

# Liquid Jets in Crossflow at Elevated Temperatures and Pressures

By

Amirreza Amighi

A thesis submitted in conformity with the requirements  
for the degree of Doctor of Philosophy  
Mechanical and Industrial Engineering  
University of Toronto

© Copyright by Amirreza Amighi 2015

UMI Number: 3715307

All rights reserved

INFORMATION TO ALL USERS

The quality of this reproduction is dependent upon the quality of the copy submitted.

In the unlikely event that the author did not send a complete manuscript and there are missing pages, these will be noted. Also, if material had to be removed, a note will indicate the deletion.



UMI 3715307

Published by ProQuest LLC (2015). Copyright in the Dissertation held by the Author.

Microform Edition © ProQuest LLC.

All rights reserved. This work is protected against unauthorized copying under Title 17, United States Code



ProQuest LLC.  
789 East Eisenhower Parkway  
P.O. Box 1346  
Ann Arbor, MI 48106 - 1346

## Abstract

# Liquid Jet in Crossflow at Elevated Temperatures and Pressures

Amirreza Amighi

Doctor of Philosophy

Mechanical and Industrial Engineering

University of Toronto

2015

An experimental study on the characterization of liquid jets injected into subsonic air crossflows is conducted. The aim of the study is to relate the droplet size and other attributes of the spray, such as breakup length, position, plume width, and time to flow parameters, including jet and air velocities, pressure and temperature as well as non-dimensional variables. Furthermore, multiple expressions are defined that would summarize the general behavior of the spray. For this purpose, an experimental setup is developed, which could withstand high temperatures and pressures to simulate conditions close to those experienced inside gas turbine engines. Images are captured using a laser based shadowgraphy system similar to a 2D PIV system. Image processing is extensively used to measure droplet size and boundaries of the spray. In total 209 different conditions are tested and over 72,000 images are captured and processed. The crossflow air temperatures are 25°C, 200°C, and 300°C; absolute crossflow air pressures are 2.1, 3.8, and 5.2 bars. Various liquid and gas velocities are tested for each given temperature and pressure in order to study the breakup mechanisms and regimes. Effects of dimensional and non-dimensional variables on droplet size are presented in detail. Several correlations for the mean droplet size, which are generated in this process, are presented. In addition, the influence of non-dimensional variables on the breakup length, time, plume area, angle, width and mean jet surface thickness are

discussed and individual correlations are provided for each parameter. The influence of each individual parameter on the droplet sizes is discussed for a better understanding of the fragmentation process. Finally, new correlations for the centerline, windward and leeward trajectories are presented and compared to the previously reported correlations.

## Acknowledgments

I would like to express my thanks and appreciation to my supervisor, Dr. Nasser Ashgriz. The completion of this work would not have been possible without his endless support, patience and guidance over the many years at MIE even prior to my Ph.D. program. Special thanks to all of my colleagues, friends and all the staff at MIE, especially Dr. M. Eslamian for his motivation, assistant and hard work in collecting data and analysis. There have been many individuals over the years that have helped and supported this project in countless different forms. Some names include: Dr. M. Ahmed, F. Sultan, R. Karami, A. Hull, J. Baptista, R. Mendel, G. Boudreau, T. Tran Do, J. Sansome, T. Bernreiter, O. Sargeant, T. Zak, F. Amighi, B. Beca and countless graduate and undergraduate students. Finally, my gratitude goes to my wife, daughters, my dear parents and my brother for their endless patience and support.

# Table of Contents

Abstract.....	ii
Acknowledgments .....	iv
Table of Contents.....	v
List of Tables .....	viii
List of Figures.....	ix
Nomenclature.....	xviii
Chapter 1 Introduction.....	1
1 Introduction.....	1
1.1 Liquid Jet Injection into a Crossflow .....	1
1.2 Liquid Jet Injection into Crossflow .....	3
1.2.1 Jet Penetration and Deformation .....	4
1.2.2 Jet Breakup Models and Theories.....	8
1.2.3 Mass Flux, Droplet Size and Velocity Distribution.....	13
1.3 Motivation of the Present Research.....	15
1.4 Objectives of the Present Research.....	16
Chapter 2 Experimental Setup and Conditions.....	17
2 Experimental Setup and Conditions .....	17
2.1 Air System .....	17
2.1.1 High volume air delivery .....	17
2.1.2 High Power Heater .....	18
2.1.3 Flow straightening system .....	19
2.1.4 Flow control system.....	19
2.1.5 Test chamber.....	21
2.1.6 Flow cooling system.....	25
2.1.7 Exhaust and flow silencing system.....	26

2.2	Liquid Injection System.....	27
2.3	Measurement System: Imaging System.....	28
2.4	Experimental Conditions and Results.....	29
Chapter 3 Image Analysis.....		38
3	Image Analysis .....	38
3.1	Image Analysis for Droplet Size.....	38
3.1.1	Initial Image Analysis.....	38
3.1.2	Data Analysis.....	42
3.2	Image Analysis for Trajectory, Breakup Length, Breakup time, and Spray Width ...	46
Chapter 4 Jet Trajectory.....		51
4	Jet Trajectory .....	51
4.1	Jet Trajectory Correlations .....	51
4.2	Discussions .....	56
4.2.1	Effect of Nozzle diameter.....	56
4.2.2	Effect of Temperature.....	57
4.2.3	Constant Momentum Flux ratio.....	59
4.2.4	Constant Air and Jet Weber Number.....	59
Chapter 5 Spray Plume Characteristics .....		62
5	Spray Plume Characteristics .....	62
5.1	Breakup Length .....	62
5.2	Stream-Wise Penetration .....	70
5.3	Cross-Stream (Jet-Wise) Penetration.....	76
5.4	Breakup Time .....	82
5.5	Plume Area .....	89
5.6	Spray Plume Angle.....	95
5.7	Mean Plume Width.....	100

5.8 Mean Jet Surface Thickness .....	105
Chapter 6.....	112
6 Global Droplet Size Based on Image Analysis.....	112
6.1 Jet Atomization Process.....	112
6.2 Effect of Dimensional Variables on the Global Droplet Size.....	120
6.2.1 Effect of Nozzle Diameter on the Global Droplet Size .....	120
6.2.2 Effect of Liquid Jet Velocity on the Global Droplet Size .....	124
6.2.3 Effect of Air Velocity on the Global Droplet Size .....	127
6.2.4 Effect of Pressure on the Global Droplet Size.....	130
6.2.5 Effect of Temperature on the Global Droplet Size.....	135
6.3 Effect of Non-Dimensional Variables on the Global Droplet Size .....	146
6.4 Correlations for the Global Droplet Size .....	151
Chapter 7 Conclusions and Recommendations .....	158
7 Conclusions and Recommendations .....	158
7.1 Conclusions .....	158
7.2 Recommendations.....	163
8 Bibliography .....	166
9 Appendices.....	175
9.1 Appendix A: Image Analysis and Calculations.....	175
9.1.1 Image Analysis: Droplet Size and Mean Plume Area/Boundary .....	175
9.1.2 Raw Data Calculations .....	176
9.1.3 Boundary Calculation .....	180
9.2 Appendix B: Estimate of Heat-up Time for the Jet .....	185
9.3 Appendix C: Circulation Heater Specifications .....	190
9.4 Appendix D: Sample Images for Each Condition .....	193



## List of Tables

Table 2.1: Summary of Fluid properties.....	30
Table 2.2: Test conditions for imaging experiments with water. ....	30
Table 2.3: List of all the conditions and results.....	31
Table 7.1: Summary of the relation between the spray parameters and the non-dimensional variables.....	161
Table 7.2: Test conditions for imaging experiments with water. ....	162
Table 7.3: Summary of all the correlations. ....	162

## List of Figures

Figure 1.1: Pratt & Whitney F100-PW-229 turbofan engine with augmentor [2].	2
Figure 1.2: Schematic representation of a jet penetration into crossflow [3].	3
Figure 1.3: Schematic representation of drop breakup model by Clark [30].	9
Figure 1.4: Relation between droplet breakup mode and Weber number [35].	9
Figure 1.5: Sketch of the merged turbulent primary- and secondary-breakup at the liquid surface [6].	10
Figure 1.6 Visualization of primary breakup process by Sallam et al. [39].	12
Figure 1.7: Detailed scheme of jet breakup in supersonic crossflow, Thomas and Schetz [46].	14
Figure 2.1: Overview of the experimental Setup.	17
Figure 2.2: Broom Wade Compressor.	18
Figure 2.3: Settling tank 2, settling tank 3, and heater.	19
Figure 2.4: (a) Flow straightening plate; (b) Flow straightening system, fuel tank and flowmeters.	20
Figure 2.5: Erdco air flowmeter.	21
Figure 2.6: Main chamber with the cooling sections before and after.	22
Figure 2.7: Main chamber and its accessories.	23
Figure 2.8: Section views of the front (a) and side (b) of the main chamber with the nozzle in place.	23
Figure 2.9: Cross-section view of the chamber and the cooling sections upstream and downstream of the chamber.	25

Figure 2.10: Cooling water tank, control valve #2 (large black valve), liquid recovery port, cooling water injection nozzle and exhaust line. ....	26
Figure 2.11: Exhaust chimney outside the Mechanical Engineering building, University of Toronto. ....	26
Figure 2.12: Schematic of the fuel system.....	28
Figure 2.13: Drawing of the adaptor for attaching the laser light sheet lens.....	29
Figure 3.1: Comparison of various thresholding techniques.....	39
Figure 3.2: Pixel value histogram of typical JICF image and the lines AB and CD display the results of triangle thresholding. ....	40
Figure 3.3: (a) A Color-inverted image with laser sheet illumination; (b) Same image after thresholding and particle analysis. Image 216001a, Case 19, $p=2.1$ bars, $T=200^{\circ}\text{C}$ , $V_{\text{Jet}}=38$ m/s, and $V_{\text{Air}}=93$ m/s. The resolution of the image is 1 pix=19 $\mu\text{m}$ . ....	40
Figure 3.4: The original image with the results superimposed. Image 216001a, Case 19, $p=2$ bars, $T=200^{\circ}\text{C}$ , $V_{\text{Jet}}=38$ m/s, and $V_{\text{Air}}=93$ m/s. ....	41
Figure 3.5: Comparison of the shadowgraph, instantaneous laser light sheet image, and time average image. The conditions are the same but the shadowgraph and instantaneous laser light sheet image are at different times. Case 55, $p=3.8$ bars, $T=25^{\circ}\text{C}$ , $V_{\text{Jet}}=24$ m/s, and $V_{\text{Air}}=41$ m/s. ....	42
Figure 3.6: Circularity of various shapes.....	43
Figure 3.7: (a) Maximum droplet size versus circularity; (b) Minimum droplet size versus circularity.....	44
Figure 3.8: Average MMD/SMD versus circularity.....	45
Figure 3.9: Some of the possible shapes for droplets with an area less than 5 pixel squared. ....	46

Figure 3.10: Effect of sample size on mean image. The images are color inverted for ease of comparison.....	47
Figure 3.10: Comparison of various thresholding techniques on mean image.....	48
Figure 3.11: (a) Mean image; (b) Same image after thresholding and particle analysis.....	48
Figure 3.12: Mean image boundaries, red outline based on Triangle threshold along with few of the plume areas superimposed.....	49
Figure 3.13: Comparison of mean image trajectory with trajectory of individual images.....	50
Figure 4.1: Graphical representation of the trajectory correlations; (a) centerline; (b) windward; (c) leeward.....	54
Figure 4.2: Comparison of various centerline trajectory correlations. $V_{Air} \approx 68$ m/s and $V_{Jet} = 19$ m/s for all cases. Momentum flux ratios are 19, 28, and 35 respectively.....	55
Figure 4.3: Comparison of initial breakup on the lee side of the jet for different nozzle diameters. Table 2.3 summarizes the conditions.....	57
Figure 4.4: Comparison of the three trajectories at three different temperatures, blue, green and red symbols represent cases at 25°C, 200°C, and 300°C respectively. (a) Cases: 49, 64, and 80. $V_{Air} \approx 65$ m/s and $V_{Jet} = 19$ m/s for all cases. Momentum flux ratios are 19, 28, and 35 respectively. (b) Cases: 102, 118, and 138. $V_{Air} \approx 49$ m/s and $V_{Jet} = 19$ m/s for all cases. Momentum flux ratios are 62, 105, and 126, respectively.....	57
Figure 4.5: Comparison of jet trajectories at three different temperatures Table 2.3 summarizes the conditions.....	58
Figure 4.6: Comparison of four cases with similar conditions and constant momentum flux ratio. Table 2.3 summarizes the conditions.....	59
Figure 4.7: Comparison of two cases with constant momentum flux ratio, and air and jet Weber numbers. Table 2.3 summarizes the conditions.....	60

Figure 4.8: Comparison of two cases with constant momentum flux ratio, and air and jet Weber numbers. Table 2.3 summarizes the conditions.....	61
Figure 5.1: Schematic representation of plume variables.....	62
Figure 5.2: Breakup length versus (a) air velocity, (b) jet velocity, (c) nozzle diameter, (d) crossflow pressure, and (e) – (h) crossflow temperature. In all the graphs the parameters are kept constant except for the parameter of interest, for example in figure (a) only air velocity is altered. The symbols do not represent the conditions since the conditions for each data series is different. Table 2.3 summarizes the conditions.....	65
Figure 5.3: Comparison of cases with varying air velocities at two temperature and pressure ranges first row at 200°C and 3.8 bar second row at 25°C and 2.1 bar.....	66
Figure 5.4: Comparison of cases at two pressure ranges.....	67
Figure 5.5: (a) Correlation of normalized breakup length; (b) – (f) Normalized breakup length vs. various non-dimensionalized numbers; (g) – (h) Normalized D32 and droplet size standard deviation vs. normalized breakup length. Table 2.3 summarizes the conditions. ....	70
Figure 5.6: Stream-wise penetration versus (a) air velocity, (b) jet velocity, (c) nozzle diameter, (d) crossflow pressure, and (e) – (h) crossflow temperature. In all the graphs the parameters are kept constant except for the parameter of interest, for example in figure (a) only air velocity is altered. The symbols do not represent the conditions since the conditions for each data series is different. Table 2.3 summarizes the conditions.....	73
Figure 5.7: (a) Correlation of normalized stream-wise penetration; (b) – (f) Normalized stream-wise penetration vs. various non-dimensionalized numbers; (g) – (h) Normalized D32 and droplet size standard deviation vs. normalized stream-wise penetration. Table 2.3 summarizes the conditions.....	76
Figure 5.8: Normalized cross-stream penetration versus (a) air velocity, (b) jet velocity, (c) nozzle diameter, (d) crossflow pressure, and (e) – (h) crossflow temperature. In all the graphs the parameters are kept constant except for the parameter of interest, for example in figure (a) only	

air velocity is altered. The symbols do not represent the conditions since the conditions for each data series is different. Table 2.3 summarizes the conditions. ....	78
Figure 5.9: (a) Correlation of normalized cross-stream penetration; (b) – (f) Normalized cross-stream penetration vs. various non-dimensionalized numbers; (g) – (h) Normalized D32 and droplet size standard deviation vs. normalized cross-stream penetration. Table 2.3 summarizes the conditions.....	82
Figure 5.10: Normalized breakup time versus (a) air velocity, (b) jet velocity, (c) nozzle diameter, (d) crossflow pressure, and (e) – (h) crossflow temperature. In all the graphs the parameters are kept constant except for the parameter of interest, for example in figure (a) only air velocity is altered. The symbols do not represent the conditions since the conditions for each data series is different. Table 2.3 summarizes the conditions.....	85
Figure 5.11: (a) Correlation of normalized breakup time; (b) – (f) Normalized mean breakup time vs. various non-dimensionalized numbers; (g) – (h) Normalized D32 and droplet size standard deviation vs. normalized breakup time. Table 2.3 summarizes the conditions. ....	89
Figure 5.12: Normalized plume area versus (a) air velocity, (b) jet velocity, (c) nozzle diameter, (d) crossflow pressure, and (e) – (h) crossflow temperature. In all the graphs the parameters are kept constant except for the parameter of interest, for example in figure (a) only air velocity is altered. The symbols do not represent the conditions since the conditions for each data series is different. Table 2.3 summarizes the conditions.....	92
Figure 5.13: (a) Correlation of normalized plume area; (b) – (f) Normalized plume area vs. various non-dimensionalized numbers; (g) – (h) Normalized D32 and droplet size standard deviation vs. normalized area plume area. Table 2.3 summarizes the conditions. ....	95
Figure 5.14: Normalized spray plume angle versus (a) air velocity, (b) jet velocity, (c) nozzle diameter, (d) crossflow pressure, and (e) – (h) crossflow temperature. In all the graphs the parameters are kept constant except for the parameter of interest, for example in figure (a) only air velocity is altered. The symbols do not represent the conditions since the conditions for each data series is different. Table 2.3 summarizes the conditions. ....	98

Figure 5.15: (a) Correlation of normalized spray plume angle; (b) – (f) Normalized spray plume angle vs. various non-dimensionalized numbers; (g) – (h) Normalized D32 and droplet size standard deviation vs. normalized spray plume angle. Table 2.3 summarizes the conditions. . 100

Figure 5.16: Normalized average plume width versus (a) air velocity, (b) jet velocity, (c) nozzle diameter, (d) crossflow pressure, and (e) – (h) crossflow temperature. In all the graphs the parameters are kept constant except for the parameter of interest, for example in figure (a) only air velocity is altered. The symbols do not represent the conditions since the conditions for each data series is different. Table 2.3 summarizes the conditions. .... 103

Figure 5.17: (a) Correlation of normalized mean plume width; (b) – (f) Normalized mean plume width vs. various non-dimensionalized numbers; (g) – (h) Normalized D32 and droplet size standard deviation vs. normalized mean plume width. Table 2.3 summarizes the conditions.. 105

Figure 5.18: Normalized mean jet surface thickness versus (a) air velocity, (b) jet velocity, (c) nozzle diameter, (d) crossflow pressure, and (e) – (h) crossflow temperature. In all the graphs the parameters are kept constant except for the parameter of interest, for example in figure (a) only air velocity is altered. The symbols do not represent the conditions since the conditions for each data series is different. Table 2.3 summarizes the conditions. .... 108

Figure 5.19: (a) Correlation of normalized mean jet surface thickness; (b) – (f) Normalized mean jet surface thickness vs. various non-dimensionalized numbers; (g) – (h) Normalized D32 and droplet size standard deviation vs. normalized mean jet surface thickness. Table 2.3 summarizes the conditions..... 111

Figure 6.1: High magnification image of jet in crossflow..... 113

Figure 6.2: Water jet in crossflow at room temperature.  $D_N=572\mu\text{m}$ ,  $p=2.1$  bars,  $V_{\text{Air}}=40\text{m/s}$ ,  $V_{\text{Jet}}=13.5$  m/s,  $q=50$ . .... 114

Figure 6.3: Close-up images of the jet exiting the nozzle at the same conditions as figure 6.2. 115

Figure 6.4: Water jet in crossflow at room temperature. The images are captured after the jet has turned in the direction of crossflow. The intact jet can be seen to the left of the image.  $D_N=572\mu\text{m}$ ,  $p=2.1$  bars,  $V_{\text{Air}}=40\text{m/s}$ ,  $V_{\text{Jet}}=6\text{m/s}$ ,  $q=10$ . .... 116

Figure 6.5: Water jet in crossflow at room temperature. $D_N=572\mu\text{m}$ , $p=2.1$ bars, $V_{\text{Air}}=40\text{m/s}$ , $V_{\text{Jet}}=17\text{m/s}$ , $q=80$ . .....	117
Figure 6.6: Correlation of SMD with dimensional variables. ....	119
Figure 6.7: (a) Sauter mean diameter vs. nozzle diameter. (b) Diameter standard deviation vs. nozzle diameter. The liquid jet velocity is kept constant at 19 m/s for all cases. All air velocities are in the range of 60 to 80 m/s. Blue series represent room temperature, green series represent 200°C, and red series represent 300°C. Each series represents a constant pressure; dashed lines represent 2.1 bars, and solid lines 3.8 bars. Table 2.3 summarizes the conditions. ....	121
Figure 6.8: Comparison of the images for conditions where all the dimensional variables are kept constant except for nozzle diameter, $D_N$ . All the images have the same scale and droplets larger than 5 pixel squared ( $D\sim 50\mu\text{m}$ ) are only shown. Table 2.3 summarizes the conditions.....	124
Figure 6.9: (a) Sauter mean diameter vs. liquid jet velocity. (b) Diameter standard deviation vs. liquid jet velocity. The air velocity is kept constant between 92 and 95 m/s for all cases. Blue series represent room temperature, green series represent 200°C, and red series represent 300°C. Each series represents a constant pressure; dashed lines represent 2.1 bars, and solid lines 3.8 bars. Nozzle diameter for all cases is 572 $\mu\text{m}$ . Table 2.3 summarizes the conditions. ....	125
Figure 6.10: Comparison of the images for conditions with all the dimensional variables kept constant except for jet velocity, $V_{\text{Jet}}$ . All the images have the same scale and droplets larger than 5 pixel squared ( $D\sim 50\mu\text{m}$ ) are only shown. Table 2.3 summarizes the conditions.....	127
Figure 6.11: (a) Sauter Mean Diameter vs. Air Velocity. (b) Diameter Standard Deviation vs. Air Velocity. The liquid jet velocity is kept constant at 19 m/s for all cases. Blue series represent room temperature, green series represents 200°C, and red series represent 300°C. Each series represents a constant pressure; dashed lines represent 2.1 bars, and solid lines 3.8 bars. Nozzle diameter for all cases is 572 $\mu\text{m}$ . Table 2.3 summarizes the conditions. ....	128
Figure 6.12: Comparison of the images for conditions with all the dimensional variables kept constant except for air velocity, $V_{\text{Air}}$ . All the images have the same scale and droplets larger than 5 pixel squared ( $D\sim 50\mu\text{m}$ ) are only shown. Table 2.3 summarizes the conditions.....	130



Figure 6.13: (a) Sauter mean diameter vs. pressure. (b) Diameter standard deviation vs. pressure. The liquid jet velocity is kept constant at 19 m/s for all cases, and air velocities are in three different ranges, 30 - 40 m/s, 60 - 70 m/s and 90 - 100 m/s. Table 2.3 summarizes the conditions. ....	131
Figure 6.14: Relation between air density and air viscosity [67]. ....	132
Figure 6.15: Comparison of conditions with similar gas densities. Table 2.3 summarizes the conditions.....	133
Figure 6.16: Comparison of the images for conditions with all the dimensional variables kept constant except for pressure, p. All the images have the same scale and droplets larger than 5 pixel squared (~50 $\mu\text{m}$ ) are only shown. Table 2.3 summarizes the conditions. ....	135
Figure 6.17: (a), (c), (e) and (g) Sauter mean diameter vs. Temperature. (b), (d), (f) and (h) Standard deviation vs. temperature. The liquid jet velocity is kept constant at 19 m/s for all cases. Air velocities are in three different ranges: green series is from 30 m/s to 40 m/s (or 40 m/s to 50 m/s depending on conditions); red series from 60 m/s to 70 m/s; and blue series from 90 m/s to 100 m/s; .....	137
Figure 6.18: Ratio of dynamic viscosity to air density (kinematic viscosity) at various air temperatures and pressures. ....	139
Figure 6.19: Effect of temperature on viscosity and surface tension. The vertical lines show the saturation temperature of water at 2.1 bars, 3.8 bars and 5.2 bars.....	142
Figure 6.20: Comparison of the images for conditions where all the dimensional variables are kept constant except for temperature, T. Table 2.3 summarizes the conditions.....	146
Figure 6.21: (a)-(p) D32 and standard deviation on droplet size vs. various non-dimensional variables. Table 2.3 summarizes the conditions. ....	151
Figure 6.22: Comparison of results from Hsiang et al. [70] with the current study. ....	152
Figure 6.23: Correlation of the SMD for primary breakup, equation (6.17). ....	153

Figure 6.24: Comparison of conditions with the stream-wise velocities and conditions but different gas and jet velocities. Table 2.3 summarizes the conditions. .... 154

Figure 6.25: Comparison of conditions with similar gas densities and stream-wise velocity. Table 2.3 summarizes the conditions..... 155

Figure 6.26: (a) and (b) correlation of the SMD for primary breakup, equation (6.18). (c) and (d) correlation of the STD for primary breakup, equation (6.20)..... 157

## Nomenclature

$A_D$	Nozzle area
$A_P$	Plume area
$C_D$	Coefficient of drag
$D$	Droplet diameter
$D_N$	Nozzle diameter
$D_{10}$	Mean diameter
$D_{32}$	Sauter mean diameter
$\frac{L}{D}$	Length over diameter for the nozzle orifice
$L_b$	Breakup length
$MMD$	Mass median diameter
$Oh_{Air}$	Air Ohnesorge number based on nozzle diameter and air properties. $Oh_{Air} = \frac{\sqrt{We_{Air}}}{Re_{Air}} = \frac{\mu_{Air}}{\sqrt{\rho_{Air}\sigma D_N}}$
$Oh_{Jet}$	Jet Ohnesorge number based on nozzle diameter and jet properties. $Oh_{Jet} = \frac{\sqrt{We_{Jet}}}{Re_{Jet}} = \frac{\mu_{Jet}}{\sqrt{\rho_{Jet}\sigma D_N}}$
$p$	Air Pressure
$q$	Momentum flux ratio. $q = \frac{We_{Jet}}{We_{Air}} = \frac{\rho_{Jet}V_{Jet}^2}{\rho_{Air}V_{Air}^2}$
$Re_{Air}$	Air Reynolds number based on nozzle diameter, air velocity and properties. $Re_{Air} = \frac{\rho_{Air}V_{Air}D_N}{\mu_{Air}}$
$Re_{Jet}$	Jet Reynolds number based on nozzle diameter, jet velocity and properties. $Re_{Jet} = \frac{\rho_{Jet}V_{Jet}D_N}{\mu_{Jet}}$
$SEM$	Droplet size standard error
$SMD$	Sauter mean diameter
$STD$	Droplet size standard deviation
$T$	Air temperature
$T_s$	Mean jet surface thickness
$t_b$	Breakup time
$t^*$	Characteristic breakup time
$V_{Air}$	Air velocity
$V_{Jet}$	Jet velocity
$V_{st}$	Stream-wise/relative velocity. $V_{st} = V_{Air} - V_{Jet}$
$We_{Air}$	Air Weber number based on nozzle diameter, air velocity and properties. $We_{Air} = \frac{\rho_{Air}V_{Air}^2 D_N}{\sigma}$
$We_{Jet}$	Jet Weber number based on nozzle diameter, jet velocity and properties. $We_{Jet} = \frac{\rho_{Jet}V_{Jet}^2 D_N}{\sigma}$

$We_{st}$	Stream-wise Weber number based on nozzle diameter, stream-wise velocity and jet properties. $We_{st} = \frac{\rho_{Jet} V_{st}^2 D_N}{\sigma}$ .
$We_{crit}$	Critical Weber number
$W_P$	Mean plume width
$x$	Stream-wise distance
$y$	Cross-stream distance
$\mu$	Dynamic viscosity
$\mu_{LN}$	Mean of log-normal distribution
$\nu$	Kinematic viscosity
$\rho$	Density
$\sigma$	Surface tension
$\sigma_{LN}$	Standard deviation of log-normal distribution
$\lambda_s$	Wavelength of surface waves
$\theta_P$	Plume Angle

#### Subscripts

$b$	Breakup point
$cl$	Center line
$cs$	Cross-section
$lw$	Leeward
$p$	Plume
$ww$	Windward

## Chapter 1 Introduction

### 1 Introduction

#### 1.1 Liquid Jet Injection into a Crossflow

Transverse injection of a liquid jet into a high velocity, high temperature and high pressure crossflow has numerous applications in fuel injection systems for advanced aircraft engines. This fuel injection technique is employed in applications such as the afterburners (augmentors), ramjets and scramjets. One of the main application areas is for the augmentors. The augmentors are mainly used for the military aircraft where rapid changes in speed and maneuvering is required; for example during take-off from the landing tarmac on the aircraft carriers. Typically, the thrust capacity of the engines can be augmented between 50% and 100% for short periods of time. Such systems are not particularly efficient but are widely used because of their low power density, low weight construction and simplicity [1].

The augmentor can be described as a large cylindrical duct attached between the gas turbine exit and the exhaust nozzle where combustion takes place. The internal components of the augmentor consist of the fuel injectors, flame holders and pilot flame. The hot gases produced in the augmentor are directed out of the exhaust nozzle. The exhaust nozzle geometry can be changed in most of the modern engines for various reasons as well as for thrust vectoring. The gas pressure and temperature change and consequently the density of the exhaust gas changes during the augmentor operation. The variable geometry exhaust nozzle is, therefore, used to stabilize and control the overall thrust and the conditions of the turbine [1].

In the augmentor, the liquid fuel is injected through multiple staggered nozzles in the form of jets where the engine exhaust gas atomizes the liquid. The droplets go through evaporation and mixing and finally are combusted. The flame is stabilized by the use of bluff bodies. This type of fuel injection is an effective method for distributing and vaporizing fuel inside the engines. It is frequently used in Rich-burn Quick-quench Lean-burn (RQL) and Lean Premixed Pre-vaporized (LLP) combustion systems. The reason for the use of such a combustion system is to reduce the pollution levels, specifically  $\text{NO}_x$ .  $\text{NO}_x$  is formed at higher temperatures, therefore by quickly

quenching the combustion, i.e. RQL, or by combusting a leaner mixture, i.e. LLP, one could try to reduce  $\text{NO}_x$  emissions. As it can be seen, environmental concerns are not the only motivation for such studies but there are also practical difficulties associated with the mentioned combustion methods. Figure 1.1 shows various parts of the engine [1].

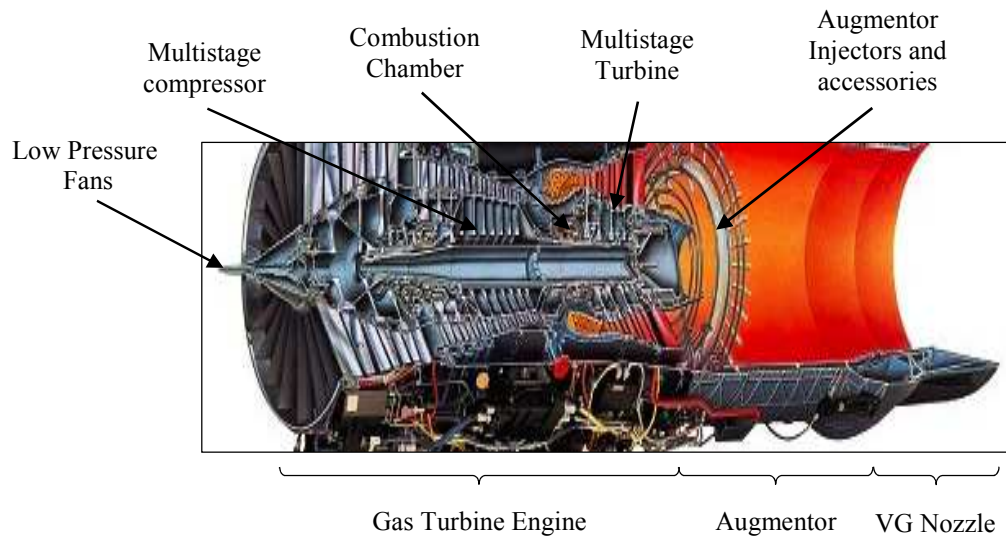


Figure 1.1: Pratt & Whitney F100-PW-229 turbofan engine with augmentor [2].

In recent years, various manufacturers are required to produce smaller and more efficient engines. These modifications have led to the reductions in the aircraft augmentor and afterburner sizes and increased the engines operating pressure. Such changes have increased the tendency for augmentors to exhibit combustion instabilities in the form of pressure fluctuations, which mostly occur at elevated pressures. These pressure fluctuations are divided into two groups; first is the “rumble” which corresponds to the low frequencies between 50 and 120 Hz; second is the “screech” which corresponds to the higher frequencies between 120 and 600 Hz. These unwanted fluctuations lead to excessive engine vibration and reduced durability. The primary cause of these fluctuations is believed to be due to irregularities in the atomization process [1].

Figure 1.2 shows a schematic of the liquid jet injected into a crossflow. The crossing air flow exerts shear and pressure forces on the jet which leads to jet deformation. The passage of air around the jet body forms a pair of kidney-shaped counter-rotating vortices. These counter-rotating vortices are responsible for the liquid shedding on the rear surface of the jet, and flattening

on the front surface of the jet. It is evident that the size and the strength of these vortices considerably affect the atomization process since they are the deciding factor on the shape and penetration of the jet. Also, depending on the size of these vortices, the number of small droplets and large ligaments are changed.

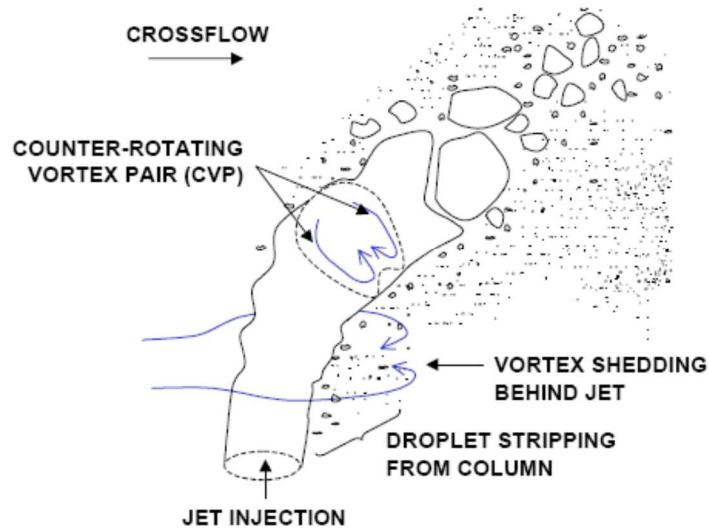


Figure 1.2: Schematic representation of a jet penetration into crossflow [3].

In addition to the droplets formed by the vortices, there are droplets and ligaments that are formed by the instability waves on the leading surface of the jet. These instability waves are produced by the passage of high velocity air over the surface of the jet. As the air accelerates over the relatively slow liquid, it creates high and low pressure areas, which lead to the formation of waves. Finally, drops and ligaments are stripped from the column due to shear forces. The rate of this mass removal and the size of the droplets and ligaments highly depend on the air Weber number, equation (1.1). Thereafter, the drops and ligaments undergo a secondary atomization until the droplets reach their minimum size.

$$We_{Air} = \frac{\rho_{Air} V_{Air}^2 D_N}{\sigma} \quad (1.1)$$

## 1.2 Liquid Jet Injection into Crossflow

The literature on the liquid jet in crossflow (JICF) can be divided into three main categories; (i) jet penetration and trajectory, (ii) jet breakup, and (iii) droplet size, velocity and flux distribution.

The first two categories have been studied extensively but due to limitations on instrumentation and difficulties associated with the measurement of size and velocity the literature is limited on the third category.

### 1.2.1 Jet Penetration and Deformation

Probably the most widely used and accepted parameter for describing the physics of the jet in crossflow is the momentum flux ratio,  $q$ . The momentum flux ratio is also known as the dynamic pressure ratio, which is the ratio of the liquid to gas Weber numbers. This definition is of a particular interest since in the past, many of the correlations are either defined based on only the momentum flux ratio or as a combination of the momentum flux ratio and the aerodynamic Weber number. Presenting the correlations based on the momentum flux ratio and aerodynamic Weber number can be misleading since it hides the jet inertia effects. In the later chapters, the presented correlations are first defined by individual Weber numbers and then in combination of both momentum flux ratio and aerodynamic Weber number. The latter combination though confusing is beneficial due to the historical continuity and an easier phenomenological explanation of the spray. The momentum flux ratio is expressed as:

$$q = \frac{We_{Jet}}{We_{Air}} = \frac{\rho_{Jet} V_{Jet}^2}{\rho_{Air} V_{Air}^2} \quad (1.2)$$

The momentum flux ratio,  $q$ , is an important parameter for predicting the jet penetration and deformation. Earlier studies have shown that the penetration and trajectory of the jet are solely defined by this parameter as it can be seen in equations (1.3) to (1.17). Schetz and Padhye [3] used this parameter to analytically define the maximum penetration distance of the spray. They considered a control volume around the jet, up to the point where the droplets reach their terminal velocity. They presented their correlation in the form of equation 1.3:

$$\left(\frac{x}{d_f}\right)_{max} = C\sqrt{q}C_D\left(\frac{d_{eq}}{d_f}\right) \quad (1.3)$$

Nejad and Schetz [4] continued the research but mostly in the supersonic region. Chen et al. [5] performed experiments with the momentum ratio ranging from 3 to 45 at room temperature, pressures between 1 and 2 bars, and at a Mach number of 0.4. They used a laser sheet imaging technique to gather their data. They presented equation (1.4).



$$\frac{y}{D_N} = 9.91q^{0.44} \left[ 1 - \exp\left(\frac{-x/D_N}{13.1}\right) \right] \left[ 1 + 1.67 \exp\left(\frac{-x/D_N}{4.77}\right) \right] \left[ 1 + 1.06 \exp\left(\frac{-x/D_N}{0.86}\right) \right] \quad (1.4)$$

Later Wu et al. [6, 7, 8, 9, 10], whose work has greatly influenced the literature, extended this concept and defined the jet trajectory as a function of momentum flux ratio. They provided a phenomenological model for the jet penetration based on their experiments. First they modeled a liquid column as a circular column and then applied a force balance to obtain the jet trajectory using a regression analysis. The coefficients for their correlations are based on their results from shadowgraphs. They also presented various breakup regimes with respect to the air Weber number. Their measurements are done at atmospheric temperatures and pressures with the momentum flux ratio ranging from 4 to 185 and the Mach numbers from 0.2 to 0.4. They provided the following correlations:

Liquid column trajectory:

$$\frac{y}{D_N} = 1.37 \sqrt{q \left( \frac{x}{D_N} \right)} \quad (1.5)$$

Height of the column fracture point:

$$\frac{y_b}{D_N} = 3.44 \sqrt{q} \quad (1.6)$$

Axial distance to the column fracture point:

$$\frac{x_b}{D_N} = 8.06 \quad (1.7)$$

Wu et al. [10] extended their work to the cross-section of the jet and the liquid mass distribution.

They offered the following equations:

Maximum spray penetration,  $y_r$ :

$$\frac{y_r}{D_N} = 4.3q^{0.33} \left( \frac{x}{D_N} \right)^{0.33} \quad (1.8)$$

The height of the maximum flux location,  $y_m$ :

$$\frac{y_m}{D_N} = 0.51q^{0.63} \left( \frac{x}{D_N} \right)^{0.41} \quad (1.9)$$

Spray width,  $Z_w$ :

$$\frac{Z_w}{D_N} = 7.86q^{0.17} \left( \frac{x}{D_N} \right)^{0.33} \quad (1.10)$$

Most of the reported correlations for the jet penetration had an exponential relation with respect to the position. Inamura et al. [11, 12] improved the form of the correlations by defining the penetration based on a logarithmic relation with respect to the position. They provided the following equations for the jet penetration and the jet width:

Jet Penetration:

$$\frac{y}{D_N} = (1.18 + 0.24D_N)q^{0.36} \ln \left[ 1.56 + (1 + 0.48d) \frac{x}{D_N} \right] \quad (1.11)$$

Jet Width:

$$\frac{Z_w}{D_N} = 1.4q^{0.18} \left( \frac{x}{D_N} \right)^{0.49} \quad (1.12)$$

Becker et al. [13] compared the results from numerical simulations to shadowgraph images and presented penetration curves for momentum ratios smaller than 18 at atmospheric pressure and temperature. Becker and Hassa [14] extended their works using shadowgraphs, Mie-scattering using laser sheets and PDA technique for the momentum ratios ranging from 1 to 40, at pressures 1.5 bars to 15 bars and room temperature. Their work remains one of the few experiments performed at higher pressures. They offered the following correlation for the jet trajectory:

$$\frac{y}{D_N} = 2.32q^{0.09} \left( \frac{x}{D_N} \right)^{0.32} \quad (1.13)$$

where  $q=1-26$ ,  $We_{Air}=360-2120$ , and  $x/d=2-18$ . Later they also provided a correlation in a logarithmic form at elevated pressures [15]. It should be noted that the correlation is not dependent on the crossflow viscosity since only pressure effects are studied. The pressure term is included in the momentum flux ratio in the form of density. They reported that the penetration is a strong function of momentum flux ratio and nozzle diameter. For these experiments  $q=3-24$ ,  $We_{Air}/D_N=1.2E-6 - 2.3E-6$ , and  $x/D_N=1.4-50$ .

$$\frac{y}{D_N} = 1.6q^{0.4} \ln \left( 1 + 3.81 \frac{x}{D_N} \right) \quad (1.14)$$

Iyogun et al. [16] studied water jet at low subsonic crossflow and determined jet trajectories. They varied momentum flux ratio from 8 to 724 as well as air Mach number from 0.07 to 0.21 at room conditions. They tested their correlation with Chen et al. [5] and presented equation 14.

$$\frac{y}{D_N} = 1.997q^{0.44} \left( \frac{x}{D_N} \right)^{0.44} \quad (1.15)$$

Masuda et al. [17] studied jet in crossflow for high-speed crossflow at pressures between 3.7 and 6.4 bars and temperatures between 350K and 475K. They varied air Mach numbers from 0.25 to 0.33 and momentum flux ratio from 2 to 30. They utilized high-speed short exposure digital shadowgraphy. They described the penetration of the spray through the following correlation for momentum flux ratios 2 to 30:

$$\frac{y}{D_N} = 0.92q^{0.50} \left( \frac{x}{D_N} \right)^{0.33} \quad (1.16)$$

Lakhamraju and Jeng [18] performed their investigation at elevated temperatures using pulsed shadowgraph technique. In their test conditions, the momentum flux ratio is varied from 1 to 50, Mach numbers from 0.2 to 0.9, temperature from 363K to 505K and at atmospheric pressure. Their results yielded the only correlation so far to include the effects of temperature. The temperature term is a combination of air density and viscosity. Once again they also used a logarithmic function to define the correlation similar to Inamura [11, 12]:

$$\frac{y}{D_N} = 1.8444q^{0.546} \ln \left[ 1 + 1.324 \left( \frac{x}{D_N} \right) \right] (T_\infty - T_0)^{-0.117} \quad (1.17)$$

Elshamy and Jeng [19] continued the investigation to discover the effect of pressure on penetration. The experiments are performed for air velocities from 39 m/s to 306 m/s, pressures up to 7 bars, momentum flux ratios from 2 to 71 and at room temperature. They concluded that as the ambient pressure increased, the penetration of the jet slightly decreased; the lower boundary of the jet rose and the spreading decreased. They suggested the following correlations:

Upper boundary:

$$\frac{y}{D_N} = 4.95 \left( \frac{x}{D_N} + 0.5 \right)^{0.279} q^{0.424} We^{-0.076} \left( \frac{p}{p_0} \right)^{-0.051} \quad (1.18)$$

Lower boundary:

$$\frac{y}{D_N} = 4.26 \left( \frac{x}{D_N} - 0.5 \right)^{0.349} q^{0.408} We^{-0.30} \left( \frac{p}{p_0} \right)^{0.111} \quad (1.19)$$

Elshamy et al. [20] also used particle image velocimetry to measure droplet velocities at the spray core and boundaries. In particular, vortices are captured in the vicinity of the injection point. More recently Bellofiore, Cavaliere, and Ragucci [21] have used similar methodology to the current study to define the boundaries of the jet in crossflow at elevated pressures and temperatures. This is one of the first correlations that also include a viscosity term.

$$\frac{y}{D_N} = 2.46 \left( \frac{x}{D_N} \right)^{0.367} q^{0.421} We^{-0.015} \left( \frac{\mu}{\mu_0} \right)^{0.033} \quad (1.20)$$

In a later study by Bellofiore et al. [22], the viscosity term in the above correlation is replaced by the crossflow Reynolds number in order to generalize the viscosity term.

$$\frac{y}{D_N} = 0.909 \left( \frac{x}{D_N} \right)^{0.35} q^{0.476} We_{Jet}^{-0.128} Re_{Air}^{0.135} \quad (1.21)$$

Additional correlations for jet penetration can be found in references [23, 24, 25, 26]. In addition to correlations, the atomization is reported to improve for jets in high pressure [27]. Pressure and temperature affect the spray behavior because they modify the air density and therefore the atomization [22]. Cavaliere et al. has suggested that predicting the jet trajectory over a wide range only based on momentum flux ratio is erroneous [27]. However, they stated that the distance of jet breakdown position mainly depends on momentum flux ratio and weakly on Weber number [28, 29]. As for temperature, it has been reported that it affects the air density mostly and to some extent the evaporation rate, but the penetration height is not affected. Vaporization of droplets at elevated pressure and temperature is not significant within a distance of 100 times the nozzle diameter [22].

## 1.2.2 Jet Breakup Models and Theories

Clark [30] presented one of the very first studies on primary jet breakup models. He used previous analysis on droplet interaction in crossflow as a basis to find a solution for jets in crossflow. In his study, he considered both the internal and external forces acting on the liquid. Figure 1.3 shows the evolution of a jet in crossflow. First the jet is distorted when it is exposed to a crossflow. The internal flow triggered by the crossflow starts to flatten the jet and finally droplets start to shed

from its edges due to instabilities. Adelberg [31] offered a similar study by a circular cylinder to explain jet breakup in a crossflow.

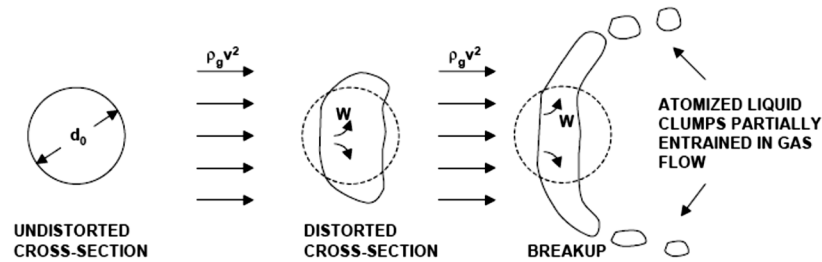


Figure 1.3: Schematic representation of drop breakup model by Clark [30].

Nguyen and Karagozian [32], Li and Karagozian [33], Heister et al. [34], Inamura [12], and Mashayek [23] have modeled the jet cross-section as an ellipse with its major axis perpendicular to the crossflow. This assumption simplifies the analytical solution meanwhile it better simulates the deformation of the jet compared to the analysis on circular cross-section. Inamura [12] modeled the liquid jet by solving the force balance equations in the direction of the axes of the jet's elliptical cross-section.

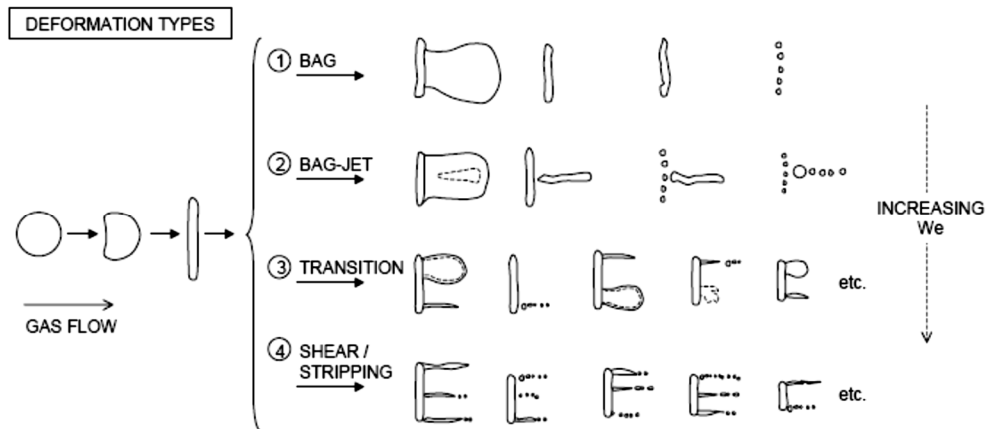


Figure 1.4: Relation between droplet breakup mode and Weber number [35].

Inamura and Nagai [36] also studied the wave formation on the liquid surface. They concluded that these waves are the main reason behind the column breakup and droplet stripping. Mazallon et al. [37] also contributed to the study of primary breakup of non-turbulent round liquid jet in gaseous crossflow. They focused on the details of the primary jet breakup regimes, jet deformation and liquid surface wavelengths. Their measurements are at room conditions for momentum flux

ratio ranging from 100 to 8000. Their results suggested qualitative similarities between the primary breakup of non-turbulent round liquid jet in crossflow and the secondary breakup of drops.

Wu and Faeth [6] have provided one of the most widely accepted theories for droplet breakup and/or formation for jet in crossflow. Figure 1.5 illustrates their theory conceptually. It is assumed that the turbulent eddy formed in the liquid phase and the air stream velocity are responsible for the formation of the initial droplet. The eddy is assumed to have an elongated shape due to larger length scales in the streamwise direction compared to cross-stream direction. The eddy is then convected into the flow based on the local mean velocity. These are the smallest drops that can be formed with such mechanism, and their size is comparable to the size of the formed eddy.

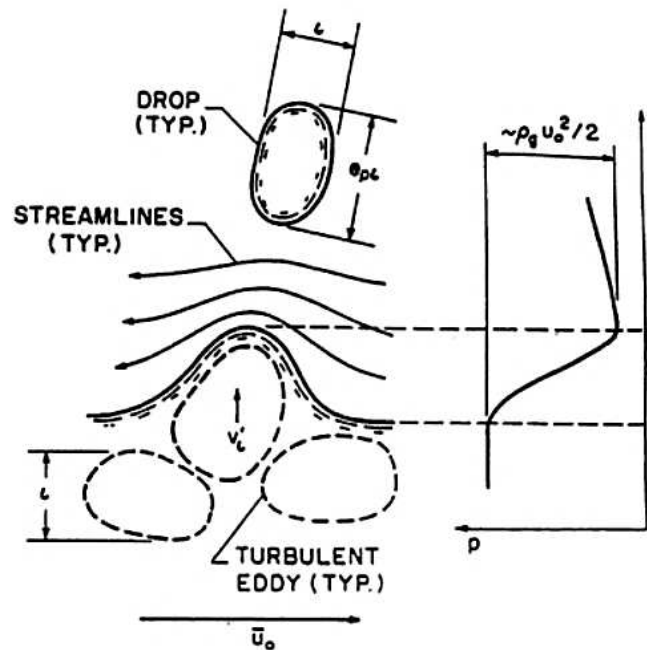


Figure 1.5: Sketch of the merged turbulent primary- and secondary-breakup at the liquid surface [6].

Mazallon et al. [37] concluded that at lower air Weber numbers, nodes appear along the column and develop until they break the jet by a mechanism similar to Rayleigh breakup. As the Weber number increases, bag-like structures appear which are very similar to bag breakup regimes observed in the secondary breakup of the drops. If the Weber number is further increased then bag-shear breakup regime starts and if the Weber number is further increased pure shear breakup happens. Figure 1.4 demonstrates the breakup regimes as described for a drop exposed to

crossflow. Wu et al. [10] and Becker and Hassa [14] also made similar observations. Wu et al. has defined a critical aerodynamic Weber number,  $We_{crit}$ , as a function of momentum flux ratio,  $q$ . If the  $We_{Air}$  is larger than  $We_{crit}$  for a given  $q$  then the dominant form of breakup is shear or surface breakup. On the other hand, if the  $We_{Aero}$  is smaller than  $We_{crit}$  for a given  $q$  then column breakup is dominant. They defined the borderline as:

$$We_{crit} \approx 10^{\frac{3.1 - \log(q)}{0.81}} \quad (1.22)$$

$$Re_{jet}^2 = \frac{q We_{Air}}{Oh_{jet}^2} \quad (1.23)$$

$$Oh_{jet}^2 = \frac{We_{jet}}{Re_{jet}^2} = \frac{\mu_{jet}^2}{\rho_{jet} \sigma D_N} \quad (1.24)$$

Madabhushi et al. [38] also have suggested that the breakup regime map be redefined in terms of turbulent transition jet Reynolds number and crossflow Weber number. Since the liquid jet turbulence as defined by the jet Reynolds number can affect the atomization characteristics while momentum flux ratio does not provide information regarding the turbulent characteristics of the jet. They proposed equation (1.23) to be used in conjunction with the existing map in order to also include the effect of jet turbulence.

They also point out one of the major issues with the breakup mapping is the transition from column to surface breakup. The transition is not very clear and subjective. However, they pointed out that for jet Reynolds numbers above 5000, the disturbances on the jet surface indicate that the jet has transitioned to the turbulence regime. Consequently, they have suggested using this threshold as a mean to identify the atomization region. That said, this is not the only criterion to identify the regions and more investigation is required.

Sallam et al. [39] suggested that the breakup regime is a function of aerodynamic Weber number,  $We_{Air}$ . Sallam has defined these regions as Column, Bag, Multimode (Bag/Shear), and Shear Breakup. Sallam used a shock tube in his experiments; he used non-turbulent jets in order to suppress the effect of jet turbulence. He also measured wavelength of liquid surface waves,  $\lambda_s$ . Figure 1.6 shows these regions with their respected  $We_{Air}$  and a corresponding image. Sallam et al. [39] found the following correlation between the surface wavelengths and the aerodynamic Weber number:

$$\lambda_s/D_p = 3.4We^{-0.45} \quad (1.25)$$

The above equation is only valid for  $We > 4$  and has a correlation coefficient of 0.82, Sallam et al. [39]. In this equation,  $D_p$  is the diameter of drops formed by the primary breakup mechanism.

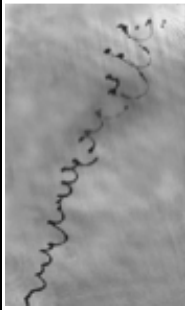


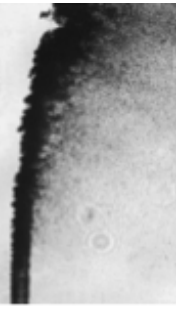
Breakup Mechanism	Column	Bag	Multimode (Bag/Shear)	Shear
$We_{Air}$	$We_{Air} \leq 4$	$4 \leq We_{Air} \leq 30$	$30 \leq We_{Air} \leq 110$	$110 \leq We_{Air}$
$\lambda_s/D_N$	$1 \leq \lambda_s/D_N$	$\lambda_s/D_N \approx 0.1$	$0.1 \leq \lambda_s/D_N \leq 1$	$\lambda_s/D_N \approx 0.1$
$V_{Air}$ [m/s]	14.6	24	30	125
$D_N = 1.0\text{mm}$				

Figure 1.6 Visualization of primary breakup process by Sallam et al. [39].

Wang et al. [40] have shown that the surface wavelength decreases not only with the increase of the gas Weber number but also with the increase of the momentum ratio. This observation suggests that both air and jet Weber numbers are significant parameters for describing the atomization process as it has been also suggested by Madabhushi et al. [41], where they related the momentum flux ratio and aerodynamic Weber numbers by the means shown in equation (1.23). Wang et al. [40] also have shown that increase in both momentum flux ratio and air Weber number will result in reduced droplet size. The relation between droplet size and momentum flux ratio is also shown by other researchers [42, 43].

More recently Linne et al. [44] employed ballistic imaging to observe the liquid core of a wide variety of jets. The main advantage of this method is the ability to capture the behavior near the jet surface. This allows for focusing on the liquid column and surface waves to see droplet stripping from the core of the liquid.



### 1.2.3 Mass Flux, Droplet Size and Velocity Distribution

This segment of research on JICF is not as well established in the literature as the previous sections. Some of the work is presented here. Oda et al. [45] showed the mass flow distributions across the cross-section of the spray plume by applying a least squares curve fit to the droplet mass flux measurements obtained with an isokinetic sampling probe. They used a 900 $\mu$ m nozzle orifice at atmospheric condition, and air velocities of 140m/s and 70m/s and jet velocities of 20m/s and 10m/s. They observed that at each location downstream of the injection nozzle, Sauter mean diameter, equation (1.26), only increases with the height from the injector, only after, the local mass flow rate starts to decrease. Their findings also showed a Gaussian distribution of mass in the normal plane to jet and a skewed Gaussian distribution in the plane of injection with maximum mass flow located further away from the center of the spray plume. Also, they predicted that as  $q$  is increased, the droplets tend to disperse farther into the crossflow in the upper region, rather than disperse across the lower region of the jet due to their higher inertia. Along the width of the jet, dispersion increased with an increased  $q$ . The results also showed that nozzle diameter did not significantly affect the distribution of the mass flux along the width of the spray.

$$D_{32} = \sum \frac{nD^3}{nD^2} \quad (1.26)$$

Wu, Hsiang and Faeth [8] used a shock wave to make their observations. They suggested the following correlation for the droplet size after secondary breakup for  $We < 103$ :

$$\rho_{Air} SMD V_{st}^2 / \sigma = 6.2 (\rho_{Jet} / \rho_{Air})^{1/4} [\mu_{Jet} / (\rho_{Jet} D_N V_{st})]^{1/2} We_{Air} \quad (1.27)$$

Later Wu et al. [10] broadened their study to observe the effect of air and jet velocity on spatial distributions of the mean droplet size and axial velocity, and of the spray volume flux using a single orifice diameter at atmospheric conditions. Their results and explanation are comparable to previous work and as with other researchers they only provided phenomenological explanation of droplet size in jet in crossflow. Nevertheless, their work has been the most influential in the field.

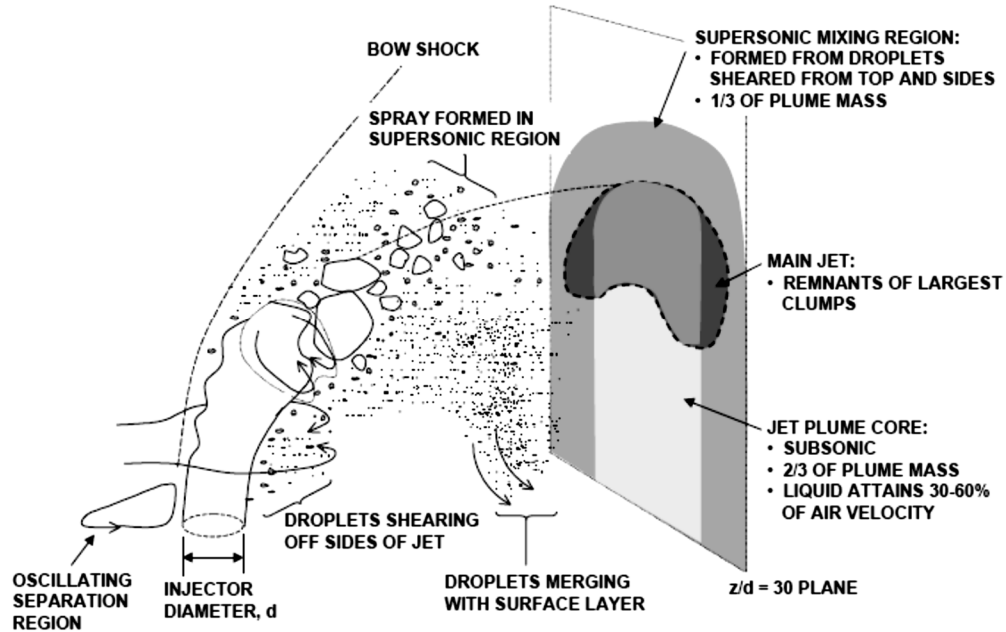


Figure 1.7: Detailed scheme of jet breakup in supersonic crossflow, Thomas and Schetz [46].

One of the more classical studies is by Thomas and Schetz [46]. Similarly, Ingebo and Foster [47], Weiss and Worsham [48] and Kihm et al. [49], performed their experiments in supersonic crossflow regime. They also provided a phenomenological explanation of droplet and mass distribution. Schetz and Padhye [3] measured Sauter mean diameter at some positions and found that increasing momentum flux ratio leads to a reduction in the droplet size. They also found that increasing nozzle orifice would increase the droplet size.

Inamura and Nagai [36] also measured droplet size and velocities and provided an explanation about the droplet distribution at subsonic crossflow velocities for 1.0 and 2.0 mm nozzles at atmospheric conditions. Most recently Madabhushi et al. [41] and Becker and Hassa [50] have completed experiments to measure droplet size in jet in crossflow. Madabhushi compared his results with the analytical work that is generated earlier and found some degree of acceptance. Becker and Hassa performed their experiments at higher pressures and found the following trend-line for their results, where  $D_{32}$  is defined as global diameter:

$$D_{32} = 429(\rho U^2)^{-0.24} \quad (1.28)$$

The most recent work to date is by Lee et al. [51] where they used a shock wave to simulate jet in crossflow. The crossflow velocities are from 36 m/s to 90 m/s for 1.0 mm and 2.0 mm nozzles. They suggested the following correlation:

$$D_{32}/\Lambda = 0.54 \left( x / \left( \Lambda We_{LA}^{1/2} \right) \right)^{0.52} \quad (1.29)$$

Where  $\Lambda$  is the radial (cross-stream) integral length scale and is  $\Lambda = D/8$  for turbulent pipe flow;  $We_{LA}$  is the Weber number based on the jet exit radial (cross-stream) integral length scale.

$$We_{LA} = \frac{\rho_{Jet} \Lambda u_{Jet}^2}{\sigma} \quad (1.30)$$

More recently Lubarsky et al. [52] also studied the dependence of droplet size and velocity on Weber number at one single constant momentum flux ratio in elevated conditions. They found that the droplet size is reduced at higher gas Weber numbers even though the momentum flux ratio is kept constant. They reported that the larger droplets are at the outer boundaries of the spray. There are other studies that have measured droplet size using Phase Doppler Particle Analyzer (PDA/PDPS), but most are short of providing correlations for droplet size and mostly just discuss various aspects of droplet size distribution [10, 15, 53, 42].

### 1.3 Motivation of the Present Research

There are several motivations behind this research. The strongest motivation is environmental. It is known that the droplet size and spray geometry are important parameters for the combustion process since they impact both vaporization and ignition of the fuel. Therefore, any advancement in the field could lead to considerable reductions in emissions. The second motivation is in regards to future propulsion systems. In recent decades, the number of travelers has grown exponentially and also there has been a great interest in high altitude travel. Many of the high altitude engines and rockets use jet in crossflow technique to achieve their goals. These systems take advantage of droplet organization inside the spray. The larger droplets have considerable inertia and penetrate more into the crossflow as compared to small droplets and therefore creating a wide range of droplet sizes. This type of droplet size distribution is especially useful in some engines where igniters are positioned close to the injector where the small droplets appear. The final motivation is academic. Jet in crossflow is considered one of the classical studies in the field of liquid fragmentation, similar to the drop impaction behavior with shock waves. In addition, the

literature review has shown that there has been a great deal of advancements in describing the droplet formation mechanisms and penetration of the jet. On the other hand, the work on droplet size is more scattered.

## 1.4 Objectives of the Present Research

The following objectives are considered in order to satisfy the above-mentioned motivations.

- Study the effect of various dimensional and non-dimensional parameters on global droplet size and obtain correlations that best describe the global droplet size.
- Literature on the jet in crossflow is limited to mostly ambient conditions. The aim is to expand the knowledge base by studying the atomization process at higher pressures and temperatures and identify the relevant and critical parameters.
- Similar to droplet size, there are very limited information on the jet trajectory at elevated conditions. It is desirable to obtain a better understanding at these conditions, especially, for the leeward boundary of the jet where it is rarely been presented due to difficulties with defining this boundary.
- Finally define various parameters for the spray plume such as area and width. to better understand the atomization region and the effects of various physical parameters.

## Chapter 2 Experimental Setup and Conditions

### 2 Experimental Setup and Conditions

A unique experimental setup is constructed to simulate conditions close to those in real gas turbine engines and augmentors, Figure 2.1. The experimental setup can be subdivided into three groups, first is the air system, second is a liquid injection system, and finally the measurement system. These systems are described in detail in the following sections.



Figure 2.1: Overview of the experimental Setup.

#### 2.1 Air System

The air system is responsible for delivery, processing and exhausting the crossflow air. This system consists of various sub-systems that are described in this section.

##### 2.1.1 High volume air delivery

Air delivery system consists of a dual stage 250 hp compressor, Broom Wade 750C, and three separate settling tanks (receivers). The compressor is capable of providing up to 750 scfm ( $\sim 22 \text{ sm}^3/\text{min}$ ) at 100 psig ( $\sim 6.7 \text{ Bar}$ ). The air is directly brought to the equipment through 2.5" and 3"

nominal pipes. Three large settling tanks are used in order to reduce the effect of flow fluctuations. The delivery system is shown in Figure 2.2, and Figure 2.3.

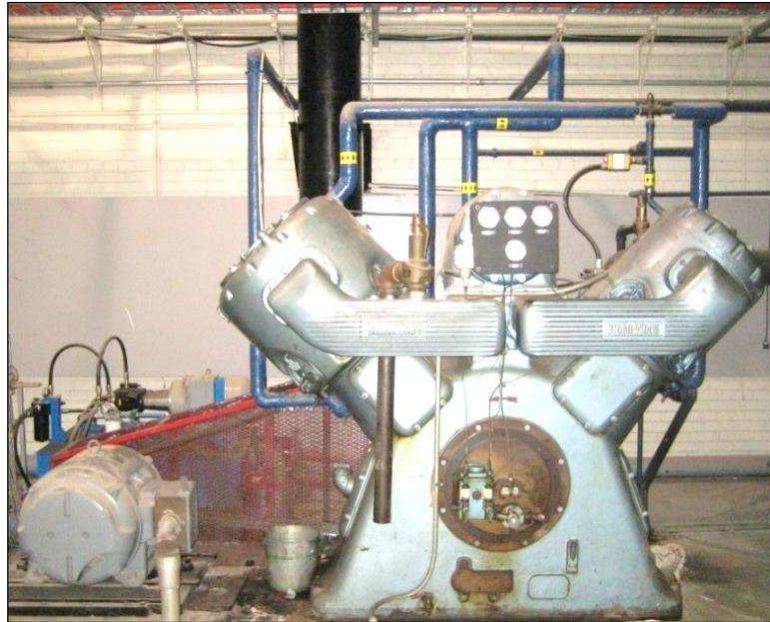


Figure 2.2: Broom Wade Compressor.

### 2.1.2 High Power Heater

This circulation heater is manufactured by Watlow Hannibal and is rated for 250 kW at 480 V, but it is configured to be operated at 150 kW and 600 V, by eliminating two of the heater banks inside the heater and rewiring the last heater bank to work with 600 V supply. The body of the heater is made of high-temperature grade stainless steel 304. The body of the heater is made of a 10" pipe, and the inlet and outlet are made of 3" pipes. All the piping has schedule 80 wall thickness. 3" - 600# flanges are used as connection points to the air delivery system. The heater is designed to heat the air to temperatures up to 730°C at 7 bars under continuous operation. The heater uses three K-type thermocouples for control and safety purposes. These thermocouples measure shell, element and process air temperatures. It is also equipped with a solid state power converter along with a PID controller to maintain the required temperature and limit the heater elements and body temperatures. All the pipes that carry the heated air to the main chamber are insulated with 2" or 3" of calcium silicate insulation depending on the location and size which can withstand temperatures up to 760°C and are chosen so that during operation the surface

temperature would not exceed approximately 45°C. Appendix C shows the engineering drawings for the circulation heater.

### 2.1.3 Flow straightening system

This system is a crucial part of the setup, see Figure 2.4. The main problem is the change from circular to rectangular cross-section of the pipe. Heated Air from the 3" line is first passed through a flow straightening plate. This plate is made of SS316 with 44 holes in various radii. Each hole has a diameter of ¼" and the plate thickness is ½", Figure 2.4 (a). The overall diameter of the plate is 5" and is placed between two flanges. The air is then passed through a ceramic honeycomb (with aspect ratio ~20, and rectangular orifices ~0.75mm) and finally through screens. The honeycomb and the screens are positioned against the 25mm x 35mm rectangular entry section of the cooling pipes. For further information about cooling pipes, refer to main chamber design.



Figure 2.3: Settling tank 2, settling tank 3, and heater.

### 2.1.4 Flow control system

This system consists of two valves, an air flowmeter, two pressure gauges and K-type thermocouples. The idea is to control the volume of air entering the heater with a butterfly valve and control the pressure inside the test chamber with a high temperature rated gate valve after the test section. Both the air flow and pressure are coupled to each other and in order to set a specific set-point an iterative process for adjustment needs to be made until the flow is stable. See Figure

2.10 for the gate valve. The flow rate is measured using a flowmeter, Figure 2.5, and the chamber pressure by one of the pressure gauges, Figure 2.7. Each pressure gauge has a span of 0 to 100 psig with accuracy of  $\pm 0.5\%$  over the span and  $\pm 0.4\%$  for every  $10^\circ\text{C}$  temperature change from  $20^\circ\text{C}$ .

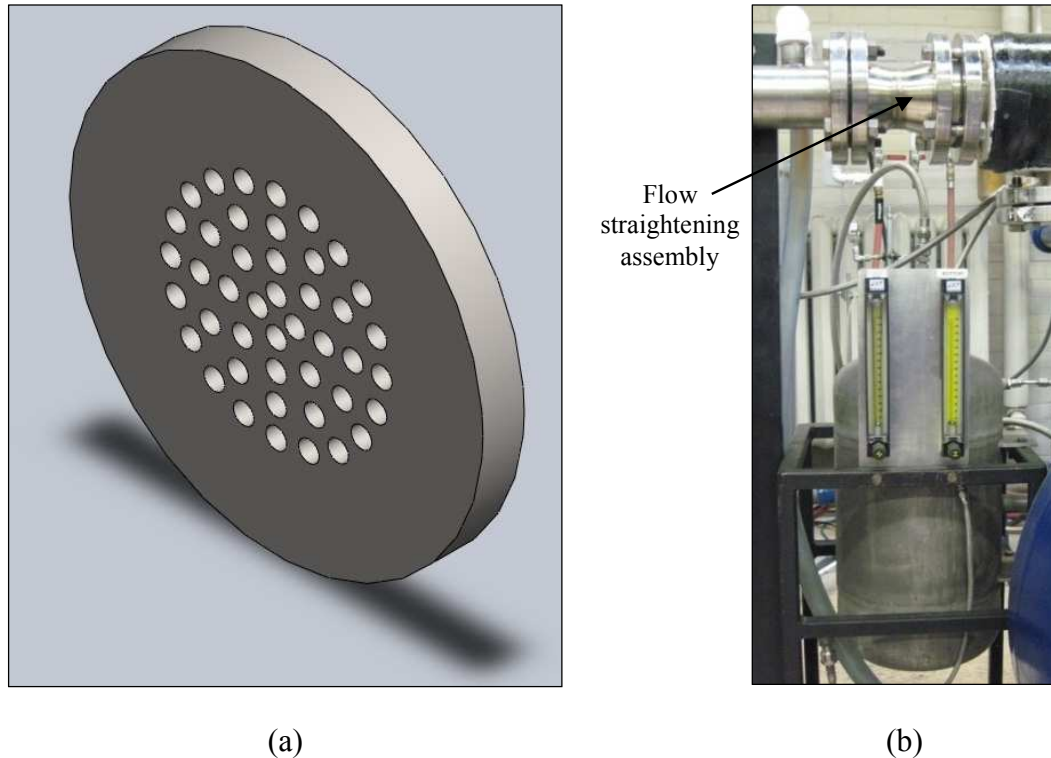


Figure 2.4: (a) Flow straightening plate; (b) Flow straightening system, fuel tank and flowmeters.

The flowmeter is an inline horizontal variable area flowmeter, made by Erdco, model Armor-Flo 1411. Inside the flowmeter, the air is passed through an orifice plate which provides a pressure drop in the main line, Figure 2.5 (a). Simultaneously, a small amount of air is bypassed by the plate and is directed through an external variable area flowmeter. The reading from the external flowmeter is directly proportional to the overall flow, since the pressure drop is the same for both the orifice plate and external flowmeter. The flowmeter system has  $\pm 2\%$  accuracy over the whole range and  $\pm 1\%$  repeatability. A thermocouple and pressure gauges are used to adjust the flowmeter calibrated reading. The flowmeter is only calibrated to work at a specific pressure and temperature and needs to be corrected when the conditions are different from the calibration. The following relation is used to correct the flowmeter reading.



$$\text{Corrected Flow rate} = \text{Scale Reading} \times \frac{\sqrt{\frac{(460 + T_1) \times SG_1}{14.7 + P_1}}}{\sqrt{\frac{(460 + T_2) \times SG_2}{14.7 + P_2}}} \quad (2.1)$$

Where:

SG1: Scale specific gravity (1.0 for this flowmeter, calibrated for air)

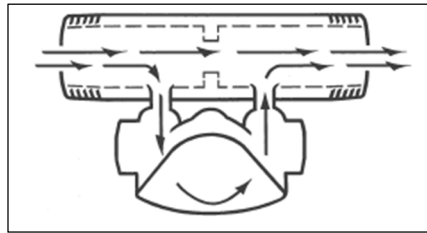
SG2: New specific gravity (1.0 if air)

P1: Scale operating pressure (70psig for this flowmeter)

P2: New operating pressure

T1: Scale operating temperature (68°F for this flowmeter)

T2: New operating temperature



(a)



(b)

Figure 2.5: Erdco air flowmeter.

### 2.1.5 Test chamber

The test chamber is designed to withstand high temperatures and pressures. The following summarizes some of the considerations for the design of the test chamber:

- Large channel cross-section area to avoid jet impingement on the walls while considering air flow limitations;
- Optical access from the two sides and bottom of the chamber. The side windows are used for imaging and measurement with PDA/PDPA. The bottom window is used for laser illumination, e.g. PIV. It can also be used for imaging;
- The bottom window can be replaced with nozzle holder and nozzles for opposed jet experiments;
- Rectangular cross-section to eliminate laser light distortion as opposed to round chambers where there is an inherent distortion of light;
- Easy nozzle access and replacement;
- Easy nozzle arrangement, i.e. single, opposed and staggered;

- Fully developed and undisturbed flow before and after the test zone;
- Capability for flow temperature profile measurement and pressure reading;
- Air and water cooling;
- Emergency water injection capabilities.

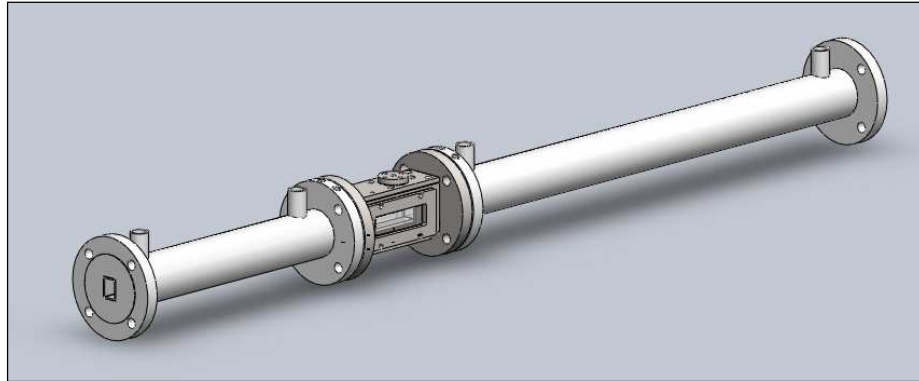


Figure 2.6: Main chamber with the cooling sections before and after.

Figure 2.6 shows a schematic of the test chamber with the cooling sections connected. Figure 2.7 shows the test chamber with all its accessories attached. The optical windows for the test chamber are made of synthetic fused silica glass, corning 7980 (quartz) because of its excellent laser transmission properties and also temperature rating. The maximum operating temperature is 1400°C. A 25mm thick glass is used in order to meet the pressure requirements. This glass can withstand pressures up to 14 bars with standard safety factor of 11 for the glass. A step is machined all around one face of the glass to allow the glass to sit flush with walls of the chamber, see Figure 2.8. The step cannot be avoided since the gaskets and glass are designed to sit flush with the wall of the chamber. The chamber is designed to be fitted with 1/16" thick Thermiculite 815 with tanged core gasket. This type of gasket can operate at temperatures as high as 850°C but due to heater power limitations graphite gaskets are used instead which can operate up to 450°C.

The channel has a cross-section of 25mm x 35mm. The penetration correlations developed by Wu et al. [9] are used to predict this cross-section area. This area is found to be large enough to avoid jet impingement and flow restrictions for the nozzles used in this study. The chamber is made of only two sections in order to make the machining and assembly of the chamber easier. The top section is T-shaped and slides over the bottom section which is U-shaped.

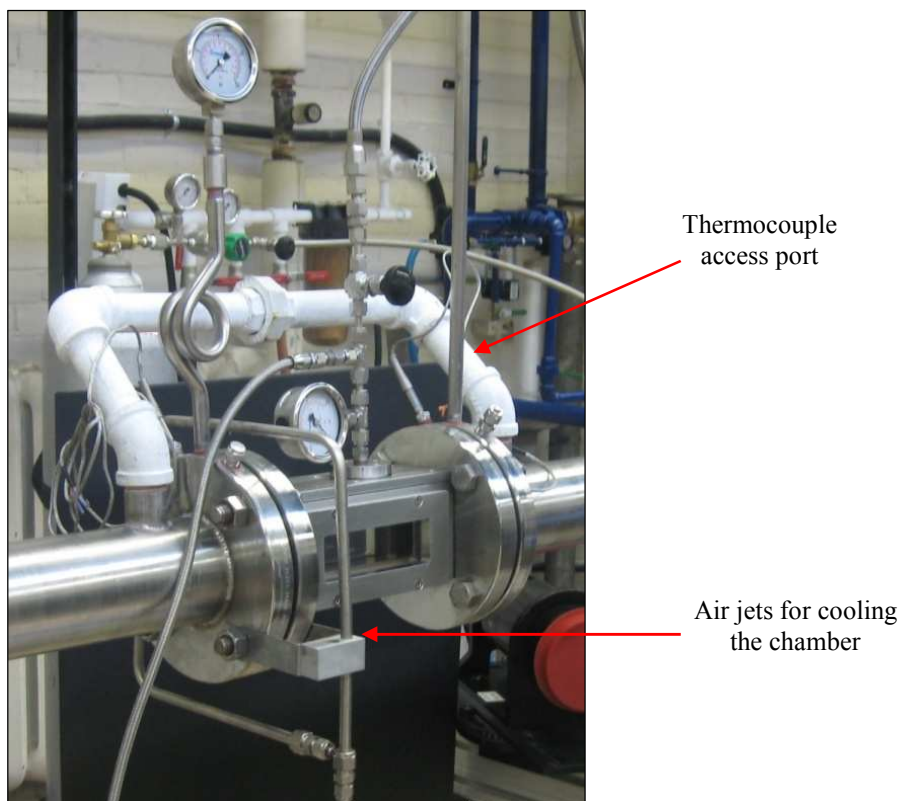


Figure 2.7: Main chamber and its accessories.

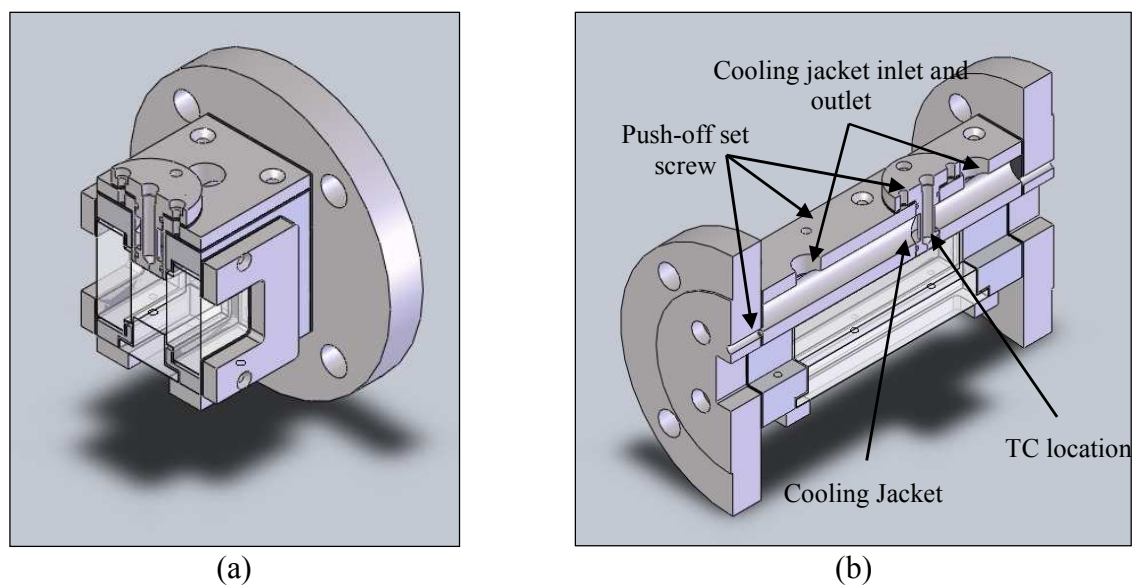


Figure 2.8: Section views of the front (a) and side (b) of the main chamber with the nozzle in place.

Figure 2.8 (a) and (b) show the section views from the side and front of the chamber. The top part of the chamber is fitted with set screws. These screws can be used to push-off the top part of the

chamber from the main body. The same feature is also added to the end flanges and nozzles. The top part of the chamber is fitted with water cooling jacket for controlling the temperature of the jet. The idea is to control the temperature of the jet by adjusting the volume flow through this cooling jacket. The temperature of the jet is monitored with a thermocouple that is inserted from the top, and the sensing tip is set at close proximity to the bottom of the nozzle.

The nozzles are designed to sit flush with the walls of the channel. They are positioned so that there is 50 mm of optical access downstream and 100 mm upstream of the injection point. The nozzles have a simple design which allows for easy exchange without disassembling of the chamber. There are two silicone O-rings that form a seal between the outside, chamber air and the cooling channel. The nozzles are first drilled from the liquid entry side with a 1/8" drill. The drill has a 90° tip. The tip is used to minimize the effect of flow separation inside the orifice. The nozzle orifices are first drilled using an EDM drill (Electric Discharge Machining) from the jet exit face of the nozzle. Afterwards a high-speed miniature drill-press is used to reach the final size for the orifice. This is the most effective technique to make circular orifices with large L/D. EDM drill can create large hole aspect ratios, especially for difficult to machine materials. The downside with the EDM drill is that the holes are not very circular because spark erosion is the primary method of removing the material. Naturally the sparks are not entirely uniform and create irregularities in the orifice. The other issue with this type of machining is that the heat generated from the machining hardens the inner wall of the orifice and makes it challenging for drilling. The benefit of using a high-speed drill to finish the orifice is that the drill makes the hole circular and reams the inner wall of the orifice to the required dimension. The process also removes any remaining burrs that can affect the jet quality especially at the jet exit.

A long and thin K-type thermocouple made by Conax Buffalo Technologies, model K-SS4-B-T3HT-MPGAV-25" is used to make the air flow temperature measurements. The thermocouple sits inside a long vertical pipe, see Figure 2.9, at the top there is compression fitting with a rubber ferrule to make the thermocouple seal. Temperature measurements can be made at different locations by adjusting the height of the thermocouple. The long pipe is required to dissipate heat from the seal. The main test section assembly also includes two cooling sections before and after the main chamber. Figure 2.6 and Figure 2.9 show the main chamber with the two cooling sections. The cooling section upstream the main chamber is 1.0 m long, and the cooling section

downstream the main chamber is 0.5 m long. The cooling water enters the downstream cooling section first and then is divided into two flows. The larger flow is directed to the upstream cooling section; the remainder is redirected and used for nozzle cooling. A plug valve is used to adjust the flow going through the chamber. The extra channel lengths upstream and downstream of the main chamber are crucial, because the air flow needs to be fully developed. The previous designs showed that if the second control valve is positioned too close to the nozzle, then the air flow is affected. This non-uniform air flow distorts the spray symmetry about its  $xz$ -plane. The cooling sections are made of an outer round pipe and an inner square pipe. The spacing between the pipes is used for passing cooling water. Multiple baffles are used to enhance the cooling of the walls at even intervals. Additionally, the main chamber is equipped with multiple cooling air jets that blast the outside surfaces of the chamber. This assembly can be seen in Figure 2.7.

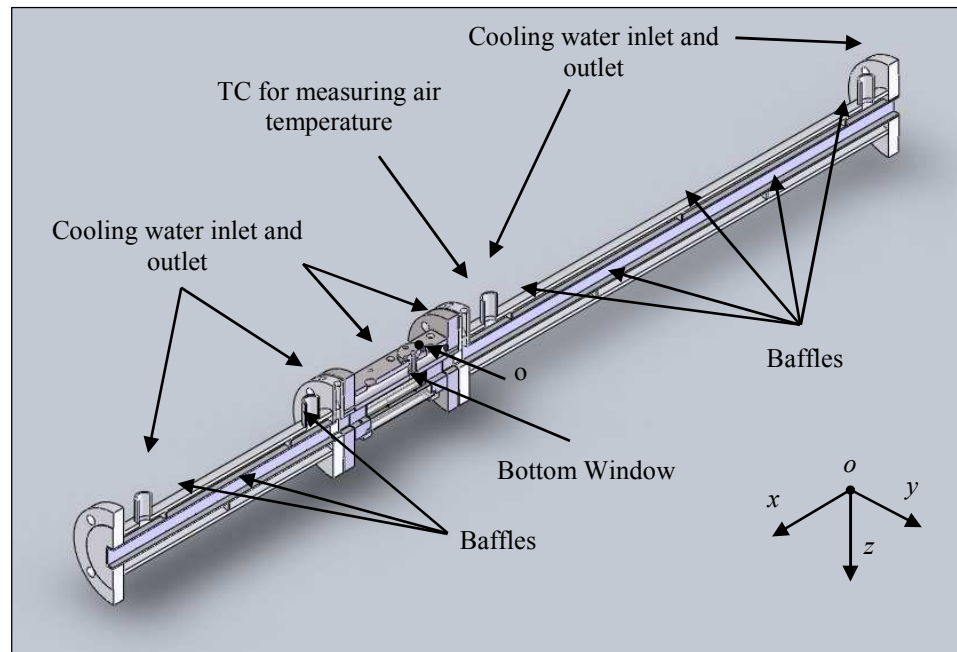


Figure 2.9: Cross-section view of the chamber and the cooling sections upstream and downstream of the chamber.

### 2.1.6 Flow cooling system

A water tank is used in order to cool the exhaust air. The exhausted hot air would first cool due to expansion after the pressure control valve, and further cooled by water injection into the pipe, the injection nozzle can be seen on Figure 2.10. The same tank can also supply the main injector

with water in case of an emergency. The excess water–fuel mixture is removed from the pipe using a liquid recovery port, see Figure 2.10. In addition to this liquid recovery port, there is a second port situated further downstream.

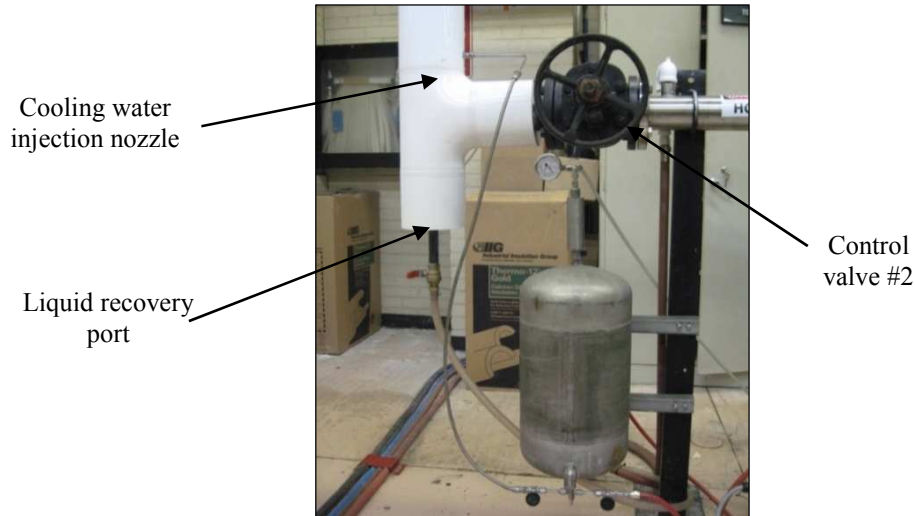


Figure 2.10: Cooling water tank, control valve #2 (large black valve), liquid recovery port, cooling water injection nozzle and exhaust line.

### 2.1.7 Exhaust and flow silencing system

The exhaust gases are directed to a chimney as seen on Figure 2.11, about 100m away using 2.5” pipes. Inside the chimney, the pipe is oriented vertically upward to reduce the noise produced by the gas expansion.



Figure 2.11: Exhaust chimney outside the Mechanical Engineering building, University of Toronto.

## 2.2 Liquid Injection System

The liquid injection system consists of three main parts; the liquid tank, flow controls and a high-pressure nitrogen tank. A schematic of the system is provided in Figure 2.12, the liquid tank and flowmeters can be seen in Figure 2.4 (b). The liquid tank is made of 304L stainless steel with multiple inlet and exit ports. Its capacity is 20 liters with working pressure up to 24 bars. For safety reasons, it is equipped with a pressure relief valve that opens at 20 bars. The tank is also electrically grounded to avoid accidental electric discharge inside the tank. To fill the tank, first it has to be depressurized then the liquid (water or Jet-A fuel) is supplied from the top of the tank. A high-pressure nitrogen cylinder provides the pressure required to drive the liquid. The liquid is driven from the bottom to a rotameter with maximum flow rate of 1370 ml/min (for water). The flowmeter has a 150 mm scale with  $\pm 2\%$  accuracy over the whole range and  $\pm 0.25\%$  repeatability. The flowmeter is calibrated with each of the nozzles whenever a different liquid than water is used. The flowmeter is equipped with a needle valve to adjust the flow rate.

An issue that rises when using this type of liquid delivery system is the solubility of nitrogen in water. Nitrogen becomes dissolved in water at higher pressures and when the liquid exits the nozzle it can potentially create bubbles and affect the atomization process. Some precautions are considered in order to avoid such problems. First, minimum amount of nitrogen pressure was applied to minimize such effects. Second, visual inspections of the jet were made to ensure the nitrogen does not affect the atomization. Third, the solubility calculations showed that the amount of nitrogen dissolved in the water were negligible. Ultimately to avoid this problem, an improvement is made to the delivery system where a super-high-pressure air-powered piston pump, Maximator model G10, is used. Essentially this pump behaves similarly to a syringe pump and measurements are made between each stroke of the piston.

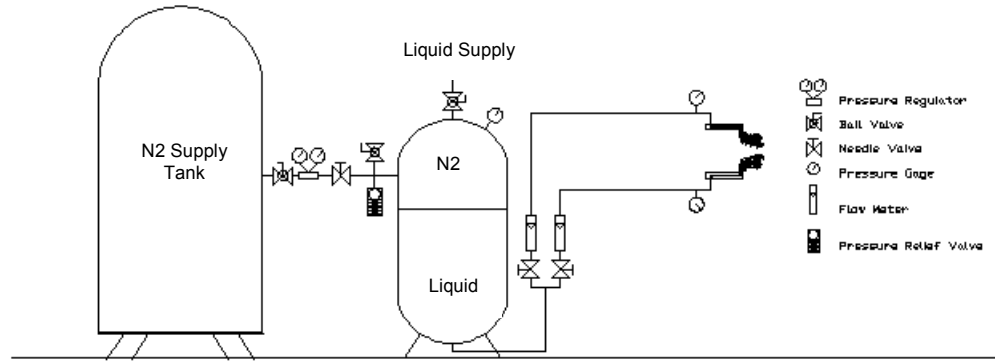


Figure 2.12: Schematic of the fuel system.

### 2.3 Measurement System: Imaging System

The system consists of the imaging hardware and software. The imaging hardware includes laser, camera and image capture software; the image capture software is Flow Manager Version 4.7 made by Dantec Dynamic A/S. The Laser is a New Wave Research solo PIV with dual laser-head system designed for Particle Image Velocimetry, PIV. The laser is Nd:YAG and has an energy output of 50 mJ for wavelength of 532 nm. A 80x60 series laser light sheet lens, Dantec Dynamics A/S, is attached using an adaptor to the front of the laser to convert the round laser beam to a laser light sheet. Figure 2.13 shows the drawing for the laser light sheet adaptor. The camera is a Flow Sense M2 8bit made by Dantec Dynamics A/S and is used with a Nikon Micro-Nikkor 60 mm lens. The camera has a resolution of 1600X1186 pixels, and each pixel represents 19.0  $\mu\text{m}$  in this study. A calibration target, 100X100 with dot spacing of 2.5 mm from Dantec Dynamics A/S, is used to determine the scale for the images. An F-C adapter is used to attach the lens to the camera. The complete system is mounted on Bosch aluminum extrusion framing and is enclosed with a black sheet metal box to avoid laser light scattering. The Assembly is then mounted on the traverse system with the laser pointing upward and the camera facing the side window of the chamber. Extra care is taken to ensure that the laser light sheet, camera, traverse and the chamber are all square to one another. Flow Manager Software is used in conjunction with a timing box and camera drivers from National Instrument to capture the images. Each image set consists of two different images. The camera is capable of capturing two simultaneous images. For the purposes of the current experiment, the image sets are captured at 15 Hz, with laser pulse duration of 0.01  $\mu\text{s}$ , and the time between each image for each image set is 100  $\mu\text{s}$ . Flow Manager is used to separate the image sets to frames A and B and finally to export the files for image analysis.



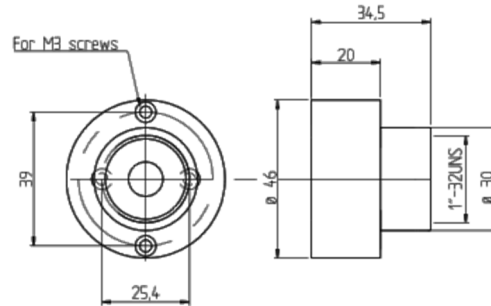


Figure 2.13: Drawing of the adaptor for attaching the laser light sheet lens.

## 2.4 Experimental Conditions and Results

Tables 2.1, 2.2 and 2.3 summarize the test conditions and results for the jet trajectory experiments. There are 209 cases for which data is captured. The total number of images captured for these cases exceed 72,000. The liquid used in all the experiments is water. Crossflow air temperatures are 25°C, 200°C, and 300°C; absolute crossflow air pressures are 2.1, 3.8, and 5.2 bars. Two nozzles with orifice diameters of 457  $\mu\text{m}$  and 572  $\mu\text{m}$  and L/D of 20 are considered. Various liquid and gas velocities are tested for each given temperature and pressure in order to study the breakup mechanisms and regimes. Most combinations of the aforementioned parameters are tested, except for 5.2 bars, where only one temperature, 200°C, is considered. Also, in few cases the required air flow rates are greater than the supply compressor capacity, and therefore, those cases are not considered. The air velocities are all in the incompressible flow regime with the Mach number ranging from 0.03 to 0.29 with average Mach number being at 0.15. For each test condition at least 300 images of the middle plain of the spray plume in the direction of the crossflow are obtained, using pulsed laser sheet illumination technique. Table 2.3 lists the details for all the conditions. Symbols presented in Table 2.1 are used to simplify the cross-reference between the conditions throughout the text except where noted otherwise for some figures. The solid filled symbols represent the 457  $\mu\text{m}$  nozzle, and the hollow symbols represent 572  $\mu\text{m}$  nozzle. In Table 2.2, the range of parameters are provided. The average and standard deviation are provided to give an idea about the range of parameters and an idea about the experimental conditions. They do not refer to the errors for the parameters.

Table 2.1: Summary of Fluid properties.

Cond. Symbol	p [Bar]	T <sub>Air</sub> [°C]	T <sub>Jet</sub> [°C]	T <sub>Sat</sub> [°C]	ρ <sub>Jet</sub> [kg/m <sup>3</sup> ]	ρ <sub>Air</sub> [kg/m <sup>3</sup> ]	σ [N/m]	V <sub>Air</sub> [m <sup>2</sup> /s]	V <sub>Jet</sub> [m <sup>2</sup> /s]	μ <sub>Air</sub> [N.S/m <sup>2</sup> ]	μ <sub>Jet</sub> [N.S/m <sup>2</sup> ]
□/■	2.1	25	25	121.3	997.10	2.42	0.072	7.638E-6	8.927E-7	1.849E-5	8.901E-4
□/■	2.1	200	25	121.3	997.10	1.52	0.072	1.716E-5	8.927E-7	2.610E-5	8.901E-4
□/■	2.1	300	25	121.3	997.10	1.25	0.072	2.380E-5	8.927E-7	2.987E-5	8.901E-4
△/▲	3.8	25	25	141.7	997.17	4.44	0.072	4.167E-6	8.925E-7	1.851E-5	8.900E-4
△/▲	3.8	200	25	141.7	997.17	2.79	0.072	9.370E-6	8.925E-7	2.611E-5	8.900E-4
△/▲	3.8	300	25	141.7	997.17	2.30	0.072	1.299E-5	8.925E-7	2.987E-5	8.900E-4
○/●	5.2	200	25	153.1	997.24	3.80	0.072	6.875E-6	8.925E-7	2.612E-5	8.900E-4

Table 2.2: Test conditions for imaging experiments with water.

	V <sub>Jet</sub> [m/s]	V <sub>Air</sub> [m/s]	q	We <sub>Aero</sub>	We <sub>Jet</sub>	Re <sub>Air</sub>	Re <sub>Jet</sub>	Oh <sub>Air</sub> [x10 <sup>3</sup> ]	Oh <sub>Jet</sub> [x10 <sup>3</sup> ]	Ma
Minimum	4.3	14.8	8	7	149	925	2783	1.368	4.392	0.03
Maximum	54.3	127.9	181	298	23282	12624	34743	4.648	4.914	0.29
Average	20.1	59.9	56	73	3738	3440	11452	2.740	4.664	0.15
Standard Deviation	11.5	25.9	42	63	4335	2446	6507	0.979	0.261	0.07

Table 2.3: List of all the conditions and results.

No.	Ref.	V <sub>Jet</sub> [m/s]	V <sub>Air</sub> [m/s]	q	We <sub>Air</sub>	We <sub>Jet</sub>	Re <sub>Air</sub>	Re <sub>Jet</sub>	Oh <sub>Air</sub> x10 <sup>3</sup>	Oh <sub>Jet</sub> x10 <sup>3</sup>	D10 [μm]	D32 [μm]	STD [μm]	MMD	Lb/DN	tb/t*	A <sub>p</sub> /A <sub>D</sub>	θ <sub>P</sub> [°]	W <sub>p</sub> /D <sub>N</sub>	t <sub>s</sub> /D <sub>N</sub> x10 <sup>3</sup>
1	□	14	95	8	172	1455	7084	8685	1.852	409.3	62.5	76.9	19.0	90.3	29.6	4.1	236.2	20.9	6.3	62.6
2	□	19	95	17	172	2910	7084	12282	1.852	486.8	60.4	72.5	17.0	86.4	31.8	4.4	252.5	29.4	6.2	62.9
3	□	30	95	42	172	7275	7084	19419	1.852	612.1	59.2	69.1	15.4	86.4	41.4	4.5	390.1	39.9	7.4	53.1
4	□	38	95	68	172	11640	7084	24564	1.852	688.4	58.1	65.8	13.8	86.4	43.1	4.0	410.7	45.8	7.5	52.5
5	□	9	61	8	71	582	4544	5493	1.852	325.5	68.5	88.8	23.9	97.1	26.1	3.4	178.2	19.8	5.4	73.3
6	□	12	61	16	71	1164	4544	7768	1.852	387.1	66.0	84.3	22.1	93.8	27.7	4.1	192.9	32.3	5.5	71.8
7	□	19	61	41	71	2910	4544	12282	1.852	486.8	63.3	78.5	19.6	90.3	36.2	4.1	294.7	41.7	6.4	61.4
8	□	24	61	66	71	4656	4544	15535	1.852	547.5	61.6	73.9	17.6	89.7	39.7	3.9	316.5	49.4	6.3	62.8
9	□	10	49	15	47	728	3701	6141	1.852	344.2	68.4	88.7	24.0	96.8	28.0	4.2	173.2	29.2	4.9	80.7
10	□	15	49	39	47	1819	3701	9710	1.852	432.8	65.6	83.0	21.5	92.3	32.2	3.7	223.8	41.7	5.5	72.0
11	□	19	49	62	47	2910	3701	12282	1.852	486.8	64.1	79.5	20.0	90.3	38.0	3.7	302.5	46.7	6.2	62.9
13	□	27	127	30	195	5820	4235	17369	3.298	578.9	57.6	65.4	13.6	84.8	49.3	5.4	605.6	30.2	9.6	40.7
14	□	43	127	75	195	14550	4235	27463	3.298	727.9	57.1	63.3	12.4	83.7	54.6	4.2	717.1	34.6	10.3	38.1
16	□	14	93	14	105	1455	3109	8685	3.298	409.3	61.3	75.0	18.2	88.0	39.9	5.1	355.4	21.8	7.0	56.1
17	□	19	93	28	105	2910	3109	12282	3.298	486.8	59.8	71.4	16.6	86.4	43.4	5.3	422.3	34.3	7.6	51.4
18	□	30	93	69	105	7275	3109	19419	3.298	612.1	58.5	68.1	15.0	86.4	47.0	4.0	502.3	40.4	8.4	46.8
20	□	9	61	13	44	582	2022	5493	3.298	325.5	67.7	88.2	23.8	94.4	26.9	4.1	197.3	30.3	5.8	68.2
21	□	12	61	26	44	1164	2022	7768	3.298	387.1	64.9	82.8	21.6	90.7	37.3	4.9	307.9	37.4	6.5	60.5
22	□	19	61	65	44	2910	2022	12282	3.298	486.8	62.2	77.2	19.2	89.7	36.3	3.4	301.9	46.1	6.5	60.1
24	□	7	49	13	29	364	1622	4342	3.298	289.4	70.0	91.6	25.0	99.1	27.3	3.9	188.6	27.3	5.4	72.4
25	□	10	49	25	29	728	1622	6141	3.298	344.2	68.8	90.0	24.5	97.1	31.3	4.3	219.4	40.7	5.5	71.3
26	□	15	49	64	29	1819	1622	9710	3.298	432.8	64.9	82.2	21.3	90.7	35.6	3.4	253.8	46.3	5.6	70.1
27	□	19	49	102	29	2910	1622	12282	3.298	486.8	63.4	79.0	19.9	90.3	35.8	2.7	253.8	46.4	5.6	70.5
32	□	14	95	16	90	1455	2285	8685	4.154	409.3	63.1	77.8	19.3	90.3	32.6	8.1	255.5	18.6	6.2	63.7
33	□	19	95	32	90	2910	2285	12282	4.154	486.8	60.8	73.2	17.3	86.8	44.6	7.9	432.0	20.2	7.6	51.6
34	□	30	95	81	90	7275	2285	19419	4.154	612.1	59.4	70.4	16.1	86.4	45.7	5.1	462.3	31.7	7.9	49.5
36	□	9	62	15	38	582	1490	5493	4.154	325.5	68.8	88.6	23.8	99.0	24.3	6.2	164.0	19.8	5.3	74.1

No.	Ref.	V <sub>Jet</sub> [m/s]	V <sub>Air</sub> [m/s]	q	We <sub>Air</sub>	We <sub>Jet</sub>	Re <sub>Air</sub>	Re <sub>Jet</sub>	Oh <sub>Air</sub> x10 <sup>3</sup>	Oh <sub>Jet</sub> x10 <sup>3</sup>	D10 [μm]	D32 [μm]	STD [μm]	MMD	L <sub>b</sub> /D <sub>N</sub>	t <sub>b</sub> /t*	A <sub>p</sub> /A <sub>D</sub>	θ <sub>P</sub> [°]	W <sub>p</sub> /D <sub>N</sub>	t <sub>s</sub> /D <sub>N</sub> x10 <sup>3</sup>
37	□	12	62	30	38	1164	1490	7768	4.154	387.1	66.1	83.9	21.9	94.4	31.2	5.7	233.2	26.5	5.9	67.0
38	□	19	62	76	38	2910	1490	12282	4.154	486.8	63.4	79.4	20.1	90.3	36.4	4.2	310.5	37.4	6.7	58.6
39	□	24	62	122	38	4656	1490	15535	4.154	547.5	62.4	77.1	19.1	90.3	38.1	3.5	306.8	45.4	6.3	62.0
40	□	7	50	15	25	364	1196	4342	4.154	289.4	70.9	92.1	25.2	100.2	25.4	6.6	141.9	15.2	4.4	89.6
41	□	10	50	29	25	728	1196	6141	4.154	344.2	69.0	89.1	23.9	99.0	27.8	5.1	173.0	27.7	4.9	80.3
42	□	15	50	74	25	1819	1196	9710	4.154	432.8	66.3	84.5	22.1	94.4	37.4	4.4	300.5	38.1	6.3	62.3
43	□	19	50	118	25	2910	1196	12282	4.154	486.8	65.1	82.1	21.1	92.2	35.7	3.3	255.4	48.9	5.6	69.9
44	△	19	92	10	298	2910	12624	12283	1.368	486.8	59.4	69.5	15.6	86.4	33.8	10.8	292.9	15.9	6.8	57.8
45	△	27	92	20	298	5821	12624	17371	1.368	578.8	58.5	66.9	14.3	86.4	35.8	8.1	334.2	22.8	7.3	53.5
46	△	43	92	49	298	14551	12624	27466	1.368	727.9	57.7	65.2	13.5	86.3	39.9	5.7	398.5	36.6	7.8	50.1
47	△	54	92	78	298	23282	12624	34743	1.368	818.6	57.1	63.2	12.4	83.7	41.4	4.7	402.8	44.3	7.6	51.3
48	△	14	65	10	150	1455	8956	8686	1.368	409.3	63.8	78.8	19.8	90.3	25.2	8.1	190.3	24.7	5.9	66.3
49	△	19	65	19	150	2910	8956	12283	1.368	486.8	61.6	74.5	18.0	89.3	31.9	7.2	247.4	33.1	6.1	64.5
50	△	30	65	48	150	7276	8956	19422	1.368	612.1	59.8	70.7	16.2	86.4	39.7	5.7	373.8	42.6	7.4	53.1
51	△	38	65	77	150	11641	8956	24567	1.368	688.4	58.5	66.7	14.2	86.4	42.1	4.8	392.3	49.2	7.3	53.6
52	△	9	41	10	60	582	5665	5493	1.368	325.5	68.4	87.6	23.4	97.0	22.1	7.1	149.0	26.0	5.3	74.1
53	△	12	41	19	60	1164	5665	7769	1.368	387.1	66.5	84.1	22.0	94.4	24.7	5.6	170.6	33.6	5.4	72.5
54	△	19	41	48	60	2910	5665	12283	1.368	486.8	64.1	79.3	20.0	90.3	31.8	4.6	221.6	46.1	5.5	71.9
55	△	24	41	77	60	4656	5665	15537	1.368	547.4	62.1	75.2	18.1	90.3	40.1	4.6	313.3	50.6	6.1	64.1
56	△	7	33	10	38	364	4478	4343	1.368	289.4	69.1	88.7	23.8	99.1	26.3	8.4	137.4	14.5	4.1	95.7
57	△	10	33	19	38	728	4478	6142	1.368	344.2	68.5	88.4	23.8	97.1	27.1	6.2	181.3	29.0	5.3	74.7
58	△	15	33	48	38	1819	4478	9711	1.368	432.8	65.9	82.7	21.4	94.4	32.2	4.6	218.6	43.7	5.3	73.5
59	△	19	33	77	38	2910	4478	12283	1.368	486.8	64.2	78.6	19.6	90.7	35.1	4.0	241.8	50.8	5.4	72.6
60	△	19	92	15	188	2910	5633	12283	2.437	486.8	58.8	68.5	15.2	86.4	31.6	8.0	267.2	16.8	6.6	59.1
61	△	27	92	31	188	5821	5633	17371	2.437	578.8	57.8	65.4	13.6	86.3	36.1	6.5	327.4	21.4	7.1	55.1
62	△	43	92	77	188	14551	5633	27466	2.437	727.9	57.0	63.4	12.5	83.3	38.1	4.3	345.8	35.9	7.1	55.1
63	△	14	68	14	102	1455	4146	8686	2.437	409.3	62.8	78.5	19.7	90.3	29.2	7.7	248.4	17.8	6.7	58.7
64	△	19	68	28	102	2910	4146	12283	2.437	486.8	60.5	73.1	17.3	86.4	28.4	5.3	223.6	30.4	6.2	63.5
65	△	30	68	71	102	7276	4146	19422	2.437	612.1	59.0	69.4	15.6	86.4	33.2	3.9	259.0	42.3	6.1	64.0

No.	Ref.	V <sub>Jet</sub> [m/s]	V <sub>Air</sub> [m/s]	q	We <sub>Air</sub>	We <sub>Jet</sub>	Re <sub>Air</sub>	Re <sub>Jet</sub>	Oh <sub>Air</sub> x10 <sup>3</sup>	Oh <sub>Jet</sub> x10 <sup>3</sup>	D10 [μm]	D32 [μm]	STD [μm]	MMD	L <sub>b</sub> /D <sub>N</sub>	t <sub>b</sub> /t*	A <sub>p</sub> /A <sub>D</sub>	θ <sub>P</sub> [°]	W <sub>p</sub> /D <sub>N</sub>	t <sub>s</sub> /D <sub>N</sub> x10 <sup>3</sup>
66	△	38	68	114	102	11641	4146	24567	2.437	688.4	57.7	64.9	13.3	86.3	37.1	3.5	293.4	49.1	6.2	63.3
67	△	9	43	14	42	582	2645	5493	2.437	325.5	67.9	88.6	24.0	94.4	23.8	6.4	167.0	20.1	5.5	71.2
68	△	12	43	28	42	1164	2645	7769	2.437	387.1	65.6	84.4	22.3	92.2	28.3	5.3	198.1	28.7	5.5	71.4
69	△	19	43	70	42	2910	2645	12283	2.437	486.8	62.9	78.0	19.5	90.3	30.2	3.6	215.7	41.9	5.6	70.0
70	△	24	43	112	42	4656	2645	15537	2.437	547.4	61.6	74.8	18.1	89.3	33.4	3.2	231.4	48.6	5.4	72.2
71	△	7	35	14	27	364	2127	4343	2.437	289.4	69.8	91.7	25.1	99.1	22.1	6.0	130.8	16.8	4.7	84.4
72	△	10	35	27	27	728	2127	6142	2.437	344.2	69.0	91.2	25.0	97.0	24.4	4.7	159.0	28.0	5.1	76.6
73	△	15	35	68	27	1819	2127	9711	2.437	432.8	65.9	84.5	22.3	92.3	28.2	3.4	187.1	41.0	5.2	75.3
74	△	19	35	108	27	2910	2127	12283	2.437	486.8	64.2	80.4	20.5	90.3	33.8	3.3	245.1	47.6	5.7	69.1
76	△	27	92	37	156	5821	4063	17371	3.070	578.8	59.0	68.2	14.9	86.4	45.7	7.5	507.5	19.9	8.7	45.0
77	△	43	92	94	156	14551	4063	27466	3.070	727.9	58.1	66.1	13.9	86.4	49.6	5.1	622.9	31.1	9.9	39.8
80	△	19	68	35	84	2910	2986	12283	3.070	486.8	61.0	73.5	17.5	88.0	36.1	6.1	327.9	24.9	7.1	55.1
81	△	30	68	87	84	7276	2986	19422	3.070	612.1	59.6	70.6	16.1	86.4	38.0	4.1	324.8	40.7	6.7	58.5
82	△	38	68	139	84	11641	2986	24567	3.070	688.4	58.6	67.5	14.6	86.4	41.6	3.5	391.4	45.5	7.4	53.1
83	△	9	43	17	34	582	1908	5493	3.070	325.5	67.3	85.8	22.6	94.4	30.0	7.3	222.9	18.8	5.8	67.3
84	△	12	43	34	34	1164	1908	7769	3.070	387.1	65.6	82.7	21.4	92.3	30.4	5.2	224.9	27.2	5.8	67.5
85	△	19	43	85	34	2910	1908	12283	3.070	486.8	63.4	78.8	19.7	90.3	35.2	3.8	294.3	41.0	6.6	59.8
86	△	24	43	136	34	4656	1908	15537	3.070	547.4	62.3	76.6	18.8	90.3	38.7	3.3	327.3	45.4	6.6	59.1
87	△	7	34	17	21	364	1506	4343	3.070	289.4	69.8	90.0	24.4	99.1	30.9	7.5	204.2	14.6	5.2	75.7
88	△	10	34	34	21	728	1506	6142	3.070	344.2	68.4	87.2	23.2	97.1	28.5	4.9	187.6	26.6	5.2	75.9
89	△	15	34	85	21	1819	1506	9711	3.070	432.8	66.4	83.9	21.8	94.4	33.3	3.6	256.9	39.5	6.1	64.8
90	△	19	34	136	21	2910	1506	12283	3.070	486.8	64.6	80.7	20.5	90.7	33.9	2.9	223.1	50.2	5.2	76.0
91	■	14	96	8	141	1165	5727	6946	2.072	409.5	65.9	82.9	21.5	94.2	31.2	10.9	268.2	20.9	6.7	58.2
92	■	19	96	17	141	2330	5727	9823	2.072	487.0	63.0	77.6	19.3	90.3	43.6	10.7	476.1	21.9	8.6	45.8
93	■	30	96	41	141	5825	5727	15531	2.072	612.4	60.6	72.5	17.0	86.4	46.0	7.1	483.8	34.4	8.3	47.5
94	■	38	96	66	141	9320	5727	19646	2.072	688.8	59.6	70.5	16.1	86.4	46.1	5.7	478.1	45.7	8.1	48.2
95	■	9	61	8	56	466	3622	4393	2.072	325.7	71.5	93.7	25.8	100.8	33.6	11.7	246.4	15.8	5.8	68.2
96	■	12	61	17	56	932	3622	6213	2.072	387.3	69.6	89.9	24.3	99.1	33.3	8.2	255.9	24.7	6.0	65.1
97	■	19	61	41	56	2330	3622	9823	2.072	487.0	65.7	83.2	21.6	93.3	42.2	6.6	417.3	36.7	7.8	50.6

No.	Ref.	V <sub>Jet</sub> [m/s]	V <sub>Air</sub> [m/s]	q	We <sub>Air</sub>	We <sub>Jet</sub>	Re <sub>Air</sub>	Re <sub>Jet</sub>	Oh <sub>Air</sub> x10 <sup>3</sup>	Oh <sub>Jet</sub> x10 <sup>3</sup>	D10 [μm]	D32 [μm]	STD [μm]	MMD	L <sub>b</sub> /D <sub>N</sub>	t <sub>b</sub> /t*	A <sub>p</sub> /A <sub>D</sub>	θ <sub>P</sub> [°]	W <sub>p</sub> /D <sub>N</sub>	t <sub>s</sub> /D <sub>N</sub> x10 <sup>3</sup>
98	■	24	61	66	56	3728	3622	12425	2.072	547.7	64.3	80.2	20.4	90.7	43.3	5.3	410.3	44.6	7.4	52.8
99	■	7	50	8	38	291	2970	3473	2.072	289.6	72.1	93.4	25.5	102.8	33.2	12.0	202.4	11.9	4.8	82.0
100	■	10	50	15	38	582	2970	4911	2.072	344.4	71.3	93.4	25.7	100.8	34.3	8.7	262.4	22.5	6.0	65.4
101	■	15	50	38	38	1456	2970	7766	2.072	433.0	68.2	87.3	23.3	97.0	39.9	6.4	331.5	36.1	6.5	60.2
102	■	19	50	62	38	2330	2970	9823	2.072	487.0	66.6	84.5	22.1	94.4	42.3	5.4	388.5	42.8	7.2	54.5
106	■	54	128	118	158	18639	3404	27784	3.690	819.1	57.7	64.5	13.0	86.4	45.5	4.2	501.4	43.2	8.6	45.4
107	■	14	95	14	86	1165	2517	6946	3.690	409.5	65.2	82.6	21.4	92.2	31.2	8.5	304.4	18.4	7.7	51.2
108	■	19	95	27	86	2330	2517	9823	3.690	487.0	62.2	76.4	18.7	90.3	37.0	7.1	339.1	25.0	7.2	54.5
109	■	30	95	68	86	5825	2517	15531	3.690	612.4	60.1	71.4	16.5	86.4	42.9	5.2	436.5	35.6	8.0	49.1
110	■	38	95	108	86	9320	2517	19646	3.690	688.8	59.4	69.4	15.5	86.4	44.3	4.3	461.3	44.8	8.2	48.0
111	■	9	61	13	35	466	1615	4393	3.690	325.7	70.9	92.7	25.4	100.2	29.3	8.1	207.4	12.9	5.6	70.6
112	■	12	61	26	35	932	1615	6213	3.690	387.3	68.4	89.1	24.0	96.8	33.5	6.5	281.7	26.7	6.6	59.4
113	■	19	61	66	35	2330	1615	9823	3.690	487.0	65.0	82.3	21.3	92.2	41.8	5.2	379.9	35.1	7.1	55.0
114	■	24	61	105	35	3728	1615	12425	3.690	547.7	63.3	79.7	20.3	90.3	41.3	4.0	385.6	42.2	7.3	53.6
115	■	7	48	13	22	291	1277	3473	3.690	289.6	72.6	95.3	26.4	102.8	30.5	8.4	217.7	12.9	5.6	70.1
116	■	10	48	26	22	582	1277	4911	3.690	344.4	71.8	94.6	26.2	100.8	30.1	5.9	206.1	23.5	5.4	73.1
117	■	15	48	66	22	1456	1277	7766	3.690	433.0	68.2	88.6	23.9	96.7	36.0	4.4	316.1	34.9	6.9	56.9
118	■	19	48	105	22	2330	1277	9823	3.690	487.0	66.3	85.1	22.4	94.4	43.3	4.2	367.0	41.1	6.7	59.0
119	■	19	127	18	129	2330	2447	9823	4.648	487.0	59.2	69.3	15.5	86.4	42.9	10.1	513.7	18.7	9.4	41.7
120	■	27	127	36	129	4660	2447	13892	4.648	579.2	58.1	66.0	13.9	86.4	35.0	5.8	321.3	35.5	7.2	54.5
121	■	43	127	90	129	11649	2447	21965	4.648	728.3	57.2	64.0	12.8	83.7	42.4	4.5	444.2	43.6	8.2	47.7
122	■	54	127	144	129	18639	2447	27784	4.648	819.1	56.7	62.5	12.0	83.2	46.3	3.9	484.2	49.5	8.2	47.9
123	■	14	95	16	72	1165	1825	6946	4.648	409.5	64.0	81.4	21.0	90.3	27.4	6.8	223.6	24.3	6.4	61.3
124	■	19	95	32	72	2330	1825	9823	4.648	487.0	61.8	76.1	18.7	89.3	30.9	5.4	268.6	33.9	6.8	57.5
125	■	30	95	81	72	5825	1825	15531	4.648	612.4	59.7	71.3	16.5	86.4	41.3	4.6	377.9	39.4	7.2	54.6
126	■	38	95	130	72	9320	1825	19646	4.648	688.8	59.3	70.1	15.9	86.4	39.8	3.5	367.8	48.1	7.3	54.1
127	■	9	60	16	29	466	1154	4393	4.648	325.7	70.8	93.3	25.7	99.6	24.0	6.0	165.9	14.0	5.4	72.5
128	■	12	60	32	29	932	1154	6213	4.648	387.3	68.8	90.5	24.7	97.0	29.8	5.2	221.8	23.8	5.9	67.1
129	■	19	60	81	29	2330	1154	9823	4.648	487.0	65.7	85.1	22.5	92.2	35.0	3.9	305.5	38.6	6.9	57.3

No.	Ref.	V <sub>Jet</sub> [m/s]	V <sub>Air</sub> [m/s]	q	We <sub>Air</sub>	We <sub>Jet</sub>	Re <sub>Air</sub>	Re <sub>Jet</sub>	Oh <sub>Air</sub> x10 <sup>3</sup>	Oh <sub>Jet</sub> x10 <sup>3</sup>	D10 [μm]	D32 [μm]	STD [μm]	MMD	L <sub>b</sub> /D <sub>N</sub>	t <sub>b</sub> /t*	A <sub>p</sub> /A <sub>D</sub>	θ <sub>P</sub> [°]	W <sub>p</sub> /D <sub>N</sub>	t <sub>s</sub> /D <sub>N</sub> x10 <sup>3</sup>
130	■	24	60	130	29	3728	1154	12425	4.648	547.7	64.1	81.8	21.1	90.3	38.7	3.4	330.5	46.5	6.7	58.6
131	■	7	48	16	18	291	925	3473	4.648	289.6	72.5	95.0	26.3	101.4	31.7	8.0	200.2	11.8	5.0	79.1
132	■	10	48	31	18	582	925	4911	4.648	344.4	70.9	94.3	26.2	99.6	31.1	5.6	228.0	23.0	5.8	68.3
133	■	15	48	79	18	1456	925	7766	4.648	433.0	68.7	91.4	25.1	96.7	33.3	3.8	260.7	38.2	6.1	63.9
134	■	19	48	126	18	2330	925	9823	4.648	487.0	67.3	88.1	23.7	94.4	38.4	3.4	311.4	46.1	6.4	61.6
135	▲	18	88	10	217	2113	9632	9356	1.531	475.3	57.5	64.8	13.3	83.7	36.9	11.8	352.4	29.3	7.5	52.4
136	▲	26	88	19	217	4227	9632	13232	1.531	565.2	57.4	64.5	13.1	83.7	41.7	9.5	428.6	32.6	8.1	48.6
137	▲	41	88	49	217	10567	9632	20921	1.531	710.7	56.7	63.3	12.6	83.2	42.0	6.0	434.6	44.8	8.1	48.3
138	▲	52	88	78	217	16908	9632	26464	1.531	799.3	56.3	62.3	12.0	82.8	44.6	5.1	442.7	52.2	7.8	50.4
139	▲	14	68	9	129	1165	7432	6947	1.531	409.5	60.2	71.9	16.9	86.4	29.7	9.9	245.2	27.2	6.5	60.5
140	▲	19	68	18	129	2330	7432	9824	1.531	487.0	59.0	69.3	15.6	86.4	33.3	7.8	306.4	36.5	7.2	54.3
141	▲	30	68	45	129	5825	7432	15533	1.531	612.4	58.2	67.2	14.6	86.3	40.3	6.0	383.4	47.4	7.5	52.6
142	▲	38	68	72	129	9320	7432	19648	1.531	688.7	57.3	64.6	13.3	83.3	45.0	5.3	458.9	53.9	8.0	49.1
143	▲	9	44	9	55	466	4823	4394	1.531	325.7	61.6	76.3	19.0	86.4	29.8	10.2	207.9	21.5	5.5	71.6
144	▲	12	44	17	55	932	4823	6213	1.531	387.3	61.5	75.3	18.5	88.0	29.3	7.1	223.1	35.0	6.0	65.6
145	▲	19	44	43	55	2330	4823	9824	1.531	487.0	59.7	71.5	16.7	86.4	39.4	6.0	335.6	47.2	6.7	58.7
146	▲	24	44	68	55	3728	4823	12427	1.531	547.7	59.2	69.5	15.8	86.4	44.1	5.3	412.1	52.2	7.3	53.5
147	▲	7	35	9	34	291	3813	3473	1.531	289.6	60.9	74.1	18.0	86.4	27.1	9.3	168.2	19.0	4.9	80.5
148	▲	10	35	17	34	583	3813	4912	1.531	344.4	61.9	76.5	19.1	88.0	30.6	7.4	219.1	30.2	5.6	69.9
149	▲	15	35	43	34	1456	3813	7767	1.531	433.0	60.2	73.0	17.5	86.4	34.2	5.2	254.4	47.8	5.8	67.2
150	▲	19	35	68	34	2330	3813	9824	1.531	487.0	59.9	71.7	16.9	86.4	42.4	5.1	361.9	51.8	6.7	58.7
153	▲	43	93	77	152	11650	4520	21968	2.727	728.2	57.5	64.9	13.3	85.7	42.8	4.9	474.2	37.3	8.7	45.2
154	▲	54	93	123	152	18641	4520	27787	2.727	819.0	57.1	63.8	12.8	83.7	46.1	4.2	535.2	42.8	9.1	43.1
155	▲	14	68	14	82	1165	3327	6947	2.727	409.5	64.3	81.8	21.2	90.3	29.2	7.8	271.5	22.1	7.3	53.7
156	▲	19	68	28	82	2330	3327	9824	2.727	487.0	62.2	77.0	19.0	90.2	32.0	6.0	300.7	30.3	7.4	53.3
157	▲	30	68	71	82	5825	3327	15533	2.727	612.4	60.1	72.4	17.0	86.4	40.6	4.8	405.1	39.9	7.8	50.1
158	▲	38	68	113	82	9320	3327	19648	2.727	688.7	59.2	69.9	15.9	86.4	42.4	4.0	424.6	47.4	7.9	49.9
159	▲	9	44	14	33	466	2122	4394	2.727	325.7	70.7	92.8	25.4	99.6	25.8	6.9	195.4	19.5	5.9	66.0
160	▲	12	44	28	33	932	2122	6213	2.727	387.3	68.2	89.5	24.2	96.3	30.8	5.8	248.8	28.7	6.3	62.0

No.	Ref.	V <sub>Jet</sub> [m/s]	V <sub>Air</sub> [m/s]	q	We <sub>Air</sub>	We <sub>Jet</sub>	Re <sub>Air</sub>	Re <sub>Jet</sub>	Oh <sub>Air</sub> x10 <sup>3</sup>	Oh <sub>Jet</sub> x10 <sup>3</sup>	D10 [μm]	D32 [μm]	STD [μm]	MMD	L <sub>b</sub> /D <sub>N</sub>	t <sub>b</sub> /t*	A <sub>p</sub> /A <sub>D</sub>	θ <sub>P</sub> [°]	W <sub>p</sub> /D <sub>N</sub>	t <sub>s</sub> /D <sub>N</sub> x10 <sup>3</sup>
161	▲	19	44	70	33	2330	2122	9824	2.727	487.0	64.7	82.5	21.4	90.7	36.7	4.4	286.9	39.9	6.1	64.0
162	▲	24	44	111	33	3728	2122	12427	2.727	547.7	63.4	80.0	20.4	90.3	39.7	3.8	353.7	47.0	7.0	56.1
163	▲	7	34	14	21	291	1678	3473	2.727	289.6	72.1	94.8	26.2	100.8	29.0	7.8	179.9	13.9	4.9	80.6
164	▲	10	34	28	21	583	1678	4912	2.727	344.4	70.1	92.8	25.6	99.1	29.5	5.6	206.9	26.0	5.5	71.4
165	▲	15	34	70	21	1456	1678	7767	2.727	433.0	67.7	88.5	23.8	94.4	34.5	4.1	255.1	36.0	5.8	67.7
166	▲	19	34	111	21	2330	1678	9824	2.727	487.0	65.5	84.2	22.1	92.2	38.3	3.6	283.0	44.2	5.8	67.6
167	▲	14	68	17	67	1165	2384	6947	3.4342	409.5	64.8	83.1	21.7	90.7	31.3	7.5	290.4	18.3	7.3	53.9
168	▲	19	68	35	67	2330	2384	9824	3.4342	487.0	62.4	78.0	19.6	89.7	32.2	5.5	284.8	29.1	7.0	56.5
169	▲	30	68	87	67	5825	2384	15533	3.4342	612.4	60.4	72.8	17.2	86.4	41.2	4.4	411.8	37.4	7.8	50.0
170	▲	38	68	139	67	9320	2384	19648	3.4342	688.7	59.3	70.3	16.0	86.4	41.5	3.5	399.0	48.7	7.6	52.0
171	▲	9	44	17	28	466	1534	4394	3.4342	325.7	69.6	90.8	24.7	99.1	28.2	6.9	232.1	14.7	6.5	60.7
172	▲	12	44	34	28	932	1534	6213	3.4342	387.3	67.7	88.2	23.7	94.4	28.4	4.9	221.5	26.0	6.1	64.2
173	▲	19	44	84	28	2330	1534	9824	3.4342	487.0	65.1	83.5	21.8	90.7	37.2	4.1	331.4	36.3	7.0	56.1
174	▲	24	44	134	28	3728	1534	12427	3.4342	547.7	64.3	81.5	21.0	90.3	37.9	3.3	320.7	46.0	6.6	59.1
175	▲	7	35	17	18	291	1223	3473	3.4342	289.6	71.4	93.9	25.9	100.8	25.7	6.3	159.1	12.9	4.9	80.9
176	▲	10	35	33	18	583	1223	4912	3.4342	344.4	70.1	92.7	25.6	99.1	31.8	5.5	229.0	23.2	5.7	69.4
177	▲	15	35	83	18	1456	1223	7767	3.4342	433.0	68.5	90.5	24.7	96.5	32.8	3.6	250.0	37.9	6.0	65.5
178	▲	19	35	132	18	2330	1223	9824	3.4342	487.0	67.2	87.5	23.4	94.4	38.4	3.3	312.2	43.5	6.4	61.5
180	●	27	81	30	157	4660	5356	13895	2.3362	579.1	59.3	69.2	15.4	86.4	48.5	8.9	601.7	20.7	9.7	40.3
181	●	43	81	74	157	11651	5356	21970	2.3362	728.2	58.4	66.9	14.3	86.4	52.8	6.1	721.6	30.9	10.7	36.6
182	●	54	81	119	157	18642	5356	27790	2.3362	819.0	57.6	64.6	13.1	86.3	50.5	4.6	549.1	43.4	8.5	46.0
183	●	14	57	15	78	1165	3787	6947	2.3362	409.5	64.1	80.1	20.3	90.3	38.1	9.9	353.8	18.1	7.3	53.8
184	●	19	57	30	78	2330	3787	9825	2.3362	487.0	61.9	76.2	18.7	89.7	45.1	8.3	465.8	22.7	8.1	48.4
185	●	30	57	74	78	5826	3787	15535	2.3362	612.4	60.5	72.7	17.1	86.4	46.6	5.4	522.7	35.3	8.8	44.6
186	●	38	57	119	78	9321	3787	19650	2.3362	688.7	59.4	69.9	15.8	86.4	45.8	4.2	474.3	46.2	8.1	48.2
187	●	9	36	15	31	466	2395	4394	2.3362	325.7	68.9	88.8	23.9	97.7	33.3	8.6	246.3	14.3	5.8	67.6
188	●	12	36	30	31	932	2395	6214	2.3362	387.3	68.1	87.2	23.2	97.0	37.8	6.9	331.2	24.0	6.9	57.0
189	●	19	36	74	31	2330	2395	9825	2.3362	487.0	65.0	82.0	21.1	92.2	45.0	3.3	439.3	35.2	7.7	51.2
190	●	24	36	119	31	3728	2395	12428	2.3362	547.7	63.5	79.3	20.0	90.3	42.6	2.9	369.6	45.8	6.8	57.6



No.	Ref.	V <sub>Jet</sub> [m/s]	V <sub>Air</sub> [m/s]	q	We <sub>Air</sub>	We <sub>Jet</sub>	Re <sub>Air</sub>	Re <sub>Jet</sub>	Oh <sub>Air</sub> x10 <sup>3</sup>	Oh <sub>Jet</sub> x10 <sup>3</sup>	D10 [μm]	D32 [μm]	STD [μm]	MMD	L <sub>b</sub> /D <sub>N</sub>	t <sub>b</sub> /t*	A <sub>p</sub> /A <sub>D</sub>	θ <sub>P</sub> [°]	W <sub>p</sub> /D <sub>N</sub>	t <sub>s</sub> /D <sub>N</sub> x10 <sup>3</sup>
191	●	7	28	15	20	291	1894	3474	2.3362	289.6	70.3	91.8	25.1	99.6	32.4	2.9	221.9	14.5	5.4	72.9
192	●	10	28	30	20	583	1894	4913	2.3362	344.4	70.2	91.4	24.9	99.6	34.4	2.9	277.5	23.2	6.3	62.0
193	●	15	28	74	20	1456	1894	7767	2.3362	433.0	68.0	87.0	23.1	97.0	40.4	3.0	326.3	35.4	6.4	61.8
194	●	19	28	119	20	2330	1894	9825	2.3362	487.0	66.2	84.0	21.9	94.4	43.0	3.0	342.3	45.5	6.3	62.7
197	○	27	42	113	53	5973	3475	17599	2.0882	582.6	58.2	66.3	14.0	86.4	43.4	4.1	424.1	37.1	7.7	51.2
199	○	12	30	45	26	1195	2457	7870	2.0882	389.6	61.5	74.4	17.8	88.9	35.8	5.3	290.2	28.0	6.4	61.7
200	○	19	30	113	26	2987	2457	12444	2.0882	489.9	60.0	71.4	16.5	86.4	38.3	3.6	350.3	39.5	7.2	54.7
201	○	25	30	181	26	4779	2457	15741	2.0882	551.0	58.7	67.8	14.8	86.4	41.8	3.1	387.1	47.4	7.3	54.0
202	○	5	19	23	11	239	1554	3520	2.0882	260.5	67.1	85.0	22.4	94.4	23.4	4.9	162.9	19.7	5.5	71.9
203	○	8	19	45	11	478	1554	4978	2.0882	309.8	65.5	82.4	21.3	92.3	30.8	4.6	225.9	27.9	5.8	68.2
204	○	12	19	113	11	1195	1554	7870	2.0882	389.6	63.9	79.3	20.0	90.3	35.7	3.3	297.9	38.9	6.6	59.9
205	○	16	19	181	11	1911	1554	9955	2.0882	438.2	62.6	76.9	18.9	90.3	35.4	2.6	283.3	47.7	6.3	62.4
206	○	4	15	23	7	149	1229	2783	2.0882	231.7	68.8	88.3	23.7	97.1	24.9	5.2	141.9	16.7	4.5	87.7
207	○	6	15	45	7	299	1229	3935	2.0882	275.5	67.6	86.4	23.0	94.4	28.9	4.3	198.1	29.2	5.4	73.1
208	○	10	15	113	7	747	1229	6222	2.0882	346.4	66.2	83.6	21.7	94.4	32.2	3.0	232.3	41.3	5.7	69.4
209	○	12	15	181	7	1195	1229	7870	2.0882	389.6	64.8	80.6	20.4	92.2	37.6	2.8	286.2	47.9	6.0	65.6
Min.		4	15	8	7	149	925	2783	1.368	231.7	56.3	62.3	12.0	82.8	22.1	2.6	130.8	11.8	4.1	36.6
Max.		54	128	181	298	23282	12624	34743	4.648	819.1	72.6	95.3	26.4	102.8	54.6	12.0	721.6	53.9	10.7	95.7
Mean		20	60	56	73	3738	3440	11452	2.740	479.7	63.7	78.9	19.7	91.2	35.8	5.5	311.1	33.4	6.6	61.1
STD		11	26	42	63	4335	2446	6507	0.979	135.1	4.4	9.2	4.0	5.0	6.7	2.0	112.4	11.3	1.2	10.7

## Chapter 3 Image Analysis

### 3 Image Analysis

#### 3.1 Image Analysis for Droplet Size

##### 3.1.1 Initial Image Analysis

Open source imaging software ImageJ and Matlab are used to analyze the images. ImageJ is used to perform all the image analysis and export raw data. Matlab is used to organize and analyze the data. First, the images are cropped and rotated so that all the images would have the same coordinate system. The coordinate is set on the center of the nozzle that is positioned 50 pixels from the border of each image. Second, an automated thresholding is used to calculate a particular threshold value for each image, and then this value is used to identify the boundaries of various structures in the spray. Finally, the ImageJ's Analyze Particle feature is used to detect individual formations and droplets. The data produced for each droplet by the software are area, x and y position of the center, perimeter, length of major and minor axis of fitted ellipse and the orientation of the ellipse. The fitted ellipse area is the same area as the particle. The information about the ellipse is then used to approximate the droplet sizes. The effective diameter of the droplet is calculated based on the assumption that the volume of the representative spherical droplet is the same as the volume of the fitted ellipsoid, equation (3.1). This method is also used by Faeth et al. [8].

$$D_{Sphere} = \sqrt[3]{D_{Major}D_{Minor}^2} \quad (3.1)$$

As it can be seen the difficulty lies with setting the correct threshold for the image and the laser light intensity. The sensitivity to the threshold value can be clearly seen from the images in Figure 3.1. The intensity of the laser light sheet has to be high enough so the smaller features and droplets which have lower light intensities become visible. Conversely, the larger features generally reflect the light at higher intensities and can effectively washout the image. This behavior can be seen at the exit of the nozzle for laminar jets in Appendix D. However, the exact value of light intensity is not the only determining factor, since each image has its own signature intensity histogram profile depending on the liquid volume, conditions, shapes, lighting conditions, etc. In order to

address the differences, each image has to be analyzed based on a particular threshold value for that particular image. Triangle threshold algorithm is used to process the images. Various thresholding algorithms are also compared to the triangle algorithm, but it is found that triangle thresholding is best suited for the current dataset. The pixel value histogram for the current data set has a Gaussian distribution with only one peak which is ideal type of intensity histogram for use with triangle thresholding algorithm. Figure 3.1 shows the comparison of different thresholding algorithms. As it can be seen, most of the thresholding algorithms either dilute the image and under-estimate the boundaries or conversely are affected by the background noise and over-estimate the spray region. The more successful thresholding algorithms are the ones that are best suited for use with single intensity distributions, such as mean, triangle, and Huang algorithms. Blaisot [54] has also used a similar technique as described above for thresholding and measuring droplet size in diesel sprays.

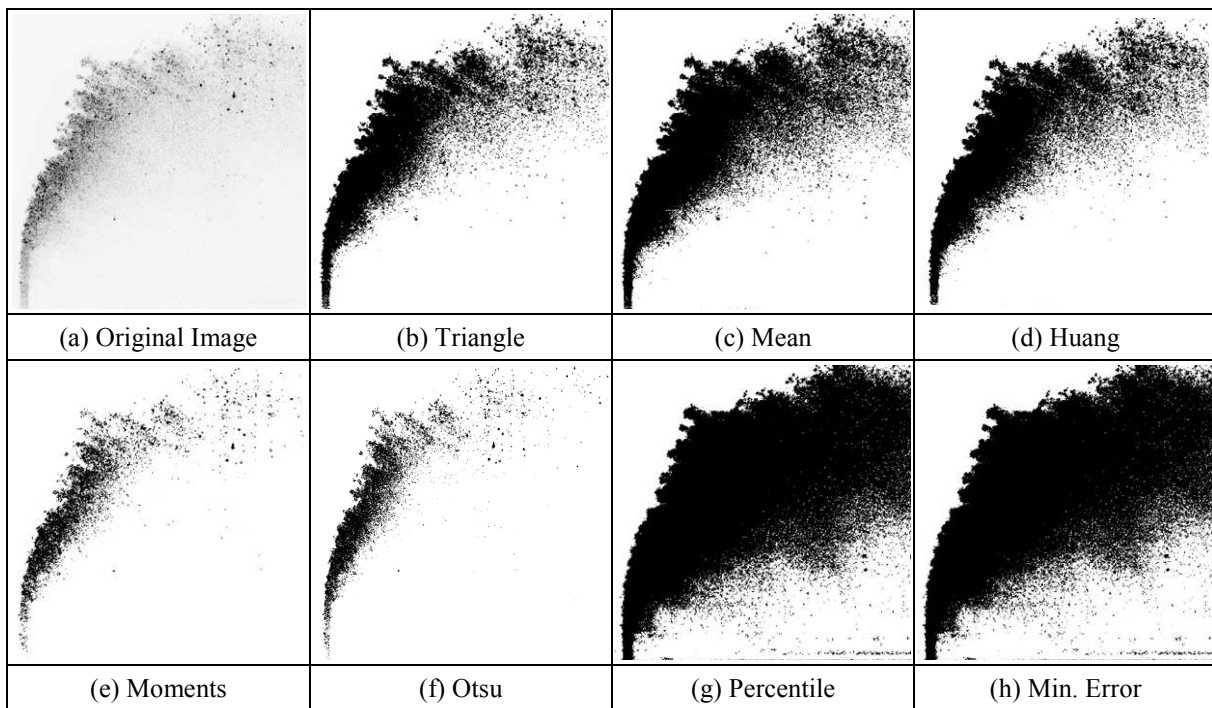


Figure 3.1: Comparison of various thresholding techniques.

The triangle algorithm is originally developed for cell detection in biology [55]. In this method a line is constructed between the maximum of the histogram, point A in Figure 3.2, on the gray level axis and the minimum value, point B, on the gray scale axis where the histogram is significantly larger than zero. Then an iterative procedure is performed by constructing a second line CD that

is perpendicular to line AB. This line CD is moved along the AB, and the threshold value is the pixel value where the value of the maximal length CD coincides with the histogram.

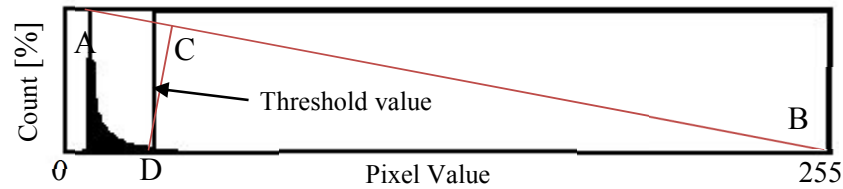


Figure 3.2: Pixel value histogram of typical JICF image and the lines AB and CD display the results of triangle thresholding.

Figure 3.2 shows the histogram for one of the cropped images. It schematically shows the triangle threshold calculations. The next step is to compare the actual grayscale image with the final processed image.

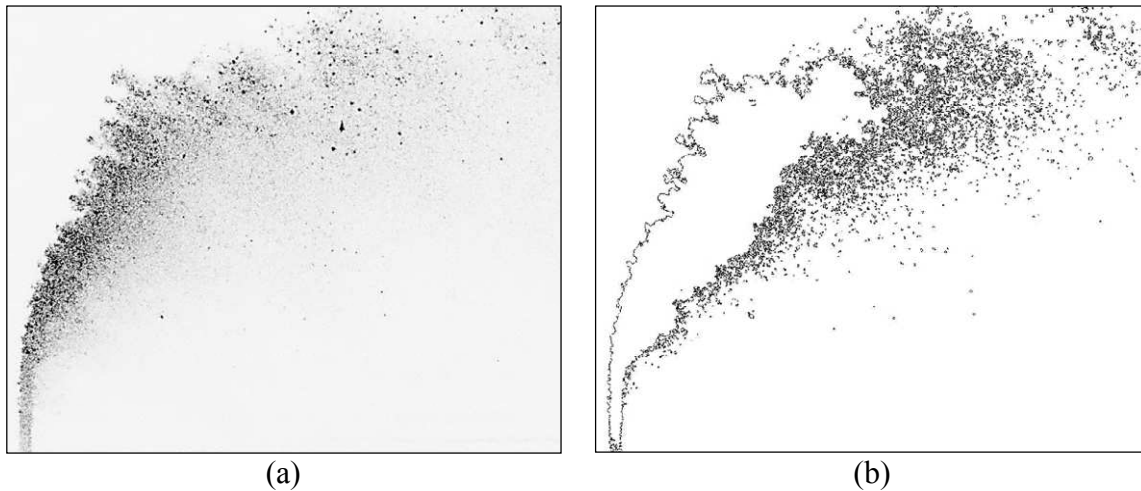


Figure 3.3: (a) A Color-inverted image with laser sheet illumination; (b) Same image after thresholding and particle analysis. Image 216001a, Case 19,  $p=2.1$  bars,  $T=200^{\circ}\text{C}$ ,  $V_{\text{Jet}}=38$  m/s, and  $V_{\text{Air}}=93$  m/s. The resolution of the image is 1 pix=19  $\mu\text{m}$ .

Figure 3.3 (a) shows a color inverted original image before image processing; Figure 3.3 (b) shows the outlines of the plumes, ligaments and droplets for the same image after image processing and particle sizing using ImageJ software. In Figure 3.4, Figure 3.3 (a) and (b) are superimposed for comparison purposes. The macro for the image processing can be found in Appendix A. As it can be seen from Figure 3.3 (b), there are two types of distinct structures present in the image, the main plume area and the drops and ligaments. The plume area is the largest area that is detected by the image processing algorithm. In this area, different structures are present and make the processing

difficult. In this area, the liquid core is still mostly intact and has not fully atomized and depending on the atomization regime there are various different types of structures that are present. Nevertheless, it allows for a clear visualization of the windward and leeward boundary of the spray. In Figure 3.4, there are bright and dark spots in the plume area. The spots appear due to disturbances that are present on the surface and cause scattering of laser light.



Figure 3.4: The original image with the results superimposed. Image 216001a, Case 19,  $p=2$  bars,  $T=200^{\circ}\text{C}$ ,  $V_{\text{Jet}}=38$  m/s, and  $V_{\text{Air}}=93$  m/s.

Figure 3.5 shows the comparison of the shadowgraph, instantaneous laser light sheet image, and time average image for case 55 taken at different times. The shadowgraph image provides a glimpse of the structures that are present in the plume area. The undulations and disturbances on the instantaneous laser light sheet image are different compared to shadowgraph image. The plume area oscillates depending on various parameters and the amplitude of these oscillations increase further downstream of the jet especially for dominantly column breakup regimes. The continually moving interface poses one of the difficulties seen by various researches for determining the trajectories of the jet. The trajectory can be defined based on the peak of these undulations, the inflection points, or the valley positions. These parameters can be difficult to measure and always depend on the methodology used to capture images and most of the time arbitrary in nature. In order to overcome this uncertainty, one of the suggestions that have been made is to use the trajectory along the maximum mass flux of the jet [26, 56]. The method for defining the boundaries of the jet for trajectory calculations is presented in section 3.2.

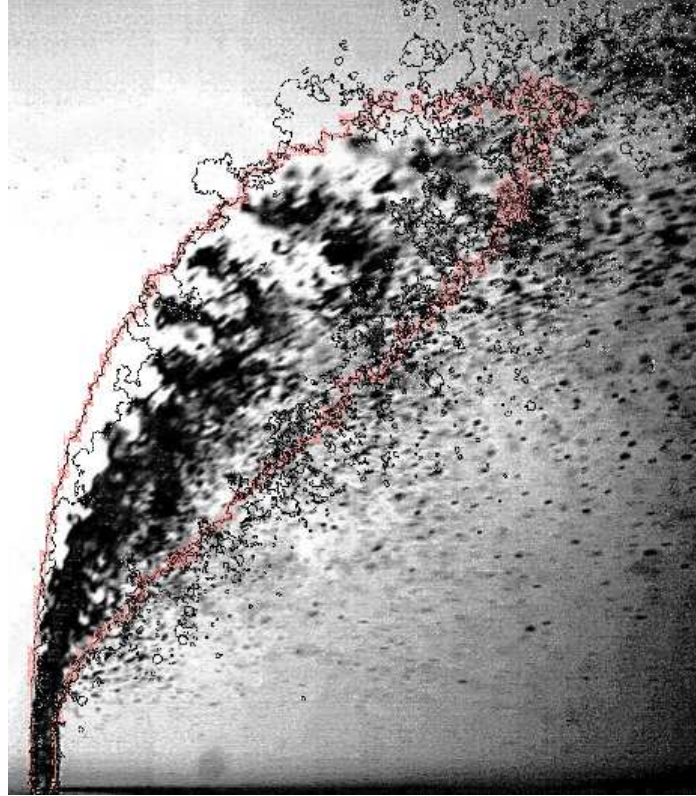


Figure 3.5: Comparison of the shadowgraph, instantaneous laser light sheet image, and time average image. The conditions are the same but the shadowgraph and instantaneous laser light sheet image are at different times. Case 55,  $p=3.8$  bars,  $T=25^{\circ}\text{C}$ ,  $V_{\text{Jet}}=24$  m/s, and  $V_{\text{Air}}=41$  m/s.

### 3.1.2 Data Analysis

The data generated from ImageJ is analyzed using Matlab to calculate the characteristics of the spray such as droplet size. The Matlab code for data analysis can be found in Appendix A. The data is first imported, and then based on the area and perimeter; circularity of each particle is calculated. Circularity is defined as the ratio of the area of the particle with the area of a circle that has the same perimeter as the particle. Circularity is defined as:

$$\text{Circularity} = \frac{4 \pi \text{Area}}{\text{Perimeter}^2} \quad (3.2)$$

Circularity is a good measure for characterizing the general shape of the droplets and its value is between 0 and 1, where 1 represents a perfect circle. With that in mind, when dealing with droplets that are only few pixels in diameter, the circularity can be larger than unity. Figure 3.6 schematically shows the circularity for various geometries [57].

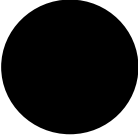
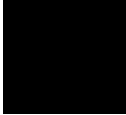
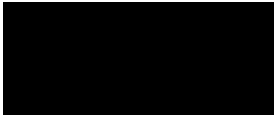
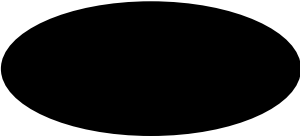
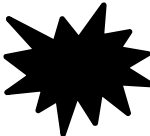
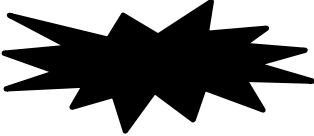
		
Circularity = 1	Circularity = 0.89	Circularity = 0.52
		
Circularity = 0.47	Circularity = 0.47	Circularity = 0.21

Figure 3.6: Circularity of various shapes.

After calculating the circularity, four types of filtering techniques are applied. First, based on circularity, any particles with a circularity value of less than 0.85 are filtered. This filter removes the main plume, secondary and tertiary plume areas in addition to the ligaments and finally the particles and reflections that are close to the wall. This stage is essential to perform in order to remove the particles that are irregular and would change the result of reported diameter sizes. Second, the minimum measurable particle area is set to 5 pixel squared where the droplets with smaller area than this threshold size are filtered. Third, the particles close to the wall are eliminated. The cut-off value is set to 10 pixels away from the walls. Finally, the noise particles, the particles that appear in multiple images, are removed by first sorting the data based on the Y-position. Then if a particle of the same size and circularity is found in the same X-position then this particle is removed from the dataset. After filtering the data, the droplet size is calculated based on equation (3.1). Finally, the global diameters for each case are calculated namely D10, D32, standard deviation, STD, standard error mean, SEM, mass median diameter, MMD, ratio of mass median diameter to sauter mean diameter, MMD/SMD, and finally the minimum and maximum size for each case. The definitions for the above variables are as follow:

$$D_{mn} = \frac{\sum D^m}{\sum D^n} \quad (3.3)$$

$$STD = \sqrt{\frac{\sum (D_i - \bar{D})^2}{n}} \quad (3.4)$$

$$SEM = \frac{STD}{\sqrt{n}} = \frac{\sqrt{\sum (D_i - \bar{D})^2}}{n} \quad (3.5)$$

$$MMD = \text{Median}\{i = 0:n|D_i\} \quad (3.6)$$

As it can be seen the first two filters require further clarification since they can be selected arbitrarily to any value. In contrast, the last two filters are intuitive and do not require further discussion. The first four experiments are chosen as the representative sample to better understand the effect of circularity and minimum filtering size. These cases are analyzed based on the circularity ranging from 0.7 to 0.95 with increments of 0.05, and also based on the minimum area from 3 to 7 with increments of 1. Based on the analysis, it is found that the circularity affects the maximum detectable size in the spray, since larger formations tend to be irregularly shaped and therefore they are readily filtered. These geometries have larger perimeters compared to their areas, and subsequently they also have smaller circularity values.

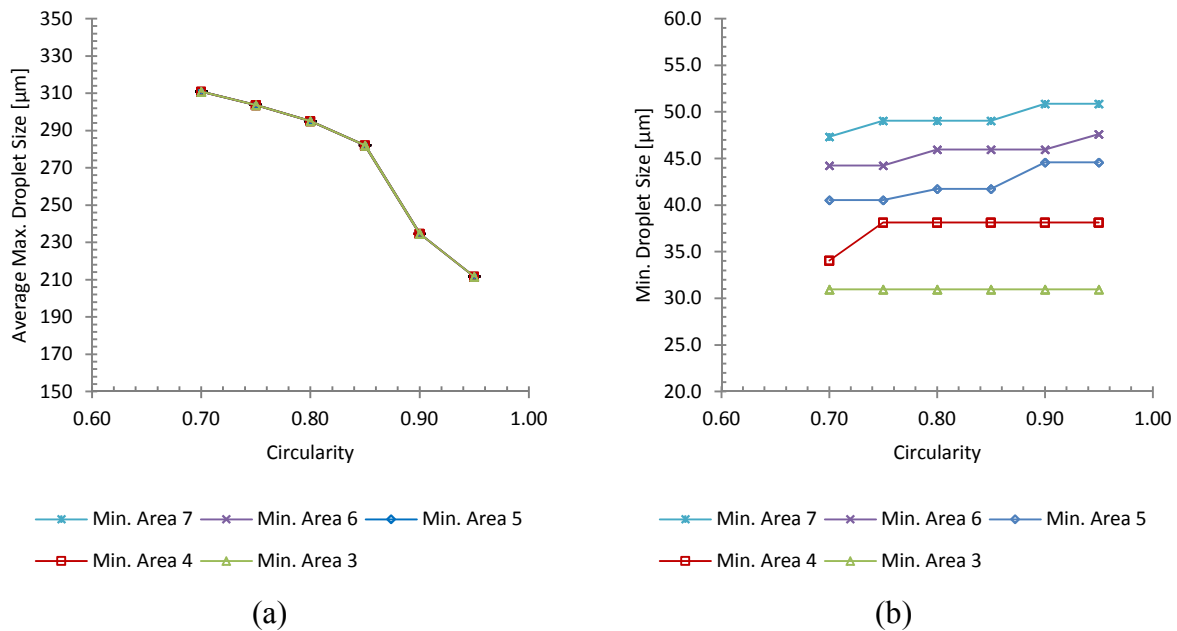


Figure 3.7: (a) Maximum droplet size versus circularity; (b) Minimum droplet size versus circularity.

Figure 3.7 (a) shows the effect of circularity on the maximum droplet size. The maximum droplet size is the average of maximum droplet sizes from multiple images for each case. As it is expected, the minimum cut-off area does not affect the maximum droplet size and only the minimum measurable size. In contrast, increasing circularity beyond 0.85 causes the maximum droplet size to decrease substantially and therefore this value is used as the limit on circularity. As for the minimum area, the previous work namely by Chavez [58, 59] has shown that the lower limit on



the resolution cannot be less than 5 pixel squared otherwise the error on the measurement is significantly increased.

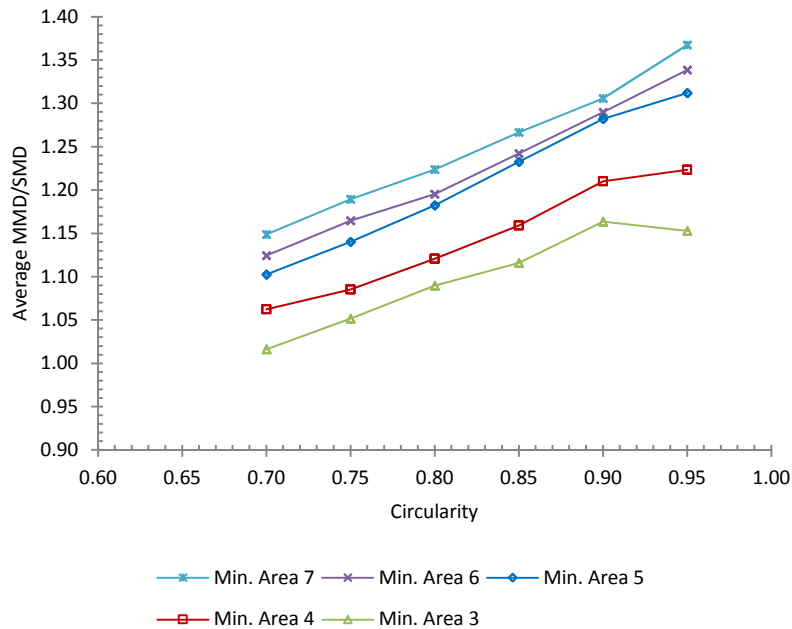


Figure 3.8: Average MMD/SMD versus circularity.

Figure 3.9 shows the various geometries for the droplets smaller than 5 pixel squared. Also, it is important to notice that circularity affects the minimum droplet size as it can be deduced from the geometries in Figure 3.9 and equation (3.2). Figure 3.7 (b) shows the effect of circularity on minimum droplet size. In order to detect smaller droplets, the resolution of the images needs to be increased by either higher resolution camera or by stitching multiple images to create the flow field. Finally, the ratio of the mass median diameter to sauter mean diameter between various set-points is considered. Based on the work by Simmons [60], Faeth [8] and others, the droplet size distribution for turbulent and non-turbulent primary breakup generally follows the universal root normal distribution of Simmons with  $MMD/SMD=1.2$ . Based on the results from Figure 3.8 and presented discussions the appropriate value for the circularity and minimum area threshold are set to 0.85 and 5 respectively for the current experiments.

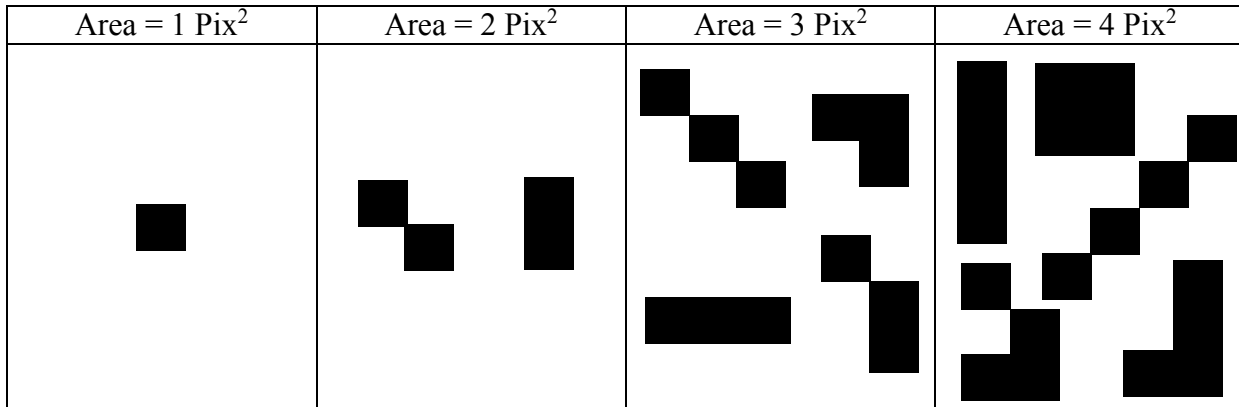


Figure 3.9: Some of the possible shapes for droplets with an area less than 5 pixel squared.

### 3.2 Image Analysis for Trajectory, Breakup Length, Breakup time, and Spray Width

Similar to the droplet size measurement, open source imaging software ImageJ and Matlab is extensively used to analyze the images. ImageJ is used to perform all the image analysis and export raw data; Matlab is used to organize and analyze the data. First, the images are cropped and rotated so that all the images would have the same coordinate system. The coordinate is set on the center of the nozzle which is positioned 50 pixels from the border of each image. Second, a mean grayscale image is created by averaging all the images for each case and creating a time average image of the spray. Third, the same triangle thresholding is used to calculate the individual threshold value for mean image, and then this value is used to identify the boundaries of the plume area.

The sample size is of great importance when the image analysis are performed on the mean images. It goes without emphasis that the larger the initial sample size the more reliable the final outcome becomes. Figure 3.10 compares the effect of sample size on the mean images. A quick visual inspection shows that the mean image changes based on the sample size but the changes becomes less apparent between mean images for 200, 250, and 300 images. The greyscale value of multiple reference points at different locations are compared between different mean images to see the effect of sample size on the mean image. Based on this comparison it is found that minimum of 250 images are required to achieve reliable mean image.

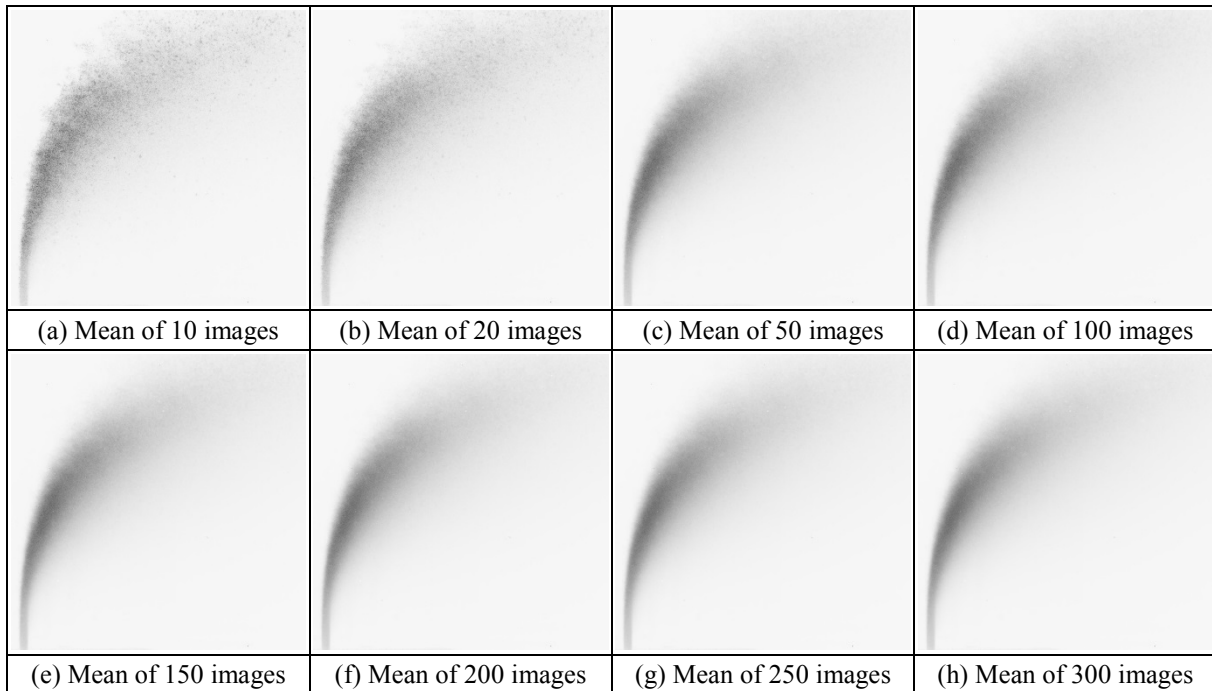


Figure 3.10: Effect of sample size on mean image. The images are color inverted for ease of comparison.

Once again the difficulty lies with setting the correct threshold value for the image; this can be clearly seen from the images in Figure 3.11. Various thresholding algorithms are compared and it is found that triangle thresholding is best suited and provides the most accurate results. Most of the thresholding algorithms either dilute the image and under-estimate the boundaries or conversely are affected by the background noise and over-estimate the spray region. The windward trajectory is less affected by the thresholding algorithm closer to the nozzle exit. On the other hand, the lee-ward trajectory is very sensitive to threshold value. This is also evident in literature where there are limited number of correlations for this trajectory. As it can be seen, the threshold value can affect the final results and consequently it is best to define the trajectory based on other variables such as mass flux. Mass flux is proportional with the light intensity. However, it is not necessary to determine the exact value of the mass flux since the maximum light intensity in each row of the image can be used as an indicator for finding the mass flux trajectory.

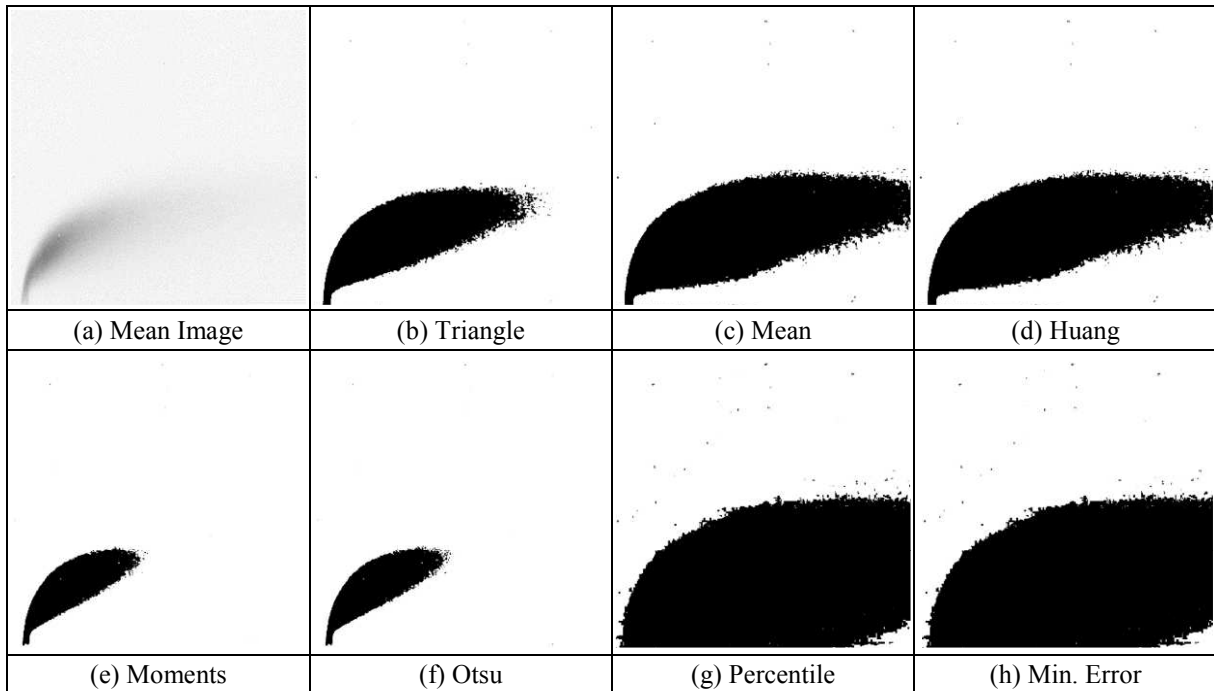


Figure 3.11: Comparison of various thresholding techniques on mean image.

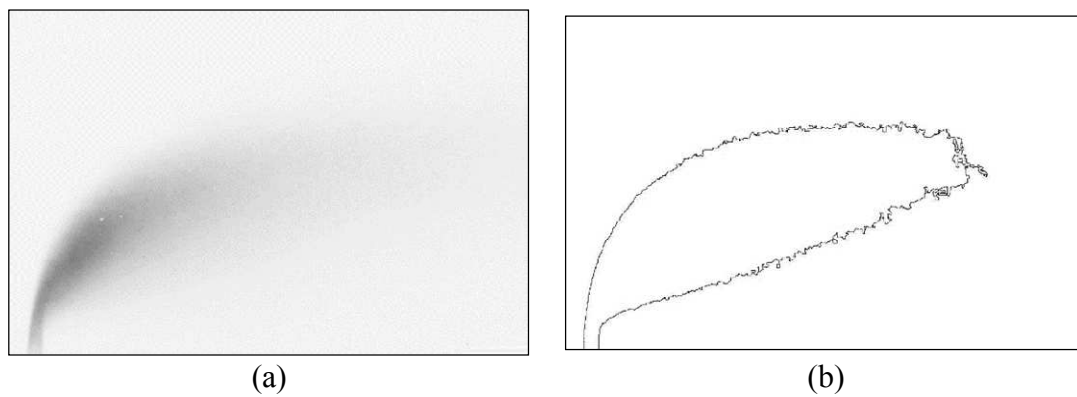


Figure 3.12: (a) Mean image; (b) Same image after thresholding and particle analysis.

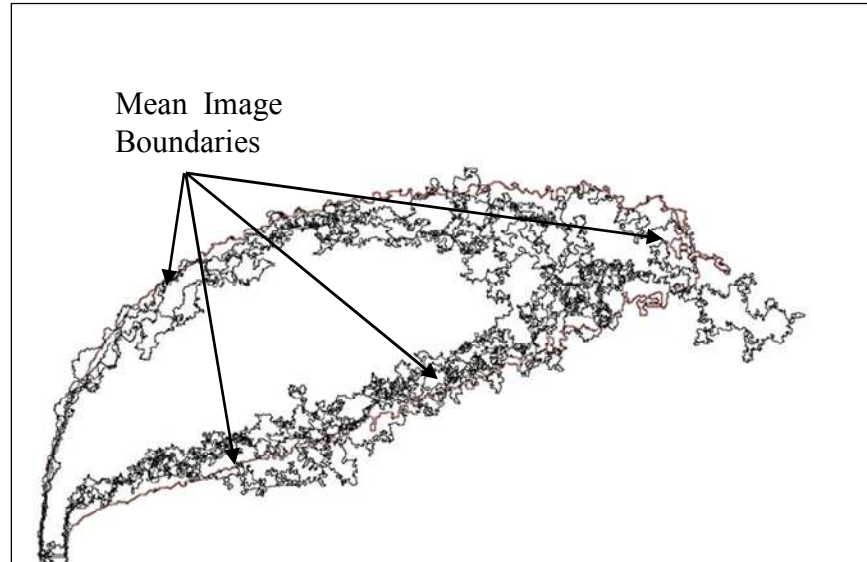


Figure 3.13: Mean image boundaries, red outline based on Triangle threshold along with few of the plume areas superimposed.

Figure 3.12 (a) shows the image of the color inverted mean image before image processing; Figure 3.12 (b) shows the outlines of the main plume area. In Figure 3.13, the outlines of the mean image plume area (red outlines) is compared to few of the actual plume areas by superimposing them. The macro for the image processing can be found in Appendix A. It is difficult to solely depend on this image to justify the accuracy of the measurement, and therefore the data from wind-ward and lee-ward boundaries of 360 images were compared to the mean image boundaries, Figure 3.14. The lower boundary, lee-ward trajectory, is very unstable and there are large undulations as it can also be seen from Figure 3.13. However the approximation of this edge based on the mean image analysis seems to be a straight line that is offset by the neck of the jet. The upper boundary, windward trajectory, is stable at the jet exit and as the jet penetrates into the crossflow it exhibits increasing instability. This can also be seen in Figure 3.14, where the spread of data across the mean image trajectory increases. The windward trajectory can be best approximated with logarithmic function similar to the correlation suggested by Inamura [11].

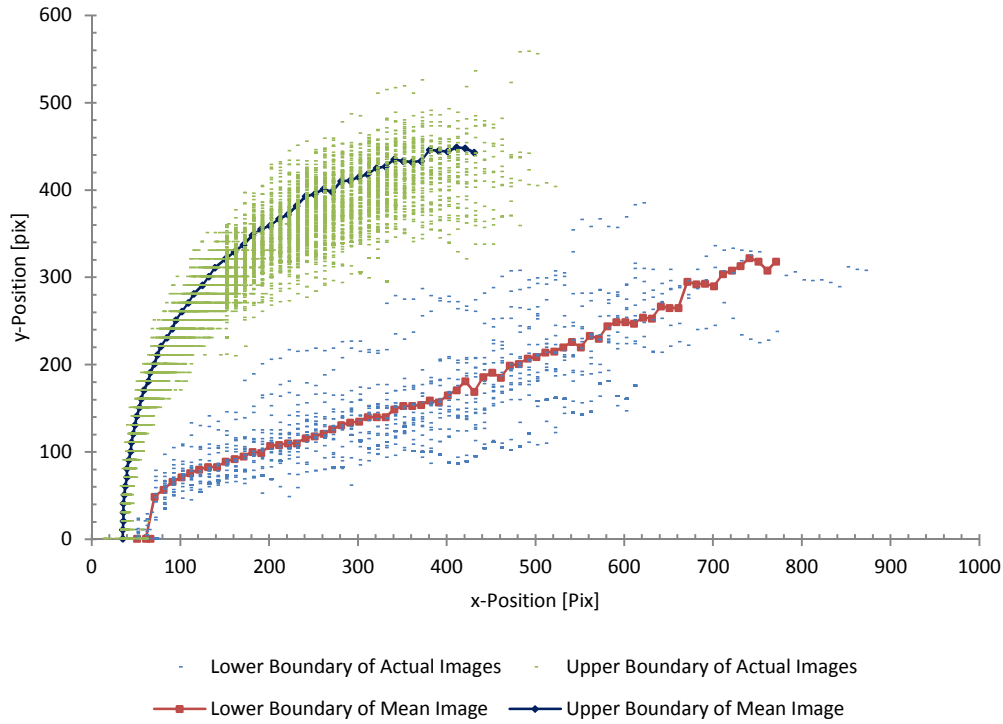


Figure 3.14: Comparison of mean image trajectory with trajectory of individual images.

Beyond the trajectory information collected from the mean image, average plume width, breakup time and length can also be obtained. Breakup time and length are well established parameters in spray analysis. In this study, breakup length is defined based on the breakup point. Breakup point is the farthest point downstream of the nozzle on the boundary of the mean image plume. Breakup length is then defined as the linear distance between the center of nozzle exit and breakup point. Breakup time is defined as the time that it takes for the jet to lose its momentum in the direction of jet and is calculated based on the jet-wise distance between the breakup point and the initial jet velocity. Finally the average plume width is defined as the ratio of mean image plume area to breakup length. The average plume width is a parameter that has not been studied extensively. There is a reference to the cross-sectional area by Wu et al. [10], which is the area perpendicular to the plume area in this study. They related normalized cross-sectional area to momentum flux ratio, given by the following equation:

$$A/A_j = 121\bar{q}^{0.34} \left(\frac{x}{d}\right)^{0.52} \quad (3.7)$$

## Chapter 4 Jet Trajectory

### 4 Jet Trajectory

#### 4.1 Jet Trajectory Correlations

In this chapter, trajectory of liquid jet in crossflow is discussed. First, the method for evaluating the trajectory is briefly described. Second, correlations for the center-line, wind-ward, and lee-ward trajectories are derived. Finally, effects of some parameters, including temperature, nozzle diameter, momentum flux ratio and Weber numbers, are described. The method for finding the boundaries are based on the discussion provided in section 3.2 on image analysis. In brief, the obtained images are first time-averaged followed by triangle thresholding for improving the boundary detection. The spray center, windward, and leeward trajectories are calculated using an automated method presented in Appendix A. The algorithm scans the image to find the highest intensity and the two boundaries in each row of the image. The light intensity is then used as the parameter that is directly proportional to the mass flux in order to identify the centerline of the spray.

The data points close to the nozzle exit and breakup point are filtered in order to improve the certainty of the correlations, especially for the wind-ward and lee-ward trajectories. However, the filtering is for different reasons. The breakup point is defined as the furthest point away from the nozzle exit on the boundaries of the spray plume. The plume area does not extend in the direction of the flow and is only limited to the dense regions of the spray where the light intensity is significant. Therefore, the wind-ward and lee-ward trajectories determined based on the plume area do not represent the actual spray trajectory. This behavior is displayed in Figure 3.14. The accuracy of the correlations improve significantly if the data points closer to the breakup point are filtered. The correlations provided are only valid for up to 90% of breakup point. This can also be seen in Figure 4.2 where the data diverges closer to the breakup point for all the three trajectories. Filtering these points does not interfere with the overall trajectory of the spray since the spray is almost completely formed within few nozzle diameters beyond the breakup point and will follow the crossflow air. As for the points closer to the nozzle exit, they are eliminated for two reasons. First, the jet does not bend in the direction of the crossflow immediately for the cases with larger

momentum flux ratios. Consequently more complex mathematical expression is required to also include these points in the correlations. One of the aims of this study is to have correlations that also help with understanding of the behavior and, therefore, it is beneficial to have a simple form for the correlation. Second, in some cases the jet does not inhibit significant disturbances on its surface at the nozzle exit and consequently it is difficult to detect the jet boundaries close to the nozzle exit. Therefore, the correlations are only valid from two nozzle diameters downstream of the nozzle exit.

Three different correlations are presented below: (i) the centerline trajectory, where most of the liquid mass is present, equation (4.1); (ii) the windward trajectory, equation (4.3); and (iii) the leeward trajectory, equation (4.5). The coefficient of determination for these correlations are 0.95, 0.94 and 0.89, respectively and the chosen variables for all the correlations are significant based on 95% confidence criterion. The standard errors for the correlations are 0.10, 0.10 and 0.22, respectively. Figure 4.1 shows the data fit to the correlations. In order to use the same coordinate system for all three correlations, the windward and leeward data are shifted by half nozzle diameter. Alternatively a logarithmic function can be used to represent the data for the windward and centerline trajectories, similar to the ones suggested by Jeng et al., equation (1.17), and linear for leeward trajectory.

$$\begin{aligned}\frac{y_{cl}}{D_N} &= 2.65 \left(\frac{x}{D_N}\right)^{0.39} We_{Air}^{-0.38} We_{Jet}^{0.65} Re_{Air}^{0.22} Re_{Jet}^{-0.47} \\ &= 2.65 \left(\frac{x}{D_N}\right)^{0.39} We_{Air}^{-0.28} We_{Jet}^{0.42} Oh_{Air}^{-0.22} Oh_{Jet}^{0.47} \\ &= 2.65 \left(\frac{x}{D_N}\right)^{0.39} q^{0.42} We_{Air}^{0.15} Oh_{Air}^{-0.22} Oh_{Jet}^{0.47}\end{aligned}\quad (4.1)$$

$$y_{cl} = 2.65x^{0.39} D_N^{0.63} V_{Air}^{-0.56} V_{Jet}^{0.84} \rho_{Air}^{-0.17} \rho_{Jet}^{0.19} \mu_{Air}^{-0.22} \mu_{Jet}^{0.47} \sigma^{-0.27} \quad (4.2)$$

$$\begin{aligned}\frac{y_{ww}}{D_N} &= 13.31 \left(\frac{x}{D_N} + 0.5\right)^{0.27} We_{Air}^{-0.35} We_{Jet}^{0.72} Re_{Air}^{0.20} Re_{Jet}^{-0.65} \\ &= 13.31 \left(\frac{x}{D_N} + 0.5\right)^{0.27} We_{Air}^{-0.25} We_{Jet}^{0.40} Oh_{Air}^{-0.20} Oh_{Jet}^{0.65} \\ &= 13.31 \left(\frac{x}{D_N} + 0.5\right)^{0.27} q^{0.40} We_{Air}^{0.14} Oh_{Air}^{-0.20} Oh_{Jet}^{0.65}\end{aligned}\quad (4.3)$$

$$y_{ww} = 13.31 \left(\frac{x}{D_N} + 0.5\right)^{0.27} D_N^{0.93} V_{Air}^{-0.50} V_{Jet}^{0.80} \rho_{Air}^{-0.35} \rho_{Jet}^{0.08} \mu_{Air}^{-0.20} \mu_{Jet}^{0.65} \sigma^{-0.38} \quad (4.4)$$



$$\begin{aligned}\frac{y_{lw}}{D_N} &= 0.054 \left( \frac{x}{D_N} - 0.5 \right)^{0.49} We_{Air}^{-0.70} We_{Jet}^{0.66} Re_{Air}^{0.42} Re_{Jet}^{-0.17} \\ &= 0.054 \left( \frac{x}{D_N} - 0.5 \right)^{0.49} We_{Air}^{-0.49} We_{Jet}^{0.57} Oh_{Air}^{-0.42} Oh_{Jet}^{0.17}\end{aligned}\quad (4.5)$$

$$\begin{aligned}&= 0.054 \left( \frac{x}{D_N} - 0.5 \right)^{0.49} q^{0.57} We_{Air}^{0.08} Oh_{Air}^{-0.42} Oh_{Jet}^{0.17} \\ y_{lw} &= 0.054 \left( \frac{x}{D_N} - 0.5 \right)^{0.49} D_N^{1.21} V_{Air}^{-0.98} V_{Jet}^{1.14} \rho_{Air}^{-0.28} \rho_{Jet}^{0.49} \mu_{Air}^{-0.42} \mu_{Jet}^{0.17} \sigma^{0.05}\end{aligned}\quad (4.6)$$

Three different forms of the same correlation are provided. The aim is to make the comparisons more intuitive. It is possible to present the correlations in this manner since the momentum flux ratio is the ratio of the two Weber numbers and the Ohnesorge number is the ratio of the square root of Weber number to Reynolds number. Various researchers have suggested that trajectory is not solely dependent on the momentum flux ratio, [52, 28, 29]. By representing the correlations in different forms it is possible to show that in fact it is the two Weber numbers and Reynolds numbers which describe the trajectory instead of the momentum flux ratio alone. Generally, the momentum flux ratio is paired with air Weber number and in some instances it is paired with jet Weber number in order to overcome the shortcomings of just using momentum flux ratio. Based on the above, both approaches are valid and simply display the different methods to set up the experiments. The other parameters that are new to this correlation are the air and jet Ohnesorge numbers and Reynolds numbers. In order to include the viscous effects, either the Reynolds number or Ohnesorge number can be used. It is beneficial to use the Ohnesorge number since it is independent of velocity and only depends on fluid properties and nozzle diameter. Jeng et al. [18] have in fact presented the same principles in a different way in their correlations for higher temperatures, equation (1.17), and pressures, equation (1.18). The viscosity term for the air only appears in the form of temperature difference and the pressure difference in the form of pressure ratio. Later on, Ragucci et al. [21, 22] presented their correlations first in the form of viscosity ratio, equation (1.20), and later on using air Reynolds number, equation (1.21). In both cases the viscosity term is present but it is compared to room conditions, which is arbitrary. It is preferable to use non-dimensionalized numbers since they represent the flow independently without the need for a reference point. The only term that is not present in many of the correlations is the jet Reynolds number. Gopala [61] in his work has shown that the initial condition of the jet and

therefore, jet Reynolds number is important for the breakup point and consequently the trajectory [61].

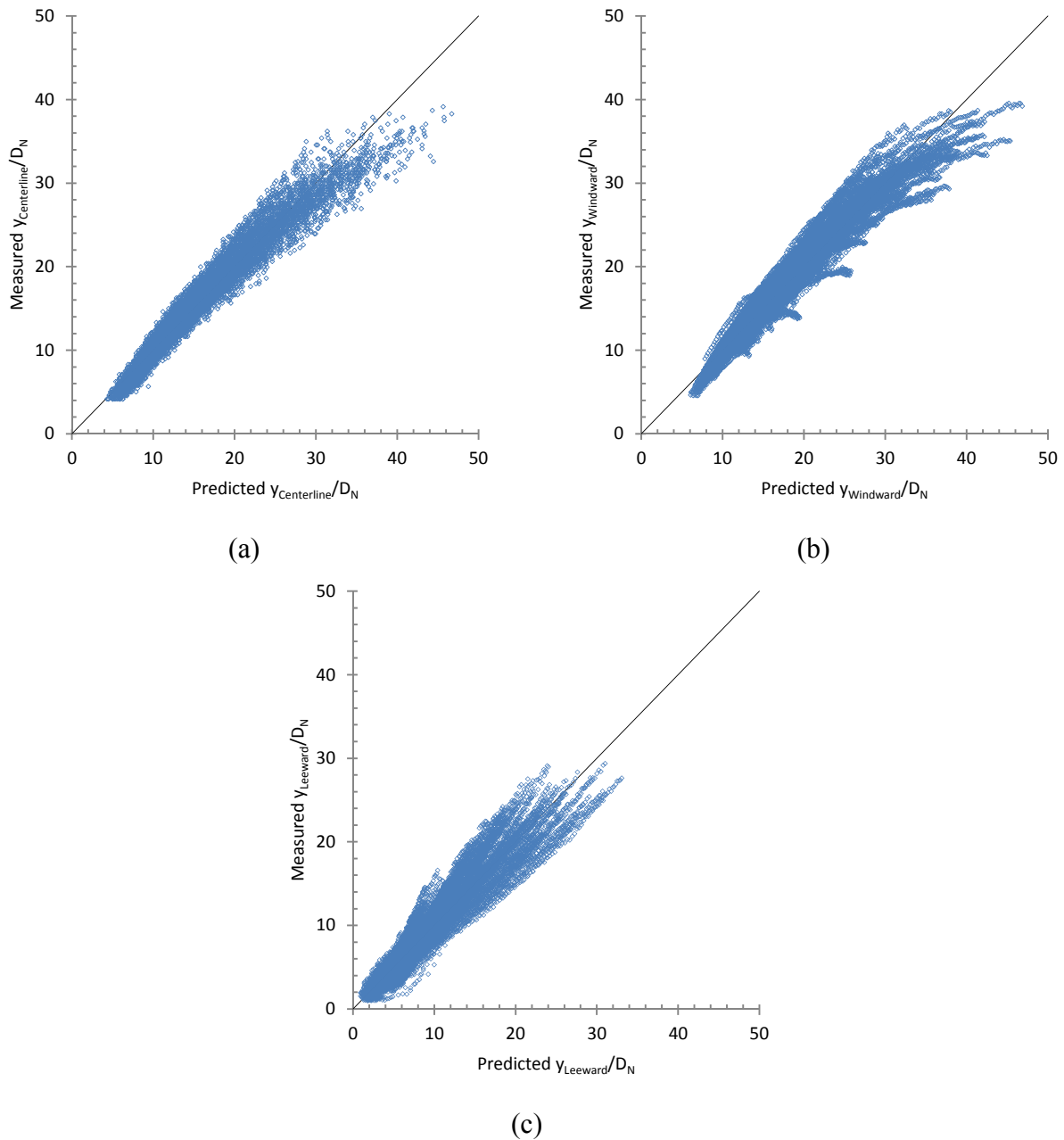


Figure 4.1: Graphical representation of the trajectory correlations; (a) centerline; (b) windward; (c) leeward.

Figure 4.2 compares the presented correlation with the correlations of Tambe et al. [53], Ragucci et al. [28, 29], and Jeng et al. [20]. The air velocity is 68 m/s and jet velocity is 19 m/s for all cases. All the cases are at 3.8 bars and the 572  $\mu\text{m}$  nozzle is used. The only variable that is different between the three cases is temperature. Momentum flux ratios are 19, 28, and 35. Based on earlier studies where the gas viscosity is not considered, the expectation would be that since the density is reducing the penetration would increase. However the penetration along the center line is almost unaffected between the three cases. As it can be seen, it is essential to include a term that includes the gas viscosity. The correlations, particularly those for elevated conditions, that lump crossflow and jet inertia terms into just momentum flux ratio and ignore the effects of gas and liquid viscosities, may be oversimplifying the flow dynamics. The presented correlation seems to best fit the data compared to others but more importantly it includes all the fluid related properties.

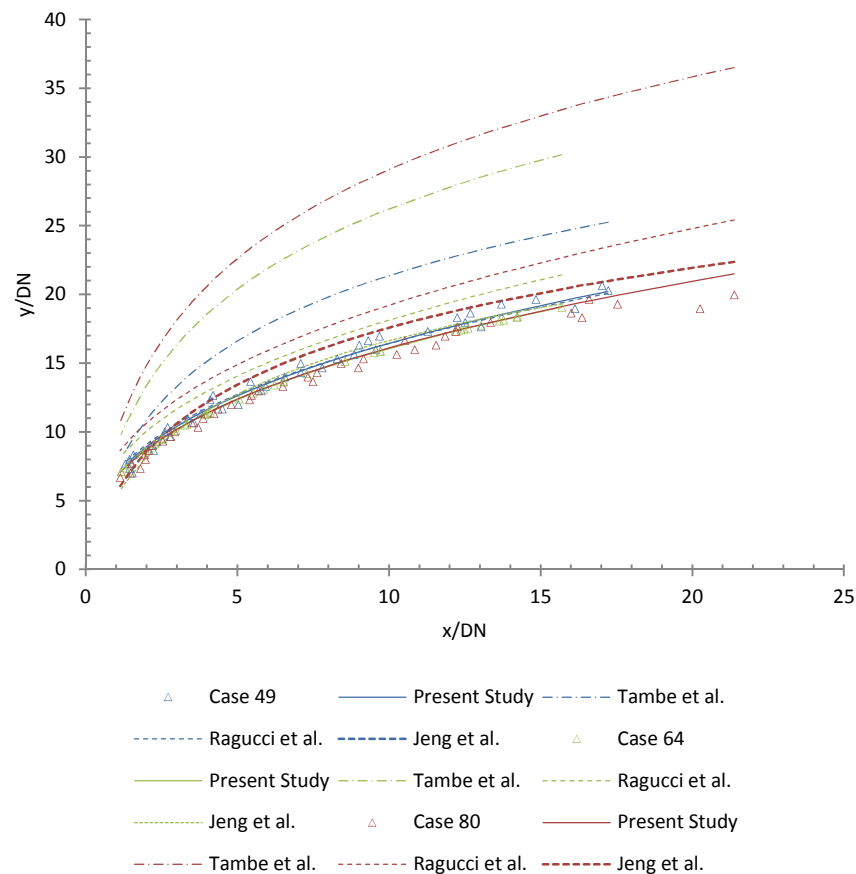
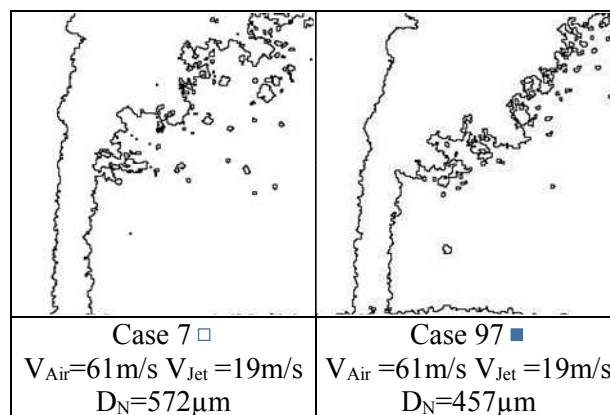


Figure 4.2: Comparison of various centerline trajectory correlations.  $V_{\text{Air}} \approx 68$  m/s and  $V_{\text{Jet}} = 19$  m/s for all cases. Momentum flux ratios are 19, 28, and 35 respectively.

## 4.2 Discussions

### 4.2.1 Effect of Nozzle diameter

Increasing the nozzle diameter increases the penetration of the jet due to increased liquid jet momentum which is expected. More interesting is the changes in the atomization process. The difference between the two nozzles that are used for these experiments is very small, only 115  $\mu\text{m}$ . The nozzle diameters are 457  $\mu\text{m}$  and 572  $\mu\text{m}$ . However, the atomization process is slightly different between the two nozzles. It is not difficult to see in Figure 4.3 that for the smaller nozzle, the lee-side of the jet is fairly different. The neck, straight portion of the jet exiting the nozzle, is shorter. The jet starts to bend much earlier due to differences in inertia and viscous forces. Also, for the smaller nozzle the liquid stretches more into the flow without breakup. This can be explained by comparing the Weber numbers and Ohnesorge numbers. Even though the momentum flux ratio in each row of Figure 4.3 is the same, the Ohnesorge numbers for the smaller nozzle are larger and vice versa for the Weber numbers. Essentially the jet exhibits more viscous behavior compared to the larger nozzle. The formations and ligaments on the lee side of the jet are much longer due to the increased viscous and decreased inertia effects. Based on this observation, it is not difficult to deduce that larger droplets are produced due to increase viscosity effects. This is an important point since increasing the nozzle diameter generally causes the droplet size to increase. This point is discussed more in depth in the section 6.2.1. The viscous effects become even more apparent when comparing each column of Figure 4.3. The air kinematic viscosity is about three times higher for the high temperature cases. The liquid is stretched more into the gas flow Even though the density is reduced.



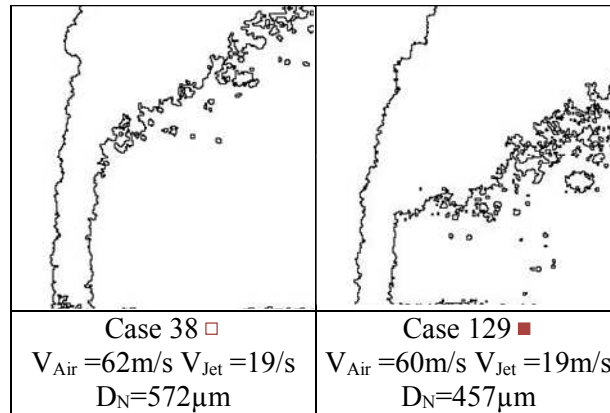


Figure 4.3: Comparison of initial breakup on the lee side of the jet for different nozzle diameters. Table 2.3 summarizes the conditions.

#### 4.2.2 Effect of Temperature

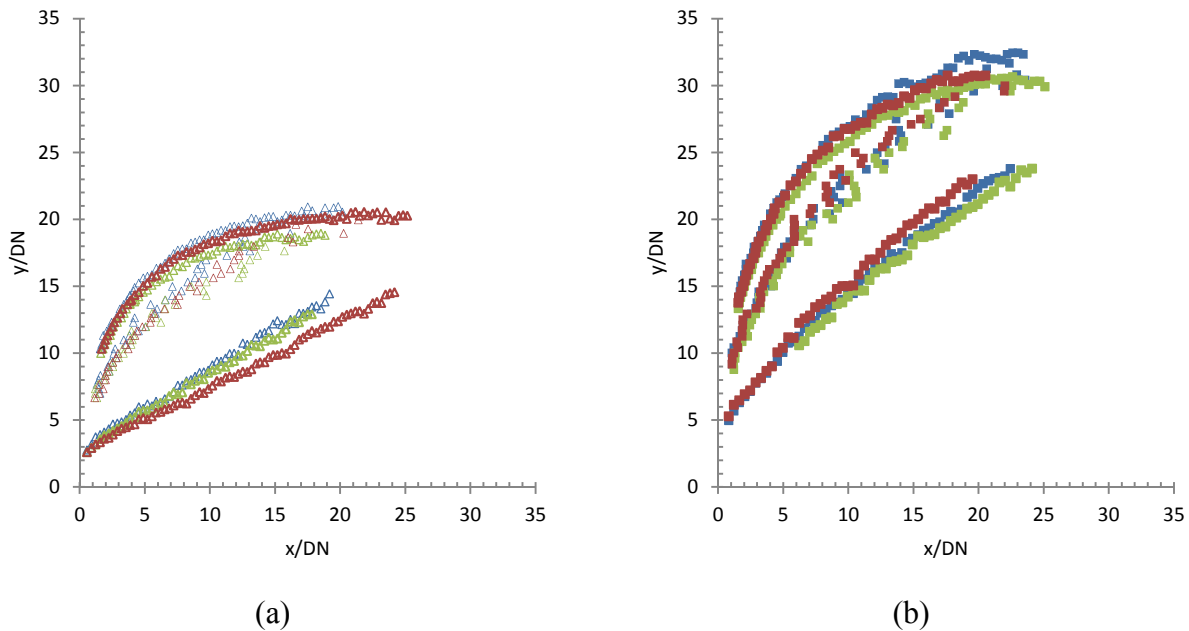


Figure 4.4: Comparison of the three trajectories at three different temperatures, blue, green and red symbols represent cases at 25°C, 200°C, and 300°C respectively. (a) Cases: 49, 64, and 80.  $V_{Air} \approx 65$  m/s and  $V_{Jet} = 19$  m/s for all cases. Momentum flux ratios are 19, 28, and 35 respectively. (b) Cases: 102, 118, and 138.  $V_{Air} \approx 49$  m/s and  $V_{Jet} = 19$  m/s for all cases. Momentum flux ratios are 62, 105, and 126, respectively.

Temperature affects both the density and viscosity of air and consequently atomization. These properties and their influence on droplet size are discussed in more detail in section 6.2.5. In this section, the spray geometry is the discussed. Figure 4.4 (a) shows three trajectories for three

different cases that have the same flow parameters except for gas temperature. These cases are 49, 64, and 80, all are at 3.8 bars and the 572  $\mu\text{m}$  nozzle is used. Similarly, Figure 4.4 (b) shows all three trajectories for cases 102, 118, 138, which are all at 2.1 bars and 457  $\mu\text{m}$  nozzle is used. The centerline trajectory for all cases is very similar and almost indistinguishable from one another considering the air density is reduced considerably. For example, air density for cases 49, 64 and 80 are 4.4  $\text{kg/m}^3$ , 2.8  $\text{kg/m}^3$ , and 2.3  $\text{kg/m}^3$  respectively. Figure 4.5 shows the actual trajectories and spray formation for all of these cases. Essentially as the temperature increases the reduction in gas density is compensated by the increase in gas viscosity and the overall trajectory is relatively unchanged. This has profound effect on droplet size since the droplet size is affected by the trajectory. Generally, as the trajectory increases the droplet size should decrease for as long as the increase in the jet trajectory is due to increases in liquid jet velocity. In chapter 6 the effects of temperature on droplet size is discussed in more detail.

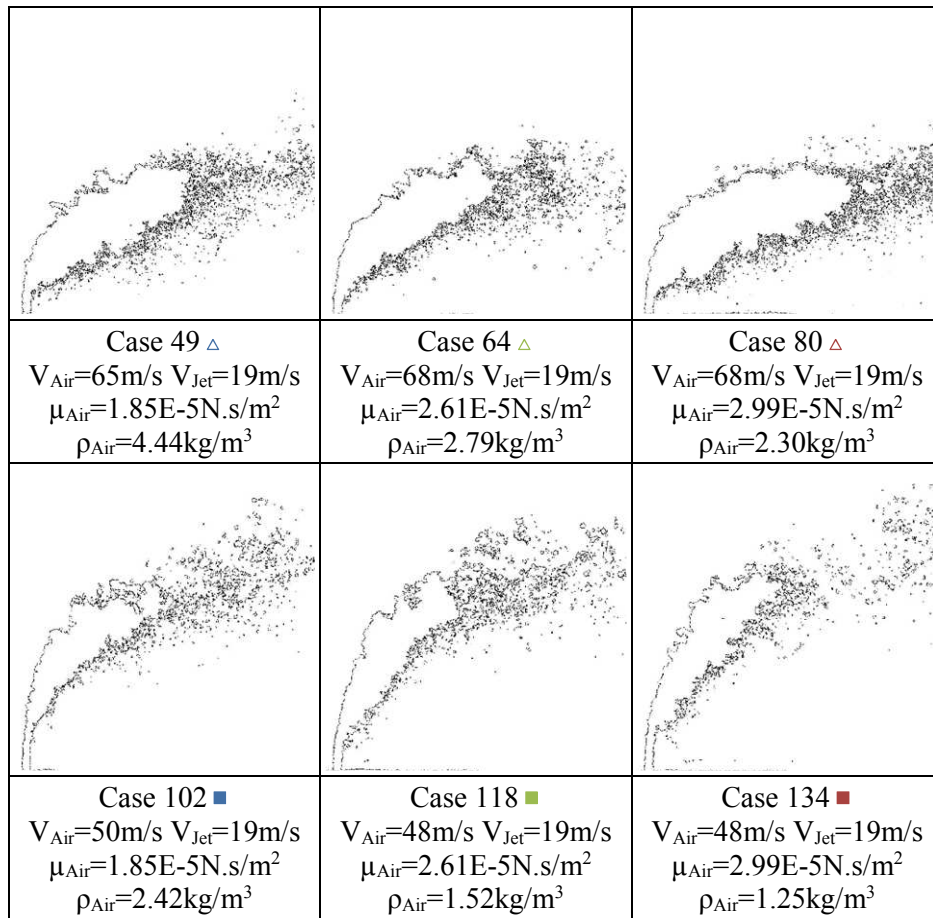


Figure 4.5: Comparison of jet trajectories at three different temperatures Table 2.3 summarizes the conditions.

### 4.2.3 Constant Momentum Flux ratio

In section 4.2.1, it is shown that momentum flux ratio cannot solely describe all the attributes of the atomization process. Images in Figure 4.6 show the atomization of four cases at 200°C and 2.1 bars. The air and jet velocities are altered so that the momentum flux ratio remains constant at 74. A quick comparison shows that as the liquid mass flow rate is reduced the amount of liquid present for atomization is also reduced and consequently the overall size and shape of the plume is reduced. Also as the air velocity is reduced the plume becomes narrower as the shear force on the jet is reduced and therefore the atomization process is changed. For example, D32 for cases 181, 185, 189, and 193 are 66.9  $\mu\text{m}$ , 72.7  $\mu\text{m}$ , 82.0  $\mu\text{m}$ , and 87  $\mu\text{m}$  respectively. Finally it is very clear that all the trajectories are altered even though the air and jet properties are kept constant. This demonstrates the need for having at least two parameters to describe the inertia effects on the trajectory for any given condition. Therefore it is more appropriate to use both the air and jet Weber numbers. Alternatively it is possible to use one of the Weber numbers along with the momentum flux ratio, since the momentum flux ratio is the ratio of the two Weber numbers. Nevertheless the momentum flux ratio is an important parameter since it can provide an estimate of the trajectory and it easy to comprehend compared to the Weber numbers.

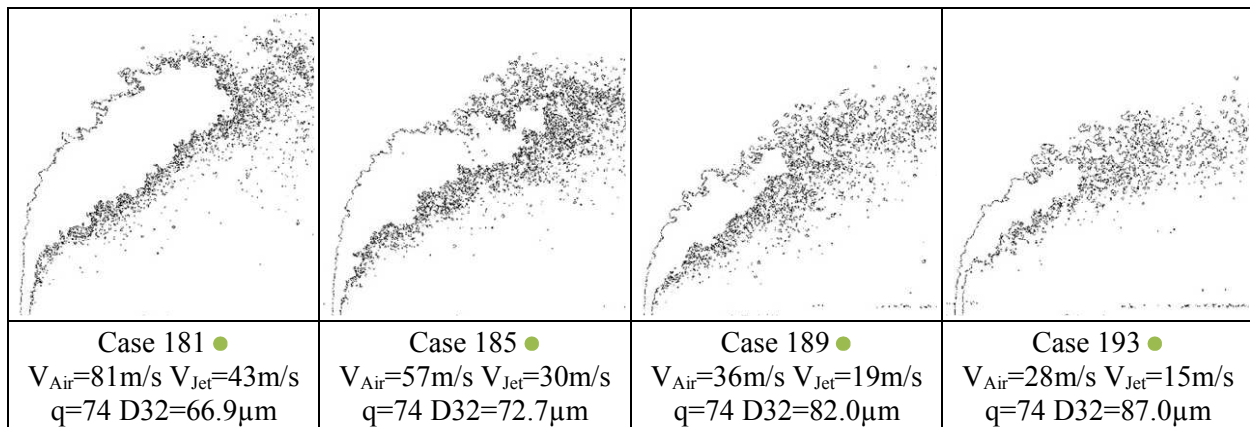


Figure 4.6: Comparison of four cases with similar conditions and constant momentum flux ratio. Table 2.3 summarizes the conditions.

### 4.2.4 Constant Air and Jet Weber Number

In this section, an example is provided to demonstrate the need for non-dimensional terms that include viscosity terms to describe the jet trajectory beyond just the Weber numbers and momentum flux ratio. For example, for the cases in Figure 4.7, the momentum flux ratio, air and

jet Weber numbers are kept constant and are 18, 129, and 2330 respectively. Even though these parameters are the same in both cases the atomization is very different between the two. The windward- and lee-ward trajectories are lowered and the jet is closer to the wall. The liquid is stretched more in the direction of the gas considering the inertia terms between the two cases are the same. The changes in the trajectory are caused by the viscosity of the gas. The gas Ohnesorge numbers for cases 140 and 119 are 0.0015 and 0.0046, respectively. The Ohnesorge number is about three times higher for case 119. This difference is due to both air temperature and pressure. Air density and viscosity for cases 140 and 119 are  $4.4 \text{ kg/m}^3$ ,  $1.3 \text{ kg/m}^3$ ,  $1.85\text{E-}5 \text{ N.s/m}^2$  and  $2.99\text{E-}5 \text{ N.s/m}^2$  respectively. The gas Weber number is kept constant even as the gas density for case 119 is reduced. The air velocity has increased to compensate for density. Based on this example there is enough evidence to show that both viscosity and density play important role in the atomization process. However, more investigation is required to justify for the effect of viscosity since the density is also reduced in this example. Therefore in the following example only the density is altered to show that viscous effects are present in the first example.

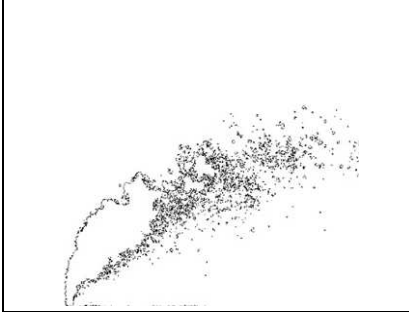

	
<p>Case 140 ■</p> <p><math>V_{\text{Air}}=68\text{m/s}</math> <math>V_{\text{Jet}}=19\text{m/s}</math></p> <p><math>\mu_{\text{Air}}=1.85\text{E-}5\text{N.s/m}^2</math> <math>\rho_{\text{Air}}=4.4\text{kg/m}^3</math></p> <p><math>We_{\text{Air}}=129.5</math> <math>We_{\text{Jet}}=2330</math> <math>q=18</math></p> <p><math>Oh_{\text{Air}}=0.0015</math></p>	<p>Case 119 ▲</p> <p><math>V_{\text{Air}}=127\text{m/s}</math> <math>V_{\text{Jet}}=19\text{m/s}</math></p> <p><math>\mu_{\text{Air}}=2.99\text{E-}5\text{N.s/m}^2</math> <math>\rho_{\text{Air}}=1.3\text{kg/m}^3</math></p> <p><math>We_{\text{Air}}=129.3</math> <math>We_{\text{Jet}}=2330</math> <math>q=18</math></p> <p><math>Oh_{\text{Air}}=0.0046</math></p>

Figure 4.7: Comparison of two cases with constant momentum flux ratio, and air and jet Weber numbers.

Table 2.3 summarizes the conditions.

In Figure 4.8, the momentum flux ratio and both Weber numbers are almost the same, but contrary to previous example only the air pressure is increased. Essentially only air density is changed. The gas densities for the two cases are  $1.5 \text{ kg/m}^3$  and  $3.8 \text{ kg/m}^3$ , respectively. In this case, the sprays are very similar and it is hard to distinguish the difference. Nevertheless there are small differences, for example the magnitude of the undulation on the windward of the jet for case 106. The other difference is the neck position and the atomization closer to the nozzle exit. In conclusion, Weber



numbers are not sufficient to describe the trajectory and other non-dimensional groups that contain viscous terms also need to be included.

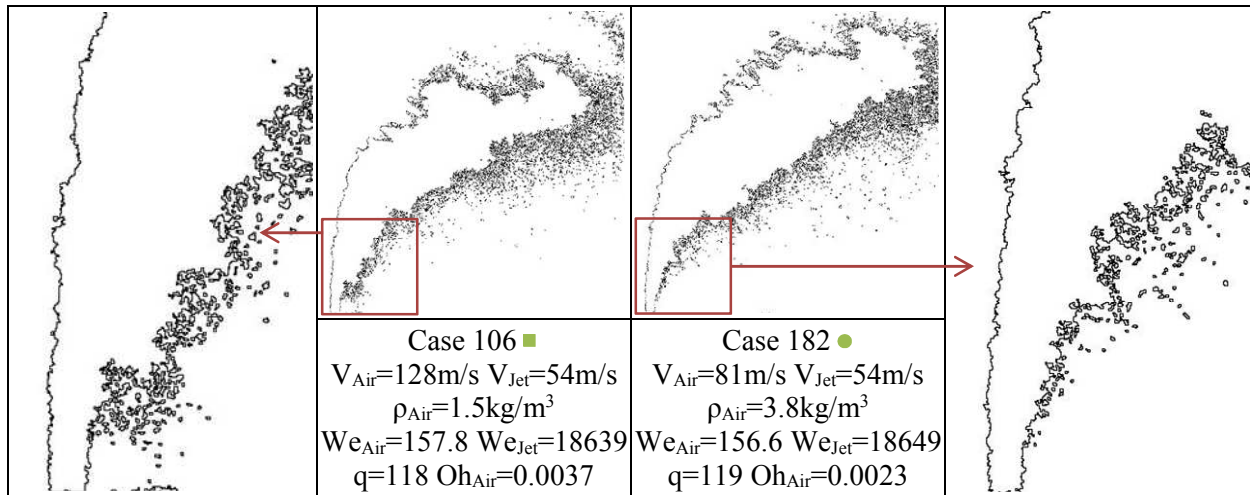


Figure 4.8: Comparison of two cases with constant momentum flux ratio, and air and jet Weber numbers.

Table 2.3 summarizes the conditions.

## Chapter 5 Spray Plume Characteristics

### 5 Spray Plume Characteristics

In this chapter, various characteristics are quantified and compared to the dimensional and non-dimensional parameters. These characteristics are breakup length and time, plume area, angle, and width, and finally mean jet surface thickness. Table 2.3 outlines the conditions and results for the presented graphs in this chapter. Figure 5.1 schematically shows the above mentioned characteristics. The breakup point is shown in red and is defined as the furthest point away from the nozzle exit on the plume perimeter. The breakup length is defined as the length of the line connecting the center of nozzle exit to the breakup point. Plume angle is the angle between the wall and the line connecting the center of nozzle exit to the breakup point. Plume area is defined based on the area of the plume. Plume width is defined as the width of a rectangle that has the same area as the plume and the same length as the breakup length.

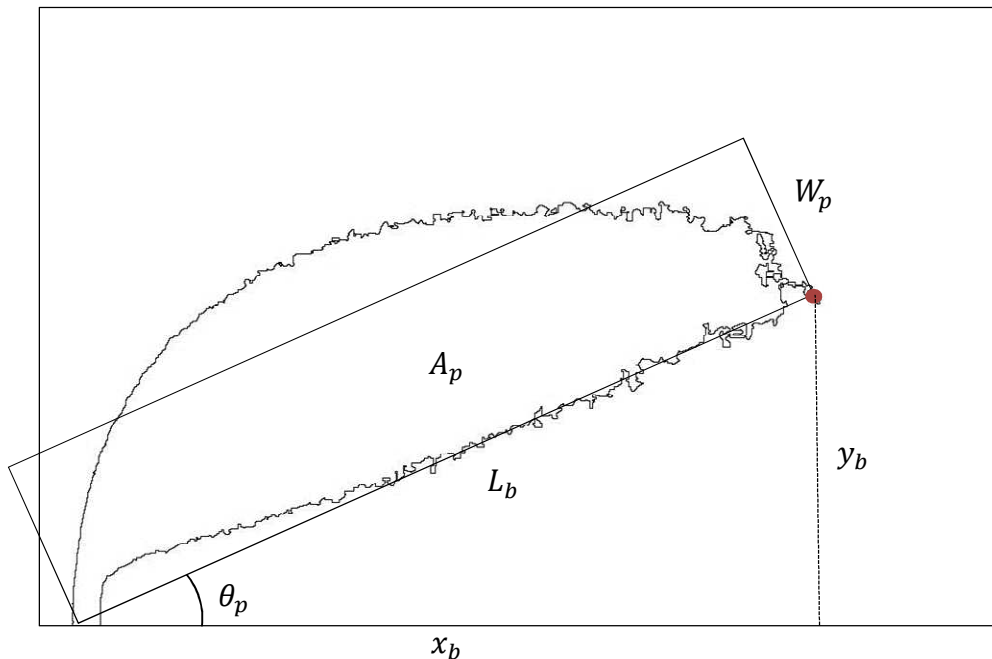
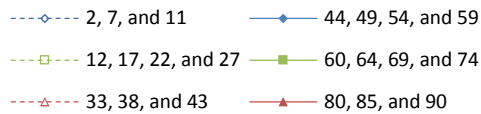
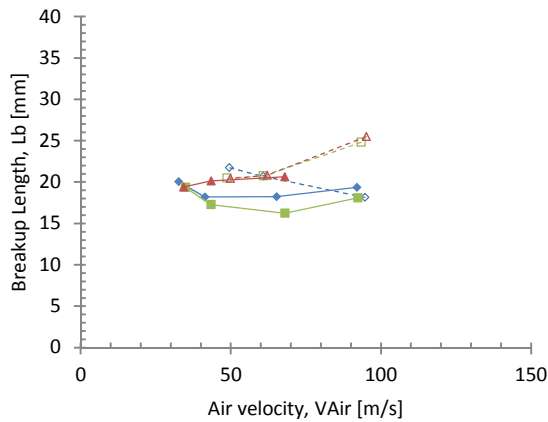


Figure 5.1: Schematic representation of plume variables.

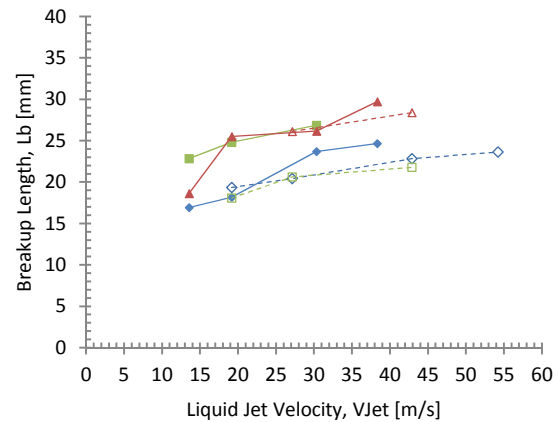
#### 5.1 Breakup Length

Breakup length is one of the most widely used parameters in spray study. In this context, it refers to the length of a straight line connecting the center of the nozzle exit to the breakup point. The

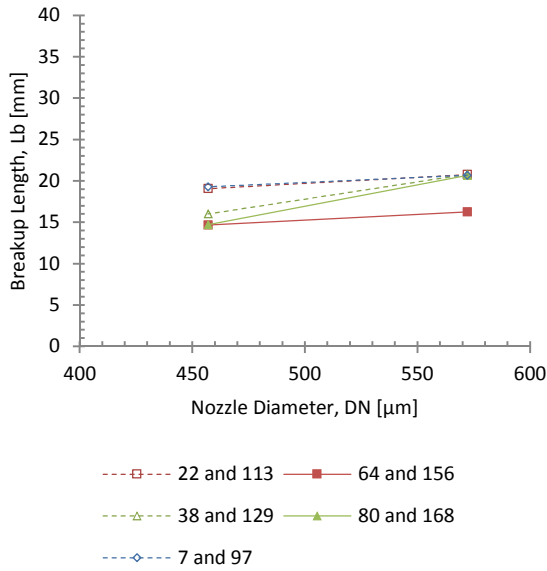
breakup point is defined as the point farthest away from the nozzle exit on the plume boundary. Figure 5.2 shows the effect of various dimensional variables versus breakup length. All the variable except for the studied parameter are kept constant in all the images for each data series. The markers for the shown data do not represent the conditions' symbols defined in previous chapters since the conditions change for each series. In each figure the jet velocity is kept constant at 19 m/s except for Figure 5.2 (b). In Figure 5.2 (e) and (f) the series presented with the dashed lines are at 2.1 bar and the series presented with the solid lines are at 3.8 bar. The nozzle diameters for Figure 5.2 (e) and (f) are 572  $\mu\text{m}$  and 457  $\mu\text{m}$  respectively. Similarly in Figure 5.2 (g) and (h) the series presented with the dashed lines are for the 457  $\mu\text{m}$  nozzle and the series presented with the solid lines are for the 572  $\mu\text{m}$  nozzle. The crossflow pressure for Figure 5.2 (g) and (h) are 2.1 bar and 3.8 bar respectively.



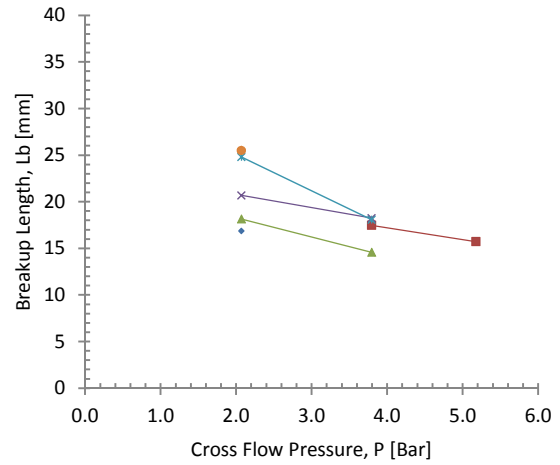
(a)



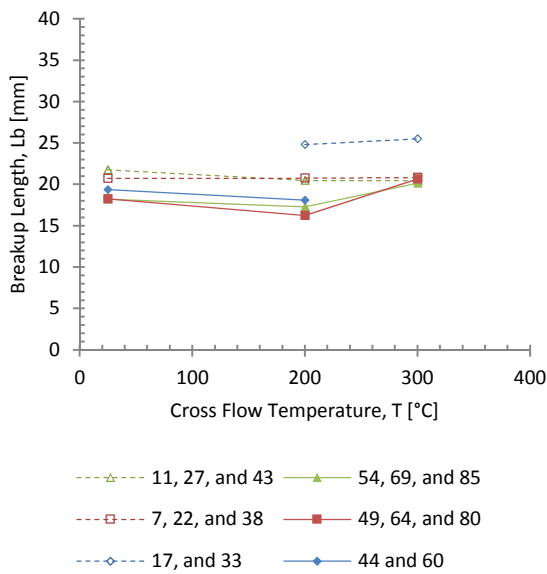
(b)



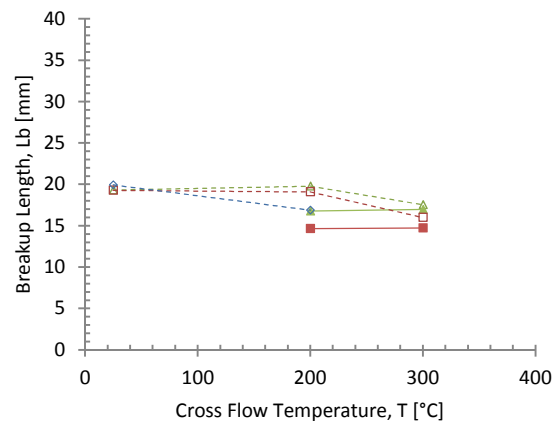
(c)



(d)



(e)



(f)

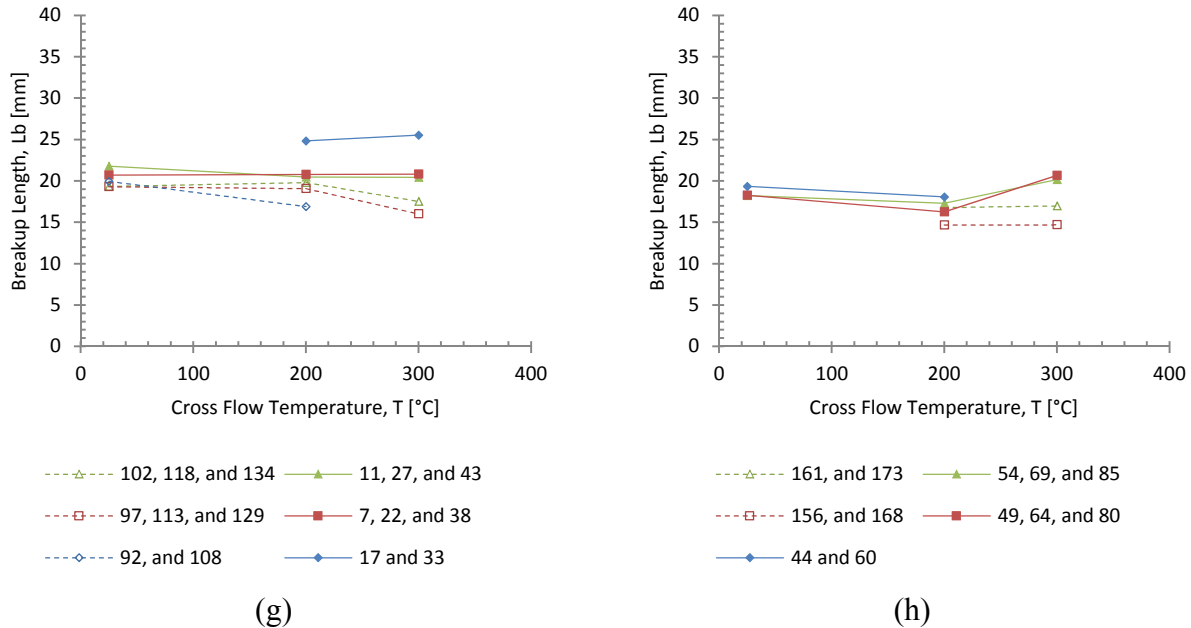


Figure 5.2: Breakup length versus (a) air velocity, (b) jet velocity, (c) nozzle diameter, (d) crossflow pressure, and (e) – (h) crossflow temperature. In all the graphs the parameters are kept constant except for the parameter of interest, for example in figure (a) only air velocity is altered. The symbols do not represent the conditions since the conditions for each data series is different. Table 2.3 summarizes the conditions.

In Figure 5.2 (a), the trend between the air velocity and breakup length is not clear. For some conditions as the air velocity is increased the breakup length is first reduced and later it increases again. In order to better understand the trend it is beneficial to express the breakup length as the vector summation of stream-wise,  $x_b$ , and cross-stream penetrations,  $y_b$ . Depending on the conditions, at lower air velocities the cross-stream, i.e. jet-wise, penetration is more significant and the jet does not bend as much in the direction of the air flow. Conversely, as the air velocity increases the spray bends more in the direction of the air flow. Finally depending on the conditions, the plume area also stretches in the direction of the air flow, which explains why the breakup length increases at higher air velocities. Figure 5.3 shows the breakup point for cases 60, 64, 69 and 74 where the gas temperature is 200°C. The breakup point is depicted by the red dot on each image. Essentially as the air velocity increases the cross-stream penetration reduces and inversely the stream-wise penetration increases. Consequently the summation of these two parameters, i.e. breakup length, would first reduced and then increase. However for the cases 2, 7, and 11 where the gas temperature is 25°C, the breakup length only decreases as the air velocity is reduced. The

main difference between the cases at higher temperature versus room temperature is density and viscosity of the gas. As the gas temperature increases the density reduces and viscosity increases and inversely the density reduces. When comparing the two rows of the Figure 5.3 the viscosity effects are quite apparent. As the gas density is reduced the expectation would be that the penetration would increase, however the images in the first row do not penetrate more in the flow but are stretched more in the direction of the flow. The plume width and curvature are fairly different between the cases at 25°C and 200°C. For cases at higher temperature and pressure breakup length increases after the initial reduction.

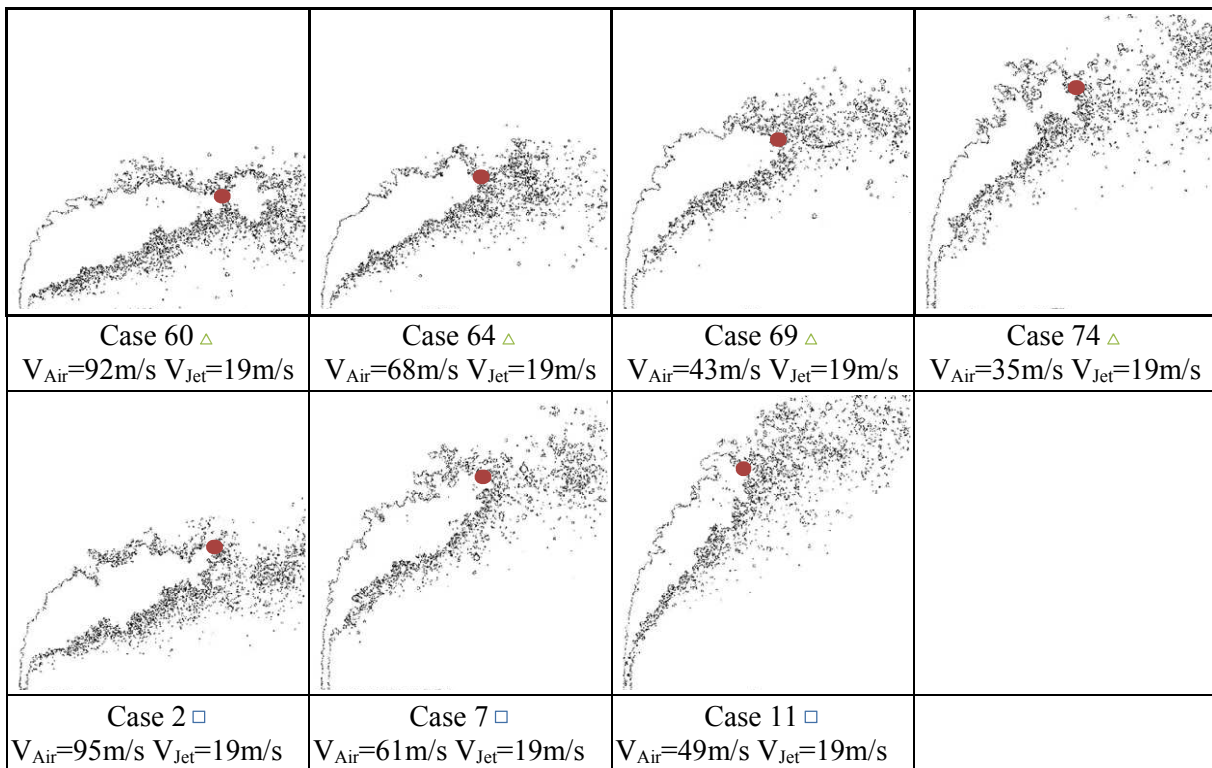


Figure 5.3: Comparison of cases with varying air velocities at two temperature and pressure ranges first row at 200°C and 3.8 bar second row at 25°C and 2.1 bar.

Figure 5.2 (b) shows the relation between the breakup length and jet velocity. As the jet velocity increases the jet-wise penetration increases and consequently breakup length increase. The increase in the jet penetration is due to the increasing liquid momentum, in other words, momentum flux ratio increases. Figure 5.2 (c) and (d) show the relation between the nozzle diameter and pressure with breakup length. As expected the breakup length increases with increased nozzle diameter due to increased jet momentum. As the pressure increases the jet is redirected earlier into the crossflow and stays intact due to increased ambient pressure. Figure 5.4

shows the comparison of two cases with all parameters kept almost constant except for pressure. Finally, Figure 5.2 (e) – (g) show the relation between temperature and breakup length. As it can be seen from these images the breakup length does not change significantly with respect to temperature. The effect of temperature is more complex to explain compared to other parameters and therefore more detailed discussion is provided in the next chapter.

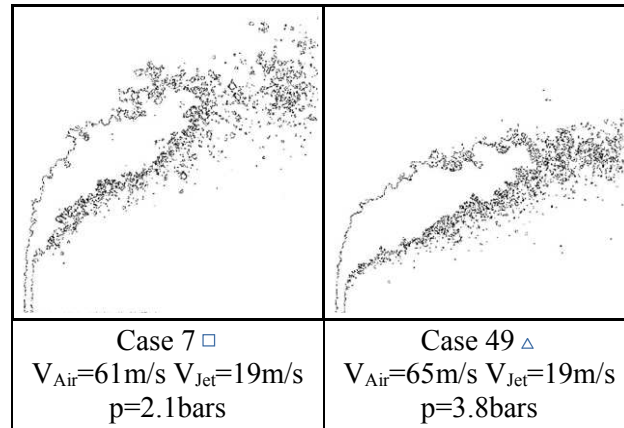


Figure 5.4: Comparison of cases at two pressure ranges.

Figure 5.5 shows the relation between normalized breakup length and various non-dimensionalized variables. In Figure 5.5 (b), the normalized breakup length is compared to the momentum flux ratio. The data shows a logarithmic relation between normalized breakup length and momentum flux ratio. This can be attributed to the fact that momentum flux ratio is a good measure of trajectory. As momentum flux ratio increases the trajectory is also increased and consequently breakup length is increased. In Figure 5.5 (c) and (d), the normalized breakup length is compared to air and liquid Weber numbers. The data shows a very good relation between normalized breakup length and liquid Weber number. Breakup length with respect to gas Weber number also shows an increasing trend but has a larger spread; this can possibly be due to instrumentation uncertainties when measuring gas volume flow rates, i.e. Erdco flowmeter. Similar behavior is seen between Reynolds numbers and normalized breakup length; see Figure 5.5 (e) and (f). The presented results are also in a good agreement with the results shown by Wang et al. [40]. Finally, the most important finding is that as the normalized breakup length increases droplet size and its standard deviation systematically reduce; see Figure 5.5 (g) and (h). It is also interesting to note that there are two different trends depending on the nozzle diameter. The slope and span of normalized breakup length on the graph does not change with different nozzles. Also the data shows the larger nozzle diameter produces finer droplets as will be discussed in the next chapter.

It should be noted breakup length does not take into account the effect of spray angle. In some cases two sprays can have similar breakup lengths but not necessary the same angle. This leads to next sections where plume angle and other plume attributes are also discussed.

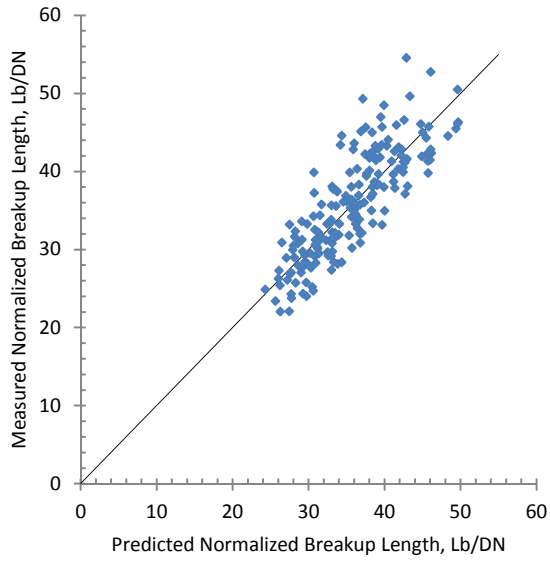
A correlation is defined based on the Weber and Reynolds numbers to capture the behavior of normalized breakup length. Similar to the previous correlations, momentum flux ratio alone is not used in the correlation for two reasons. First, it is not a truly independent variable since it can be defined as the ratio of the two Weber numbers, and therefore statistically can be omitted. Secondly, Weber and Reynolds numbers are more intuitive to use and are less specific to just the current study. A second correlation is also provided based on Weber and Ohnesorge numbers in order to combine the inertia terms into just Weber numbers and provide a better understanding for viscous and surface tension effects. It should be noted that Ohnesorge number is the ratio of square root of Weber number to Reynolds number. Therefore similar to  $q$ , it can be a dependent variable if used with both Weber and Reynolds numbers, and so it can be either used with only one or the other. Otherwise, statistically there is not a difference between the correlations.

$$\begin{aligned}\frac{L_b}{D_N} &= 1084We_{Air}^{-0.04}We_{Jet}^{0.58}Re_{Air}^{0.01}Re_{Jet}^{-0.84} \\ &= 1084We_{Air}^{-0.04}We_{Jet}^{0.16}Oh_{Air}^{-0.01}Oh_{Jet}^{0.84} \\ &= 1084q^{0.16}We_{Air}^{0.12}Oh_{Air}^{-0.01}Oh_{Jet}^{0.84}\end{aligned}\quad (5.1)$$

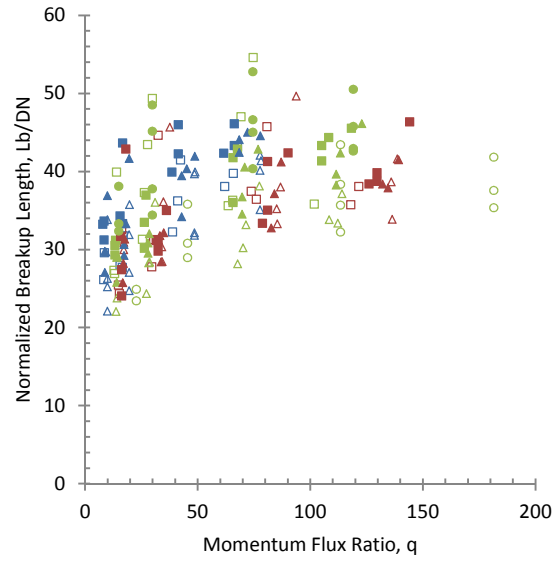
$$L_b = e^{9.90}D_N^{0.71}V_{Air}^{-0.08}V_{Jet}^{0.32}\rho_{Air}^{-0.04}\rho_{Jet}^{-0.26}\mu_{Air}^{-0.01}\mu_{Jet}^{0.84}\sigma^{-0.54}\quad (5.2)$$

The above correlations have  $R^2$  value of 0.70 and based on t-test all the variables are significant except for the Reynolds and Ohnesorge numbers for air. The statistical analysis based on 95% confidence criterion shows that the gas viscosity term is not significant and so Ohnesorge and Reynolds numbers of air can be eliminated from the above correlations. Three different forms of the same correlation are provided to help better explain the impact of various parameters. The final form is of interest since it shows both the effect of inertia terms and viscosity terms. Essentially as momentum flux ratio, Weber number of gas and viscosity of jet increase, then the breakup length also increases. Figure 5.5 (a) displays the above correlations in graphical form.

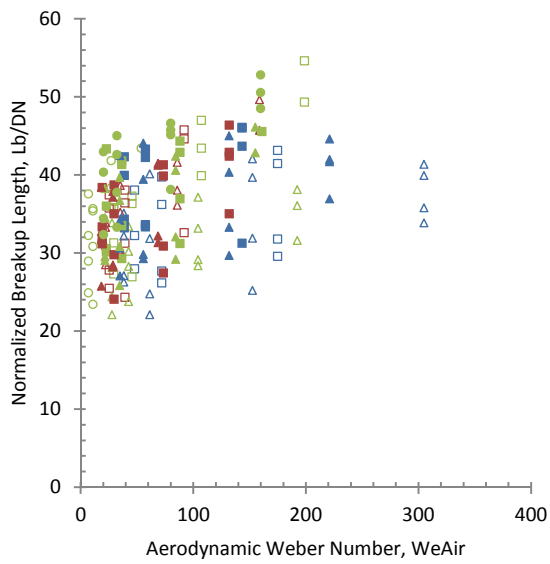




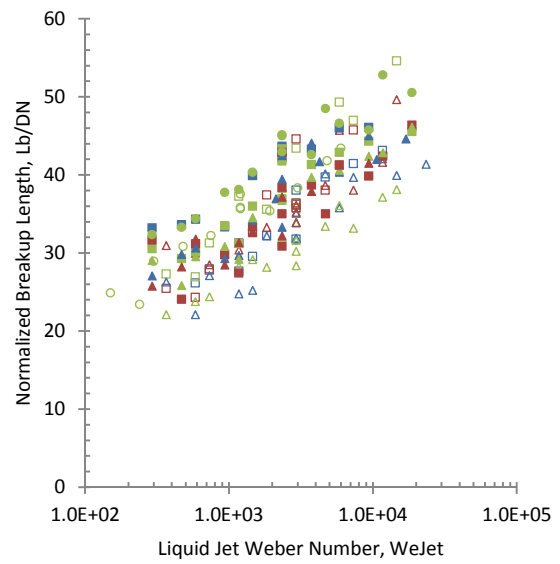
(a)



(b)



(c)



(d)

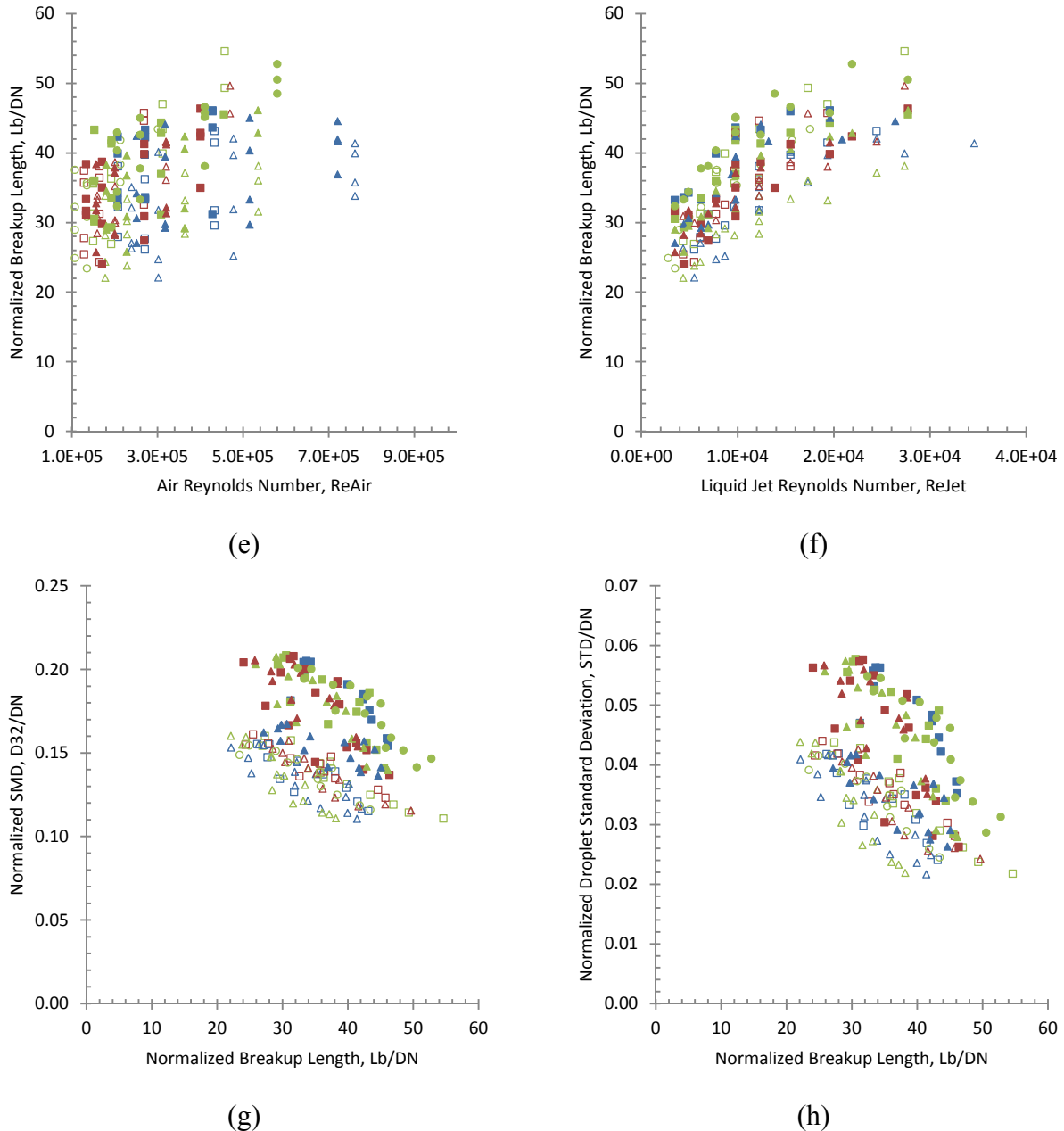
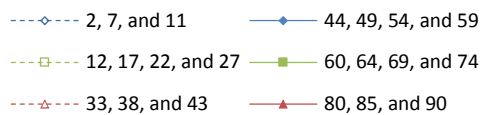
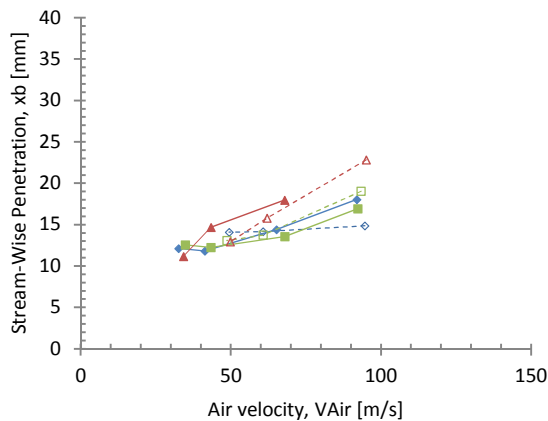


Figure 5.5: (a) Correlation of normalized breakup length; (b) – (f) Normalized breakup length vs. various non-dimensionalized numbers; (g) – (h) Normalized D32 and droplet size standard deviation vs. normalized breakup length. Table 2.3 summarizes the conditions.

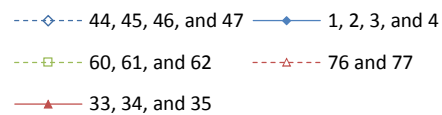
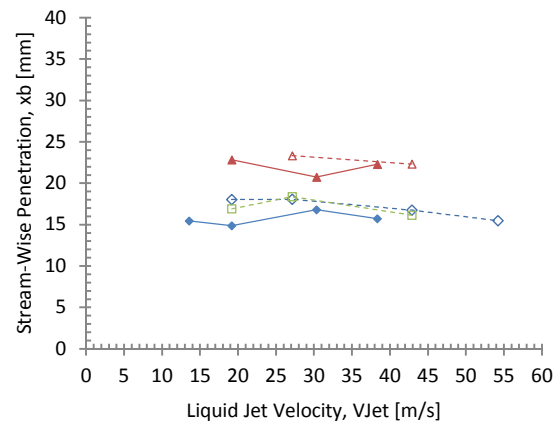
## 5.2 Stream-Wise Penetration

Stream-wise penetration is the length between the nozzle exit and the breakup point in the crossflow direction and is denoted by  $x_b$  in Figure 5.1. It is the furthest point the jet reaches in the crossflow direction. Based on the discussions on breakup length and its relation with air velocity

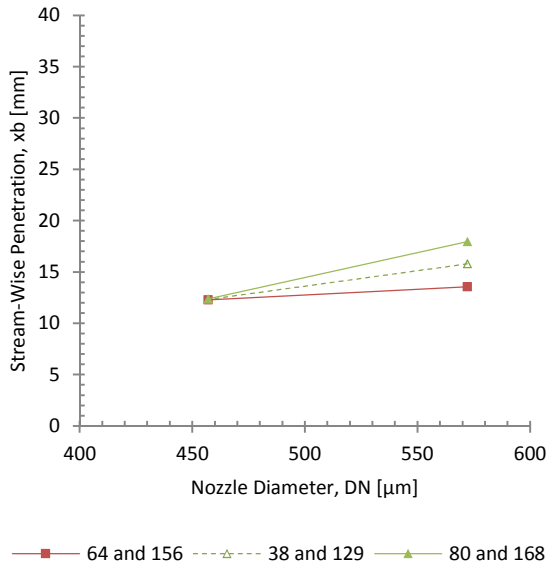
it is beneficial to define stream-wise penetration. Previously Wu et al [6, 7, 8, 9, 10] has shown that the normalized stream-wise penetration is a constant, equation (1.7). However, more recently Gopala [61] have shown that this parameter actually depends on parameters such as the aerodynamic Weber number and momentum flux ratio as well as liquid type. Figure 5.6 shows the effect of various dimensional variables versus stream-wise penetration. In all the images all the variable except for the studied parameter are kept constant for each data series. The markers for the shown data do not represent the conditions' symbols defined in previous chapters. In each figure the jet velocity is kept constant at 19 m/s except for Figure 5.6 (b). In Figure 5.6 (e) and (f) the series presented with the dashed lines are at 2.1 bar and the series presented with the solid lines are at 3.8 bar. The nozzle diameters for Figure 5.6 (e) and (f) are 572  $\mu\text{m}$  and 457  $\mu\text{m}$  respectively. Similarly in Figure 5.6 (g) and (h) the series presented with the dashed lines are for the 457  $\mu\text{m}$  nozzle and the series presented with the solid lines are for the 572  $\mu\text{m}$  nozzle. The crossflow pressure for Figure 5.6 (g) and (h) are 2.1 bar and 3.8 bar respectively. As it can be seen in Figure 5.6 (a) and (b), as the air velocity increases the stream-wise penetration also increases. As the air velocity increases the jet bends more and is redirected in the direction of airflow. Conversely when the jet velocity increases the stream-wise penetration decreases but it is not affected as dramatically compared to cases where the air velocity is altered.



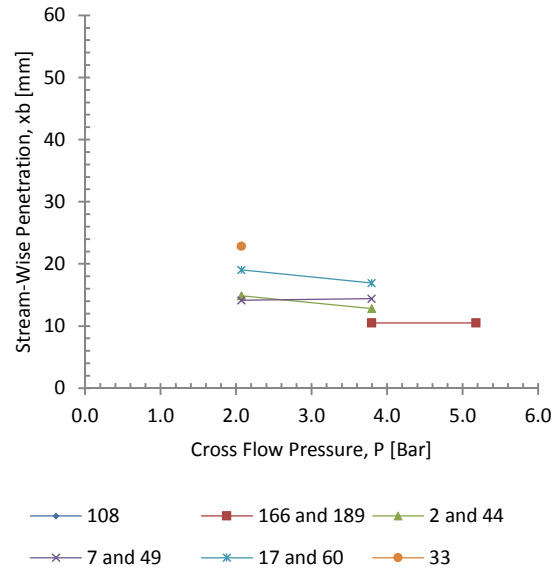
(a)



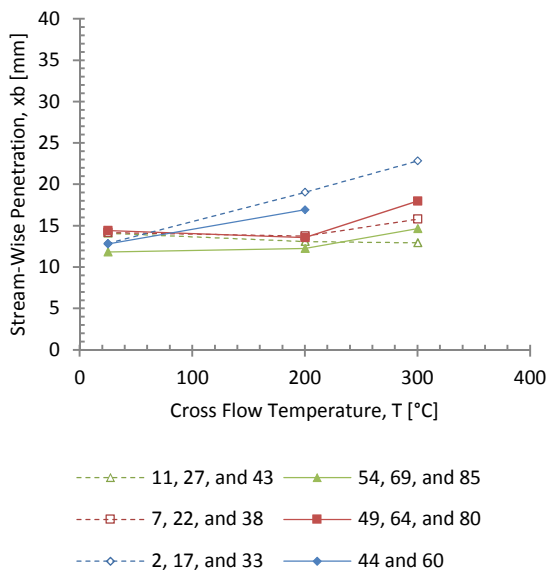
(b)



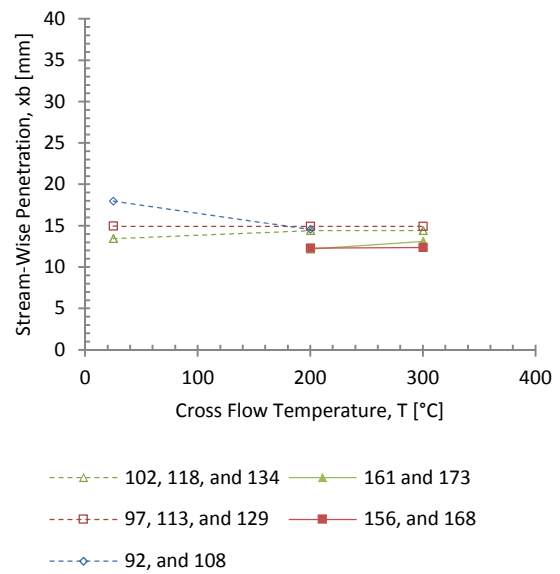
(c)



(d)



(e)



(f)

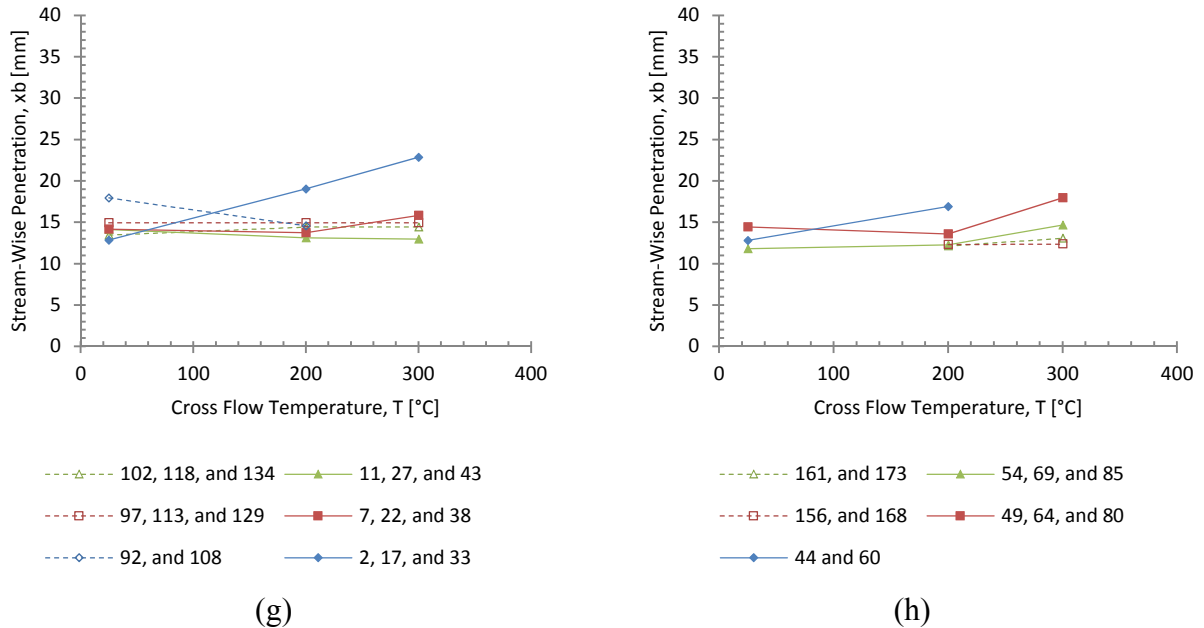


Figure 5.6: Stream-wise penetration versus (a) air velocity, (b) jet velocity, (c) nozzle diameter, (d) crossflow pressure, and (e) – (h) crossflow temperature. In all the graphs the parameters are kept constant except for the parameter of interest, for example in figure (a) only air velocity is altered. The symbols do not represent the conditions since the conditions for each data series is different. Table 2.3 summarizes the conditions.

Figure 5.6 (c) displays the relation between the stream-wise penetration and nozzle diameter. As expected, as the nozzle diameter increases the liquid penetrates more in the both stream-wise and cross-stream direction mainly due increased liquid momentum. Figure 5.6 (c) displays the relation between the stream-wise penetration and pressure. As the pressure is increased the liquid is more confined and is extended more in the direction of the gas flow. Finally, as the temperature increases, Figure 5.6 (e) – (h), the stream-wise penetration also increases. Although the gas density reduces at higher temperatures the effect of increased gas viscosity becomes more apparent. The shear forces on the jet increase and cause the liquid jet to stretch in the direction of the gas flow. A more comprehensive explanation for the effect of both pressure and temperature is provided in chapter regarding droplet size.

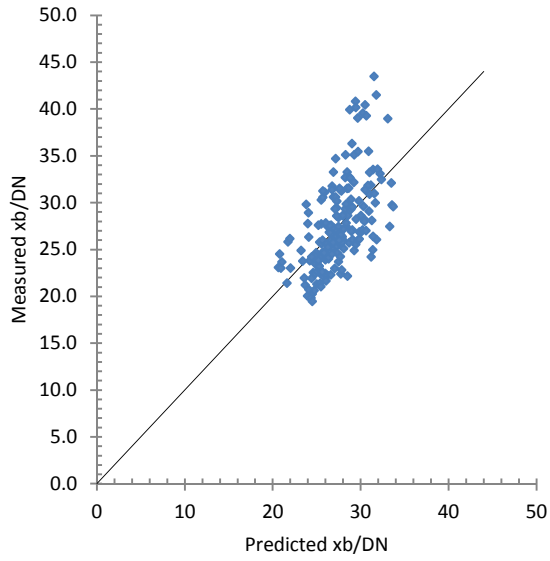
Figure 5.5 shows the relation between normalized stream-wise penetration and various non-dimensionalized variables. In Figure 5.5 (b), the normalized stream-wise penetration is compared to the momentum flux ratio. The data does not show a strong relation between normalized stream-

wise penetration and momentum flux ratio. The momentum flux ratio is the ratio of jet to gas momentum ratios. As it is shown earlier the liquid velocity does not affect the stream-wise penetration as much as the gas velocity. In Figure 5.5 (c) and (d), the normalized stream-wise penetration is compared to air and liquid Weber numbers. The data shows a good relation between normalized stream-wise penetration and Weber number. Finally, the relation between the stream-wise penetration and sauter mean diameter is shown in Figure 5.5 (g) and (h). The data shows that as the stream-wise penetration increases the droplet size and standard deviation reduces.

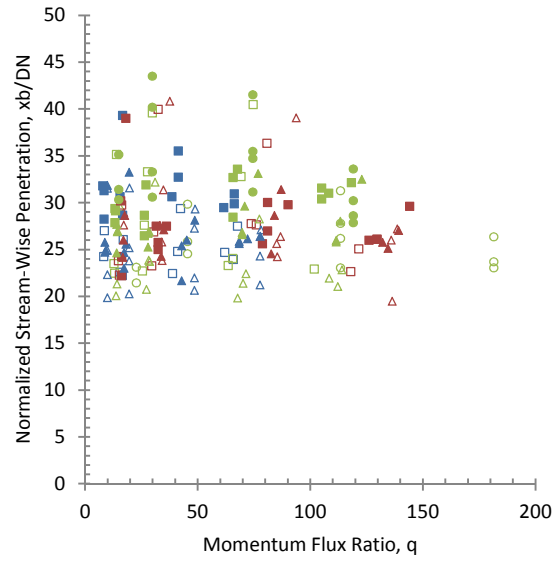
$$\begin{aligned}\frac{x_b}{D_N} &= 3709We_{Air}^{0.14}We_{Jet}^{0.45}Re_{Air}^{-0.10}Re_{Jet}^{-0.88} \\ &= 3709We_{Air}^{0.09}We_{Jet}^{0.01}Oh_{Air}^{0.10}Oh_{Jet}^{0.88} \\ &= 3709q^{0.01}We_{Air}^{0.10}Oh_{Air}^{0.10}Oh_{Jet}^{0.88}\end{aligned}\quad (5.3)$$

$$x_b = 3709D_N^{0.61}V_{Air}^{0.18}V_{Jet}^{0.02}\rho_{Air}^{0.04}\rho_{Jet}^{-0.43}\mu_{Air}^{0.10}\mu_{Jet}^{0.88}\sigma^{-0.59}\quad (5.4)$$

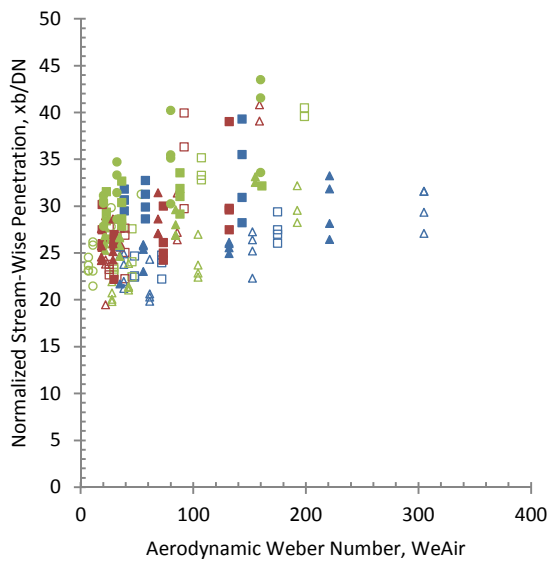
A correlation is defined based on non-dimensional parameters to capture the behavior of normalized stream-wise penetration. The above correlations have  $R^2$  value of 0.37 and although not a very strong correlation the t-test reveals that all the variables are significant except for the variables containing jet velocity, e.g. jet Weber number and momentum flux ratio. The statistical analysis is based on %95 confidence criterion. The second correlation reveals that increasing air Weber number and air and jet Ohnesorge numbers increases the stream-wise penetration. As the gas and liquid viscosity increase the jet is kept intact and elongates in the gas direction. Figure 5.5 (a) displays the above correlations in graphical form.



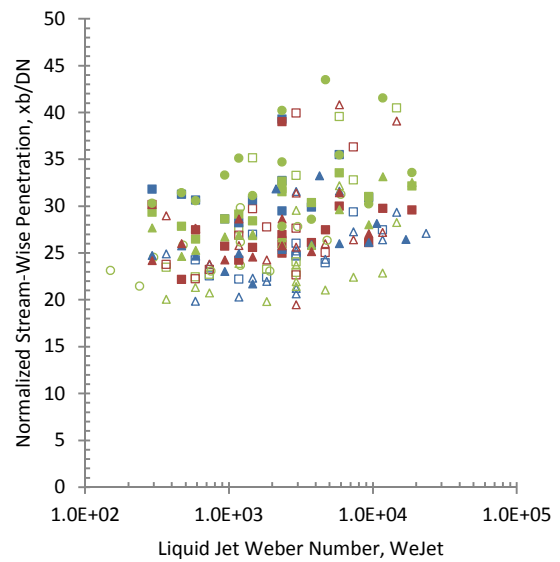
(a)



(b)



(c)



(d)

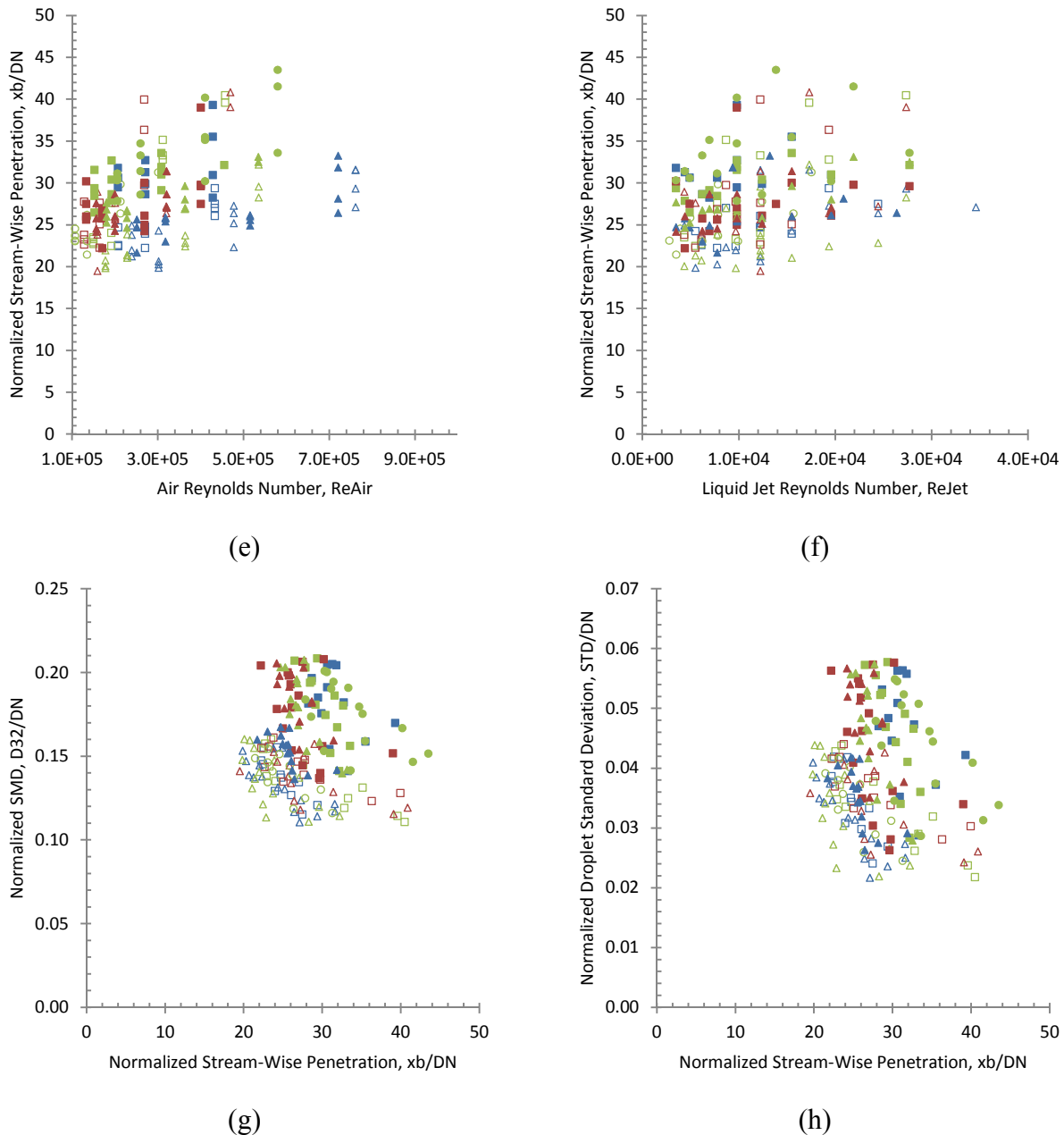


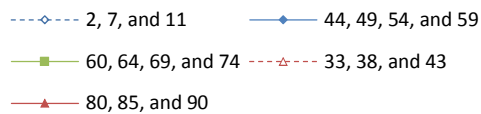
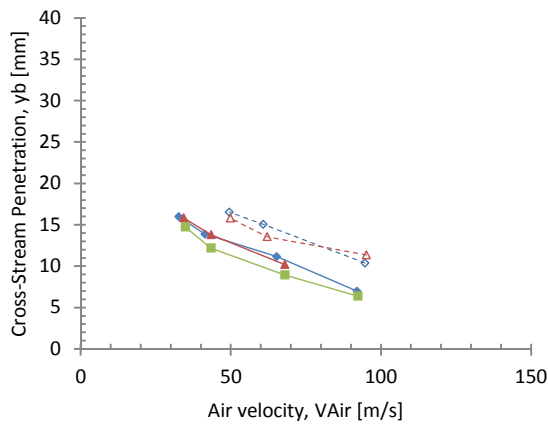
Figure 5.7: (a) Correlation of normalized stream-wise penetration; (b) – (f) Normalized stream-wise penetration vs. various non-dimensionalized numbers; (g) – (h) Normalized  $D_{32}$  and droplet size standard deviation vs. normalized stream-wise penetration. Table 2.3 summarizes the conditions.

### 5.3 Cross-Stream (Jet-Wise) Penetration

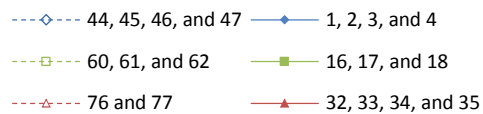
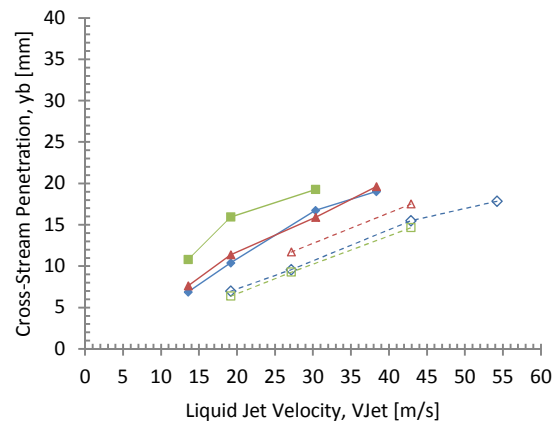
Cross-stream or jet-wise penetration is the length between the nozzle exit and the breakup point in the jet direction and is denoted by  $y_b$  in Figure 5.1. It is the furthest point the jet reaches in the jet direction. Figure 5.8 shows the effect of various dimensional variables versus cross-stream



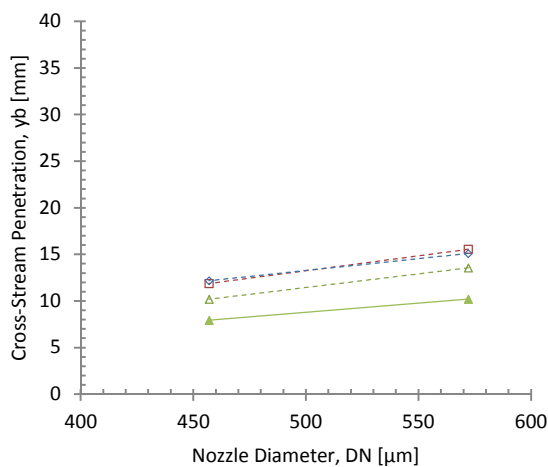
penetration. In all the images all the variable except for the studied parameter are kept constant for each data series. The markers for the shown data do not represent the conditions' symbols defined in previous chapters. In each figure the jet velocity is kept constant at 19 m/s except for Figure 5.8 (b). In Figure 5.8 (e) and (f) the series presented with the dashed lines are at 2.1 bar and the series presented with the solid lines are at 3.8 bar. The nozzle diameters for Figure 5.8 (e) and (f) are 572  $\mu\text{m}$  and 457  $\mu\text{m}$  respectively. Similarly in Figure 5.8 (g) and (h) the series presented with the dashed lines are for the 457  $\mu\text{m}$  nozzle and the series presented with the solid lines are for the 572  $\mu\text{m}$  nozzle. The crossflow pressure for Figure 5.8 (g) and (h) are 2.1 bar and 3.8 bar, respectively.



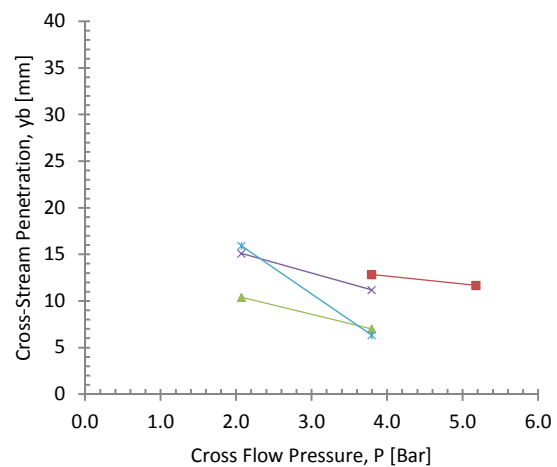
(a)



(b)



(c)



(d)

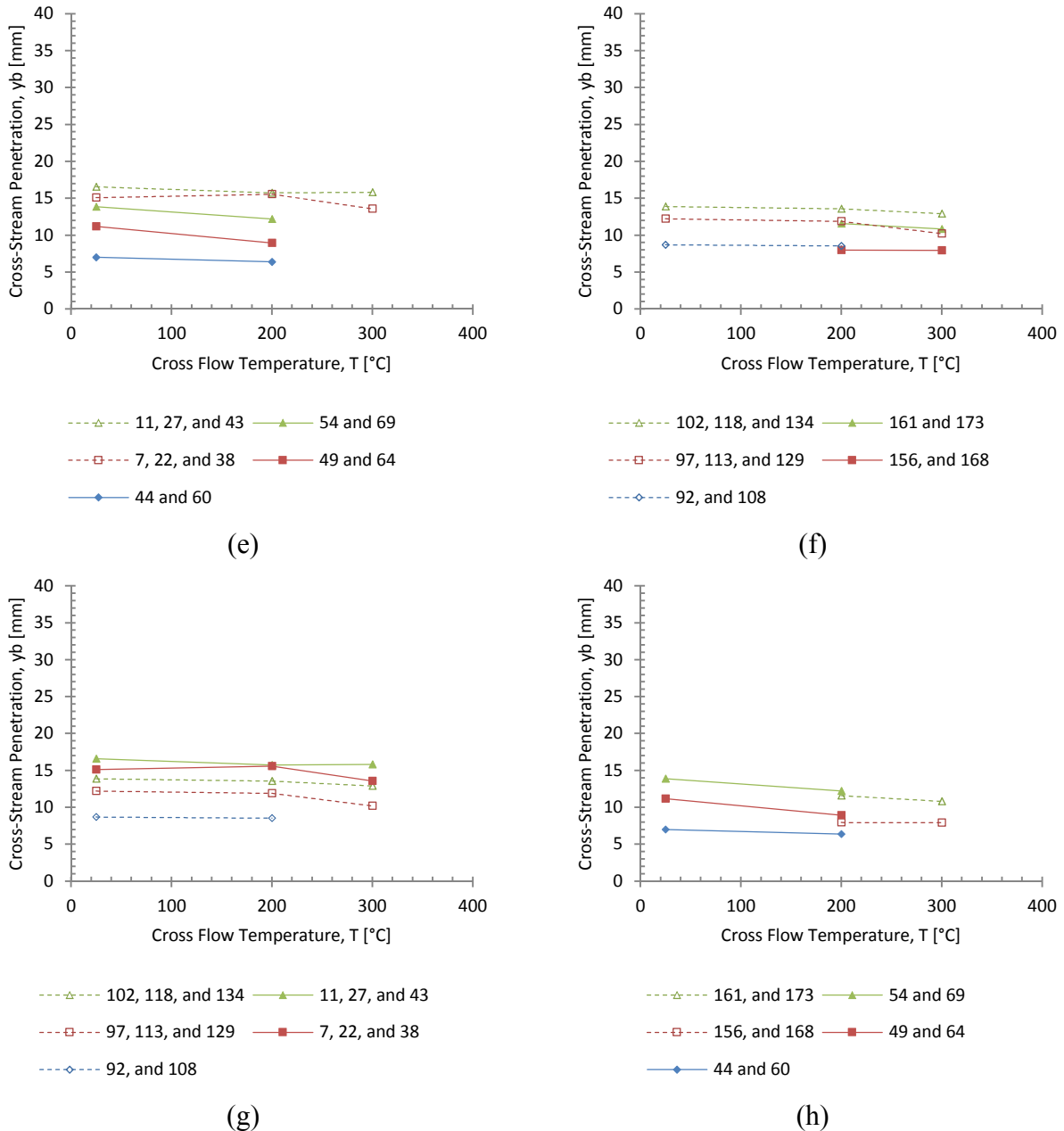


Figure 5.8: Normalized cross-stream penetration versus (a) air velocity, (b) jet velocity, (c) nozzle diameter, (d) crossflow pressure, and (e) – (h) crossflow temperature. In all the graphs the parameters are kept constant except for the parameter of interest, for example in figure (a) only air velocity is altered. The symbols do not represent the conditions since the conditions for each data series is different. Table 2.3 summarizes the conditions.

Figure 5.8 (a) and (b) show the relation between cross-stream penetration and air and jet velocities. As the air velocity increases the jet-wise penetration reduces and on the other hand as the jet

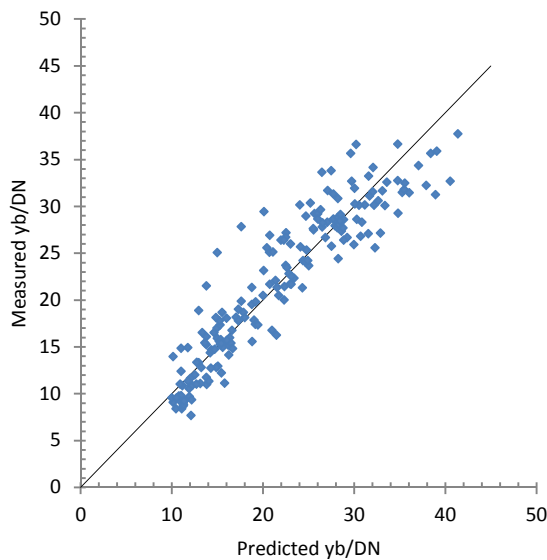
velocity increases the penetration also increases. This is many due to the momentum of the liquid versus and the air. Figure 5.8 (c) shows the relation between cross-stream penetration and nozzle diameter. As expected the cross-stream penetration is higher for the larger nozzle diameter, mainly due to the increased momentum of the jet. Figure 5.8 (d) displays the relation between cross-stream penetration and pressure. As the air pressure increases the air density also increases and the drag force on the jet increases and causes the jet to bend more in the direction of gas flow. Finally, in Figure 5.8 (e) – (f) the relation between the cross-stream penetration and temperature are shown. Based on these results as the gas temperature increases the penetration slightly reduces. The reduction in the penetration can be attributed to the increased gas viscosity even though the gas density is reduced.

$$\begin{aligned}\frac{y_b}{D_N} &= 27.33We_{Air}^{-0.38}We_{Jet}^{0.79}Re_{Air}^{0.19}Re_{Jet}^{-0.69} \\ &= 27.33We_{Air}^{-0.29}We_{Jet}^{0.45}Oh_{Air}^{-0.19}Oh_{Jet}^{0.69} \\ &= 27.33q^{0.45}We_{Air}^{0.16}Oh_{Air}^{-0.19}Oh_{Jet}^{0.69}\end{aligned}\quad (5.5)$$

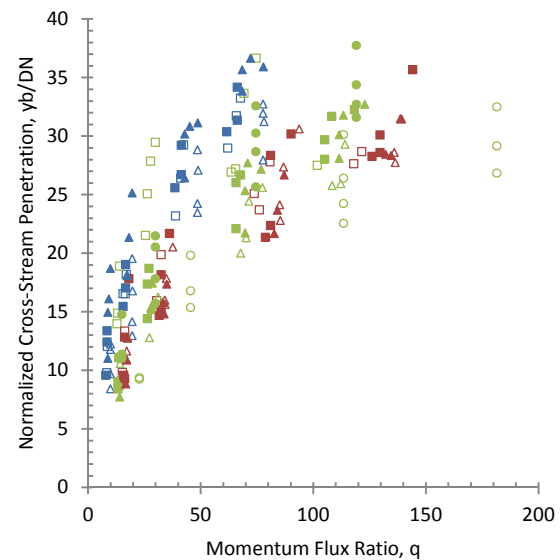
$$y_b = 27.33D_N^{0.91}V_{Air}^{-0.58}V_{Jet}^{0.90}\rho_{Air}^{-0.20}\rho_{Jet}^{0.11}\mu_{Air}^{-0.19}\mu_{Jet}^{0.69}\sigma^{-0.41}\quad (5.6)$$

Next, three equivalent correlations are defined based on four non-dimensional numbers to capture the behavior of normalized cross-stream penetration. The above correlations have  $R^2$  value of 0.86 and based on t-test all the variables are significant. The statistical analysis is based on %95 confidence criterion. The second correlation is the most convenient to discuss since the velocity terms are only present in the form of Weber numbers. Figure 5.9 (a) displays the above correlations in graphical form. Figure 5.9 (c) and (d) show the relation between the cross-stream penetration and Weber numbers. As it is discussed earlier as the gas Weber number increases, (i.e. gas velocity, nozzle diameter and gas density) then the cross-stream penetration reduces mostly due to the increased inertia of the crossflow air. In contrast, increasing the jet Weber number increases the cross-stream penetration. It is interesting to note that the jet Weber number has the larger exponent and consequently the more dominate parameter compared to the air Weber number. Figure 5.9 (e) and (f) show the relation between the cross-stream penetration and Reynolds numbers. Reynolds numbers or preferably Ohnesorge can be used to observe the effect of viscosity on the cross-stream penetration. As the gas Ohnesorge number increases the cross-stream penetration reduces due to increased shear force on the body of the jet. On the other hand, as the liquid Ohnesorge number

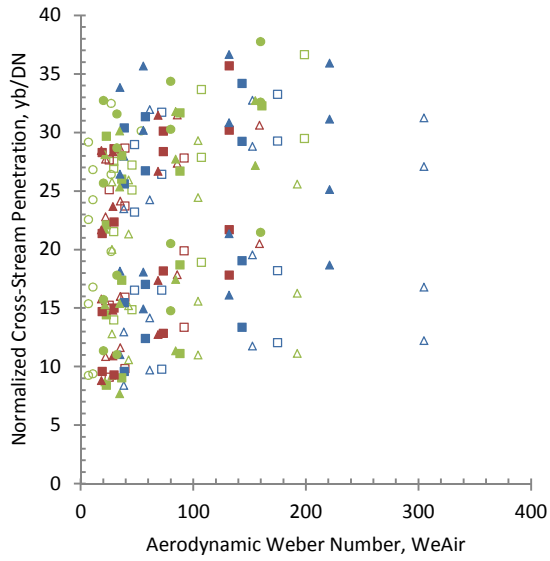
increases the penetration increases. This can be achieved by either increasing the liquid viscosity and/or reducing liquid density, surface tension and/or nozzle diameter. An important point to notice is the effect of liquid properties and velocity compared to the gas. Generally, the influence of gas properties and velocity is less noticeable compared to the jet properties and velocity. Figure 5.9 (b) shows the effect of momentum flux ratio on cross-stream penetration. Once again since momentum flux ratio is the product of the two Weber number on its own is not comprehensive and require at least one the Weber numbers. However, as the momentum flux ratio increases the cross-stream penetration increases. This finding can be miss leading since at higher gas velocities the crossflow penetration is reduced even if the momentum flux ratio is kept constant. This behavior specially becomes more apparent at higher momentum flux ratios as it can be seen in Figure 5.9 (b). Finally in Figure 5.9 (g) and (h) the relation between the cross-stream penetration with droplet size and standard deviation is examined. As the cross-stream penetration increases the droplet size and standard deviation systematically reduces. However the effects are not as profound as in the case of stream-wise penetration.



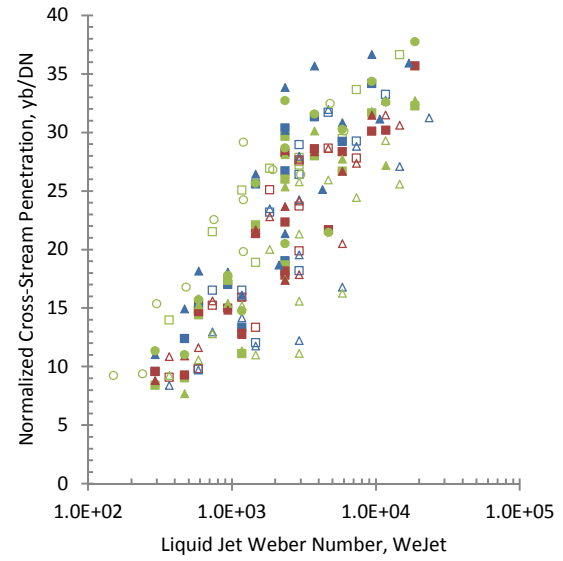
(a)



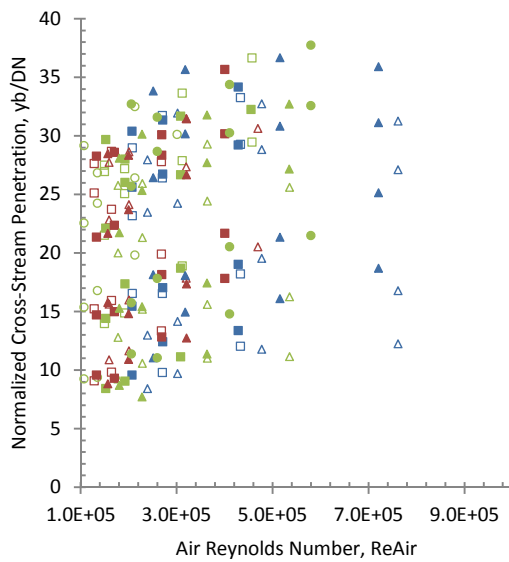
(b)



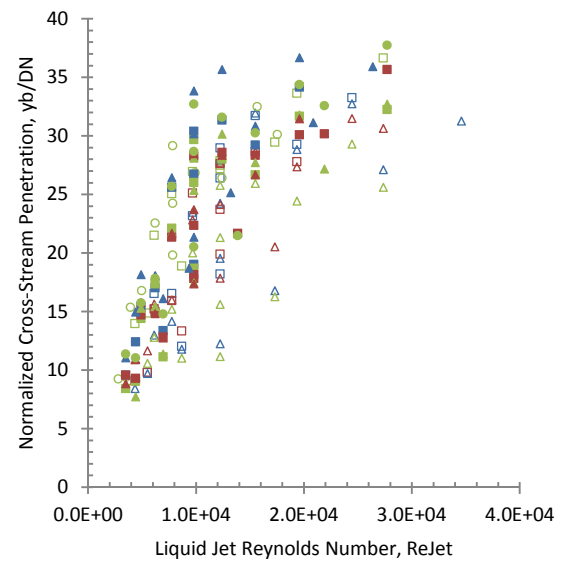
(c)



(d)



(e)



(f)

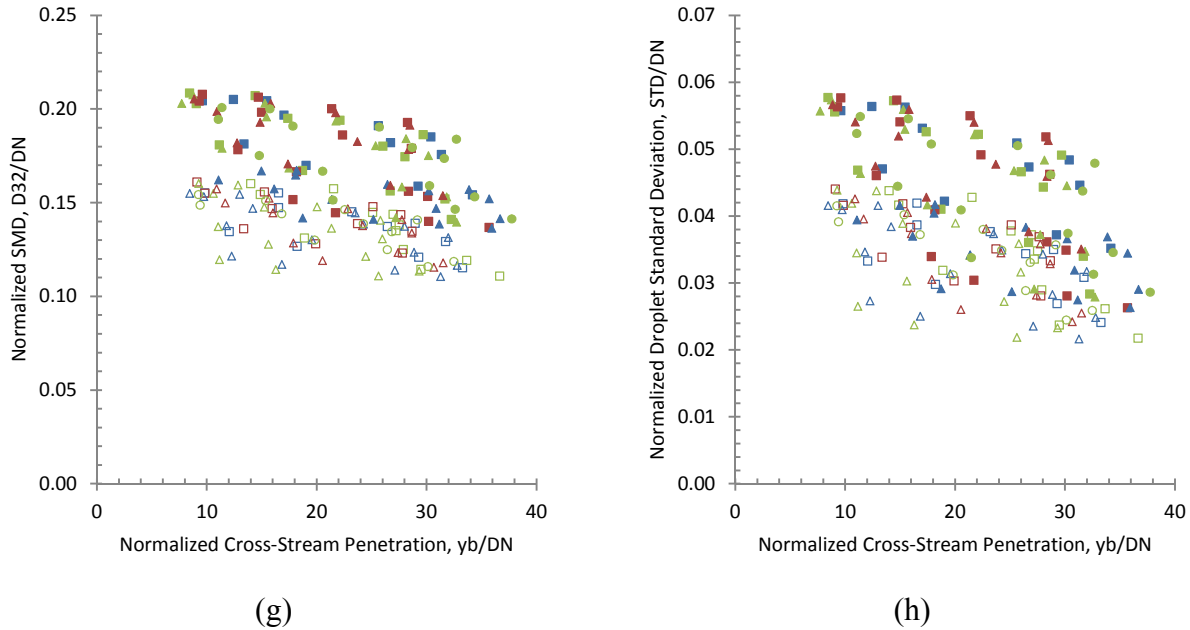


Figure 5.9: (a) Correlation of normalized cross-stream penetration; (b) – (f) Normalized cross-stream penetration vs. various non-dimensionalized numbers; (g) – (h) Normalized D32 and droplet size standard deviation vs. normalized cross-stream penetration. Table 2.3 summarizes the conditions.

## 5.4 Breakup Time

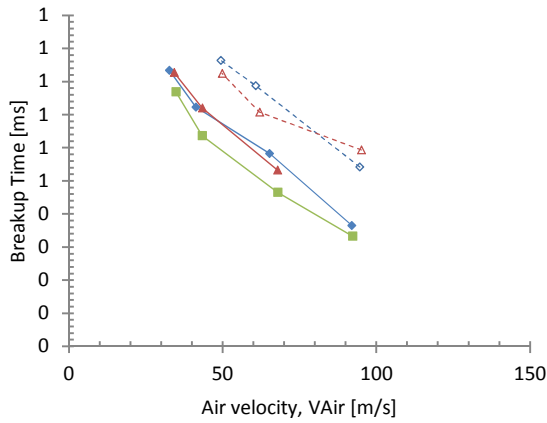
The breakup time is another important parameter. The breakup time is widely used in the spray and combustion studies. It is widely used in the design of combustion chambers along with breakup length. In current study it is particularly of interest since it helps in the understanding of heat transfer to the fluid. As the local temperature of liquid changes the physical properties namely density and viscosity are also altered, see appendix D for detailed discussion. In this study it is defined based on equation (5.7), which physically refers to time it take for a droplet to reach the breakup point. It is assumed that the droplets have lost their initial momentum and are only traveling in the gas stream-wise direction once they reach the breakup point. It is then normalized by non-dimensional time defined in equation (5.8).

$$t_b = \frac{y_b}{V_{Jet}} \quad (5.7)$$

$$\frac{t_b}{t^*} = \frac{t_b}{\frac{\rho_{Jet} D_N}{\sqrt{\rho_{Air} V_{Air}}}} = \frac{t_b}{\sqrt{q} \frac{D_N}{V_{Jet}}} = C \quad (5.8)$$

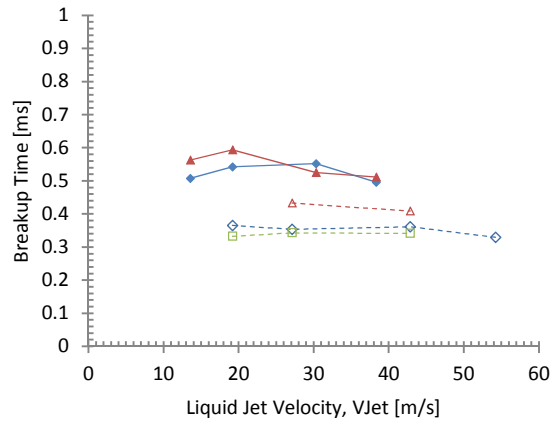
Previously it has been shown that the breakup is constant and does not exhibit change over limited conditions. Wu et al. [9] and Sallam et al. [39] have previously reported values at about 2.5 and 3.5 for momentum flux ratio value of 20. More recently Gopala [61] has expanded on this aspect of research and shown that in fact non-dimensionalized time changes as the primary variables change. Gopala's [61] results show that normalized breakup time follow a logarithmic trend with respect to momentum flux ratio. They did not provide a unified correlation to define normalized breakup time; instead they have correlated breakup time with each parameter individually to show the trend between individual parameters and breakup time. One of the differences that exist between the two studies is the actual numerical value of normalized time. Their values range from 1 to 3 while the values of current research are from 3 to 12. This difference is mostly due to the fact that Gopala used a dye which fluoresces the liquid column once illuminated by laser and consequently have been able to capture more detailed imaging of the jet breakup point. Generally there are environmental hazards associated with use of such dye and the current research facility is not able to accommodate for such chemicals. They also used a blow down tank similar to Sallam for their experiments which inherently transient in nature. Finally, in the current study the velocities have been varied in order to achieve the momentum flux ratios with different flow intensities. This essentially explains the multiple values seen for single momentum flux ratio, Figure 5.11 (b). The normalized time varies considerably at lower momentum flux ratios but as the momentum flux ratio increases the normalized breakup time asymptotically reaches the lower limit of approximately 3. On the other hand, at lower end of momentum flux ratio it can reach as high as 12 based on the results of current study.

Figure 5.10 shows the effect of various dimensional variables versus breakup time. In all the images all the variable except for the studied parameter are kept constant for each data series. The markers for the shown data do not represent the conditions' symbols defined in previous chapters. In each figure the jet velocity is kept constant at 19 m/s except for Figure 5.10 (b). In Figure 5.10 (e) and (f) the series presented with the dashed lines are at 2.1 bar and the series presented with the solid lines are at 3.8 bar. The nozzle diameters for Figure 5.10 (e) and (f) are 572  $\mu\text{m}$  and 457  $\mu\text{m}$  respectively. Similarly in Figure 5.10 (g) and (h) the series presented with the dashed lines are for the 457  $\mu\text{m}$  nozzle and the series presented with the solid lines are for the 572  $\mu\text{m}$  nozzle. The crossflow pressure for Figure 5.10 (g) and (h) are 2.1 bar and 3.8 bar respectively.



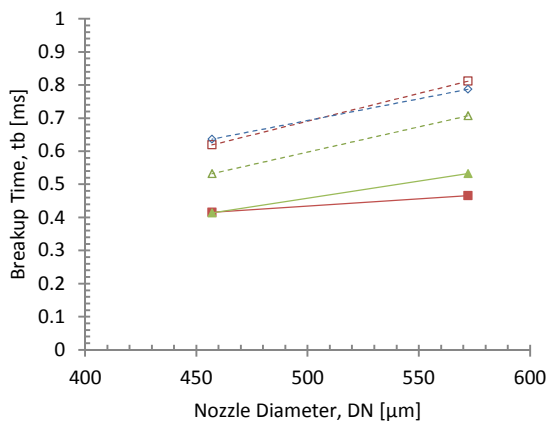
---◇--- 2, 7, and 11      ---◆--- 44, 49, 54, and 59  
 ---■--- 60, 64, 69, and 74      - - -△- - - 33, 38, and 43  
 ---▲--- 80, 85, and 90

(a)



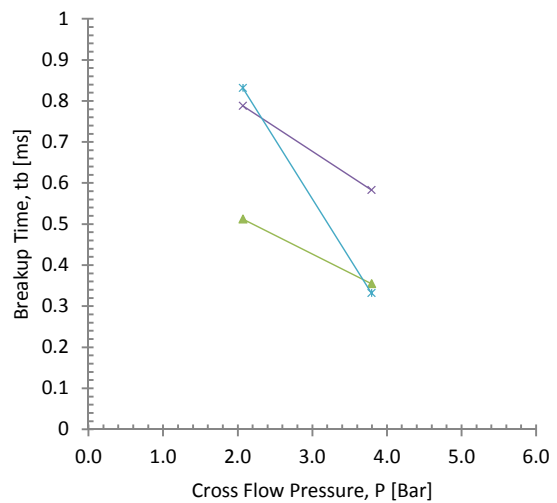
---◇--- 44, 45, 46, and 47      ---◆--- 1, 2, 3, and 4  
 ---□--- 60, 61, and 62      - - -△- - - 76 and 77  
 ---▲--- 32, 33, 34, and 35

(b)



- - -□- - - 22 and 113      ---■--- 64 and 156  
 - - -△- - - 38 and 129      ---▲--- 80 and 168  
 ---◇--- 7 and 97

(c)



---▲--- 2 and 44      ---×--- 7 and 49      ---\*--- 17 and 60

(d)



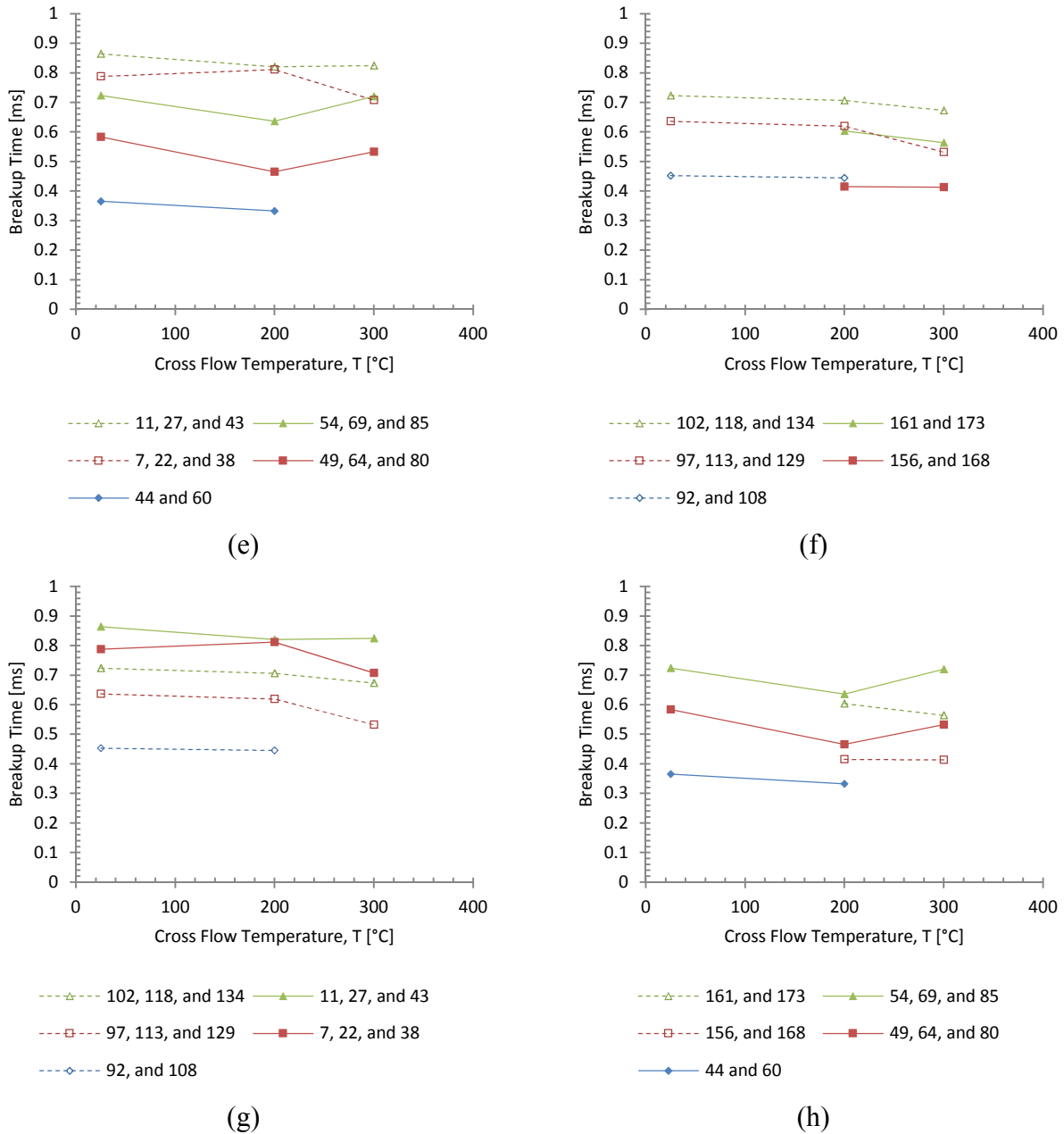


Figure 5.10: Normalized breakup time versus (a) air velocity, (b) jet velocity, (c) nozzle diameter, (d) crossflow pressure, and (e) – (h) crossflow temperature. In all the graphs the parameters are kept constant except for the parameter of interest, for example in figure (a) only air velocity is altered. The symbols do not represent the conditions since the conditions for each data series is different. Table 2.3 summarizes the conditions.

Figure 5.10 (a) and (b) show the effect of air and jet velocity on the breakup time. The breakup time reduces as both of these variables increase due to increased force on the body of the jet. In

contrast as the nozzle diameter increases the breakup time is delayed due to the larger diameter of the jet, Figure 5.10 (c). The larger jet has more momentum and penetrates more in the flow and consequently the breakup time increases. As expected increasing pressure leads to shorter breakup times, Figure 5.10 (d). However, the temperature changes in current range does not show a clear effect on the breakup time, Figure 5.10 (e) – (h). Similar to pressure, temperature changes the gas density but unlike pressure, it also changes the gas viscosity. The two changes seem to cancel each other. For the current range of temperatures the effects are negligible.

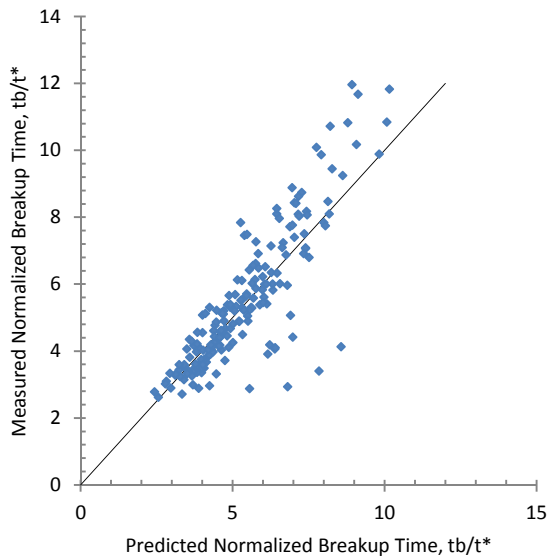
Similar to previous section Weber, Reynolds and Ohnesorge numbers are used to define three correlations for the normalized breakup time, Figure 5.11 (a). The coefficient of determination for these correlations is 0.72 and it is found that statically the chosen variables are all significant based on 95% confidence criterion. In this case also a third equation is also provided for which breakup time is directly correlated to the non-dimensional variables, equation (5.10). The coefficient of determination for this correlation is 0.82. It is more intuitive to use equation (5.10) for explaining the behavior of the jet since the normalized breakup time inherently includes the momentum flux ratio and one of the velocities terms. Once again by rearranging equation (5.10) one can see that momentum flux ratio would have a power of -0.30, which means as the trajectory is increased the breakup time decreases. Equation (5.10) shows that as the aerodynamic forces are increased the breakup time is decreased. Images in each row of Figure 6.12 clearly show this behavior. As the air velocity is reduced the aerodynamic forces on the jet is reduces and the jet penetrates more into the crossflow air and the breakup time increases, as shown earlier. Equation (5.10) also suggests that when the liquid jet Weber number is increased, the breakup time is reduced. In fact this is fairly easy to verify since by increasing jet Weber number the inertia forces can overcome surface tension forces easier, and consequently the breakup time is reduced. Finally, viscosity of the liquid jet plays an important role. As the viscosity is increased one can anticipate the breakup to take place later, in equation (5.10) as the viscosity increases Reynolds number would decrease and breakup time is reduced. The data shows that the viscosity of the jet and the initial condition of the jet play an important role in the atomization process. Essentially both aerodynamic and turbulent breakup mechanisms are inseparable in the breakup process.

$$\begin{aligned} \frac{t_b}{t^*} &= e^{10.80} We_{Air}^{0.39} We_{Jet}^{0.51} Re_{Air}^{0.03} Re_{Jet}^{-1.61} \\ &= e^{10.80} We_{Air}^{0.40} We_{Jet}^{-0.30} Oh_{Air}^{-0.03} Oh_{Jet}^{1.61} \\ &= 4e^{10.80} q^{-0.30} We_{Air}^{0.11} Oh_{Air}^{-0.03} Oh_{Jet}^{1.61} \end{aligned} \quad (5.9)$$

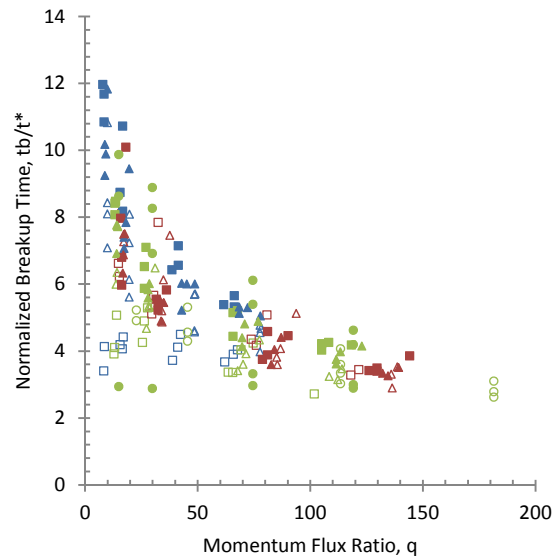
$$\begin{aligned} t_b &= e^{-5.00} We_{Air}^{-0.11} We_{Jet}^{-0.99} Re_{Air}^{0.03} Re_{Jet}^{1.39} \\ &= e^{-5.00} We_{Air}^{-0.10} We_{Jet}^{-0.30} Oh_{Air}^{-0.03} Oh_{Jet}^{-1.39} \\ &= e^{-5.00} q^{-0.30} We_{Air}^{-0.39} Oh_{Air}^{-0.03} Oh_{Jet}^{-1.39} \end{aligned} \quad (5.10)$$

$$t_b = e^{-5.00} D_N^{0.31} V_{Air}^{-0.20} V_{Jet}^{-0.60} \rho_{Air}^{-0.09} \rho_{Jet}^{0.40} \mu_{Air}^{-0.03} \mu_{Jet}^{-1.39} \sigma^{1.11} \quad (5.11)$$

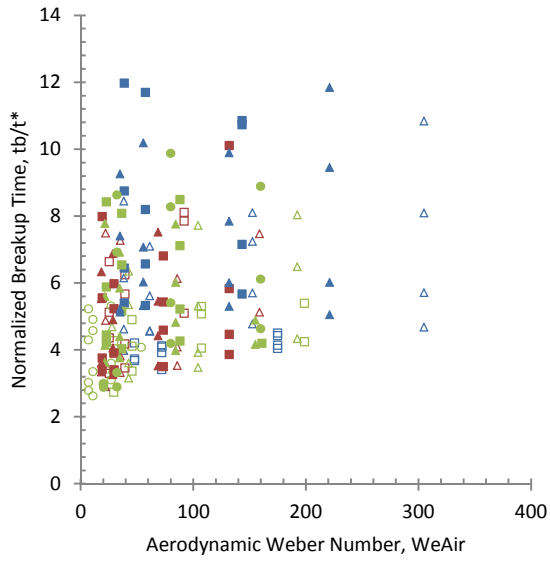
Figure 5.11 (g) and (h) show that the droplet size does not relate to breakup time very well. The breakup time for various test conditions can be the same and so it is possible to have different droplet size for a given breakup time. For jet in crossflow at elevated temperatures, the droplet size is highly dependable on gas viscosity. A more detail discussion is provided in the next chapter.



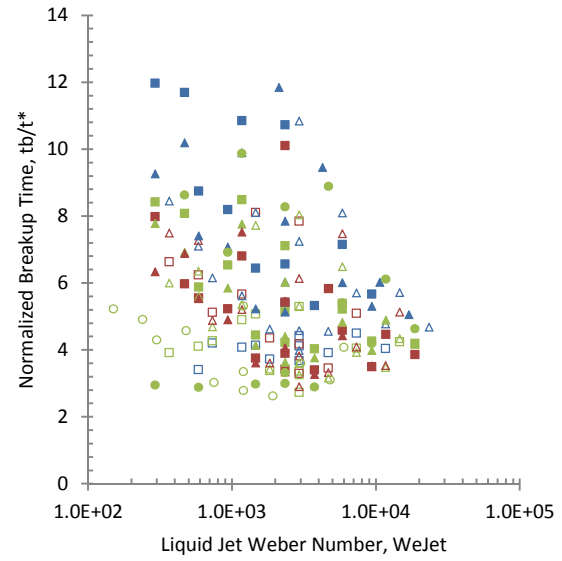
(a)



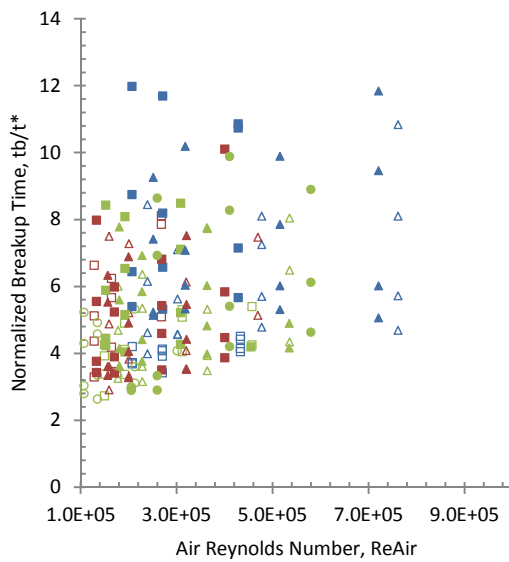
(b)



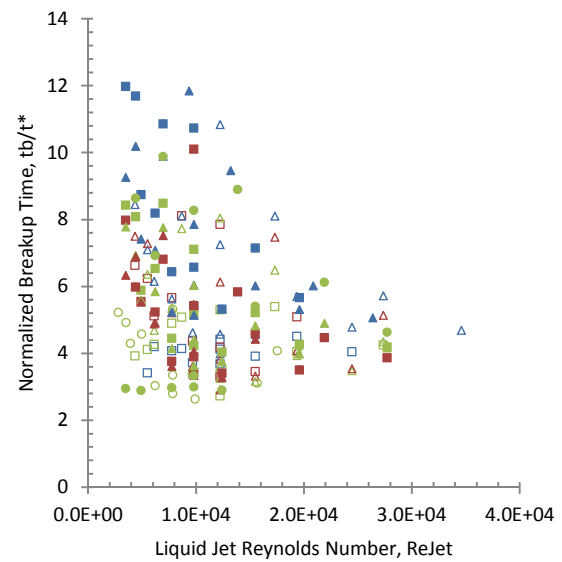
(c)



(d)



(e)



(f)

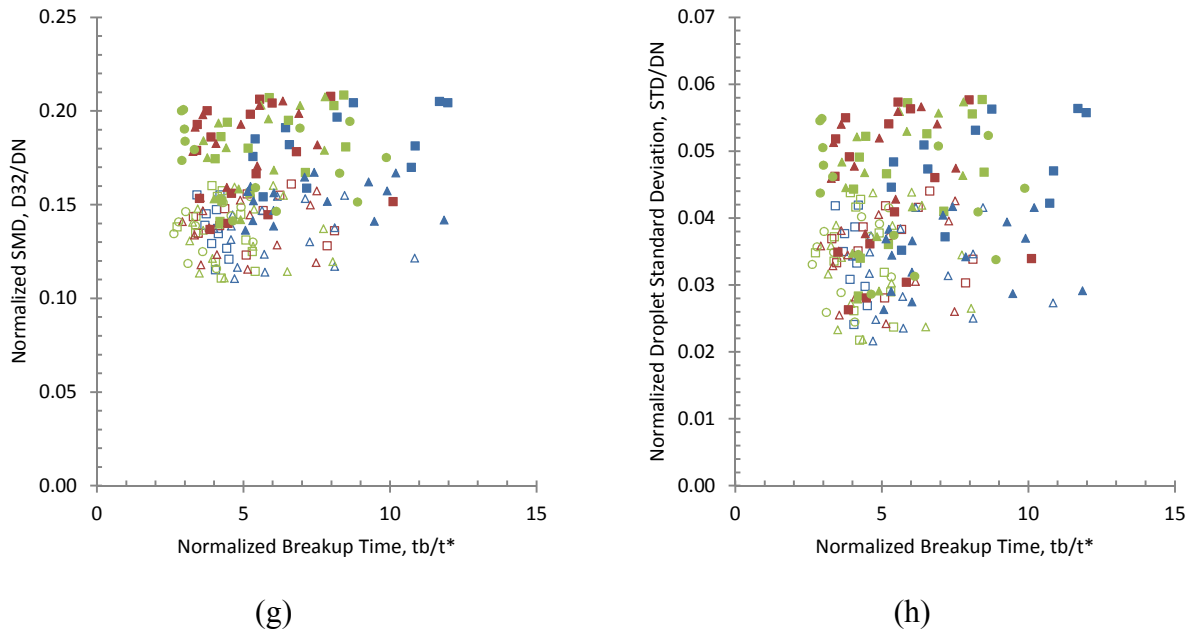


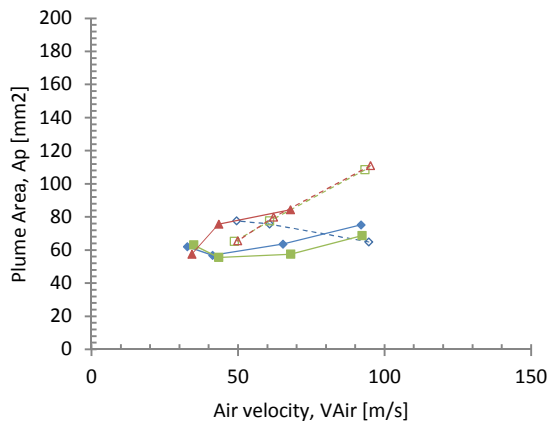
Figure 5.11: (a) Correlation of normalized breakup time; (b) – (f) Normalized mean breakup time vs. various non-dimensionalized numbers; (g) – (h) Normalized D32 and droplet size standard deviation vs. normalized breakup time. Table 2.3 summarizes the conditions.

## 5.5 Plume Area

The plume area is the largest intact area that is measured by the image processing algorithm as defined earlier in chapter 3. The spray area can be associated as a measure of the effectiveness of atomization and droplet dispersion. This becomes more apparent when looking at the next two sections on mean spray width and mean jet surface thickness. Plume area solely on its own can be an ambiguous concept since it encapsulates multiple behaviors into one parameter. For example, There can be two plume areas of similar dimension but when comparing the imaging one can be very slender and long and the other much wider and shorter. Consequently the dispersion, droplet formation, and ultimately the atomization process is different for these cases. Nevertheless, the data presented here will try to show how the plume area is affected by various parameters and how it affects droplet size.

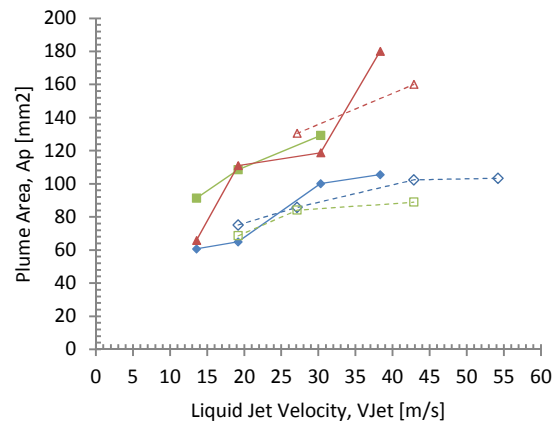
Figure 5.12 shows the effect of various dimensional variables versus plume area. In all the images all the variable except for the studied parameter are kept constant for each data series. The markers for the shown data do not represent the conditions' symbols defined in previous chapters. In each figure the jet velocity is kept constant at 19 m/s except for Figure 5.12 (b). In Figure 5.12 (e) and

(f) the series presented with the dashed lines are at 2.1 bar and the series presented with the solid lines are at 3.8 bar. The nozzle diameters for Figure 5.12 (e) and (f) are 572  $\mu\text{m}$  and 457  $\mu\text{m}$  respectively. Similarly in Figure 5.12 (g) and (h) the series presented with the dashed lines are for the 457  $\mu\text{m}$  nozzle and the series presented with the solid lines are for the 572  $\mu\text{m}$  nozzle. The crossflow pressure for Figure 5.12 (g) and (h) are 2.1 bar and 3.8 bar respectively. It is not difficult to recognize that an increase in jet velocity, density, viscosity and/or nozzle diameter causes the plume area to increase, Figure 5.12 (b) and (c). In contrast gas velocity, pressure, and temperature effects are subdued, Figure 5.12 (a) and (d) – (h). In order to better understand the relation between the gas properties and plume area it is beneficial to compare the parameters in the non-dimensional form.



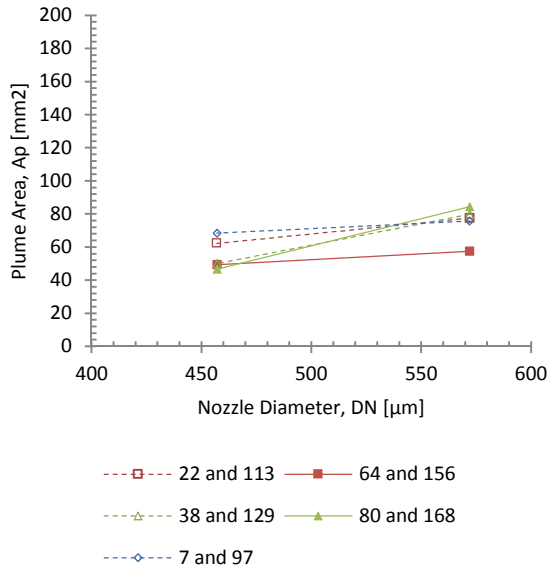
- ◇--- 2, 7, and 11
- ◇--- 44, 49, 54, and 59
- 17, 22, and 27
- 60, 64, 69, and 74
- △--- 28, 33, 38, and 43
- △--- 80, 85, and 90

(a)

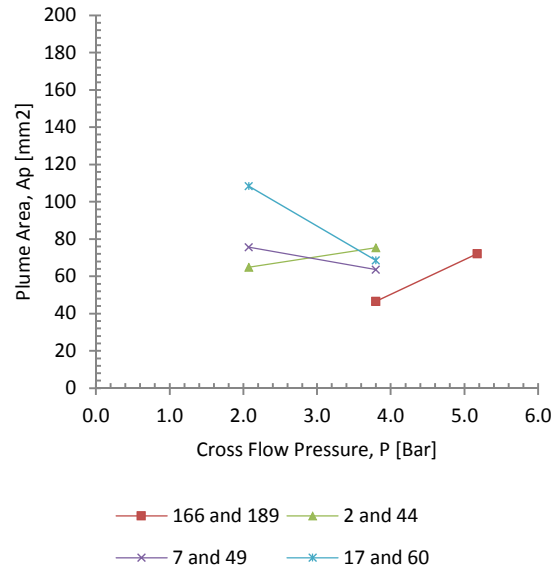


- ◇--- 44, 45, 46, and 47
- ◇--- 1, 2, 3, and 4
- 60, 61, and 62
- 16, 17, and 18
- △--- 76 and 78
- △--- 32, 33, 34, and 35

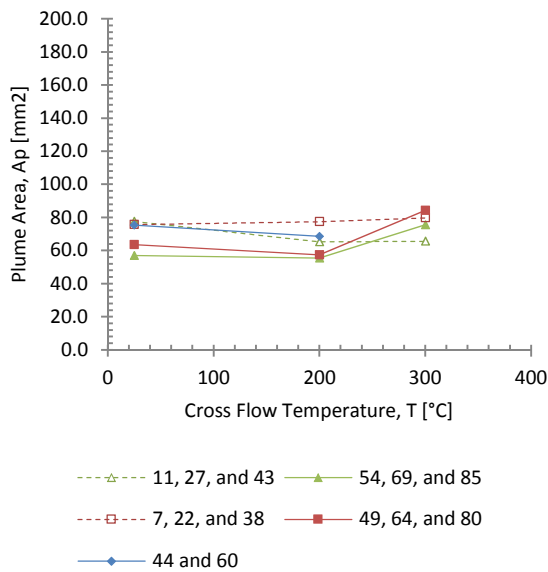
(b)



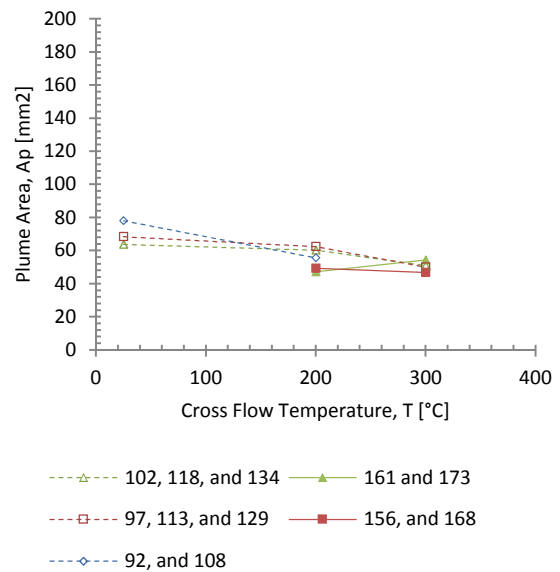
(c)



(d)



(e)



(f)

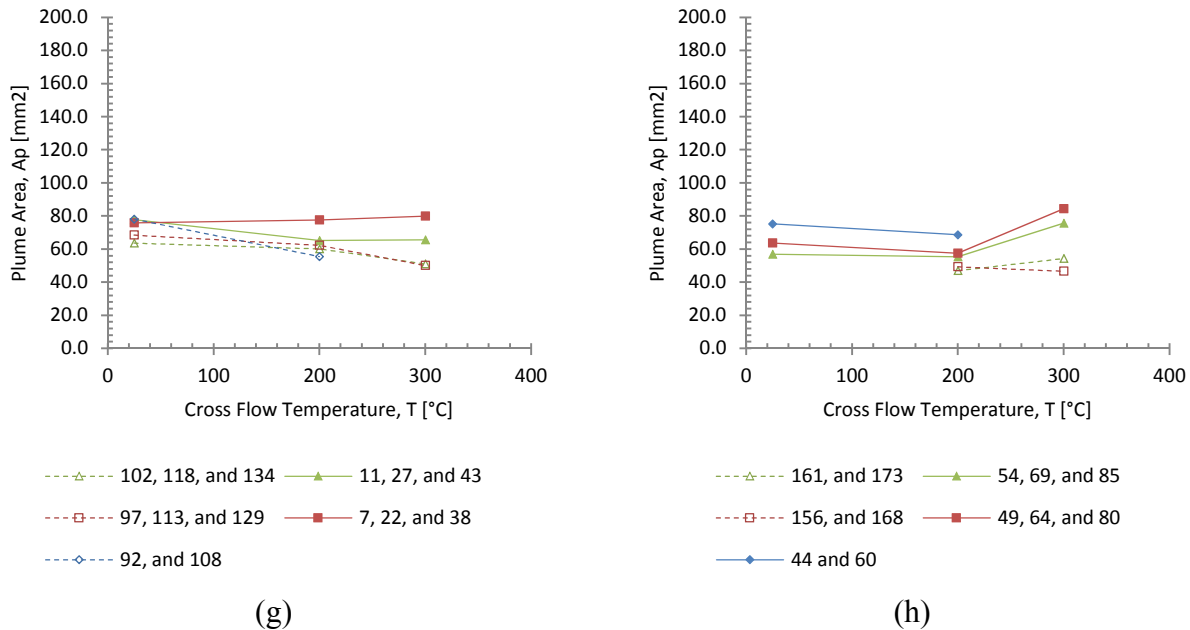


Figure 5.12: Normalized plume area versus (a) air velocity, (b) jet velocity, (c) nozzle diameter, (d) crossflow pressure, and (e) – (h) crossflow temperature. In all the graphs the parameters are kept constant except for the parameter of interest, for example in figure (a) only air velocity is altered. The symbols do not represent the conditions since the conditions for each data series is different. Table 2.3 summarizes the conditions.

Figure 5.13 (b) – (f) show the effects of momentum flux ratio, gas and liquid Weber and Reynolds numbers on normalized plume area. The plume area is normalized by the orifice area. Generally speaking as the Weber and Ohnesorge numbers increase plume area also increases. However due to the observed scatter and the convoluted nature of plume area it is difficult to draw any solid conclusions. For instance, the effect of gas Weber and Ohnesorge numbers compared to their liquid counterparts are negligible, see equation (5.12). That said the importance of plume area becomes clearer when looking at Figure 5.13 (g) and (h). They show the relation of normalized plume area with droplet size and standard deviation. As the plume area increases the droplet size and standard deviation is almost linearly reduced. It is interesting to note that even though at first glance the data displays a wider spread for smaller sizes it is not actually a spread in data. The data for each condition does not deviate radically but rather as the conditions change the slope that relates the two parameters change. This suggests that as pressure and nozzle diameter change the slope in Figure 5.13 (g) also changes. In other words, as these parameters increase, the area also increases



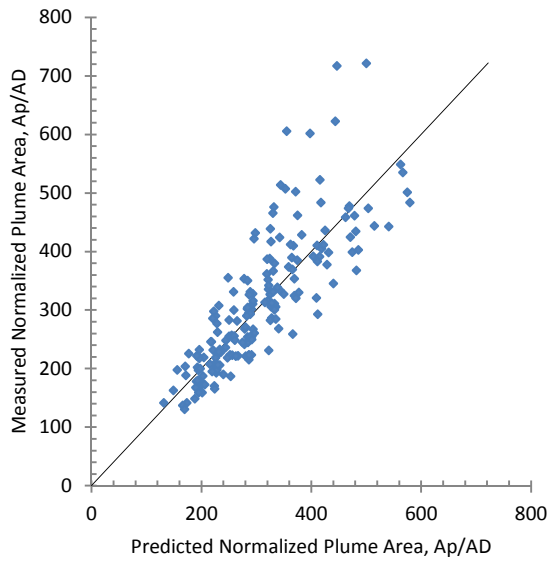
and consequently droplet size decreases. This leads itself to the discussions in the next chapter on droplet size.

$$\begin{aligned}\frac{A_p}{A_D} &= e^{13.01} We_{Air}^{0.04} We_{Jet}^{1.09} Re_{Air}^{-0.05} Re_{Jet}^{-1.68} \\ &= e^{13.01} We_{Air}^{0.02} We_{Jet}^{0.25} Oh_{Air}^{0.05} Oh_{Jet}^{1.68} \\ &= e^{13.01} q^{0.25} We_{Air}^{0.27} Oh_{Air}^{0.05} Oh_{Jet}^{1.68}\end{aligned}\quad (5.12)$$

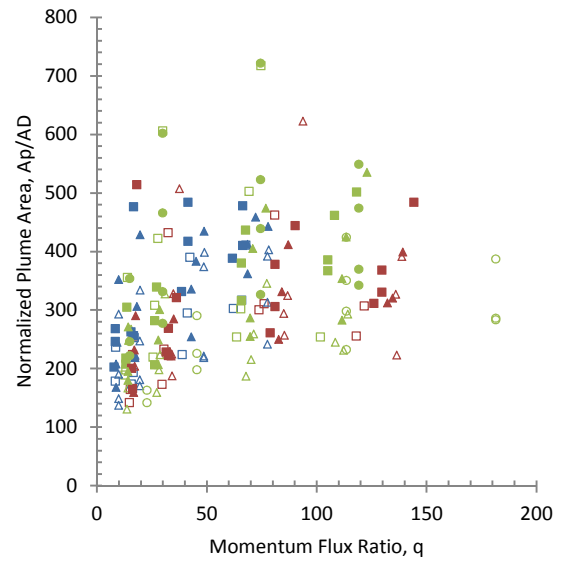
$$A_p = e^{13.25} D_N^{1.41} V_{Air}^{0.04} V_{Jet}^{0.50} \rho_{Air}^{-0.01} \rho_{Jet}^{-0.59} \mu_{Air}^{0.02} \mu_{Jet}^{1.68} \sigma^{-1.14}\quad (5.13)$$

Similar to previous section Weber, Reynolds and Ohnesorge numbers are used to define three interchangeable correlations for the normalized breakup length, Figure 5.13 (a). The coefficient of determination for these correlations is 0.75 and it is found that statically the chosen variables are all significant based on 95% confidence criterion. The data displays strong relation with jet properties and conditions while gas properties and conditions are found to be statistically insignificant. Normalized plume area is a measure of mass of liquid that is available during primary atomization. Therefore, it is the liquid jet properties and conditions that should affect this parameter the most. Parameters related to air only change the geometry of the plume. Finally, it is safe to assume that momentum flux ratio alone does not affect normalized plume area, Figure 5.13 (b) – (f).

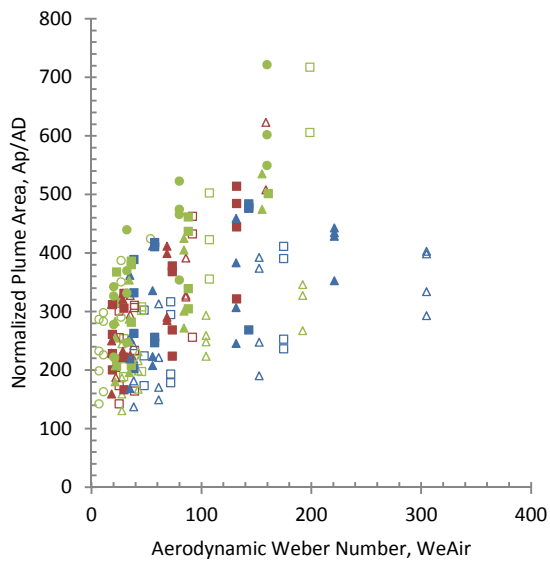
Another way to verify the statistical observations is to compare images in Figure 6.12 where only air velocity is altered. In these images the breakup length and plume width change for each row of images but the plume area does not change significantly. Essentially the air velocity does not significantly affect plume area. There are two opposed mechanisms that are in play, as the air velocity increases the plume is bent more but at the same time it is stretched more in the air flow direction. On the other hand as the velocity decreases the jet penetrates more in the crossflow but the plume takes on a more slender shape. This is specially becomes more apparent for the cases at higher temperature where gas viscosity is also in play. For example, when comparing images in Figure 6.20 where only gas temperature is changed, i.e. gas density and viscosity, and there are small changes in the normalized area. On the other hand when comparing images in Figure 6.10 the plume area is considerably increasing as the liquid jet velocity is increasing.



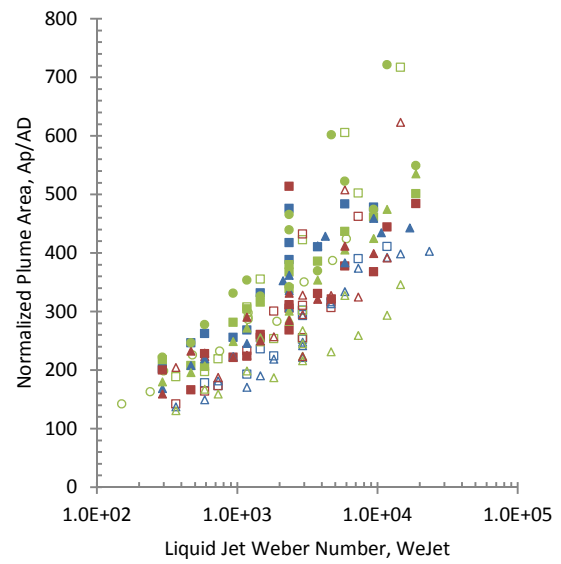
(a)



(b)



(c)



(d)

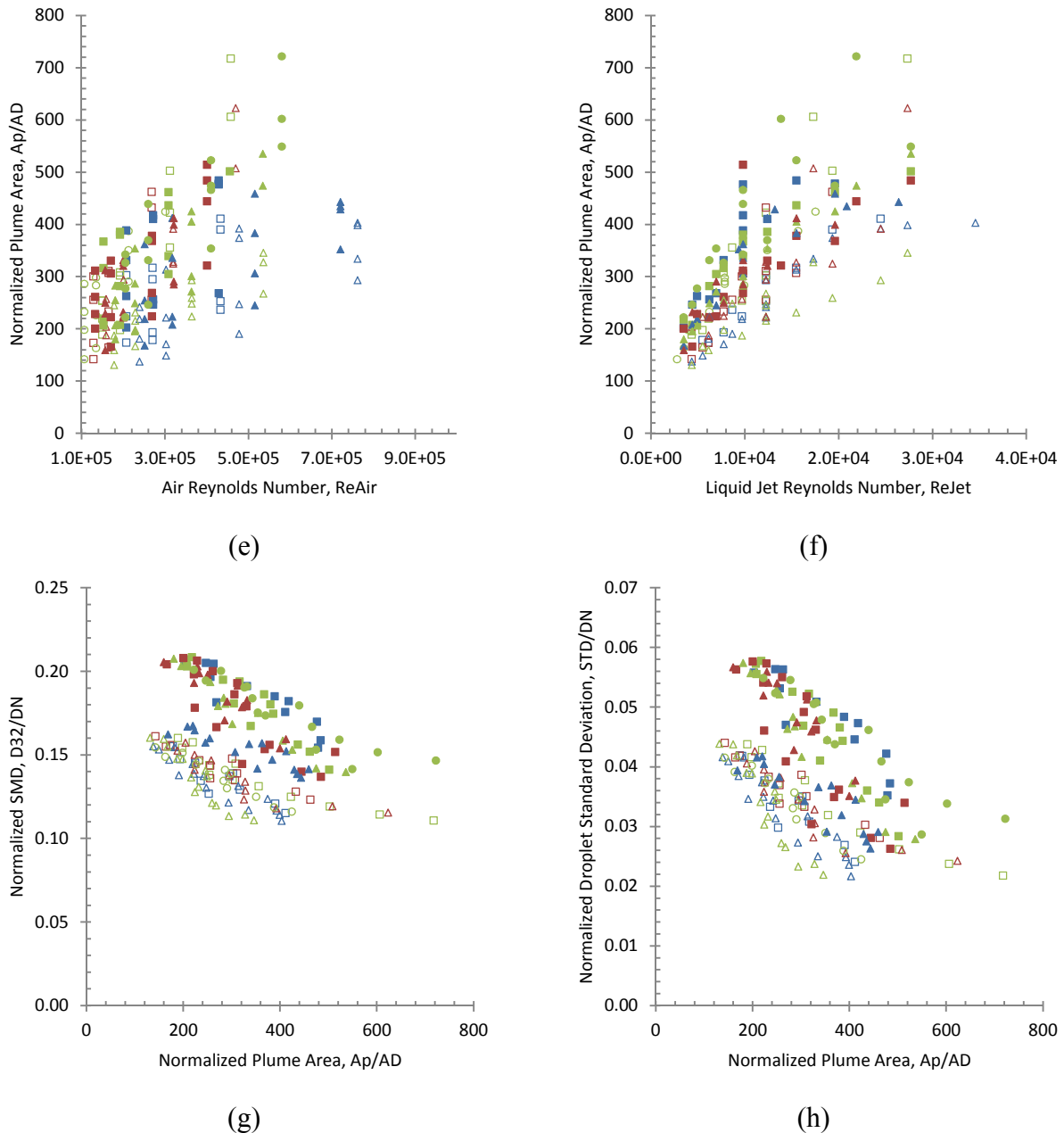
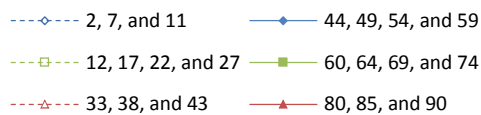
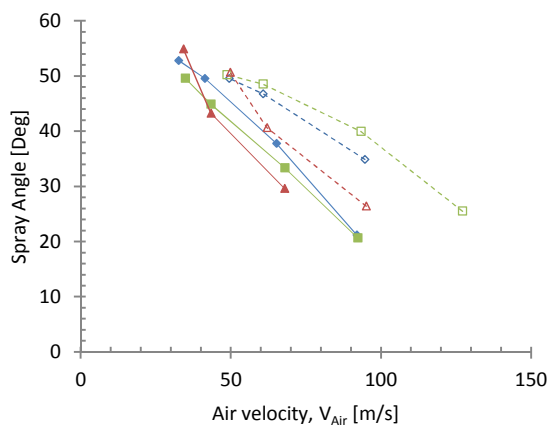


Figure 5.13: (a) Correlation of normalized plume area; (b) – (f) Normalized plume area vs. various non-dimensionalized numbers; (g) – (h) Normalized  $D_{32}$  and droplet size standard deviation vs. normalized area plume area. Table 2.3 summarizes the conditions.

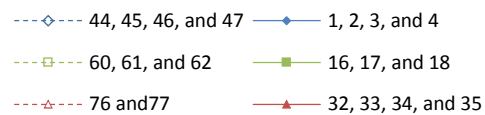
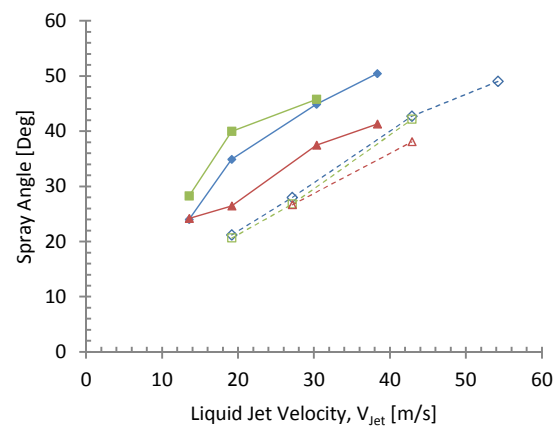
## 5.6 Spray Plume Angle

Spray plume angle is defined as the angle between the chamber wall that houses the nozzle and the imaginary line the center of the nozzle exit to the breakup point. In a way this is very similar to the spray angle that is widely recognized in spray studies. Plume angle is essentially a measure

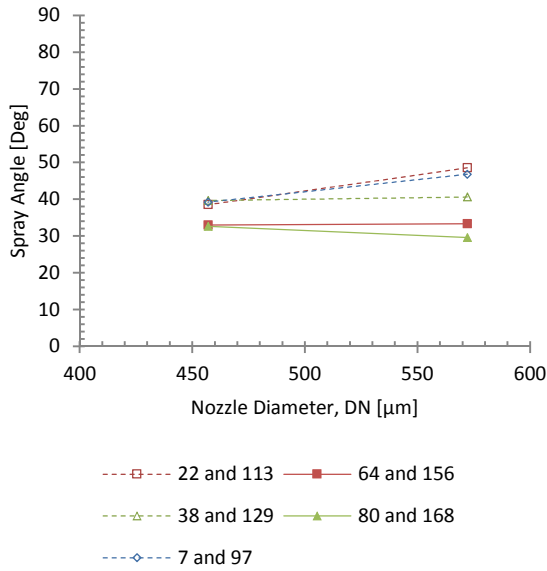
of the dispersion of the liquid jet into crossflow. Figure 5.14 shows the effect of various dimensional variables versus spray plume angle. In all the images all the variable except for the studied parameter are kept constant for each data series. The markers for the shown data do not represent the conditions' symbols defined in previous chapters. In each figure the jet velocity is kept constant at 19 m/s except for Figure 5.14 (b). In Figure 5.14 (e) and (f) the series presented with the dashed lines are at 2.1 bar and the series presented with the solid lines are at 3.8 bar. The nozzle diameters for Figure 5.14 (e) and (f) are 572  $\mu\text{m}$  and 457  $\mu\text{m}$  respectively. Similarly in Figure 5.14 (g) and (h) the series presented with the dashed lines are for the 457  $\mu\text{m}$  nozzle and the series presented with the solid lines are for the 572  $\mu\text{m}$  nozzle. The crossflow pressure for Figure 5.14 (g) and (h) are 2.1 bar and 3.8 bar respectively. Figure 5.14 (a) and (b) show the relation between the plume angle and the gas and jet velocities. As the gas velocity increases and jet velocity decreases the plume angle decreases. In Figure 5.14 (c) as the nozzle diameter increases the plume angle increases. Plume angle is heavily dependent on gas properties as oppose to the other parameters discussed earlier. Figure 5.14 (d) show that as the pressure increases the plume angle decreases which essentially means as the gas density increases the plume angle reduces. However, in Figure 5.14 (e) – (h) as the temperature increases the plume angle in most cases is reduced. This observation suggests that increasing the temperature not only causes the gas density to reduce but also increases the gas viscosity, which explain reduction in plume angle.



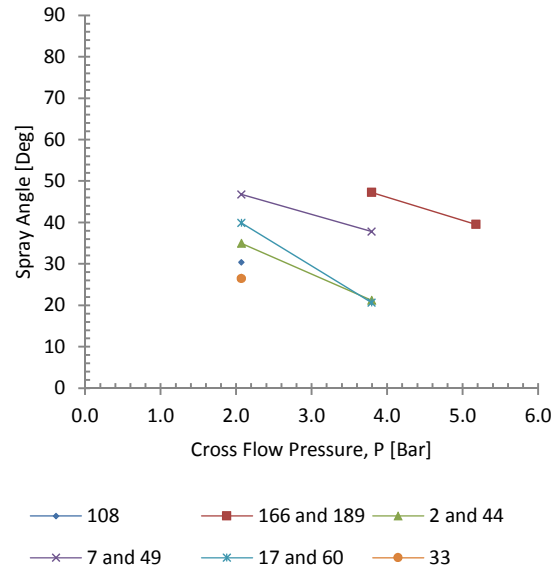
(a)



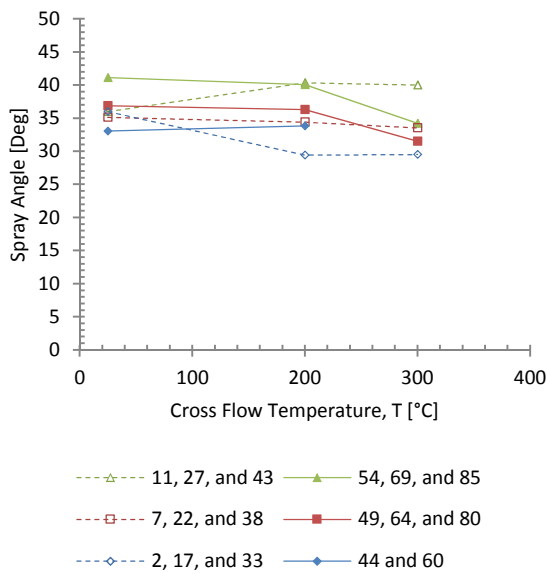
(b)



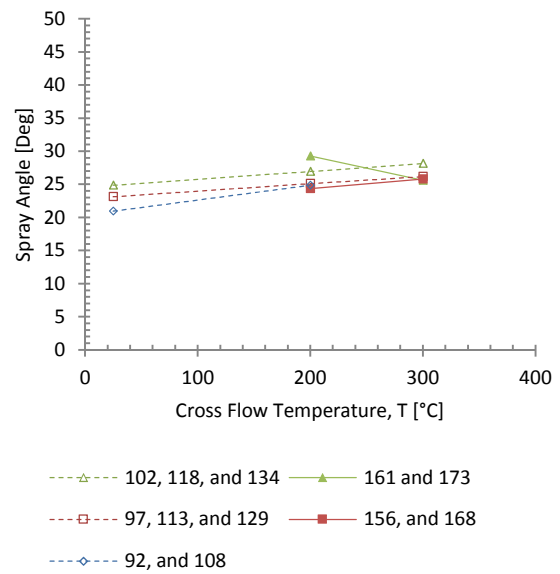
(c)



(d)



(e)



(f)

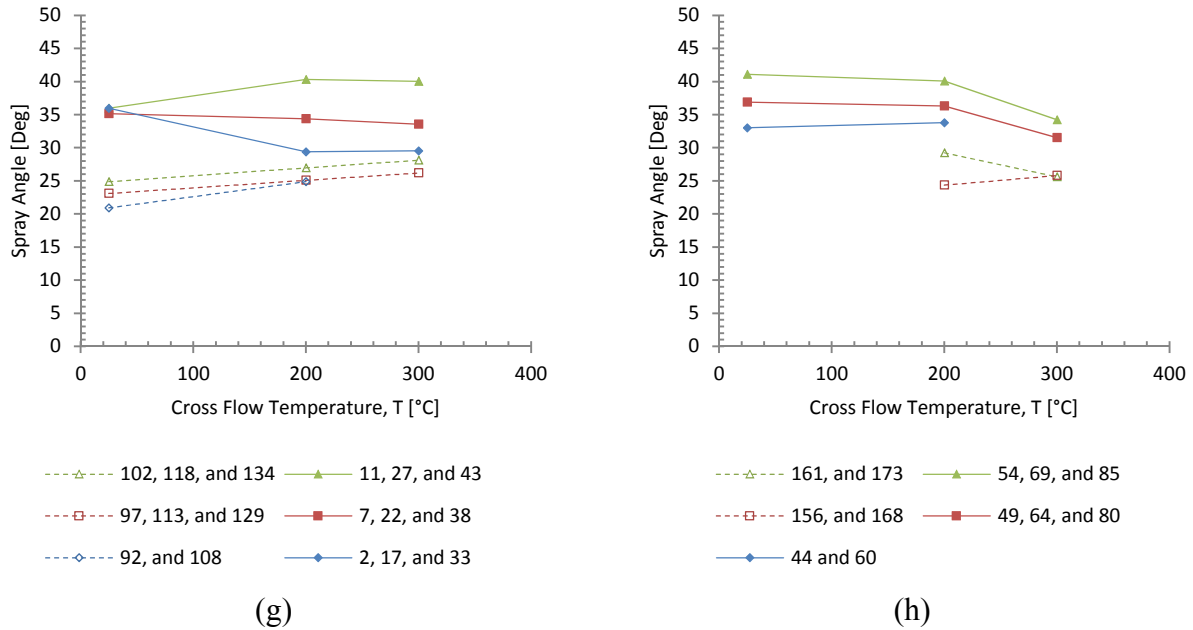


Figure 5.14: Normalized spray plume angle versus (a) air velocity, (b) jet velocity, (c) nozzle diameter, (d) crossflow pressure, and (e) – (h) crossflow temperature. In all the graphs the parameters are kept constant except for the parameter of interest, for example in figure (a) only air velocity is altered. The symbols do not represent the conditions since the conditions for each data series is different. Table 2.3 summarizes the conditions.

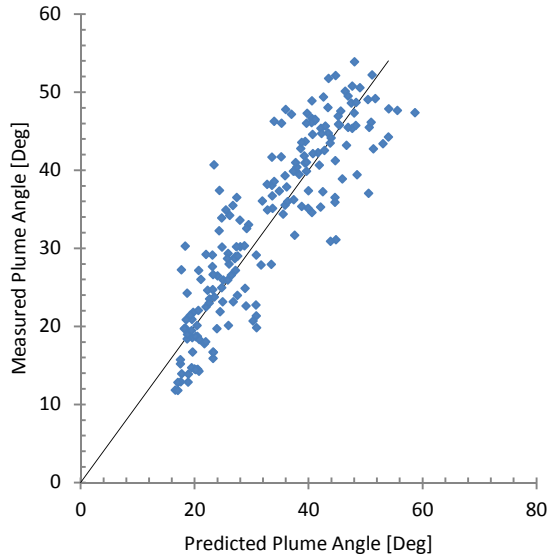
Figure 5.15 (b) – (f) show the relation between the non-dimensionalized parameters and plume angle. The plume angle shows strong relation with momentum flux ratio very similar to breakup length and time. The plume angle seems to follow a logarithmic trend with respect of momentum flux ratio. A more detailed examination of Figure 5.15 (b) also shows the temperature effects on plume angle. Spray plume angle generally reduces the overall droplet size as it is seen in Figure 5.15 (g) and (h). As discussed and anticipated, as the air Weber number increases the spray angle decreases. Similar conclusion can be made regarding liquid Weber number.

$$\begin{aligned}
 \theta_p &= 0.89 We_{Air}^{-0.49} We_{Jet}^{0.39} Re_{Air}^{0.28} Re_{Jet}^{0.03} \\
 &= 0.89 We_{Air}^{-0.35} We_{Jet}^{0.41} Oh_{Air}^{-0.28} Oh_{Jet}^{-0.03} \\
 &= 0.89 q^{0.41} We_{Air}^{0.06} Oh_{Air}^{-0.28} Oh_{Jet}^{-0.03}
 \end{aligned} \tag{5.14}$$

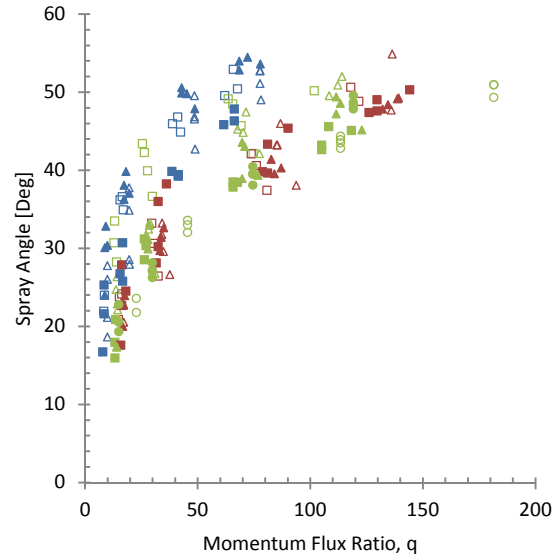
$$\theta_p = 0.89 D_N^{0.22} V_{Air}^{-0.70} V_{Jet}^{0.82} \rho_{Air}^{-0.21} \rho_{Jet}^{0.43} \mu_{Air}^{-0.28} \mu_{Jet}^{-0.03} \sigma^{0.01} \tag{5.15}$$

Similar to previous sections a correlation is developed to explain the behavior of plume angle, equation (5.14). The coefficient of determination for this correlations is 0.77 and it is found that statically the chosen

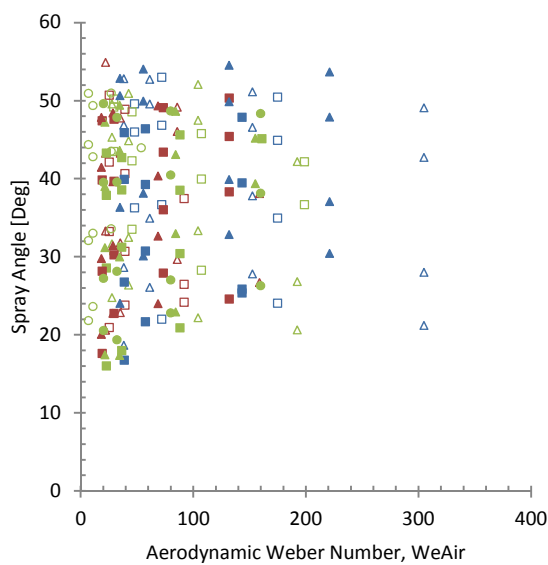
variables are all significant based on 95% confidence criterion. The influence liquid Reynolds number is not strong which is similar to previous findings where penetration is only defined as a function of momentum flux ratio and Aerodynamic Weber number.



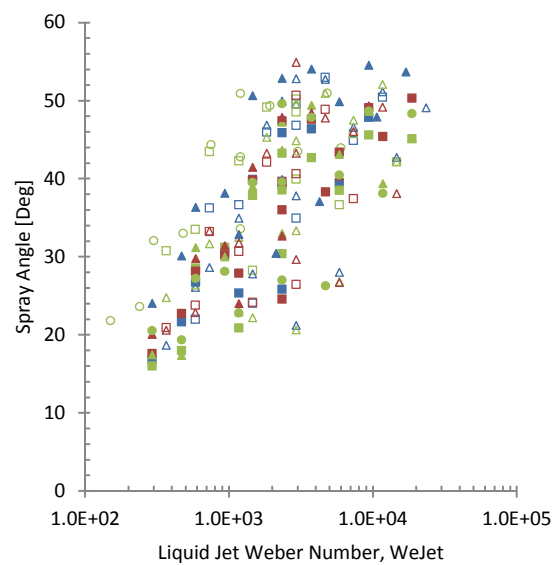
(a)



(b)



(c)



(d)

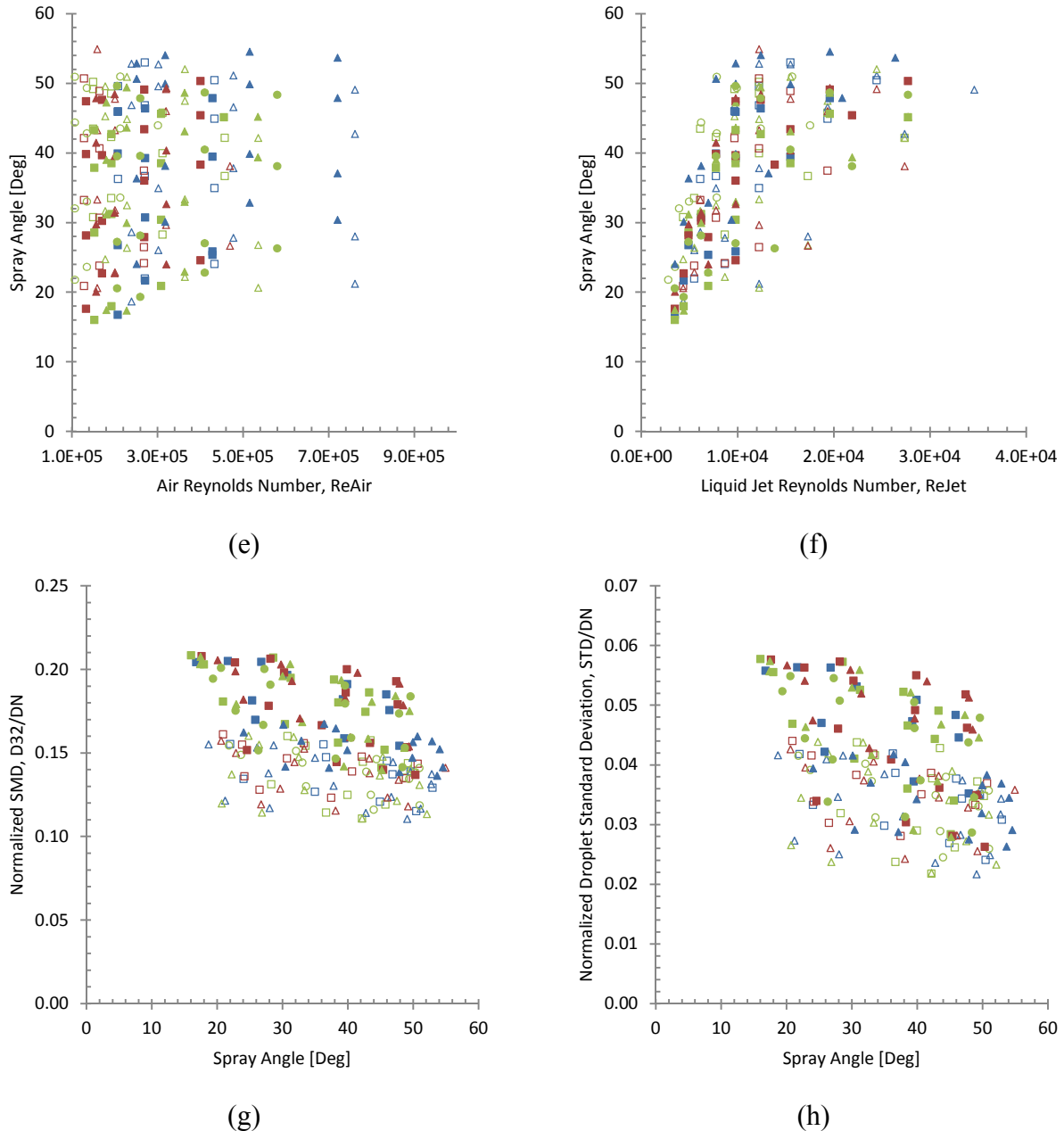


Figure 5.15: (a) Correlation of normalized spray plume angle; (b) – (f) Normalized spray plume angle vs. various non-dimensionalized numbers; (g) – (h) Normalized D32 and droplet size standard deviation vs. normalized spray plume angle. Table 2.3 summarizes the conditions.

## 5.7 Mean Plume Width

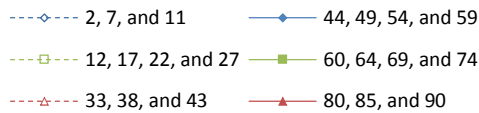
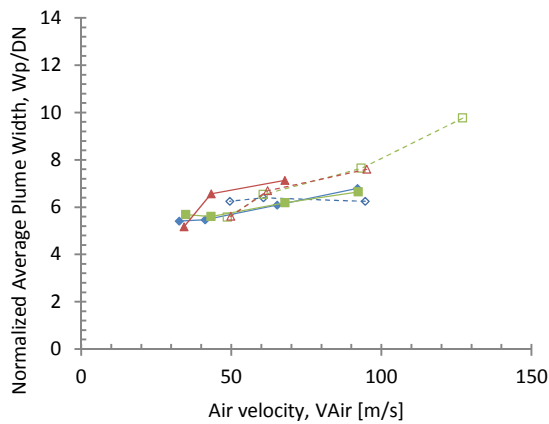
Mean plume width is defined as the ratio of mean plume area and breakup length, equation (5.16). This parameter is defined to help better understand the spray geometry, i.e. shape. As discussed in the previous section plume area is not a good parameter for the comparison since it encapsulates



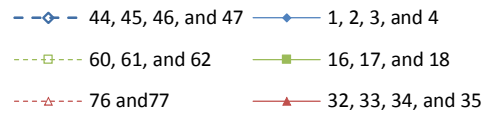
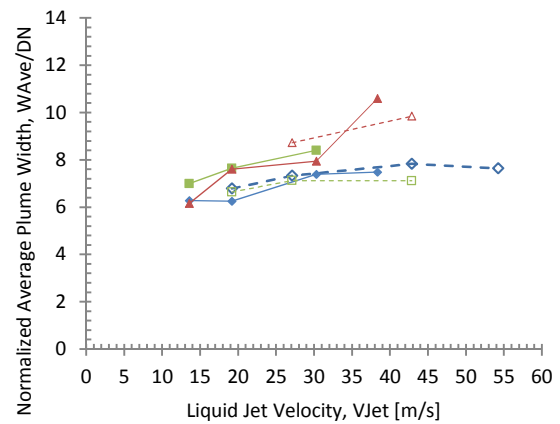
both breakup length and plume width. Plume width is a good measure of dispersion and conceptually must be affected by liquid viscosity and surface tension, since as the liquid viscosity increases it is anticipated that the plume width would also increase due to liquid viscous forces. Conversely, as the liquid surface tension increases then the plume width would decrease.

$$W_P = \frac{A_P}{L_B} \quad (5.16)$$

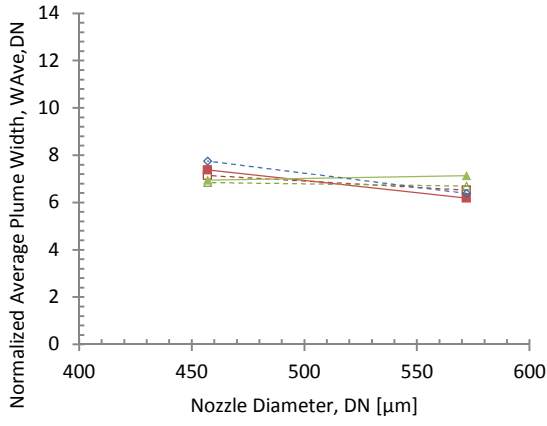
Figure 5.16 shows the effect of various dimensional variables versus mean plume width. In all the images all the variable except for the studied parameter are kept constant for each data series. The markers for the shown data do not represent the conditions' symbols defined in previous chapters. In each figure the jet velocity is kept constant at 19 m/s except for Figure 5.16 (b). In Figure 5.16 (e) and (f) the series presented with the dashed lines are at 2.1 bar and the series presented with the solid lines are at 3.8 bar. The nozzle diameters for Figure 5.16 (e) and (f) are 572  $\mu\text{m}$  and 457  $\mu\text{m}$  respectively. Similarly in Figure 5.16 (g) and (h) the series presented with the dashed lines are for the 457  $\mu\text{m}$  nozzle and the series presented with the solid lines are for the 572  $\mu\text{m}$  nozzle. The crossflow pressure for Figure 5.16 (g) and (h) are 2.1 bar and 3.8 bar respectively.



(a)

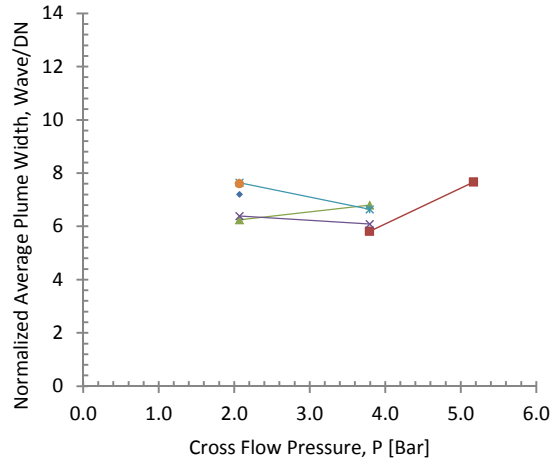


(b)



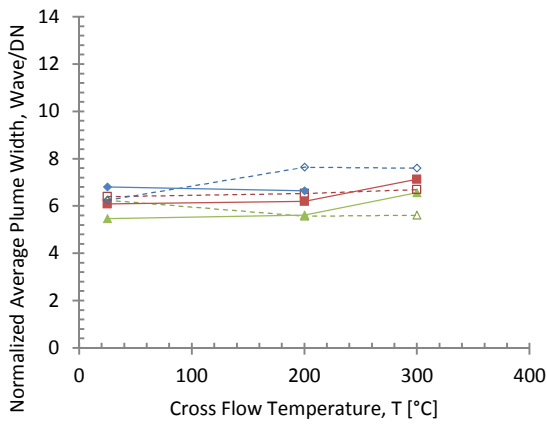
- 22 and 113    ---■--- 64 and 156
- △--- 38 and 129    ---▲--- 80 and 168
- ◇--- 7 and 97

(c)



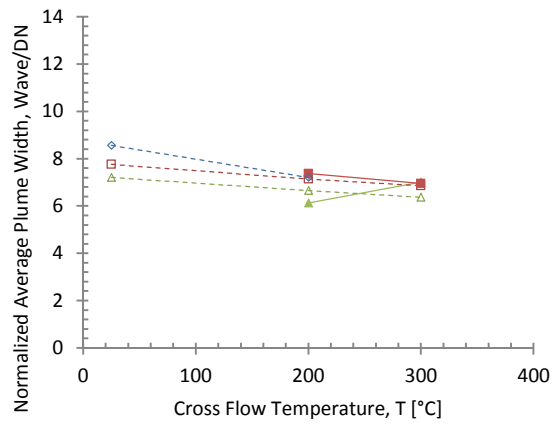
- ◇--- 108    ---■--- 166 and 189    ---▲--- 2 and 44
- ×--- 7 and 49    ---\*--- 17 and 60    ---○--- 33

(d)



- △--- 11, 27, and 43    ---▲--- 54, 69, and 85
- 7, 22, and 38    ---■--- 49, 64, and 80
- ◇--- 2, 17, and 33    ---●--- 44 and 60

(e)



- △--- 102, 118, and 134    ---▲--- 161 and 173
- 97, 113, and 129    ---■--- 156, and 168
- ◇--- 92, and 108

(f)

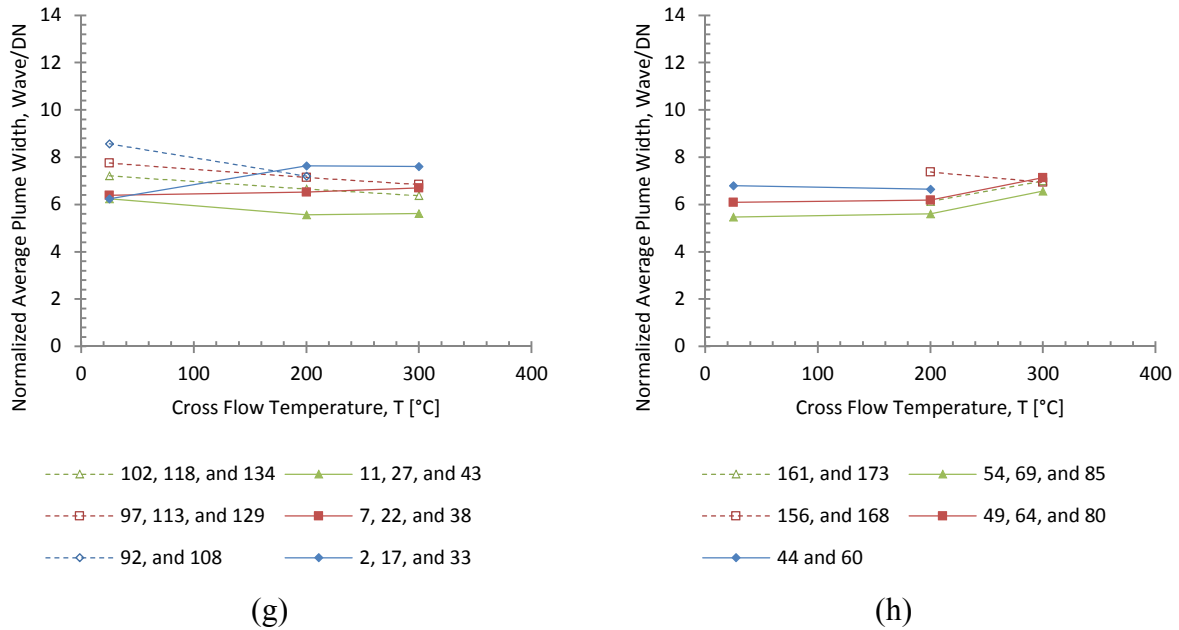


Figure 5.16: Normalized average plume width versus (a) air velocity, (b) jet velocity, (c) nozzle diameter, (d) crossflow pressure, and (e) – (h) crossflow temperature. In all the graphs the parameters are kept constant except for the parameter of interest, for example in figure (a) only air velocity is altered. The symbols do not represent the conditions since the conditions for each data series is different. Table 2.3 summarizes the conditions.

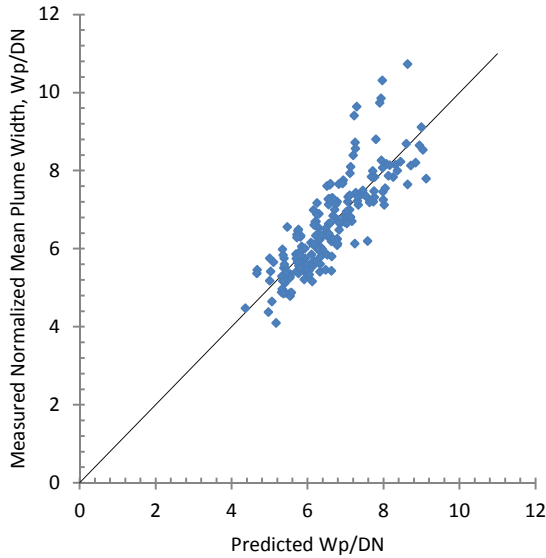
Once again, a correlation is developed to explain the effect various flow parameters as well as fluid properties, equation (5.17). The coefficient of determination for this correlations is 0.73 and it is found that statically the chosen variables are all significant based on 95% confidence criterion. As it can be seen the variables that impact the normalized plume width are liquid Weber number and Reynolds number. This essentially means that the liquid momentum and viscosity has an important role in the atomization process.

$$\begin{aligned}
 \frac{W_P}{D_N} &= 324.8 W_{Air}^{0.09} W_{Jet}^{0.52} Re_{Air}^{-0.06} Re_{Jet}^{-0.84} \\
 &= 324.8 W_{Air}^{0.06} W_{Jet}^{0.09} Oh_{Air}^{0.06} Oh_{Jet}^{0.84} \\
 &= 324.8 q^{0.09} W_{Air}^{0.15} Oh_{Air}^{0.06} Oh_{Jet}^{0.84}
 \end{aligned} \tag{5.17}$$

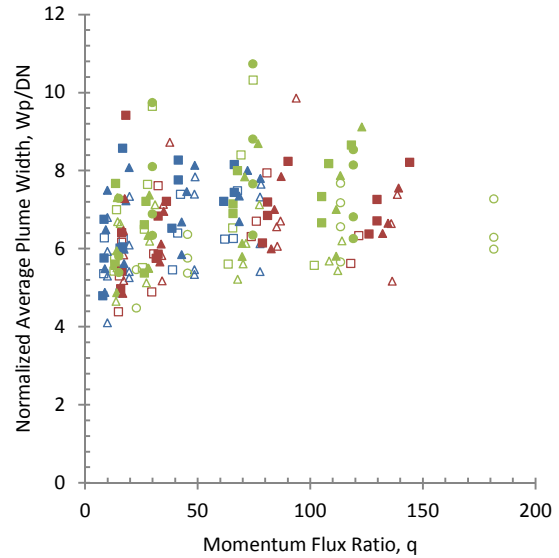
$$W_P = 324.8 D_N^{0.70} V_{Air}^{0.12} V_{Jet}^{0.18} \rho_{Air}^{0.03} \rho_{Jet}^{-0.33} \mu_{Air}^{0.06} \mu_{Jet}^{0.84} \sigma^{-0.6} \tag{5.18}$$

Figure 5.17 (b) – (f) show the impact of various non-dimensionalized numbers on normalized plume width. Once again liquid properties are the determining parameters for mean plume width.

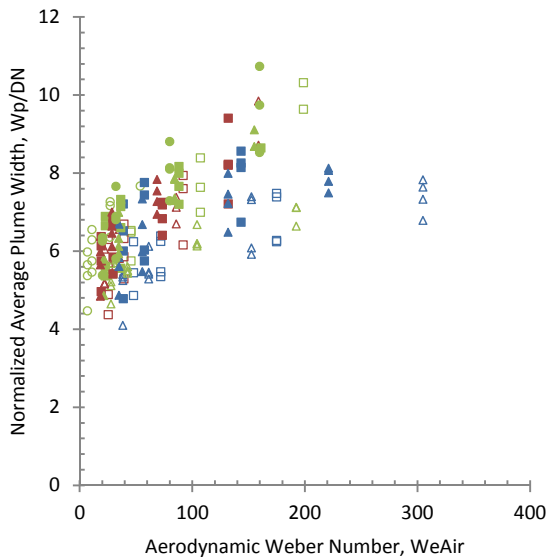
However, the influence of gas related non-dimensional variables can be seen in Figure 5.17 (c) and (e). As these parameters are increased, essentially the density, viscosity and velocity of gas, shear forces on the plume are increased and consequently the mean plume width is also increased. Finally, Figure 5.17 (g) and (h) show the relation between plume width and droplet size and its standard deviation. The figures show that as the plume width increases the droplet size systematically decreases.



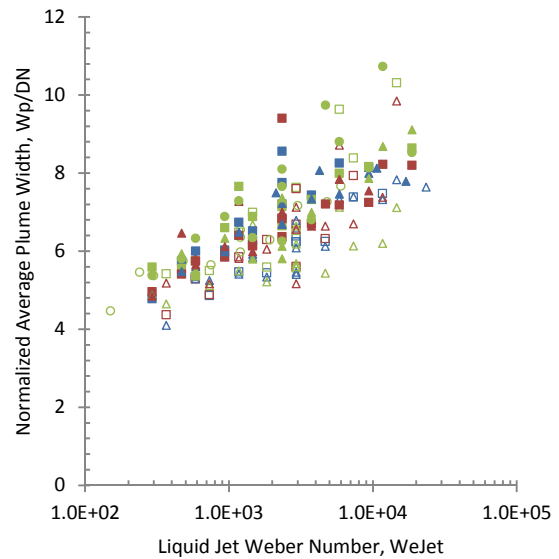
(a)



(b)



(c)



(d)

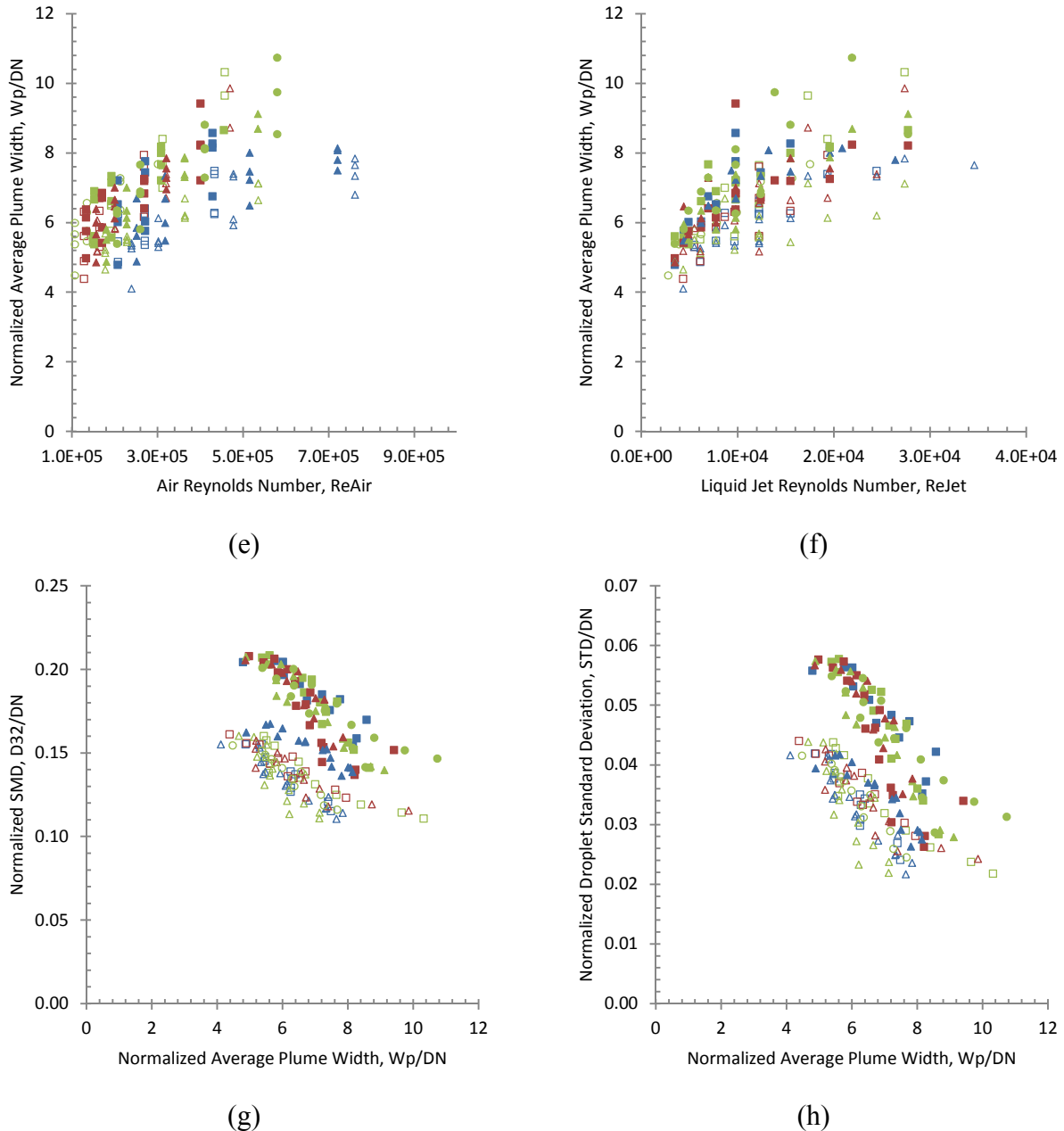


Figure 5.17: (a) Correlation of normalized mean plume width; (b) – (f) Normalized mean plume width vs. various non-dimensionalized numbers; (g) – (h) Normalized  $D_{32}$  and droplet size standard deviation vs. normalized mean plume width. Table 2.3 summarizes the conditions.

## 5.8 Mean Jet Surface Thickness

The atomization process in jet in crossflow does not produce a sheet similar to nozzles specifically designed to employ this type of atomization. Mean jet surface thickness is designed to quantify the relative thickness of the formations inside the plume area where the spray is very dense and the jet

is still intact. The ligament thickness is generally can be related to the size of initially formed droplets in atomization process. It is very difficult to actually measure this parameter for the current study but in any case an attempt is made to calculate a mean value for this parameter based on some of the measured imaging parameters and spray conditions. The primary purpose is not to actually present this data as a finding but to verify the droplet size measuring technique independently and also give an insight to the parameters that would impact ligament thickness and ultimately droplet size and the atomization process. A series of simple assumptions are made in order to derive an expression for jet surface thickness. Liquid mass balance is performed on the mean cross-section of the plume and at the nozzle exit, equation (5.19). It is assumed that the liquid density does not change during atomization and so the mass balance can be simplified, equation (5.20). It is assumed that the surface velocity is the same as the crossflow velocity. As for the cross section area, it is assumed that the cross section of the plume takes a crescent shape similar to the cross-section of a deformed droplet in crossflow, Figure 1.3. The crescent is formed by the drag forces on the front of the jet and by the counter rotating vortices formed downstream of the jet and cause the jet to flatten in the front and stretch to the sides. The area of the crescent can then be defined based on mean plume width and jet surface thickness, equation (5.21). Finally, an expression is derived for the jet surface thickness, equation (5.22), and for the normalized jet surface thickness, equation (5.23). The jet surface thickness is a function of nozzle diameter, breakup length and plume area.

$$\dot{m}_{Nozzle\ Exit} = \dot{m}_{Plume\ Cross-Section} \quad (5.19)$$

$$\rho_{Jet} A_{Nozzle} V_{Jet} = \rho_{Jet} A_{Cross-Section} V_{Cross-section} \quad (5.20)$$

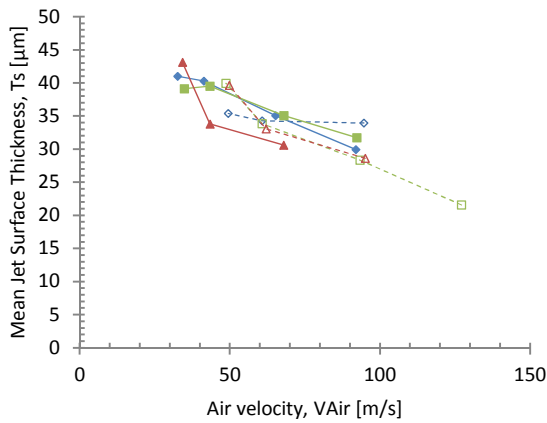
$$\frac{\pi}{4} D_N^2 V_{Jet} = 2T_s W_p V_{CS} = 2T_s \frac{A_p}{B_L} V_{CS} \quad (5.21)$$

$$T_s = \frac{\pi D_N^2}{8 W_p} = \frac{\pi D_N^2 B_L}{8 A_p} \quad (5.22)$$

$$\frac{T_s}{D_N} = \frac{\pi D_N}{8 W_p} = \frac{\pi D_N B_L}{8 A_p} \quad (5.23)$$

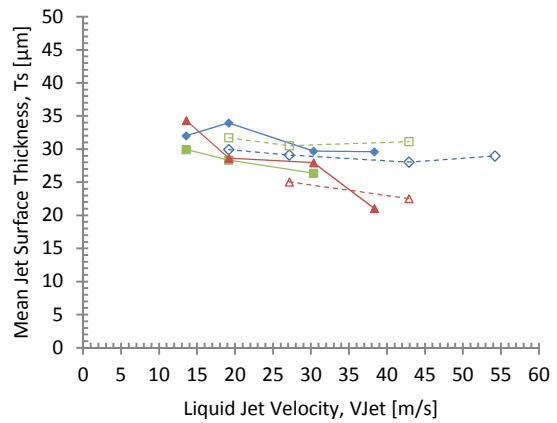
Figure 5.18 shows the effect of various dimensional variables versus normalized mean jet surface thickness. In all the images all the variable except for the studied parameter are kept constant for each data series. The markers for the shown data do not represent the conditions' symbols defined

in previous chapters. In each figure the jet velocity is kept constant at 19 m/s except for Figure 5.18 (b). In Figure 5.18 (e) and (f) the series presented with the dashed lines are at 2.1 bar and the series presented with the solid lines are at 3.8 bar. The nozzle diameters for Figure 5.18 (e) and (f) are 572  $\mu\text{m}$  and 457  $\mu\text{m}$  respectively. Similarly in Figure 5.18 (g) and (h) the series presented with the dashed lines are for the 457  $\mu\text{m}$  nozzle and the series presented with the solid lines are for the 572  $\mu\text{m}$  nozzle. The crossflow pressure for Figure 5.18 (g) and (h) are 2.1 bar and 3.8 bar respectively.



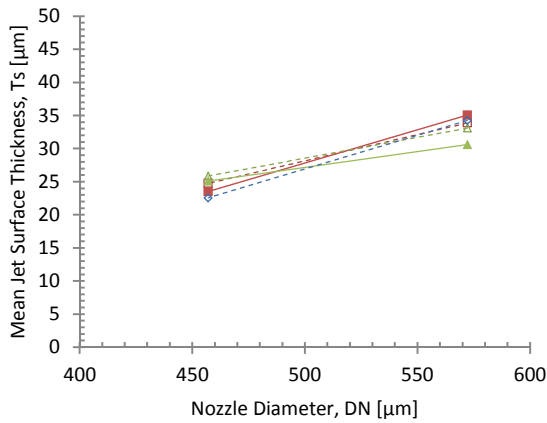
- ◇--- 2, 7, and 11
- 12, 17, 22, and 27
- △--- 33, 38, and 43
- ◇--- 44, 49, 54, and 59
- 60, 64, 69, and 74
- △--- 80, 85, and 90

(a)



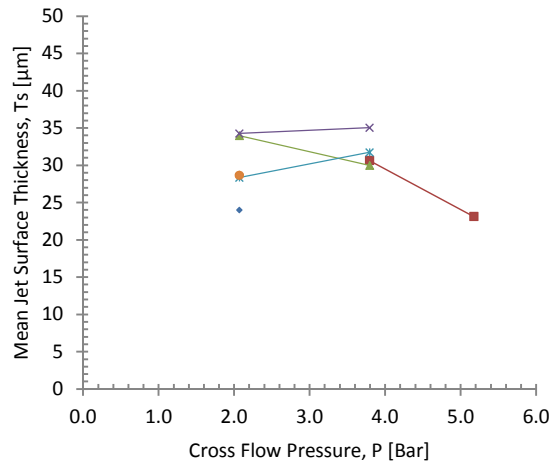
- ◇--- 44, 45, 46, and 47
- 60, 61, and 62
- △--- 76 and 77
- ◇--- 1, 2, 3, and 4
- 16, 17, and 18
- △--- 32, 33, 34, and 35

(b)



- 22 and 113
- △--- 38 and 129
- ◇--- 7 and 97
- 64 and 156
- △--- 80 and 168

(c)



- ◇--- 108
- △--- 166 and 189
- ◇--- 7 and 49
- △--- 2 and 44
- ◇--- 17 and 60
- ◇--- 33

(d)

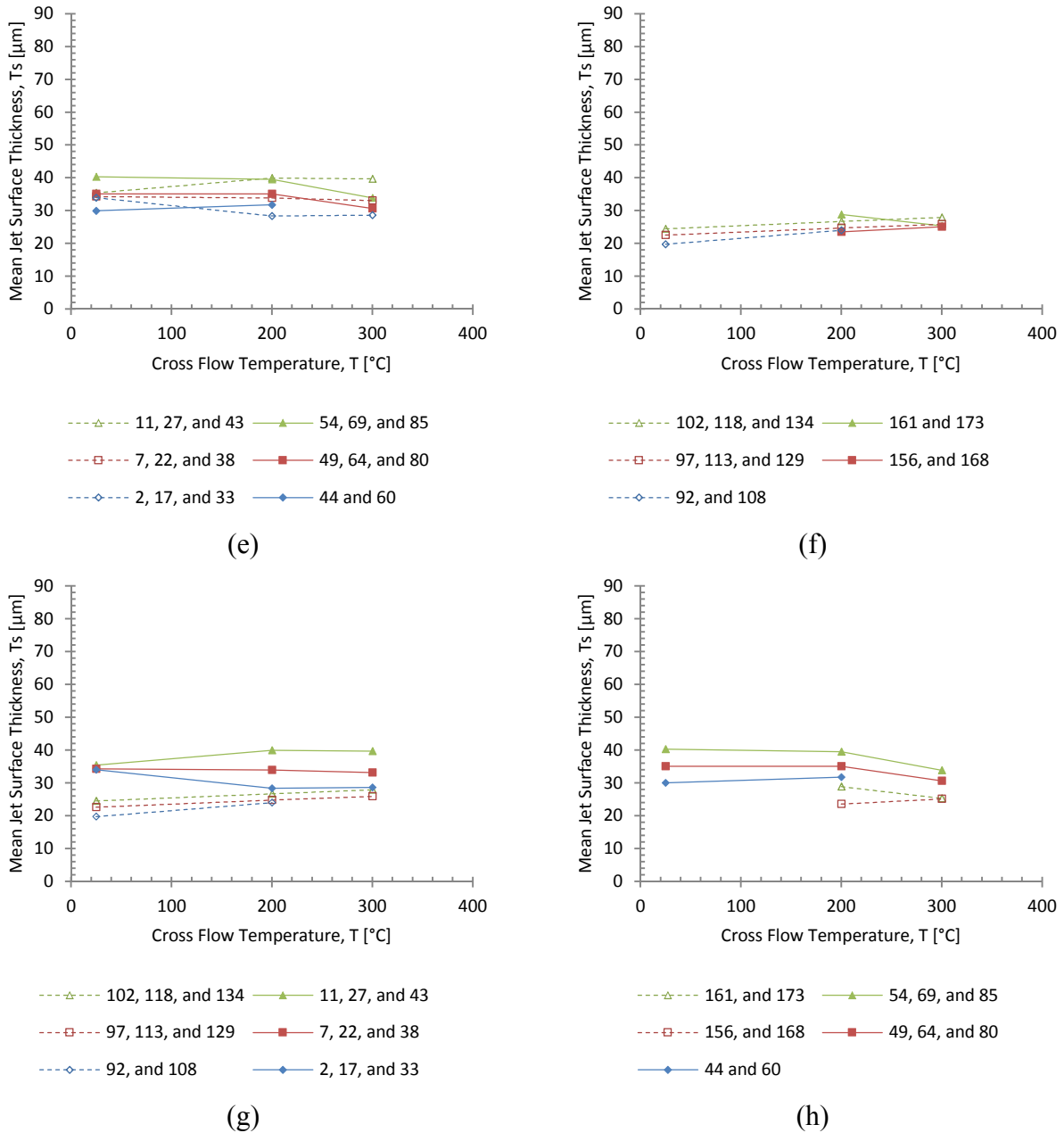


Figure 5.18: Normalized mean jet surface thickness versus (a) air velocity, (b) jet velocity, (c) nozzle diameter, (d) crossflow pressure, and (e) – (h) crossflow temperature. In all the graphs the parameters are kept constant except for the parameter of interest, for example in figure (a) only air velocity is altered. The symbols do not represent the conditions since the conditions for each data series is different. Table 2.3 summarizes the conditions.

Once again a correlation is developed to explain the relation between mean jet surface thickness and various non-dimensionalized variables, equation (5.24). The coefficient of determination for

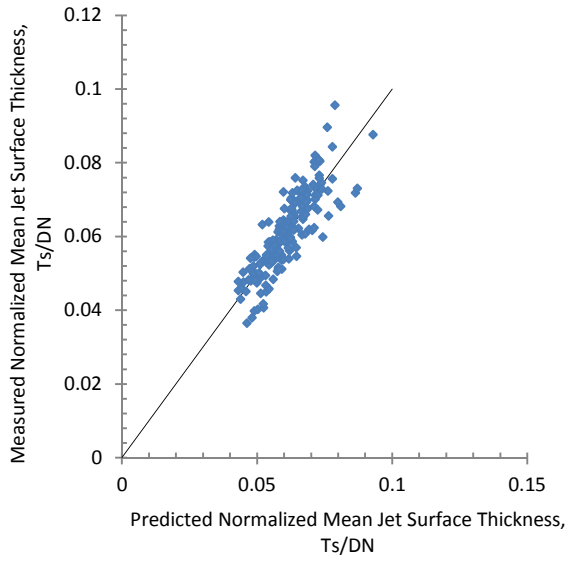


this correlations is 0.73 and it is found that statically the chosen variables are all significant based on 95% confidence criterion, Figure 5.19 (a). It is interesting to note that this correlation is very similar to the correlation provided for mean plume width, equation (5.17). The two parameters are inversely proportional and therefore only the exponents' signs are reversed and the correlation's constant is different.

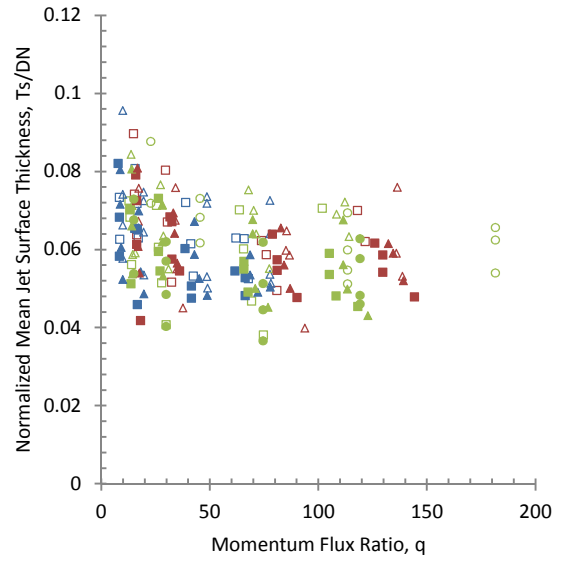
$$\begin{aligned}\frac{T_s}{D_N} &= e^{-6.72} We_{Air}^{-0.09} We_{Jet}^{-0.52} Re_{Air}^{0.06} Re_{Jet}^{0.84} \\ &= e^{-6.72} We_{Air}^{-0.06} We_{Jet}^{-0.09} Oh_{Air}^{-0.06} Oh_{Jet}^{-0.84} \\ &= e^{-6.72} q^{-0.09} We_{Air}^{-0.15} Oh_{Air}^{-0.06} Oh_{Jet}^{-0.84}\end{aligned}\quad (5.24)$$

$$T_s = e^{-6.72} D_N^{1.30} V_{Air}^{-0.12} V_{Jet}^{-0.18} \rho_{Air}^{-0.03} \rho_{Jet}^{0.33} \mu_{Air}^{-0.06} \mu_{Jet}^{-0.84} \sigma^{0.60}\quad (5.25)$$

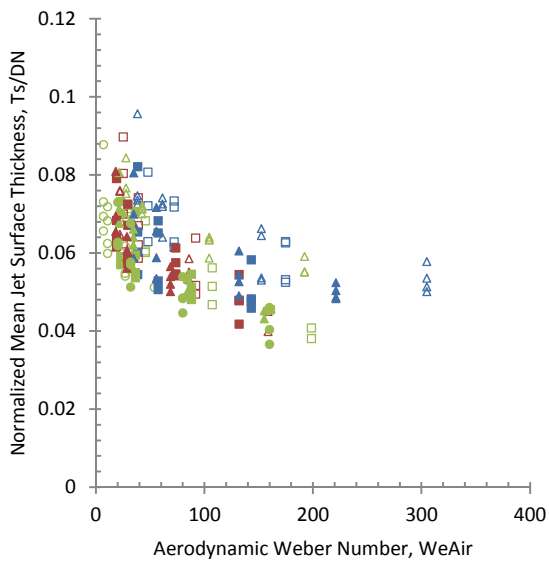
Equation (5.24) and Figure 5.19 (b) through (f) show the effects of various parameters on the spray. The inertia terms have an inverse relation with the mean jet surface thickness. As the liquid and gas Weber numbers increase the mean jet surface thickness is reduced. Alternatively this can be viewed as the combination of momentum flux and aerodynamic Weber number. When the penetration of the jet is increased then the jet surface thickness is reduced. As the aerodynamic Weber number increases then the shear force also increases which reduces the jet surface thickness as well. Finally, the effect of viscosity can be seen by comparing Ohnesorge numbers. An increase in liquid viscosity leads to the jet surface thinning. As the liquid viscosity increases the liquid becomes more elastic and less prone to tears and breakup. This essentially allows the liquid to stay intact and the jet surface stretches and leads to thinning of the jet surface. As it can be seen from the empirical correlation, liquid viscosity plays an important role. One of the goals of looking at mean jet surface thickness is to compare the results with droplet size. Figure 5.19 (g) and (h) show that as the jet surface thickness increases the droplet size and standard deviation of the droplet size also increase.



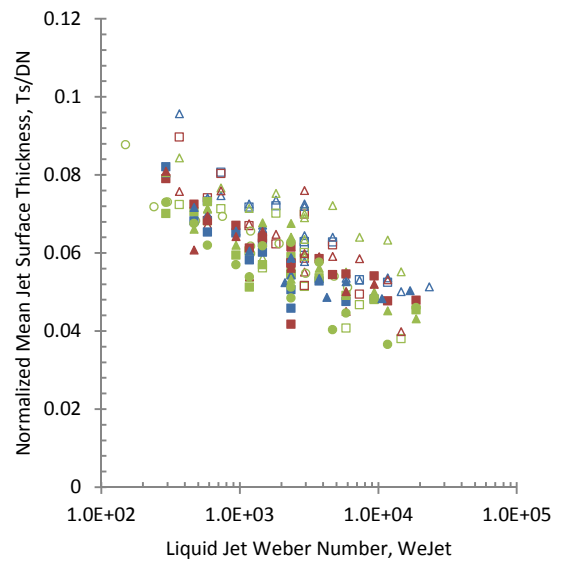
(a)



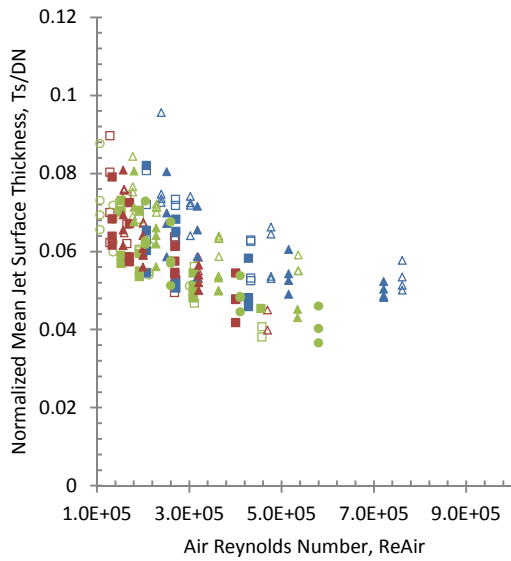
(b)



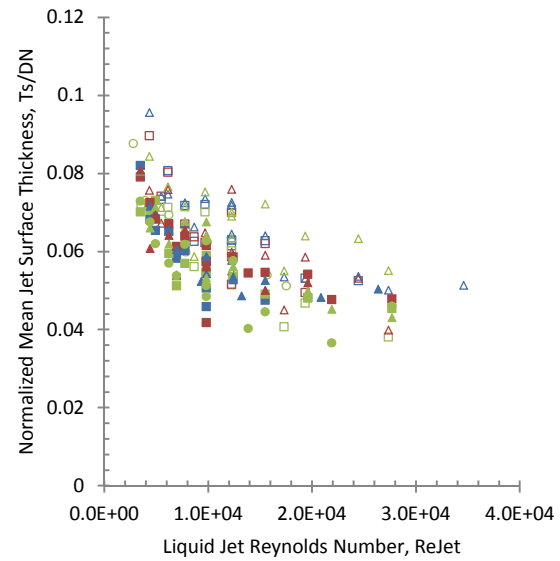
(c)



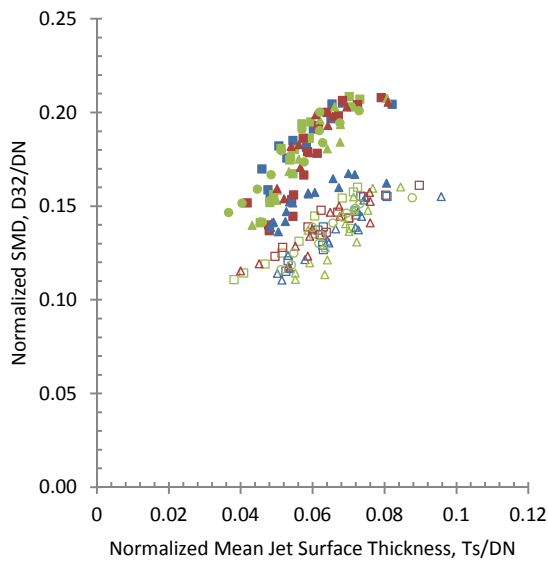
(d)



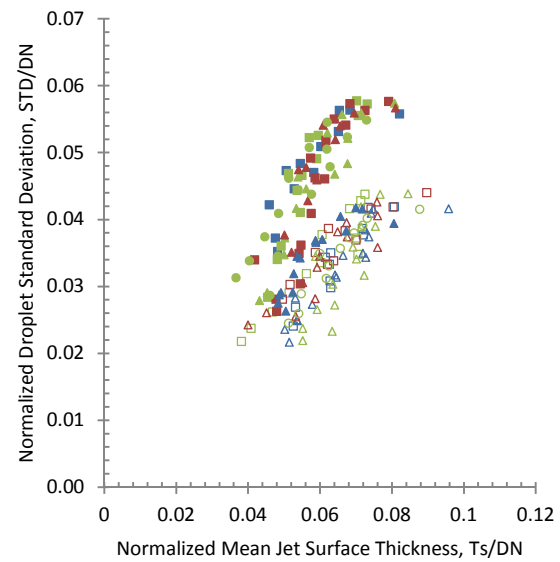
(e)



(f)



(g)



(h)

Figure 5.19: (a) Correlation of normalized mean jet surface thickness; (b) – (f) Normalized mean jet surface thickness vs. various non-dimensionalized numbers; (g) – (h) Normalized D32 and droplet size standard deviation vs. normalized mean jet surface thickness. Table 2.3 summarizes the conditions.

## Chapter 6

# 6 Global Droplet Size Based on Image Analysis

## 6.1 Jet Atomization Process

This section presents results on the droplet sizes produced by the jet in crossflow atomization process. Figure 6.1 shows a water jet in crossflow at room conditions. This image is captured using a Nikon DSLR D300 in combination with a long distance microscope lens with a rear reflector mirror. The lighting is provided by a Nano-Flash using a spark as the light source. The spark duration is only a few nano-seconds to freeze the image. The shadowgraph images that will follow have longer exposure times, about 9  $\mu$ s, and some droplets appear as streaks in the images. The image in Figure 6.1 has a light gradient from bright center to dark corners due to the light energy losses in the lens. The bright area in the center is the silhouette of the arc. The image shows that, initially the leeside surface of the jet is undisturbed and smooth. This relatively smooth and straight part of the jet is referred to as the neck of the jet. The large disturbances that are observed further downstream on the jet surface are generally initiated from the windward surface of the jet [61]. The disturbances present themselves as transverse waves which can then be categorized by their direction of propagation; jet-wise and wind-wise. The jet-wise waves propagate in the direction of the jet flow and wind-wise wave propagate in the direction of the air flow. These disturbances are always present but depending on the spray parameters their influence is different which leads to different breakup regimes. These regimes have been categorized as dominantly column breakup, surface/shear breakup and multimode breakup, generally referred to as bag breakup regime.

The jet-wise waves have much larger amplitude and are the waves that are responsible for column fracture and the so called column breakup mechanism. The parts of the spray that atomize in this manner generally form the larger drops and ligaments. These are the large droplets that are observed away from the atomization region and can be few hundred microns in size prior to the secondary atomization [61]. The large separated drops and ligaments will then exhibit secondary and tertiary breakups [62, 63]. Generally, the smaller droplets are measured in the center and closer to the jet body but, the larger droplets are generally on the peripheries due to momentum and

breakup mechanisms. Many researchers have shown this behavior using Phase Doppler Particle Analyzer, PDA/PDPA [10, 15, 42].

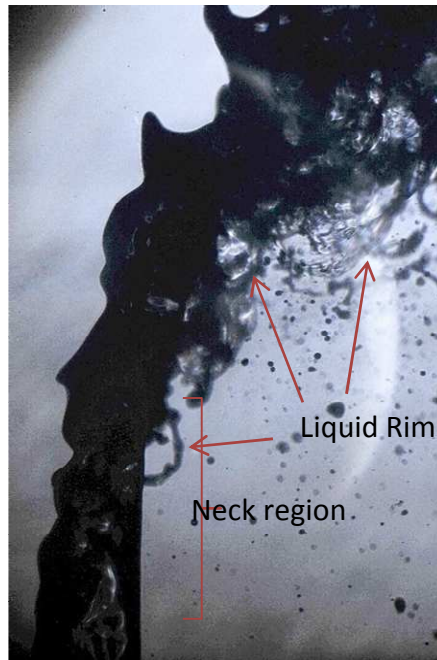


Figure 6.1: High magnification image of jet in crossflow.

On the other hand, the wind-wise waves on the jet have smaller wavelengths. These are the waves that are responsible for smaller formation such as bags, ligaments and droplets on the sides of the jet. For small aerodynamic forces, the waves do not grow due to the surface tension and liquid viscous forces, and the breakup is dominated by jet-wise waves. This is what is known as column breakup regime. For moderate aerodynamic forces, the crests of the wind wise waves form a rim. Eventually, the aerodynamic forces form bag formations between this rim and jet body. This is known as bag breakup regime where column breakup still contributes to the overall atomization, Figure 6.1. Finally for strong aerodynamic forces, a similar behavior takes place but the rims disintegrate much earlier compared to the previous case. The droplets are formed by the breakup of this rim, similar to Rayleigh breakup mechanism. In addition, the turbulent characteristics of the jet itself contributed in making this breakup process very complex [64]. This is commonly known as the surface/shear breakup regime, where usually momentum flux ratios are higher and the jet does not bend as much in the direction of the air. This type of breakup is observed to be more stable due to smaller undulations on the jet surface in the jet-wise direction and generally produces more uniform and relatively smaller droplet sizes along the jet.

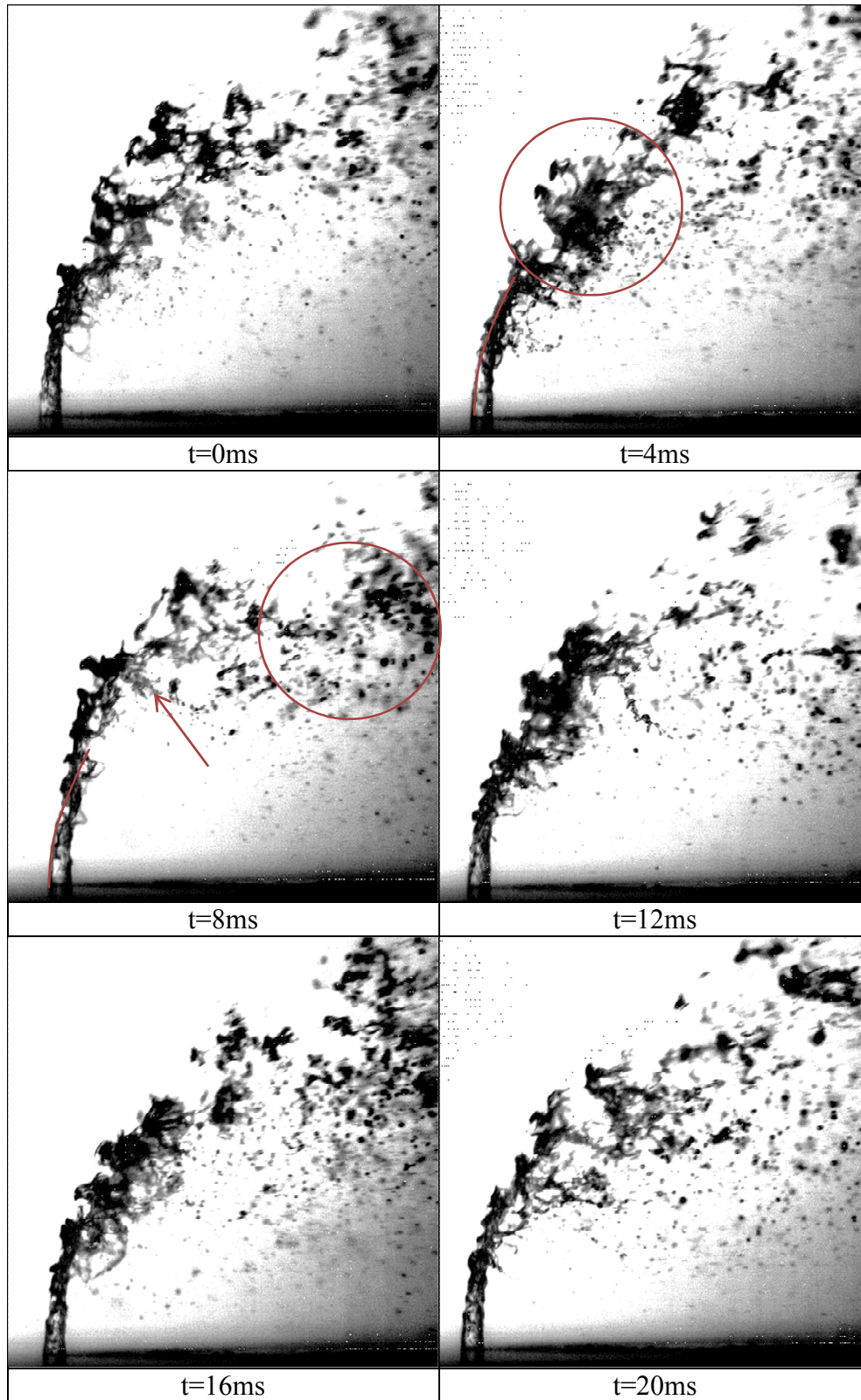


Figure 6.2: Water jet in crossflow at room temperature.  $D_N=572\mu\text{m}$ ,  $p=2.1\text{ bars}$ ,  $V_{\text{Air}}=40\text{m/s}$ ,  $V_{\text{Jet}}=13.5\text{ m/s}$ ,  $q=50$ .

Figure 6.2 displays the evolution of a jet in crossflow where both mechanisms are present. The images are captured using a high-speed camera. The time difference between each image is 4 ms. The liquid is water and air is at room temperature and 2.1 bars. Air and jet velocities are 39 m/s and 13.5 m/s, respectively, the nozzle diameter is 572  $\mu\text{m}$ , and the momentum flux ratio is 50. The breakup mechanism is dominantly column breakup but bag formations are also present close to the jet exit, Figure 6.3. The undulations cause the jet to disintegrate but also there seems to be a feedback response to the jet based on the formations downstream of the nozzle. For example, in the second time frame of Figure 6.2 there is a large formation that is transported downstream in the next time frame. This formation creates a backpressure and causes the jet to buckle upwards in the next time frame. This can be seen when comparing the jet trajectories. The trajectory of the jet in the second time frame is shown in both second and third time frames in red. The windward trajectory of the jet is very different when comparing the two images. The trajectory has increased in the third time frame. This is probably the cause for some of the combustion instabilities observed in various engines as it is discussed in earlier chapters. Figure 6.3 shows the larger segment of the jet as it exits the nozzle. The conditions are the same but the time difference between consecutive images is only 125  $\mu\text{s}$ . The small disturbances on the windward surface of the jet grow very quickly and cause the column to fracture. Small bag and ligament formations are also present on the side of the jet.

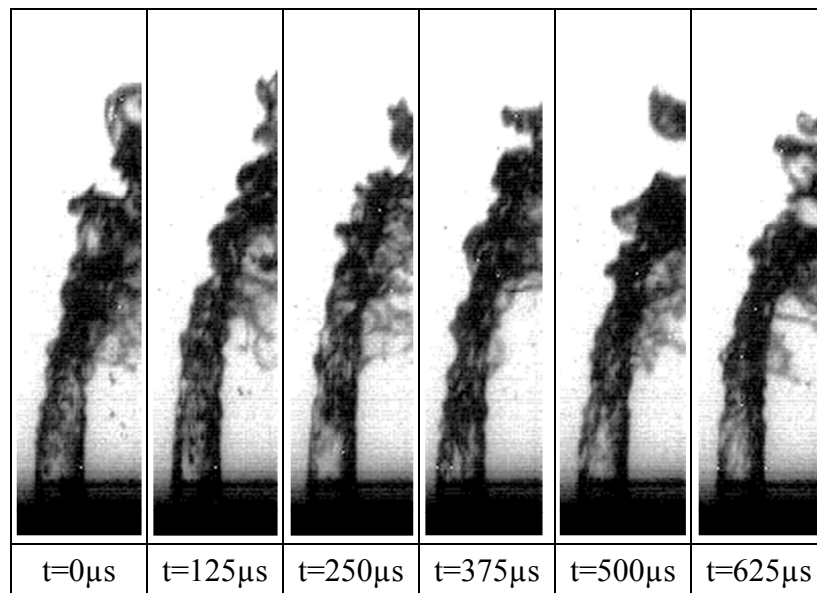


Figure 6.3: Close-up images of the jet exiting the nozzle at the same conditions as figure 6.2.

Figure 6.4 shows a series of images to demonstrate the formation of the larger droplets on the windward surface of the jet at lower aerodynamic Weber numbers and momentum flux ratios where the column breakup is more dominant. The conditions are the same as figure 6.2 except that the jet velocity is reduced to 6 m/s and momentum flux ratio is reduced to 10. The images are captured after the jet is bent in the direction of the crossflow. The jet can be seen on the left side of some images after it exits the nozzle. The jet does not penetrate significantly in this case and is close to the nozzle exit. As expected the surface breakup is not even present in this case. The images display the breakup of the top surface of the jet. The formed crests are stretched due to aerodynamic forces and are finally separated. In this series of images the dominating breakup mechanism is initiated by the larger waves formed on the windward surface of the jet.

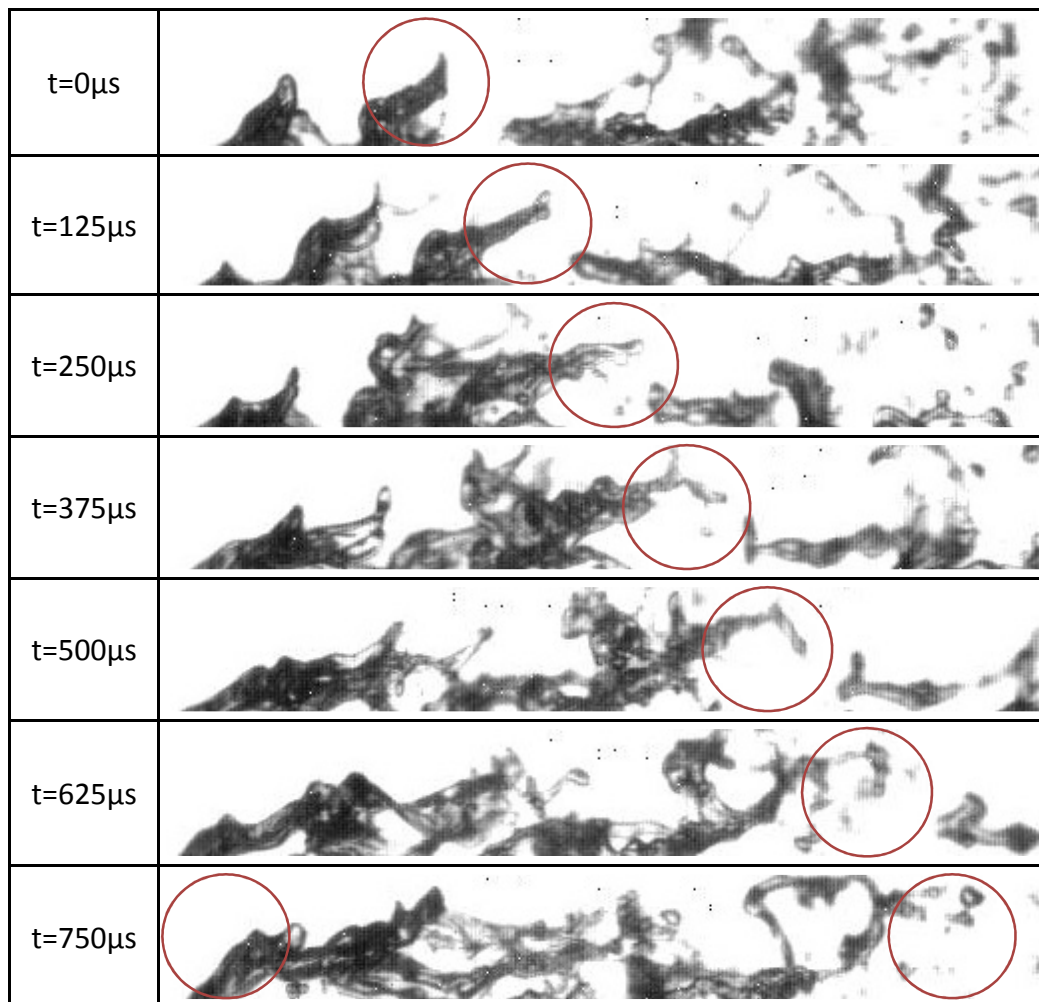


Figure 6.4: Water jet in crossflow at room temperature. The images are captured after the jet has turned in the direction of crossflow. The intact jet can be seen to the left of the image.  $D_N=572\mu\text{m}$ ,  $p=2.1$  bars,

$$V_{\text{Air}}=40\text{m/s}, V_{\text{Jet}}=6\text{m/s}, q=10.$$



Figure 6.5 shows a close-up image of the jet as it exits the nozzle at a higher jet velocity to demonstrate the formation of the smaller droplets on the sides of the jet. The jet velocity is 17 m/s and the momentum flux ratio is 80. The column breakup type structures that are observed earlier are not present in this case. The amplitude and wavelengths on the windward surface are reduced and do not contribute to the overall breakup as significantly when compared to the earlier examples. There are smaller ligament structures that appear to separate from the side surface of the jet. These seem to appear as the rim discussed earlier are breaking and are responsible for smaller droplets. These rim structures give rise to bag formation previously observed in the field. It is anticipated that as the aerodynamic forces increases the overall size of these structures will reduce. Similar behavior is also reported by Sallam et al. in their work [64]. In addition to the aerodynamic forces, the jet initial conditions as well as nozzle properties play an important role. It has been reported that the turbulence of the jet is an important factor in the type of breakup. The nozzle properties have been compared most recently by Gopala [61] and Brown et al. [65]. Many of the observations in this section are in agreement with more recent observations by Linne et al. which they employed both ballistic imaging and shadowgraphy [63, 44].

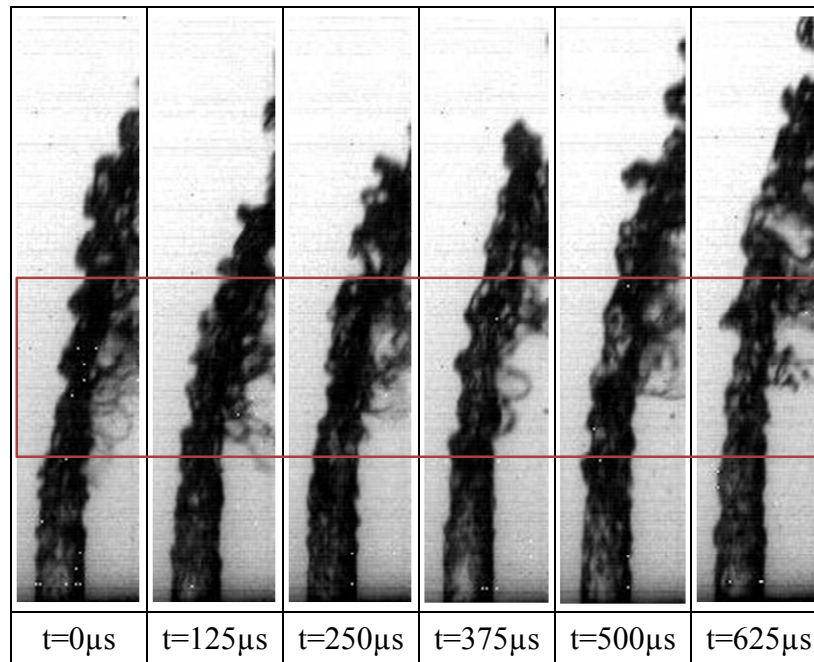


Figure 6.5: Water jet in crossflow at room temperature.  $D_N=572\mu\text{m}$ ,  $p=2.1$  bars,  $V_{\text{Air}}=40\text{m/s}$ ,  $V_{\text{Jet}}=17\text{m/s}$ ,  $q=80$ .

The above discussions demonstrate that the droplet size can vary significantly depending on the region of interest and conditions of air and jet. In any case it is useful to define a global droplet size which can represent the spray in general and would allow for a more effective comparison between various cases. It should be noted that it is possible to have different conditions where the global droplet size is similar but the atomization process is quite different. In this context the global droplet size is defined as the average size of all the droplets in each image independent of position. The individual droplet size is calculated based on the major and minor axis of an ellipse that has the same cross-section area as the droplets. Then the effective diameter of the droplet is calculated based on the assumption that the volume of the spherical droplet is the same as the volume of the measured ellipsoid, equation (3.1). This method is also used by Faeth et al. [8]. Finally, D10 and D32 are calculated based on the individual droplet sizes. A standard error mean, SEM, is calculated for the mean diameter and it is found that this error is generally in the order of 0.05  $\mu\text{m}$  with standard deviation of 0.030  $\mu\text{m}$ , and therefore, relatively insignificant to the following analysis. Subsequently, error bars are not shown on the figures. On the other hand, standard deviation, STD, is significant and is a good indicator of the span of the data and the shape of the histogram. Additionally, based on the histogram analysis of the data, Mass Median Diameter is calculated for all the cases and it is found that MMD/SMD is about 1.2 with standard deviation of 0.1. The MMD/SMD ranges between 1.1 and 1.4. Based on previous work on structure of dense sprays and breakup of turbulent and non-turbulent sprays, the distribution generally follows the universal root-normal distribution function defined by Simmons with MMD/SMD=1.2, [60, 66, 8]. The details of these calculations are given in appendix A. The spray follows the log-normal distribution, and therefore, the presented data also includes the mean and variance of the log-normal distribution, which is given by:

$$f(D) = \frac{1}{\sqrt{2\pi}\sigma_{LN}D} e^{-\frac{[\ln(D)-\mu_{LN}]^2}{2\sigma_{LN}^2}} \quad (6.1)$$

$$D10 = e^{\mu_{LN} + \sigma_{LN}^2/2} \quad (6.2)$$

$$STD^2 = e^{2\mu_{LN} + \sigma_{LN}^2} (e^{\sigma_{LN}^2} - 1) \quad (6.3)$$

At first, the dimensional variables are all correlated with the results and then individual parameters are compared in the following sections, and finally some correlations based on non-dimensionalized numbers are compared and presented. The dimensional variables are nozzle

diameter,  $D_N$ , liquid jet velocity,  $V_{Jet}$ , air velocity,  $V_{Air}$ , air pressure,  $p$ , and air temperature,  $T$ . Air pressure and temperature are combined into density, viscosity and surface tension. The following correlation summarizes the various effects considered in these experiments:

$$SMD = 300D_N^{-1/5}V_{Jet}^{-1/8}V_{Air}^{-1/8}\rho_{Jet}^0\rho_{Air}^{-1/5}\mu_{Jet}^0\mu_{Air}^{-1/12}\sigma^0 \quad (6.4)$$

The data is presented in graphical form in Figure 6.6. The coefficient of determination,  $R^2$ , is 0.84 and standard error of 0.05 and the standard errors for the constant, nozzle diameter, jet and air velocities, density, and viscosity are 0.03, 0.03, 0.01, 0.01, 0.03, and 0.02, respectively. The units for the nozzle diameter and droplet size are  $\mu\text{m}$ ; all other variables are in SI units. Based on t-test all considered variable are statistically significant. It should be noted that the correlation does not show any change with respect to density, viscosity and surface tension of the jet since only water is used in the present study. The effect of temperature and pressure on these parameters is relatively small so that the results do not vary significantly with respect to them. Consequently the final correlations which are presented are in non-dimensional form to help better understand the effect of these variables as well.

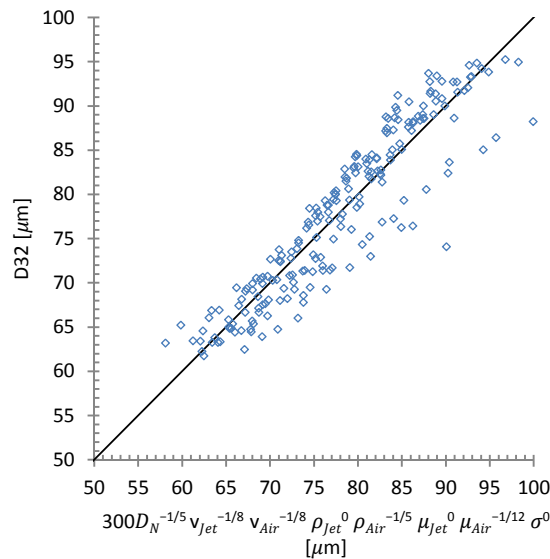


Figure 6.6: Correlation of SMD with dimensional variables.

## 6.2 Effect of Dimensional Variables on the Global Droplet Size

### 6.2.1 Effect of Nozzle Diameter on the Global Droplet Size

All the dimensional variables are kept constant in order to observe the effect of nozzle diameter on the global droplet size. The dimensional variables that are kept constant are pressure,  $p$ , temperature,  $T$ , air velocity,  $V_{Air}$ , and liquid jet velocity,  $V_{Jet}$ . Table 2.3 summarizes the conditions and results of the compared cases. As it can be seen from Figure 6.7, droplet size is reduced when the nozzle diameter is increased. This is opposite to the general understanding that increasing the nozzle diameter would increase the droplet size. The breakup mechanism is highly dependent on the drag force on the jet, spray geometry and penetration. Drag force can be defined with the generalized form of equation (6.5), where for this study it can be assumed that the effective velocity is the vectorial summation of the jet and air velocities.

$$F_D = \frac{1}{2} C_d \rho A v_{Effective}^2 \quad (6.5)$$

$$v_{Effective}^2 = v_{Air}^2 + v_{Jet}^2 \quad (6.6)$$

In-order to better understand the effect of drag force, the jet can be approximated as a solid vertical cylinder with the same length as the height of the breakup point suggested by Wu et al. [9], equation (1.6). It is also possible to have more complex modeling but most of the correlations for the jet penetration, width, etc. are fairly simple and are based on nozzle diameter and momentum flux ratio. Thus it is not necessary for complex modeling to have a general understanding of the topic in hand. Just based on the above assumption, the coefficient of drag and frontal area can be approximated using equations (6.7) and (6.8) for comparison of conditions with the same momentum flux ratio. The coefficient of drag of a cylinder is a function of  $L/D$  of the cylinder and based on the correlation from Wu et al. [9], then it only becomes a function of momentum flux ratio which does not have any dependency on diameter. Thus the coefficient of drag for two cases with the same momentum flux ratio, densities and velocities can be assumed to be the same. Note that this cannot be generalized to just momentum flux ratio as it will be shown later in the chapter. Also, a similar approach can be applied to the frontal area estimation. Finally, the approximation for the current nozzles and experiments results in 60% increase in drag force for the cases with larger nozzles, which essentially explains the reduction in droplet size as the nozzle size is increased, equation (6.9).

$$C_D = f\left(\frac{L}{D_N}\right)_{Cylinder} = f\left(\frac{y_b}{D_N}\right) = f\left(\frac{3.44D_N\sqrt{q}}{D_N}\right) = f(\sqrt{q}) \quad (6.7)$$

$$A = \frac{\pi D_N L}{2} = \frac{3.44\pi D_N^2 \sqrt{q}}{2} \quad (6.8)$$

$$\frac{F_{D1}}{F_{D2}} = \frac{C_{D1} A_1}{C_{D2} A_2} = \frac{D_{N1}^2}{D_{N2}^2} \sim 1.6 \quad (6.9)$$

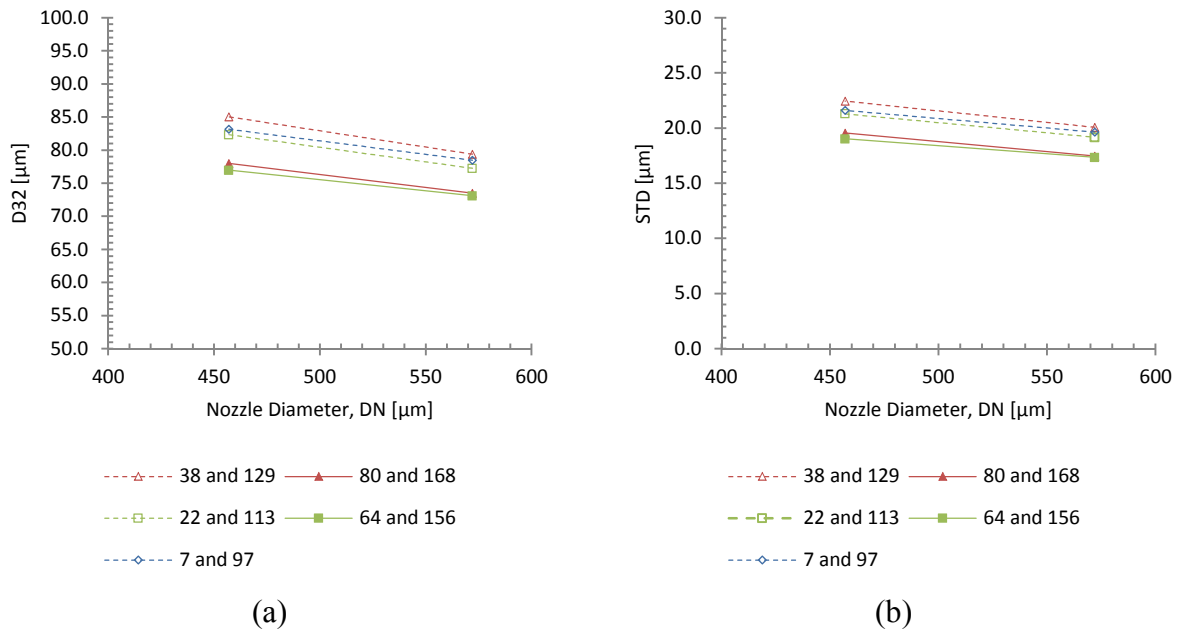

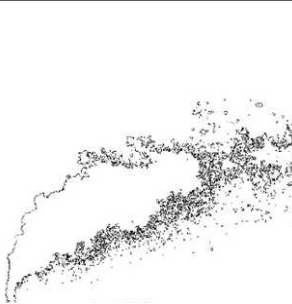
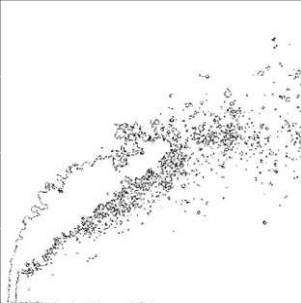

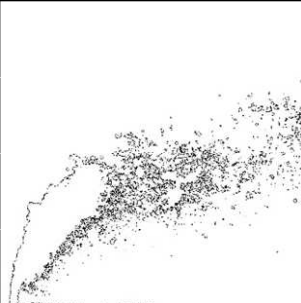

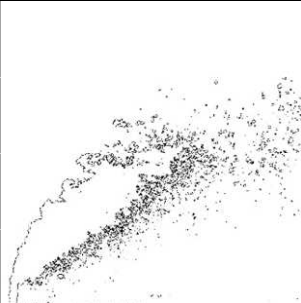



Figure 6.7: (a) Sauter mean diameter vs. nozzle diameter. (b) Diameter standard deviation vs. nozzle diameter. The liquid jet velocity is kept constant at 19 m/s for all cases. All air velocities are in the range of 60 to 80 m/s. Blue series represent room temperature, green series represent 200°C, and red series represent 300°C. Each series represents a constant pressure; dashed lines represent 2.1 bars, and solid lines 3.8 bars. Table 2.3 summarizes the conditions.

As an example, cases 64 and 156 can be compared. In case of case 64, 572 $\mu$ m nozzle, the breakup point coordinates are (13.6mm, 8.9mm). For case 156, 467 $\mu$ m nozzle, the breakup point coordinates are (12.3mm, 8.0mm). The penetration in the direction of jet is about 11% higher for the case with larger nozzle diameter. This can also be seen from the images in Figure 6.8. Images in the left column have the larger nozzle diameter, 572  $\mu$ m, versus 467  $\mu$ m. Also, the standard deviation and maximum droplet size is reduced with the larger nozzle. As before, this is mostly due to better atomization as the penetration is increased. As the penetration is increased the breakup

mechanism is mostly dominated by shear breakup versus breakup due to column breakup. This discussion leads itself to one of the issues with defining the spray characteristics simply by momentum flux ratio. The momentum flux ratio for all the data presented in the section is kept constant, but the Weber numbers for the air and jet are varied. By definition, the momentum flux ratio is simply the ratio of jet to air Weber numbers. For example, the momentum flux ratio for both cases 64 and 156 is 28, on the other hand jet and air Weber number for case 64 are 2910 and 102, respectively and for case 156 are 2330 and 82, respectively. The difference in Weber numbers is due to nozzle size difference, about 25% higher. Weber number represents the ratio of inertial forces to surface tension forces acting on the fluid, and it is expected that the droplet size would decrease when the Weber numbers are higher. It is also essential to observe the Reynolds numbers. Reynolds numbers for both jet and air increase by 25% by increasing the nozzle diameter. The breakup length can be used as a measure to demonstrate the effect of increase in jet Reynolds number and average spray plume width for air and jet Reynolds number. This can also be seen from the correlations in previous chapter. For example, the jet and air Reynolds numbers for case 64 are 12,283 and 4,146, respectively and for case 156 are 9,824 and 3,327, respectively. The breakup lengths are 16.2mm vs. 14.6mm, and average spray plume widths are 3.5mm vs. 3.4mm for cases 64 and 156 respectively.

	
Case 156 ▲ $V_{Air}=68 \text{ m/s}$ $V_{Jet}=19 \text{ m/s}$ $D_N=467\mu\text{m}$	Case 64 △ $V_{Air}=68 \text{ m/s}$ $V_{Jet}=19 \text{ m/s}$ $D_N=572\mu\text{m}$
	
Case 97 ■ $V_{Air}=61 \text{ m/s}$ $V_{Jet}=19 \text{ m/s}$ $D_N=467\mu\text{m}$	Case 7 □ $V_{Air}=61 \text{ m/s}$ $V_{Jet}=19 \text{ m/s}$ $D_N=572\mu\text{m}$
	
Case 113 ■ $V_{Air}=61 \text{ m/s}$ $V_{Jet}=19 \text{ m/s}$ $D_N=467\mu\text{m}$	Case 22 □ $V_{Air}=61 \text{ m/s}$ $V_{Jet}=19 \text{ m/s}$ $D_N=572\mu\text{m}$
	
Case 129 ■ $V_{Air}=60 \text{ m/s}$ $V_{Jet}=19 \text{ m/s}$ $D_N=467\mu\text{m}$	Case 38 □ $V_{Air}=62 \text{ m/s}$ $V_{Jet}=19 \text{ m/s}$ $D_N=572\mu\text{m}$

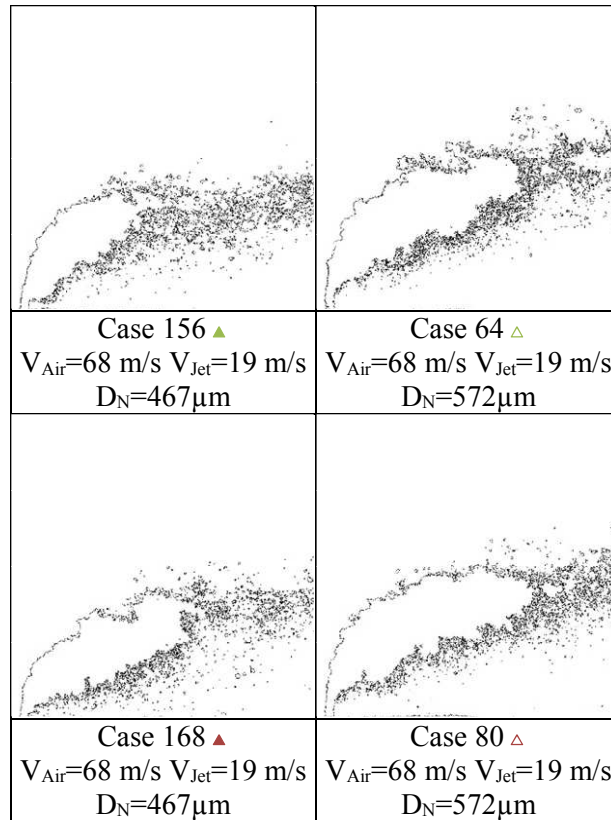


Figure 6.8: Comparison of the images for conditions where all the dimensional variables are kept constant except for nozzle diameter,  $D_N$ . All the images have the same scale and droplets larger than 5 pixel squared ( $D \sim 50 \mu\text{m}$ ) are only shown. Table 2.3 summarizes the conditions.

### 6.2.2 Effect of Liquid Jet Velocity on the Global Droplet Size

Similar to the previous section, all the dimensional variables are kept constant in order to observe the effect of jet velocity on the global droplet size. The dimensional variables that are kept constant are pressure,  $p$ , temperature,  $T$ , nozzle diameter,  $D_N$ , and air velocity,  $V_{Air}$ . Table 2.3 summarizes the conditions and results of the compared cases. Figure 6.9 shows the effect of liquid jet velocity on the global droplet size. As the liquid jet velocity is increased the droplet size decreases, and similarly the standard deviation on the droplet size is reduced. The reductions in standard deviation hint that the atomization is more uniform along the jet axis and the atomization transitions towards shear breakup. It should be noted that the air velocity for all the cases is between 92 m/s and 95 m/s. At higher liquid flow rates the exposure of jet to air increases and shear force on the jet body increases. Based on the discussions in the previous section the drag force can be assumed to be a function of momentum flux ratio and the nozzle diameter, and as these parameters increase the



droplet size decreases. Alternatively, as the jet velocity is increased the jet Reynolds number increases and the jet becomes more turbulent which explains the reduction in size.

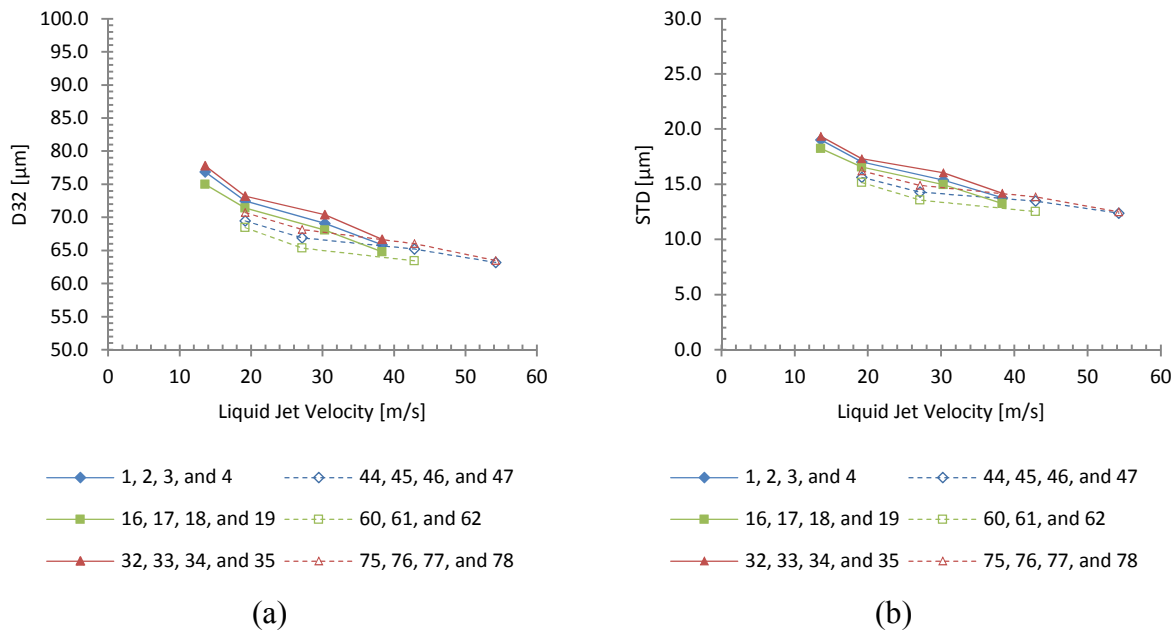
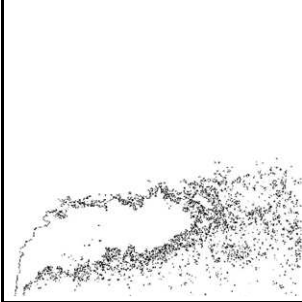
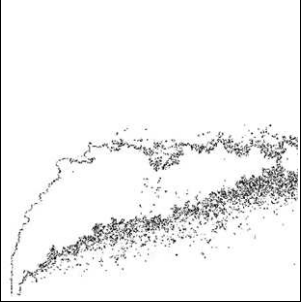
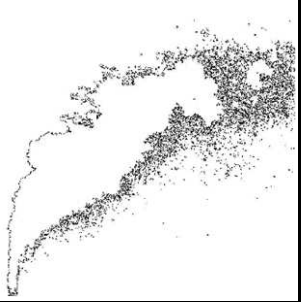
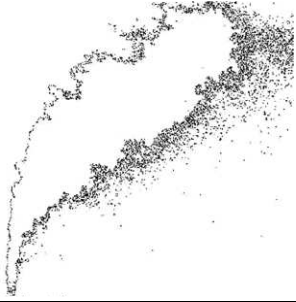
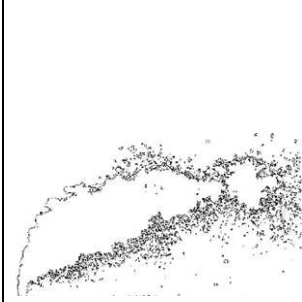






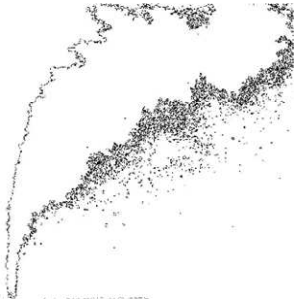
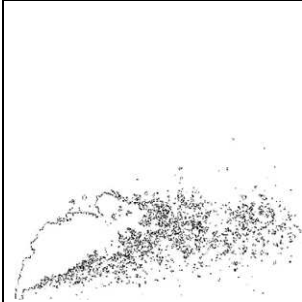
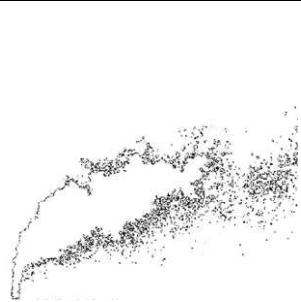
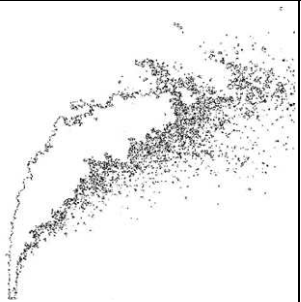
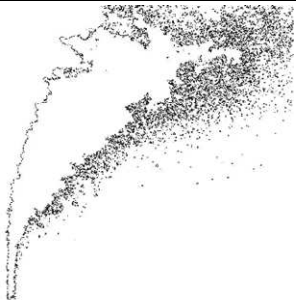


Figure 6.9: (a) Sauter mean diameter vs. liquid jet velocity. (b) Diameter standard deviation vs. liquid jet velocity. The air velocity is kept constant between 92 and 95 m/s for all cases. Blue series represent room temperature, green series represent 200°C, and red series represent 300°C. Each series represents a constant pressure; dashed lines represent 2.1 bars, and solid lines 3.8 bars. Nozzle diameter for all cases is 572 μm. Table 2.3 summarizes the conditions.

Figure 6.10 shows a sample image for the cases presented in Figure 6.9. The jet velocity is increased from left to right in each row of the table while other parameters are kept constant. When comparing figures in any row of Figure 6.10, it can be seen that the main plume area width and breakup length increase when the jet velocity is increased, which is a clear indication of the effect of inertial forces on the jet. For example, for case 16, 17, 18, and 19, the breakup lengths are 16.9mm, 18.2mm, 23.7mm and 24.7mm respectively, and the average plume widths are 3.6mm, 3.6mm, 4.2mm, and 4.3mm respectively. In addition to the effects of jet velocity, other aspects of the spray can be seen by comparing the columns. For example, the droplet size for high pressure cases is smaller compare to low pressure cases. A temperature pattern is also present where the droplet size initially is reduced when temperature is increased and after it increases again, these behaviors are discussed in more detail in the following sections. Additionally, the plume seems to elongate as the temperature is increased due to increase in kinematic viscosity.

			
Case 44 $\Delta$ $V_{Air}=92m/s$ $V_{Jet}=19m/s$	Case 45 $\Delta$ $V_{Air}=92m/s$ $V_{Jet}=27m/s$	Case 46 $\Delta$ $V_{Air}=92m/s$ $V_{Jet}=43m/s$	Case 47 $\Delta$ $V_{Air}=92m/s$ $V_{Jet}=54m/s$
			
Case 60 $\Delta$ $V_{Air}=92m/s$ $V_{Jet}=19m/s$	Case 61 $\Delta$ $V_{Air}=92m/s$ $V_{Jet}=27m/s$	Case 62 $\Delta$ $V_{Air}=92m/s$ $V_{Jet}=43m/s$	
			
Case 75 $\Delta$ $V_{Air}=92m/s$ $V_{Jet}=19m/s$	Case 76 $\Delta$ $V_{Air}=92m/s$ $V_{Jet}=27m/s$	Case 77 $\Delta$ $V_{Air}=92m/s$ $V_{Jet}=43m/s$	Case 78 $\Delta$ $V_{Air}=92m/s$ $V_{Jet}=54m/s$
			
Case 1 $\square$ $V_{Air}=95m/s$ $V_{Jet}=14m/s$	Case 2 $\square$ $V_{Air}=95m/s$ $V_{Jet}=19m/s$	Case 3 $\square$ $V_{Air}=95m/s$ $V_{Jet}=30m/s$	Case 4 $\square$ $V_{Air}=95m/s$ $V_{Jet}=38m/s$

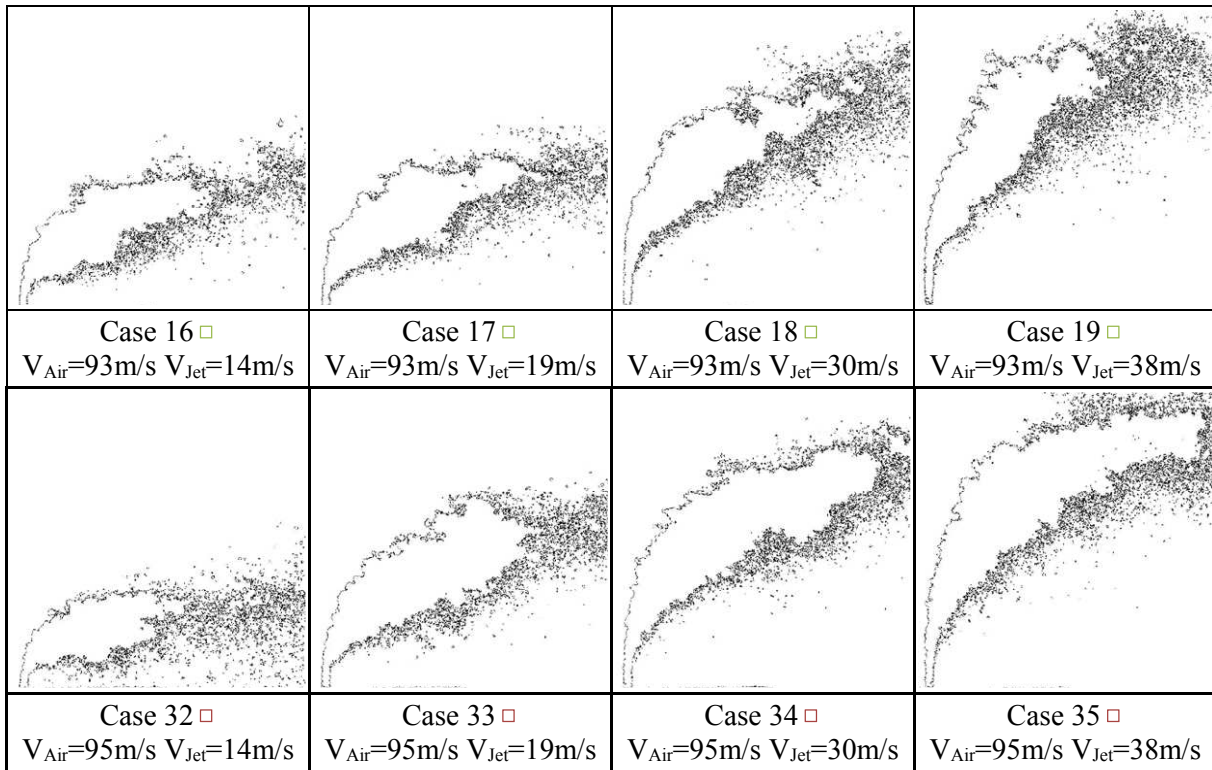


Figure 6.10: Comparison of the images for conditions with all the dimensional variables kept constant except for jet velocity,  $V_{Jet}$ . All the images have the same scale and droplets larger than 5 pixel squared ( $D \sim 50 \mu\text{m}$ ) are only shown. Table 2.3 summarizes the conditions.

### 6.2.3 Effect of Air Velocity on the Global Droplet Size

Similar to the previous section, all the dimensional variables are kept constant in order to observe the effect of air velocity on the global droplet size. The dimensional variables that are kept constant are pressure,  $p$ , temperature,  $T$ , nozzle diameter,  $D_N$ , and liquid jet velocity,  $V_{Jet}$ . Table 2.3 summarizes the conditions and results of the compared cases. Figure 6.11 shows the effect of air velocity on atomization. As the air velocity increases the global droplet size decreases. This can also be seen from the images in Figure 6.12. As expected, as the air velocity is reduced the penetration is increased due to increase in the momentum flux ratio. It should be noted that even when the penetration increases it is not necessarily guarantee smaller droplet sizes. In the presented cases, penetration is increased due to reduction in the crossflow momentum and therefore drag force on the jet body is reduced. This can be easily seen by comparing the primary plume widths between the cases in any row of Figure 6.12. The spray width is reduced due to the reduction on the drag force for the same mass flow rate of liquid. Hassa et al. [15] and Amighi [42] have shown

that as the air velocity increases the droplet size reduces for kerosene jets in crossflow. They both used Phase Doppler Particle Analyzer, PDA/PDPS, to measure droplet size at elevated pressure. Alternatively a similar approach can be taken to previous section to better understand the effect of air velocity on the drag force. Equation (6.10) summarizes the observations based on the previous assumptions. An interesting observation is that the drag force is a function of both the momentum flux ratio and the velocities. It is therefore possible to have various cases with the same momentum flux ratio but different air and jet velocities. It is not difficult to then see that the drag force is different for such cases and consequently the breakup mechanisms and ultimately the droplet size would be different.

$$F_D = \frac{1}{2} C_d \rho A v_{Effective}^2 = f(D^2, \rho, \sqrt{q}, v_{Air}^2 + v_{jet}^2) \quad (6.10)$$

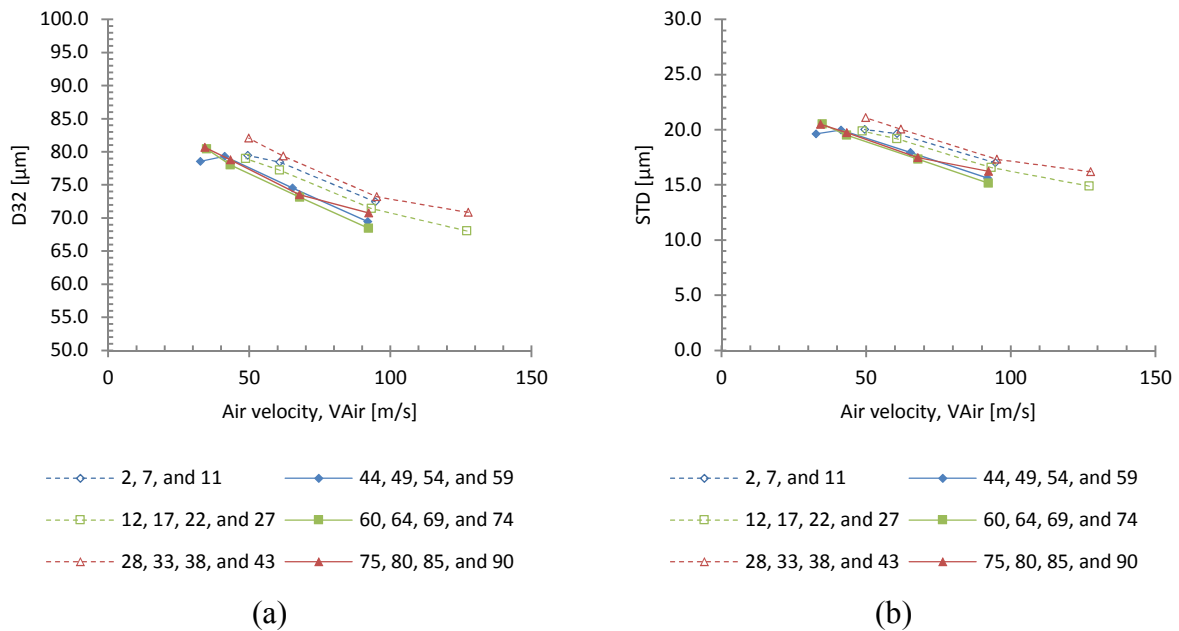
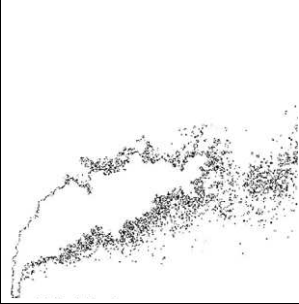


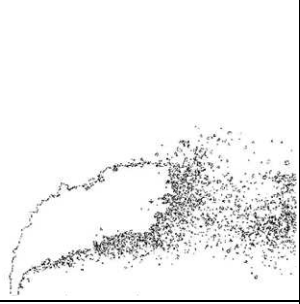
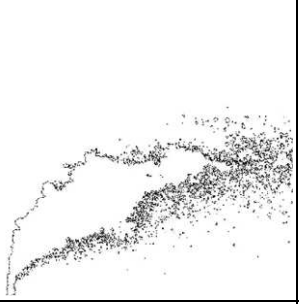
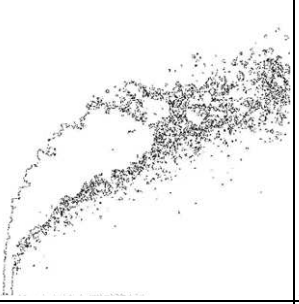
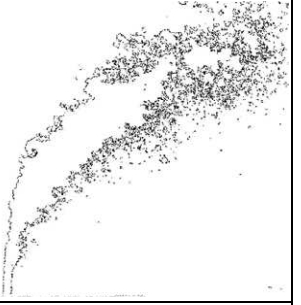
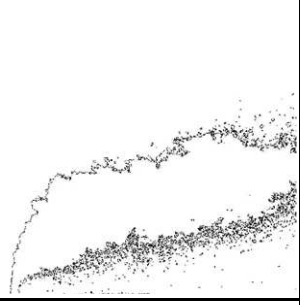
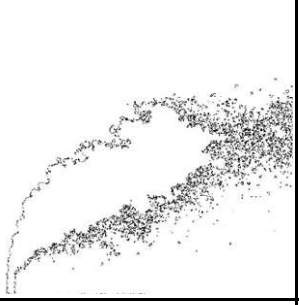
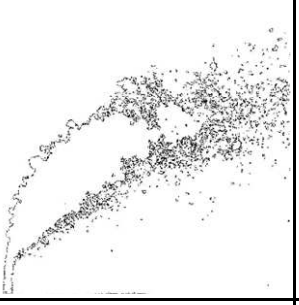
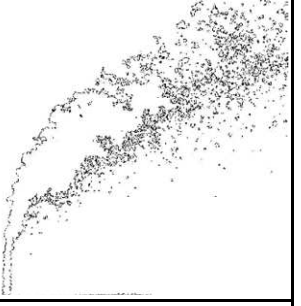
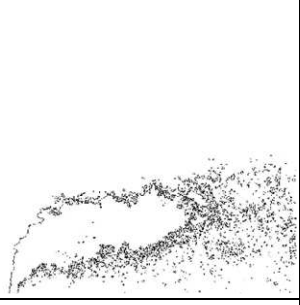
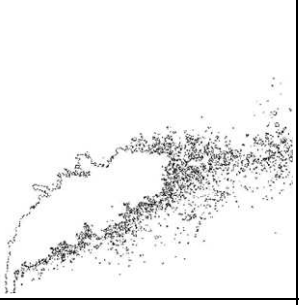
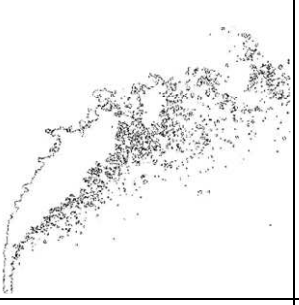
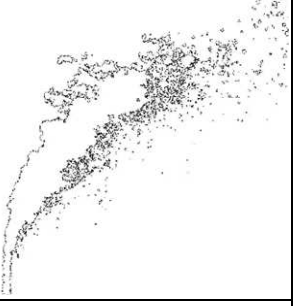


Figure 6.11: (a) Sauter Mean Diameter vs. Air Velocity. (b) Diameter Standard Deviation vs. Air Velocity. The liquid jet velocity is kept constant at 19 m/s for all cases. Blue series represent room temperature, green series represents 200°C, and red series represent 300°C. Each series represents a constant pressure; dashed lines represent 2.1 bars, and solid lines 3.8 bars. Nozzle diameter for all cases is 572 μm. Table 2.3 summarizes the conditions.

			
	Case 2 □ $V_{Air}=95\text{m/s}$ $V_{Jet}=19\text{m/s}$	Case 7 □ $V_{Air}=61\text{m/s}$ $V_{Jet}=19\text{m/s}$	Case 11 □ $V_{Air}=49\text{m/s}$ $V_{Jet}=19\text{m/s}$
			
Case 12 □ $V_{Air}=127\text{m/s}$ $V_{Jet}=19\text{m/s}$	Case 17 □ $V_{Air}=93\text{m/s}$ $V_{Jet}=19\text{m/s}$	Case 22 □ $V_{Air}=61\text{m/s}$ $V_{Jet}=19\text{m/s}$	Case 27 □ $V_{Air}=49\text{m/s}$ $V_{Jet}=19\text{m/s}$
			
Case 28 □ $V_{Air}=128\text{m/s}$ $V_{Jet}=19\text{m/s}$	Case 33 □ $V_{Air}=95\text{m/s}$ $V_{Jet}=19\text{m/s}$	Case 38 □ $V_{Air}=62\text{m/s}$ $V_{Jet}=19\text{m/s}$	Case 43 □ $V_{Air}=50\text{m/s}$ $V_{Jet}=19\text{m/s}$
			
Case 44 △ $V_{Air}=92\text{m/s}$ $V_{Jet}=19\text{m/s}$	Case 49 △ $V_{Air}=65\text{m/s}$ $V_{Jet}=19\text{m/s}$	Case 54 △ $V_{Air}=41\text{m/s}$ $V_{Jet}=19\text{m/s}$	Case 59 △ $V_{Air}=33\text{m/s}$ $V_{Jet}=19\text{m/s}$

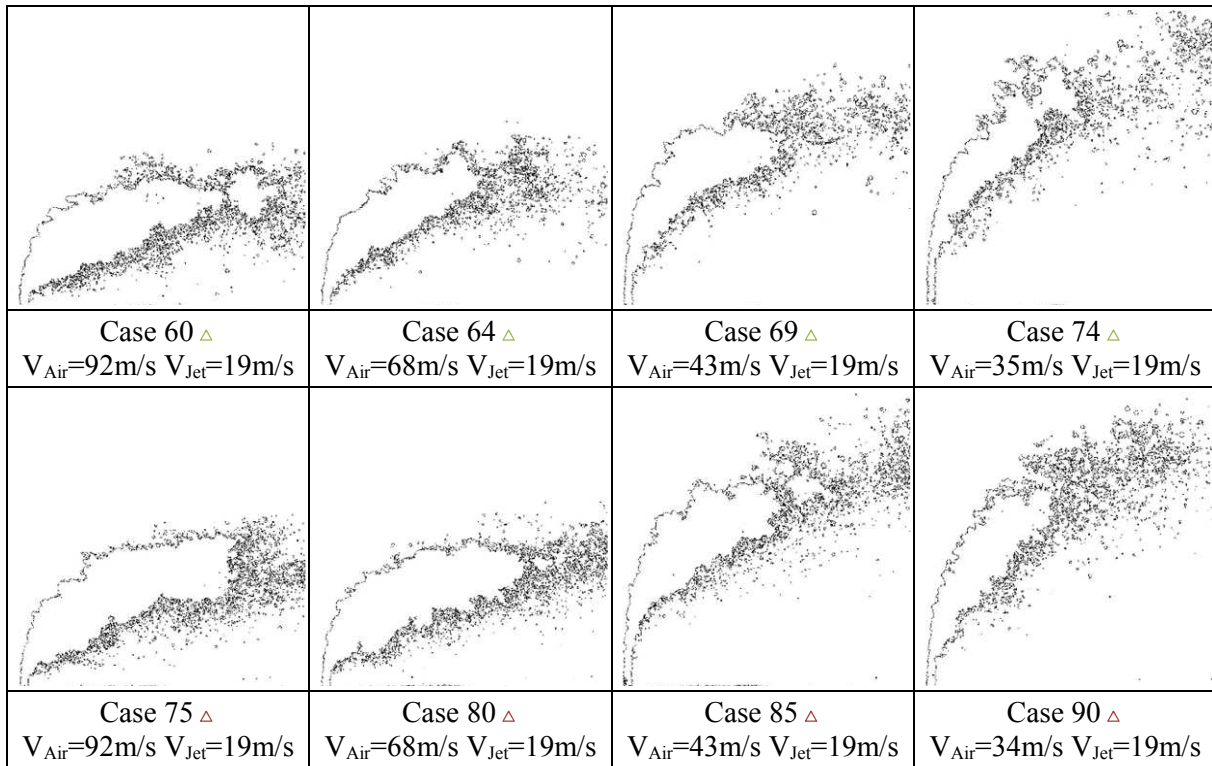


Figure 6.12: Comparison of the images for conditions with all the dimensional variables kept constant except for air velocity,  $V_{Air}$ . All the images have the same scale and droplets larger than 5 pixel squared ( $D \sim 50 \mu\text{m}$ ) are only shown. Table 2.3 summarizes the conditions.

#### 6.2.4 Effect of Pressure on the Global Droplet Size

In this section, similar to the previous sections, all the dimensional variables are kept constant in order to observe the effect of pressure. The dimensional variables that are kept constant are temperature,  $T$ , nozzle diameter,  $D_N$ , air velocity,  $V_{Air}$ , and liquid jet velocity,  $V_{Jet}$ . Table 2.3 summarizes the conditions and results of the compared cases. Generally, when the crossflow pressure increases the atomization is enhanced and droplet size is reduced. By increasing pressure, the density and viscosity of the gas, although negligible, is increased which in effect increases the drag force on the jet and improves atomization. The other effects of pressure are on the saturation temperature of the liquid. As pressure increases the saturation temperature increases and the evaporation takes places at higher temperatures, that said other parameters also needs to be considered for evaporation beyond just saturation temperature as it is discussed in more detail in Appendix D.

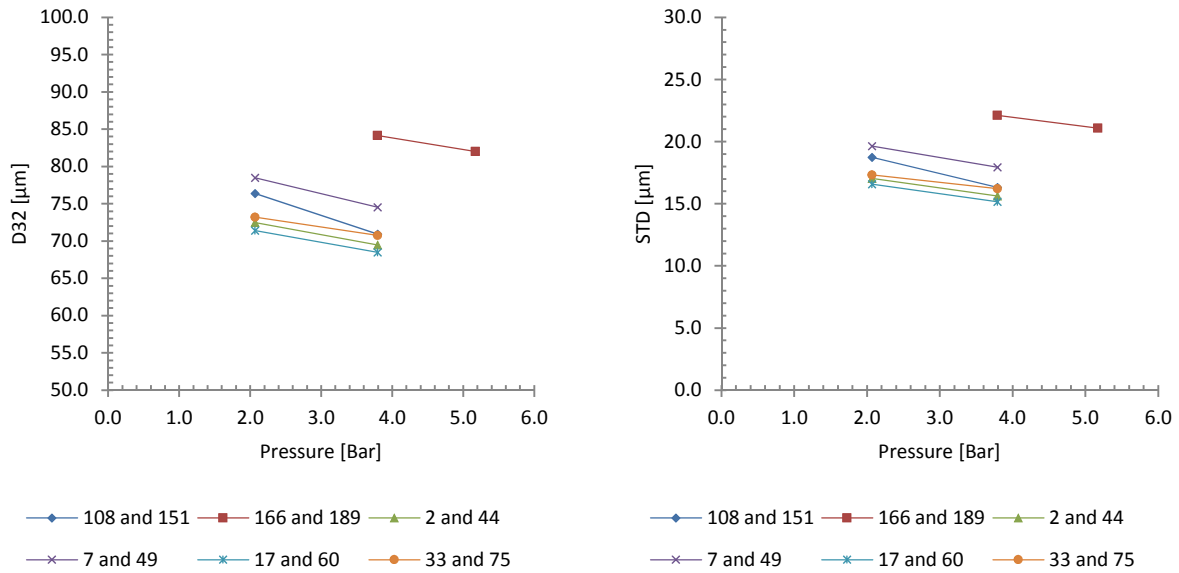


Figure 6.13: (a) Sauter mean diameter vs. pressure. (b) Diameter standard deviation vs. pressure. The liquid jet velocity is kept constant at 19 m/s for all cases, and air velocities are in three different ranges, 30 - 40 m/s, 60 - 70 m/s and 90 - 100 m/s. Table 2.3 summarizes the conditions.

Figure 6.13 shows the effect of pressure on SMD and STD. Each of the series shown represents condition where all dimensional variables are kept constant to see the effect of pressure. The liquid jet velocity is kept constant at 19 m/s, and air velocities are in three different ranges of 30 m/s to 40 m/s, 60 m/s to 70 m/s and 90 m/s to 100 m/s. As it can be seen, increasing crossflow pressure decreases the sauter mean diameter. This can be mainly contributed to increased inertial forces on the jet. As the density is increased the number of large droplets is reduced, which results in smaller SMD and standard deviation for the cases with higher pressure. Essentially as the pressure is increased the drag-force on the jet and the individual droplets is also increased causing them to break into smaller droplets. Air velocity is also very critical on the droplet size as it can be seen by comparison of cases 108 and 151 versus 166 and 189. This essentially shows the importance of inertial forces on the atomization process. The temperature, nozzle diameter and liquid jet velocity is the same in all four cases but air velocity is about two and half times higher for cases 108 and 151, which result in smaller droplets even though the pressure is lower.

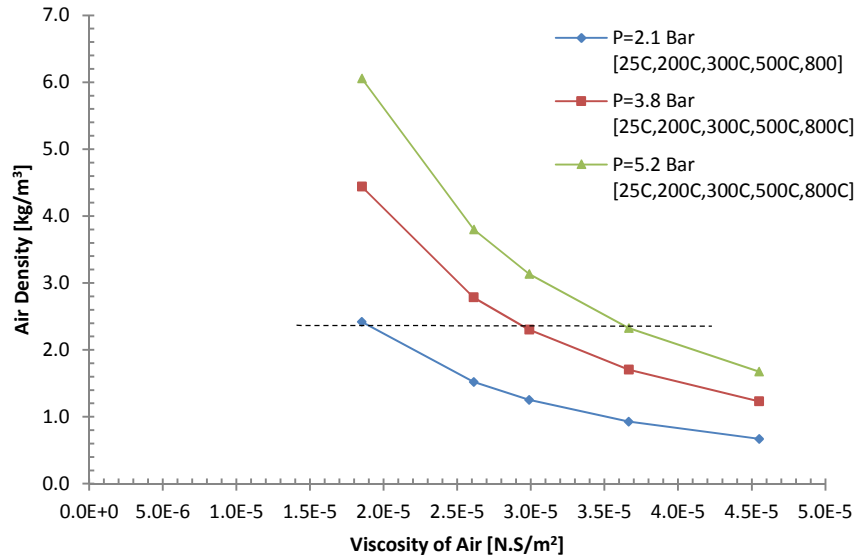


Figure 6.14: Relation between air density and air viscosity [67].

Figure 6.14 shows the relation between air density and air viscosity at various pressures and temperatures. As the air pressure is increased the air density is also increased but as the temperature is increased the viscosity is increased and density is slightly reduced as expected. It is possible to infer that at higher temperatures the viscous forces will have a greater effect on the breakup. Therefore, increasing pressure is not necessarily improving atomization since at higher temperatures the density of gas does not increase as substantially comparing to lower temperatures. In other words the effect of inertial forces due to pressure will become less prominent. For example, as it can be seen in Figure 6.15, SMD for case 2 ( $p=2.1$  bars,  $T=25^{\circ}\text{C}$ ) is  $76.6\mu\text{m}$  with standard deviation of  $24\mu\text{m}$ , and SMD for case 75 ( $p=3.8$  bars,  $T=300^{\circ}\text{C}$ ) is  $72.5\mu\text{m}$  with standard deviation of  $22.6\mu\text{m}$ . In both cases, the gas densities and velocities are almost the same, which indicates that the inertial forces are the same. But viscosity of the air is higher due to increased temperature. The viscosity has increased by a factor of almost 1.6. This forces the jet to have an increased width and length, leading to smaller droplets size. It is also important to note that the momentum flux ratio for both cases is also the same, which hints that the trajectories are very close to each other but as it can be seen both the droplet size and atomization is significantly altered.



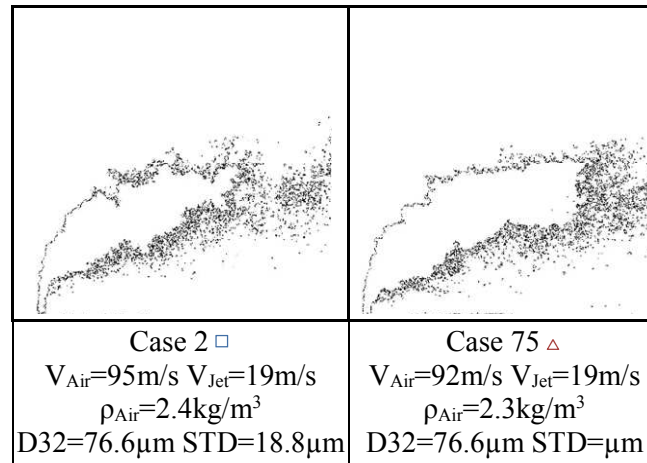
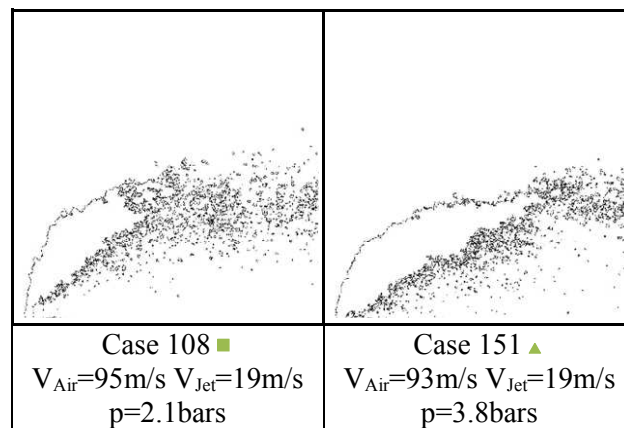
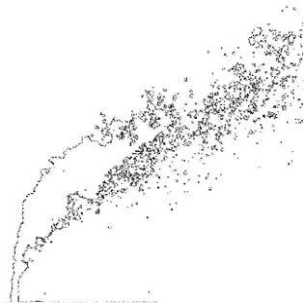
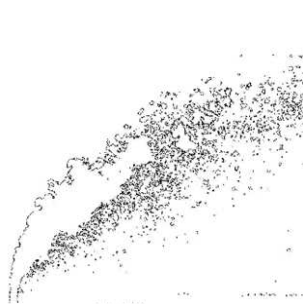
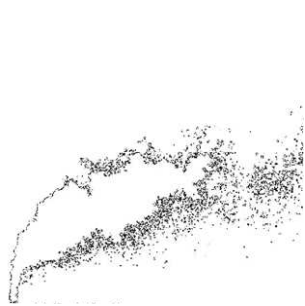
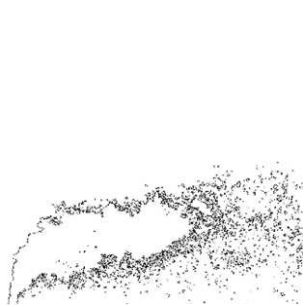


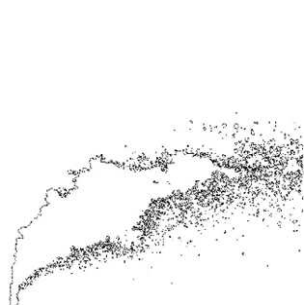



Figure 6.15: Comparison of conditions with similar gas densities. Table 2.3 summarizes the conditions.

Figure 6.16 shows the processed image for the cases presented in Figure 6.13. As it can be seen, in all the images as the pressure is increased the jet trajectory is reduced due to increase drag force on the jet. The drag force is increased only due to increase in air density by pressure while the viscosity for all practical purposes is almost unchanged. It should be noted that in all the comparisons the liquid mass flow rate is constant. Also, as the pressure increases the main plume area is stretched in the direction of airflow as it stays intact. This can be attributed to the increased density of the gas, which confines the spray into a narrower region and reduces dispersion. The increased pressure enhances the atomization process and in effect reduces the deviation in droplets and produces a more uniform spray.



	
Case 166 ▲ $V_{Air}=34\text{m/s}$ $V_{Jet}=19\text{m/s}$ $p=3.8\text{bars}$	Case 189 ● $V_{Air}=36\text{m/s}$ $V_{Jet}=19\text{m/s}$ $p=5.2\text{bars}$
	
Case 2 □ $V_{Air}=95\text{m/s}$ $V_{Jet}=19\text{m/s}$ $p=2.1\text{bars}$	Case 44 △ $V_{Air}=92\text{m/s}$ $V_{Jet}=19\text{m/s}$ $p=3.8\text{bars}$
	
Case 7 □ $V_{Air}=61\text{m/s}$ $V_{Jet}=19\text{m/s}$ $p=2.1\text{bars}$	Case 49 △ $V_{Air}=65\text{m/s}$ $V_{Jet}=19\text{m/s}$ $p=3.8\text{bars}$
	
Case 17 □ $V_{Air}=93\text{m/s}$ $V_{Jet}=19\text{m/s}$ $p=2.1\text{bars}$	Case 60 △ $V_{Air}=92\text{m/s}$ $V_{Jet}=19\text{m/s}$ $p=3.8\text{bars}$

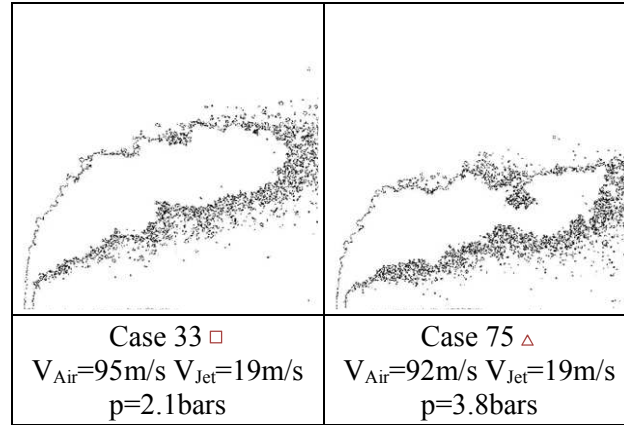
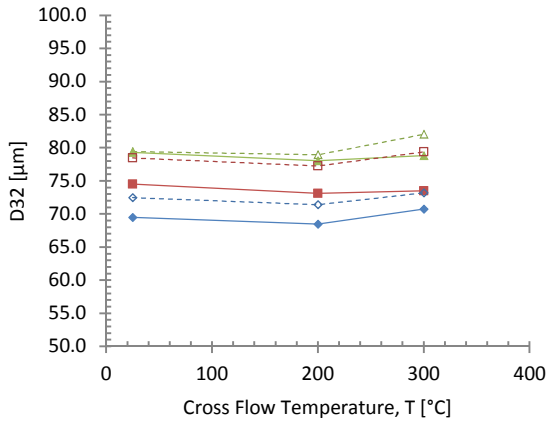


Figure 6.16: Comparison of the images for conditions with all the dimensional variables kept constant except for pressure,  $p$ . All the images have the same scale and droplets larger than 5 pixel squared ( $\sim 50 \mu\text{m}$ ) are only shown. Table 2.3 summarizes the conditions.

### 6.2.5 Effect of Temperature on the Global Droplet Size

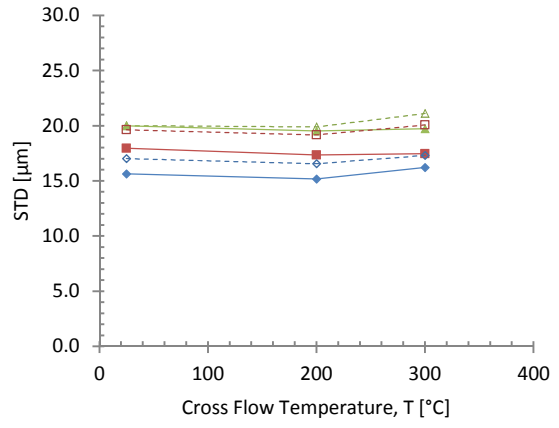
Similar to the previous sections, all the dimensional variables are kept constant in order to observe the effect of temperature on the global droplet size. The dimensional variables that are kept constant are the pressure,  $p$ , nozzle diameter,  $D_N$ , air velocity,  $V_{Air}$ , and liquid jet velocity,  $V_{Jet}$ . Table 2.3 summarizes the conditions and results of the compared cases. Generally, there are two distinct effects that are expected when the gas temperature is changed; first, the gas properties such as the density and viscosity are effected and depending on the heat transfer rates, the surface tension between the two mediums and ultimately the liquid properties such as viscosity and density are effected; second, depending on the temperature difference and the amount of energy available, the evaporation takes place which also effects the droplet size at the location of measurement.

Figure 6.17 shows the effect of temperature on sauter mean diameter and standard deviation. Each of the series shown represents condition where all dimensional variables are kept constant to observe the effect of temperature. The liquid jet velocity is kept constant at 19 m/s for all the cases. Air velocities are in three different ranges of 30 m/s to 40 m/s (green series), 60 m/s to 70 m/s (red series) and 90 m/s to 100 m/s (blue series). Each series are then organized to represents either a constant pressure, dashed lines are 2.1 bars, and solid lines are 3.8 bars, or constant nozzle diameter, dashed lines are  $457 \mu\text{m}$  and solid lines are  $572 \mu\text{m}$ .



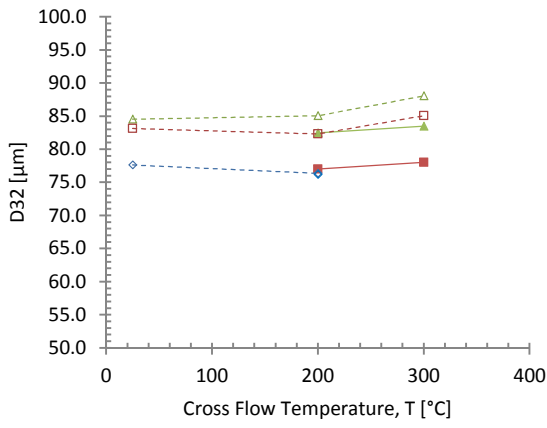
---△--- 11, 27, and 43    ---▲--- 54, 69, and 85  
 ---□--- 7, 22, and 38    ---■--- 49, 64, and 80  
 ---◇--- 2, 17, and 33    ---◆--- 44, 60, and 75

(a)



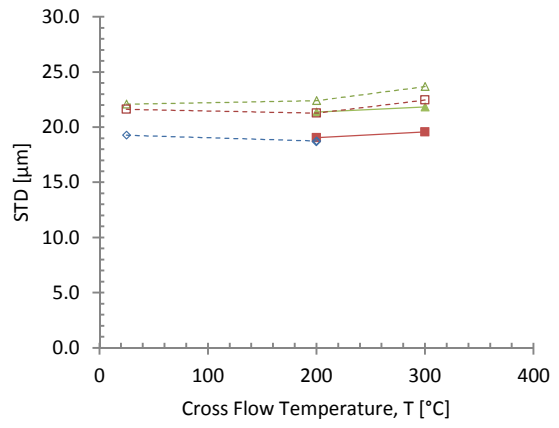
---△--- 11, 27, and 43    ---▲--- 54, 69, and 85  
 ---□--- 7, 22, and 38    ---■--- 49, 64, and 80  
 ---◇--- 2, 17, and 33    ---◆--- 44, 60, and 75

(b)



---△--- 102, 118, and 134    ---▲--- 161 and 173  
 ---□--- 97, 113, and 129    ---■--- 156, and 168  
 ---◇--- 92, and 108    ---◆--- 184

(c)



---△--- 102, 118, and 134    ---▲--- 161 and 173  
 ---□--- 97, 113, and 129    ---■--- 156, and 168  
 ---◇--- 92, and 108    ---◆--- 184

(d)

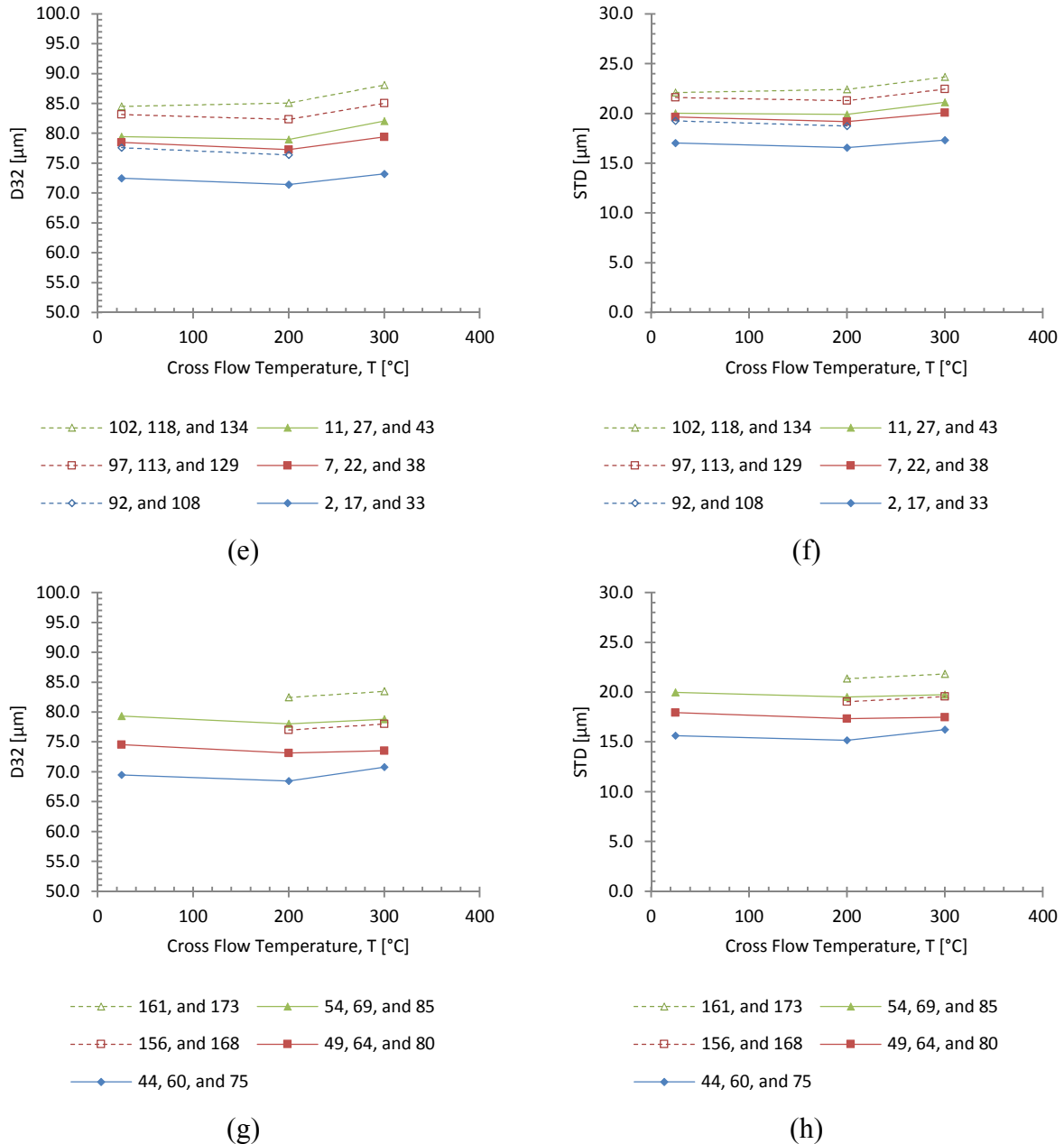


Figure 6.17: (a), (c), (e) and (g) Sauter mean diameter vs. Temperature. (b), (d), (f) and (h) Standard deviation vs. temperature. The liquid jet velocity is kept constant at 19 m/s for all cases. Air velocities are in three different ranges: green series is from 30 m/s to 40 m/s (or 40 m/s to 50 m/s depending on conditions); red series from 60 m/s to 70 m/s; and blue series from 90 m/s to 100 m/s;

- For Figure 6.17 (a) and (b) each series represents a constant pressure; dashed lines represent 2.1 bars, and solid lines 3.8 bars. Nozzle diameter is 572 μm for all cases;
- For Figure 6.17 (c) and (d) each series represents a constant pressure; dashed lines represent 2.1 bars, and solid lines 3.8 bars. Nozzle diameter is 457 μm for all cases;

- For Figure 6.17 (e) and (f) each series represents a constant nozzle size; solid lines represent 572  $\mu\text{m}$ , and dashed lines 475  $\mu\text{m}$ . Pressure is 2.1 bars for all cases.
- For Figure 6.17 (g) and (h) Each series represents a nozzle diameter; solid lines represent 572  $\mu\text{m}$ , and dashed lines 475  $\mu\text{m}$ . Pressure is kept at 3.8 bars for all cases.

Prior to explaining the spray behavior at various temperatures, the observations from the previous sections can be verified. The droplet sizes for cases at higher pressure are smaller, Figure 6.17 (a) – (d), and also droplet sizes for cases with smaller nozzle are larger, Figure 6.17 (e) – (h). Among all cases increasing the crossflow temperature first causes a slight decrease in sauter mean diameter and standard deviation and as the temperature is further increased the droplet size slightly increases, Figure 6.17. The changes are observed for both nozzles and pressures and various gas velocities. It should be noted that the changes are very subtle compared to the cases where other parameters are changed. However, the same pattern is observed in various different conditions even from figures presented in previous sections (e.g. Figure 6.9 also shows the same pattern when jet velocities are changed). Additionally the numbers of droplets measured are significant ranging from  $\sim 71,000$  to  $\sim 1,880,000$  droplets and on average  $\sim 710,000$  droplets for each case. Finally, same behavior is seen even with different circularity set-points in the droplet measurement algorithm. Although the actual measured sizes for different circularity set-points are different the results show similar pattern. Therefore it is safe to accept the changes are not coincidental and oblige further investigation.

In short, the reason for the initial reduction in droplet size is the change in gas properties and the increase is caused by higher evaporation rates. The properties of liquid specifically density, dynamic viscosity and surface tension are all temperature dependent and consequently time dependent due to heat transfer rates. Therefore, it is necessary to discuss heating and evaporation of the jet and droplets in order to better understand this behavior. A discussion is provided in Appendix D regarding heat transfer to the jet and droplets as well as calculation for evaporation rates for the droplets. As it can be seen, the discussion is multifaceted and consequently the best order for the discussions has to be the same order as the atomization process. First, the gas and liquid properties during initial jet breakup are discussed, followed by heat-up time of the formed droplets and finally the droplet evaporation rates and its effect on overall size.

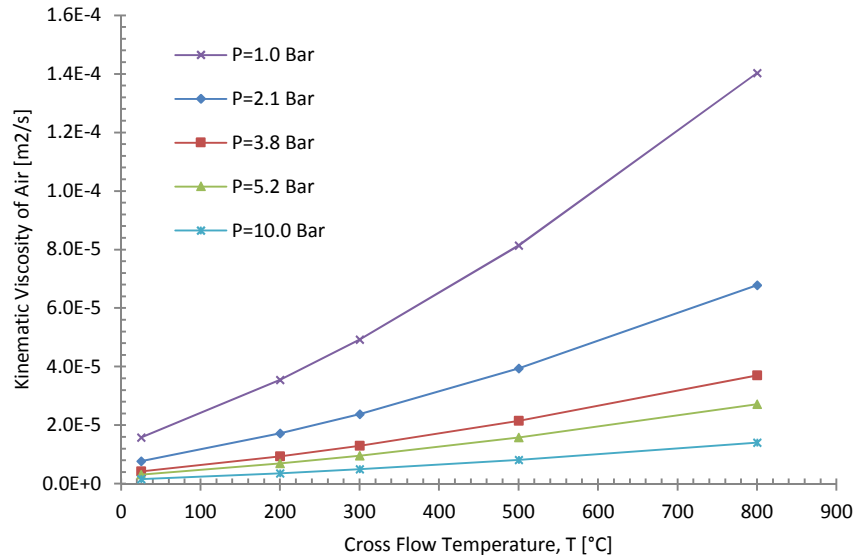


Figure 6.18: Ratio of dynamic viscosity to air density (kinematic viscosity) at various air temperatures and pressures.

It is important to define an interface or effective temperature for the spray plume. When the liquid is introduced into the high temperature crossflow the liquid will absorb the heat from the air. For the current study, the highest effective temperature for the spray plume is the saturated temperature for the liquid at the given pressure. The crossflow air contains sufficient amount of energy to bring the temperature of the liquid up to its saturation temperature. In most cases there is excess energy, which is available for evaporation. The liquid essentially acts as a temperature regulator, where the temperature will not increase beyond the saturation temperature at the given pressure. The important issue to consider is the time that is required for the change in temperature versus the breakup time. In Appendix D, the details regarding heat-up time is shown. During the initial phase of atomization the jet is still intact. The jet is assumed to be cylindrical with the same diameter as the nozzle. The calculations based on lumped capacitance method for the jet body shows that the heat-up time is on average 12 s versus 0.6 ms for the breakup time. This essentially means that during initial jet breakup the liquid will remain at the same temperature as the liquid reservoir for all practical purposes. In addition to lump capacitance method for verifying this result, various temperature schemes for the jet is also considered but the data fit is found to be best for the case where the liquid temperature is unaffected by the crossflow air and the liquid is at the same

pressure as the crossflow air. Consequently all the properties calculated for the liquid are at the initial temperature and crossflow pressure.

During the initial stages of atomization only gas properties are affected by temperature. These properties are mainly gas density and viscosity. As the temperature is increased the gas density is reduced and viscosity is increased. The kinematic viscosity at a given pressure which is the ratio of density to dynamic viscosity, increases as the temperature increases, Figure 6.18. It is important to note that as the pressure is increased the change in kinematic viscosity with respect to temperature is reduced. This can also be seen when comparing Figure 6.17 (a) – (d), where the changes in droplet size for cases at 2.1 bars is larger than cases at 3.8 bars. As the kinematic viscosity is increased air Reynolds number is reduced and the coefficient of drag is increased. This can also be seen in the images of Figure 6.20 where the plume width is increased as the temperature is increased. The mass flow rate of the liquid is kept constant and as the drag is increased the liquid ligaments, sheets, and other formation will be smaller which then lead to smaller droplets and ligament formations.

Referring back to Figure 6.14 where the relation between air density and viscosity is shown, at lower pressures as the temperature is increased, air viscosity increases dramatically and density reduces less substantially, at higher pressures the effect is reversed. Images in Figure 6.20 show that the trajectory is almost unaffected while the gas density is almost reduced by half when comparing high and low temperature cases, i.e.  $q$  is increased by factor of 2. Due to increase in gas viscosity, the trajectory increases ever slightly, this is also noticeable by comparing mean plume width. In addition to droplet size it is important to introduce the viscosity term to trajectory correlations since momentum flux ratio cannot solely describe the physics. Consequently the penetration and droplet size depend on both air density and viscosity. This can also be seen in the results reported by Hassa et al. at room temperature. Even though their experiments are performed at room temperature, pressure for their experiments ranged from 2 bars to 8 bars. Phase Doppler Particle Analyzer data show that as the pressure is increased the droplet size reduces but eventually the trends plateau even though gas density is further increased by increasing pressure [15]. This can be explained by comparing the kinematic viscosity changes in Figure 6.18 at a constant temperature.



The next step in atomization is the heat-up and evaporation of the jet, ligaments and droplets. Evaporation also plays an important role in the measured droplet size. Evaporation reduces the size of individual droplets. As the temperature and evaporation rate increase smaller droplets would completely evaporate while the larger droplets are still measurable even though smaller in size. This in effect creates a shift in droplet size histogram and results in a perceived increase in droplet size at higher temperatures. This can be seen when comparing the data between D10 and D32, D32 as a statistical measure is more sensitive to large diameters and is not altered by smaller droplets as much. This can also be verified by comparing the standard deviation of the droplet size where it also increases with increased evaporation and suggests that the distribution is widened. Generally, the rate of reduction in diameter due to evaporations is higher for smaller droplets than larger droplets. Evaporation takes place on the surface and because surface to volume ratio of large drops is higher than smaller drops even at constant evaporation rates the diameter for the smaller drop would reduce faster. Generally, evaporation of a suspended droplet follows D-squared law. The heat-up process speeds up significantly after the primary breakup based on the calculations shown in Appendix D. The sauter mean diameter is used to represent the average size for the formed bodies. The heat-up time is significantly reduced based on the results obtained from lumped capacitance method. The heat-up time ranges from 8 ms to 1.1 s with the average at 310 ms. Evaporation rates are then calculated and the average droplet life range is from 14 ms to 180 ms with the average at 58 ms.

Another way to show the effect of evaporation on droplet size is to compare the effects of air velocity, nozzle diameter and pressure. As the air velocity is increased the evaporation rate also increases, and the slopes between cases at 200°C and 300°C are also increased, Figure 6.17, i.e. the slope of the solid green line is larger than the solid red and solid red is larger compare to solid blue. Additionally the droplet size increase is delayed for the larger nozzle where evaporation rate are lower. Finally the cases at lower air pressure where the evaporation rates are higher, the slope in the last segment of the figures is higher. These observations verify the effect of evaporation on droplet size.

In addition to the effect of gas temperature on gas properties and evaporation, the liquid density, viscosity and surface tension are also affected. These mostly apply to secondary atomization. As temperature is increased all of these parameters are reduced and there is a coupling effect between

the viscosity and surface tension. Surface tension has a linear relation with temperature, while viscosity follows an inverse power law relation. Effect of temperature on surface tension can be calculated based on Eötvös rule [68], which is:

$$\sigma = \frac{k(T_c - T)}{\hat{V}^{2/3}} \quad (6.11)$$

where  $T_c$  is critical temperature so that beyond this temperature the surface temperature has a value of zero,  $k$  is a constant with a typical value of  $2.1 \times 10^{-7}$  [J K<sup>-1</sup> mol<sup>-2/3</sup>] for various liquids and  $\hat{V}$  is molar volume. Viscosity relation with temperature can be generally calculated based on Reynolds equation:

$$\mu_{Jet}(T) = \mu_0 e^{-bT} \quad (6.12)$$

And for water the following empirical relation [69] can be used:

$$\mu_{Jet}(T) = 2.414 \times 10^{-5} 10^{\frac{247.8}{T-140}} \quad (6.13)$$

Where  $T$  [K] is the liquid temperature and  $\mu_{Jet}$  [N.s/m<sup>2</sup>] is the viscosity of the liquid jet. The correlation is accurate within 2.5% from 0°C to 370°C.

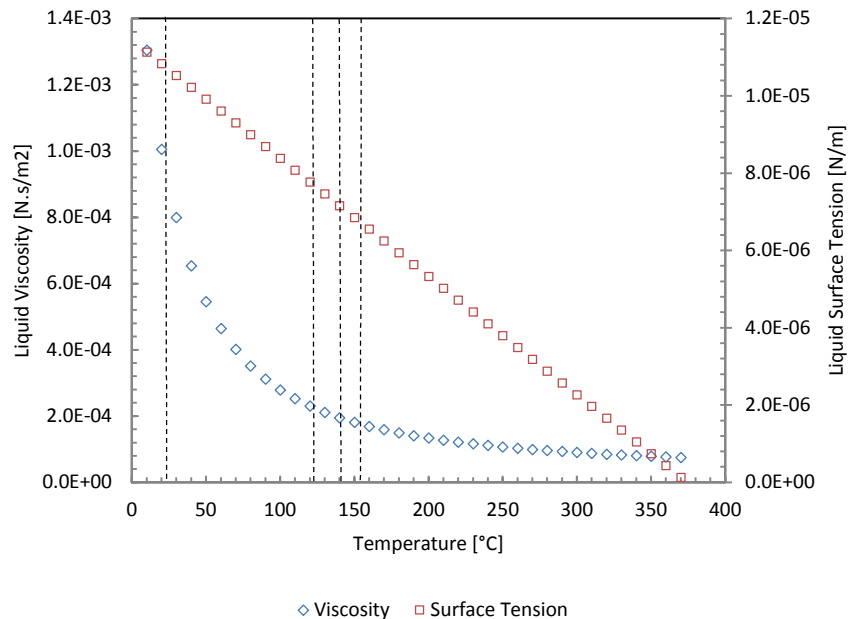
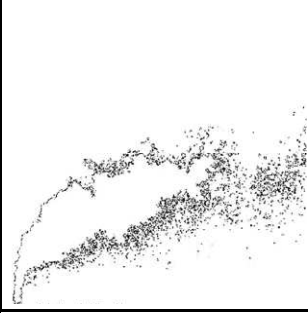
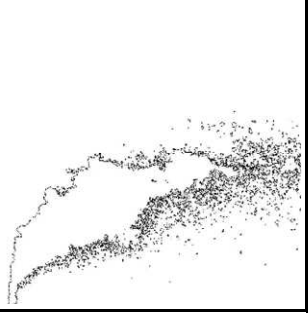
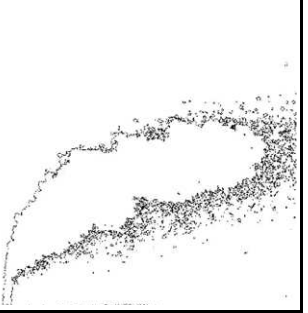
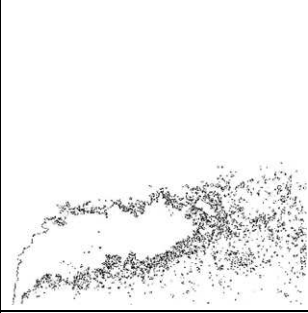
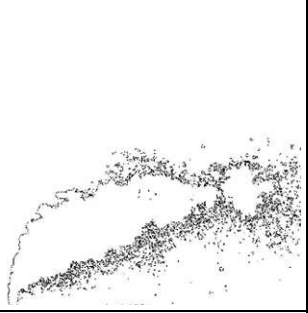
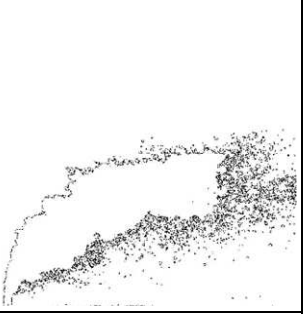
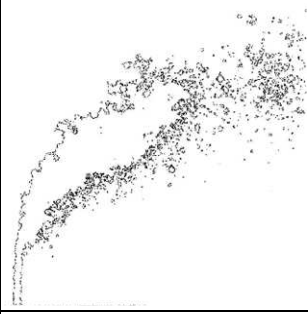
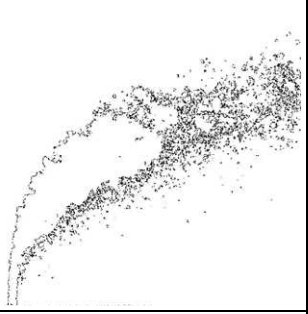
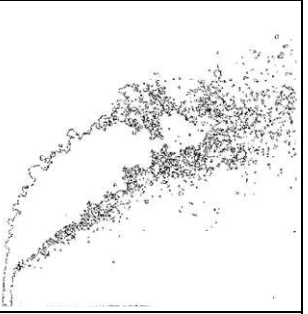

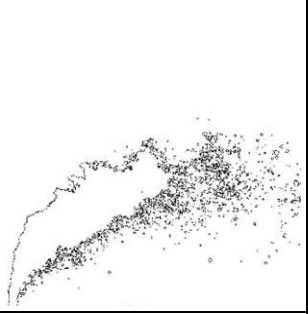
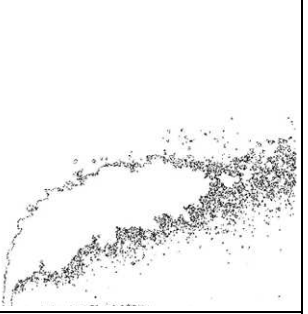


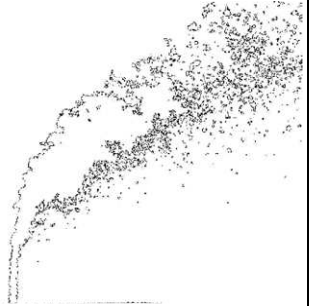

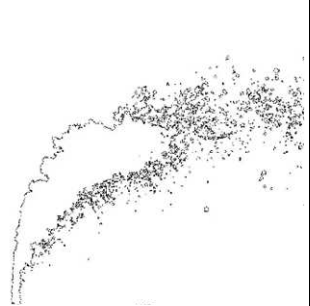
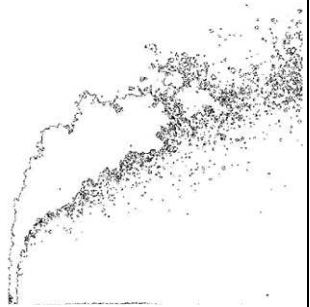
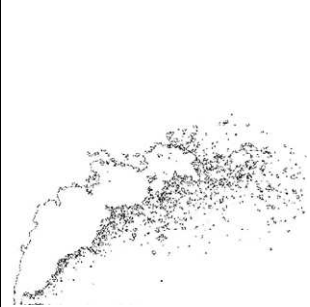




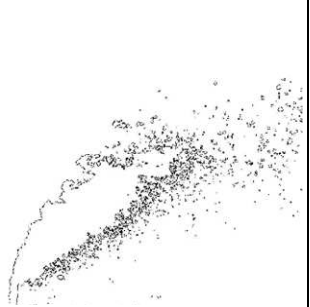


Figure 6.19: Effect of temperature on viscosity and surface tension. The vertical lines show the saturation temperature of water at 2.1 bars, 3.8 bars and 5.2 bars.

Based on the above correlations and Figure 6.19, it can be seen that beyond a specific temperature the change in viscosity is negligible while surface temperature is further reduced. As it can be seen, there is a significant change in viscosity between the first two temperatures while there is a lesser change in viscosity between the last two temperatures. On the other hand, surface tension is reduced linearly. Therefore, the droplet size follows a similar relation to viscosity even due surface tension is further reduced. It should be noted that since atomization takes place on the surface of the liquid, both the liquid surface tension and viscosity influences are present even if the liquid volume may not be at the equilibrium temperature. Ultimately as the gas temperature is increased, the liquid interface reaches saturation temperature earlier. This behavior becomes more significant at higher temperatures where the heat transfer to the jet body is larger. That said, as the gas temperature is increased, the liquid properties are limited by the saturation temperature of the liquid. Figure 6.20 shows the processed images for the aforementioned cases where the liquid mass flow rate is constant for all cases. The liquid properties of cases in the center and right column are very similar as the gas properties change. In all the images, as the temperature is increased the drag force on the jet is also increased which leads to an increased plume width. Subsequently, the dispersion is also improved due to increased gas viscosity and reduction in gas density. Conversely the cases that are at higher pressures lead to narrower plume width and reduced dispersion since pressure does not affect the gas viscosity but the density is reduced linearly, Figure 6.14.

		
Case 2 □ $V_{Air}=95\text{m/s}$ $V_{Jet}=19\text{m/s}$ $T=25^\circ\text{C}$	Case 17 □ $V_{Air}=93\text{m/s}$ $V_{Jet}=19\text{m/s}$ $T=200^\circ\text{C}$	Case 33 □ $V_{Air}=95\text{m/s}$ $V_{Jet}=19\text{m/s}$ $T=300^\circ\text{C}$
		
Case 44 △ $V_{Air}=92\text{m/s}$ $V_{Jet}=19\text{m/s}$ $T=25^\circ\text{C}$	Case 60 △ $V_{Air}=92\text{m/s}$ $V_{Jet}=19\text{m/s}$ $T=200^\circ\text{C}$	Case 75 △ $V_{Air}=92\text{m/s}$ $V_{Jet}=19\text{m/s}$ $T=300^\circ\text{C}$
		
Case 7 □ $V_{Air}=61\text{m/s}$ $V_{Jet}=19\text{m/s}$ $T=25^\circ\text{C}$	Case 22 □ $V_{Air}=61\text{m/s}$ $V_{Jet}=19\text{m/s}$ $T=200^\circ\text{C}$	Case 38 □ $V_{Air}=62\text{m/s}$ $V_{Jet}=19\text{m/s}$ $T=300^\circ\text{C}$
		
Case 49 △ $V_{Air}=65\text{m/s}$ $V_{Jet}=19\text{m/s}$ $T=25^\circ\text{C}$	Case 64 △ $V_{Air}=68\text{m/s}$ $V_{Jet}=19\text{m/s}$ $T=200^\circ\text{C}$	Case 80 △ $V_{Air}=68\text{m/s}$ $V_{Jet}=19\text{m/s}$ $T=300^\circ\text{C}$

		
Case 11 □ $V_{Air}=49\text{m/s}$ $V_{Jet}=19\text{m/s}$ $T=25^{\circ}\text{C}$	Case 27 □ $V_{Air}=49\text{m/s}$ $V_{Jet}=19\text{m/s}$ $T=200^{\circ}\text{C}$	Case 43 □ $V_{Air}=50\text{m/s}$ $V_{Jet}=19\text{m/s}$ $T=300^{\circ}\text{C}$
		
Case 54 △ $V_{Air}=41\text{m/s}$ $V_{Jet}=19\text{m/s}$ $T=25^{\circ}\text{C}$	Case 69 △ $V_{Air}=43\text{m/s}$ $V_{Jet}=19\text{m/s}$ $T=200^{\circ}\text{C}$	Case 85 △ $V_{Air}=43\text{m/s}$ $V_{Jet}=19\text{m/s}$ $T=300^{\circ}\text{C}$
		
Case 92 ■ $V_{Air}=96\text{m/s}$ $V_{Jet}=19\text{m/s}$ $T=25^{\circ}\text{C}$	Case 108 ■ $V_{Air}=95\text{m/s}$ $V_{Jet}=19\text{m/s}$ $T=200^{\circ}\text{C}$	Case 124 ■ $V_{Air}=95\text{m/s}$ $V_{Jet}=19\text{m/s}$ $T=300^{\circ}\text{C}$
		
Case 97 ■ $V_{Air}=61\text{m/s}$ $V_{Jet}=19\text{m/s}$ $T=25^{\circ}\text{C}$	Case 113 ■ $V_{Air}=61\text{m/s}$ $V_{Jet}=19\text{m/s}$ $T=200^{\circ}\text{C}$	Case 129 ■ $V_{Air}=60\text{m/s}$ $V_{Jet}=19\text{m/s}$ $T=300^{\circ}\text{C}$

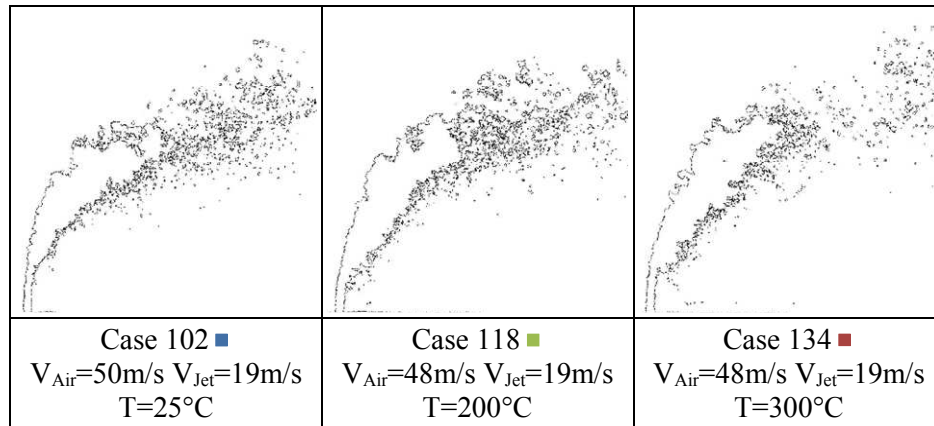


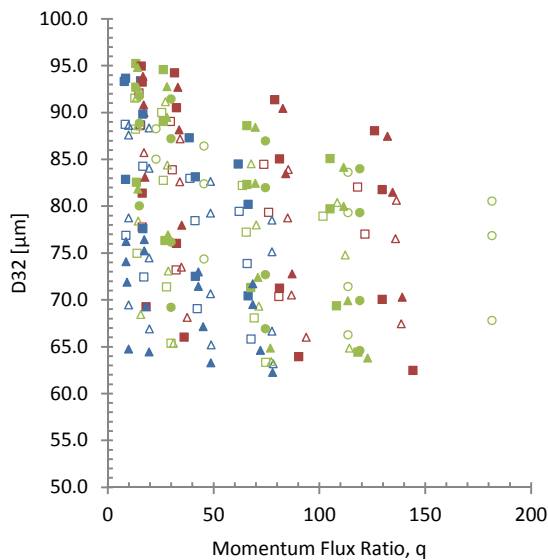
Figure 6.20: Comparison of the images for conditions where all the dimensional variables are kept constant except for temperature,  $T$ . Table 2.3 summarizes the conditions.

### 6.3 Effect of Non-Dimensional Variables on the Global Droplet Size

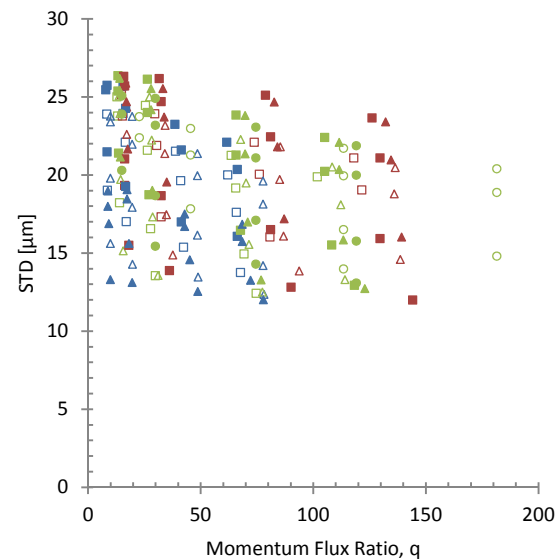
In this section, effects of various non-dimensionalized numbers on droplet size are discussed. These non-dimensional variables are the momentum flux ratio, jet and air Weber, Reynolds, and Ohnesorge numbers, and finally density ratio. Momentum flux ratio is one of the more important parameters in the current study. Historically and rightfully, it has been widely used and shown that it relates to the trajectory very well. In contrary, the current research shows that momentum flux ratio does not solely represent droplet size. This can be seen from the results in Figure 6.21 (a) and (b). Even though, many of the conditions have the same momentum flux ratio the droplet size varies considerably. Momentum flux ratio is the ratio of the jet and air Weber numbers. It is possible to have the same momentum flux ratio with different Weber numbers, which results in different type of atomization, as shown in the previous sections.

Similar conclusion can be made in regards to density ratio. This variable does not display any sensitivity to the velocity variations, as it can be seen in Figure 6.21 (o) and (p). On the other hand, Weber numbers and Reynolds numbers for liquid and gas capture the physics more consistently, Figure 6.21 (c) – (j). Figure 6.21 (c) – (j) show that as these variables increase, the droplet size and standard deviation on droplet size decreases. It is interesting to note that in all of these figures as Weber number and Reynolds numbers increase the data seem to converge and vice versa as they are reduced the variation on the droplet size increases. Also droplet size shows less variation for a given liquid Weber and Reynolds numbers versus air Weber and Reynolds numbers. This information can be taken as an indication on the sensitivity of droplet size on the nozzle geometry

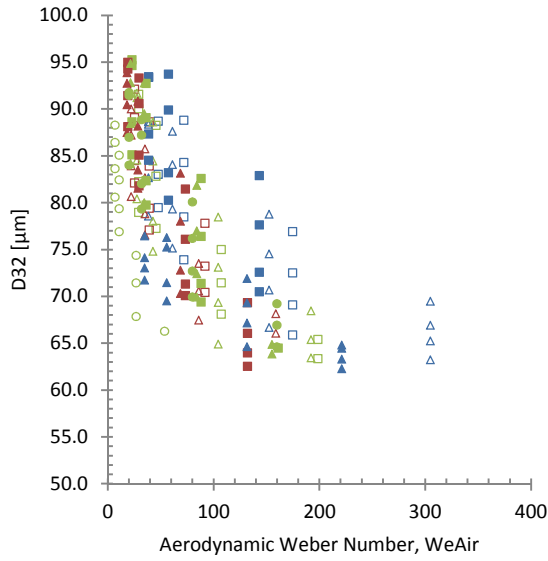
and initial jet conditions. Finally, it is easy to see that Weber and Reynolds numbers are the best suited variables to define a global correlation for droplet size. The correlations presented in the next section have three different forms. The first correlation is based on just the Weber and Reynolds numbers, the second is based on the Weber and Ohnesorge numbers; and the third is based on the momentum flux ratio, gas Weber number and gas and liquid Ohnesorge numbers. The reason for the three forms is that such correlations only require four independent non-dimensional groups. It is intuitive and more general to use Weber and Reynolds to derive the initial correlation, but the velocity terms will be present in both Weber and Reynolds number and consequently to separate the effect of physical properties from velocity it is beneficial to present the correlation with Weber and Ohnesorge numbers. Finally, due to the form presented in previous the studies it is helpful to use the momentum flux ratio and gas Weber number instead of the gas and liquid Weber numbers.



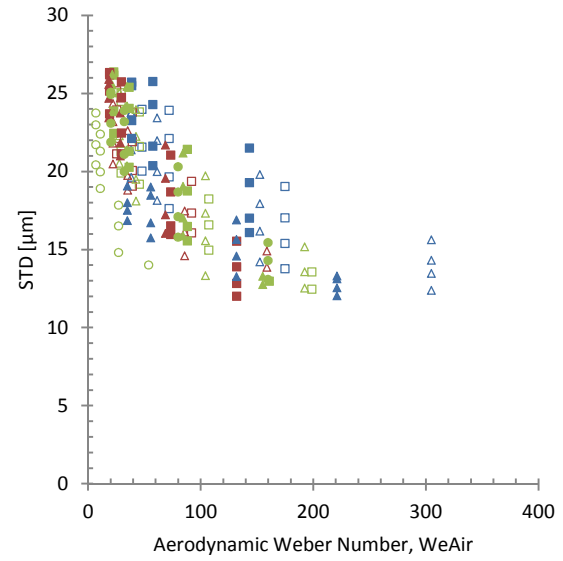
(a)



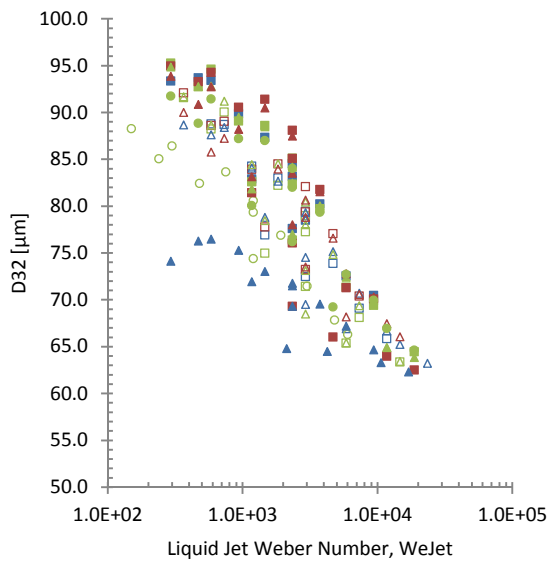
(b)



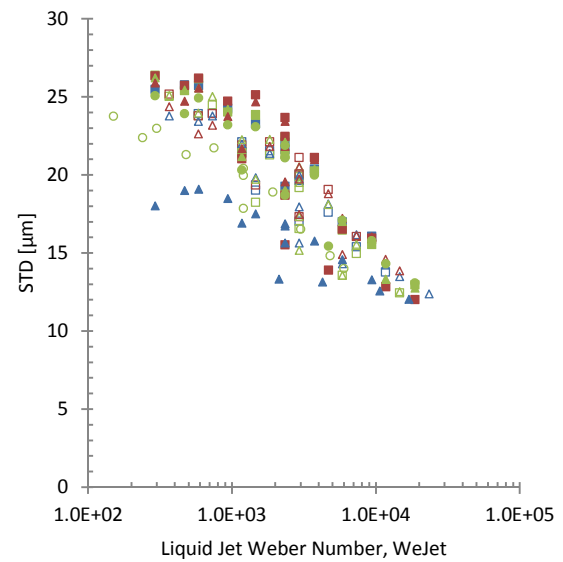
(c)



(d)

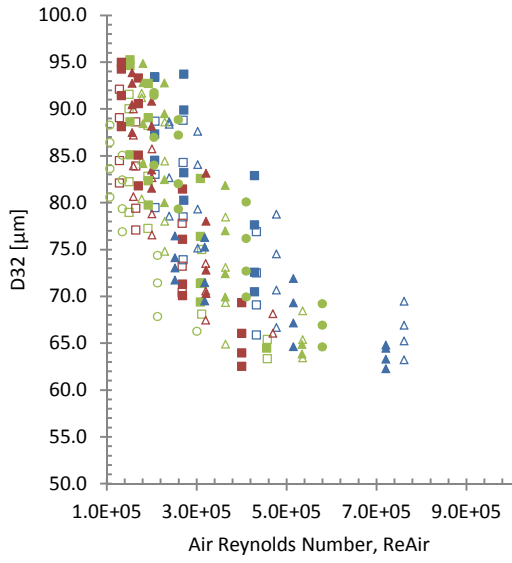


(e)

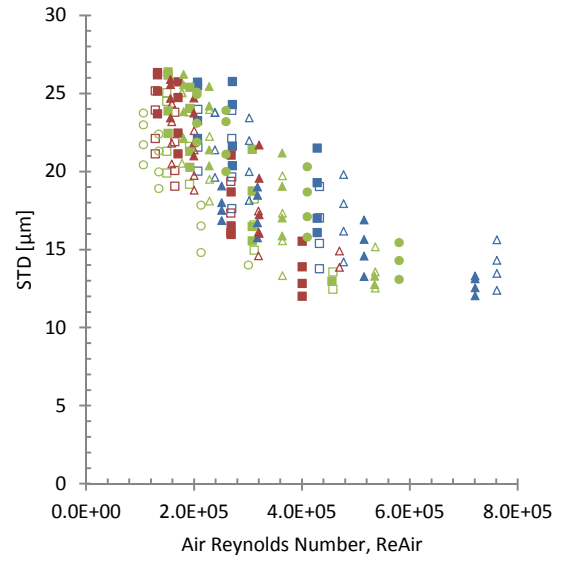


(f)

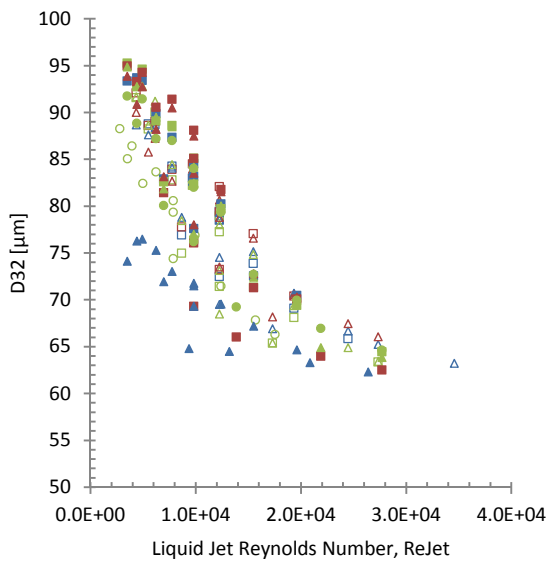




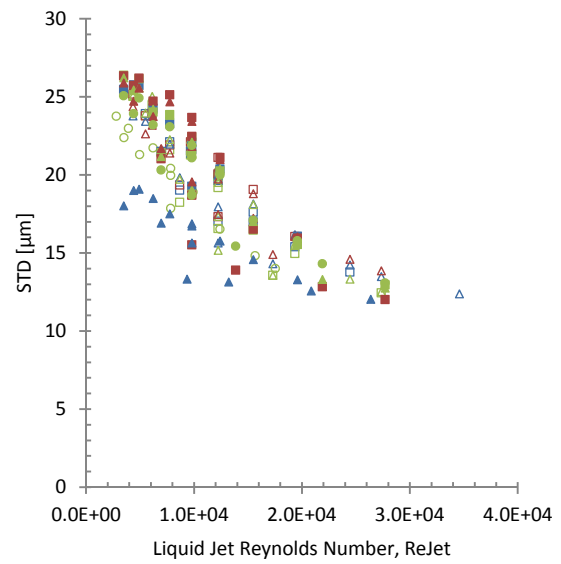
(g)



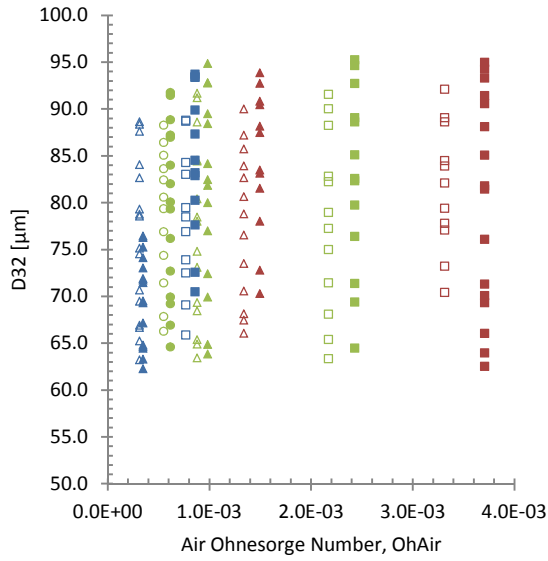
(h)



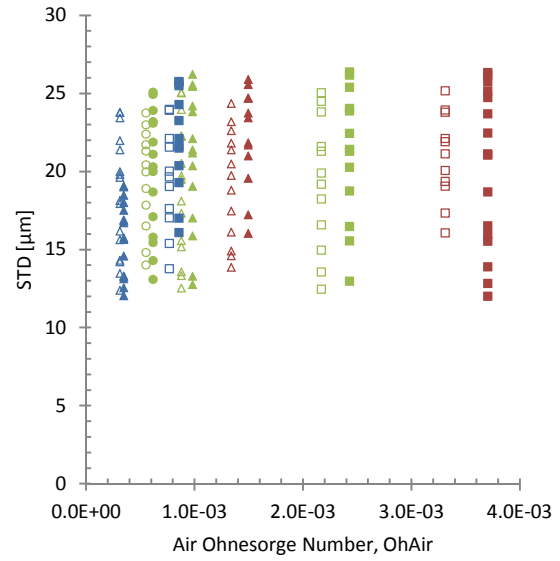
(i)



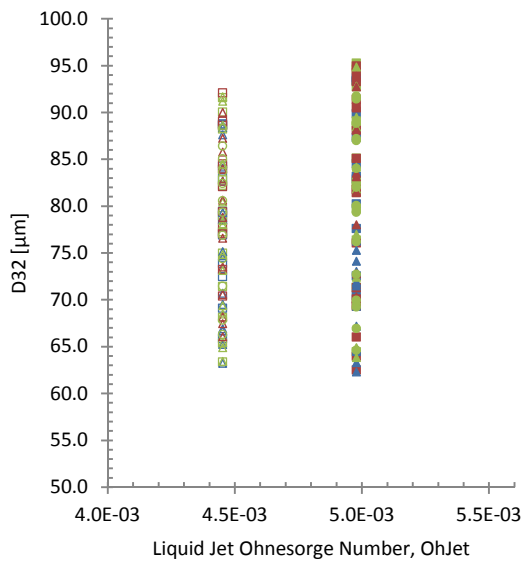
(j)



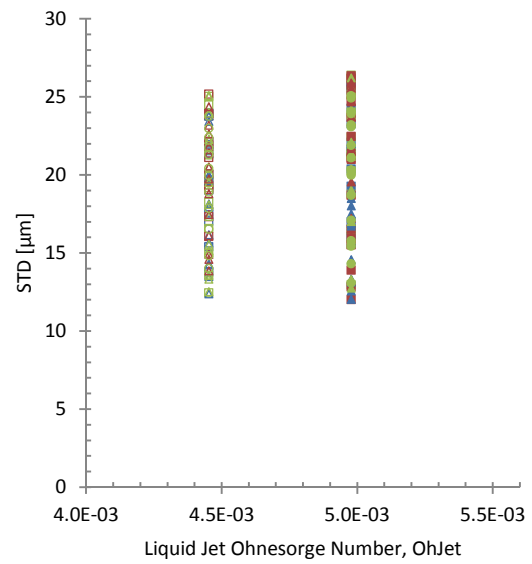
(k)



(l)



(m)



(n)

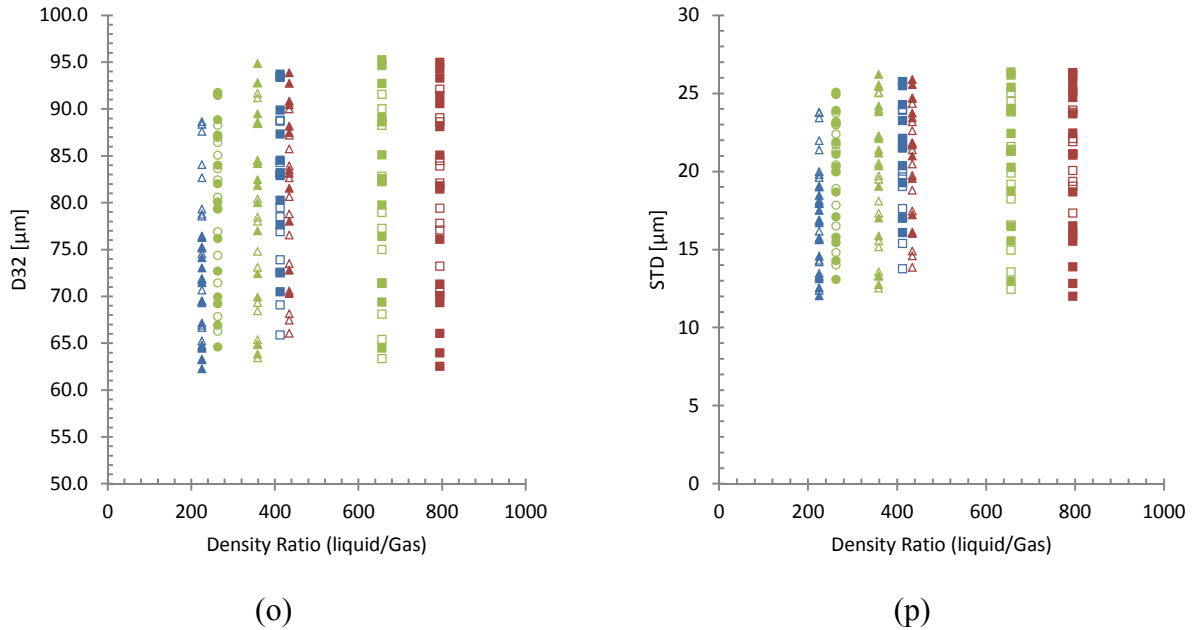


Figure 6.21: (a)-(p) D32 and standard deviation on droplet size vs. various non-dimensional variables.

Table 2.3 summarizes the conditions.

## 6.4 Correlations for the Global Droplet Size

In this section, few correlations are presented and compared as a function of various non-dimensional variables. The correlation by Hsiang et al. is considered as a starting point [70]. It is derived based on the phenomenological understanding of the atomization process:

$$\frac{SMD}{D_N} = C_s \left( \frac{\rho_{Air}}{\rho_{Jet}} \right)^{-0.25} \left( \frac{\rho_{Jet} D_N V_{st}}{\mu_{Jet}} \right)^{-0.5} \quad (6.14)$$

$$\left( \frac{\rho_{Air} SMD V_{st}^2}{\sigma} \right) = 6.2 \left( \frac{\rho_{Air}}{\rho_{Jet}} \right)^{-0.25} \left( \frac{\rho_{Jet} D_N V_{st}}{\mu_{Jet}} \right)^{-0.5} We_{Air} \quad (6.15)$$

They performed their experiments at room condition and had a stream of droplets injected inside a shock tube. They assumed that the boundary layer thickness is comparable to the droplet size and the relative (stream-wise) velocity is comparable to the relative velocity at the time of breakup. Equation (6.15) is then evolved by re-arranging equation (6.14) and using linear regression to determine the constant of correlation. The data used for the fit of the above correlation is the droplet size for primary breakup. The data did not vary greatly for the density ratio and the authors recommended further investigation.

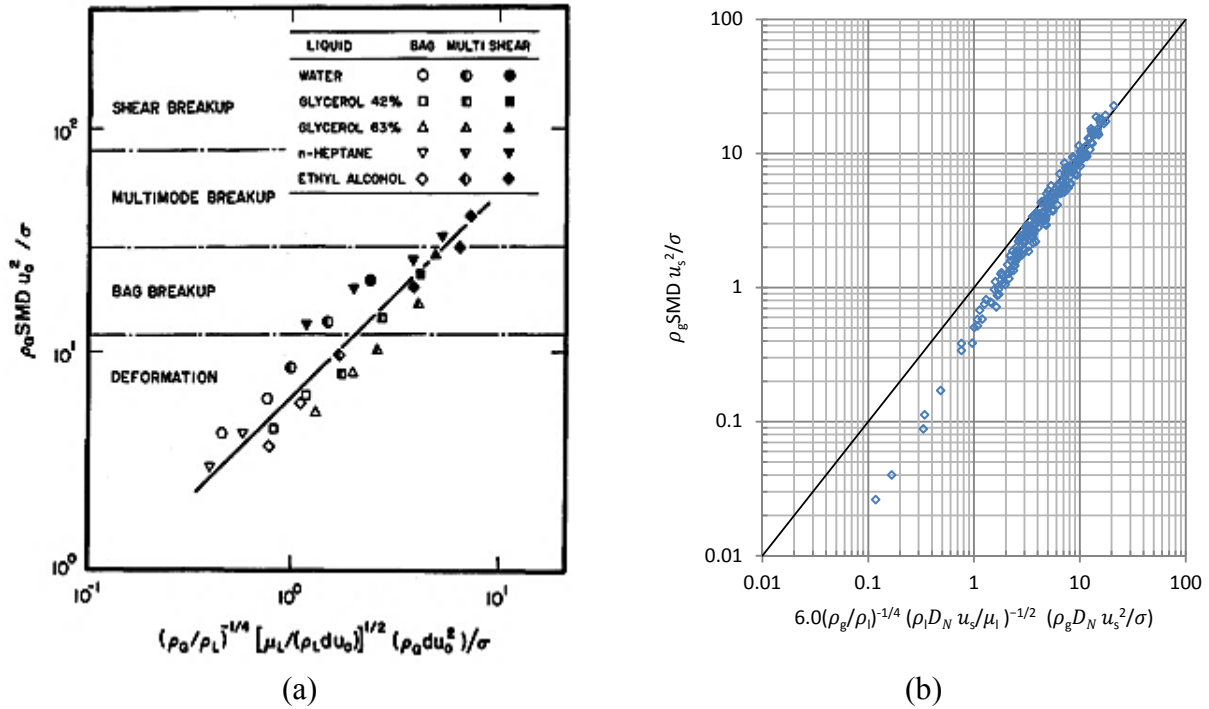


Figure 6.22: Comparison of results from Hsiang et al. [70] with the current study.

The above correlation is a good starting point for the development of a correlation for the current study. The following correlation is the result of nonlinear regression analysis to fit the current study's data to the form suggested by Hsiang et al. [70]:

$$\left( \frac{\rho_{Air} SMD V_{st}^2}{\sigma} \right) = 6.0 \left( \frac{\rho_{Air}}{\rho_{Jet}} \right)^{-0.25} \left( \frac{\rho_{Jet} D_N V_{st}}{\mu_{Jet}} \right)^{-0.5} We_{Air} \quad (6.16)$$

The coefficient of determination for the above equation is 0.97 and the standard error for the dependent variable, i.e. left side of the correlation, is 0.1. In equation (6.16) the exponents are forced to be constant and also the constant term is forced to be zero, i.e. the mean of errors is zero. This can produce biased results. The standard error of the dependent variable is fairly large due to the method of analysis. The range of values for the dependent variable is 0 – 100 versus 0 – 10 for the study by Hsiang et al. [70].

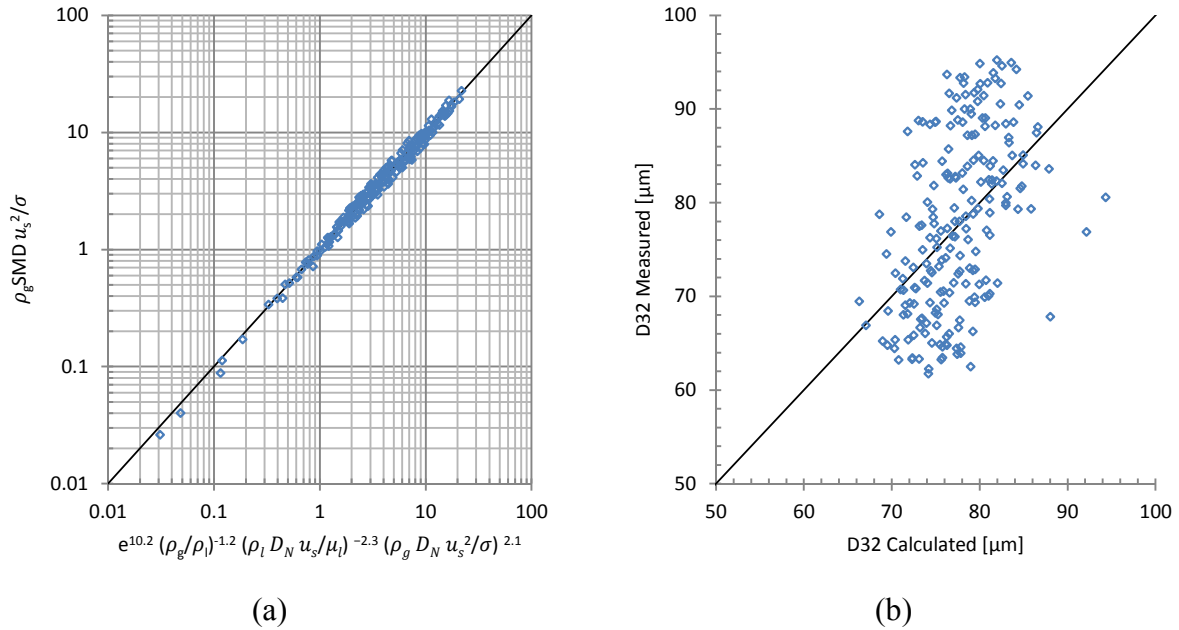


Figure 6.23: Correlation of the SMD for primary breakup, equation (6.17).

The following modified correlation is the result of allowing the correlation to fit the data without forcing any of the exponents to remain constant, Figure 6.23.

$$\left( \frac{\rho_{Air} \text{SMD } V_{st}^2}{\sigma} \right) = e^{10.2} \left( \frac{\rho_{Air}}{\rho_{Jet}} \right)^{-1.2} \left( \frac{\rho_{Jet} D_N V_{st}}{\mu_{Jet}} \right)^{-2.3} \left( \frac{\rho_{Air} D_N V_{st}^2}{\sigma} \right)^{2.1} \quad (6.17)$$

The coefficient of determination for the above equation is 0.99 and the standard error for the dependent variable, i.e. left side of the correlation, is 0.1. The standard errors for the exponents from left to right are 0.07, 0.07, and 0.13, respectively. The standard error for the correlation constant is 0.7. T-test and F-test are performed to check for the significance of the individual variables and the correlation as a whole. It is found that all the variables and correlation are statistically significant and exceed the 99.5% confidence level. The standard error for the correlation constant is fairly significant. Figure 6.23 shows the plot of measurements of SMD for primary breakup. Additionally, when computing SMD based on the current data, the mean error is 5% with standard deviation of 4%. The error is large enough to suggest that calculating SMD based on this correlation can lead to inaccuracies even though the error on the left side of the correlation is small.

The other issues with this type of correlation is related to the air and jet velocities as well as gas temperature and pressure. In equation (6.17) the effect of two velocity terms is simplified to the

relative velocity term. For example, the compared cases in the Figure 6.24 have the same relative velocity and conditions but because the jet and gas velocities are different then the atomization process is altered. As it can be seen, although the trajectory is not significantly different the droplet size is reduced and the droplet concentration is increased on the leeside of the jet for case 86. The SMD for case 86 is  $76.6 \mu\text{m}$  with standard deviation of  $18.8 \mu\text{m}$ , while SMD for case 89 is  $83.9 \mu\text{m}$  with standard deviation of  $21.8 \mu\text{m}$ .

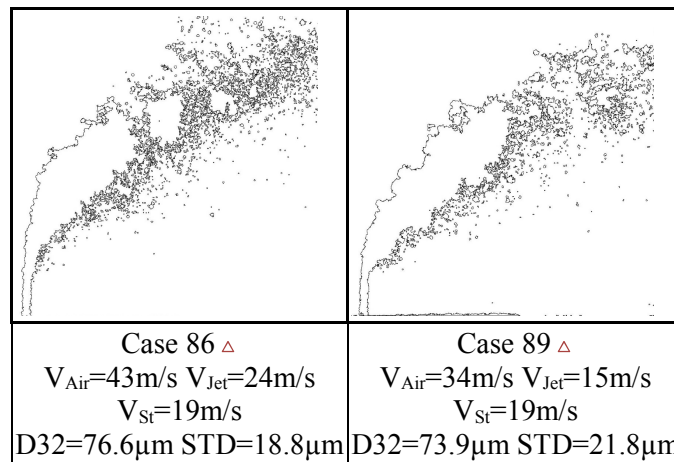


Figure 6.24: Comparison of conditions with the stream-wise velocities and conditions but different gas and jet velocities. Table 2.3 summarizes the conditions.

Moreover, in the equation (6.17) the effect of temperature and pressure is also omitted. These two parameters are coupled into the density ratio term in the correlation and the effect of gas viscosity is not present. For example in Figure 6.25, two cases are compared that have the same gas density and velocities but the pressure and temperature are different. Both cases have the same stream-wise velocity,  $19 \text{ m/s}$  and gas density. SMD for case 2 ( $p=2.1 \text{ bars}$ ,  $T=25^\circ\text{C}$ ) is  $76.6 \mu\text{m}$  with standard deviation of  $24 \mu\text{m}$ , and SMD for case 75 ( $p=3.8 \text{ bars}$ ,  $T=300^\circ\text{C}$ ) is  $72.5 \mu\text{m}$  with standard deviation of  $22.6 \mu\text{m}$ . In both cases the gas densities are almost the same but the droplet size is different due to gas viscosity. The viscosity has increased by a factor of almost 1.6. Equation (6.17) does not account for the changes in gas viscosity.

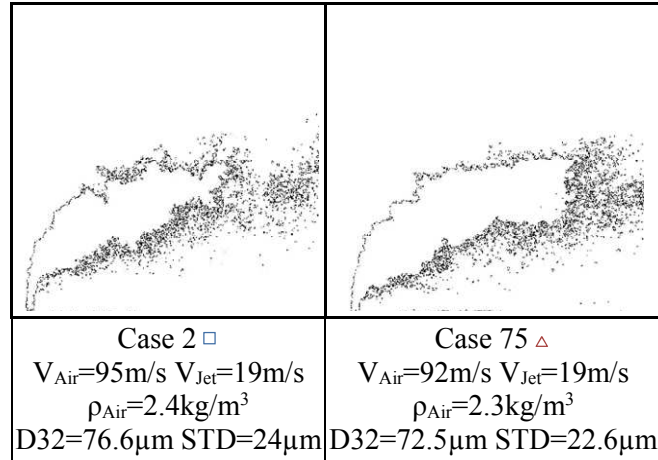


Figure 6.25: Comparison of conditions with similar gas densities and stream-wise velocity. Table 2.3 summarizes the conditions.

Alternatively equation (6.18) is presented for which liquid and gas effects are presented separately. Two separate non-dimensional groups, Weber and Reynolds numbers, are used to show the effects of viscosity, density and surface tension for each fluid. The correlation can then be rearranged with a combination of different non-dimensional group. These correlations are interchangeable due to the relation between the individual non-dimensional groups. The result is the following correlation:

$$\begin{aligned} \frac{SMD}{D_N} &= e^{10.34} We_{Air}^{-0.02} We_{Jet}^{0.98} Re_{Air}^{-0.04} Re_{Jet}^{-2.1} \\ &= e^{10.34} We_{Air}^{-0.04} We_{Jet}^{-0.07} Oh_{Air}^{0.04} Oh_{Jet}^{2.1} \\ &= e^{10.34} q^{-0.07} We_{Air}^{-0.11} Oh_{Air}^{0.04} Oh_{Jet}^{2.1} \end{aligned} \quad (6.18)$$

$$SMD = e^{10.34} D_N^{-0.18} V_{Air}^{-0.08} V_{Jet}^{-0.14} \rho_{Air}^{-0.06} \rho_{Jet}^{-1.12} \mu_{Air}^{0.04} \mu_{Jet}^{2.1} \sigma^{-0.96} \quad (6.19)$$

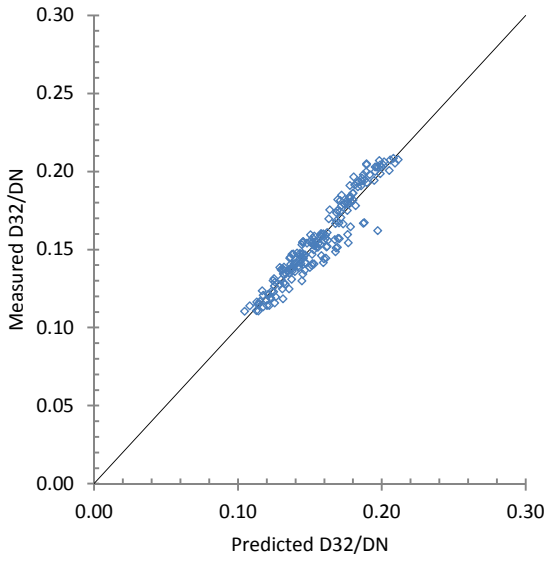
$$\begin{aligned} \frac{STD}{D_N} &= e^{9.90} We_{Air}^{-0.04} We_{Jet}^{0.95} Re_{Air}^{-0.07} Re_{Jet}^{-2.15} \\ &= e^{9.90} We_{Air}^{-0.08} We_{Jet}^{-0.12} Oh_{Air}^{0.07} Oh_{Jet}^{2.15} \\ &= e^{9.90} q^{-0.12} We_{Air}^{-0.20} Oh_{Air}^{0.07} Oh_{Jet}^{2.15} \end{aligned} \quad (6.20)$$

$$STD = e^{9.90} D_N^{-0.31} V_{Air}^{-0.16} V_{Jet}^{-0.24} \rho_{Air}^{-0.12} \rho_{Jet}^{-1.12} \mu_{Air}^{0.07} \mu_{Jet}^{2.15} \sigma^{2.11} \quad (6.21)$$

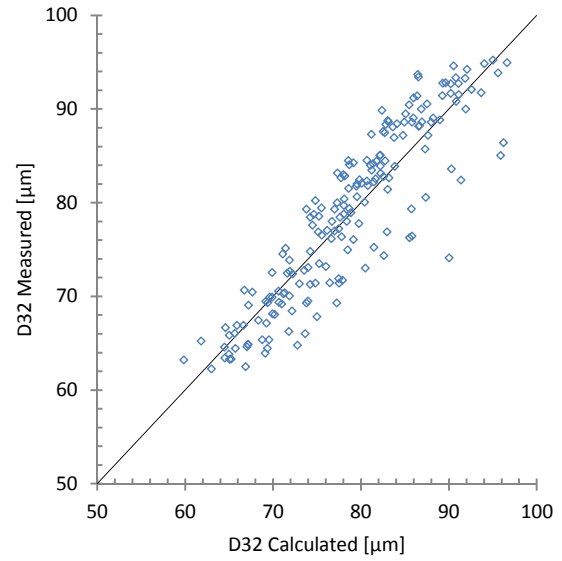
The coefficient of determination for the equation (6.18) is 0.91 and the standard error for the dependent variable, i.e. left side of the correlation, is 0.05. The standard errors for the exponents from left to right are 0.005, 0.005, 0.011, and 0.068, respectively. The standard error for the correlation constant is 0.36. Similar to the previous correlations, the statistical analysis shows that

all the variables are significant. Statistically the correlation shows an improvement compared to equation (6.17). The mean error is reduced to 3% and standard deviation of error is also reduced to 3%, Figure 6.23 (b) versus Figure 6.26 (b). Also all the standard errors are reduced in this correlation specifically the standard error for the correlation coefficient. Finally, the  $D^2$  Law can be used to determine droplet size downstream of the injector. The initial droplet size can be evaluated from the above correlation and evaporation rates from Appendix D. Equation (6.18) is rearranged, equation (6.19), to show the effect of individual dimensional parameters. As it can be seen, in both equations (6.18) and (6.19), the coefficient of the correlation is fairly large. This is mainly due to the limited data points for nozzle diameter, liquid viscosity and surface tension and also the error associated with measuring the gas velocity in the main chamber. Finally, Equation (6.20) shows the relation between the standard deviation of droplet size and non-dimensional variables. Generally, correlations for standard deviation are not provided. However, correlation of standard deviation is a valuable tool since it provides information about the shape of the droplet size distribution that otherwise is not available just by using the sauter mean diameter. The coefficient of determination for the equation (6.20) is 0.86 and the standard error for the dependent variable, i.e. left side of the correlation, is 0.65. The standard errors for the exponents from left to right are 0.170, 0.062, 0.020, and 0.123 respectively. The standard error for the correlation constant is 0.36. Similar to the previous correlations, the statistical analysis shows that all the variables are significant.

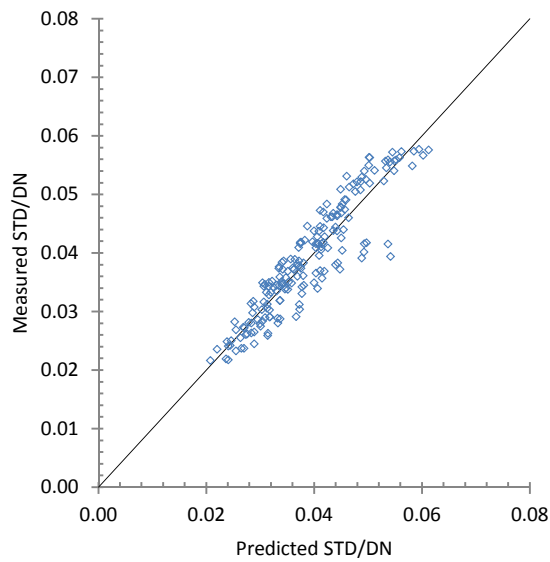




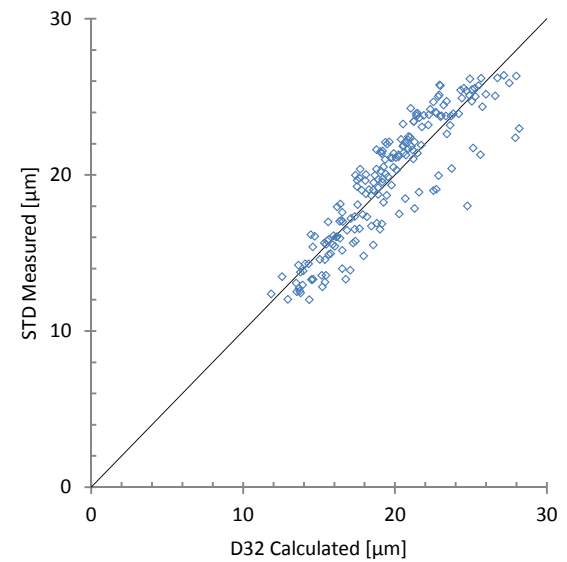
(a)



(b)



(c)



(d)

Figure 6.26: (a) and (b) correlation of the SMD for primary breakup, equation (6.18). (c) and (d) correlation of the STD for primary breakup, equation (6.20).

## Chapter 7 Conclusions and Recommendations

### 7 Conclusions and Recommendations

#### 7.1 Conclusions

The present research has four different attributes and contributions to the field of liquid jet in crossflows: (i) A new method of analyzing LJICF using direct imaging technique; (ii) characterization of the breakup regimes of LJICF; (iii) development of correlations for the jet trajectories; and (iv) development of correlations for the global average droplet sizes generated by LJICF.

(i) The breakup and atomization of water jet in continuous subsonic crossflow is studied using laser light sheet illumination technique and shadowgraphy. Overall 209 tests which are at three different crossflow temperatures and pressures are studied. A method for analyzing the images is developed and employed to measure the droplet size, trajectories and other spray parameters. An automated algorithm is used to individually process 72,000 images. The threshold level is defined based on the triangle criterion for each image contingent on the individual light intensity distributions. A separate algorithm is then used to determine the edges of threshold images and droplet size. The droplet size results are then filtered based on minimum size and circularity. A similar process is also used to find the boundaries and other attributes related to the spray plume but instead the process is performed on the time averaged image for each case. The comparison between the shadowgraph images and individual processed images with the time averaged images show that this technique is suitable to find the windward and leeward boundaries of the jet. The following summarizes some of the findings from the present work.

(ii) There are three atomization regimes, dominantly column breakup, dominantly surface/shear breakup, and multimode regime. In the dominantly column breakup regime, the waves on the windward face of the jet grow and eventually the undulations in combination with the aerodynamic forces cause the breakup of the jet. The separated secondary plumes will then exhibit secondary breakup. In the dominantly surface/shear breakup regime, the disturbances are smaller and produce more uniform droplet sizes along the jet. Some of the disturbances on the windward surface of the jet are due to the aerodynamic effects and the others are due to jet conditions and turbulence. In

the multimode regime both breakup mechanisms are present. The borderline between the regimes is not clear and generally it is arbitrarily defined since both mechanisms are always present.

(iii) Trajectories of liquid jets in crossflow for a wide range of flow conditions are studied. Three correlations are presented for windward, leeward and centerline trajectories. There are inconsistencies that exist in literature regarding the windward and leeward boundaries mainly due to jet undulations and the method used for finding these boundaries. On the other hand, centerline trajectory is more consistent and therefore a better benchmark for defining trajectory. Also, the results show that the gas viscosity has to be considered when developing correlations. The correlations that include this term are generally better in predicting the trajectory. Momentum flux ratio is generally used to define the trajectories. However the results indicate that the trajectory and atomization change when the air and jet velocities are changed while keeping momentum flux ratio constant. Therefore it is beneficial to describe the trajectory based on air and jet Weber numbers or momentum flux ratio in combination with one of the Weber numbers. Also, examples are given where both Weber numbers are kept constant but the atomization is changed and therefore other terms beyond inertia terms are required to describe the spray behavior. The observed differences are due to viscous effects caused by both air and jet, and therefore Ohnesorge numbers in combination with Weber numbers is used to describe the trajectories.

(iv) The global average droplet size of a sprays formed by various LJICFs are studied. Effects of various parameters on the global droplet sizes are considered. For the range of parameters in the current study the following observations are made:

- Increasing the nozzle diameter from 457  $\mu\text{m}$  to 572  $\mu\text{m}$  leads to a higher jet penetration and a reduction in droplet size. This is contrary to the general knowledge that increase in nozzle diameter, increases the average droplet size. The observed results are only valid for the range of nozzles tested here. The reduction in the droplet size indicates that one can obtain an optimized nozzle size, minimize the average droplet size, while keeping all other parameters constant. In the current study, the momentum flux ratio is kept constant between the examined cases but the Weber and Reynolds numbers for both air and jet increase as the nozzle diameter increases. Increase in these parameters leads to better atomization.

- Increasing the jet velocity leads to a higher jet penetration and causes a reduction in the droplet size. In this case, as the jet velocity increases the Reynolds number of the jet increases and the jet becomes more turbulent. The atomization regime changes to shear breakup regime and even though the air velocity is kept constant the atomization improves. This indicates that the jet turbulence plays an important role in the atomization process. Increasing the jet velocity also leads to an increase in both plume width and breakup length.
- Increasing the air velocity leads to a lower penetration but causes a reduction in droplet size. As the air velocity is reduced, the atomization regime shifts to dominantly column breakup and droplet size increases. It should be noted that in this case plume width becomes narrower. As the air velocity increases the dynamic pressure on the jet, i.e. air Weber number, increases and atomization is enhanced.
- Increasing the crossflow pressure enhances the atomization, reducing the average droplet size. By increasing the pressure, the density is increased, which in effect increases the drag force on the jet and improves the atomization. An increase in pressure increases the dynamic pressure on the jet, thus reducing the jet penetration, increasing the plume width, thus enhancing the shear type of breakup. Also as the pressure increases the saturation temperature of the liquid increases, therefore, delaying the droplet evaporation.
- For the range of parameters studied here, small increases in the gas temperature, first slightly decreases the global droplet size, followed by slight increase in the global droplet size. This behavior is also not intuitive since increases in the gas temperature should increase evaporation, thus reducing the droplet sizes. However, for the limited range of parameters considered here, the effect of viscosity change with temperature played an important role in the atomization process. As the temperature increases the kinematic viscosity of the gas increases, resulting in increasing the drag force. In addition, at higher temperatures the evaporation rates are higher, resulting in the disappearance of the smaller droplets. Therefore, the mean droplet size shortly after atomization region appears larger. Two cases with similar gas densities and other relevant parameters are compared. It is shown that the case having a higher temperature (higher dynamic viscosity) produces finer

droplets. Therefore, the observed initial reduction of droplet size is due to increased gas viscosity. And the observed increase in the average droplet size with further increase in temperature is due to the evaporation of small droplets. The crossflow pressure mostly influences the gas density which essentially influences the dynamic pressure on the jet. At elevated temperatures the effect of pressure on density is reduced since the density is a function of both pressure and temperature. However, the gas viscosity increases at higher temperatures and becomes more prominent, Figure 6.14. Beyond density and viscosity, as the crossflow pressure increases the saturation temperature of the liquid jet also increases which delays the evaporation process. Essentially the influence of pressure on atomization will be reduced as the temperature increases. Therefore, it might be beneficial for various reasons to operate the engines at lower to moderate pressures when the gas temperatures are higher.

- Correlations for both droplet size and standard deviation based on air and jet Weber and Reynolds numbers are obtained. It is shown that the correlations can be rearranged to have Ohnesorge number replace the Reynolds number so that the velocity effects are only included in one term. Finally the Weber numbers can be rearranged so that the overall correlation is based on momentum flux ratio in combination with air Weber number and air and jet Ohnesorge numbers. The global droplet size correlation shows a stronger relation between size and jet parameters versus air parameters, mainly due to liquid density and viscosity.

Various spray parameters such as breakup length, time, plume area, plume angle, mean plume width and thickness are defined and compared to the non-dimensional variables. Table 7.1 summarizes the effects of increasing any of the non-dimensional variables on spray parameters. Extra caution needs to be considered when using this table since the non-dimensional variables have common variables.

Table 7.1: Summary of the relation between the spray parameters and the non-dimensional variables.

	D32	STD	$L_b/D_N$	$t_b/t^*$	$A_p/A_D$	$\angle$	$W_p/D_N$	$T_s/D_N$
q	↑	↓	↓	↑	↓	↓	↑	↑

$We_{Air}$	↑	↓	↓	↑	↑	↑	↓	↑	↓
$We_{Jet}$	↑	↓	↓	↑	↓	↑	↑	↑	↓
$Re_{Air}$	↑	↓	↓	↑	↑	↑	↓	↑	↓
$Re_{Jet}$	↑	↓	↓	↑	↓	↑	↑	↑	↓
$Oh_{Air}$	↑	↑	↑	↑	↑	↓	↑	↓	↑
$Oh_{Jet}$	↑	↑	↑	↑	↑	↑	↑	↑	↑

Table 7.3 summarizes all the correlations developed in the current study. These correlations are based on the conditions provided in Table 7.2. The liquid properties are calculated based on the air pressure and initial liquid temperature. The air pressure is used instead of tank pressure since the atomization process doesnot happen inside the nozzle and the liquid would be at the same pressure as the air during the atomization process. As for the gas properties, they are calculated based on the initial temperature and pressure of air. It is assumed that the air and liquid temperature and consequently both viscoisties and surface tension is unaffected during the initial atomization process.

Table 7.2: Test conditions for imaging experiments with water.

	$V_{Jet}$ [m/s]	$V_{Air}$ [m/s]	T [°C]	p [Bar]	$D_N$ [μm]	q	$We_{Air}$	$We_{Jet}$	$Re_{Air}$	$Re_{Jet}$	$Oh_{Air}$ [x10 <sup>3</sup> ]	$Oh_{Jet}$ [x10 <sup>3</sup> ]	Ma
Min.	4.3	14.8	25	2.1	457	8	7	149	925	2783	1.368	4.392	0.03
Max.	54.3	127.9	300	5.2	572	181	298	23282	12624	34743	4.648	4.914	0.29

Table 7.3: Summary of all the correlations.

$$\frac{y_{cl}}{D_N} = 2.65 \left( \frac{x}{D_N} \right)^{0.39} We_{Air}^{-0.28} We_{Jet}^{0.42} Oh_{Air}^{-0.22} Oh_{Jet}^{0.47} \quad (7.1)$$

$$\frac{y_{ww}}{D_N} = 13.31 \left( \frac{x}{D_N} + 0.5 \right)^{0.27} We_{Air}^{-0.25} We_{Jet}^{0.40} Oh_{Air}^{-0.20} Oh_{Jet}^{0.65} \quad (7.2)$$

$$\frac{y_{lw}}{D_N} = 0.054 \left( \frac{x}{D_N} - 0.5 \right)^{0.49} We_{Air}^{-0.49} We_{Jet}^{0.57} Oh_{Air}^{-0.42} Oh_{Jet}^{0.17} \quad (7.3)$$

$$\frac{L_b}{D_N} = 1084 We_{Air}^{-0.04} We_{Jet}^{0.16} Oh_{Air}^{-0.01} Oh_{Jet}^{0.84} \quad (7.4)$$

$$\frac{x_b}{D_N} = 3709 We_{Air}^{0.09} We_{Jet}^{0.01} Oh_{Air}^{0.10} Oh_{Jet}^{0.88} \quad (7.5)$$

$$\frac{y_b}{D_N} = 27.33 We_{Air}^{-0.29} We_{Jet}^{0.45} Oh_{Air}^{-0.19} Oh_{Jet}^{0.69} \quad (7.6)$$

$$\frac{t_b}{t^*} = e^{10.80} We_{Air}^{0.40} We_{Jet}^{-0.30} Oh_{Air}^{-0.03} Oh_{Jet}^{1.61} \quad (7.7)$$

$$\frac{A_p}{A_D} = e^{13.01} We_{Air}^{0.02} We_{Jet}^{0.25} Oh_{Air}^{0.05} Oh_{Jet}^{1.68} \quad (7.8)$$

$$\theta_p = 0.89 We_{Air}^{-0.35} We_{Jet}^{0.41} Oh_{Air}^{-0.28} Oh_{Jet}^{-0.03} \quad (7.9)$$

$$\frac{W_p}{D_N} = 324.8 We_{Air}^{0.06} We_{Jet}^{0.09} Oh_{Air}^{0.06} Oh_{Jet}^{0.84} \quad (7.10)$$

$$\frac{T_s}{D_N} = e^{-6.72} We_{Air}^{-0.06} We_{Jet}^{-0.09} Oh_{Air}^{-0.06} Oh_{Jet}^{-0.84} \quad (7.11)$$

$$\frac{SMD}{D_N} = e^{10.34} We_{Air}^{-0.04} We_{Jet}^{-0.07} Oh_{Air}^{0.04} Oh_{Jet}^{2.1} \quad (7.12)$$

$$\frac{STD}{D_N} = e^{9.90} We_{Air}^{-0.08} We_{Jet}^{-0.12} Oh_{Air}^{0.07} Oh_{Jet}^{2.15} \quad (7.13)$$

## 7.2 Recommendations

There are various areas that still require further investigation and clarification. Some of these aspects are presented here. The transition between various breakup mechanisms is not very clear and a unified definition is needed to better describe the regimes. The problem arises since both atomization processes, i.e. column and surface breakup, are always present. Historically the regimes are defined based on the images of the jet. This can be problematic since it is difficult to capture all the details on the jet and therefore, the classification is biased depending on the method used. Instead, droplet size might be a better tool for defining the atomization regimes. Inherently, droplet size is the result of jet behavior and potentially can be used as a tool to identify the regimes. Generally, the larger droplets are further away from the nozzle and it varies significantly along the jet for cases that are dominantly column breakup. There is in fact a transition in mean droplet size when moving away from the nozzle exit. This sudden increase can then be attributed to the breakup zones.

The other issue regarding the atomization map is the non-dimensionalized numbers that are used to define the critical values. So far in the literature the map is defined mainly with momentum flux ratio and air Weber number and in some cases jet Reynolds number. But based on the findings of this work there are four non-dimensional groups that define the atomization process and therefore the new map will need to include all of these parameters. These parameters are the Weber and

Reynolds numbers of both air and jet or alternatively Ohnesorge numbers can be used instead of Reynolds numbers in a similar manner to the presented correlations.

In recent years, more emphasis has been given to the injector design. Many have studied the effect of  $L/D$ , inlet angles and other attributes of the orifice and successfully have shown that these parameters are indeed important. It goes without saying that there are many different combinations for the nozzle geometry and consequently it is difficult to unify and relate the findings with spray parameters. One suggestion would be to have the jet properties such as turbulence intensities, “jet surface roughness”, etc. as the defining parameter instead of  $L/D$  or other parameters for the orifice. The benefit is that many nozzle combinations would probably have similar effect on the jet behavior.

In the current study, only water is used for the tests. Although there are obvious technical benefits for using water it is important to demonstrate the behavior of various fuels since most common hydrocarbon based fuels have lower density, viscosity, surface tension and boiling points and in case of some bio-fuels they have solid contents which would have implications on the atomization. It is of great interest to see the influence of fuel properties on the jet and atomization since many of the obtained correlations show strong relation with liquid Weber, Reynolds, and Ohnesorge numbers.

In this study, it is shown that the evaporation does not alter primary breakup. It is anticipated that at higher crossflow temperatures, the evaporation might affect the primary atomization by creating nucleation sites for the formation of bubbles. It is of interest to see how the jet surface structures and ultimately droplet size will be affected by early evaporation. Evaporation aside, the jet liquid properties such as surface tension and viscosity will also be reduced at higher temperatures which will influence the atomization.

Generally compressing gas is energy intensive and therefore it can be beneficial to define a critical pressure where the atomization process will not greatly enhance beyond this critical pressure.

One of the issues that is introduced and discussed is the liquid properties at elevated temperatures and their influence on both atomization and evaporation. Preheating the liquid reduces viscosity and surface tension which in return can potentially reduce the energy requirements for the



atomization. Therefore, it is interesting to see if the atomization requirements, i.e. pressure, temperature, flow rates, nozzle diameter, can actually be reduced by preheating the liquid.

## 8 Bibliography

- [1] H. B. Ebrahimi, "Overview of Gas Turbine Augmentor Design, operation And Combustion Oscillation," in *ILASS Americas*, Toronto, 2006.
- [2] [Online]. Available: <http://www.f-15e.info/joomla/technology/engines/101-engines>.
- [3] J. A. Schetz and A. Padhye, "Penetration and breakup of liquids in subsonic airstreams," *AIAA Journal*, vol. 15, no. 10, pp. 1385-1390, 1977.
- [4] A. S. Nejad and J. A. Schetz, "Effects of properties and location in the plume on droplet diameter for injection in a supersonic stream," *AIAA Journal*, vol. 21, no. 7, pp. 956-961, 1983.
- [5] T. H. Chen, C. R. Smith, D. G. Schommer and A. S. Nejad, "Multi-zone behavior of transverse liquid jet in high speed flow," *31st Aerospace Sciences Meeting and Exhibit*, 1993.
- [6] P.-K. Wu and G. M. Faeth, "Aerodynamic Effects on Primary Breakup of Turbulent Liquids," in *31st Aerospace Sciences Meeting & Exhibit*, Reno, NV, 1993.
- [7] P. -K. Wu, L. P. Hsiang and G. M. Faeth, "Chapter 9: Aerodynamic effects on primary and secondary spray breakup," in *Spray Combustion Measurements and Model Simulation, Volume 5; Volume 171*, AIAA, 1994, pp. 247-279.
- [8] P. K. Wu, L. P. Hsiang and G. M. Faeth, "Aerodynamic effects on primary and secondary breakup," *Liquid rocket engine combustion instability*, vol. 169, pp. 247-279, 1995.
- [9] P.-K. Wu, K. A. Kirkendall, R. P. Fuller and A. S. Nejad, "Breakup Processes of Liquid Jets in Subsonic Cross Flows," *Journal of Propulsion and Power*, vol. 13, no. 1, January-February 1997.

- [10] P.-K. Wu, K. A. Kirkendall, R. P. Fuller and A. S. Nejad, "Spray Structures of Liquid Jets Atomized in Subsonic Cross Flows," *Journal of Propulsion and Power*, vol. 14, no. 2, March-April 1998.
- [11] T. Inamura, N. Nagai, T. Watanabe and N. Yasuyanagi, "Disintegration of liquid and slurry jets traversing subsonic airstreams," *Experimental Heat Transfer, Fluid Mechanics, and Thermodynamics*, pp. 1522-1529, 1993.
- [12] T. Inamura, "Trajectory of a liquid jet traversing subsonic airstreams," *Journal of Propulsion and Power*, vol. 16, no. 1, pp. 155-157, 2000.
- [13] M. Rachner, J. Becker, C. Hassa and T. Doerr, "Modelling of the Atomization of a Plain Liquid Fuel Jet in Cross Flow at Gas Turbine Conditions," *Aerospace Science and Technology*, vol. 6, pp. 495-506, 2002.
- [14] J. Becker and C. Hassa, "Breakup and Atomization of a Kerosene Jet in Cross Flow at Elevated Pressure," *Atomization and Sprays*, vol. 11, pp. 49-67, 2002.
- [15] S. Freitag and C. Hassa, "Spray Characteristics of a Kerosene Jet in Crossflow of Air at Elevated Pressure," in *ILASS2008*, Lake Como, Italy, 2008.
- [16] C. O. Iyogun, M. Birouk, N. Popplewell and H. M. Soliman, "Trajectory of water jet exposed to low subsonic cross flow," *Atomization and Spray Journal*, 2005.
- [17] B. J. Masuda, R. L. Hack, V. G. McDonell, G. W. Oskam and D. J. Cramb, "Some observations of liquid jet in crossflow," *ILASS Americas, 18th annual conference on liquid atomization and spray systems*, May 2005.
- [18] R. R. Lakhamraju and S. M. Jeng, "Liquid Jet Breakup Studies in Subsonic Airstream at Elevated Temperatures," *ILASS Americas, 18th annual conference on liquid atomization and spray systems*, May 2005.

- [19] O. M. Elshamy and S. M. Jeng, "Study of Liquid Jet in Crossflow at Elevated Ambient Pressures," *ILASS Americas, 18th Annual Conference on Liquid and Atomization and Spray Systems*, May 2005.
- [20] O. Elshamy, S. Tambe, J. Cai and S.-M. Jeng, "Structure of Liquid Jets in Subsonic Crossflow at Elevated Ambient Pressures," *44th Aerospace Sciences Meeting & Exhibit, AIAA Paper*, p. 1224, 2006.
- [21] A. Bellofiore, A. Cavaliere and R. Ragucci, "Experimental and Numerical Study of Liquid Jets Injected in High-Density Air Crossflow," University of Studies of Naples Federico II Department of Chemical Engineering, Naples, Italy, 2006.
- [22] A. Bellofiore, A. Cavaliere and R. Ragucci, "Air Density Effect on the Atomization of Liquid Jets in Crossflow," *Combustion Science and Technology*, vol. 179, no. 1-2, pp. 319-342, January 2007.
- [23] A. Mashayek, A. Jafari and N. Ashgriz, "Improved Model for the Penetration of Liquid Jets in Subsonic Crossflows," *AIAA Journal*, vol. 46, no. 11, p. 2674–2686, 2008.
- [24] E. Lubarsky, D. Shcherbik, O. Bibik, Y. Gopala and B. T. Zinn, "Fuel Jet in Cross Flow - Experimental Study of Spray Characteristics," *Advanced Fluid Dynamics*, 2012.
- [25] S.-Y. No, "Empirical Correlations for Penetration Height of Liquid Jet in Cross Flow—A Review," in *Proceeding of the 24th Annual Conf. on Liquid Atomization and Spray Systems*, Estoril, Portugal, September 2006.
- [26] A. Amighi, M. Eslamian and N. Ashgriz, "Trajectory of Liquid Jets in High Pressure and High Temperature Crossflows," in *Proceedings of the 11th International Conference on Liquid Atomization and Spray Systems*, Vail, CO, 2009.

- [27] A. Cavaliere, R. Ragucci and C. Noviello, "Bending and Break-Up of a Liquid Jet in a High Pressure Airflow,," *Experimental Thermal and Fluid Science*,, vol. 27, no. 4, p. 449–454, 2003.
- [28] R. Ragucci, A. Bellofiore, G. Carulli and A. Cavaliere, "Momentum Coherence Breakdown of Bending Atomizing Liquid Jet,," in *9th International Conf. on Liquid Atomization and Spray Systems*, Sorrento, Italy, July 2003.
- [29] R. Ragucci, A. Bellofiore and A. Cavaliere, "Breakup and Breakdown of Bent Kerosene Jets in Gas Turbine Conditions," *Proceedings of the Combustion Institute*, vol. 31, no. 2, pp. 2231-2238, 2007.
- [30] B. J. Clark, "Breakup of a liquid jet in a traverse flow of gas," 1964.
- [31] M. Adelberg, "Breakup rate and penetration of a liquid jet in a gas stream," *AIAA Journal*, vol. 5, pp. 1408-1415, August 1967.
- [32] T. T. Nguyen and A. R. Karagozian, "Liquid fuel jet in subsonic cross flow," *Journal of propulsion and power*, vol. 8, no. 1, pp. 21-29, 1992.
- [33] H. S. Li and A. R. Karagozian, "Breakup of a liquid jet in supersonic cross flow," *AIAA Journal*, vol. 30, no. 7, pp. 1919-1921, 1992.
- [34] S. D. Heister, T. T. Nguyen and A. R. Karagozian, "Moddeling of liquid jets injected transversely inot a supersonic crossflow," *AIAA Journal*, vol. 27, no. 12, pp. 1727-1734, 1989.
- [35] M. Y. Leong, V. G. McDonell and S. G. Samuelsen, "Effect of Ambient Pressure on an Airblast Spray Injected into a Crossflow," *Journal of Propulsion and Power*, vol. 17, no. 5, pp. 1076-1084, September-October 2001.
- [36] T. Inamura and N. Nagai, "Spray Characteristics of Liquid Jet Traversing Subsonic Airstreams," *Journal of Propulsion and Power*, vol. 13, no. 2, pp. 250-256, March-April 1997.

- [37] J. Mazallon, Z. Dai and G. M. Faeth, "Primary Breakup of nonturbulent round liquid jets in gas crossflows," *Atomization and Sprays*, vol. 9, no. 3, pp. 291-311, 1999.
- [38] R. K. Madabhushi, M. Y. Leong, M. Arienti, C. T. Brown and V. G. McDonell, "On The Breakup Regime Map of Liquid Jet in Crossflow," in *ILASS Americas, 19th Annual Conference on Liquid Atomization and Spray Systems*, Toronto, Canada, 2006.
- [39] K. A. Sallam, C. Aalburg and G. M. Faeth, "Breakup of Round Nonturbulent Liquid Jets in Gaseous Crossflow," *AIAA Journal*, vol. 42, no. 12, pp. 2529-2540, 2004.
- [40] S.-l. Wang, Y. Huang, F. Wang, Z.-l. Liu and L. Liu, "On the Breakup Process of Round Liquid Jets in Gaseous Crossflows at Low Weber Number," in *ASME Turbo Expo 2013: Turbine Technical Conference and Exposition*, San Antonio, Texas, 2013.
- [41] R. K. Madabhushi, M. Y. Leong and D. J. Hautman, "Simulation of the Breakup of a Liquid Jet in Cross Flow at Atmospheric Conditions," *Proceedings of ASME Turbo Expo 2004*, 2004.
- [42] A. Amighi, "Droplet Size Distribution for Jets in Crossflows at High Temperature and Pressure," M.S. Thesis, University of Toronto, Toronto, Canada, 2008.
- [43] V. S. Iyengar, S. Kumarasamy, S. Jangam and M. Pulumathi, "Drop Size Characteristics of Forward Angled Injectors in Subsonic Cross Flows," in *ASME 2013 Gas Turbine India Conference*, Bangalore, Karnataka, India, 2013.
- [44] M. A. Linne, M. E. Paciaroni, D. Sedarsky, J. R. Gord and T. R. Meyer, "Ballistic Imaging of the Liquid Core for a Jet in Crossflow," *ILASS Americas, 18th Annual Conference on Liquid and Atomization and Spray Systems*, May 2005.
- [45] T. Oda, H. Hiroyasu, M. Arai and K. Nishida, "Characterization of Liquid Jet Atomization across a High-Speed Airstream," *JSME International Journal*, vol. 37, no. 4, pp. 937-944, 1994.

- [46] R. H. Thomas and J. A. Schetz, "Distributions Across the Plume of Transverse Liquid and Slurry Jets in Supersonic Airflow," *AIAA Journal*, vol. 23, no. 12, pp. 1892-1901, 1985.
- [47] R. D. Ingebo and H. H. Foster, "Drop Size Distribution for Crosscurrent Breakup of Liquid Jets in Air Streams," 1957.
- [48] C. Weiss and C. Worsham, "Atomization in High Velocity Air Streams," *ARS Journal*, vol. 29, pp. 252-259, 1959.
- [49] K. D. Kihm, G. M. Lyn and S. Y. Son, "Atomization of Cross-Injecting Sprays Into Convective Air Stream," *Atomization and Spray*, vol. 5, no. 4-5, pp. 417-433, 1995.
- [50] J. Becker and C. Hassa, "Plain jet kerosene injection into high temperature, high pressure crossflow with and without flimer plate," *8th international conference on liquid atomization and spray systems*, July 2000.
- [51] K. Lee, C. Aalburg, F. J. Diez, G. M. Faeth and K. A. Sallam, "Primary Breakup of Turbulent Round Liquid Jets in Uniform Cross Flows," *AIAA Journal*, vol. 45, no. 8, pp. 1907-1916, August 2007.
- [52] E. Lubarsky, J. R. Reichel, B. T. Zinn and R. McAmis, "Spray in Crossflow: Dependence on Weber Number," *Journal of Engineering for Gas Turbines and Power*, vol. 132, no. 2, 2010.
- [53] S. B. Tambe, S.-M. Jeng, H. Mongia and G. Hsiao, "Liquid Jets in Subsonic Crossflows," *43rd AIAA Aerospace Sciences Meeting and Exhibit, AIAA Paper*, January 2005.
- [54] J. B. Blaisot and J. Yon, "Droplet Size and Morphology Characterization for Dense Sprays by Image Processing: Application to the Diesel Spray," *Experiments in Fluids*, vol. 39, pp. 977-994, 2005.
- [55] G. W. Zack, W. E. Rogers and S. A. Latt, "Automatic measurement of sister chromatid exchange frequency," *J Histochem Cytochem.*, pp. 741-53, July 1977.

- [56] M. Herrmann, M. Arienti and M. Soteriou, "The Impact of Density Ratio on the Liquid Core Dynamics of a Turbulent Liquid Jet Injected Into a Crossflow," *Journal of Engineering for Gas Turbines and Power*, vol. 133, 2011.
- [57] Malvern Instruments, "Particle Size and Shape Measurement Using Image Analysis".
- [58] A. Chavez and F. Mayinger, "Single- and Double-Pulsed Holography for Characterization of Spray of Refrigerant R113 Injected into its Own Saturated Vapor," in *Proc. of the 1st World Conf. on Exp. Heat Transfer, Fluid Mechanics and Thermodynamics.*, Dubrovnik, 1988.
- [59] A. Chavez and F. Mayinger, "Evaluation of Pulsed Laser Holograms of Spray Droplets by Applying Digital Image Processing," in *9th International Conference on Heat Transfer*, Jerusalem, 1990.
- [60] H. C. Simmons, "The Correlation of Drop-Size Distributions in Fuel Nozzle Sprays—Part I: The Drop-Size/Volume-Fraction Distribution," *J. Eng. Power*, vol. 99, no. 3, pp. 309-314, 1977.
- [61] Y. Gopala, "Breakup characteristics of liquid jet in subsonic crossflow," PhD Thesis, Georgia Institute of Technology, 2012.
- [62] D. Sedarsky, M. Paciaroni, E. Berrocal, P. Petterson, J. Zelina, J. Gord and M. Linne, "Model validation image data for breakup of a liquid jet in crossflow: part I," *Experiments in Fluids*, vol. 49, no. 2, pp. 391-408, 2010.
- [63] D. Sedarsky, M. Paciaroni, E. Berrocal, P. Petterson, J. Zelina, J. Gord and M. Linne, "Model validation image data for breakup of a liquid jet in crossflow: Part I," *Experiments in Fluids*, vol. 49, pp. 391-408, 2010.
- [64] A. R. Osta and K. A. Sallam, "Nozzle-Geometry Effects on Upwind-Surface Properties of Turbulent Liquid Jets in Gaseous Crossflow," *Journal of Propulsion and Power*, vol. 26, no. 5, pp. 936-946, 2010.



- [65] C. Brown, U. Mondragon and V. McDonell, "Liquid Jet in Crossflow: Consideration of Injector Geometry and Liquid Physical Properties," in *ILASS Americas, 25th Annual Conference on Liquid Atomization and Spray Systems*, Pittsburgh, 2013.
- [66] M. H. Belz, *Statistical Methods in the Process Industries*, New York: Wiley, 1973, pp. 103-104.
- [67] [Online]. Available: [http://www.peacesoftware.de/einigewerte/luft\\_e.html](http://www.peacesoftware.de/einigewerte/luft_e.html).
- [68] [Online]. Available: [http://en.wikipedia.org/wiki/Eötvös\\_rule](http://en.wikipedia.org/wiki/Eötvös_rule).
- [69] [Online]. Available: [http://en.wikipedia.org/wiki/Temperature\\_dependence\\_of\\_liquid\\_viscosity](http://en.wikipedia.org/wiki/Temperature_dependence_of_liquid_viscosity).
- [70] L. -P. Hsiang and G. M. Faeth, "Near-limit drop deformation and secondary breakup," *Int. J. Multiphase Flow*, vol. 18, no. 5, pp. 635-652, 1992.
- [71] F. X. Tanner, "Evaporating Sprays," in *Handbook of Atomization and Sprays Theory and Applications*, N. Ashgriz, Ed., Springer, 2011, p. 263.
- [72] B. Abramzon and W. A. Sirignano, "Droplet vaporization model for spray combustion calculations," *Int. J. Heat Mass Transfer*, vol. 32, no. 9, pp. 1605-1618, 1989.
- [73] B. Abramzon and S. Sazhin, "Convective vaporization of a fuel droplet with thermal radiation absorption," *Fuel*, vol. 85, pp. 32-46, 2006.
- [74] S. R. Turns, *An Introduction to Combustion: Concepts and Applications*, McGraw-Hill, 1996.
- [75] S. S. Sazhin, "Advanced models of fuel droplet heating and evaporation," *Progress in Energy and Science*, vol. 32, pp. 162-214, 2006.

- [76] M. Y. Leong, V. G. McDonell and G. S. Samuelsen, "Mixing of an airblast-atomized fuel spray injected into a cross flow of air," 2000.
- [77] L. -P. Hsiang and G. M. Faeth, "Drop Properties after secondary breakup," *Int. J. Multiphase Flow*, vol. 19, no. 5, pp. 721-735, 1993.
- [78] L. -P. Hsiang and G. M. Faeth, "Drop deformation and breakup due to shock wave and steady disturbances," in *32nd Aerospace Sciences Meeting & Exhibit*, Reno, NV, 1994.

## 9 Appendices

### 9.1 Appendix A: Image Analysis and Calculations

#### 9.1.1 Image Analysis: Droplet Size and Mean Plume Area/Boundary

The following macro is used to process the images after cropping and centering the images for both determining droplet size and mean plume area/boundary calculation. The difference between the two is given by using raw images versus mean image. The only difference between the two is that for determining the boundary the minimum size is chosen so that only main plume is calculated. The area information is then combined with breakup length from the results from Matlab to calculate spray plume width.

```

requires("1.43n");
dir = getDirectory("/.../...");
list = getFileList(dir);
setOption("display labels", true);
setBatchMode(true);
run("Clear Results");
for (i=0; i<list.length; i++) {
    path = dir+list[i];
    showProgress(i, list.length);
    IJ.redirectErrorMessages();
    open(path);
    if (nImages>=1) {
        setAutoThreshold("Triangle dark");
        run("Analyze Particles...", "size=0-Infinity circularity=0.0-1.00 show=Nothing display");
        saveAs("Jpeg",path);
    } else
        print("Error opening "+path);
}

```

## 9.1.2 Raw Data Calculations

The following Matlab ‘.m’ file is used to process the data generated from ImageJ. The data from ImageJ are in .txt format with the following information in each column: Particle Number, Image ID, Area, X-position, Y-position, and Perimeter.

```
clear
clc
Scalemm=25/1314.5246;
Scaleum=25000/1314.5246;
%DataSummary case number, image count, unfiltered number of particles,
%filtered number of particles, Percent filtered, D10, D32, Std. Deviation STD, Std. Error of
%mean SEM
DataSummary=zeros(416,15);

for CaseNumber=197:416
    %197-204 206-259 261-288 293-368 373-403 405-416
    disp(CaseNumber);
    clock
    %import data
    Step=1;
    disp(Step);
    tic
    FileName = ['Results B ' num2str(CaseNumber) '.txt'];
    if exist(FileName, 'file')
        % File exists. Do ...

        %IMPORTFILE(FileName)
        % Imports data from the specified file
        % FILETOREAD1: file to read

        % Import the file Col. 1-4 are Area, X, Y, Peri., 5:circularity, 6:Image ID
        newdata = importdata(FileName);

        % Create new variables in the base workspace from those fields.
        vars = fieldnames(newdata);
        for i = 1:length(vars)
            assignin('base', vars {i}, newdata.(vars {i}));
        end
        toc

        %Count the number of images for each case and record the first and last
        %particle number each case
        Step=Step+1;
        disp(Step);
        tic

        j=1;
        for i=2:(length(textdata)-1)
            TF = strcmp(textdata(i,2),textdata(i+1,2));
            if TF==0
                j=j+1;
            end
        end
        DataSummary(CaseNumber,1)=CaseNumber;
        DataSummary(CaseNumber,2)=j;
        DataSummary(CaseNumber,3)=length(data);

        %Seperate the data for each Image
        j=1;
        imagerange=zeros(DataSummary(CaseNumber,2),3);
        imagerange(1,1)=1;
        imagerange(1,2)=1;
        imagerange(DataSummary(CaseNumber,2),3)=length(textdata)-1;

        for i=2:(length(textdata)-1)
```

```

TF = strcmp(textdata(i,2),textdata(i+1,2));
if TF==0
    imagerange(j,3)=i-1;
    imagerange(j+1,1)=j+1;
    imagerange(j+1,2)=i;
    j=j+1;
end
end

data=newdata.data;

clear TF;
clear newdata;
clear textdata;
clear vars;

toc

%Filter by Size
Step=Step+1;
disp(Step);
tic

%Sort the data by Area
data=sortrows(data,1);

%find the cutoff circularity value
Arealmt=7;
cutoffArea=0;
i=1;
while data(i,1)<Arealmt
    cutoffArea=i;
    i=i+1;
end

%Delete the rows with circularity less than limit
data=data((cutoffArea+1):end,:);

clear Arealmt;
clear cutoffArea;

toc

%Filter by Circularity
Step=Step+1;
disp(Step);
tic
%Add Circularity to the eight col. of data

for i=1:length(data)
    data(i,8)=4*pi*data(i,1)/(data(i,4))^2;
end

%Sort the data by Circularity
data=sortrows(data,8);

%find the cutoff circularity value
circlmt=0.95;
cutoffcirc=0;
i=1;
while data(i,8)<circlmt
    cutoffcirc=i;
    i=i+1;
end

%Delete the rows with circularity less than limit
data=data((cutoffcirc+1):end,:);

clear circlmt;
clear cutoffcirc;

```

```

toc

%Filter by Y position
Step=Step+1;
disp(Step);
tic
% Sort the data based on the X-position first and then Y-position
data=sortrows(data,2);
data=sortrows(data,3);
%delete all the droplets that are positioned below y=10pix~0.2mm

%find the cutoff y value
ylmt=10;
cutoffy=0;
i=1;
while data(i,3)<ylmt
    cutoffy=i;
    i=i+1;
end

%Delete the rows with y position less than limit
data=data((cutoffy+1):end,:);

clear ylmt;
clear cutoffy;

toc

%Filter the scattered noise above the spray
Step=Step+1;
disp(Step);
tic
%find the cutoff droplet area
Arealmt=10;
cutoffArea=length(data);
i=length(data);
while data(i,1)<Arealmt
    cutoffArea=i;
    i=i-1;
end

%Delete the rows with y position less than limit
data=data(1:(cutoffArea-1),:);

clear Arealmt;
clear cutoffArea;

toc

%Filter the repeated particles
Step=Step+1;
disp(Step);
tic

DataSummary(CaseNumber,4)=length(data);
DataSummary(CaseNumber,5)=100-DataSummary(CaseNumber,4)/DataSummary(CaseNumber,3)*100;

toc

%calculate variables
Step=Step+1;
disp(Step);
tic

%create calculation matrices
DropletCount=zeros(length(data),1);
Dum=zeros(length(data),1);
MMD=zeros(length(data),1);
Dum2=zeros(length(data),1);

```

```

Dum3=zeros(length(data),1);
DumSum=zeros(length(data),1);
Dum2Sum=zeros(length(data),1);
Dum3Sum=zeros(length(data),1);
D10um=zeros(length(data),1);
D32um=zeros(length(data),1);
y=zeros(length(data),1);

for i=1:length(data)
    DropletCount(i,1)=i;
    data(i,9)=((data(i,5))*(data(i,6))^2)^(1/3)*Scaleum;
    Dum(i,1)=data(i,9);
    MMD(i,1)=pi*(Dum(i,1)^3)/6;
    Dum2(i,1)=Dum(i,1)^2;
    Dum3(i,1)=Dum(i,1)^3;
    y(i,1)=data(i,3);
end

DumSum(1,1)=Dum(1,1);
Dum2Sum(1,1)=Dum2(1,1);
Dum3Sum(1,1)=Dum3(1,1);

for i=2:length(data)
    DumSum(i,1)=Dum(i,1)+DumSum(i-1,1);
    Dum2Sum(i,1)=Dum2(i,1)+Dum2Sum(i-1,1);
    Dum3Sum(i,1)=Dum3(i,1)+Dum3Sum(i-1,1);
end

%Calculate Moving D10 and D32

for i=1:length(data)
    D10um(i,1)=DumSum(i,1)/DropletCount(i,1);
    D32um(i,1)=Dum3Sum(i,1)/Dum2Sum(i,1);
end

DataSummary(CaseNumber,6)=D10um(length(D10um),1);
DataSummary(CaseNumber,7)=D32um(length(D32um),1);
DataSummary(CaseNumber,8)=std(Dum);
DataSummary(CaseNumber,9)=std(Dum)/sqrt(length(Dum));
DataSummary(CaseNumber,10)=((median(MMD))^(1/3))*6/pi;
DataSummary(CaseNumber,11)=(((median(MMD))^(1/3))*6/pi)/D32um(length(D32um),1);
pd = lognfit(Dum,0.01);
DataSummary(CaseNumber,16)= pd(1);
DataSummary(CaseNumber,17)= pd(2);
pd = gamfit(Dum,0.01);
DataSummary(CaseNumber,12)= pd(1);
DataSummary(CaseNumber,13)= pd(2);
DataSummary(CaseNumber,14)= min(Dum);
DataSummary(CaseNumber,15)= max(Dum);

%Save Dum
FileName = ['Dum ' num2str(CaseNumber) '.txt'];
dlmwrite(FileName, Dum, 'delimiter', '\t', 'precision', 6);
%Save the data
FileName = ['Data ' num2str(CaseNumber) '.txt'];
dlmwrite(FileName, data, 'delimiter', '\t', 'precision', 6);

clear Dum;
clear DMM;
clear Dum2;
clear Dum2Sum;
clear Dum3;
clear Dum3Sum;
clear DumSum;
clear DropletCount;
clear pd;

end
end

dlmwrite('Data Summary.txt', DataSummary, 'delimiter', '\t', 'precision', 6);

```

### 9.1.3 Boundary Calculation

The following Matlab ‘.m’ file is used to process the data generated from ImageJ. The boundary image which is generated by ImageJ’s processing mean image is used to generate the data regarding the boundaries. The windward trajectory is determined by first horizontally scanning image from the left hand-side of the image and after a threshold vertically scanning the image from the top. As for the leeward trajectory the scanning direction is changed from left to right and top to bottom. In order to reduce the size of the data base the step size for the scanning is set to 10 pixels. The program also finds the breakup point by scanning the image in two directions; first, vertically from top to bottom and second, horizontally from right to left.

```
clear
clc
Scalemm=25/1314.5246;
Scaleum=25000/1314.5246;
BinaryThreshold=256/2;
lowercount=0;
uppercount=0;
maxcount=0;
BreakupLength=0;
%TrajectoryDataSummary case number, xbreakup, ybreakup, breakup length,
%image size x, image size y

for CaseNumber=197:416

    %197-204 206-259 261-288 293-368 373-403 405-416
    disp(CaseNumber);
    clock

    Step=1;
    disp(Step);
    tic
    FileName = ['/Users/amirrezaamighi/Desktop/PhD Thesis/Image Trajectory/' num2str(CaseNumber)];
    if exist(FileName, 'file')

        % iF file exists. Do ...

        %IMPORTFILE(FileName)
        % Imports data from the specified file
        % FILETOREAD1: file to read

        listOfJpegs = dir(['/Users/amirrezaamighi/Desktop/PhD Thesis/Image Trajectory/' num2str(CaseNumber) '/*.jpg']);
        JpegNumber = numel(listOfJpegs);
        ImageCount=JpegNumber;
        TrajectoryDataSummary=zeros(JpegNumber,7);

    toc

    Step=Step+1;
    disp(Step);
    tic

    for k=1:JpegNumber
        %find if the imagenumber is odd or even for different file
        %names
        if mod(k,2)
            % disp('odd')
            if (k/2+0.5)<10
                ImageFileName=['/Users/amirrezaamighi/Desktop/PhD Thesis/Image Trajectory/' num2str(CaseNumber) '/' num2str(CaseNumber)
'000' num2str(k/2+0.5) '_a.jpg'];
```



```

end
if (k/2+0.5)>=10 && i<100
    ImageFileName=['/Users/amirrezaamighi/Desktop/PhD Thesis/Image Trajectory/' num2str(CaseNumber) '/' num2str(CaseNumber)
'00' num2str(k/2+0.5) '_a.jpg'];
end
if (k/2+0.5)>=100
    ImageFileName=['/Users/amirrezaamighi/Desktop/PhD Thesis/Image Trajectory/' num2str(CaseNumber) '/' num2str(CaseNumber)
'0' num2str(k/2+0.5) '_a.jpg'];
end

else

%       disp('even')
if (k/2)<10
    ImageFileName=['/Users/amirrezaamighi/Desktop/PhD Thesis/Image Trajectory/' num2str(CaseNumber) '/' num2str(CaseNumber)
'000' num2str(k/2) '_b.jpg'];
end
if (k/2)>=10 && i<100
    ImageFileName=['/Users/amirrezaamighi/Desktop/PhD Thesis/Image Trajectory/' num2str(CaseNumber) '/' num2str(CaseNumber)
'00' num2str(k/2) '_b.jpg'];
end
if (k/2)>=100
    ImageFileName=['/Users/amirrezaamighi/Desktop/PhD Thesis/Image Trajectory/' num2str(CaseNumber) '/' num2str(CaseNumber)
'0' num2str(k/2) '_b.jpg'];
end
end

if exist(ImageFileName, 'file')

%IMPORTFILE(fileName)
% Imports data from the specified file
% FILETOREAD1: file to read

ImageFileName
imagedata = imread(ImageFileName);
%       imagedata = fliplr(imagedata);
imagedatasize=size(imagedata);
TrajectoryDataSummary(CaseNumber,1)=CaseNumber;
TrajectoryDataSummary(CaseNumber,2)=JpegNumber;
TrajectoryDataSummary(CaseNumber,6)=imagedatasize(1,2); %x,i,col
TrajectoryDataSummary(CaseNumber,7)=imagedatasize(1,1); %y,j,row

toc

Step=Step+1;
disp(Step);
tic

%Find breakup point

%Scan the binary image to find the breakup point. scan columns
endloop1=0;
endloop2=0;

i=0; %x-position
j=0; %y-position
for i=TrajectoryDataSummary(CaseNumber,6):-1:1

    for j=TrajectoryDataSummary(CaseNumber,7):-1:1

        if imagedata(j,i) < BinaryThreshold
            endloop1=1;
            TrajectoryDataSummary(CaseNumber,3)=i;
            TrajectoryDataSummary(CaseNumber,4)=j;
        end

        if endloop1==1
            break
        end
    end
end

```

```

end

if endloop1==1
break
end

end

endloop1=0;

toc

%Find lower trajectory
Step=Step+1;
disp(Step);
tic

i=0; %x-position
j=0; %y-position

for j=1:10:TrajectoryDataSummary(CaseNumber,7)
for i=TrajectoryDataSummary(CaseNumber,6):-1:1

    if imagedata(j,i) < BinaryThreshold

        lowercount=lowercount+1;

        LowerBoundary(lowercount,1)=CaseNumber;
        LowerBoundary(lowercount,2)=i;
        LowerBoundary(lowercount,3)=j;

        endloop1=1;

        if LowerBoundary(lowercount,2)>50
            endloop2=1;
        end

        if endloop1==1
            break
        end

    end

end

if endloop2==1
    break
end
endloop1=0;

end

endloop2=0;

for i=51:10:0.9*TrajectoryDataSummary(CaseNumber,3)
for j=1:TrajectoryDataSummary(CaseNumber,7)

    if imagedata(j,i) < BinaryThreshold

        lowercount=lowercount+1;

        LowerBoundary(lowercount,1)=CaseNumber;
        LowerBoundary(lowercount,2)=i;
        LowerBoundary(lowercount,3)=j;

        endloop1=1;

        if endloop1==1
            break
        end

    end

end

```

```

end

endloop1=0;

end

toc

%Find upper trajectory
Step=Step+1;
disp(Step);
tic

i=0; %x-position
j=0; %y-position

for j=1:10:TrajectoryDataSummary(CaseNumber,7)
    for i=1:TrajectoryDataSummary(CaseNumber,6)

        if imagedata(j,i) < BinaryThreshold

            uppercount=uppercount+1;

            UpperBoundary(uppercount,1)=CaseNumber;
            UpperBoundary(uppercount,2)=i;
            UpperBoundary(uppercount,3)=j;

            endloop1=1;

            if UpperBoundary(uppercount,2)>150
                endloop2=1;
            end

            if j>1
                BreakupLength=sqrt((i-UpperBoundary(uppercount-1,2))^2+(j-UpperBoundary(uppercount-1,3))^2)+BreakupLength
            end

            if endloop1==1
                break
            end

        end

    end

    if endloop2==1
        break
    end

    endloop1=0;

end

endloop2=0;

maxupper=0;

for i=151:10:0.5*TrajectoryDataSummary(CaseNumber,3)
    for j=TrajectoryDataSummary(CaseNumber,7):-1:1

        if imagedata(j,i) < BinaryThreshold

            uppercount=uppercount+1;

            UpperBoundary(uppercount,1)=CaseNumber;
            UpperBoundary(uppercount,2)=i;
            UpperBoundary(uppercount,3)=j;

            if maxupper<UpperBoundary(uppercount,3)
                maxupper=UpperBoundary(uppercount,3);
            end

        end

    end

end

```

```

        endloop1=1;

        BreakupLength=sqrt((i-UpperBoundary(uppercount-1,2))^2+(j-UpperBoundary(uppercount-1,3))^2)+BreakupLength;

        if endloop1==1
            break
        end

    end

end

endloop1=0;

end
endloop2=0;

for i=1:length(UpperBoundary)

    if maxupper<UpperBoundary(1,3)
        maxupper=UpperBoundary(1,3);
    end
end

toc

else
    JpegNumber=JpegNumber+1;
end

end

end

clear CaseNumber;
clear FileName;

FileName = 'Conditions.txt';
Conditions = dlmread(FileName);

for i=1:length(MaxTrajectory)
    for j=1:length(Conditions)
        if Conditions(j,1)==MaxTrajectory(i,1)
            MaxTrajectory(i,4:26)=Conditions(j,2:24);
        end
    end
end

for i=1:length(LowerBoundary)
    for j=1:length(Conditions)
        if Conditions(j,1)==LowerBoundary(i,1)
            LowerBoundary(i,4:26)=Conditions(j,2:24);
        end
    end
end

for i=1:length(UpperBoundary)
    for j=1:length(Conditions)
        if Conditions(j,1)==UpperBoundary(i,1)
            UpperBoundary(i,4:26)=Conditions(j,2:24);
        end
    end
end

dlmwrite('Trajectory Data Summary.txt', TrajectoryDataSummary, 'delimiter', '\t', 'precision', 6);
dlmwrite('Upper Trajectory.txt', UpperBoundary, 'delimiter', '\t', 'precision', 6);
dlmwrite('Lower Trajectory.txt', LowerBoundary, 'delimiter', '\t', 'precision', 6);
dlmwrite('Max Trajectory.txt', MaxTrajectory, 'delimiter', '\t', 'precision', 6);

```

## 9.2 Appendix B: Estimate of Heat-up Time for the Jet

In this section a method for estimating heat-up time for the jet and droplets as well as evaporation rate are discussed. One of the difficulties with the analysis at higher temperatures is approximation of liquid temperature and how it effects other liquid properties namely density, surface tension and viscosity. As expected all three parameters are affected by temperature and not as significantly by the pressure. At first the heat-up time for the jet is calculated so that the mentioned physical properties of liquid for the atomization process can be determined. Second, similar calculation is used to determine the heat-up time for the average droplet size in the spray. Finally, evaporation rates are calculated so that the effect of evaporation at early stages of atomization can be understood.

The breakup time also needs to be considered due to time dependency of evaporation and heat-up time. The breakup time has been studied by various researchers and is defined by (9.1). For the current study the breakup time ranges from 0.6 ms to 133 ms with the average at 67 ms. Non-dimensionalized breakup time generally follows the form of (9.2), where C is a constant and based on the literature review by Gopala [61] its value ranges from 1.6 to 3.44, depending on the study. For the current study the range is from 2.6 to 12.0 with the average at 5.5.

$$t_b = \frac{y_B}{V_{Jet}} \quad (9.1)$$

$$\frac{t_b}{t^*} = \frac{t_b}{\sqrt{\frac{\rho_{Jet} D_N}{\rho_{Air} V_{Air}}}} = C \quad (9.2)$$

There are two aspects for calculating a reasonable time scales; first, there must be sufficient energy to have the transition from low temperature liquid to saturated liquid and finally to the gas phase; and secondly, the duration of these transitions and if it is in the same time scale as the jet breakup times. The spray goes through an initial transient heat-up phase before the steady state evaporation takes place for which  $D^2$  Law can be employed as an approximation. It is assumed that the heat-up temperature i.e. interface temperature would be the saturation temperature at a given ambient pressure. This is a valid assumption for as long as the energy required by heating-up the liquid is available and can be transferred from the gas. The energy required for heating-up can be calculated as follows:

$$\dot{Q}_{hl} = \dot{m}_l C_{p,l} (T_s - T_0) \quad (9.3)$$

$$\dot{Q}_{El} = \dot{m}_l h_{fg} \quad (9.4)$$

Where  $\dot{m}_l$  is the mass flow rate of the jet,  $h_{fg}$  is the latent heat of evaporation,  $T_s$  is the saturated temperature and  $T_0$  is the initial liquid jet temperature. In order to evaporate the liquid, there must be sufficient energy for the liquid to reach the saturated temperature and significantly more energy is needed to change the phase. The energy available from the gas can be calculated based on the first law of thermodynamics:

$$\dot{Q}_g = \dot{m}_g (h_\infty - h_s) \quad (9.5)$$

Based on the above calculations the free stream gas temperature must be high enough for the evaporation to take place. When the free stream gas temperature is not high, the jet temperature would never reach the saturation temperature and diffusion would be the dominating factor. For the current study, all the high temperature cases satisfy the above requirement, i.e.  $\dot{Q}_g > \dot{Q}_{hl}$ . The following ratio is defined to better understand the process:

$$C_E = \frac{\dot{Q}_{hl} + \dot{Q}_{el}}{\dot{Q}_g} \quad (9.6)$$

For the cases where  $C_E > 1$ , the rate of evaporation is not substantial and the dominating factor for change in atomization process is governed by the property change of the gas and liquid. Conversely, evaporation becomes the primary process in droplet size reduction for the cases where  $C_E < 1$ . This is especially noticeable for cases with smaller nozzle diameters where the liquid mass flow rate is lower than the cases with larger nozzle.

The next important step would be to determine the time required to reach this saturation temperature. If this time is the same as the breakup time, then it is safe to assume that the liquid properties should be based on the saturation temperature. The following is a short summary from reference [71] and more details can be found in the text.

The heating-up process is transient and lumped capacitance assumption is an accepted method to estimate heat-up times. In this method, it is assumed that the temperature within the jet and droplets is spatially uniform and is only time dependent. This can be justified for the sprays with small

droplet sizes. The Biot number is the ratio of convective heat transfer to an object versus the internal heat conduction. For cases where Biot number is smaller than 0.1, the above-mentioned assumption for internal droplet temperature is valid. The Biot number is given by:

$$Bi = \frac{h_q d}{K_l} \quad (9.7)$$

Where  $h_q$  is the convective heat transfer rate,  $d$  is the characteristic length, which for a droplet is  $D_{32}/6$  and for Jet  $D_N/4$ , and  $K_l$  is the thermal conductivity of the liquid. The characteristic length for the purposes of this analysis is assumed to be based on  $D_{32}$  for the droplet heat-up calculations and jet diameter for the jet heat-up calculations. For a single spherical droplet the diameter is the variable that represents the volume and surface of that droplet. Therefore, the effective diameter has to represent these two variables since in heat transfer the volume and surface play an important role. The effective diameter is defined by ratio of volume to surface, (9.8). A liquid jet then can be approximated as a cylinder but since the diameter of the nozzle compare to the overall length of the jet is insignificant and does not play a major role in heat transfer the surfaces at the ends of the cylinder can be ignored, (9.9). It should be noted that this assumption over-estimates the time scale since it does not consider mass removal from the jet as it would be the case in the actual spray.

$$D_{f-sphere} = \frac{V}{S} = \frac{D}{6} \quad (9.8)$$

$$D_{f-cylinder} = \frac{V}{S} \sim \frac{\left(\frac{\pi}{4} D^2 l\right)}{(\pi D l)} = \frac{D}{4} \quad (9.9)$$

When the Biot number is less than 0.1 the following relation can be used to calculate the time required for the heat-up time.

$$\theta = e^{-Bi.Fo} \quad (9.10)$$

$$\theta = \frac{T_s - T_\infty}{T_0 - T_\infty} \quad (9.11)$$

$$Fo = \frac{\alpha t}{d^2} \quad (9.12)$$

$$t = -Ln \left( \frac{T_s - T_\infty}{T_0 - T_\infty} \right) \left( \frac{h_q}{K_l} \cdot \frac{\alpha}{d} \right)^{-1} \quad (9.13)$$

Where  $\theta$  is the non-dimensionalized temperature, and  $Fo$  is the Fourier number, which is the ratio of thermal diffusivity to thermal storage, and  $\alpha$  is the thermal diffusivity of the liquid. As it can be

seen the difficulty for determining the heat-time is estimating the convective heat transfer coefficient. The convective heat transfer rate can be determined using the Nusselt number. The following correlation by Ranz and Marshal is for forced convection in a spray with small Reynolds number below 200:

$$Nu = \frac{h_q d}{K_g} \quad (9.14)$$

$$Nu = 2 + 0.6Re_d^{1/2} Pr_d^{1/3} \quad (9.15)$$

For the current study the Reynolds number are larger the 200 and beyond the limits for the above correlation and therefore the following modified Ranz and Marshal correlations is used.

$$Nu_0 = (2 + 0.552Re_d^{1/2} Pr_d^{1/3}) \quad (9.16)$$

$$Nu^* = 2 + (Nu_0 - 2)/F_T \quad (9.17)$$

$$F_T = (1 + B)^{0.7} \frac{\ln(1 + B)}{B} \quad (9.18)$$

$$B_T = \frac{C_{pg}(T_\infty - T_s)}{L^*} \quad (9.19)$$

$$L^* = \frac{q_s}{q_s - q_{ls}} L \quad (9.20)$$

Where the Reynolds and Prandtl number is based on the characteristic the defined lengths and gas velocity and properties,  $B_h^*$  is the heat transfer number, and  $L^*$  is the adjusted latent heat. Based on the above calculations and assumptions it is found that for the current study the average Biot number is about  $3.1E-4$  for the spray and  $5.9E-4$  for the jet. The heat-up time for the average droplet in the spray ranged from 16 ms to 4.9 s with the average at 1.1 s. On the other hand, the heat-up time for the jet ranged from 0.4 s to 44 s with the average at 12 s.

As presented earlier, the breakup time for the jet based on the current study is smaller than heat-up time of the jet and it is safe to assume for the current study that the liquid would still be at initial conditions, crossflow pressure and inlet liquid temperature, by the time the primary jet breakup is complete. On the other hand, once the primary breakup takes place then the heat-up times for the droplets are much shorter and evaporation starts to take place.



The next step is to determine evaporation rate to better understand the breakup and evaporation process. The process for the following calculations is based on the combination of work done by Abramzon and Sirignano [72] and Sazhin [73] as well as Turns [74]. The evaporation model of droplet by Abramzon [73] is considered for calculating the evaporation rate of the droplets. Once the evaporation rate is known, then D<sup>2</sup> Law, (9.21), can be used cautiously to estimate droplet size at various locations, where D<sub>0</sub> is based on the correlations in section 6.4. In order to calculate the evaporation rate, it is assumed that the droplets are at saturation temperature, and properties for the evaporation rates are based on film temperature. The film temperature is approximated by the weighted average between liquid and gas (2/3 liquid and 1/3 gas) similar to the methodology used in evaporation models by Sirignano [72], Abramzon [73], and Sazhin [75]. One of the difficulties with this type of analysis is defining a characteristic length for the liquid because the spray is highly irregular and has various heat transfer rates by convection and conduction as well as advection. Once again D<sub>32</sub> is used as the characteristic length for the calculations.

$$D^2 = D_0^2 - Kt \quad (9.21)$$

$$K = \frac{4k_g}{\rho_l C_{pg}} Nu^* \ln(1 + B_T) \quad (9.22)$$

$$C_{pg} = C_{pWater}(\bar{T}) \quad (9.23)$$

$$k_g = 0.4k_{Water}(\bar{T}) + 0.6k_{Air}(\bar{T}) \quad (9.24)$$

$$B_T = \frac{C_{pg}(T_\infty - T_{Sat.})}{C_{pWater}(T_{Sat.} - T_0) + h_{fg}} \quad (9.25)$$

The evaporation constant K is given in (9.22) is based on thermal properties of the spray.  $C_{p,Water}$  and  $C_{p,Air}$ ,  $k_{g,Water}$  and  $k_{g,Air}$  are calculated at the film temperature and pressure. Then approximation of Law and Williams, (9.24), for burning droplet is used to calculate the film average thermal conductivity and vapor specific heat at constant pressure. Based on these calculations the average droplet life range is from 14 ms to 180 ms with the average at 58 ms. The average droplet life is about 100 times the breakup time. Mean distance traveled by droplet can be estimated by assuming the droplets are traveling at the crossflow speed. The distance travelled by mean droplets ranges from 1 m to 5 m with the average at 2.7 m.

### 9.3 Appendix C: Circulation Heater Specifications

REVISIONS			
REV.	DESCRIPTION	DATE	APPROVED
0	INITIAL ISSUE	01-10-06	

PRODUCT FEATURES	
SERIAL NUMBER	706-06K12164
DESIGN DATA	
DESIGNED, MANUFACTURED AND STAMPED IN ACCORDANCE WITH ASME SECTION VIII, DIV. 1, 2004 EDITION 2005 ADDENDA	
DESIGN PRESSURE	95 PSIG
DESIGN TEMPERATURE	1350°F (732.2°C)
MDMT	-20°F (-28.9°C)
HYDROTEST PRESSURE	852 PSIG
CORROSION ALLOWANCE	NONE
RADIOGRAPHY	NONE
OTHER NDE	NONE
FWHT	NONE
INSPECTION	PER ASME SECTION VIII
MATERIAL SPECIFICATIONS	
SHELL	10 NPS STD. SCH. SA-312-TP304H SMLS
SHELL FLANGE	10" CLASS 600 RFWN SA-182-F304H
WELD CAP	10 NPS STD. SCH. SA-403-304H
VESSEL SUPPORTS	1/4" PLATE SA-240-304H
N1 INLET	CONNECTION 3" CLASS 600 RFWN SA-182-F304H NECK 3 NPS STD. SCH. SA-312-TP304H SMLS
N2 OUTLET	CONNECTION 3" CLASS 600 RFWN SA-182-F304H NECK 3 NPS STD. SCH. SA-312-TP304H SMLS
N3 VENT	CONNECTION N/A N/A NECK N/A N/A
N4 DRAIN	CONNECTION N/A N/A NECK N/A N/A
N5 PROCESS THERMOCOUPLE	CONNECTION 1/2 NPT CL 3000 CPLG SA-182-F304H NECK 1/2 NPS SCH. BD SA-312-TP304H SMLS
N6 SHELL LIMIT THERMOCOUPLE	CONNECTION 1/2 NPT CL 3000 CPLG SA-182-F304H NECK 1/2 NPS SCH. BD SA-312-TP304H SMLS

ITEM	CUT LENGTH
N1	141 1/2"
N2	141 1/2"
N3	N/A
N4	N/A
N5	6" TOE
N6	5 3/4" TOE
N7	N/A
SHELL	119 3/4"

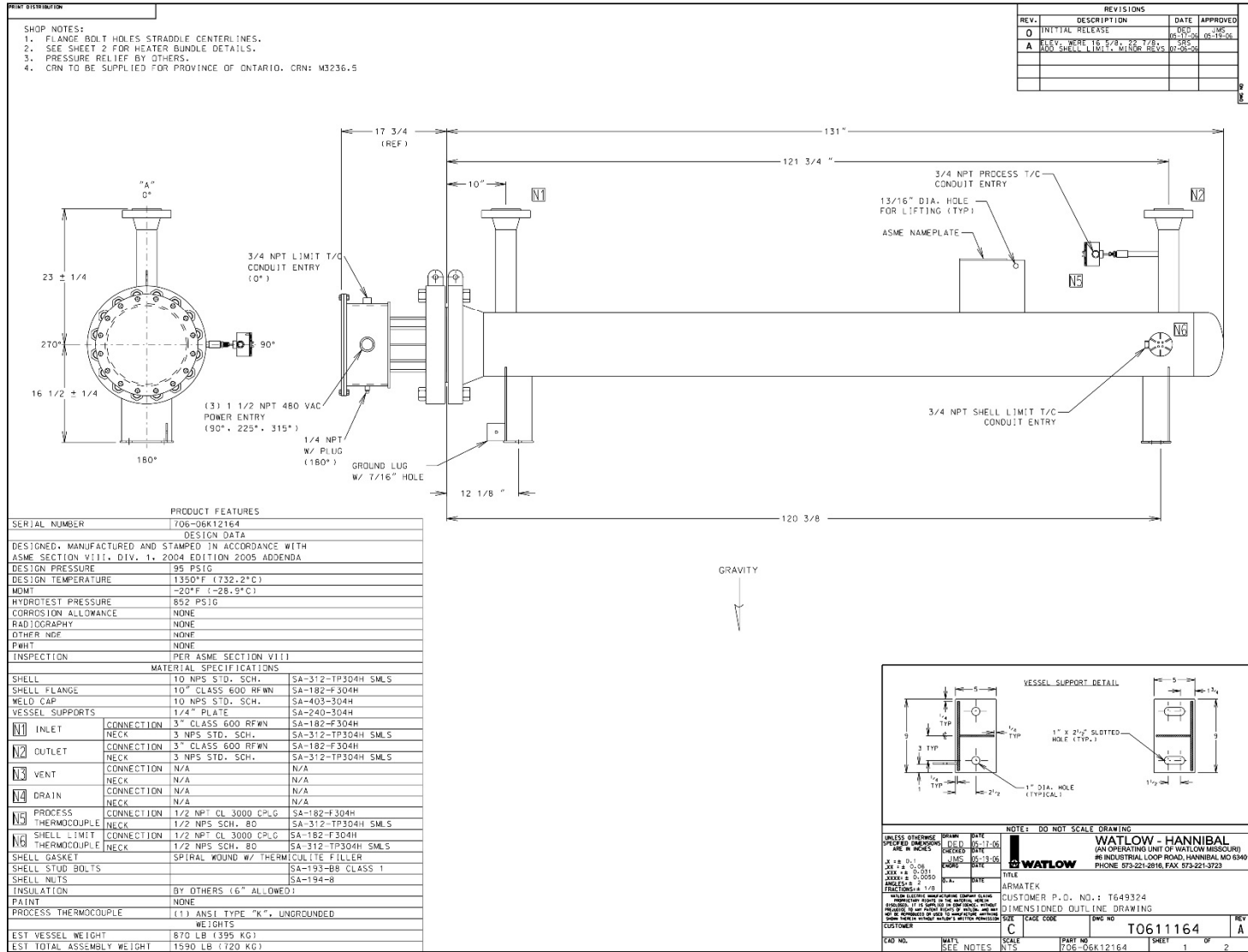
1194 National Board Number	
Certified by WATLOW HANNIBAL, MD USA (573)221-2816	
Maximum Allowable Working Pressure	95 psig at 1350 °F
Minimum Design Metal Temperature	-20 °F at Maximum Allowable Working Pressure 95 psig
706-06K12164 (Manufacturer's Serial Number) 2006 (Year Built) CRN: M3236.5	

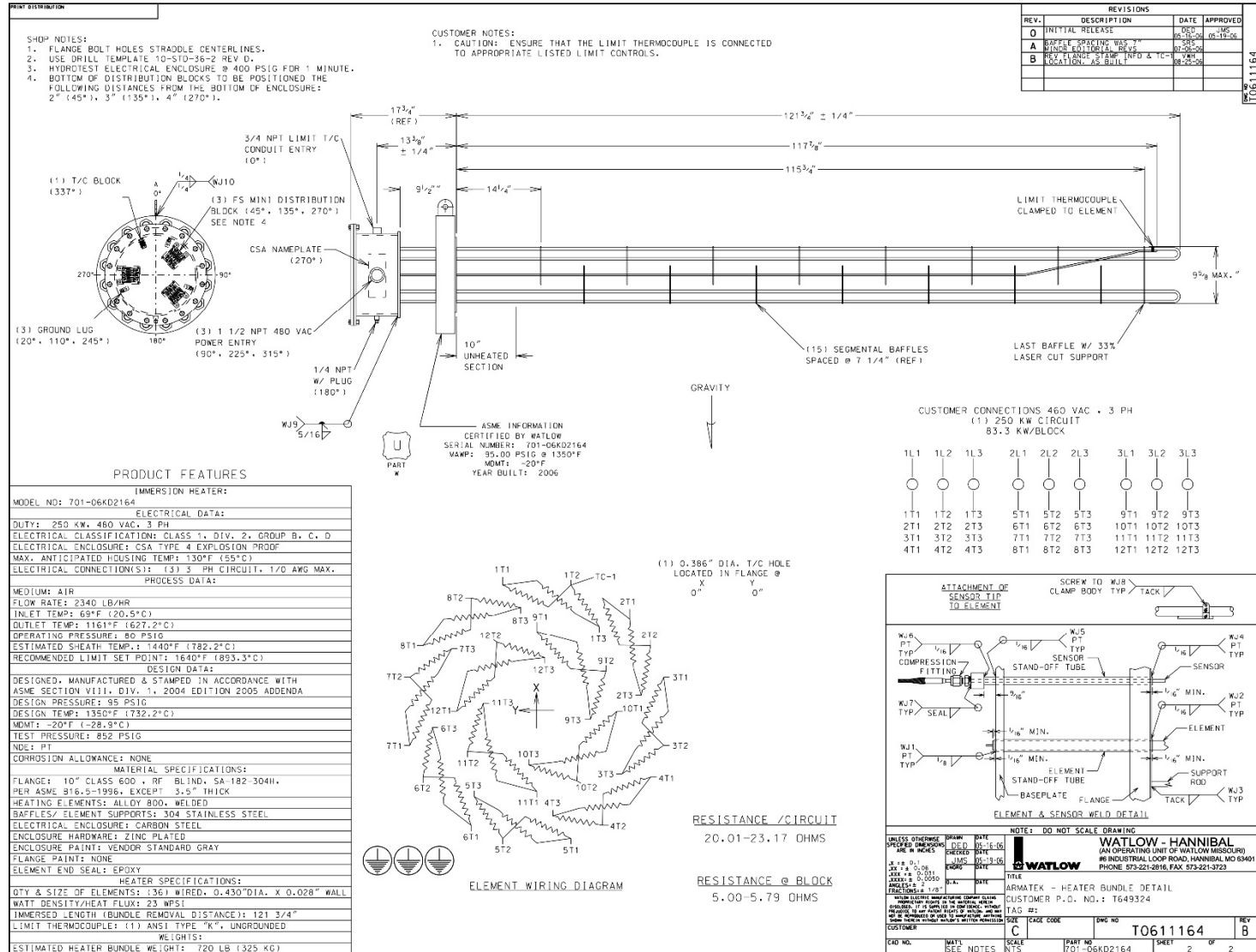
UNLESS OTHERWISE SPECIFIED DIMENSIONS ARE IN INCHES	DRAWN	DATE	DATE
1:1 & 2:1	SRS	01-10-06	
JUL 7 8 0 06	ENGR		
APR 18 8 00 06	DATE		
ANGLES 2	DATE		
TOLERANCES 1/8	DATE		

NOTE: DO NOT SCALE DRAWING	
WATLOW - HANNIBAL (AN OPERATING UNIT OF WATLOW MISSOURI) 86 INDUSTRIAL LOOP ROAD, HANNIBAL, MO 63401 PHONE 573-221-2816, FAX 573-221-3723	
TITLE	ARMATEK
CUSTOMER P.O. NO.	T649324
VESSEL WELD MAP	
CUSTOMER	C
DWG NO	T0611164
SHEET	0
CAD NO.	WATL
SCALE	
PART NO	706-06K12164
SHEET	01

NOTES

- ALL NOZZLE LOADINGS ARE CONSIDERED NEUTRAL.
- ALL GROOVE WELDS ARE REQUIRED TO HAVE 100% PENETRATIONS. IF COMPLETE PENETRATIONS CANNOT BE OBTAINED FROM ONE SIDE, BACKWELDING IS ALLOWED.
- ALL WELD SIZES SHOWN ARE MINIMUM.
- FLANGE BOLT HOLES STRADDLE CENTERLINE OF VESSEL.
- INSPECTION: PER ASME SECTION VIII.
- NOZZLE N6 DOES NOT PENETRATE SHELL.
- CRN TO BE SUPPLIED FOR PROVINCE OF ONTARIO.

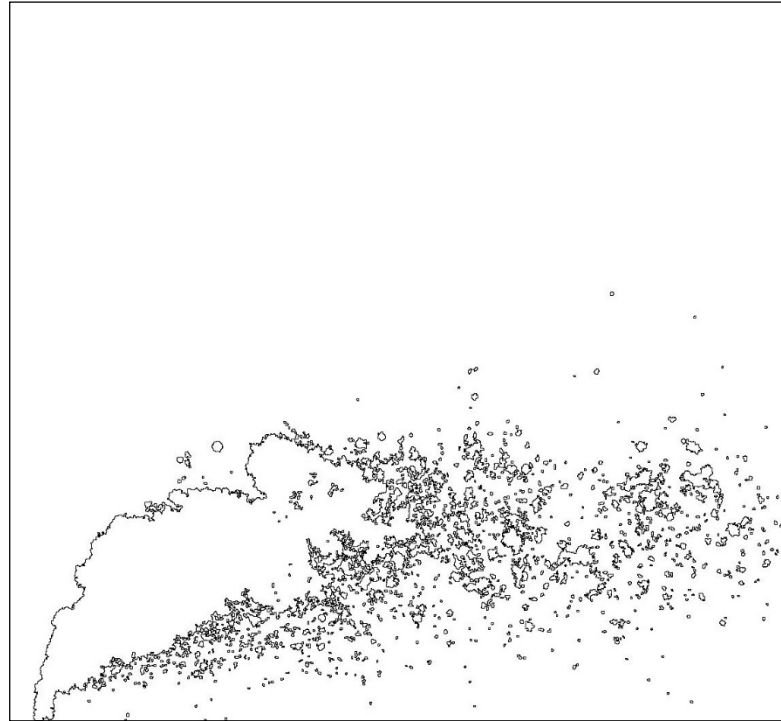




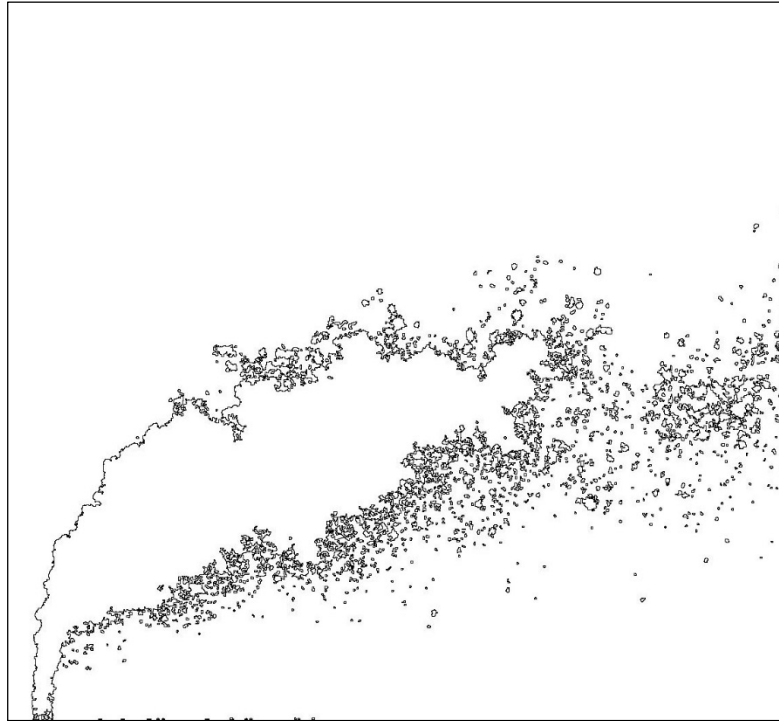
## 9.4 Appendix D: Sample Images for Each Condition

In this section a sample image for each case is shown. The table above each image summarizes the conditions and global droplet size. The fluid properties are shown in the form of a symbol. The relation between the fluid properties and symbols are summarized in Table 2.2, the range of parameters are provided. The average and standard deviation are provided to give an idea about the range of parameters and an idea about the experimental conditions. They do not refer to the errors for the parameters. Table 2.1. The solid filled symbols represent the 457  $\mu\text{m}$  nozzle and the hollow symbols represent the 572  $\mu\text{m}$  nozzles.

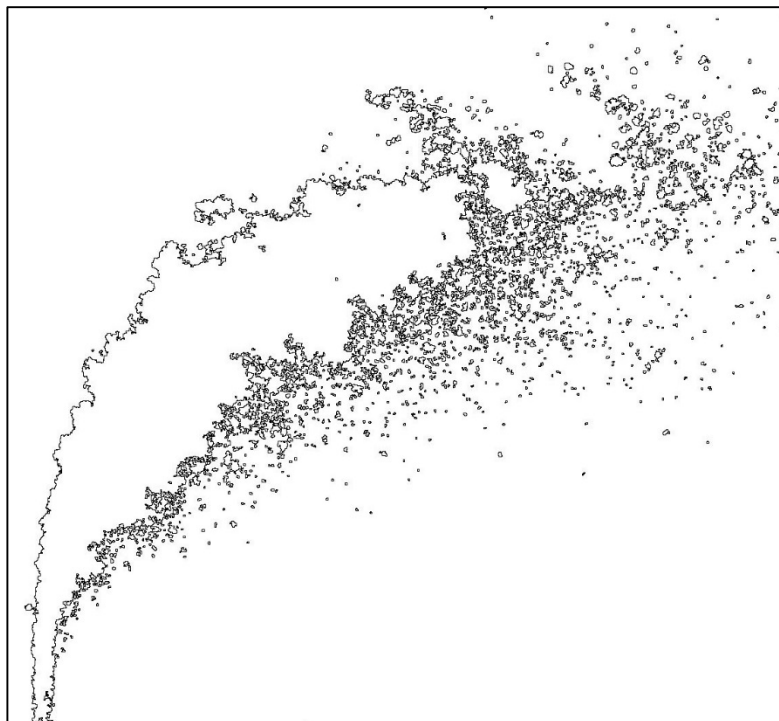
No.	Ref.	$V_{\text{Jet}}$ [m/s]	$V_{\text{Air}}$ [m/s]	q	$We_{\text{Air}}$	$We_{\text{Jet}}$	$Re_{\text{Air}}$	$Re_{\text{Jet}}$	$Oh_{\text{Air}}$ $\times 10^3$	$Oh_{\text{Jet}}$ $\times 10^3$	D10 [ $\mu\text{m}$ ]	D32 [ $\mu\text{m}$ ]
1	□	14	95	8	172	1455	7084	8685	1.852	409.3	62.5	76.9



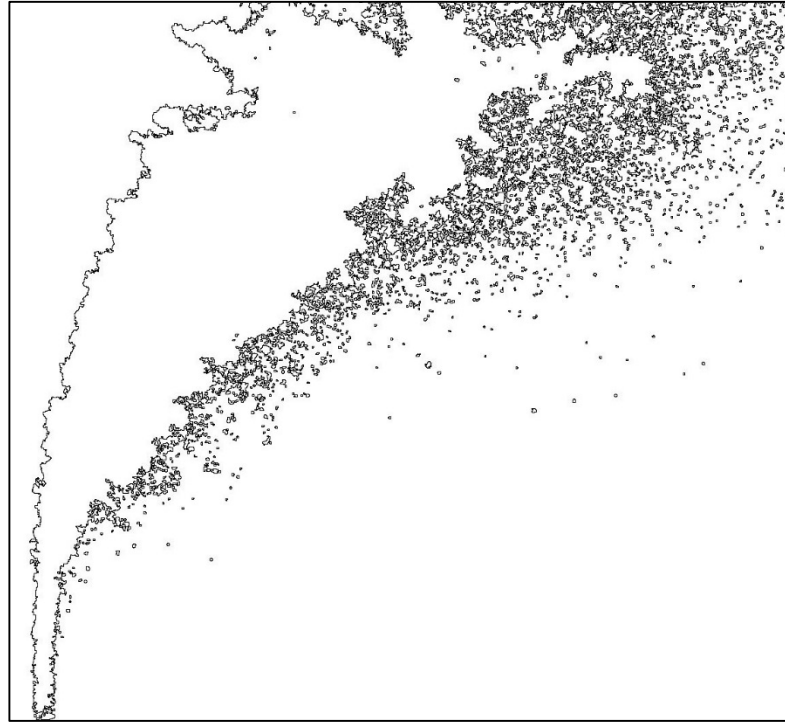
No.	Ref.	$V_{\text{Jet}}$ [m/s]	$V_{\text{Air}}$ [m/s]	q	$We_{\text{Air}}$	$We_{\text{Jet}}$	$Re_{\text{Air}}$	$Re_{\text{Jet}}$	$Oh_{\text{Air}}$ $\times 10^3$	$Oh_{\text{Jet}}$ $\times 10^3$	D10 [ $\mu\text{m}$ ]	D32 [ $\mu\text{m}$ ]
2	□	19	95	17	172	2910	7084	12282	1.852	486.8	60.4	72.5



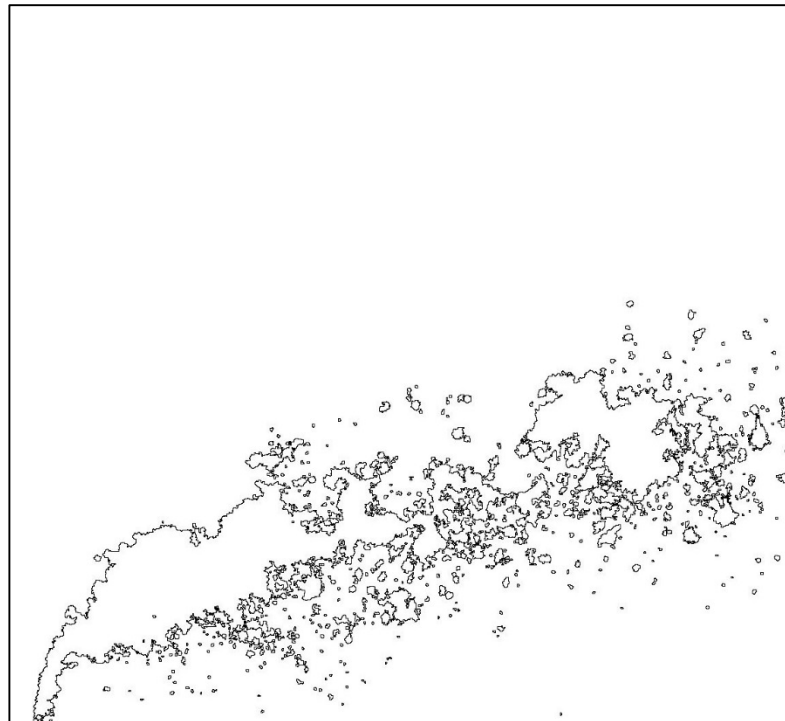
No.	Ref.	$V_{\text{Jet}}$ [m/s]	$V_{\text{Air}}$ [m/s]	q	$We_{\text{Air}}$	$We_{\text{Jet}}$	$Re_{\text{Air}}$	$Re_{\text{Jet}}$	$Oh_{\text{Air}}$ $\times 10^3$	$Oh_{\text{Jet}}$ $\times 10^3$	D10 [ $\mu\text{m}$ ]	D32 [ $\mu\text{m}$ ]
3	□	30	95	42	172	7275	7084	19419	1.852	612.1	59.2	69.1



No.	Ref.	$V_{\text{Jet}}$ [m/s]	$V_{\text{Air}}$ [m/s]	q	$We_{\text{Air}}$	$We_{\text{Jet}}$	$Re_{\text{Air}}$	$Re_{\text{Jet}}$	$Oh_{\text{Air}}$ $\times 10^3$	$Oh_{\text{Jet}}$ $\times 10^3$	D10 [ $\mu\text{m}$ ]	D32 [ $\mu\text{m}$ ]
4	□	38	95	68	172	11640	7084	24564	1.852	688.4	58.1	65.8



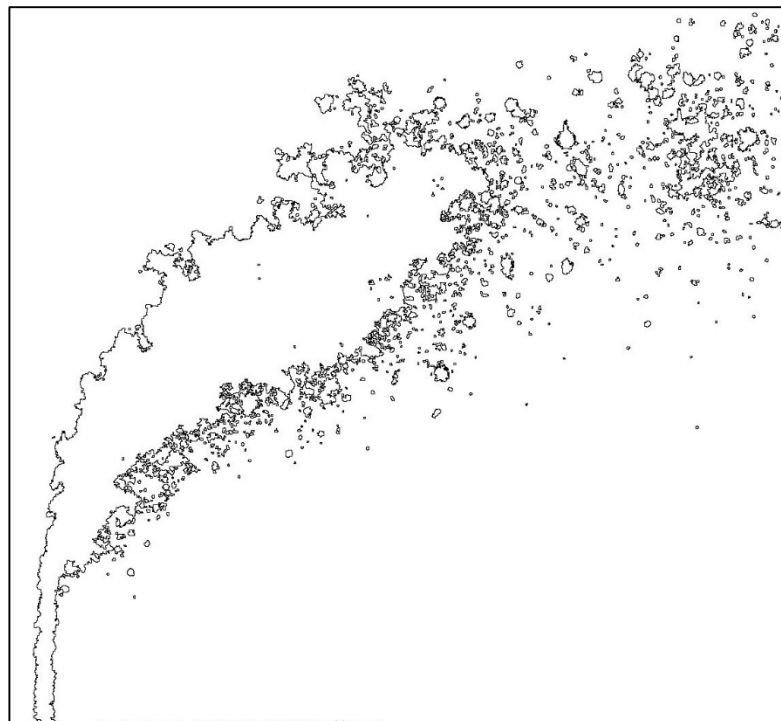
No.	Ref.	$V_{\text{Jet}}$ [m/s]	$V_{\text{Air}}$ [m/s]	q	$We_{\text{Air}}$	$We_{\text{Jet}}$	$Re_{\text{Air}}$	$Re_{\text{Jet}}$	$Oh_{\text{Air}}$ $\times 10^3$	$Oh_{\text{Jet}}$ $\times 10^3$	D10 [ $\mu\text{m}$ ]	D32 [ $\mu\text{m}$ ]
5	□	9	61	8	71	582	4544	5493	1.852	325.5	68.5	88.8



No.	Ref.	$V_{\text{Jet}}$ [m/s]	$V_{\text{Air}}$ [m/s]	q	$We_{\text{Air}}$	$We_{\text{Jet}}$	$Re_{\text{Air}}$	$Re_{\text{Jet}}$	$Oh_{\text{Air}}$ $\times 10^3$	$Oh_{\text{Jet}}$ $\times 10^3$	D10 [ $\mu\text{m}$ ]	D32 [ $\mu\text{m}$ ]
6	□	12	61	16	71	1164	4544	7768	1.852	387.1	66.0	84.3

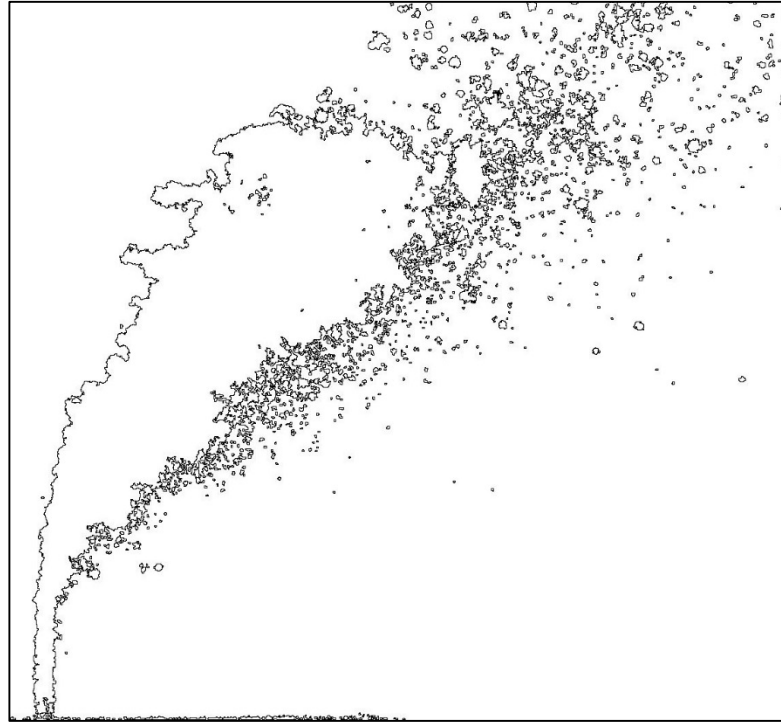


No.	Ref.	$V_{\text{Jet}}$ [m/s]	$V_{\text{Air}}$ [m/s]	q	$We_{\text{Air}}$	$We_{\text{Jet}}$	$Re_{\text{Air}}$	$Re_{\text{Jet}}$	$Oh_{\text{Air}}$ $\times 10^3$	$Oh_{\text{Jet}}$ $\times 10^3$	D10 [ $\mu\text{m}$ ]	D32 [ $\mu\text{m}$ ]
7	□	19	61	41	71	2910	4544	12282	1.852	486.8	63.3	78.5

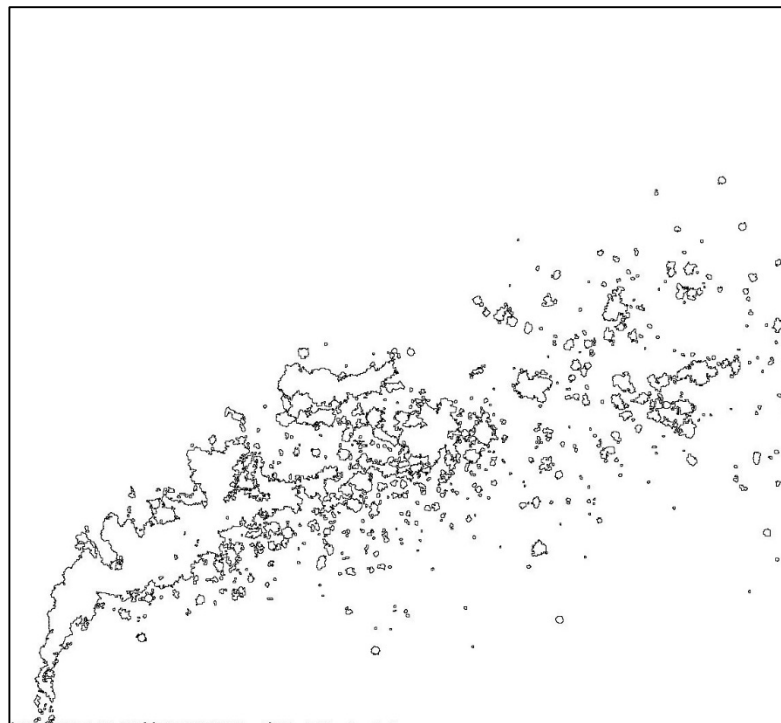




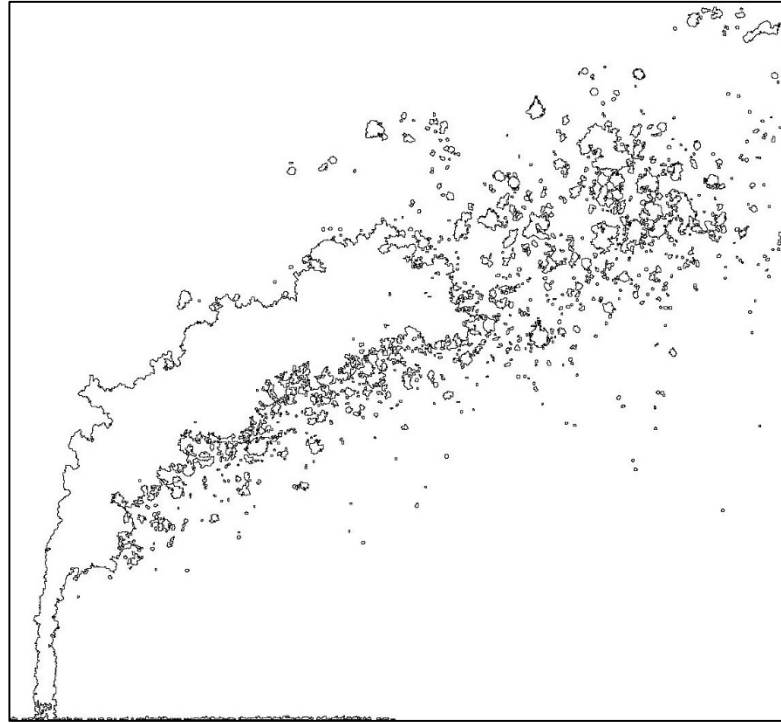
No.	Ref.	$V_{Jet}$ [m/s]	$V_{Air}$ [m/s]	q	$We_{Air}$	$We_{Jet}$	$Re_{Air}$	$Re_{Jet}$	$Oh_{Air}$ $\times 10^3$	$Oh_{Jet}$ $\times 10^3$	D10 [ $\mu m$ ]	D32 [ $\mu m$ ]
8	□	24	61	66	71	4656	4544	15535	1.852	547.5	61.6	73.9



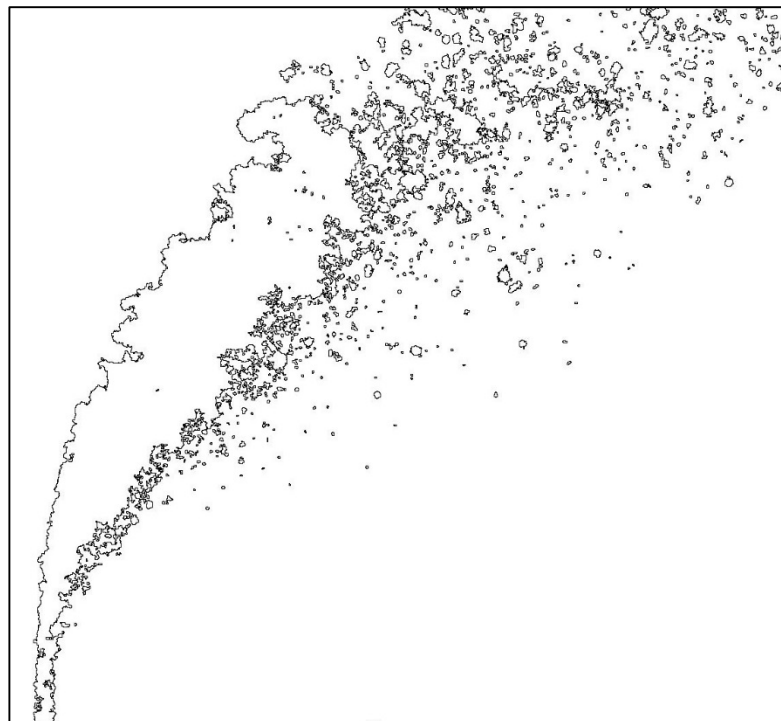
No.	Ref.	$V_{Jet}$ [m/s]	$V_{Air}$ [m/s]	q	$We_{Air}$	$We_{Jet}$	$Re_{Air}$	$Re_{Jet}$	$Oh_{Air}$ $\times 10^3$	$Oh_{Jet}$ $\times 10^3$	D10 [ $\mu m$ ]	D32 [ $\mu m$ ]
9	□	10	49	15	47	728	3701	6141	1.852	344.2	68.4	88.7



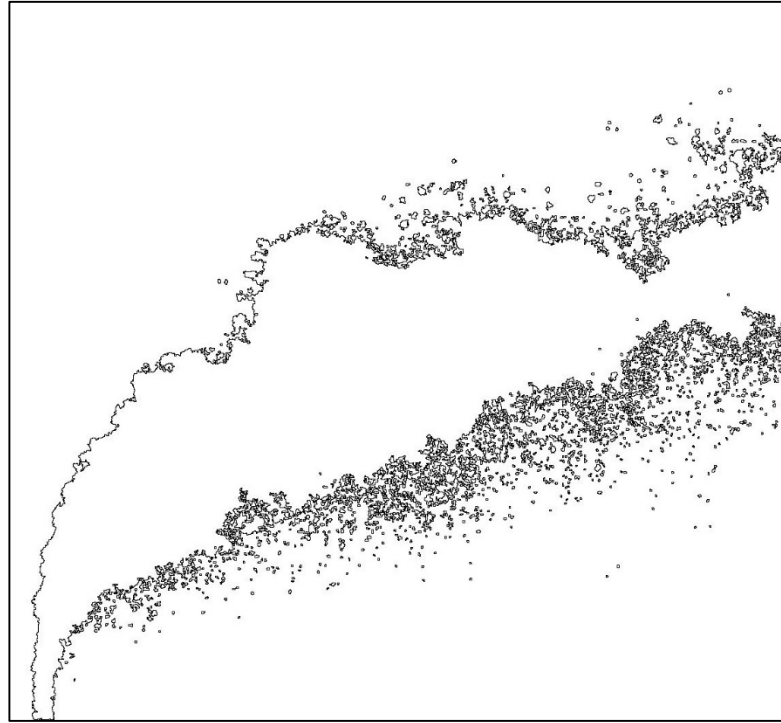
No.	Ref.	$V_{\text{Jet}}$ [m/s]	$V_{\text{Air}}$ [m/s]	q	$We_{\text{Air}}$	$We_{\text{Jet}}$	$Re_{\text{Air}}$	$Re_{\text{Jet}}$	$Oh_{\text{Air}}$ $\times 10^3$	$Oh_{\text{Jet}}$ $\times 10^3$	D10 [ $\mu\text{m}$ ]	D32 [ $\mu\text{m}$ ]
10	□	15	49	39	47	1819	3701	9710	1.852	432.8	65.6	83.0



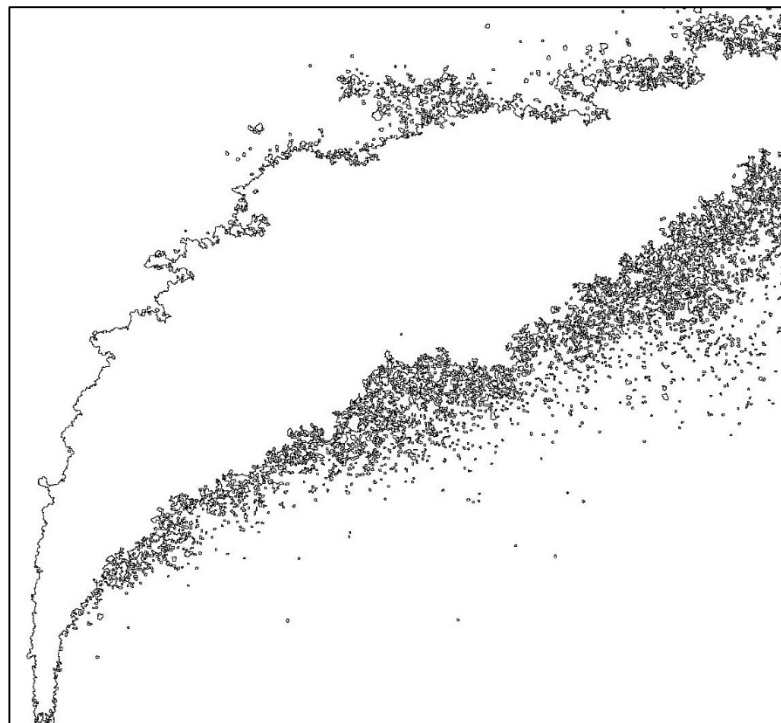
No.	Ref.	$V_{\text{Jet}}$ [m/s]	$V_{\text{Air}}$ [m/s]	q	$We_{\text{Air}}$	$We_{\text{Jet}}$	$Re_{\text{Air}}$	$Re_{\text{Jet}}$	$Oh_{\text{Air}}$ $\times 10^3$	$Oh_{\text{Jet}}$ $\times 10^3$	D10 [ $\mu\text{m}$ ]	D32 [ $\mu\text{m}$ ]
11	□	19	49	62	47	2910	3701	12282	1.852	486.8	64.1	79.5



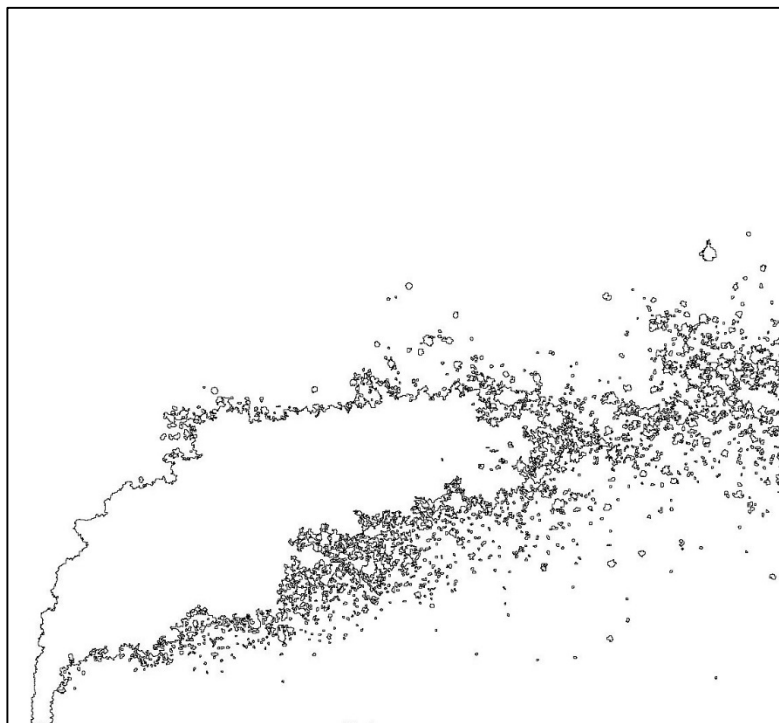
No.	Ref.	$V_{\text{Jet}}$ [m/s]	$V_{\text{Air}}$ [m/s]	q	$We_{\text{Air}}$	$We_{\text{Jet}}$	$Re_{\text{Air}}$	$Re_{\text{Jet}}$	$Oh_{\text{Air}}$ $\times 10^3$	$Oh_{\text{Jet}}$ $\times 10^3$	D10 [ $\mu\text{m}$ ]	D32 [ $\mu\text{m}$ ]
13	□	27	127	30	195	5820	4235	17369	3.298	578.9	57.6	65.4



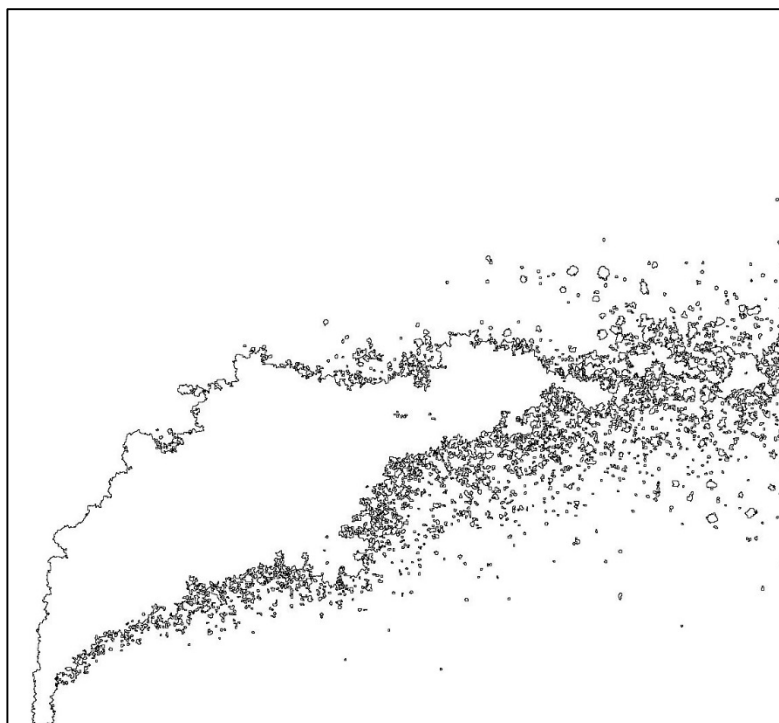
No.	Ref.	$V_{\text{Jet}}$ [m/s]	$V_{\text{Air}}$ [m/s]	q	$We_{\text{Air}}$	$We_{\text{Jet}}$	$Re_{\text{Air}}$	$Re_{\text{Jet}}$	$Oh_{\text{Air}}$ $\times 10^3$	$Oh_{\text{Jet}}$ $\times 10^3$	D10 [ $\mu\text{m}$ ]	D32 [ $\mu\text{m}$ ]
14	□	43	127	75	195	14550	4235	27463	3.298	727.9	57.1	63.3



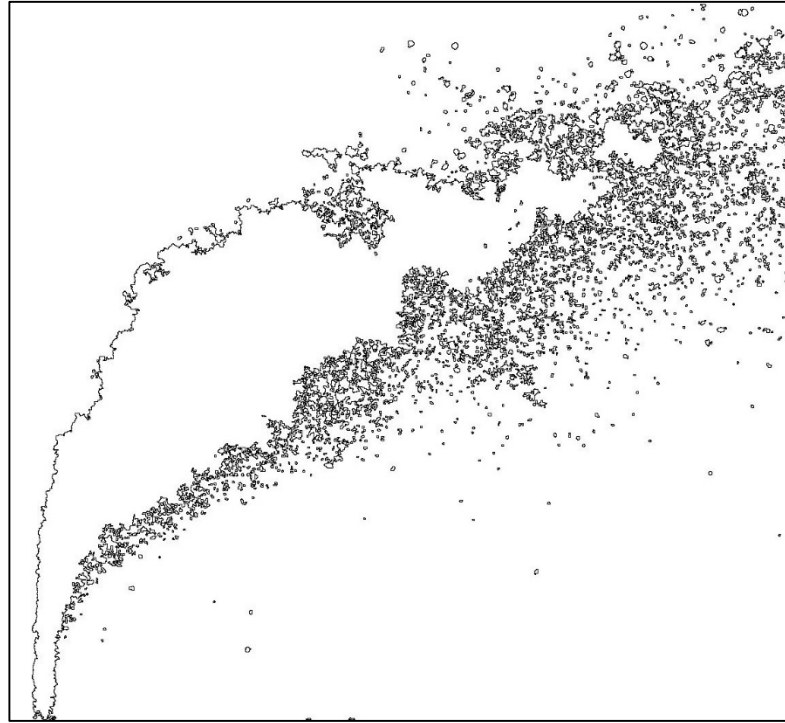
No.	Ref.	$V_{\text{Jet}}$ [m/s]	$V_{\text{Air}}$ [m/s]	q	$We_{\text{Air}}$	$We_{\text{Jet}}$	$Re_{\text{Air}}$	$Re_{\text{Jet}}$	$Oh_{\text{Air}}$ $\times 10^3$	$Oh_{\text{Jet}}$ $\times 10^3$	D10 [ $\mu\text{m}$ ]	D32 [ $\mu\text{m}$ ]
16	□	14	93	14	105	1455	3109	8685	3.298	409.3	61.3	75.0



No.	Ref.	$V_{\text{Jet}}$ [m/s]	$V_{\text{Air}}$ [m/s]	q	$We_{\text{Air}}$	$We_{\text{Jet}}$	$Re_{\text{Air}}$	$Re_{\text{Jet}}$	$Oh_{\text{Air}}$ $\times 10^3$	$Oh_{\text{Jet}}$ $\times 10^3$	D10 [ $\mu\text{m}$ ]	D32 [ $\mu\text{m}$ ]
17	□	19	93	28	105	2910	3109	12282	3.298	486.8	59.8	71.4



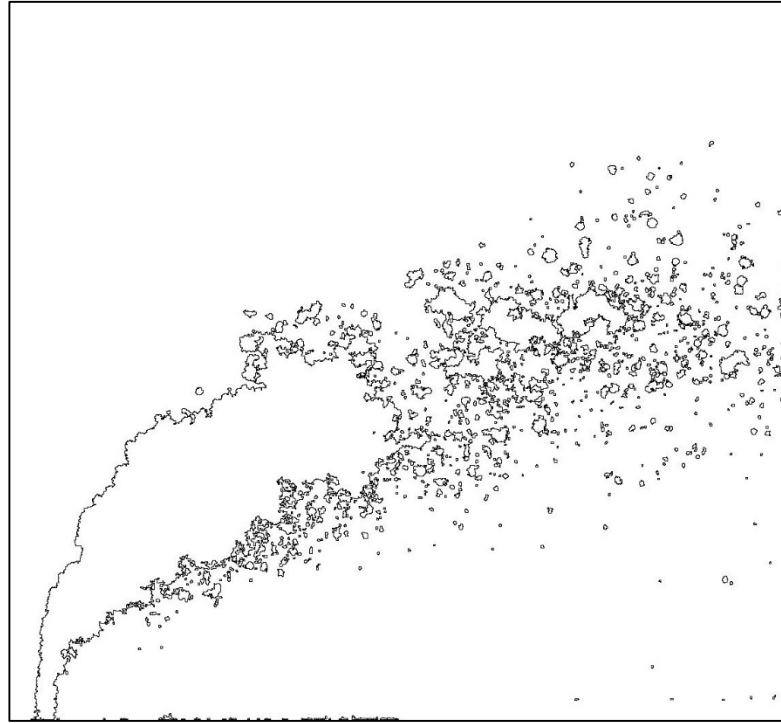
No.	Ref.	$V_{\text{Jet}}$ [m/s]	$V_{\text{Air}}$ [m/s]	q	$We_{\text{Air}}$	$We_{\text{Jet}}$	$Re_{\text{Air}}$	$Re_{\text{Jet}}$	$Oh_{\text{Air}}$ $\times 10^3$	$Oh_{\text{Jet}}$ $\times 10^3$	D10 [ $\mu\text{m}$ ]	D32 [ $\mu\text{m}$ ]
18	□	30	93	69	105	7275	3109	19419	3.298	612.1	58.5	68.1



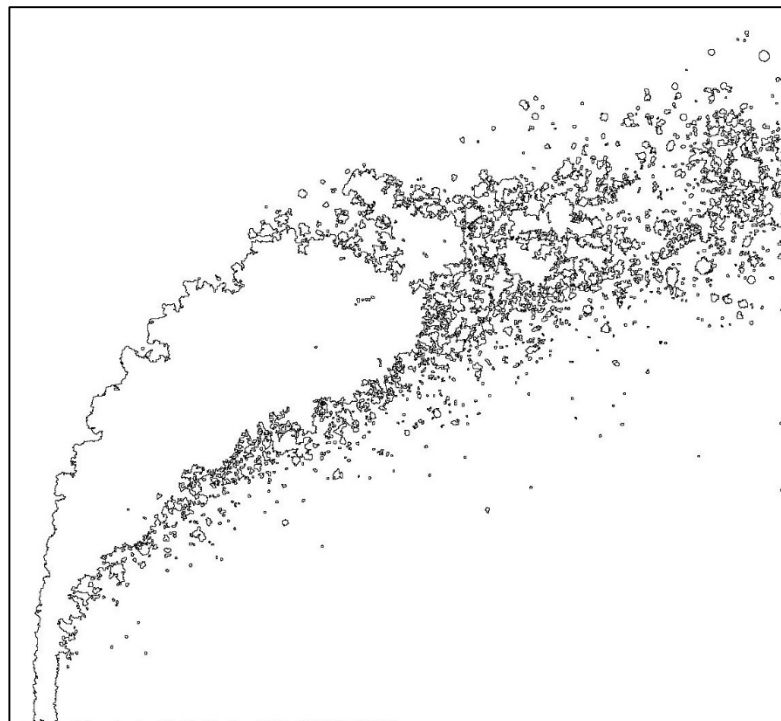
No.	Ref.	$V_{\text{Jet}}$ [m/s]	$V_{\text{Air}}$ [m/s]	q	$We_{\text{Air}}$	$We_{\text{Jet}}$	$Re_{\text{Air}}$	$Re_{\text{Jet}}$	$Oh_{\text{Air}}$ $\times 10^3$	$Oh_{\text{Jet}}$ $\times 10^3$	D10 [ $\mu\text{m}$ ]	D32 [ $\mu\text{m}$ ]
20	□	9	61	13	44	582	2022	5493	3.298	325.5	67.7	88.2



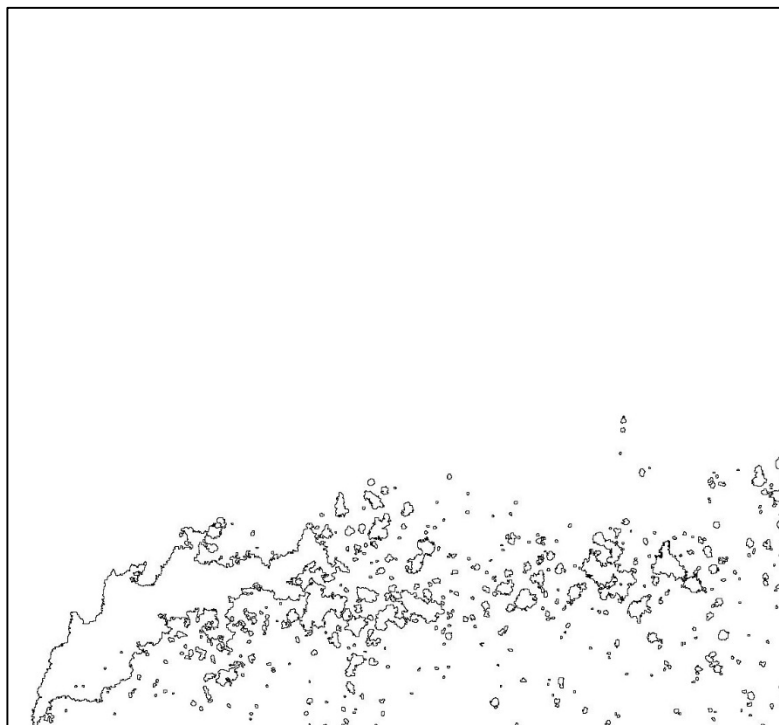
No.	Ref.	$V_{\text{Jet}}$ [m/s]	$V_{\text{Air}}$ [m/s]	q	$We_{\text{Air}}$	$We_{\text{Jet}}$	$Re_{\text{Air}}$	$Re_{\text{Jet}}$	$Oh_{\text{Air}}$ $\times 10^3$	$Oh_{\text{Jet}}$ $\times 10^3$	D10 [ $\mu\text{m}$ ]	D32 [ $\mu\text{m}$ ]
21	□	12	61	26	44	1164	2022	7768	3.298	387.1	64.9	82.8



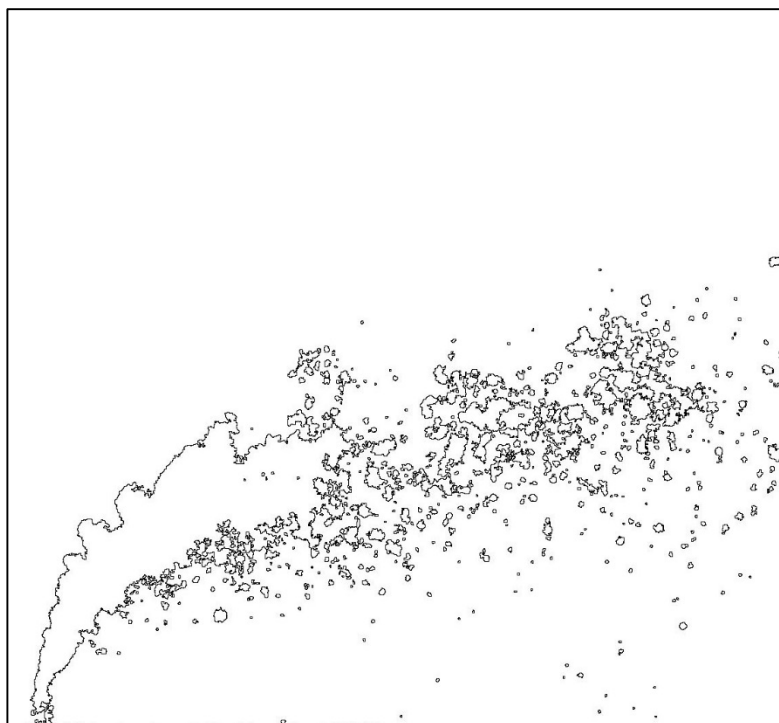
No.	Ref.	$V_{\text{Jet}}$ [m/s]	$V_{\text{Air}}$ [m/s]	q	$We_{\text{Air}}$	$We_{\text{Jet}}$	$Re_{\text{Air}}$	$Re_{\text{Jet}}$	$Oh_{\text{Air}}$ $\times 10^3$	$Oh_{\text{Jet}}$ $\times 10^3$	D10 [ $\mu\text{m}$ ]	D32 [ $\mu\text{m}$ ]
22	□	19	61	65	44	2910	2022	12282	3.298	486.8	62.2	77.2



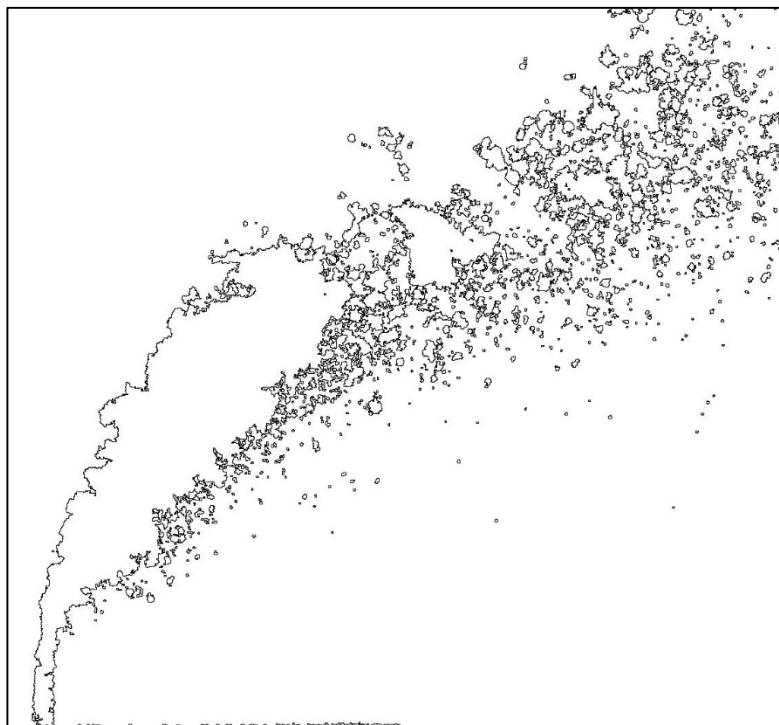
No.	Ref.	$V_{Jet}$ [m/s]	$V_{Air}$ [m/s]	q	$We_{Air}$	$We_{Jet}$	$Re_{Air}$	$Re_{Jet}$	$Oh_{Air}$ $\times 10^3$	$Oh_{Jet}$ $\times 10^3$	D10 [ $\mu m$ ]	D32 [ $\mu m$ ]
24	□	7	49	13	29	364	1622	4342	3.298	289.4	70.0	91.6



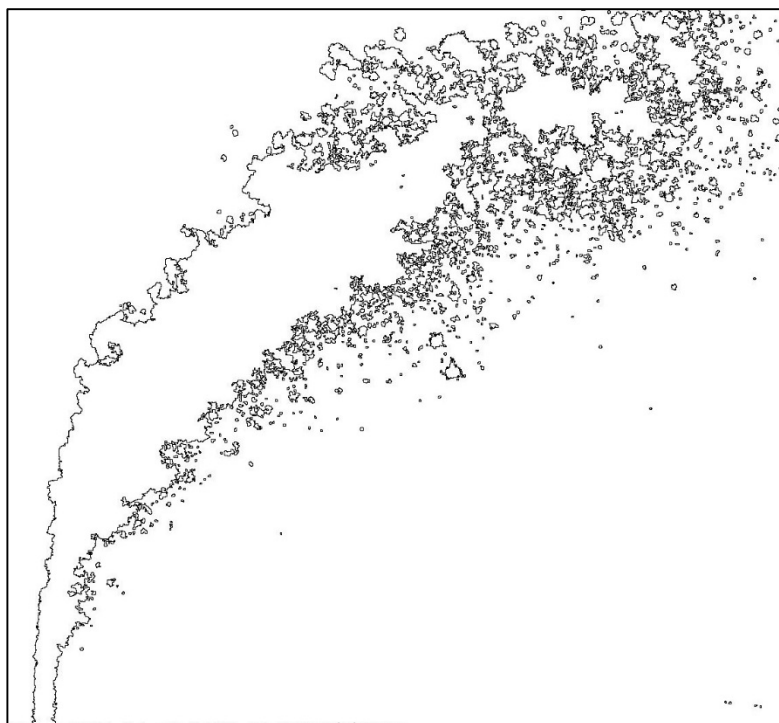
No.	Ref.	$V_{Jet}$ [m/s]	$V_{Air}$ [m/s]	q	$We_{Air}$	$We_{Jet}$	$Re_{Air}$	$Re_{Jet}$	$Oh_{Air}$ $\times 10^3$	$Oh_{Jet}$ $\times 10^3$	D10 [ $\mu m$ ]	D32 [ $\mu m$ ]
25	□	10	49	25	29	728	1622	6141	3.298	344.2	68.8	90.0



No.	Ref.	$V_{\text{Jet}}$ [m/s]	$V_{\text{Air}}$ [m/s]	q	$We_{\text{Air}}$	$We_{\text{Jet}}$	$Re_{\text{Air}}$	$Re_{\text{Jet}}$	$Oh_{\text{Air}}$ $\times 10^3$	$Oh_{\text{Jet}}$ $\times 10^3$	D10 [ $\mu\text{m}$ ]	D32 [ $\mu\text{m}$ ]
26	□	15	49	64	29	1819	1622	9710	3.298	432.8	64.9	82.2

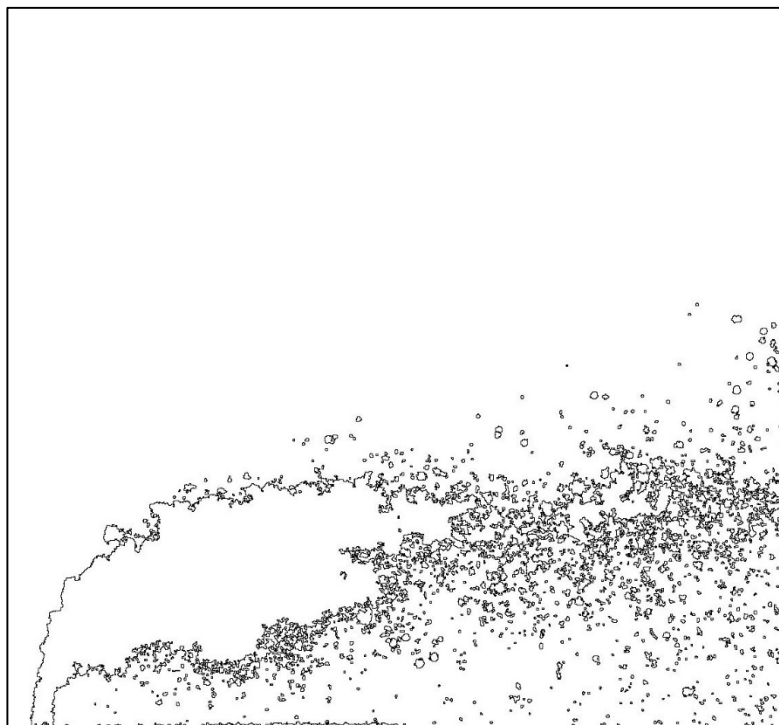


No.	Ref.	$V_{\text{Jet}}$ [m/s]	$V_{\text{Air}}$ [m/s]	q	$We_{\text{Air}}$	$We_{\text{Jet}}$	$Re_{\text{Air}}$	$Re_{\text{Jet}}$	$Oh_{\text{Air}}$ $\times 10^3$	$Oh_{\text{Jet}}$ $\times 10^3$	D10 [ $\mu\text{m}$ ]	D32 [ $\mu\text{m}$ ]
27	□	19	49	102	29	2910	1622	12282	3.298	486.8	63.4	79.0

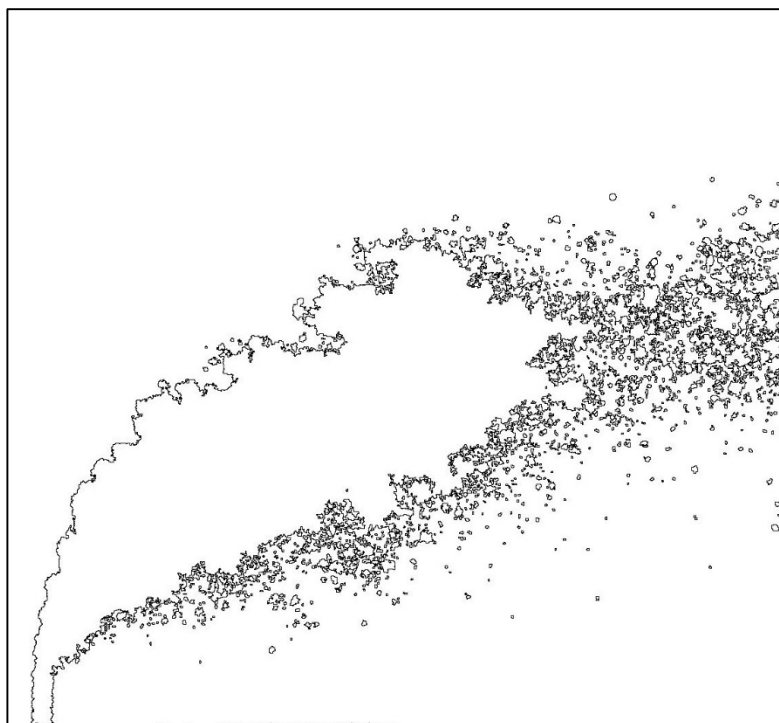




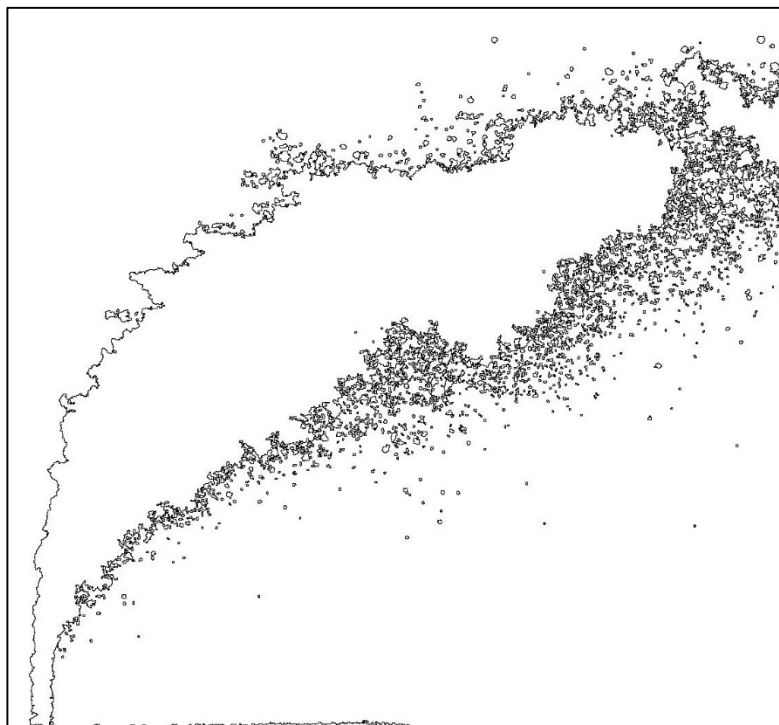
No.	Ref.	$V_{\text{Jet}}$ [m/s]	$V_{\text{Air}}$ [m/s]	q	$We_{\text{Air}}$	$We_{\text{Jet}}$	$Re_{\text{Air}}$	$Re_{\text{Jet}}$	$Oh_{\text{Air}}$ $\times 10^3$	$Oh_{\text{Jet}}$ $\times 10^3$	D10 [ $\mu\text{m}$ ]	D32 [ $\mu\text{m}$ ]
32	□	14	95	16	90	1455	2285	8685	4.154	409.3	63.1	77.8



No.	Ref.	$V_{\text{Jet}}$ [m/s]	$V_{\text{Air}}$ [m/s]	q	$We_{\text{Air}}$	$We_{\text{Jet}}$	$Re_{\text{Air}}$	$Re_{\text{Jet}}$	$Oh_{\text{Air}}$ $\times 10^3$	$Oh_{\text{Jet}}$ $\times 10^3$	D10 [ $\mu\text{m}$ ]	D32 [ $\mu\text{m}$ ]
33	□	19	95	32	90	2910	2285	12282	4.154	486.8	60.8	73.2



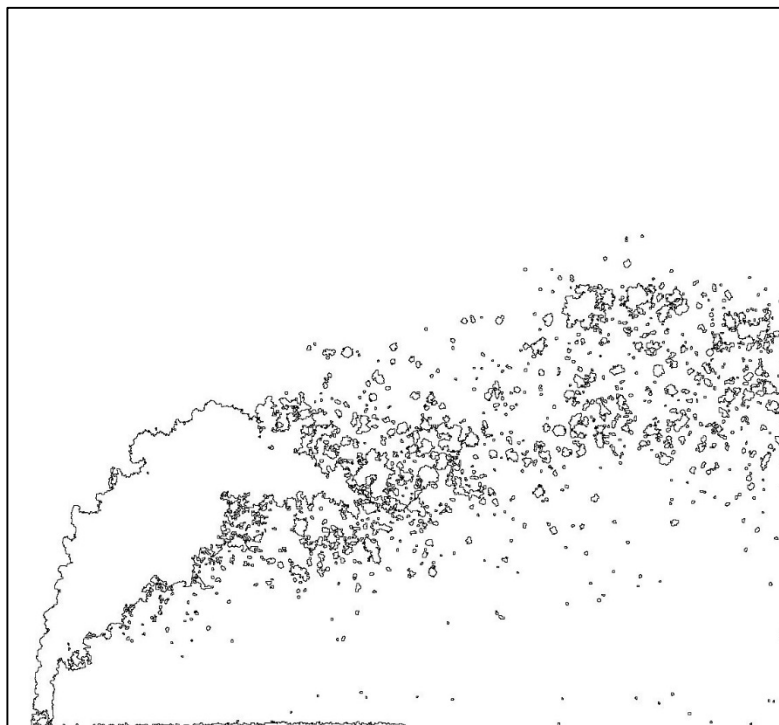
No.	Ref.	$V_{\text{Jet}}$ [m/s]	$V_{\text{Air}}$ [m/s]	q	$We_{\text{Air}}$	$We_{\text{Jet}}$	$Re_{\text{Air}}$	$Re_{\text{Jet}}$	$Oh_{\text{Air}}$ $\times 10^3$	$Oh_{\text{Jet}}$ $\times 10^3$	D10 [ $\mu\text{m}$ ]	D32 [ $\mu\text{m}$ ]
34	□	30	95	81	90	7275	2285	19419	4.154	612.1	59.4	70.4



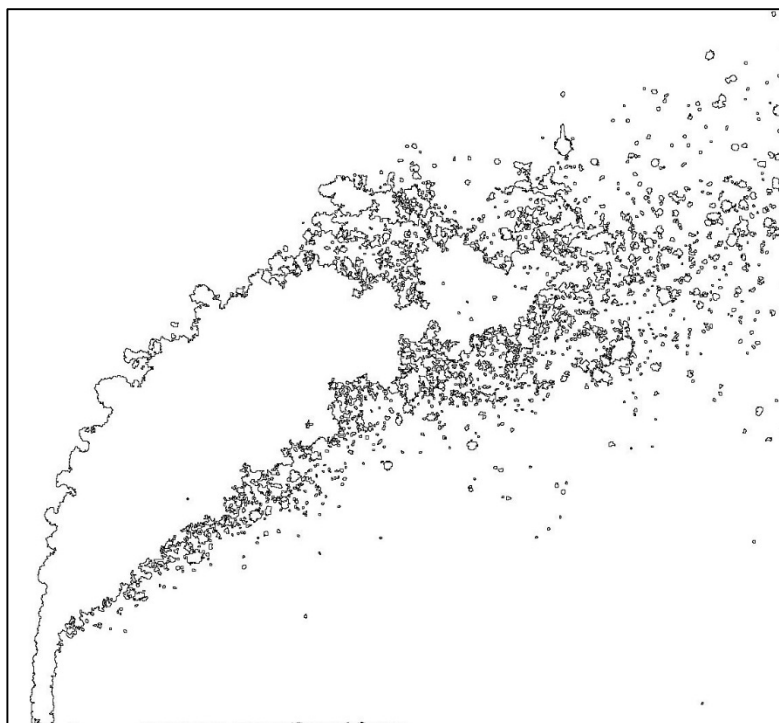
No.	Ref.	$V_{\text{Jet}}$ [m/s]	$V_{\text{Air}}$ [m/s]	q	$We_{\text{Air}}$	$We_{\text{Jet}}$	$Re_{\text{Air}}$	$Re_{\text{Jet}}$	$Oh_{\text{Air}}$ $\times 10^3$	$Oh_{\text{Jet}}$ $\times 10^3$	D10 [ $\mu\text{m}$ ]	D32 [ $\mu\text{m}$ ]
36	□	9	62	15	38	582	1490	5493	4.154	325.5	68.8	88.6



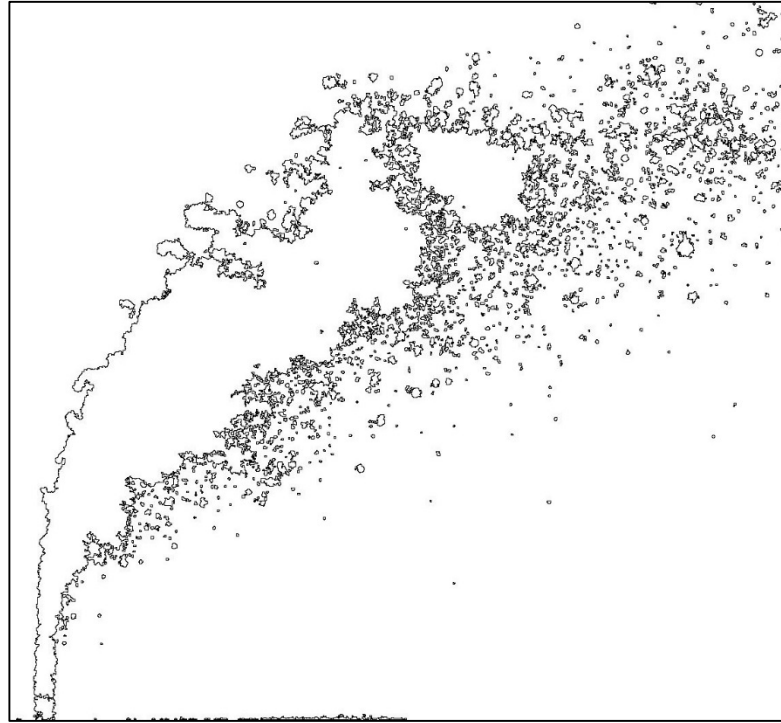
No.	Ref.	$V_{\text{Jet}}$ [m/s]	$V_{\text{Air}}$ [m/s]	q	$We_{\text{Air}}$	$We_{\text{Jet}}$	$Re_{\text{Air}}$	$Re_{\text{Jet}}$	$Oh_{\text{Air}}$ $\times 10^3$	$Oh_{\text{Jet}}$ $\times 10^3$	D10 [ $\mu\text{m}$ ]	D32 [ $\mu\text{m}$ ]
37	□	12	62	30	38	1164	1490	7768	4.154	387.1	66.1	83.9



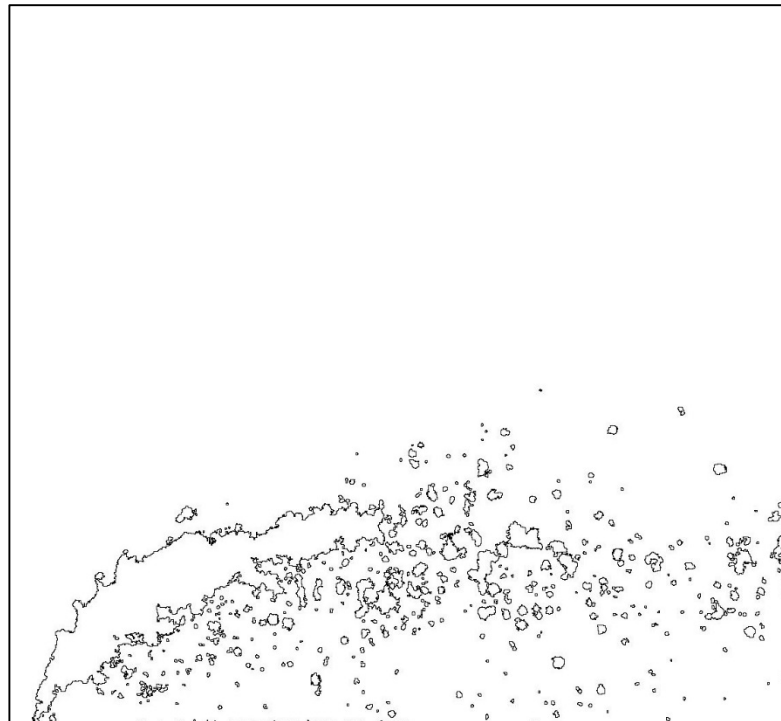
No.	Ref.	$V_{\text{Jet}}$ [m/s]	$V_{\text{Air}}$ [m/s]	q	$We_{\text{Air}}$	$We_{\text{Jet}}$	$Re_{\text{Air}}$	$Re_{\text{Jet}}$	$Oh_{\text{Air}}$ $\times 10^3$	$Oh_{\text{Jet}}$ $\times 10^3$	D10 [ $\mu\text{m}$ ]	D32 [ $\mu\text{m}$ ]
38	□	19	62	76	38	2910	1490	12282	4.154	486.8	63.4	79.4



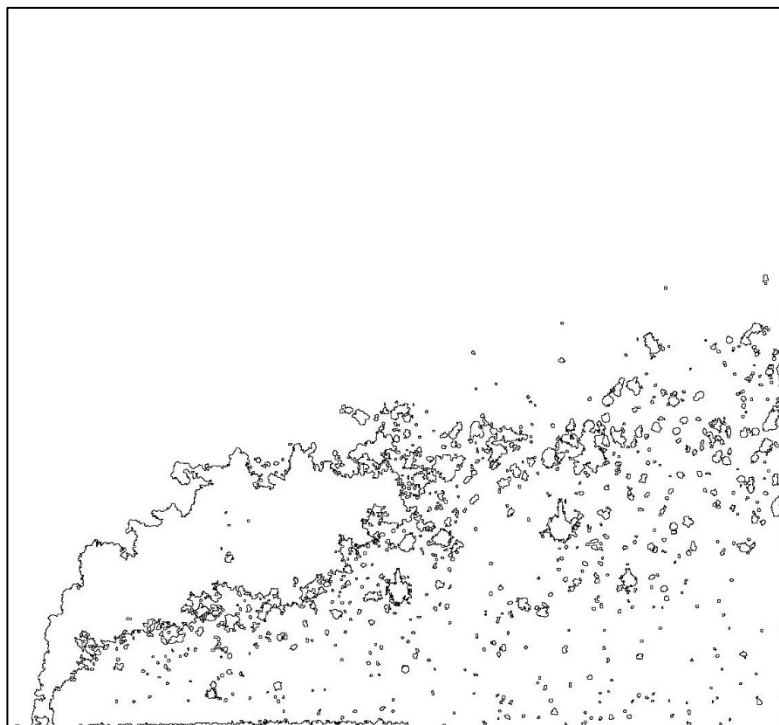
No.	Ref.	$V_{\text{Jet}}$ [m/s]	$V_{\text{Air}}$ [m/s]	q	$We_{\text{Air}}$	$We_{\text{Jet}}$	$Re_{\text{Air}}$	$Re_{\text{Jet}}$	$Oh_{\text{Air}}$ $\times 10^3$	$Oh_{\text{Jet}}$ $\times 10^3$	D10 [ $\mu\text{m}$ ]	D32 [ $\mu\text{m}$ ]
39	□	24	62	122	38	4656	1490	15535	4.154	547.5	62.4	77.1



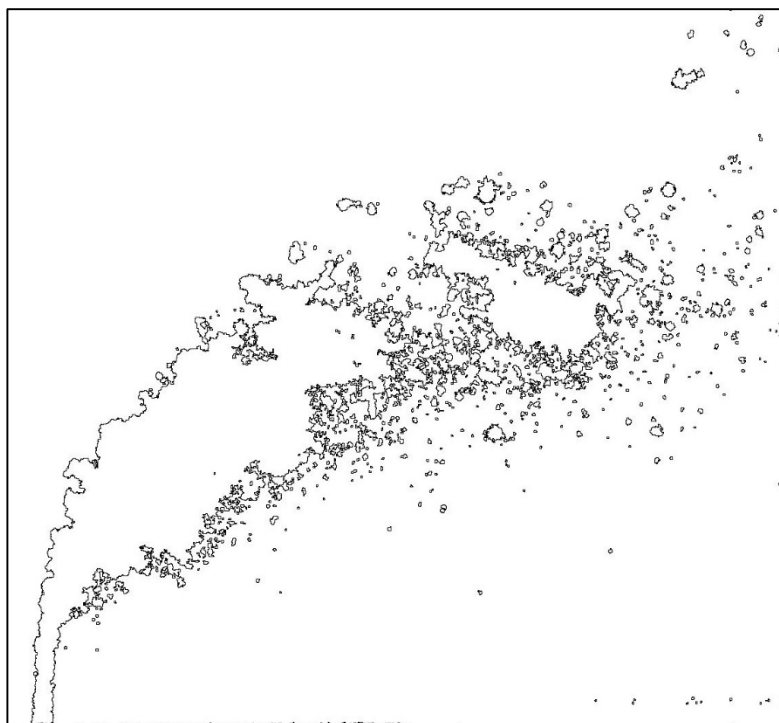
No.	Ref.	$V_{\text{Jet}}$ [m/s]	$V_{\text{Air}}$ [m/s]	q	$We_{\text{Air}}$	$We_{\text{Jet}}$	$Re_{\text{Air}}$	$Re_{\text{Jet}}$	$Oh_{\text{Air}}$ $\times 10^3$	$Oh_{\text{Jet}}$ $\times 10^3$	D10 [ $\mu\text{m}$ ]	D32 [ $\mu\text{m}$ ]
40	□	7	50	15	25	364	1196	4342	4.154	289.4	70.9	92.1



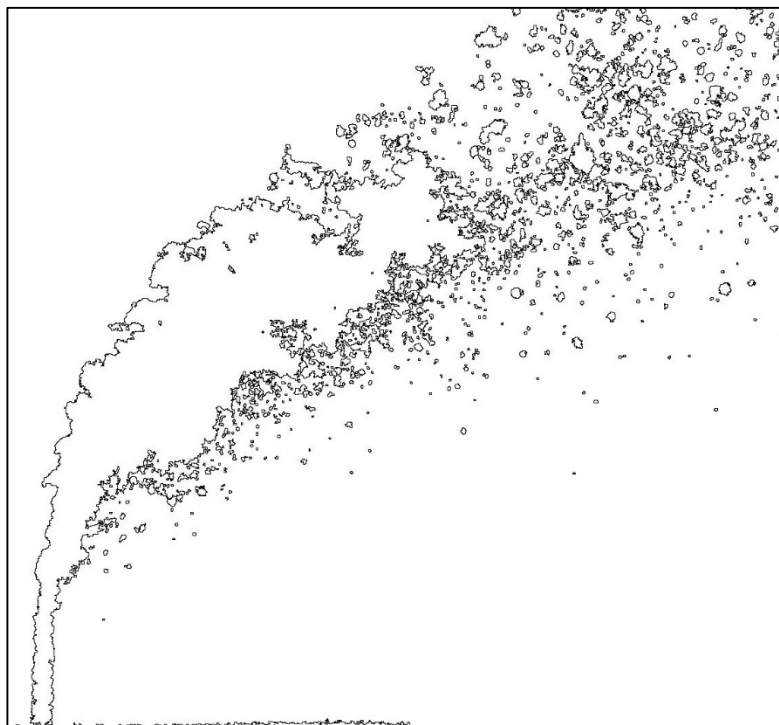
No.	Ref.	$V_{\text{Jet}}$ [m/s]	$V_{\text{Air}}$ [m/s]	q	$We_{\text{Air}}$	$We_{\text{Jet}}$	$Re_{\text{Air}}$	$Re_{\text{Jet}}$	$Oh_{\text{Air}}$ $\times 10^3$	$Oh_{\text{Jet}}$ $\times 10^3$	D10 [ $\mu\text{m}$ ]	D32 [ $\mu\text{m}$ ]
41	□	10	50	29	25	728	1196	6141	4.154	344.2	69.0	89.1



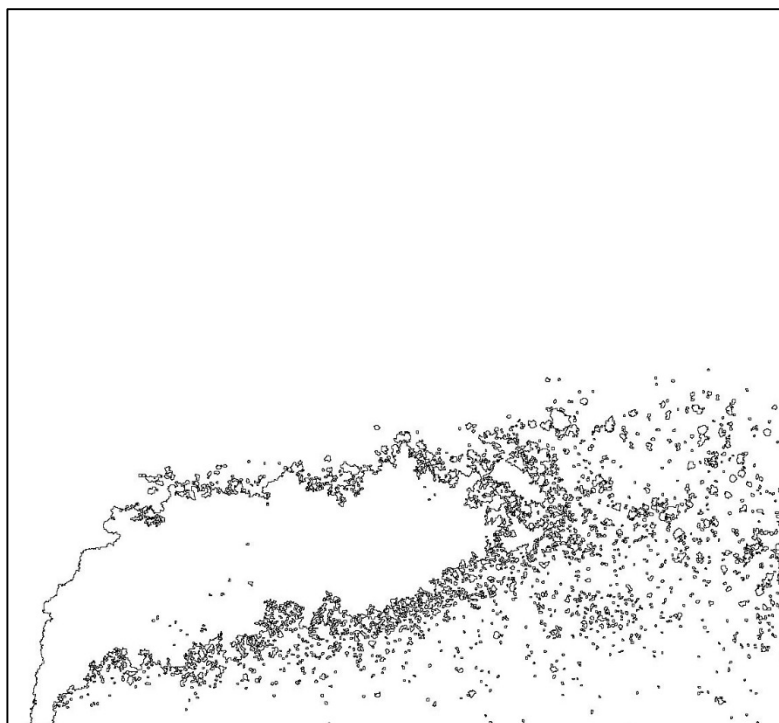
No.	Ref.	$V_{\text{Jet}}$ [m/s]	$V_{\text{Air}}$ [m/s]	q	$We_{\text{Air}}$	$We_{\text{Jet}}$	$Re_{\text{Air}}$	$Re_{\text{Jet}}$	$Oh_{\text{Air}}$ $\times 10^3$	$Oh_{\text{Jet}}$ $\times 10^3$	D10 [ $\mu\text{m}$ ]	D32 [ $\mu\text{m}$ ]
42	□	15	50	74	25	1819	1196	9710	4.154	432.8	66.3	84.5



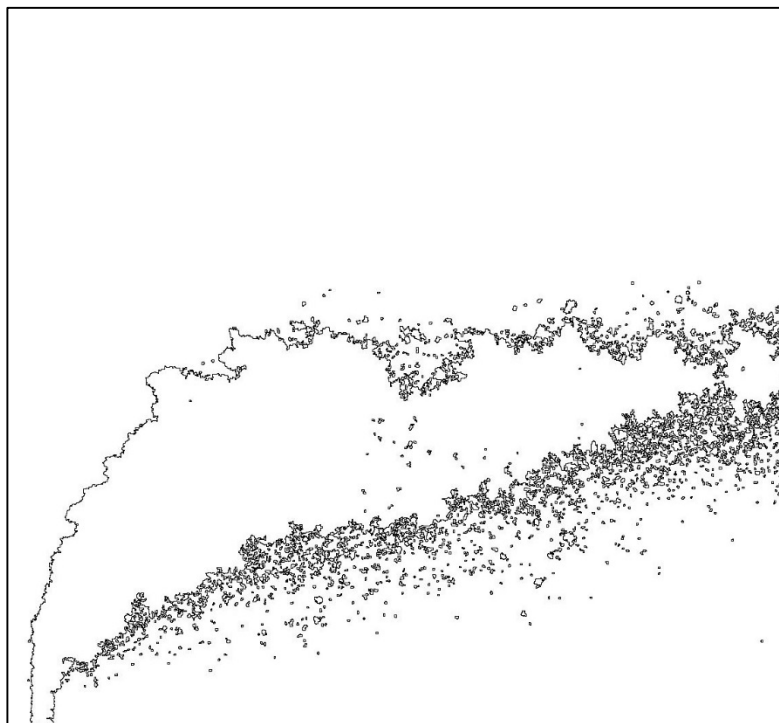
No.	Ref.	$V_{\text{Jet}}$ [m/s]	$V_{\text{Air}}$ [m/s]	q	$We_{\text{Air}}$	$We_{\text{Jet}}$	$Re_{\text{Air}}$	$Re_{\text{Jet}}$	$Oh_{\text{Air}}$ $\times 10^3$	$Oh_{\text{Jet}}$ $\times 10^3$	D10 [ $\mu\text{m}$ ]	D32 [ $\mu\text{m}$ ]
43	□	19	50	118	25	2910	1196	12282	4.154	486.8	65.1	82.1



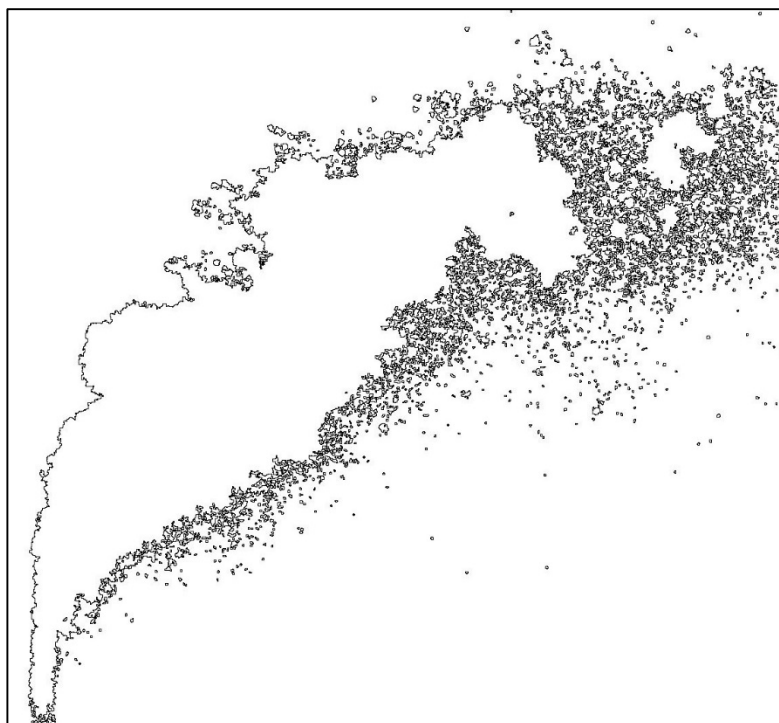
No.	Ref.	$V_{\text{Jet}}$ [m/s]	$V_{\text{Air}}$ [m/s]	q	$We_{\text{Air}}$	$We_{\text{Jet}}$	$Re_{\text{Air}}$	$Re_{\text{Jet}}$	$Oh_{\text{Air}}$ $\times 10^3$	$Oh_{\text{Jet}}$ $\times 10^3$	D10 [ $\mu\text{m}$ ]	D32 [ $\mu\text{m}$ ]
44	△	19	92	10	298	2910	12624	12283	1.368	486.8	59.4	69.5



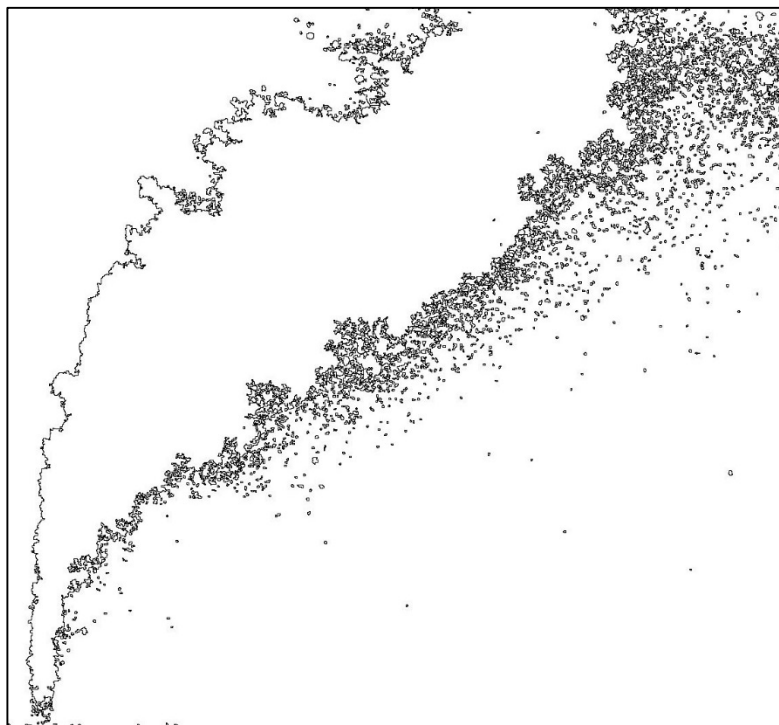
No.	Ref.	$V_{\text{Jet}}$ [m/s]	$V_{\text{Air}}$ [m/s]	q	$We_{\text{Air}}$	$We_{\text{Jet}}$	$Re_{\text{Air}}$	$Re_{\text{Jet}}$	$Oh_{\text{Air}}$ $\times 10^3$	$Oh_{\text{Jet}}$ $\times 10^3$	D10 [ $\mu\text{m}$ ]	D32 [ $\mu\text{m}$ ]
45	$\Delta$	27	92	20	298	5821	12624	17371	1.368	578.8	58.5	66.9



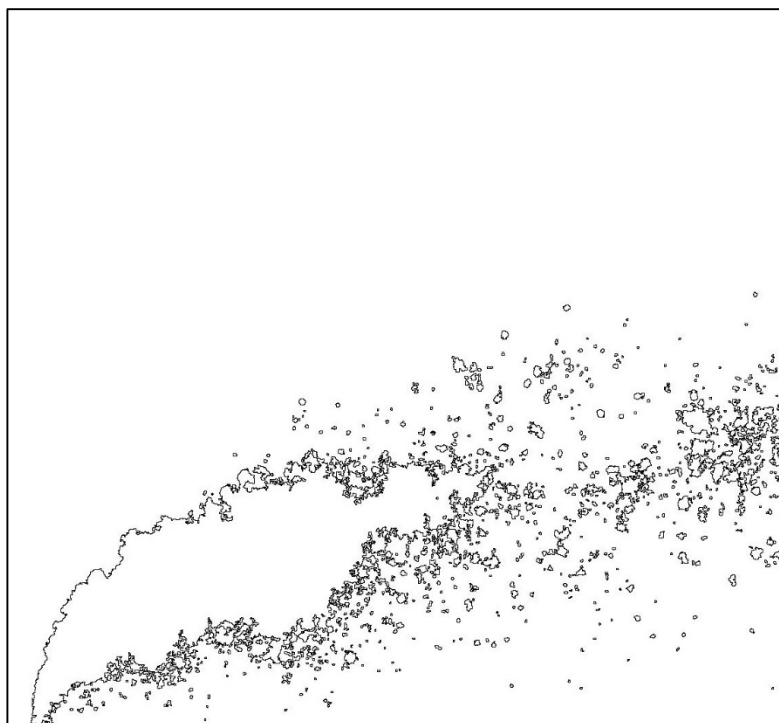
No.	Ref.	$V_{\text{Jet}}$ [m/s]	$V_{\text{Air}}$ [m/s]	q	$We_{\text{Air}}$	$We_{\text{Jet}}$	$Re_{\text{Air}}$	$Re_{\text{Jet}}$	$Oh_{\text{Air}}$ $\times 10^3$	$Oh_{\text{Jet}}$ $\times 10^3$	D10 [ $\mu\text{m}$ ]	D32 [ $\mu\text{m}$ ]
46	$\Delta$	43	92	49	298	14551	12624	27466	1.368	727.9	57.7	65.2



No.	Ref.	$V_{Jet}$ [m/s]	$V_{Air}$ [m/s]	q	$We_{Air}$	$We_{Jet}$	$Re_{Air}$	$Re_{Jet}$	$Oh_{Air}$ $\times 10^3$	$Oh_{Jet}$ $\times 10^3$	D10 [ $\mu m$ ]	D32 [ $\mu m$ ]
47	$\Delta$	54	92	78	298	23282	12624	34743	1.368	818.6	57.1	63.2

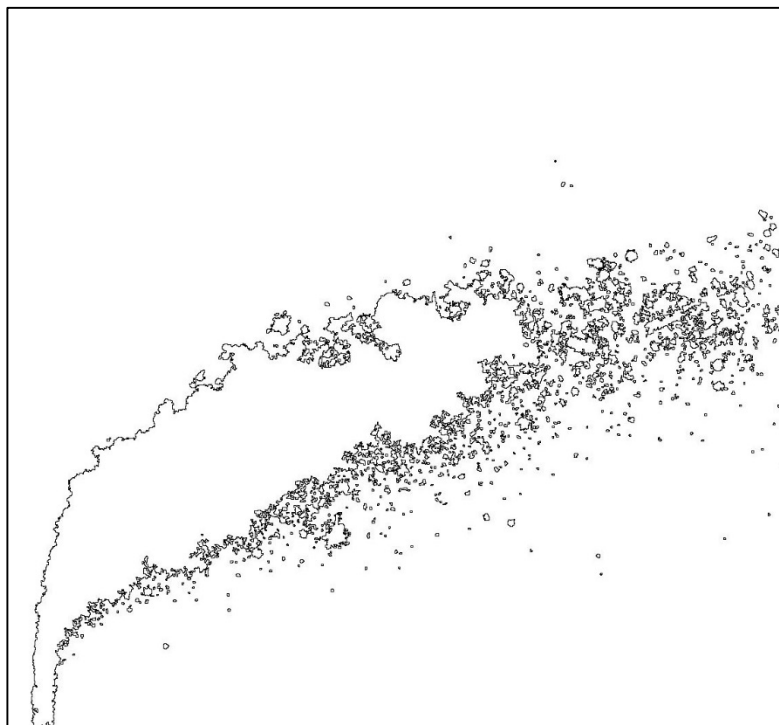


No.	Ref.	$V_{Jet}$ [m/s]	$V_{Air}$ [m/s]	q	$We_{Air}$	$We_{Jet}$	$Re_{Air}$	$Re_{Jet}$	$Oh_{Air}$ $\times 10^3$	$Oh_{Jet}$ $\times 10^3$	D10 [ $\mu m$ ]	D32 [ $\mu m$ ]
48	$\Delta$	14	65	10	150	1455	8956	8686	1.368	409.3	63.8	78.8

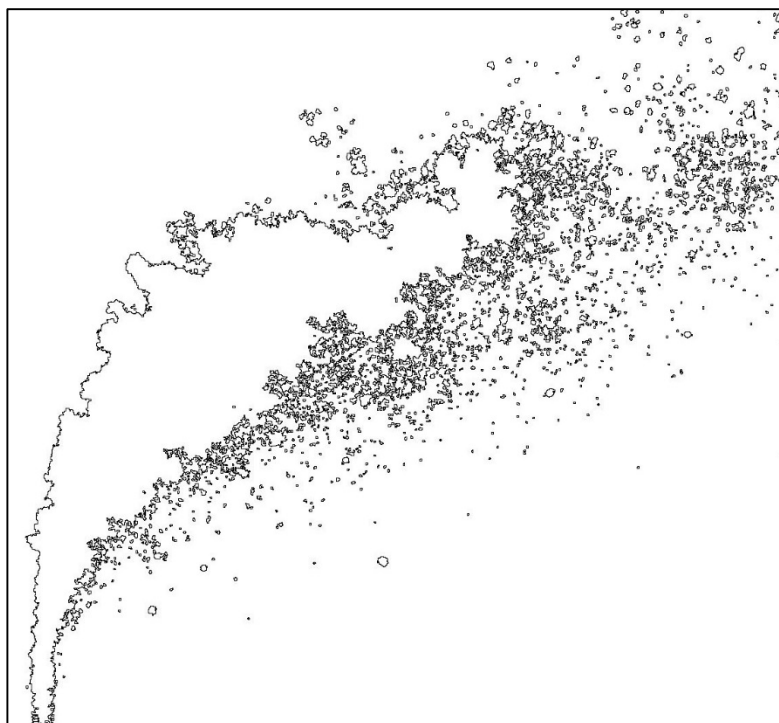




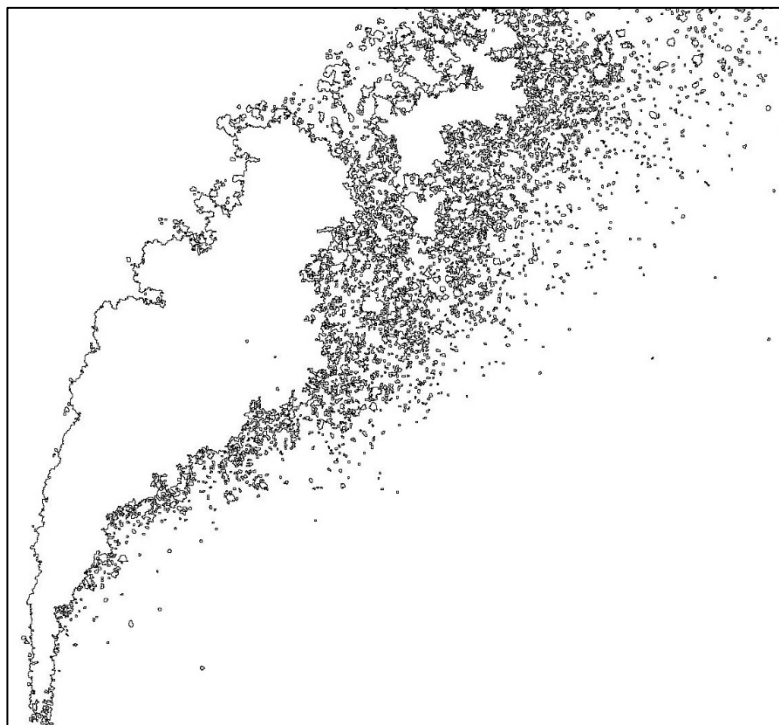
No.	Ref.	$V_{\text{Jet}}$ [m/s]	$V_{\text{Air}}$ [m/s]	q	$We_{\text{Air}}$	$We_{\text{Jet}}$	$Re_{\text{Air}}$	$Re_{\text{Jet}}$	$Oh_{\text{Air}}$ $\times 10^3$	$Oh_{\text{Jet}}$ $\times 10^3$	D10 [ $\mu\text{m}$ ]	D32 [ $\mu\text{m}$ ]
49	$\Delta$	19	65	19	150	2910	8956	12283	1.368	486.8	61.6	74.5



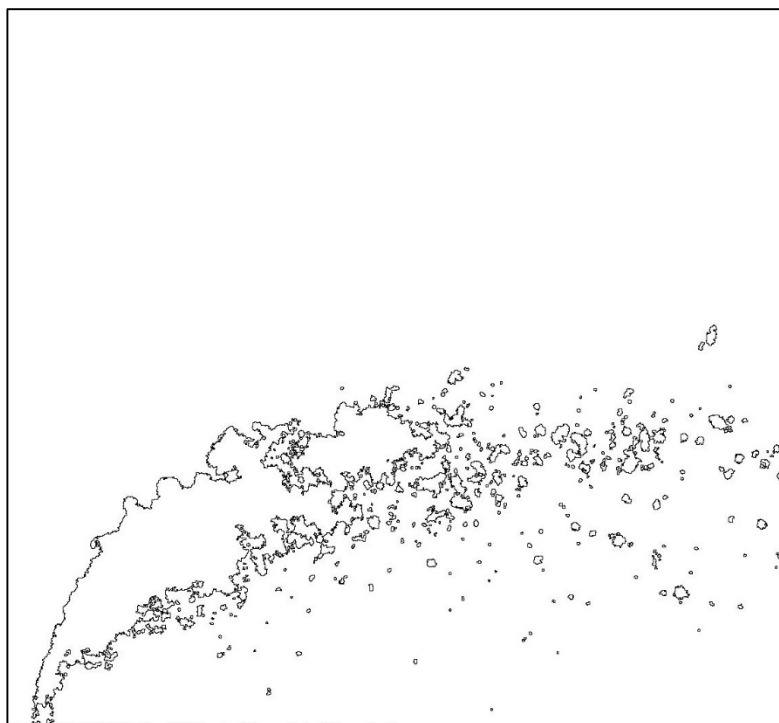
No.	Ref.	$V_{\text{Jet}}$ [m/s]	$V_{\text{Air}}$ [m/s]	q	$We_{\text{Air}}$	$We_{\text{Jet}}$	$Re_{\text{Air}}$	$Re_{\text{Jet}}$	$Oh_{\text{Air}}$ $\times 10^3$	$Oh_{\text{Jet}}$ $\times 10^3$	D10 [ $\mu\text{m}$ ]	D32 [ $\mu\text{m}$ ]
50	$\Delta$	30	65	48	150	7276	8956	19422	1.368	612.1	59.8	70.7



No.	Ref.	$V_{\text{Jet}}$ [m/s]	$V_{\text{Air}}$ [m/s]	q	$We_{\text{Air}}$	$We_{\text{Jet}}$	$Re_{\text{Air}}$	$Re_{\text{Jet}}$	$Oh_{\text{Air}}$ $\times 10^3$	$Oh_{\text{Jet}}$ $\times 10^3$	D10 [ $\mu\text{m}$ ]	D32 [ $\mu\text{m}$ ]
51	$\Delta$	38	65	77	150	11641	8956	24567	1.368	688.4	58.5	66.7



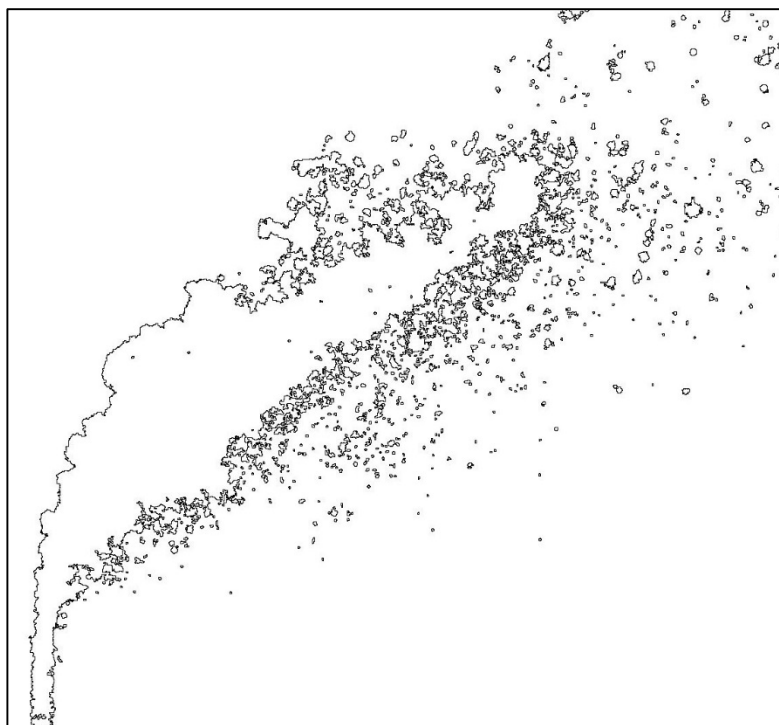
No.	Ref.	$V_{\text{Jet}}$ [m/s]	$V_{\text{Air}}$ [m/s]	q	$We_{\text{Air}}$	$We_{\text{Jet}}$	$Re_{\text{Air}}$	$Re_{\text{Jet}}$	$Oh_{\text{Air}}$ $\times 10^3$	$Oh_{\text{Jet}}$ $\times 10^3$	D10 [ $\mu\text{m}$ ]	D32 [ $\mu\text{m}$ ]
52	$\Delta$	9	41	10	60	582	5665	5493	1.368	325.5	68.4	87.6



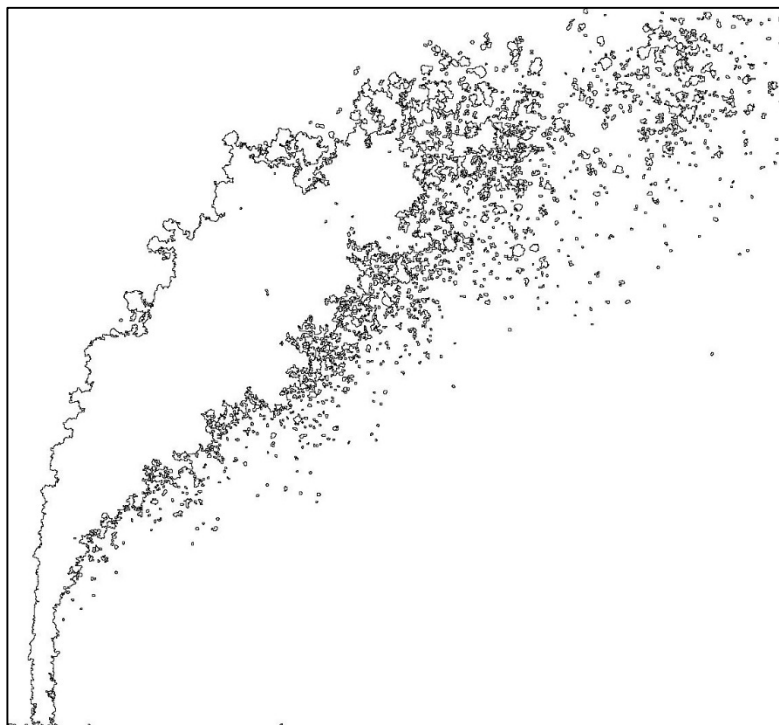
No.	Ref.	$V_{\text{Jet}}$ [m/s]	$V_{\text{Air}}$ [m/s]	q	$We_{\text{Air}}$	$We_{\text{Jet}}$	$Re_{\text{Air}}$	$Re_{\text{Jet}}$	$Oh_{\text{Air}}$ $\times 10^3$	$Oh_{\text{Jet}}$ $\times 10^3$	D10 [ $\mu\text{m}$ ]	D32 [ $\mu\text{m}$ ]
53	$\Delta$	12	41	19	60	1164	5665	7769	1.368	387.1	66.5	84.1



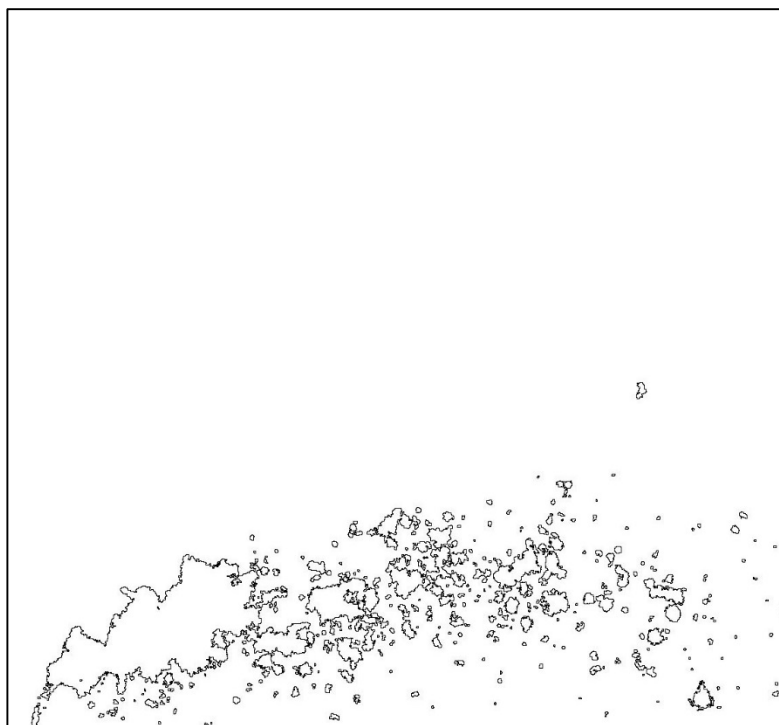
No.	Ref.	$V_{\text{Jet}}$ [m/s]	$V_{\text{Air}}$ [m/s]	q	$We_{\text{Air}}$	$We_{\text{Jet}}$	$Re_{\text{Air}}$	$Re_{\text{Jet}}$	$Oh_{\text{Air}}$ $\times 10^3$	$Oh_{\text{Jet}}$ $\times 10^3$	D10 [ $\mu\text{m}$ ]	D32 [ $\mu\text{m}$ ]
54	$\Delta$	19	41	48	60	2910	5665	12283	1.368	486.8	64.1	79.3



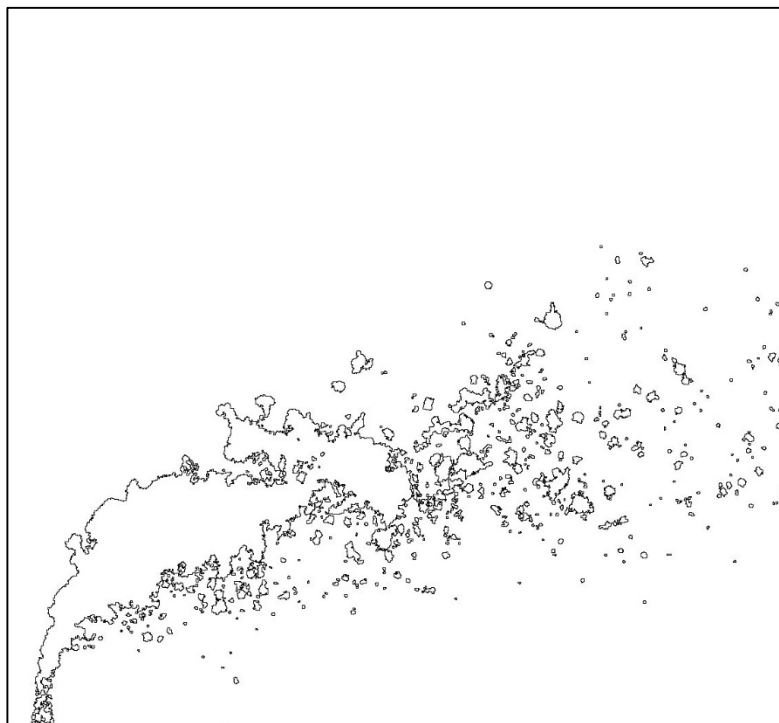
No.	Ref.	$V_{\text{Jet}}$ [m/s]	$V_{\text{Air}}$ [m/s]	q	$We_{\text{Air}}$	$We_{\text{Jet}}$	$Re_{\text{Air}}$	$Re_{\text{Jet}}$	$Oh_{\text{Air}}$ $\times 10^3$	$Oh_{\text{Jet}}$ $\times 10^3$	D10 [ $\mu\text{m}$ ]	D32 [ $\mu\text{m}$ ]
55	$\Delta$	24	41	77	60	4656	5665	15537	1.368	547.4	62.1	75.2



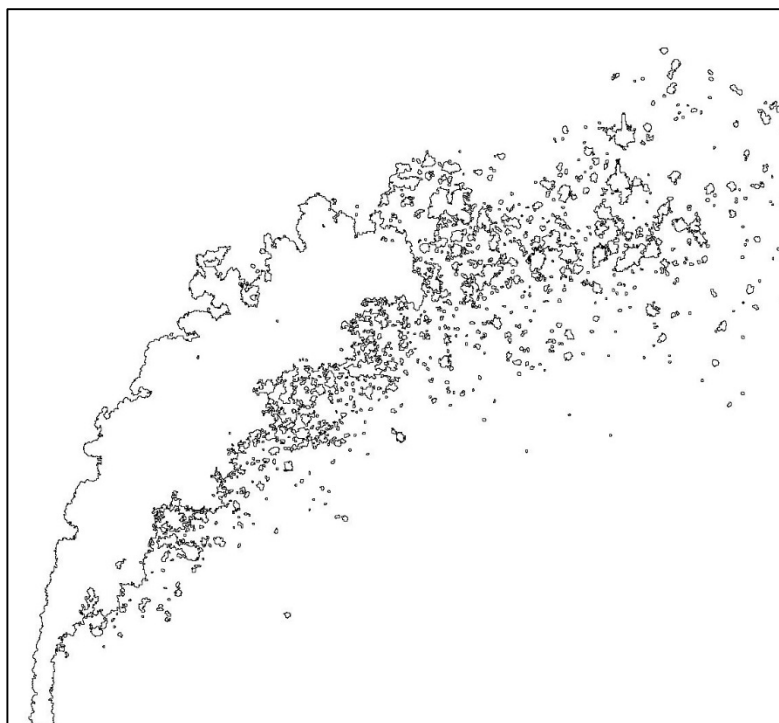
No.	Ref.	$V_{\text{Jet}}$ [m/s]	$V_{\text{Air}}$ [m/s]	q	$We_{\text{Air}}$	$We_{\text{Jet}}$	$Re_{\text{Air}}$	$Re_{\text{Jet}}$	$Oh_{\text{Air}}$ $\times 10^3$	$Oh_{\text{Jet}}$ $\times 10^3$	D10 [ $\mu\text{m}$ ]	D32 [ $\mu\text{m}$ ]
56	$\Delta$	7	33	10	38	364	4478	4343	1.368	289.4	69.1	88.7



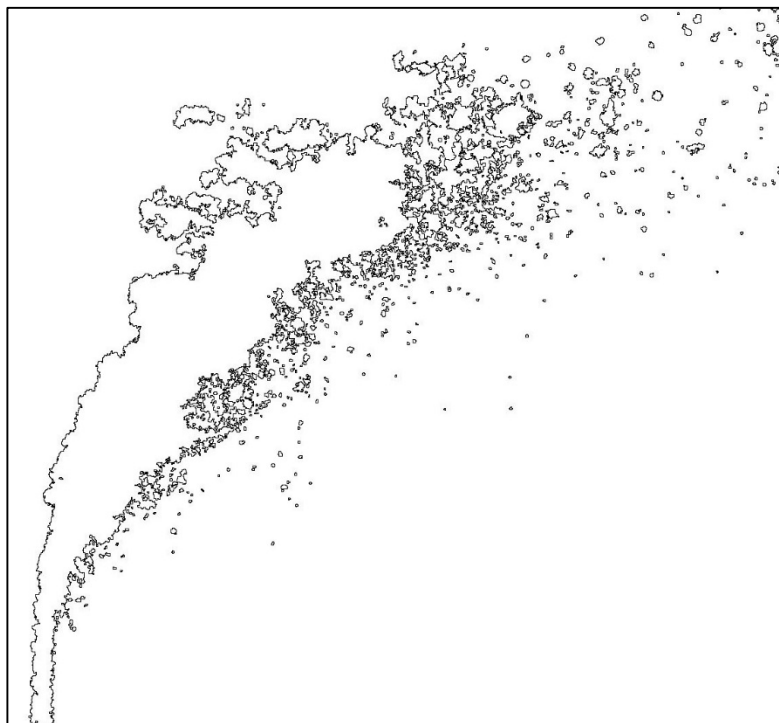
No.	Ref.	$V_{\text{Jet}}$ [m/s]	$V_{\text{Air}}$ [m/s]	q	$We_{\text{Air}}$	$We_{\text{Jet}}$	$Re_{\text{Air}}$	$Re_{\text{Jet}}$	$Oh_{\text{Air}}$ $\times 10^3$	$Oh_{\text{Jet}}$ $\times 10^3$	D10 [ $\mu\text{m}$ ]	D32 [ $\mu\text{m}$ ]
57	$\Delta$	10	33	19	38	728	4478	6142	1.368	344.2	68.5	88.4



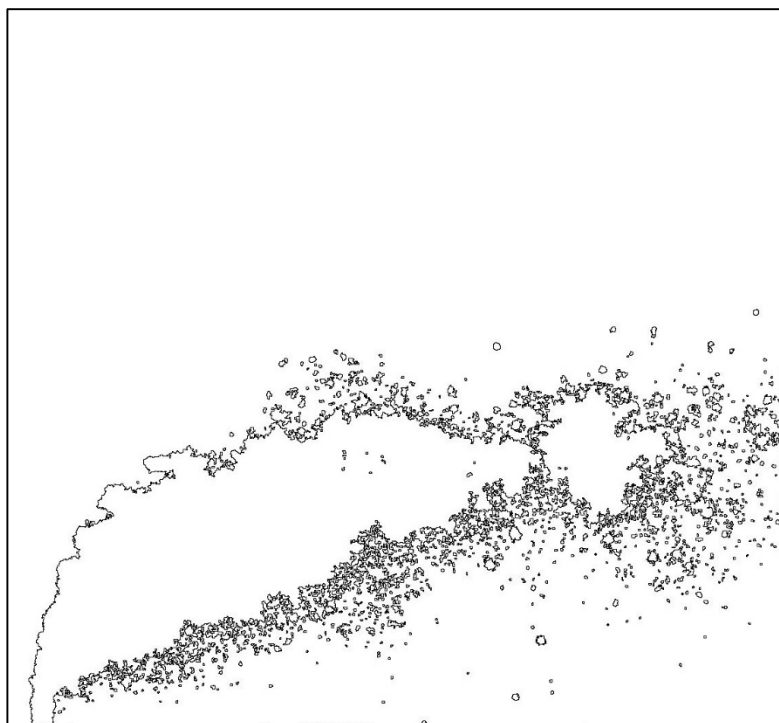
No.	Ref.	$V_{\text{Jet}}$ [m/s]	$V_{\text{Air}}$ [m/s]	q	$We_{\text{Air}}$	$We_{\text{Jet}}$	$Re_{\text{Air}}$	$Re_{\text{Jet}}$	$Oh_{\text{Air}}$ $\times 10^3$	$Oh_{\text{Jet}}$ $\times 10^3$	D10 [ $\mu\text{m}$ ]	D32 [ $\mu\text{m}$ ]
58	$\Delta$	15	33	48	38	1819	4478	9711	1.368	432.8	65.9	82.7



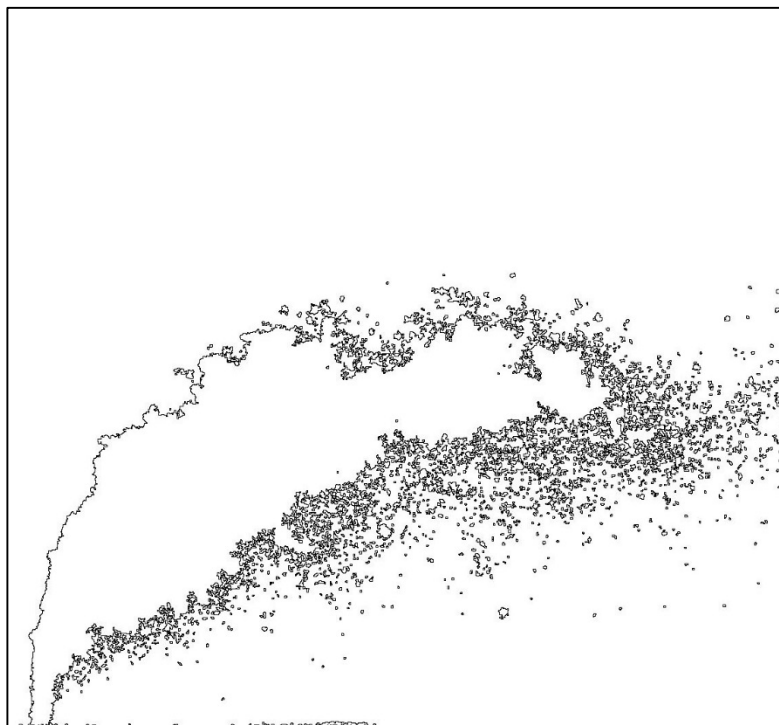
No.	Ref.	$V_{\text{Jet}}$ [m/s]	$V_{\text{Air}}$ [m/s]	q	$We_{\text{Air}}$	$We_{\text{Jet}}$	$Re_{\text{Air}}$	$Re_{\text{Jet}}$	$Oh_{\text{Air}}$ $\times 10^3$	$Oh_{\text{Jet}}$ $\times 10^3$	D10 [ $\mu\text{m}$ ]	D32 [ $\mu\text{m}$ ]
59	$\triangle$	19	33	77	38	2910	4478	12283	1.368	486.8	64.2	78.6



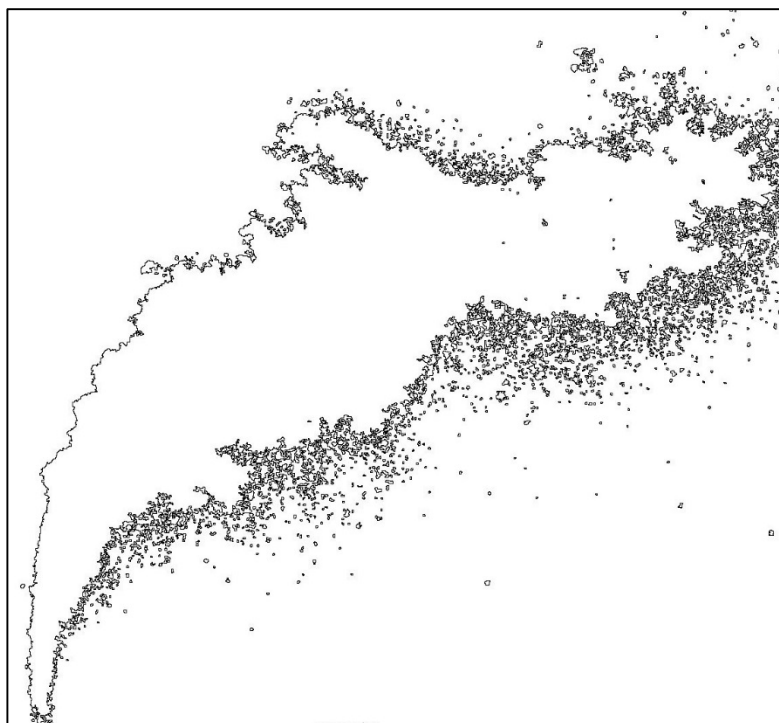
No.	Ref.	$V_{\text{Jet}}$ [m/s]	$V_{\text{Air}}$ [m/s]	q	$We_{\text{Air}}$	$We_{\text{Jet}}$	$Re_{\text{Air}}$	$Re_{\text{Jet}}$	$Oh_{\text{Air}}$ $\times 10^3$	$Oh_{\text{Jet}}$ $\times 10^3$	D10 [ $\mu\text{m}$ ]	D32 [ $\mu\text{m}$ ]
60	$\triangle$	19	92	15	188	2910	5633	12283	2.437	486.8	58.8	68.5



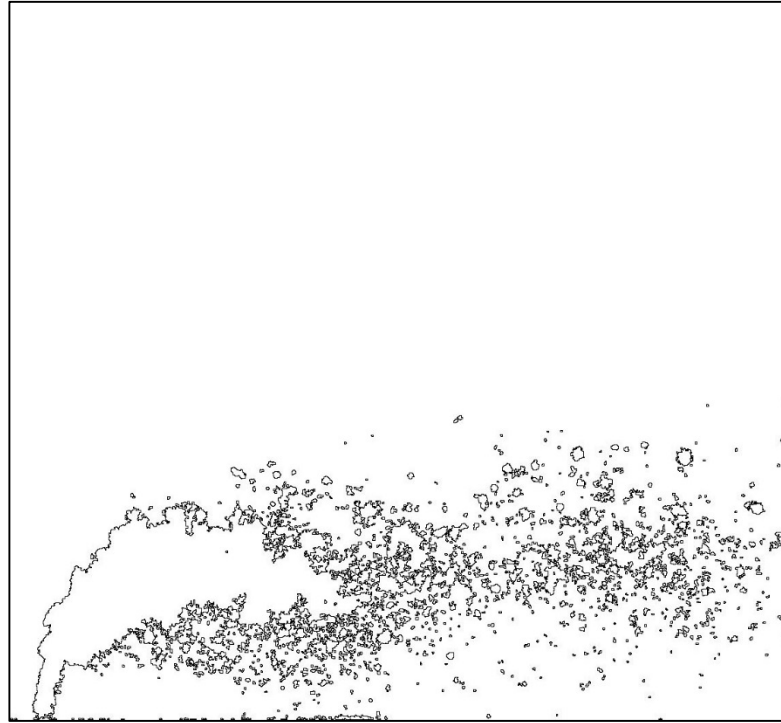
No.	Ref.	$V_{\text{Jet}}$ [m/s]	$V_{\text{Air}}$ [m/s]	q	$We_{\text{Air}}$	$We_{\text{Jet}}$	$Re_{\text{Air}}$	$Re_{\text{Jet}}$	$Oh_{\text{Air}}$ $\times 10^3$	$Oh_{\text{Jet}}$ $\times 10^3$	D10 [ $\mu\text{m}$ ]	D32 [ $\mu\text{m}$ ]
61	$\triangle$	27	92	31	188	5821	5633	17371	2.437	578.8	57.8	65.4



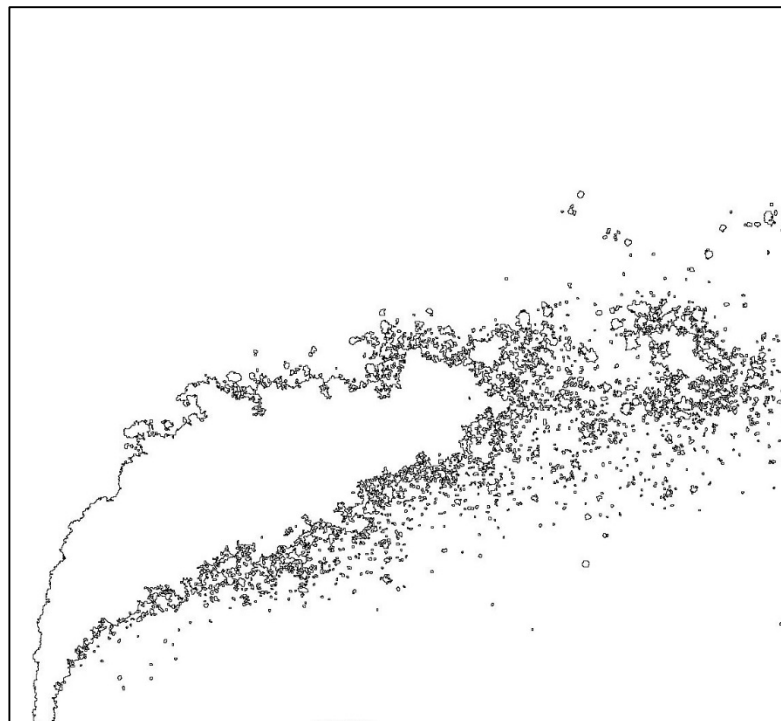
No.	Ref.	$V_{\text{Jet}}$ [m/s]	$V_{\text{Air}}$ [m/s]	q	$We_{\text{Air}}$	$We_{\text{Jet}}$	$Re_{\text{Air}}$	$Re_{\text{Jet}}$	$Oh_{\text{Air}}$ $\times 10^3$	$Oh_{\text{Jet}}$ $\times 10^3$	D10 [ $\mu\text{m}$ ]	D32 [ $\mu\text{m}$ ]
62	$\triangle$	43	92	77	188	14551	5633	27466	2.437	727.9	57.0	63.4



No.	Ref.	$V_{\text{Jet}}$ [m/s]	$V_{\text{Air}}$ [m/s]	q	$We_{\text{Air}}$	$We_{\text{Jet}}$	$Re_{\text{Air}}$	$Re_{\text{Jet}}$	$Oh_{\text{Air}}$ $\times 10^3$	$Oh_{\text{Jet}}$ $\times 10^3$	D10 [ $\mu\text{m}$ ]	D32 [ $\mu\text{m}$ ]
63	$\triangle$	14	68	14	102	1455	4146	8686	2.437	409.3	62.8	78.5

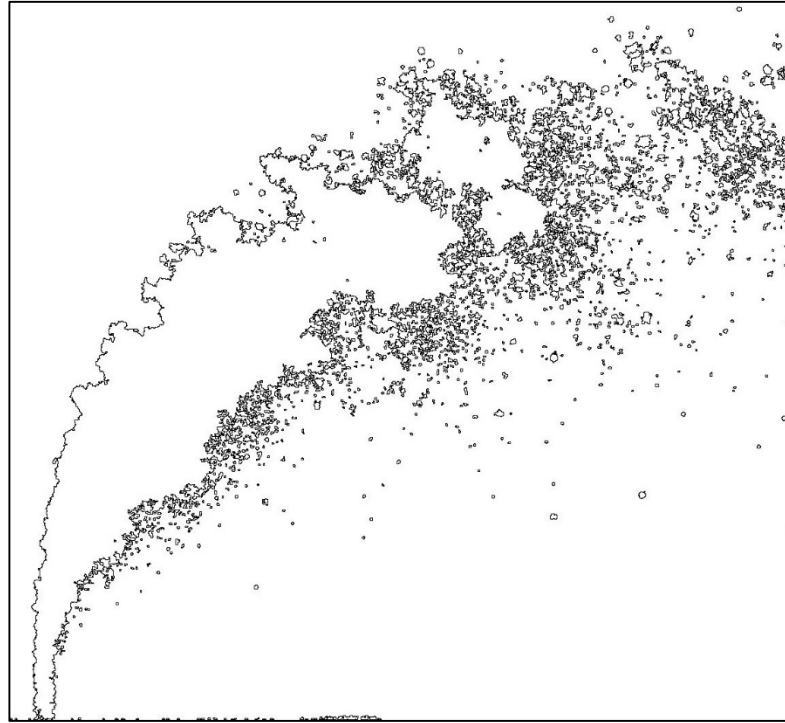


No.	Ref.	$V_{\text{Jet}}$ [m/s]	$V_{\text{Air}}$ [m/s]	q	$We_{\text{Air}}$	$We_{\text{Jet}}$	$Re_{\text{Air}}$	$Re_{\text{Jet}}$	$Oh_{\text{Air}}$ $\times 10^3$	$Oh_{\text{Jet}}$ $\times 10^3$	D10 [ $\mu\text{m}$ ]	D32 [ $\mu\text{m}$ ]
64	$\triangle$	19	68	28	102	2910	4146	12283	2.437	486.8	60.5	73.1

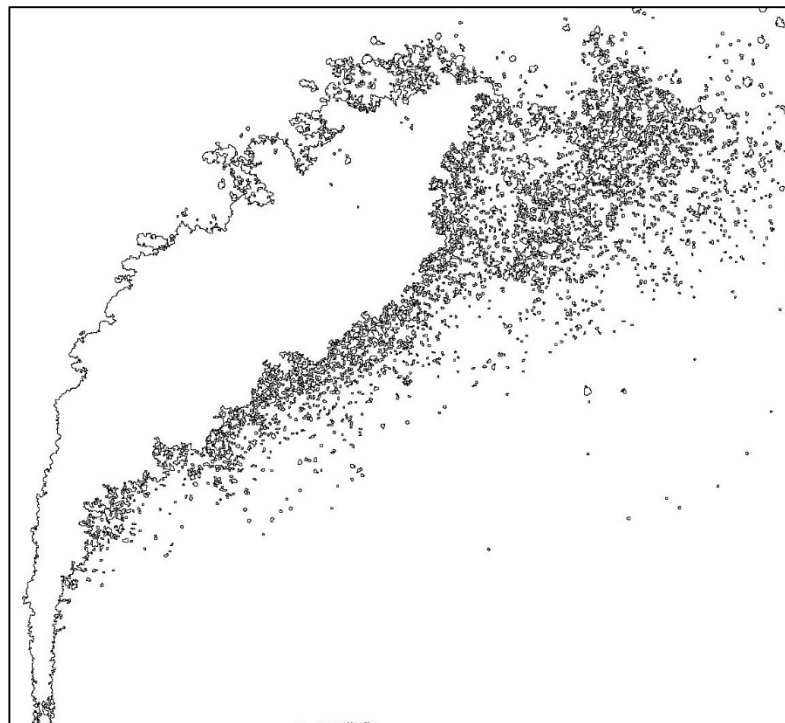




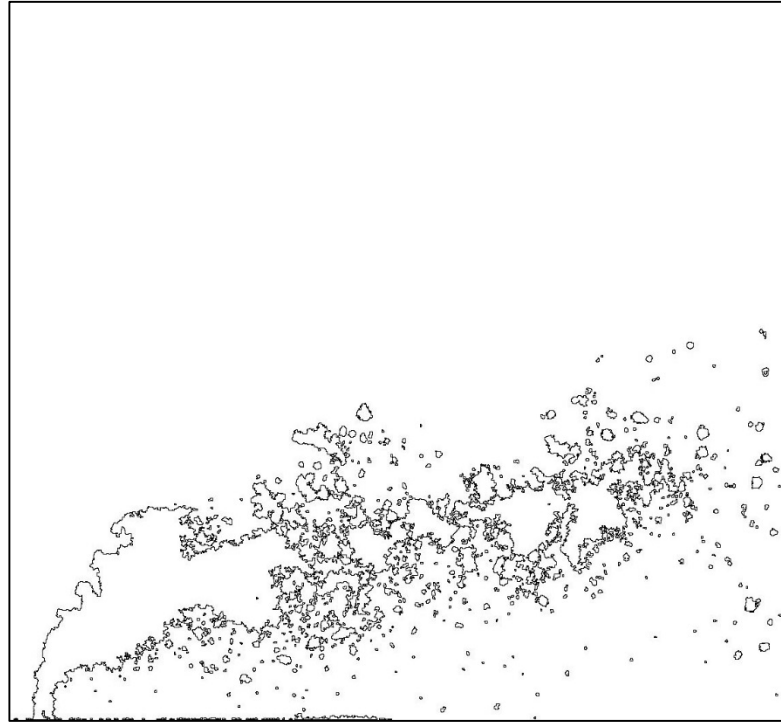
No.	Ref.	$V_{\text{Jet}}$ [m/s]	$V_{\text{Air}}$ [m/s]	q	$We_{\text{Air}}$	$We_{\text{Jet}}$	$Re_{\text{Air}}$	$Re_{\text{Jet}}$	$Oh_{\text{Air}}$ $\times 10^3$	$Oh_{\text{Jet}}$ $\times 10^3$	D10 [ $\mu\text{m}$ ]	D32 [ $\mu\text{m}$ ]
65	$\triangle$	30	68	71	102	7276	4146	19422	2.437	612.1	59.0	69.4



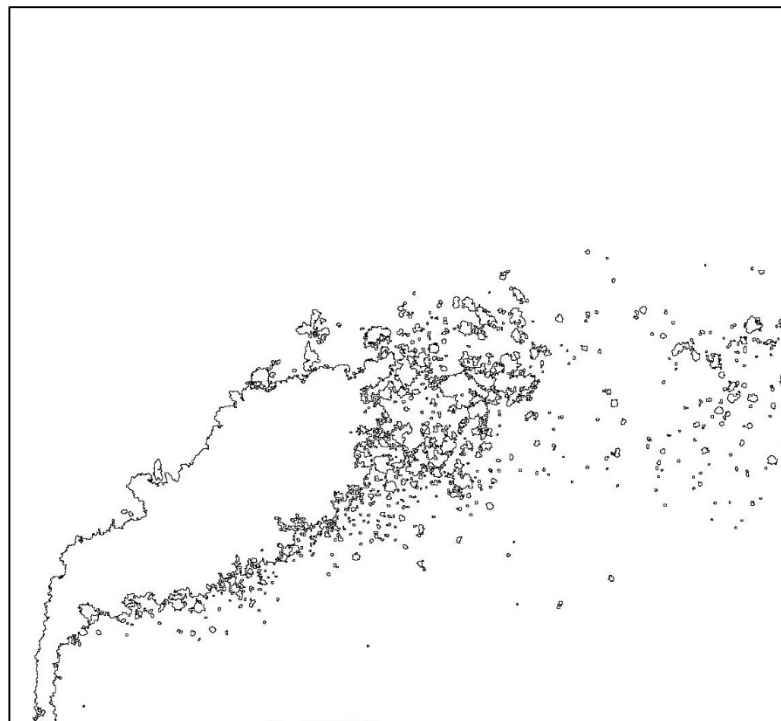
No.	Ref.	$V_{\text{Jet}}$ [m/s]	$V_{\text{Air}}$ [m/s]	q	$We_{\text{Air}}$	$We_{\text{Jet}}$	$Re_{\text{Air}}$	$Re_{\text{Jet}}$	$Oh_{\text{Air}}$ $\times 10^3$	$Oh_{\text{Jet}}$ $\times 10^3$	D10 [ $\mu\text{m}$ ]	D32 [ $\mu\text{m}$ ]
66	$\triangle$	38	68	114	102	11641	4146	24567	2.437	688.4	57.7	64.9



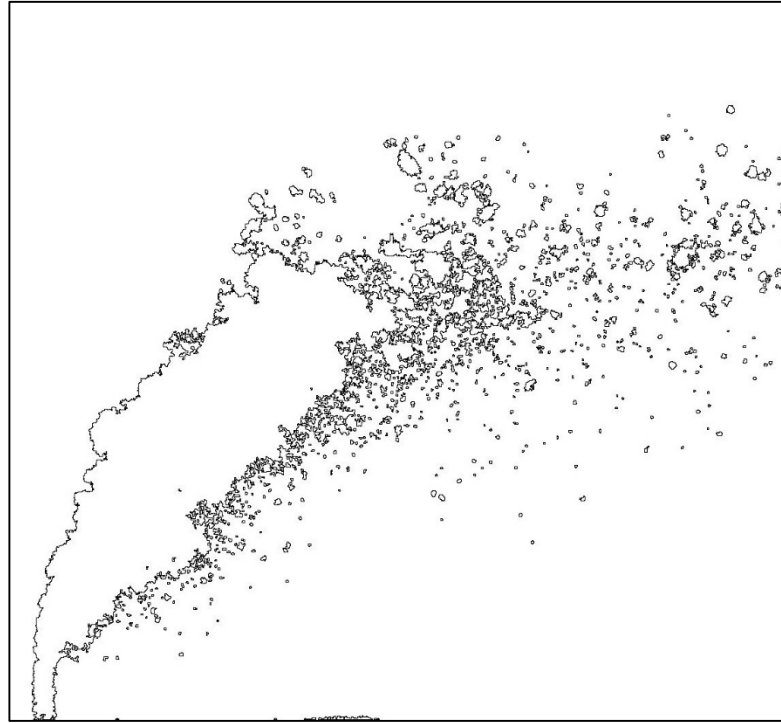
No.	Ref.	$V_{\text{Jet}}$ [m/s]	$V_{\text{Air}}$ [m/s]	q	$We_{\text{Air}}$	$We_{\text{Jet}}$	$Re_{\text{Air}}$	$Re_{\text{Jet}}$	$Oh_{\text{Air}}$ $\times 10^3$	$Oh_{\text{Jet}}$ $\times 10^3$	D10 [ $\mu\text{m}$ ]	D32 [ $\mu\text{m}$ ]
67	$\triangle$	9	43	14	42	582	2645	5493	2.437	325.5	67.9	88.6



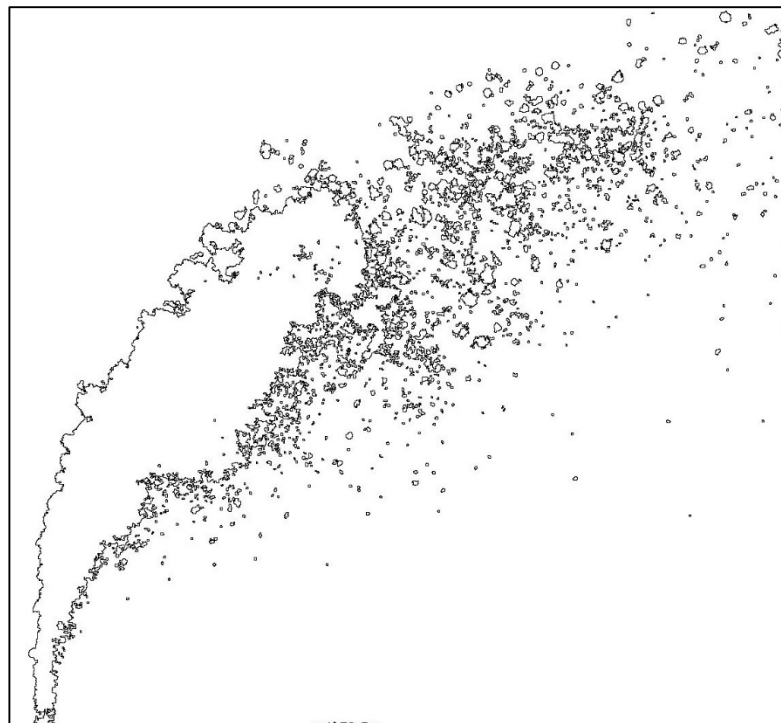
No.	Ref.	$V_{\text{Jet}}$ [m/s]	$V_{\text{Air}}$ [m/s]	q	$We_{\text{Air}}$	$We_{\text{Jet}}$	$Re_{\text{Air}}$	$Re_{\text{Jet}}$	$Oh_{\text{Air}}$ $\times 10^3$	$Oh_{\text{Jet}}$ $\times 10^3$	D10 [ $\mu\text{m}$ ]	D32 [ $\mu\text{m}$ ]
68	$\triangle$	12	43	28	42	1164	2645	7769	2.437	387.1	65.6	84.4



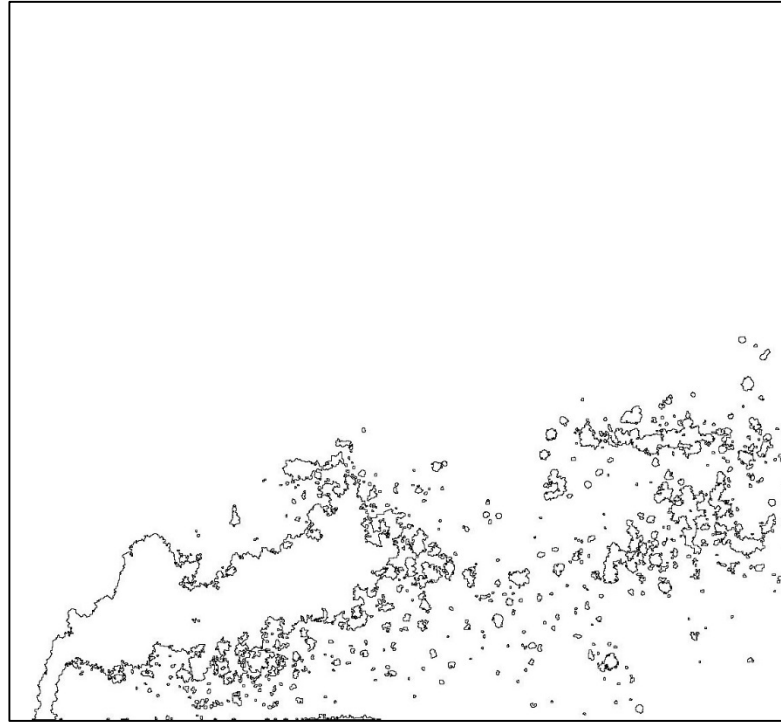
No.	Ref.	$V_{\text{Jet}}$ [m/s]	$V_{\text{Air}}$ [m/s]	q	$We_{\text{Air}}$	$We_{\text{Jet}}$	$Re_{\text{Air}}$	$Re_{\text{Jet}}$	$Oh_{\text{Air}}$ $\times 10^3$	$Oh_{\text{Jet}}$ $\times 10^3$	D10 [ $\mu\text{m}$ ]	D32 [ $\mu\text{m}$ ]
69	$\triangle$	19	43	70	42	2910	2645	12283	2.437	486.8	62.9	78.0



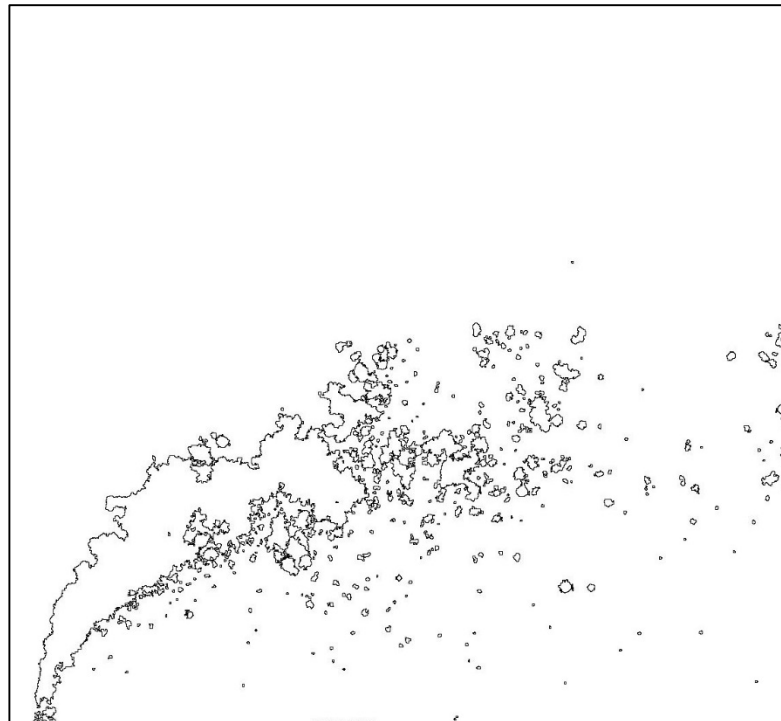
No.	Ref.	$V_{\text{Jet}}$ [m/s]	$V_{\text{Air}}$ [m/s]	q	$We_{\text{Air}}$	$We_{\text{Jet}}$	$Re_{\text{Air}}$	$Re_{\text{Jet}}$	$Oh_{\text{Air}}$ $\times 10^3$	$Oh_{\text{Jet}}$ $\times 10^3$	D10 [ $\mu\text{m}$ ]	D32 [ $\mu\text{m}$ ]
70	$\triangle$	24	43	112	42	4656	2645	15537	2.437	547.4	61.6	74.8



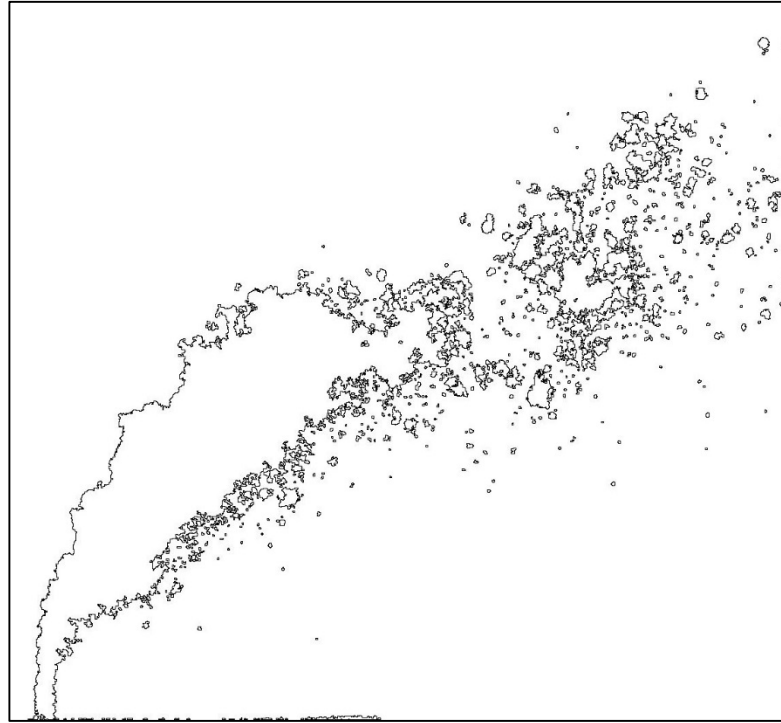
No.	Ref.	$V_{Jet}$ [m/s]	$V_{Air}$ [m/s]	q	$We_{Air}$	$We_{Jet}$	$Re_{Air}$	$Re_{Jet}$	$Oh_{Air}$ $\times 10^3$	$Oh_{Jet}$ $\times 10^3$	D10 [ $\mu m$ ]	D32 [ $\mu m$ ]
71	$\Delta$	7	35	14	27	364	2127	4343	2.437	289.4	69.8	91.7



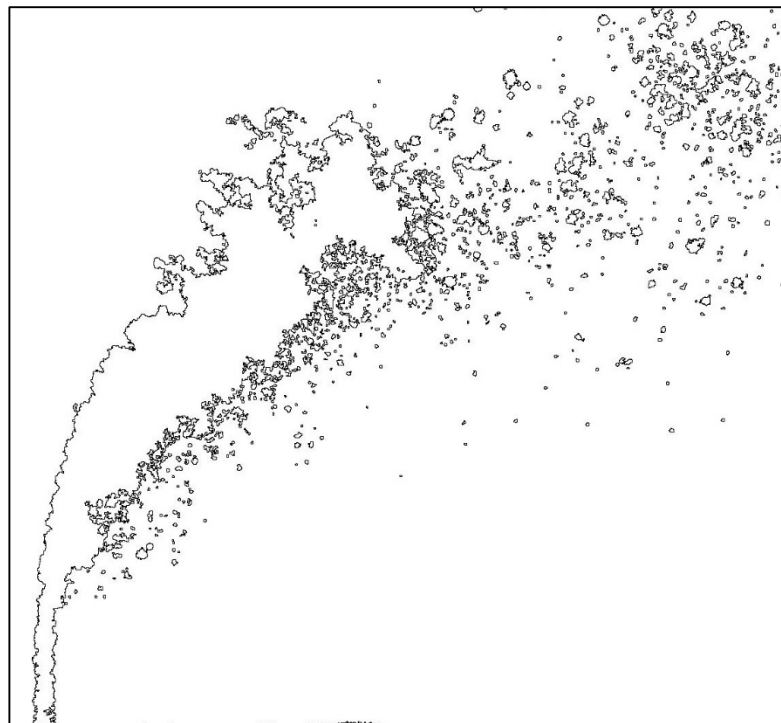
No.	Ref.	$V_{Jet}$ [m/s]	$V_{Air}$ [m/s]	q	$We_{Air}$	$We_{Jet}$	$Re_{Air}$	$Re_{Jet}$	$Oh_{Air}$ $\times 10^3$	$Oh_{Jet}$ $\times 10^3$	D10 [ $\mu m$ ]	D32 [ $\mu m$ ]
72	$\Delta$	10	35	27	27	728	2127	6142	2.437	344.2	69.0	91.2



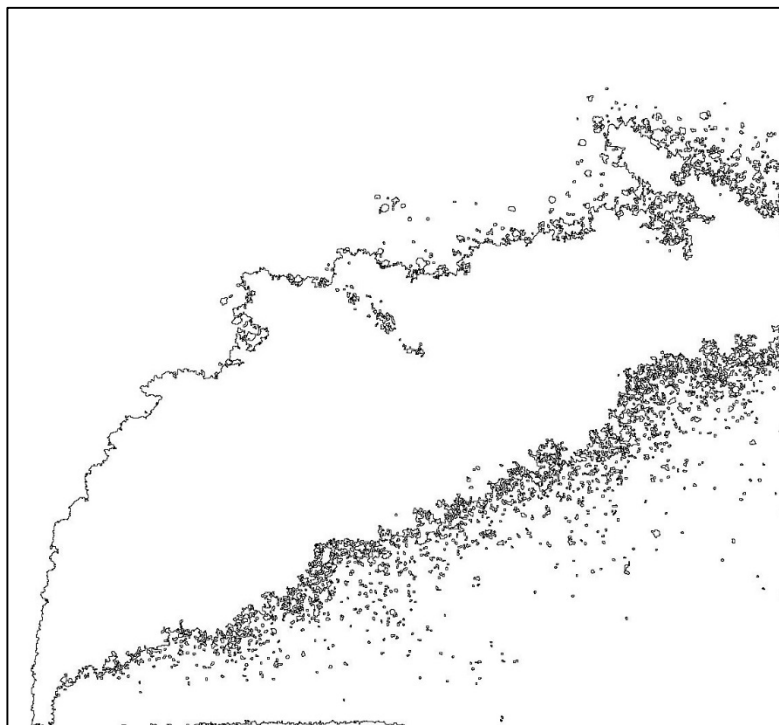
No.	Ref.	$V_{\text{Jet}}$ [m/s]	$V_{\text{Air}}$ [m/s]	q	$We_{\text{Air}}$	$We_{\text{Jet}}$	$Re_{\text{Air}}$	$Re_{\text{Jet}}$	$Oh_{\text{Air}}$ $\times 10^3$	$Oh_{\text{Jet}}$ $\times 10^3$	D10 [ $\mu\text{m}$ ]	D32 [ $\mu\text{m}$ ]
73	$\triangle$	15	35	68	27	1819	2127	9711	2.437	432.8	65.9	84.5



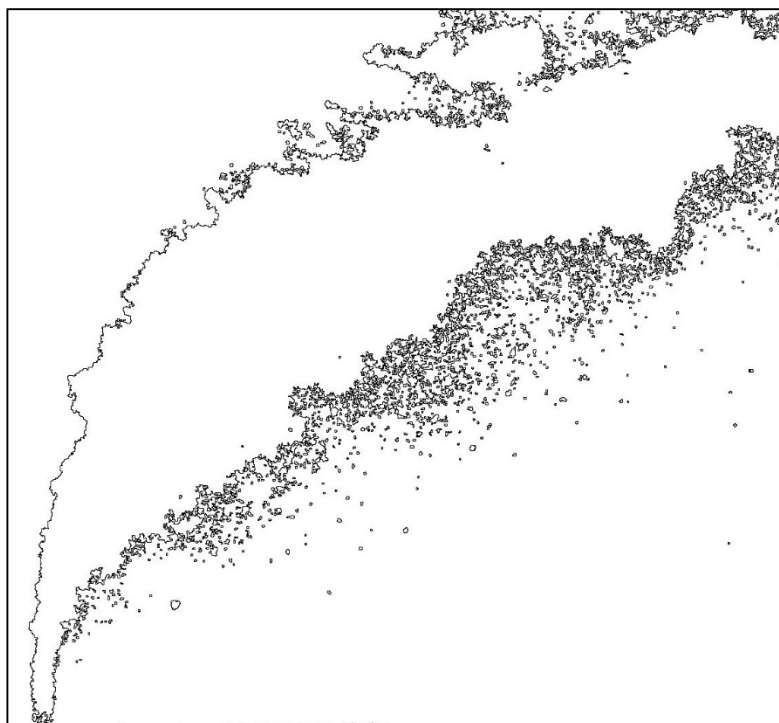
No.	Ref.	$V_{\text{Jet}}$ [m/s]	$V_{\text{Air}}$ [m/s]	q	$We_{\text{Air}}$	$We_{\text{Jet}}$	$Re_{\text{Air}}$	$Re_{\text{Jet}}$	$Oh_{\text{Air}}$ $\times 10^3$	$Oh_{\text{Jet}}$ $\times 10^3$	D10 [ $\mu\text{m}$ ]	D32 [ $\mu\text{m}$ ]
74	$\triangle$	19	35	108	27	2910	2127	12283	2.437	486.8	64.2	80.4



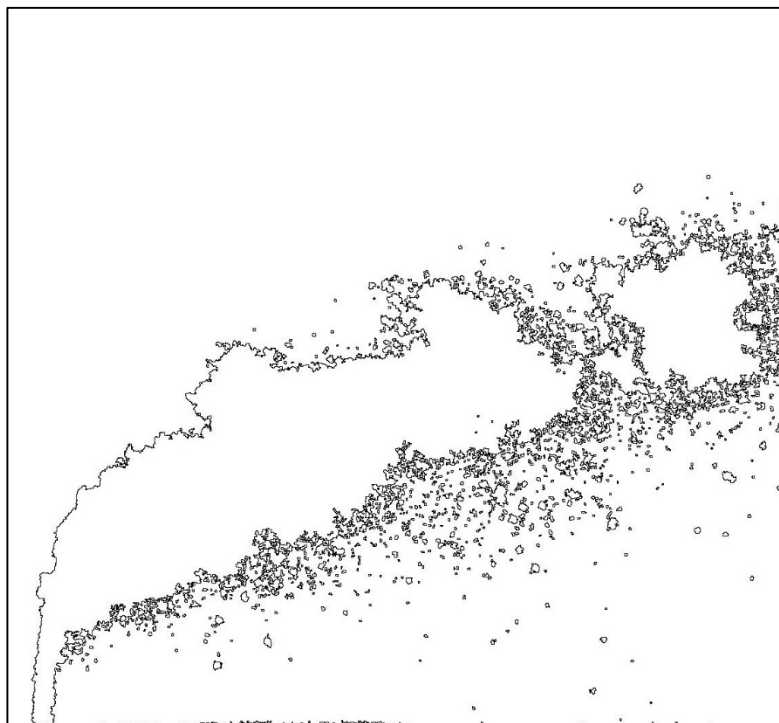
No.	Ref.	$V_{\text{Jet}}$ [m/s]	$V_{\text{Air}}$ [m/s]	q	$We_{\text{Air}}$	$We_{\text{Jet}}$	$Re_{\text{Air}}$	$Re_{\text{Jet}}$	$Oh_{\text{Air}}$ $\times 10^3$	$Oh_{\text{Jet}}$ $\times 10^3$	D10 [ $\mu\text{m}$ ]	D32 [ $\mu\text{m}$ ]
76	$\triangle$	27	92	37	156	5821	4063	17371	3.070	578.8	59.0	68.2



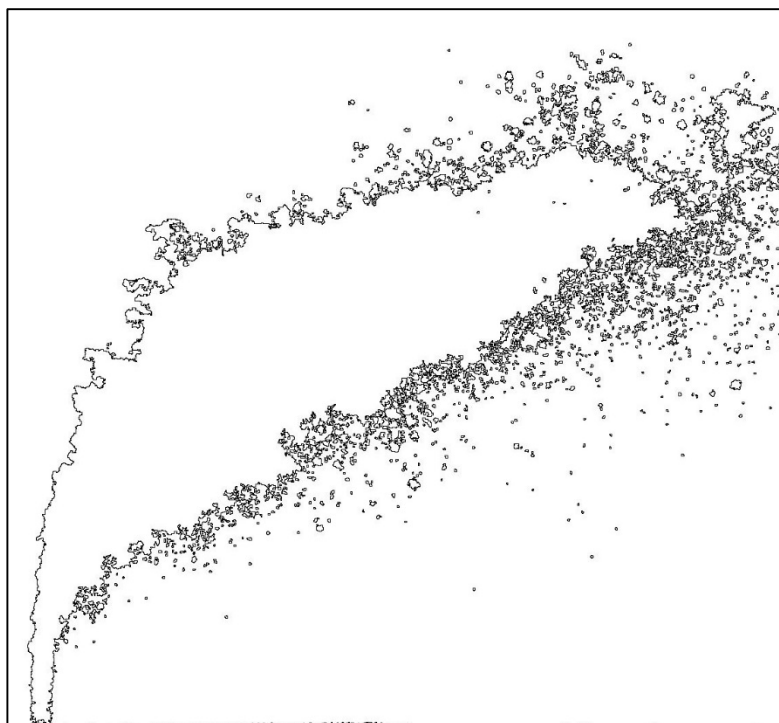
No.	Ref.	$V_{\text{Jet}}$ [m/s]	$V_{\text{Air}}$ [m/s]	q	$We_{\text{Air}}$	$We_{\text{Jet}}$	$Re_{\text{Air}}$	$Re_{\text{Jet}}$	$Oh_{\text{Air}}$ $\times 10^3$	$Oh_{\text{Jet}}$ $\times 10^3$	D10 [ $\mu\text{m}$ ]	D32 [ $\mu\text{m}$ ]
77	$\triangle$	43	92	94	156	14551	4063	27466	3.070	727.9	58.1	66.1



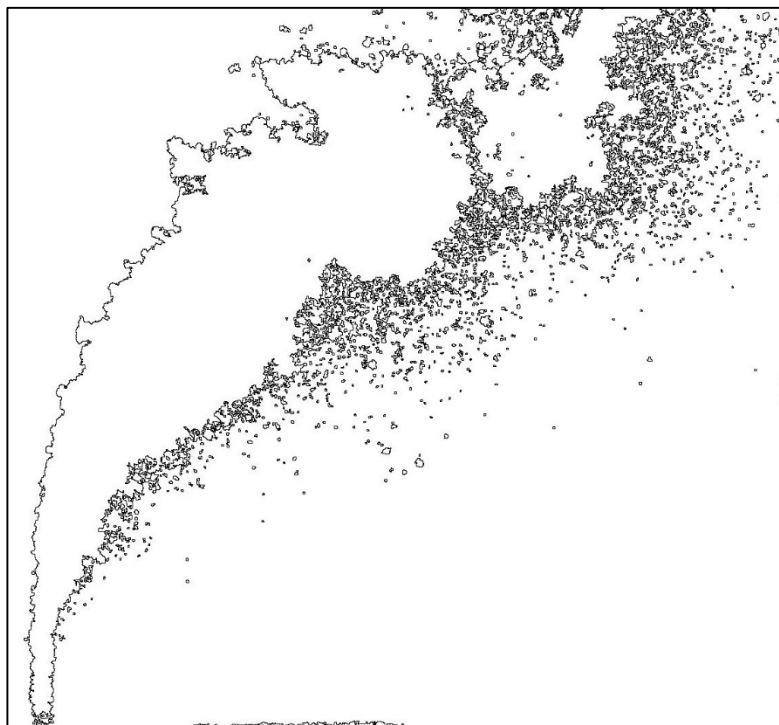
No.	Ref.	$V_{\text{Jet}}$ [m/s]	$V_{\text{Air}}$ [m/s]	q	$We_{\text{Air}}$	$We_{\text{Jet}}$	$Re_{\text{Air}}$	$Re_{\text{Jet}}$	$Oh_{\text{Air}}$ $\times 10^3$	$Oh_{\text{Jet}}$ $\times 10^3$	D10 [ $\mu\text{m}$ ]	D32 [ $\mu\text{m}$ ]
80	$\triangle$	19	68	35	84	2910	2986	12283	3.070	486.8	61.0	73.5



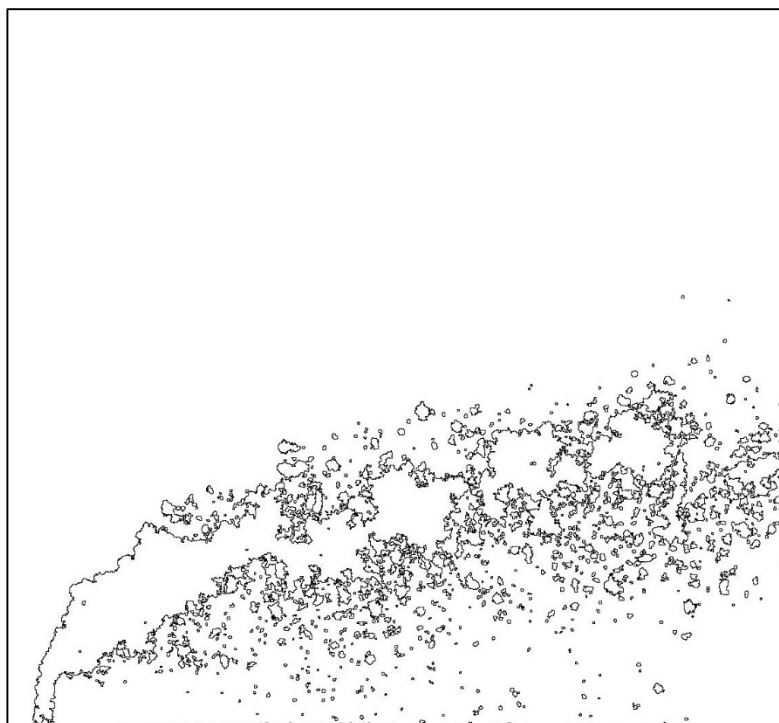
No.	Ref.	$V_{\text{Jet}}$ [m/s]	$V_{\text{Air}}$ [m/s]	q	$We_{\text{Air}}$	$We_{\text{Jet}}$	$Re_{\text{Air}}$	$Re_{\text{Jet}}$	$Oh_{\text{Air}}$ $\times 10^3$	$Oh_{\text{Jet}}$ $\times 10^3$	D10 [ $\mu\text{m}$ ]	D32 [ $\mu\text{m}$ ]
81	$\triangle$	30	68	87	84	7276	2986	19422	3.070	612.1	59.6	70.6



No.	Ref.	$V_{\text{Jet}}$ [m/s]	$V_{\text{Air}}$ [m/s]	q	$We_{\text{Air}}$	$We_{\text{Jet}}$	$Re_{\text{Air}}$	$Re_{\text{Jet}}$	$Oh_{\text{Air}}$ $\times 10^3$	$Oh_{\text{Jet}}$ $\times 10^3$	D10 [ $\mu\text{m}$ ]	D32 [ $\mu\text{m}$ ]
82	$\Delta$	38	68	139	84	11641	2986	24567	3.070	688.4	58.6	67.5

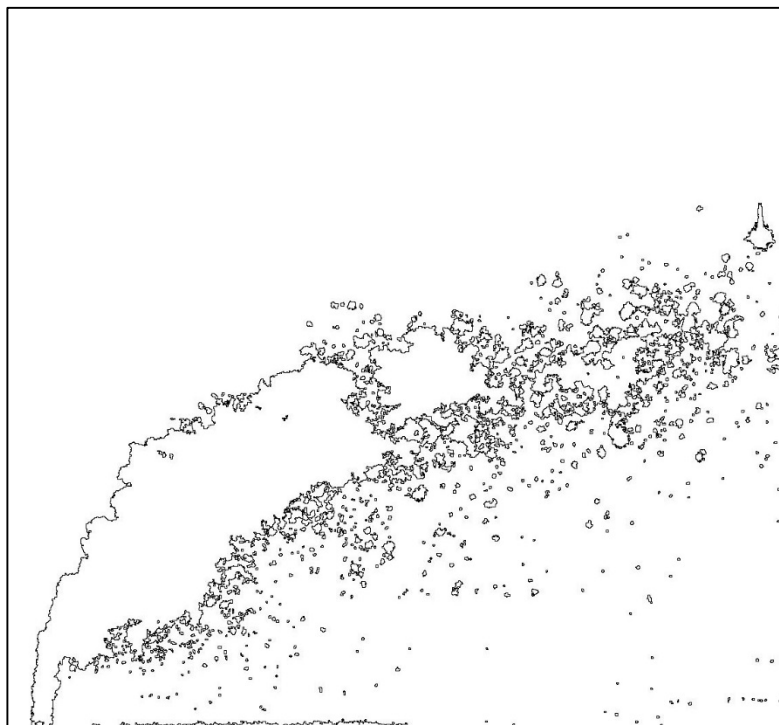


No.	Ref.	$V_{\text{Jet}}$ [m/s]	$V_{\text{Air}}$ [m/s]	q	$We_{\text{Air}}$	$We_{\text{Jet}}$	$Re_{\text{Air}}$	$Re_{\text{Jet}}$	$Oh_{\text{Air}}$ $\times 10^3$	$Oh_{\text{Jet}}$ $\times 10^3$	D10 [ $\mu\text{m}$ ]	D32 [ $\mu\text{m}$ ]
83	$\Delta$	9	43	17	34	582	1908	5493	3.070	325.5	67.3	85.8

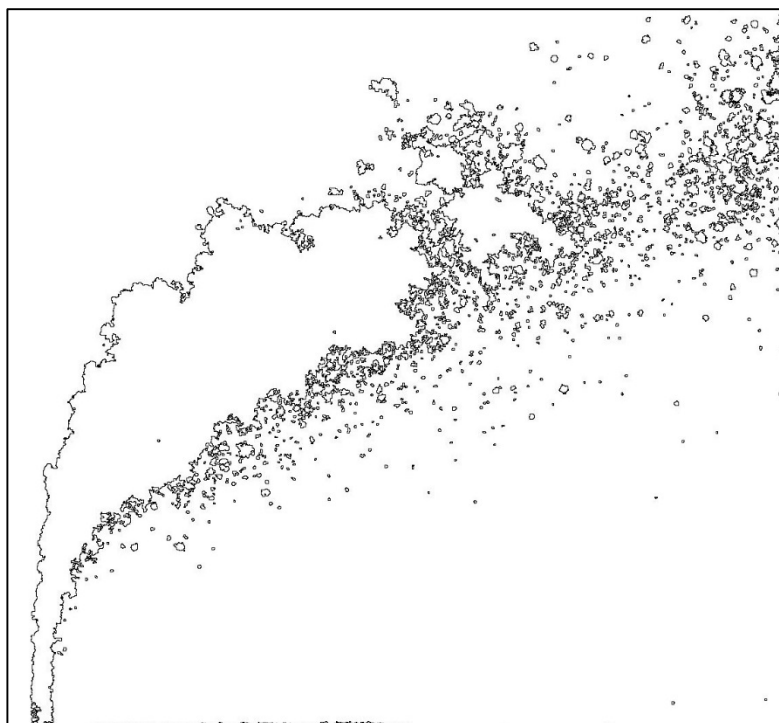




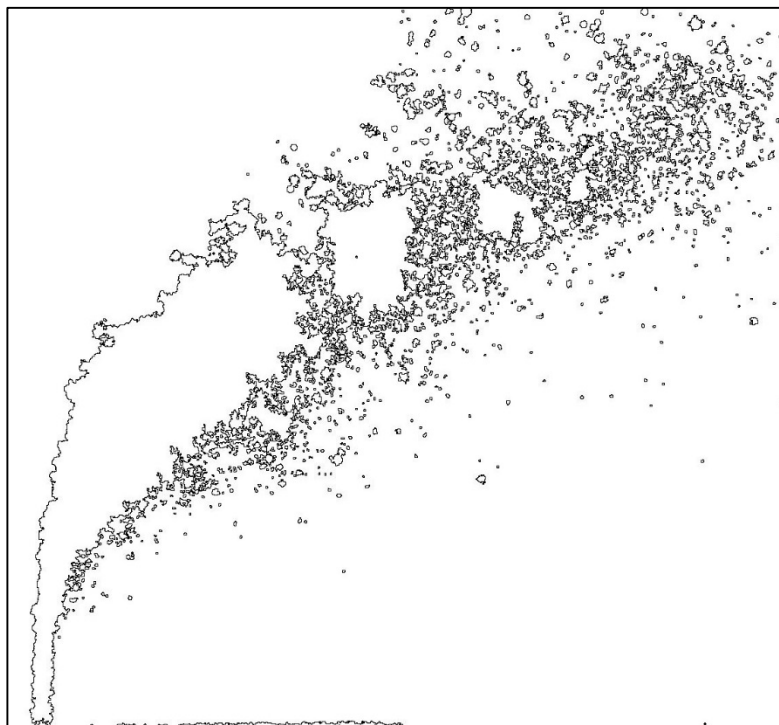
No.	Ref.	$V_{Jet}$ [m/s]	$V_{Air}$ [m/s]	q	$We_{Air}$	$We_{Jet}$	$Re_{Air}$	$Re_{Jet}$	$Oh_{Air}$ $\times 10^3$	$Oh_{Jet}$ $\times 10^3$	D10 [ $\mu m$ ]	D32 [ $\mu m$ ]
84	$\Delta$	12	43	34	34	1164	1908	7769	3.070	387.1	65.6	82.7



No.	Ref.	$V_{Jet}$ [m/s]	$V_{Air}$ [m/s]	q	$We_{Air}$	$We_{Jet}$	$Re_{Air}$	$Re_{Jet}$	$Oh_{Air}$ $\times 10^3$	$Oh_{Jet}$ $\times 10^3$	D10 [ $\mu m$ ]	D32 [ $\mu m$ ]
85	$\Delta$	19	43	85	34	2910	1908	12283	3.070	486.8	63.4	78.8



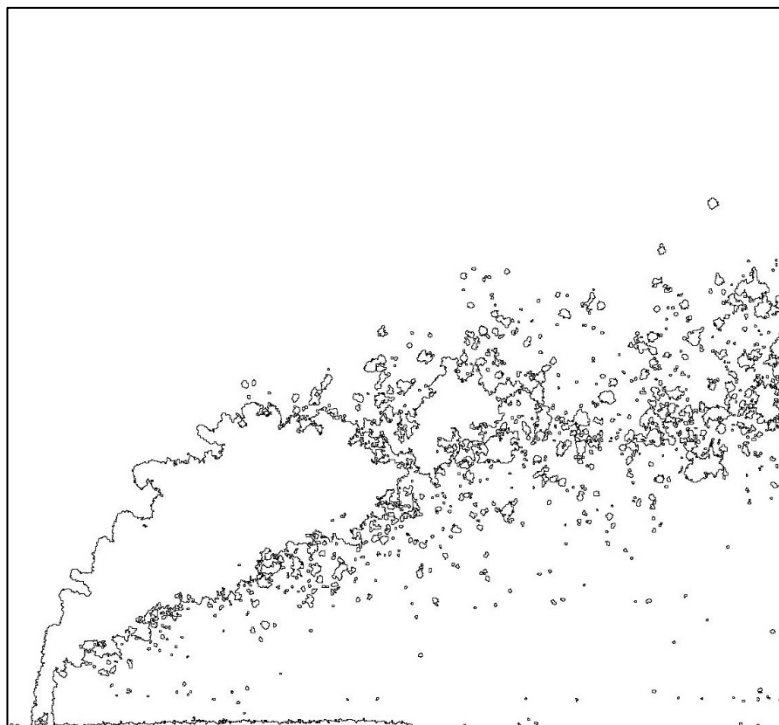
No.	Ref.	$V_{\text{Jet}}$ [m/s]	$V_{\text{Air}}$ [m/s]	q	$We_{\text{Air}}$	$We_{\text{Jet}}$	$Re_{\text{Air}}$	$Re_{\text{Jet}}$	$Oh_{\text{Air}}$ $\times 10^3$	$Oh_{\text{Jet}}$ $\times 10^3$	D10 [ $\mu\text{m}$ ]	D32 [ $\mu\text{m}$ ]
86	$\triangle$	24	43	136	34	4656	1908	15537	3.070	547.4	62.3	76.6



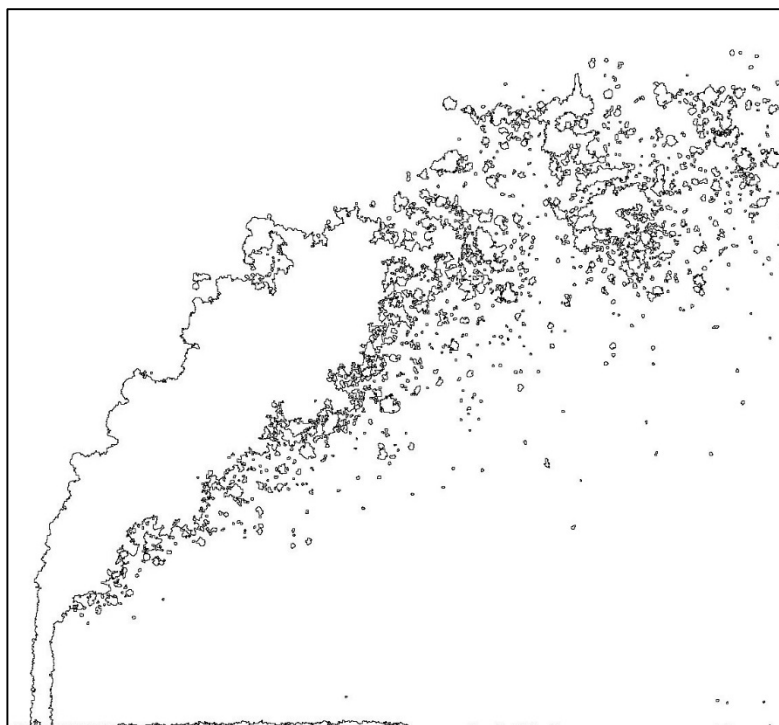
No.	Ref.	$V_{\text{Jet}}$ [m/s]	$V_{\text{Air}}$ [m/s]	q	$We_{\text{Air}}$	$We_{\text{Jet}}$	$Re_{\text{Air}}$	$Re_{\text{Jet}}$	$Oh_{\text{Air}}$ $\times 10^3$	$Oh_{\text{Jet}}$ $\times 10^3$	D10 [ $\mu\text{m}$ ]	D32 [ $\mu\text{m}$ ]
87	$\triangle$	7	34	17	21	364	1506	4343	3.070	289.4	69.8	90.0



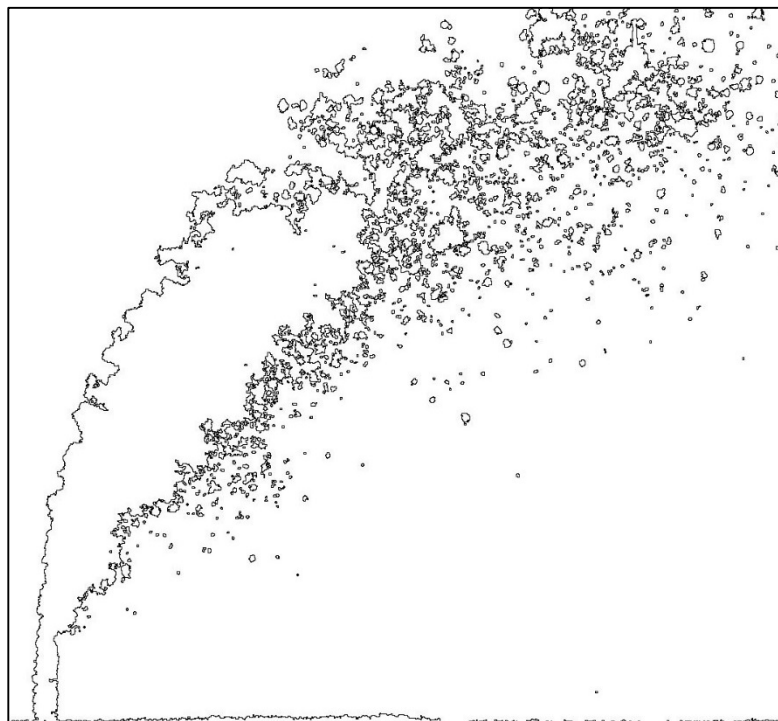
No.	Ref.	$V_{\text{Jet}}$ [m/s]	$V_{\text{Air}}$ [m/s]	q	$We_{\text{Air}}$	$We_{\text{Jet}}$	$Re_{\text{Air}}$	$Re_{\text{Jet}}$	$Oh_{\text{Air}}$ $\times 10^3$	$Oh_{\text{Jet}}$ $\times 10^3$	D10 [ $\mu\text{m}$ ]	D32 [ $\mu\text{m}$ ]
88	$\Delta$	10	34	34	21	728	1506	6142	3.070	344.2	68.4	87.2



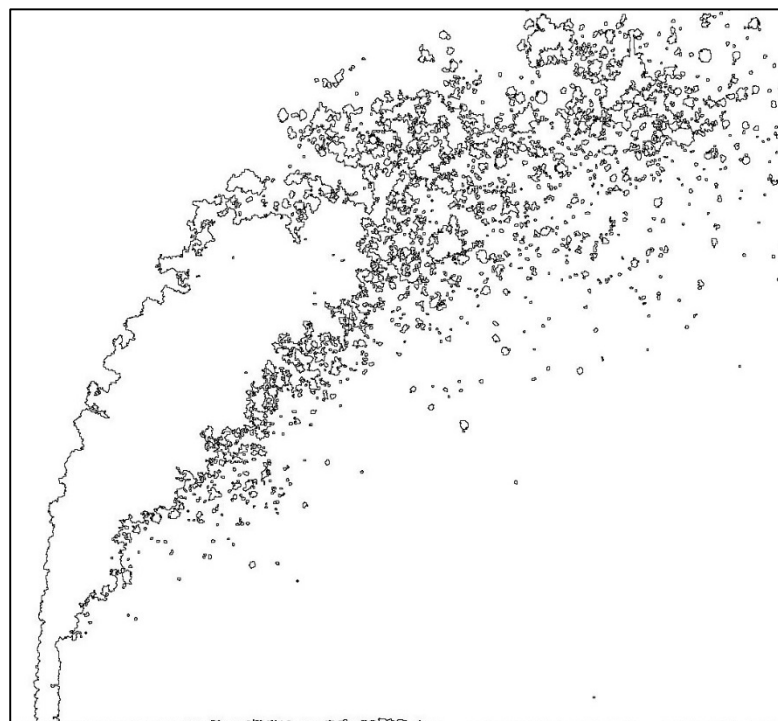
No.	Ref.	$V_{\text{Jet}}$ [m/s]	$V_{\text{Air}}$ [m/s]	q	$We_{\text{Air}}$	$We_{\text{Jet}}$	$Re_{\text{Air}}$	$Re_{\text{Jet}}$	$Oh_{\text{Air}}$ $\times 10^3$	$Oh_{\text{Jet}}$ $\times 10^3$	D10 [ $\mu\text{m}$ ]	D32 [ $\mu\text{m}$ ]
89	$\Delta$	15	34	85	21	1819	1506	9711	3.070	432.8	66.4	83.9



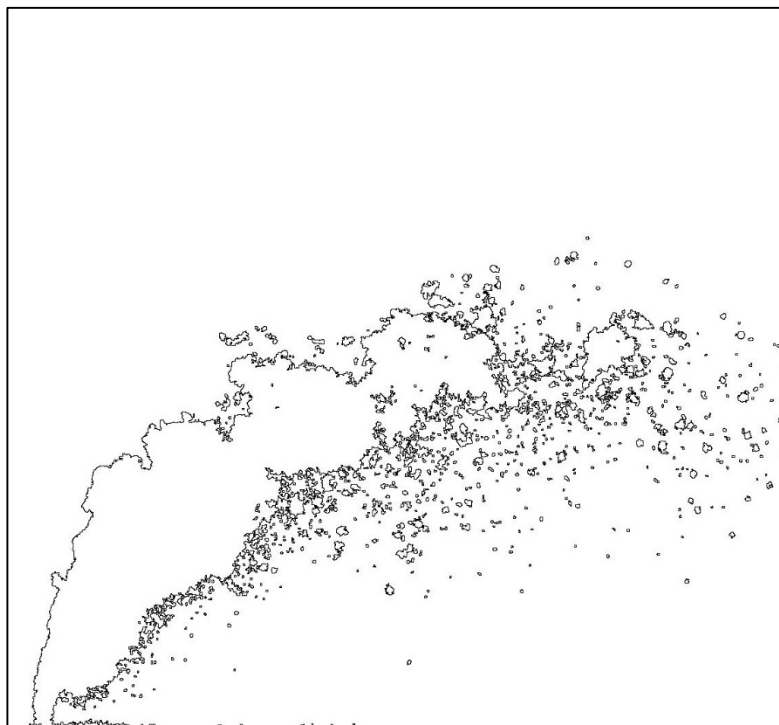
No.	Ref.	$V_{\text{Jet}}$ [m/s]	$V_{\text{Air}}$ [m/s]	q	$We_{\text{Air}}$	$We_{\text{Jet}}$	$Re_{\text{Air}}$	$Re_{\text{Jet}}$	$Oh_{\text{Air}}$ $\times 10^3$	$Oh_{\text{Jet}}$ $\times 10^3$	D10 [ $\mu\text{m}$ ]	D32 [ $\mu\text{m}$ ]
90	$\triangle$	19	34	136	21	2910	1506	12283	3.070	486.8	64.6	80.7



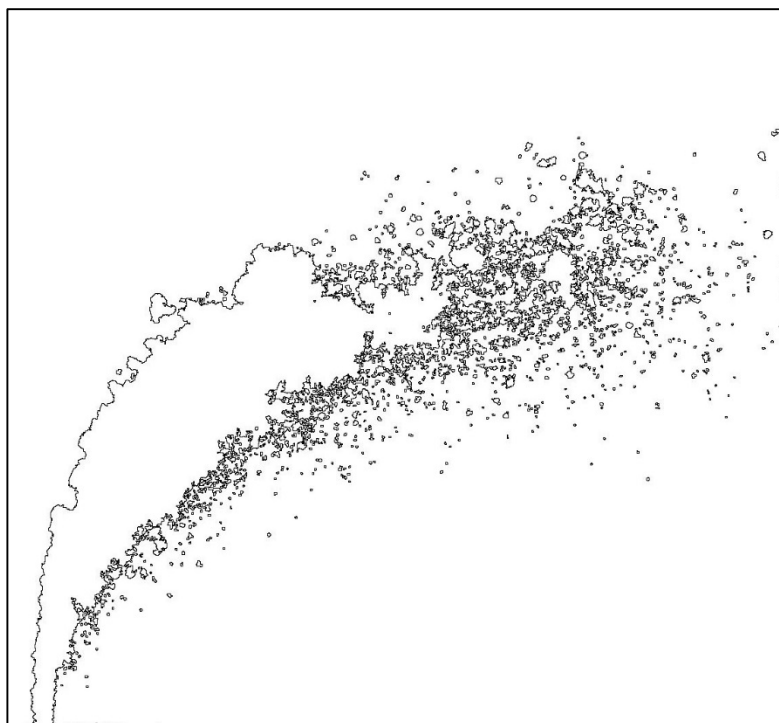
No.	Ref.	$V_{\text{Jet}}$ [m/s]	$V_{\text{Air}}$ [m/s]	q	$We_{\text{Air}}$	$We_{\text{Jet}}$	$Re_{\text{Air}}$	$Re_{\text{Jet}}$	$Oh_{\text{Air}}$ $\times 10^3$	$Oh_{\text{Jet}}$ $\times 10^3$	D10 [ $\mu\text{m}$ ]	D32 [ $\mu\text{m}$ ]
91	$\blacksquare$	14	96	8	141	1165	5727	6946	2.072	409.5	65.9	82.9



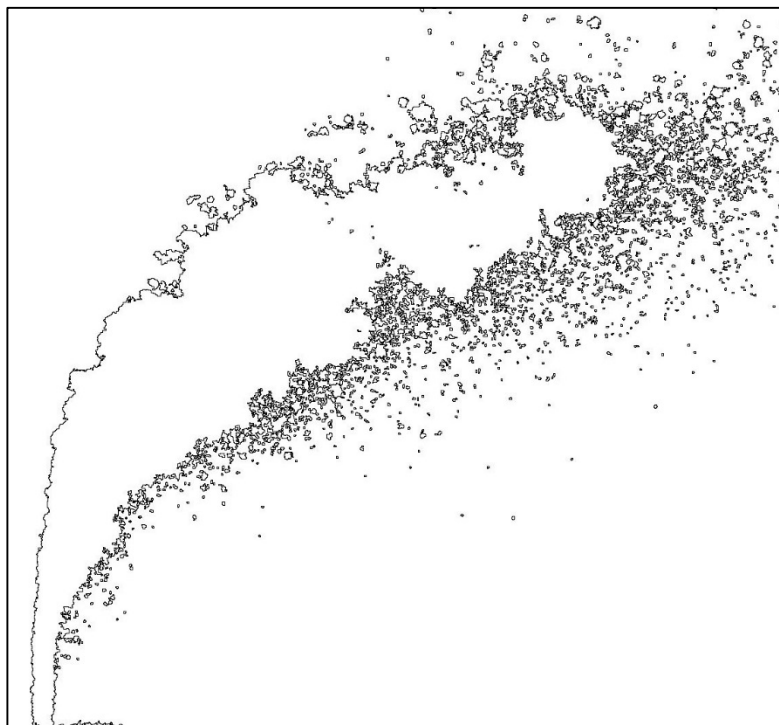
No.	Ref.	$V_{\text{Jet}}$ [m/s]	$V_{\text{Air}}$ [m/s]	q	$We_{\text{Air}}$	$We_{\text{Jet}}$	$Re_{\text{Air}}$	$Re_{\text{Jet}}$	$Oh_{\text{Air}}$ $\times 10^3$	$Oh_{\text{Jet}}$ $\times 10^3$	D10 [ $\mu\text{m}$ ]	D32 [ $\mu\text{m}$ ]
92	■	19	96	17	141	2330	5727	9823	2.072	487.0	63.0	77.6



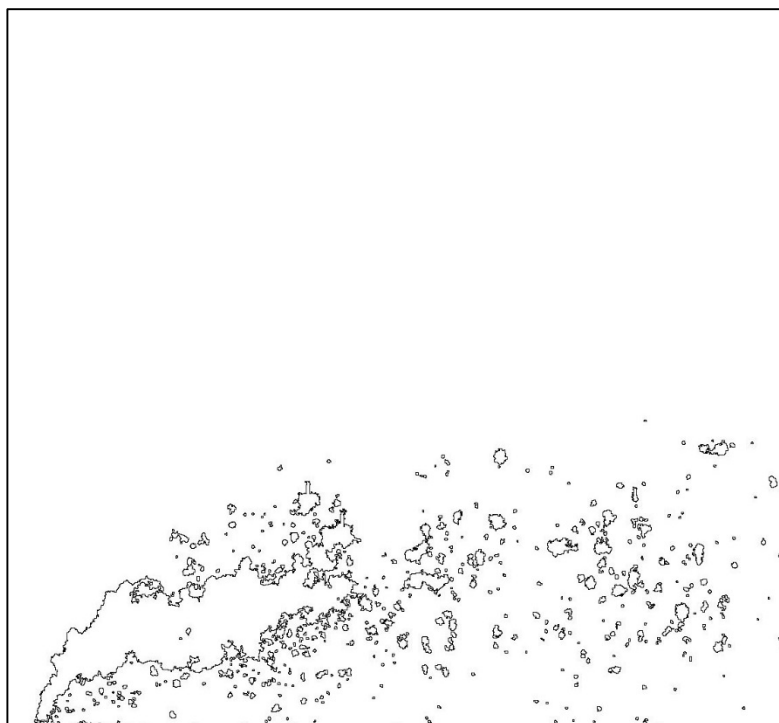
No.	Ref.	$V_{\text{Jet}}$ [m/s]	$V_{\text{Air}}$ [m/s]	q	$We_{\text{Air}}$	$We_{\text{Jet}}$	$Re_{\text{Air}}$	$Re_{\text{Jet}}$	$Oh_{\text{Air}}$ $\times 10^3$	$Oh_{\text{Jet}}$ $\times 10^3$	D10 [ $\mu\text{m}$ ]	D32 [ $\mu\text{m}$ ]
93	■	30	96	41	141	5825	5727	15531	2.072	612.4	60.6	72.5



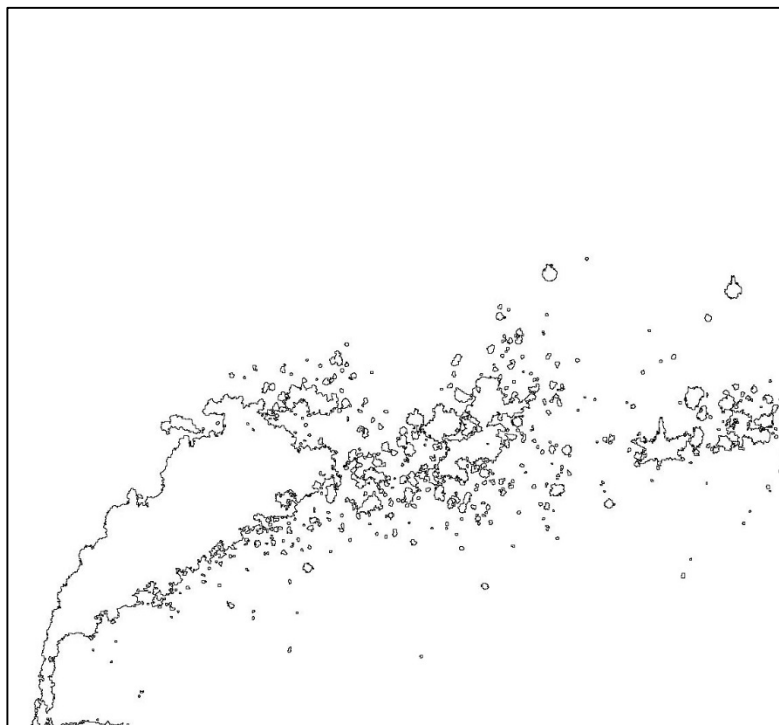
No.	Ref.	$V_{Jet}$ [m/s]	$V_{Air}$ [m/s]	q	$We_{Air}$	$We_{Jet}$	$Re_{Air}$	$Re_{Jet}$	$Oh_{Air}$ $\times 10^3$	$Oh_{Jet}$ $\times 10^3$	D10 [ $\mu m$ ]	D32 [ $\mu m$ ]
94	■	38	96	66	141	9320	5727	19646	2.072	688.8	59.6	70.5



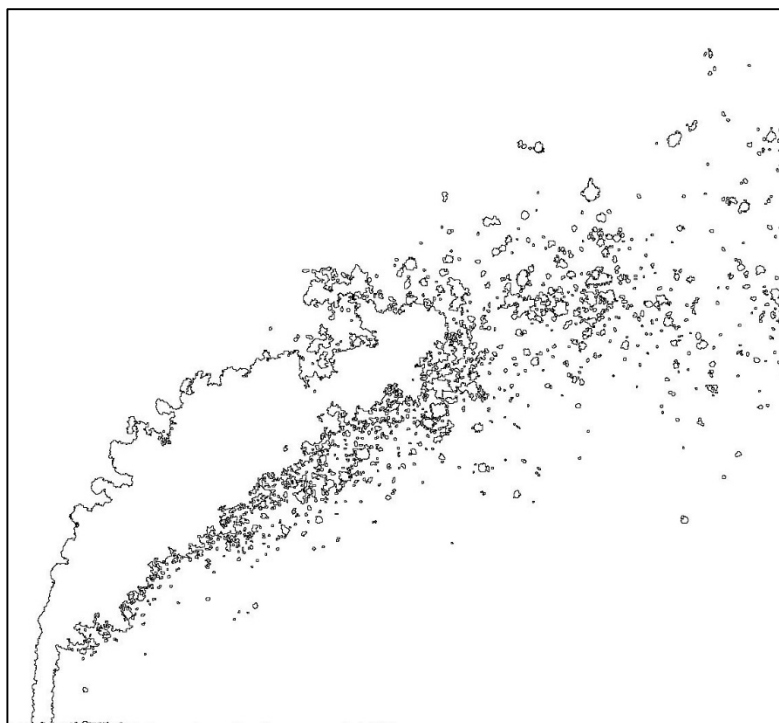
No.	Ref.	$V_{Jet}$ [m/s]	$V_{Air}$ [m/s]	q	$We_{Air}$	$We_{Jet}$	$Re_{Air}$	$Re_{Jet}$	$Oh_{Air}$ $\times 10^3$	$Oh_{Jet}$ $\times 10^3$	D10 [ $\mu m$ ]	D32 [ $\mu m$ ]
95	■	9	61	8	56	466	3622	4393	2.072	325.7	71.5	93.7



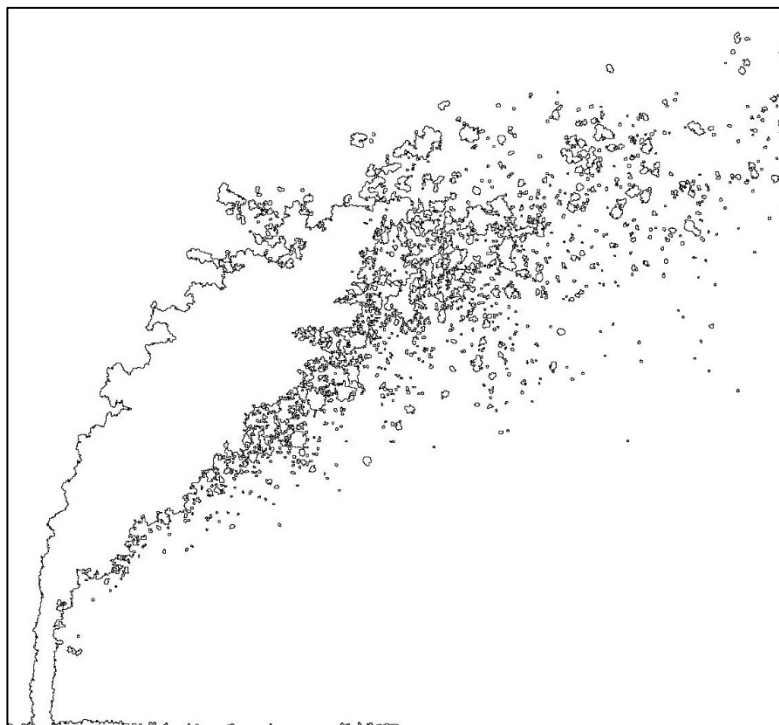
No.	Ref.	$V_{Jet}$ [m/s]	$V_{Air}$ [m/s]	q	$We_{Air}$	$We_{Jet}$	$Re_{Air}$	$Re_{Jet}$	$Oh_{Air}$ $\times 10^3$	$Oh_{Jet}$ $\times 10^3$	D10 [ $\mu m$ ]	D32 [ $\mu m$ ]
96	■	12	61	17	56	932	3622	6213	2.072	387.3	69.6	89.9



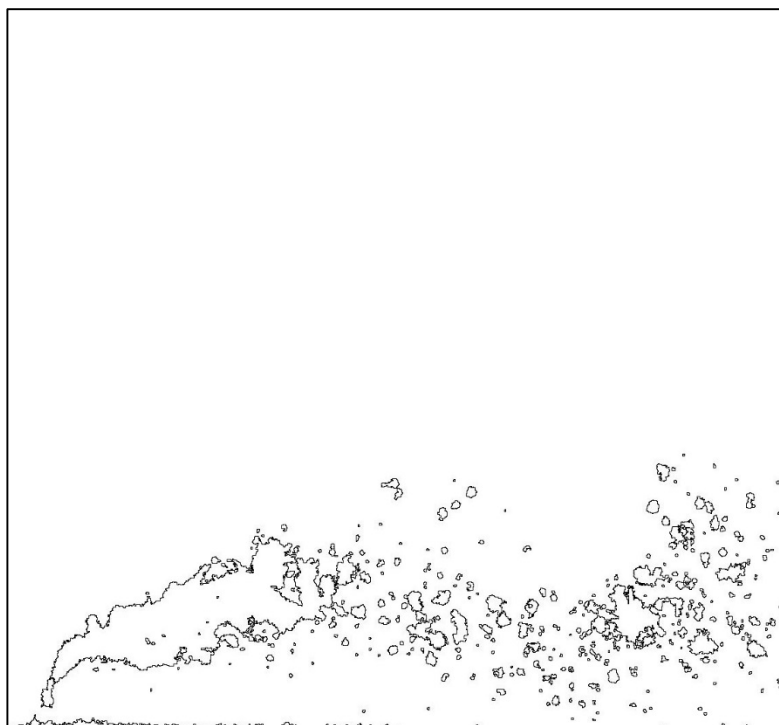
No.	Ref.	$V_{Jet}$ [m/s]	$V_{Air}$ [m/s]	q	$We_{Air}$	$We_{Jet}$	$Re_{Air}$	$Re_{Jet}$	$Oh_{Air}$ $\times 10^3$	$Oh_{Jet}$ $\times 10^3$	D10 [ $\mu m$ ]	D32 [ $\mu m$ ]
97	■	19	61	41	56	2330	3622	9823	2.072	487.0	65.7	83.2



No.	Ref.	$V_{\text{Jet}}$ [m/s]	$V_{\text{Air}}$ [m/s]	q	$We_{\text{Air}}$	$We_{\text{Jet}}$	$Re_{\text{Air}}$	$Re_{\text{Jet}}$	$Oh_{\text{Air}}$ $\times 10^3$	$Oh_{\text{Jet}}$ $\times 10^3$	D10 [ $\mu\text{m}$ ]	D32 [ $\mu\text{m}$ ]
98	■	24	61	66	56	3728	3622	12425	2.072	547.7	64.3	80.2

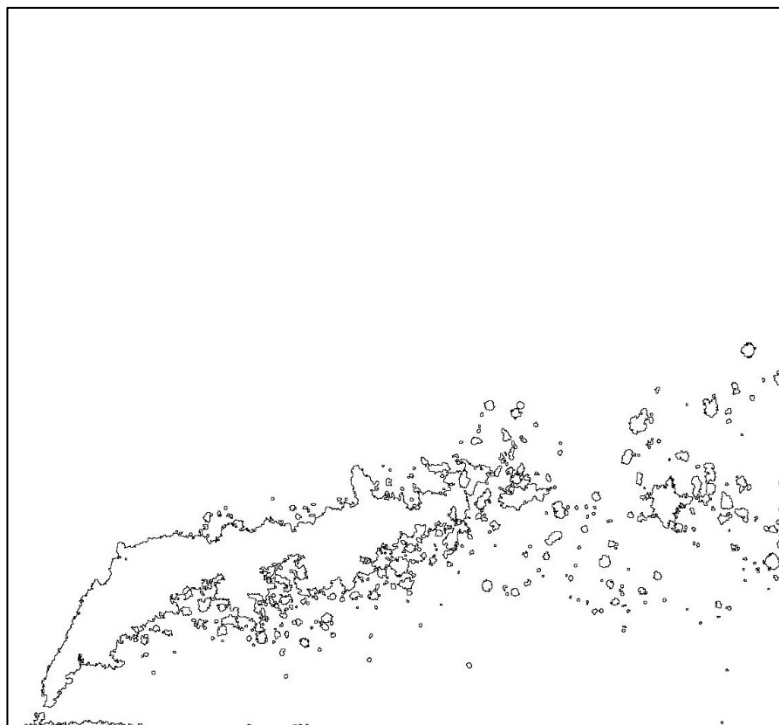


No.	Ref.	$V_{\text{Jet}}$ [m/s]	$V_{\text{Air}}$ [m/s]	q	$We_{\text{Air}}$	$We_{\text{Jet}}$	$Re_{\text{Air}}$	$Re_{\text{Jet}}$	$Oh_{\text{Air}}$ $\times 10^3$	$Oh_{\text{Jet}}$ $\times 10^3$	D10 [ $\mu\text{m}$ ]	D32 [ $\mu\text{m}$ ]
99	■	7	50	8	38	291	2970	3473	2.072	289.6	72.1	93.4

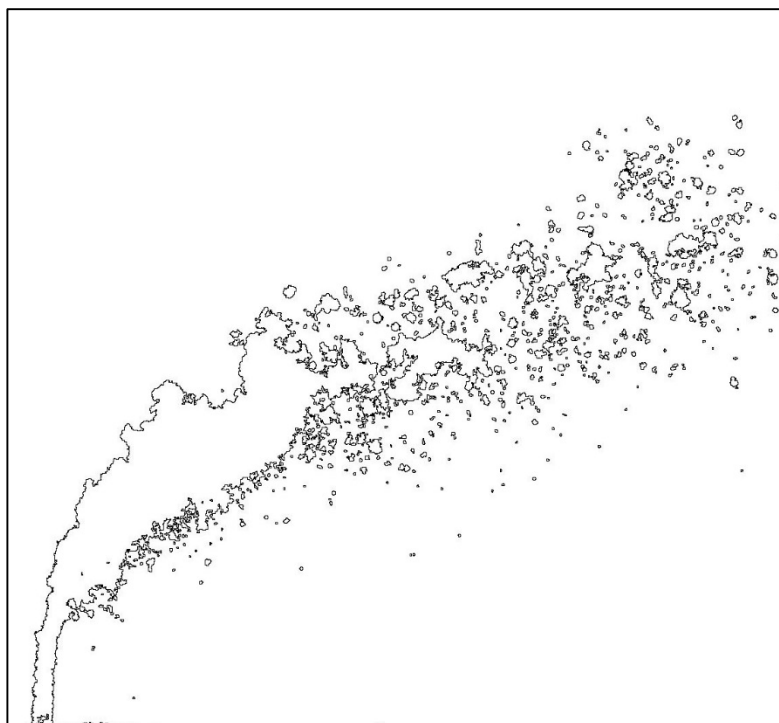




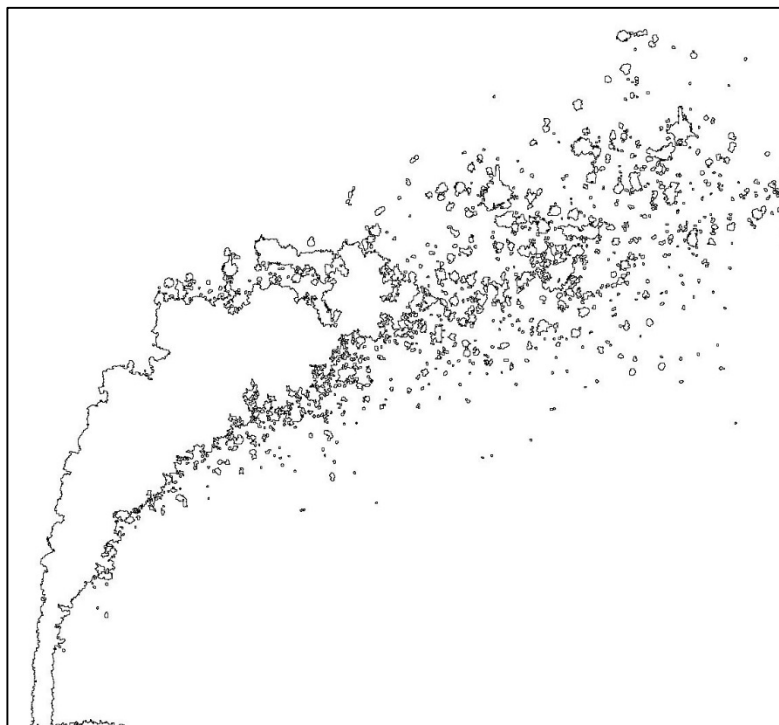
No.	Ref.	$V_{\text{Jet}}$ [m/s]	$V_{\text{Air}}$ [m/s]	q	$We_{\text{Air}}$	$We_{\text{Jet}}$	$Re_{\text{Air}}$	$Re_{\text{Jet}}$	$Oh_{\text{Air}}$ $\times 10^3$	$Oh_{\text{Jet}}$ $\times 10^3$	D10 [ $\mu\text{m}$ ]	D32 [ $\mu\text{m}$ ]
100	■	10	50	15	38	582	2970	4911	2.072	344.4	71.3	93.4



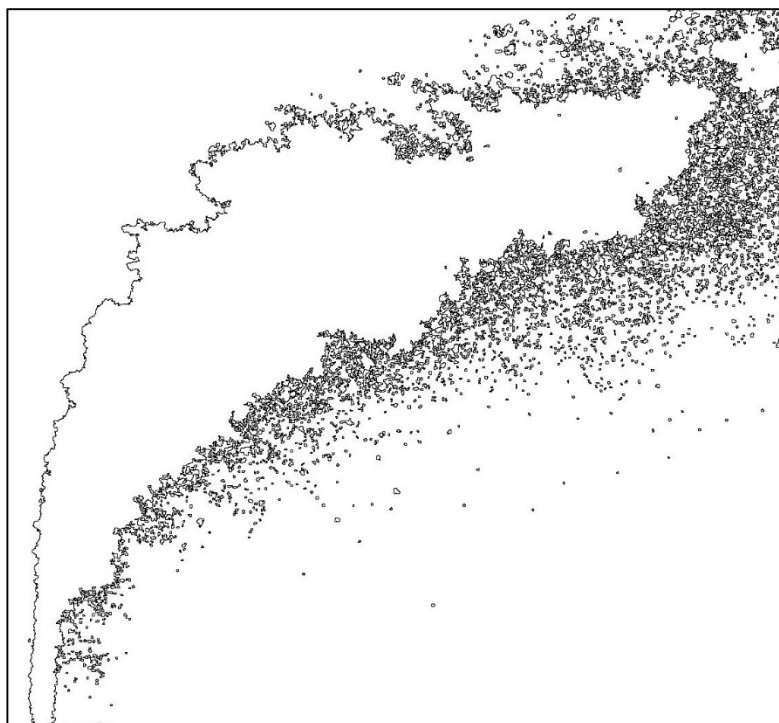
No.	Ref.	$V_{\text{Jet}}$ [m/s]	$V_{\text{Air}}$ [m/s]	q	$We_{\text{Air}}$	$We_{\text{Jet}}$	$Re_{\text{Air}}$	$Re_{\text{Jet}}$	$Oh_{\text{Air}}$ $\times 10^3$	$Oh_{\text{Jet}}$ $\times 10^3$	D10 [ $\mu\text{m}$ ]	D32 [ $\mu\text{m}$ ]
101	■	15	50	38	38	1456	2970	7766	2.072	433.0	68.2	87.3



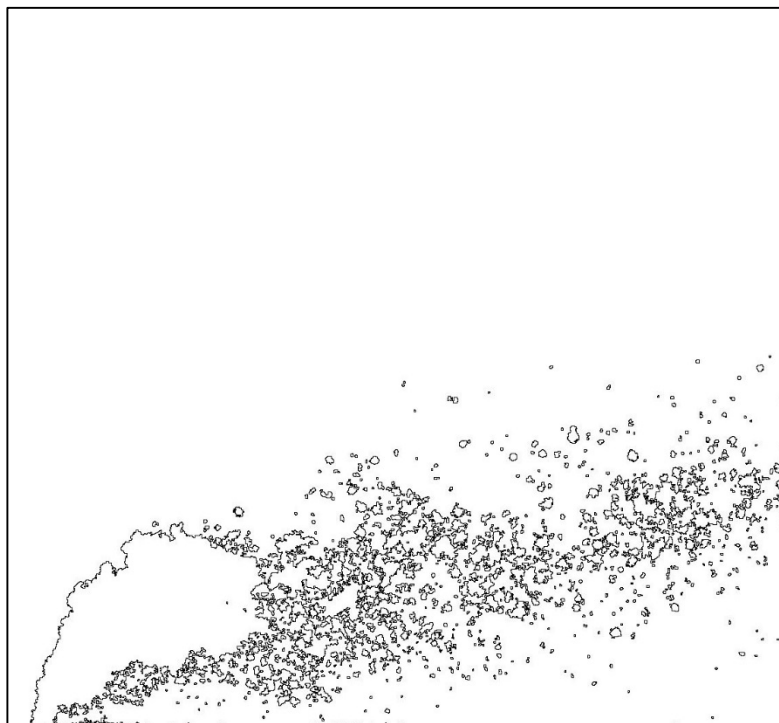
No.	Ref.	$V_{\text{Jet}}$ [m/s]	$V_{\text{Air}}$ [m/s]	q	$We_{\text{Air}}$	$We_{\text{Jet}}$	$Re_{\text{Air}}$	$Re_{\text{Jet}}$	$Oh_{\text{Air}}$ $\times 10^3$	$Oh_{\text{Jet}}$ $\times 10^3$	D10 [ $\mu\text{m}$ ]	D32 [ $\mu\text{m}$ ]
102	■	19	50	62	38	2330	2970	9823	2.072	487.0	66.6	84.5



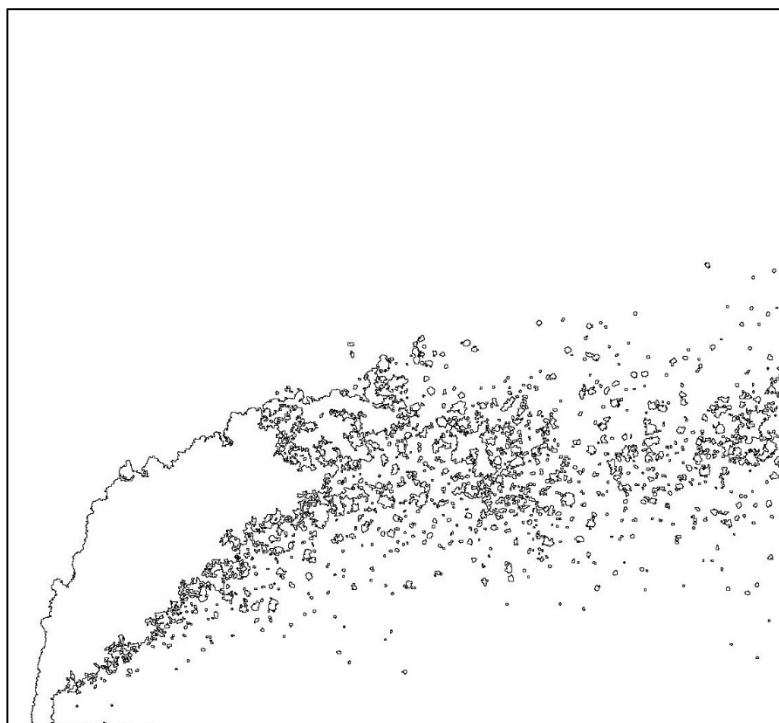
No.	Ref.	$V_{\text{Jet}}$ [m/s]	$V_{\text{Air}}$ [m/s]	q	$We_{\text{Air}}$	$We_{\text{Jet}}$	$Re_{\text{Air}}$	$Re_{\text{Jet}}$	$Oh_{\text{Air}}$ $\times 10^3$	$Oh_{\text{Jet}}$ $\times 10^3$	D10 [ $\mu\text{m}$ ]	D32 [ $\mu\text{m}$ ]
106	■	54	128	118	158	18639	3404	27784	3.690	819.1	57.7	64.5



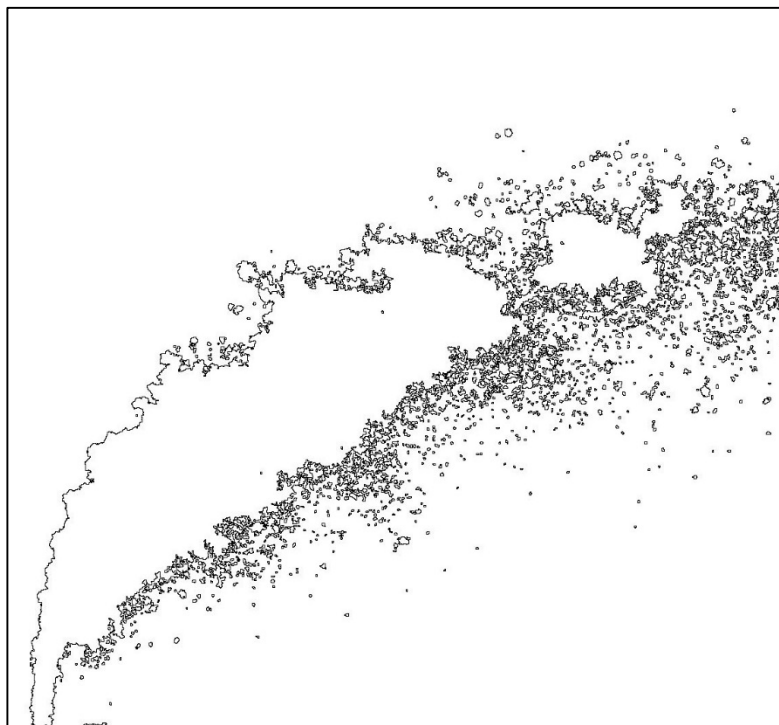
No.	Ref.	$V_{\text{Jet}}$ [m/s]	$V_{\text{Air}}$ [m/s]	q	$We_{\text{Air}}$	$We_{\text{Jet}}$	$Re_{\text{Air}}$	$Re_{\text{Jet}}$	$Oh_{\text{Air}}$ $\times 10^3$	$Oh_{\text{Jet}}$ $\times 10^3$	D10 [ $\mu\text{m}$ ]	D32 [ $\mu\text{m}$ ]
107	■	14	95	14	86	1165	2517	6946	3.690	409.5	65.2	82.6



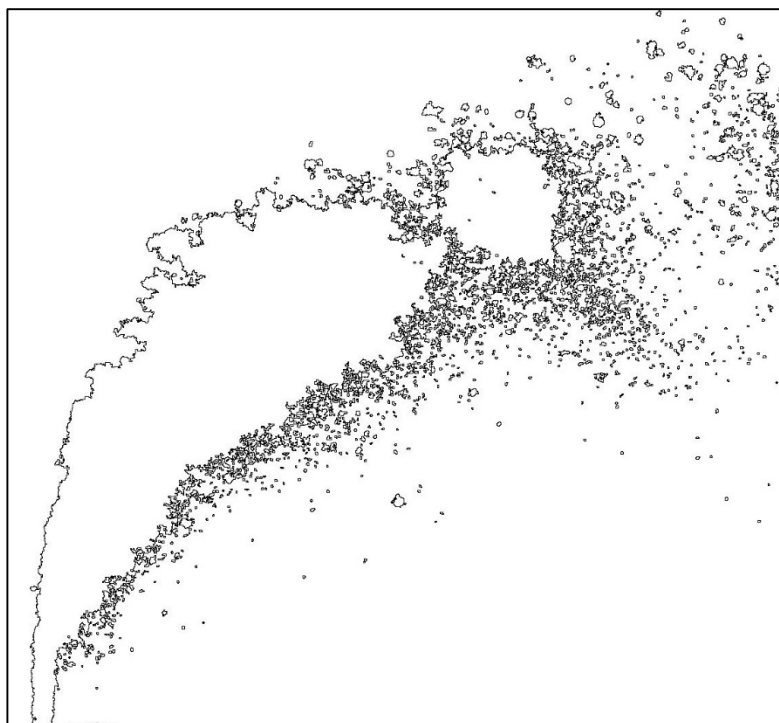
No.	Ref.	$V_{\text{Jet}}$ [m/s]	$V_{\text{Air}}$ [m/s]	q	$We_{\text{Air}}$	$We_{\text{Jet}}$	$Re_{\text{Air}}$	$Re_{\text{Jet}}$	$Oh_{\text{Air}}$ $\times 10^3$	$Oh_{\text{Jet}}$ $\times 10^3$	D10 [ $\mu\text{m}$ ]	D32 [ $\mu\text{m}$ ]
108	■	19	95	27	86	2330	2517	9823	3.690	487.0	62.2	76.4



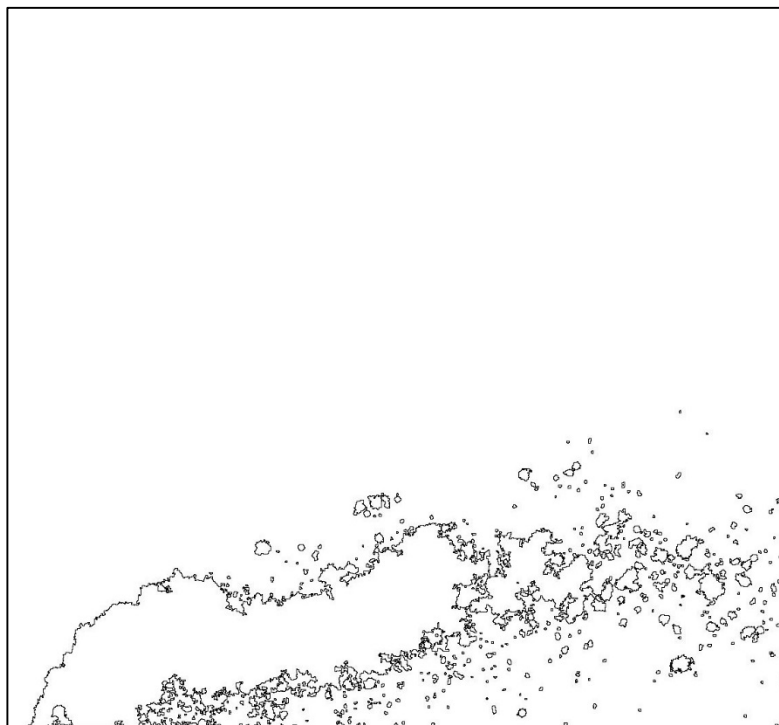
No.	Ref.	$V_{\text{Jet}}$ [m/s]	$V_{\text{Air}}$ [m/s]	q	$We_{\text{Air}}$	$We_{\text{Jet}}$	$Re_{\text{Air}}$	$Re_{\text{Jet}}$	$Oh_{\text{Air}}$ $\times 10^3$	$Oh_{\text{Jet}}$ $\times 10^3$	D10 [ $\mu\text{m}$ ]	D32 [ $\mu\text{m}$ ]
109	■	30	95	68	86	5825	2517	15531	3.690	612.4	60.1	71.4



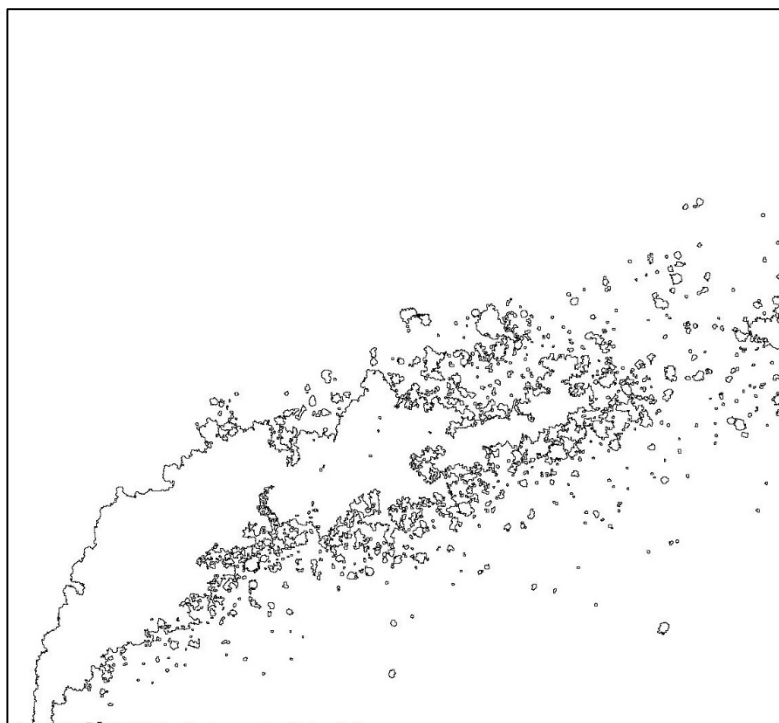
No.	Ref.	$V_{\text{Jet}}$ [m/s]	$V_{\text{Air}}$ [m/s]	q	$We_{\text{Air}}$	$We_{\text{Jet}}$	$Re_{\text{Air}}$	$Re_{\text{Jet}}$	$Oh_{\text{Air}}$ $\times 10^3$	$Oh_{\text{Jet}}$ $\times 10^3$	D10 [ $\mu\text{m}$ ]	D32 [ $\mu\text{m}$ ]
110	■	38	95	108	86	9320	2517	19646	3.690	688.8	59.4	69.4



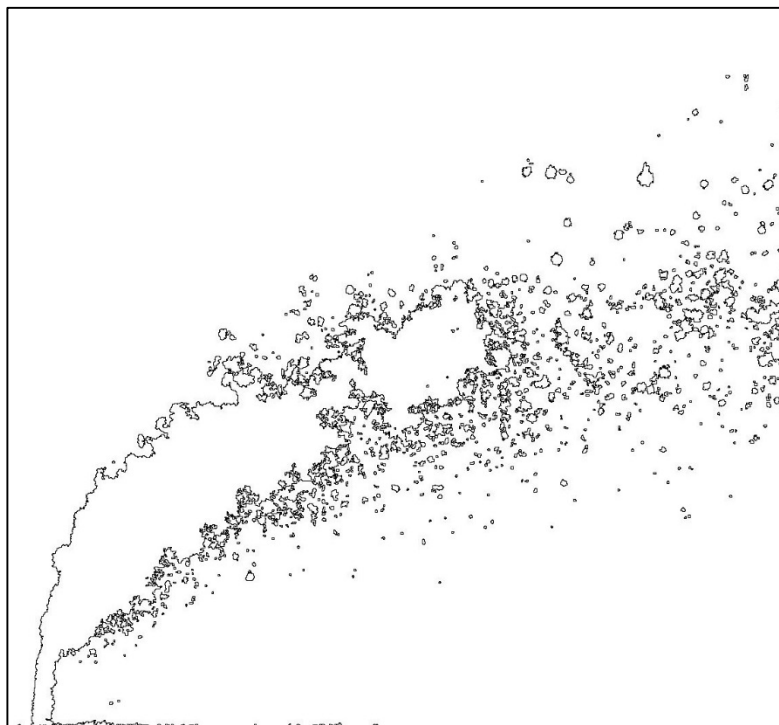
No.	Ref.	$V_{\text{Jet}}$ [m/s]	$V_{\text{Air}}$ [m/s]	q	$We_{\text{Air}}$	$We_{\text{Jet}}$	$Re_{\text{Air}}$	$Re_{\text{Jet}}$	$Oh_{\text{Air}}$ $\times 10^3$	$Oh_{\text{Jet}}$ $\times 10^3$	D10 [ $\mu\text{m}$ ]	D32 [ $\mu\text{m}$ ]
111	■	9	61	13	35	466	1615	4393	3.690	325.7	70.9	92.7



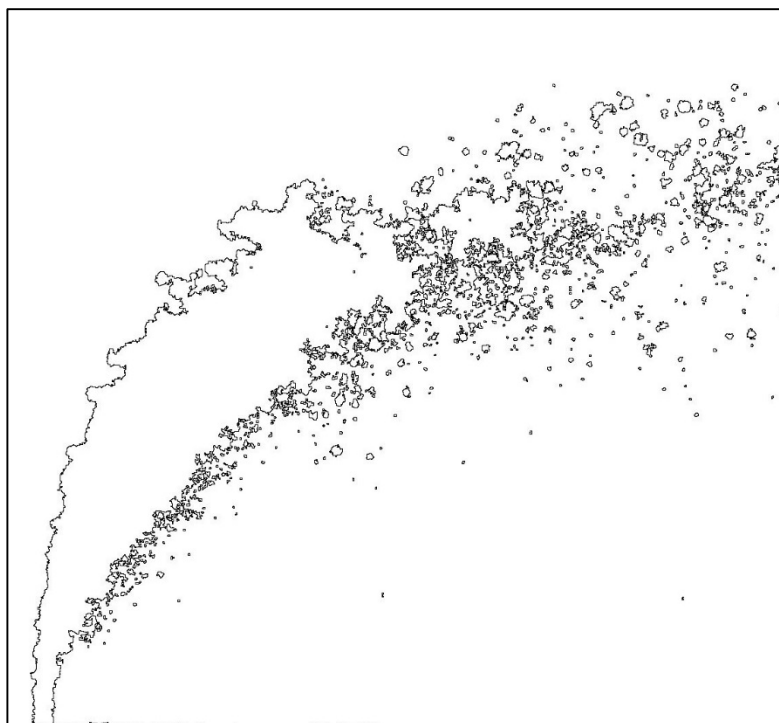
No.	Ref.	$V_{\text{Jet}}$ [m/s]	$V_{\text{Air}}$ [m/s]	q	$We_{\text{Air}}$	$We_{\text{Jet}}$	$Re_{\text{Air}}$	$Re_{\text{Jet}}$	$Oh_{\text{Air}}$ $\times 10^3$	$Oh_{\text{Jet}}$ $\times 10^3$	D10 [ $\mu\text{m}$ ]	D32 [ $\mu\text{m}$ ]
112	■	12	61	26	35	932	1615	6213	3.690	387.3	68.4	89.1



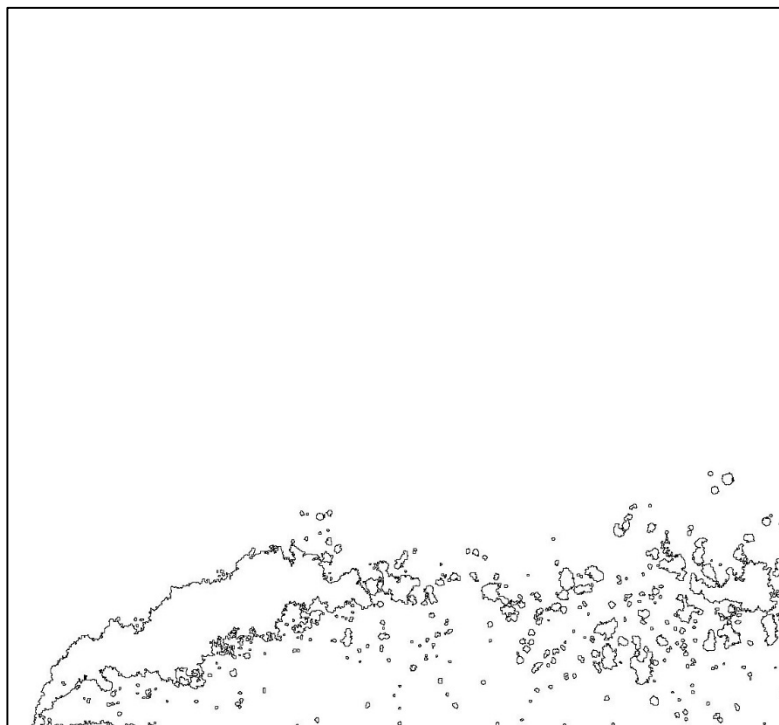
No.	Ref.	$V_{\text{Jet}}$ [m/s]	$V_{\text{Air}}$ [m/s]	q	$We_{\text{Air}}$	$We_{\text{Jet}}$	$Re_{\text{Air}}$	$Re_{\text{Jet}}$	$Oh_{\text{Air}}$ $\times 10^3$	$Oh_{\text{Jet}}$ $\times 10^3$	D10 [ $\mu\text{m}$ ]	D32 [ $\mu\text{m}$ ]
113	■	19	61	66	35	2330	1615	9823	3.690	487.0	65.0	82.3



No.	Ref.	$V_{\text{Jet}}$ [m/s]	$V_{\text{Air}}$ [m/s]	q	$We_{\text{Air}}$	$We_{\text{Jet}}$	$Re_{\text{Air}}$	$Re_{\text{Jet}}$	$Oh_{\text{Air}}$ $\times 10^3$	$Oh_{\text{Jet}}$ $\times 10^3$	D10 [ $\mu\text{m}$ ]	D32 [ $\mu\text{m}$ ]
114	■	24	61	105	35	3728	1615	12425	3.690	547.7	63.3	79.7



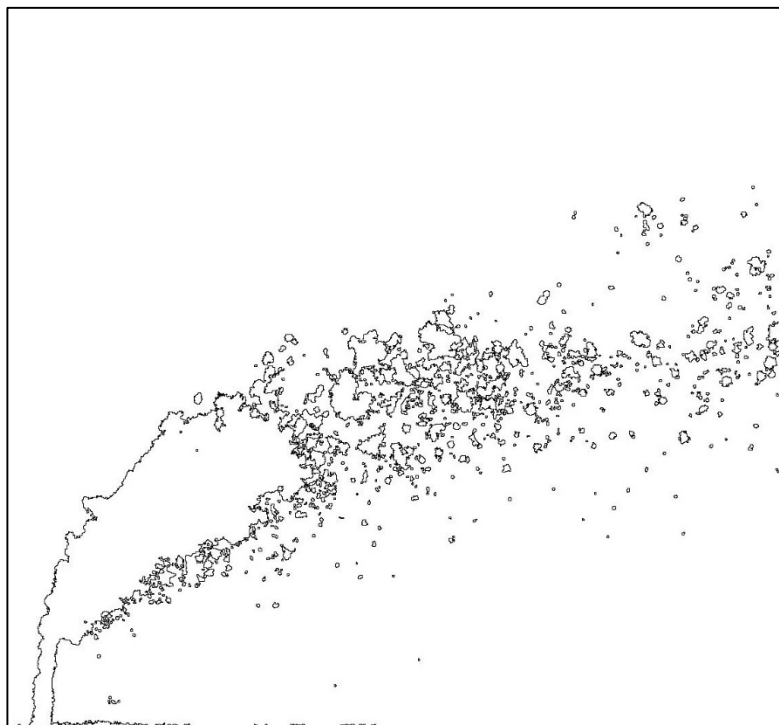
No.	Ref.	$V_{Jet}$ [m/s]	$V_{Air}$ [m/s]	q	$We_{Air}$	$We_{Jet}$	$Re_{Air}$	$Re_{Jet}$	$Oh_{Air}$ $\times 10^3$	$Oh_{Jet}$ $\times 10^3$	D10 [ $\mu m$ ]	D32 [ $\mu m$ ]
115	■	7	48	13	22	291	1277	3473	3.690	289.6	72.6	95.3



No.	Ref.	$V_{Jet}$ [m/s]	$V_{Air}$ [m/s]	q	$We_{Air}$	$We_{Jet}$	$Re_{Air}$	$Re_{Jet}$	$Oh_{Air}$ $\times 10^3$	$Oh_{Jet}$ $\times 10^3$	D10 [ $\mu m$ ]	D32 [ $\mu m$ ]
116	■	10	48	26	22	582	1277	4911	3.690	344.4	71.8	94.6



No.	Ref.	$V_{\text{Jet}}$ [m/s]	$V_{\text{Air}}$ [m/s]	q	$We_{\text{Air}}$	$We_{\text{Jet}}$	$Re_{\text{Air}}$	$Re_{\text{Jet}}$	$Oh_{\text{Air}}$ $\times 10^3$	$Oh_{\text{Jet}}$ $\times 10^3$	D10 [ $\mu\text{m}$ ]	D32 [ $\mu\text{m}$ ]
117	■	15	48	66	22	1456	1277	7766	3.690	433.0	68.2	88.6

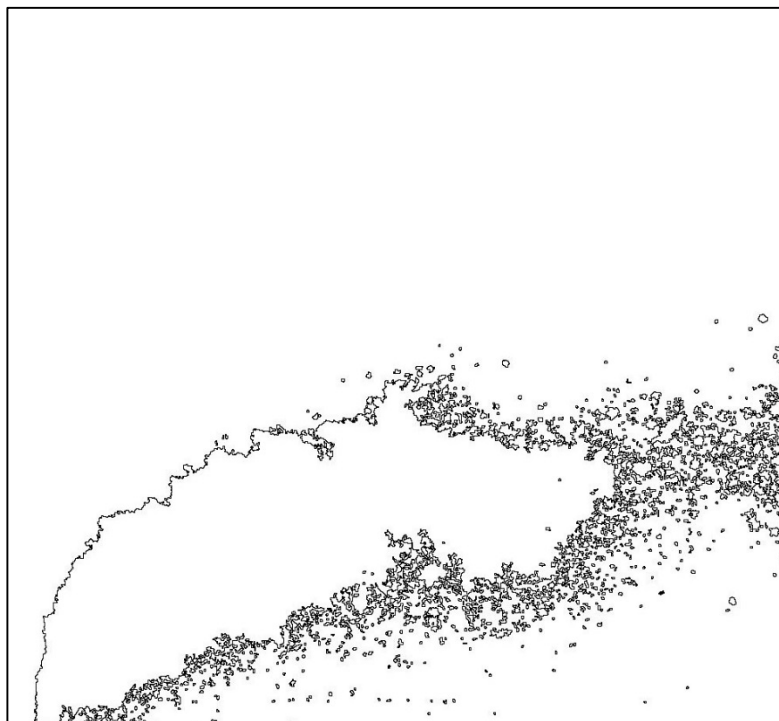


No.	Ref.	$V_{\text{Jet}}$ [m/s]	$V_{\text{Air}}$ [m/s]	q	$We_{\text{Air}}$	$We_{\text{Jet}}$	$Re_{\text{Air}}$	$Re_{\text{Jet}}$	$Oh_{\text{Air}}$ $\times 10^3$	$Oh_{\text{Jet}}$ $\times 10^3$	D10 [ $\mu\text{m}$ ]	D32 [ $\mu\text{m}$ ]
118	■	19	48	105	22	2330	1277	9823	3.690	487.0	66.3	85.1

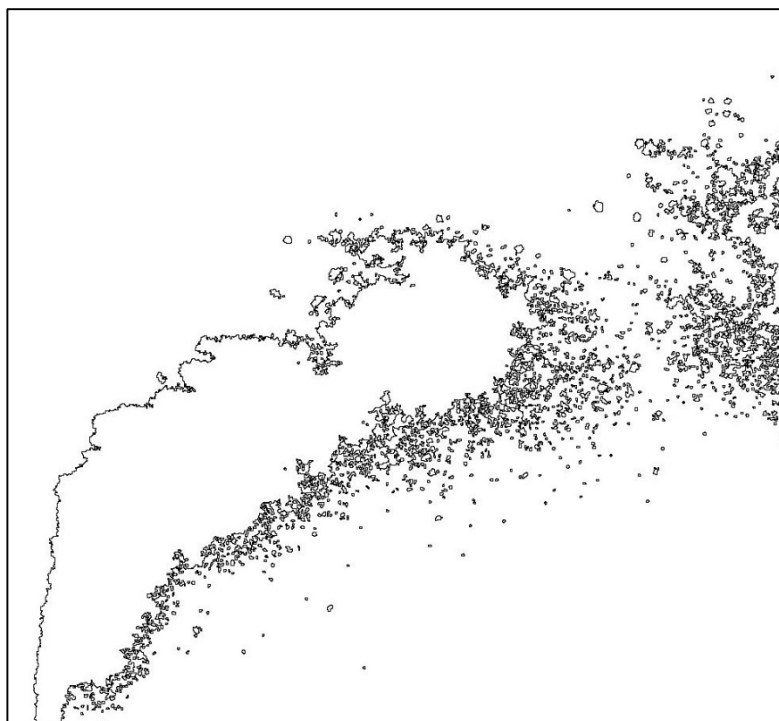




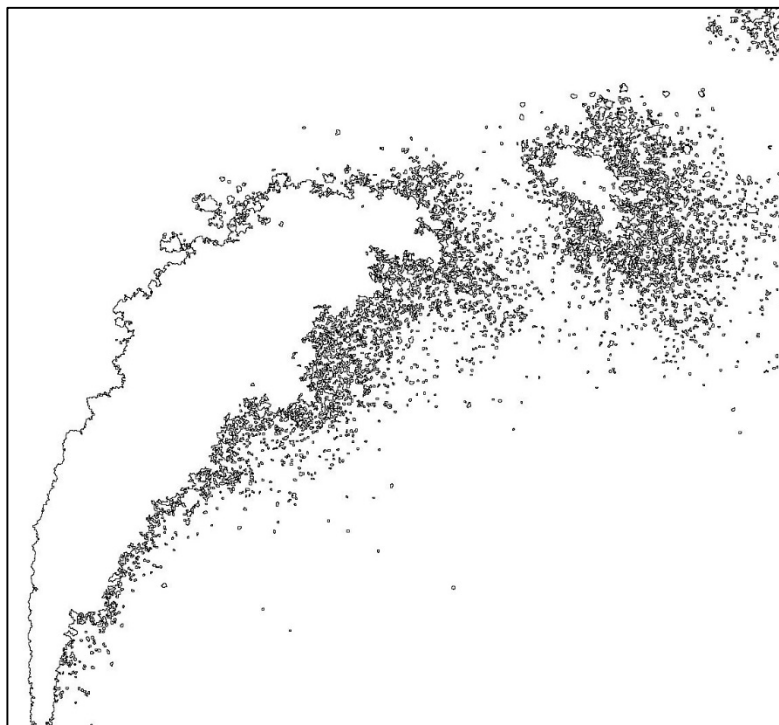
No.	Ref.	$V_{\text{Jet}}$ [m/s]	$V_{\text{Air}}$ [m/s]	q	$We_{\text{Air}}$	$We_{\text{Jet}}$	$Re_{\text{Air}}$	$Re_{\text{Jet}}$	$Oh_{\text{Air}}$ $\times 10^3$	$Oh_{\text{Jet}}$ $\times 10^3$	D10 [ $\mu\text{m}$ ]	D32 [ $\mu\text{m}$ ]
119	■	19	127	18	129	2330	2447	9823	4.648	487.0	59.2	69.3



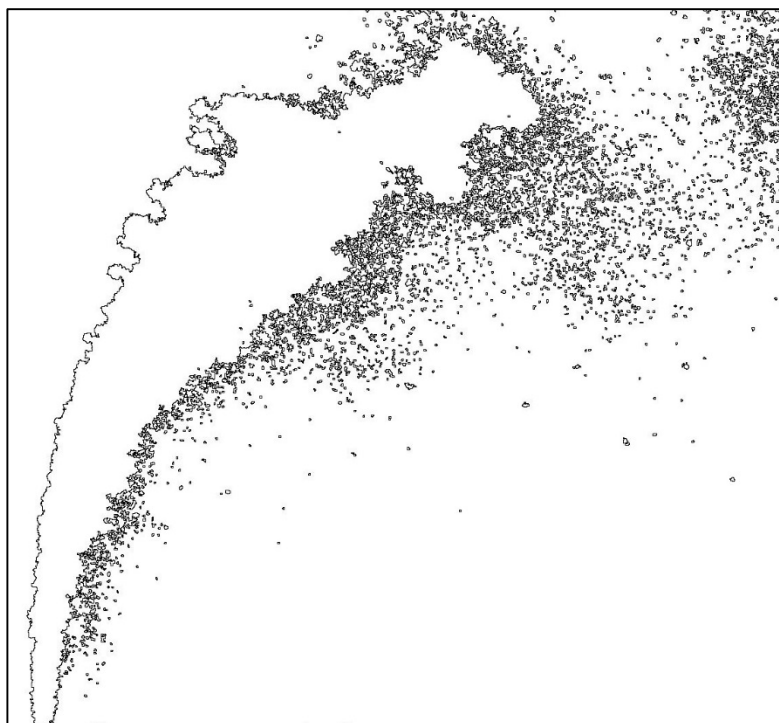
No.	Ref.	$V_{\text{Jet}}$ [m/s]	$V_{\text{Air}}$ [m/s]	q	$We_{\text{Air}}$	$We_{\text{Jet}}$	$Re_{\text{Air}}$	$Re_{\text{Jet}}$	$Oh_{\text{Air}}$ $\times 10^3$	$Oh_{\text{Jet}}$ $\times 10^3$	D10 [ $\mu\text{m}$ ]	D32 [ $\mu\text{m}$ ]
120	■	27	127	36	129	4660	2447	13892	4.648	579.2	58.1	66.0



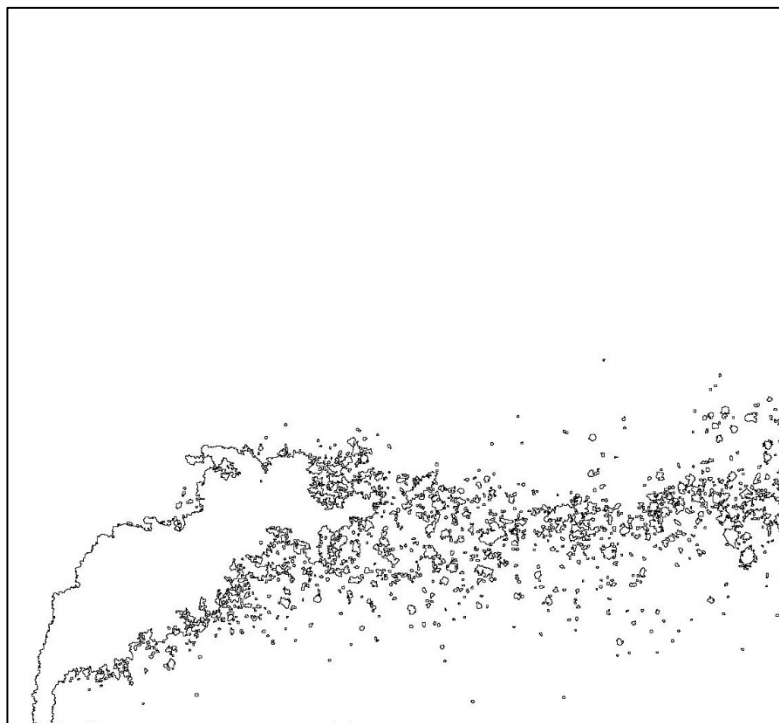
No.	Ref.	$V_{\text{Jet}}$ [m/s]	$V_{\text{Air}}$ [m/s]	q	$We_{\text{Air}}$	$We_{\text{Jet}}$	$Re_{\text{Air}}$	$Re_{\text{Jet}}$	$Oh_{\text{Air}}$ $\times 10^3$	$Oh_{\text{Jet}}$ $\times 10^3$	D10 [ $\mu\text{m}$ ]	D32 [ $\mu\text{m}$ ]
121	■	43	127	90	129	11649	2447	21965	4.648	728.3	57.2	64.0



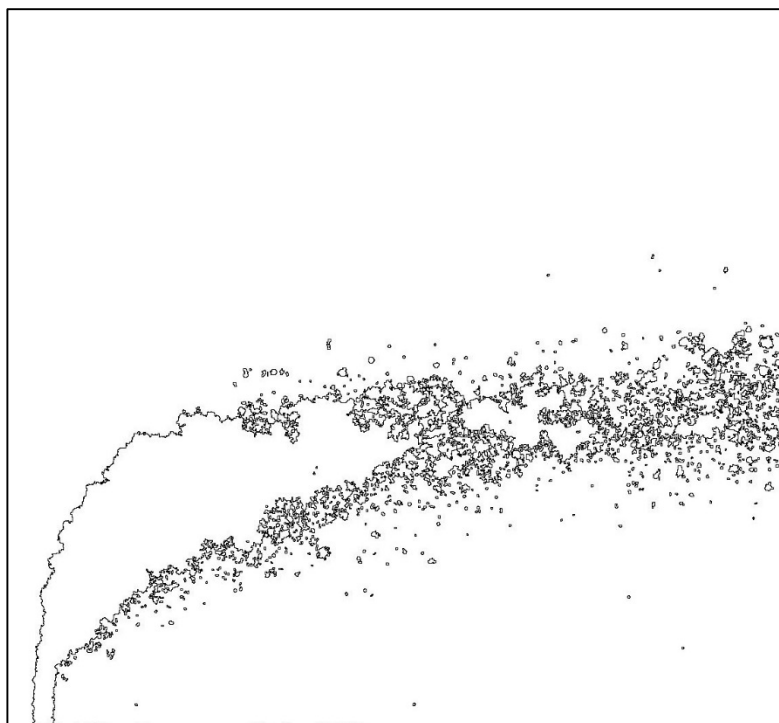
No.	Ref.	$V_{\text{Jet}}$ [m/s]	$V_{\text{Air}}$ [m/s]	q	$We_{\text{Air}}$	$We_{\text{Jet}}$	$Re_{\text{Air}}$	$Re_{\text{Jet}}$	$Oh_{\text{Air}}$ $\times 10^3$	$Oh_{\text{Jet}}$ $\times 10^3$	D10 [ $\mu\text{m}$ ]	D32 [ $\mu\text{m}$ ]
122	■	54	127	144	129	18639	2447	27784	4.648	819.1	56.7	62.5



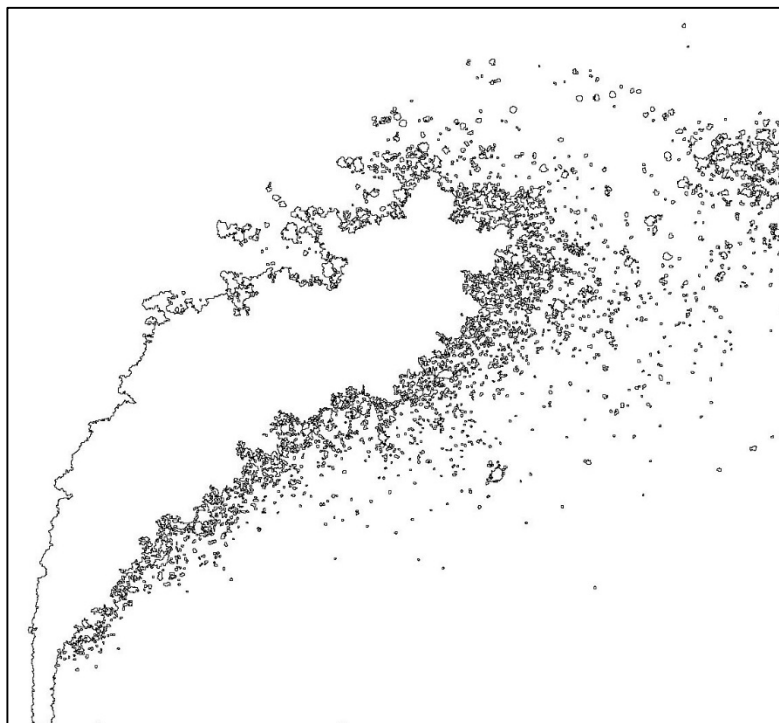
No.	Ref.	$V_{\text{Jet}}$ [m/s]	$V_{\text{Air}}$ [m/s]	q	$We_{\text{Air}}$	$We_{\text{Jet}}$	$Re_{\text{Air}}$	$Re_{\text{Jet}}$	$Oh_{\text{Air}}$ $\times 10^3$	$Oh_{\text{Jet}}$ $\times 10^3$	D10 [ $\mu\text{m}$ ]	D32 [ $\mu\text{m}$ ]
123	■	14	95	16	72	1165	1825	6946	4.648	409.5	64.0	81.4



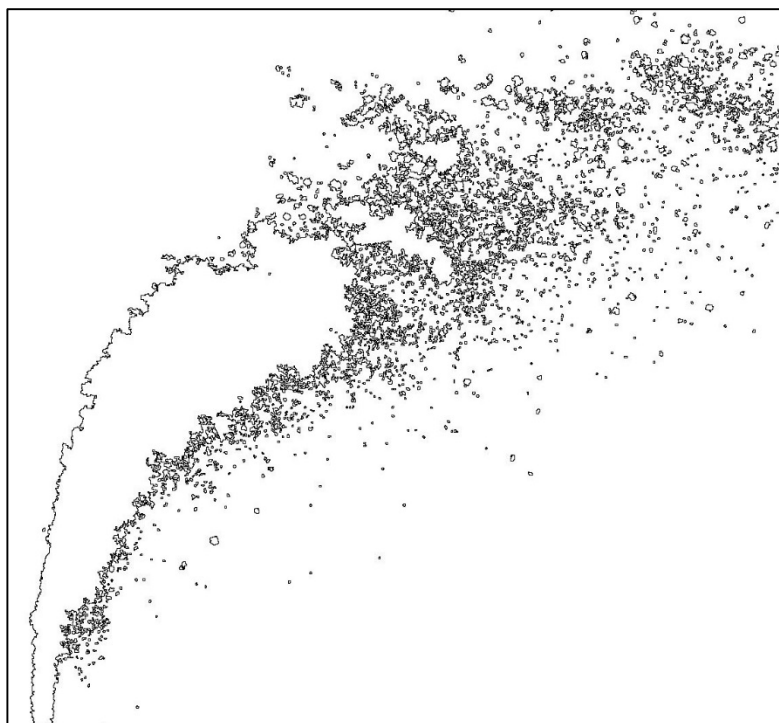
No.	Ref.	$V_{\text{Jet}}$ [m/s]	$V_{\text{Air}}$ [m/s]	q	$We_{\text{Air}}$	$We_{\text{Jet}}$	$Re_{\text{Air}}$	$Re_{\text{Jet}}$	$Oh_{\text{Air}}$ $\times 10^3$	$Oh_{\text{Jet}}$ $\times 10^3$	D10 [ $\mu\text{m}$ ]	D32 [ $\mu\text{m}$ ]
124	■	19	95	32	72	2330	1825	9823	4.648	487.0	61.8	76.1



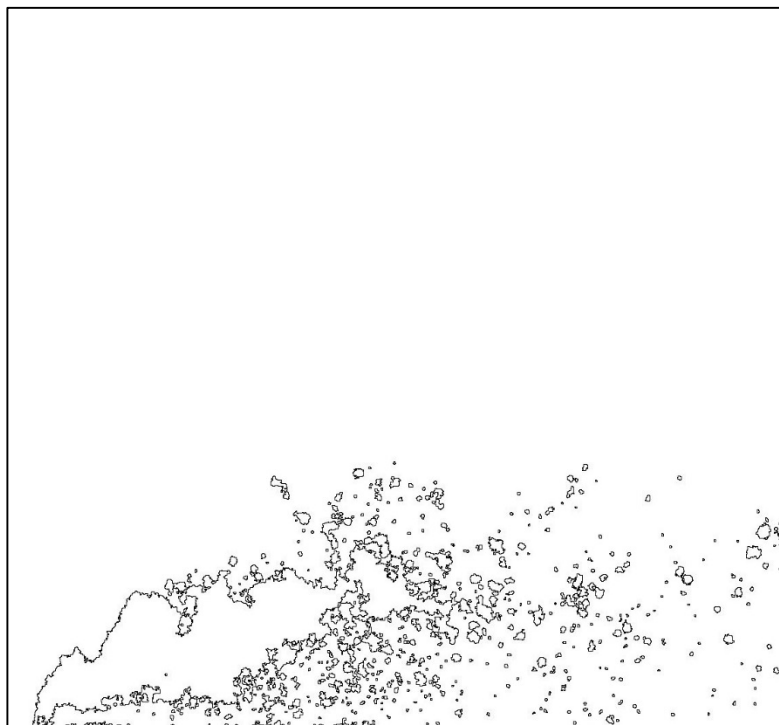
No.	Ref.	$V_{Jet}$ [m/s]	$V_{Air}$ [m/s]	q	$We_{Air}$	$We_{Jet}$	$Re_{Air}$	$Re_{Jet}$	$Oh_{Air}$ $\times 10^3$	$Oh_{Jet}$ $\times 10^3$	D10 [ $\mu m$ ]	D32 [ $\mu m$ ]
125	■	30	95	81	72	5825	1825	15531	4.648	612.4	59.7	71.3



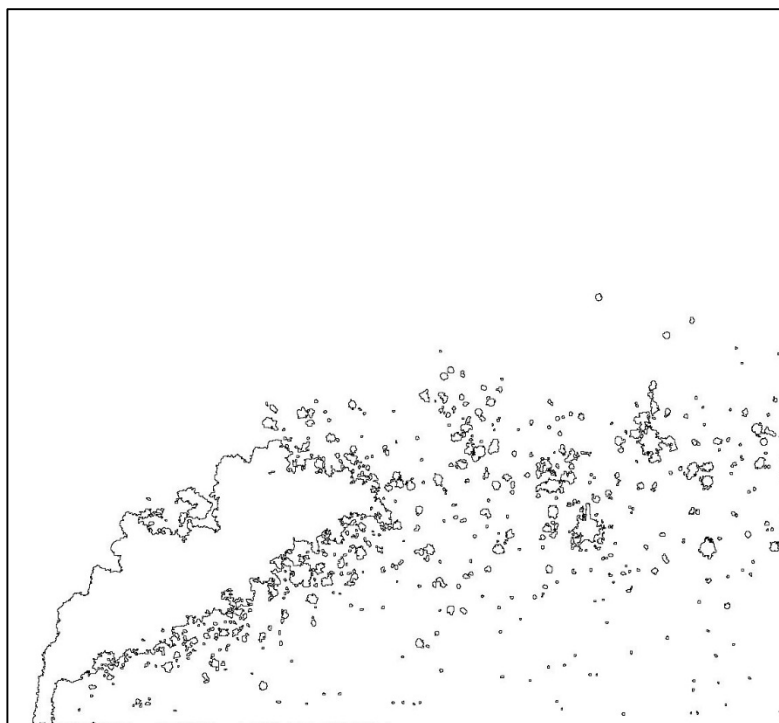
No.	Ref.	$V_{Jet}$ [m/s]	$V_{Air}$ [m/s]	q	$We_{Air}$	$We_{Jet}$	$Re_{Air}$	$Re_{Jet}$	$Oh_{Air}$ $\times 10^3$	$Oh_{Jet}$ $\times 10^3$	D10 [ $\mu m$ ]	D32 [ $\mu m$ ]
126	■	38	95	130	72	9320	1825	19646	4.648	688.8	59.3	70.1



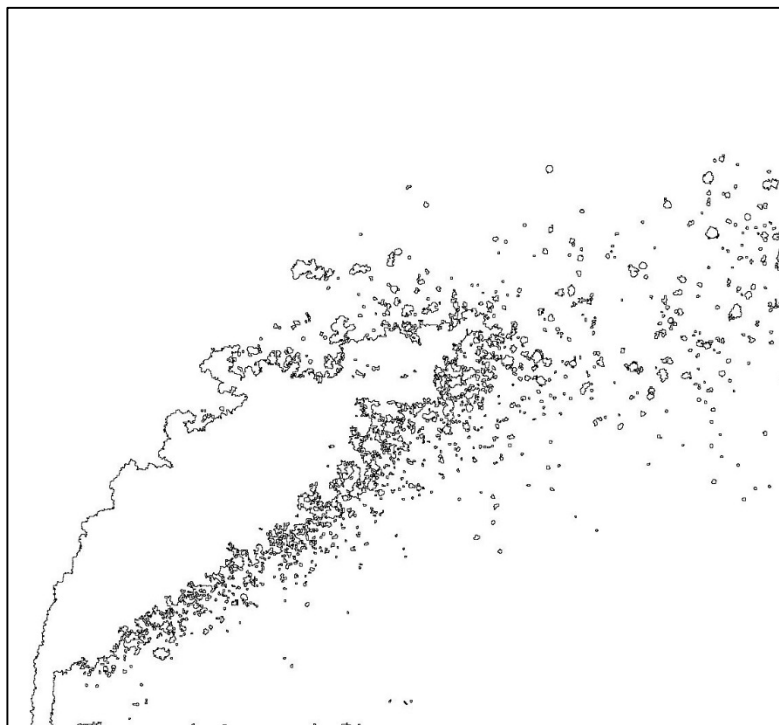
No.	Ref.	$V_{\text{Jet}}$ [m/s]	$V_{\text{Air}}$ [m/s]	q	$We_{\text{Air}}$	$We_{\text{Jet}}$	$Re_{\text{Air}}$	$Re_{\text{Jet}}$	$Oh_{\text{Air}}$ $\times 10^3$	$Oh_{\text{Jet}}$ $\times 10^3$	D10 [ $\mu\text{m}$ ]	D32 [ $\mu\text{m}$ ]
127	■	9	60	16	29	466	1154	4393	4.648	325.7	70.8	93.3



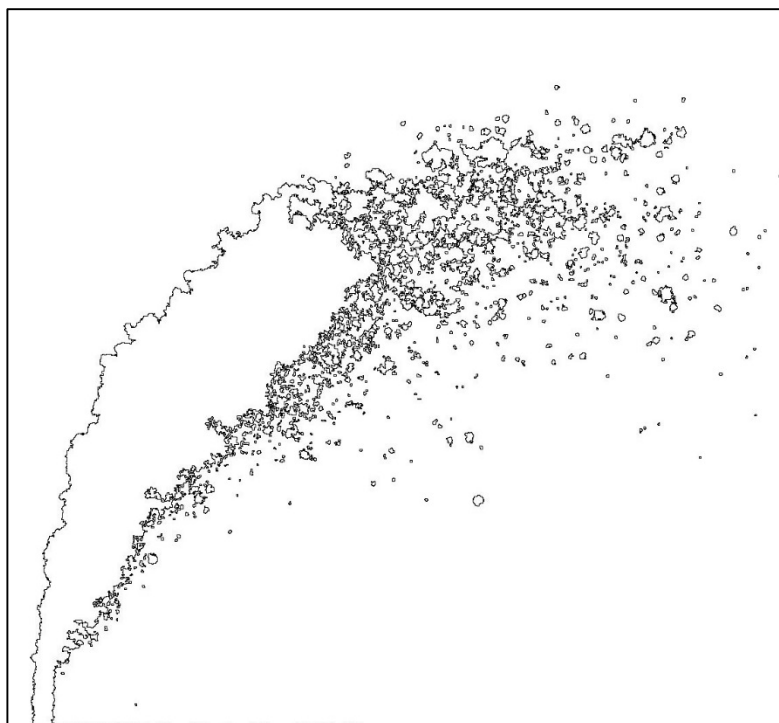
No.	Ref.	$V_{\text{Jet}}$ [m/s]	$V_{\text{Air}}$ [m/s]	q	$We_{\text{Air}}$	$We_{\text{Jet}}$	$Re_{\text{Air}}$	$Re_{\text{Jet}}$	$Oh_{\text{Air}}$ $\times 10^3$	$Oh_{\text{Jet}}$ $\times 10^3$	D10 [ $\mu\text{m}$ ]	D32 [ $\mu\text{m}$ ]
128	■	12	60	32	29	932	1154	6213	4.648	387.3	68.8	90.5



No.	Ref.	$V_{\text{Jet}}$ [m/s]	$V_{\text{Air}}$ [m/s]	q	$We_{\text{Air}}$	$We_{\text{Jet}}$	$Re_{\text{Air}}$	$Re_{\text{Jet}}$	$Oh_{\text{Air}}$ $\times 10^3$	$Oh_{\text{Jet}}$ $\times 10^3$	D10 [ $\mu\text{m}$ ]	D32 [ $\mu\text{m}$ ]
129	■	19	60	81	29	2330	1154	9823	4.648	487.0	65.7	85.1



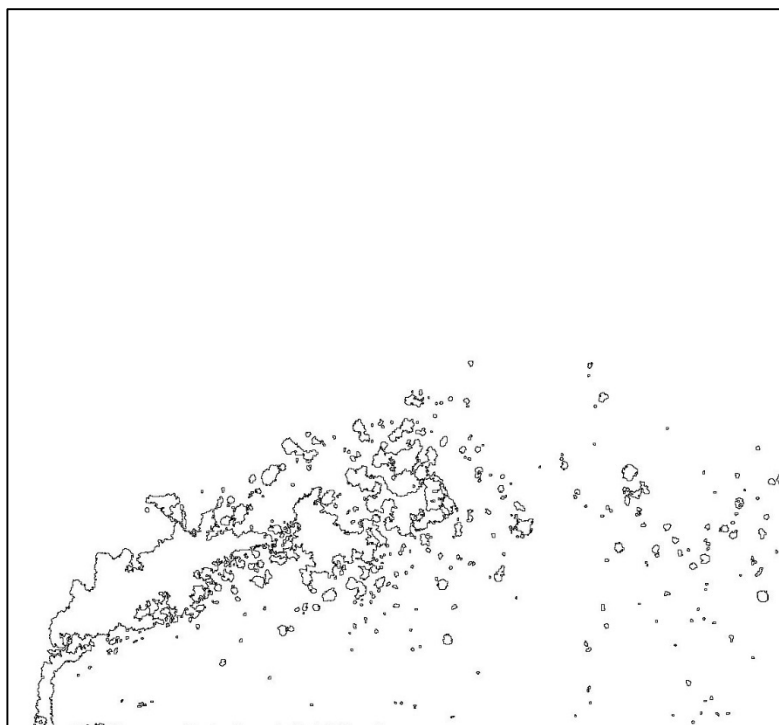
No.	Ref.	$V_{\text{Jet}}$ [m/s]	$V_{\text{Air}}$ [m/s]	q	$We_{\text{Air}}$	$We_{\text{Jet}}$	$Re_{\text{Air}}$	$Re_{\text{Jet}}$	$Oh_{\text{Air}}$ $\times 10^3$	$Oh_{\text{Jet}}$ $\times 10^3$	D10 [ $\mu\text{m}$ ]	D32 [ $\mu\text{m}$ ]
130	■	24	60	130	29	3728	1154	12425	4.648	547.7	64.1	81.8



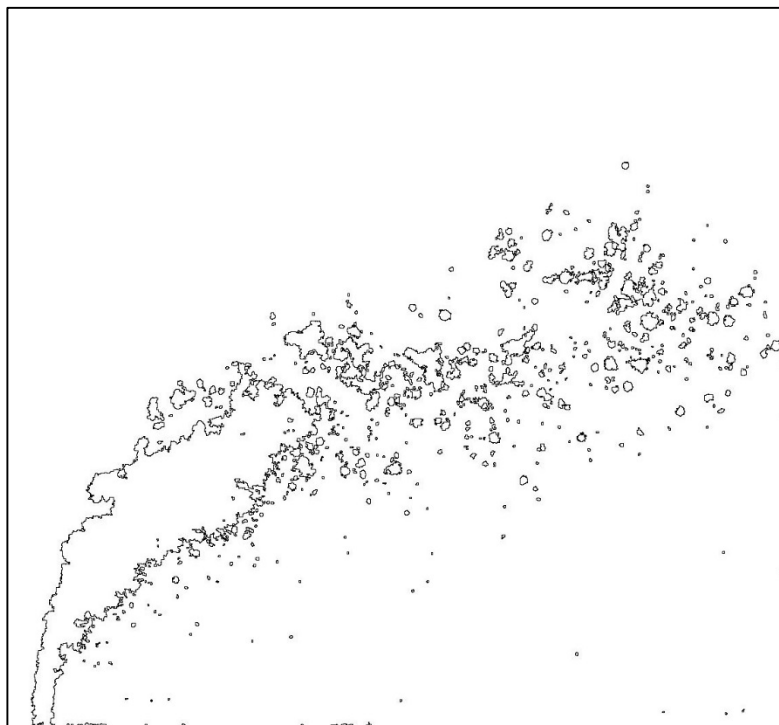
No.	Ref.	$V_{\text{Jet}}$ [m/s]	$V_{\text{Air}}$ [m/s]	q	$We_{\text{Air}}$	$We_{\text{Jet}}$	$Re_{\text{Air}}$	$Re_{\text{Jet}}$	$Oh_{\text{Air}}$ $\times 10^3$	$Oh_{\text{Jet}}$ $\times 10^3$	D10 [ $\mu\text{m}$ ]	D32 [ $\mu\text{m}$ ]
131	■	7	48	16	18	291	925	3473	4.648	289.6	72.5	95.0



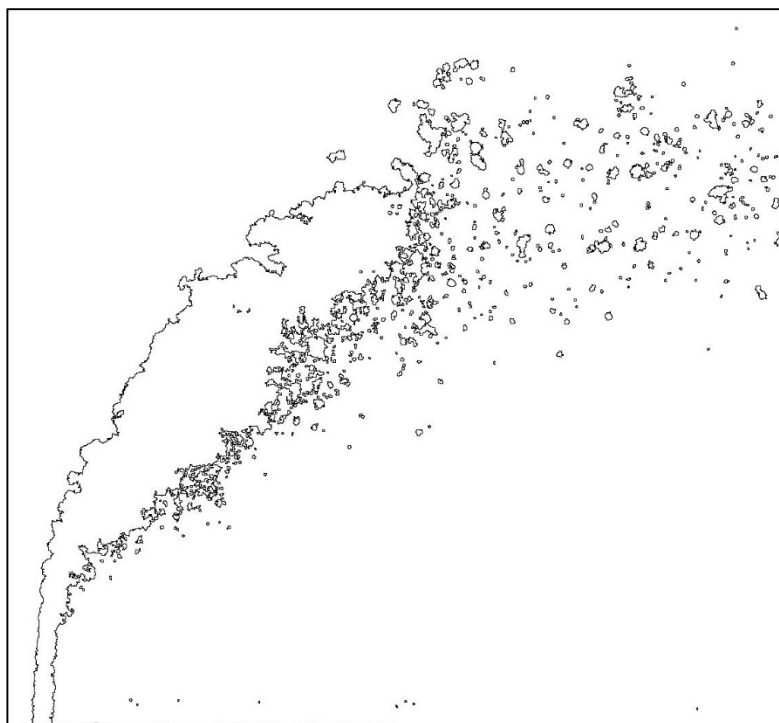
No.	Ref.	$V_{\text{Jet}}$ [m/s]	$V_{\text{Air}}$ [m/s]	q	$We_{\text{Air}}$	$We_{\text{Jet}}$	$Re_{\text{Air}}$	$Re_{\text{Jet}}$	$Oh_{\text{Air}}$ $\times 10^3$	$Oh_{\text{Jet}}$ $\times 10^3$	D10 [ $\mu\text{m}$ ]	D32 [ $\mu\text{m}$ ]
132	■	10	48	31	18	582	925	4911	4.648	344.4	70.9	94.3



No.	Ref.	$V_{\text{Jet}}$ [m/s]	$V_{\text{Air}}$ [m/s]	q	$We_{\text{Air}}$	$We_{\text{Jet}}$	$Re_{\text{Air}}$	$Re_{\text{Jet}}$	$Oh_{\text{Air}}$ $\times 10^3$	$Oh_{\text{Jet}}$ $\times 10^3$	D10 [ $\mu\text{m}$ ]	D32 [ $\mu\text{m}$ ]
133	■	15	48	79	18	1456	925	7766	4.648	433.0	68.7	91.4

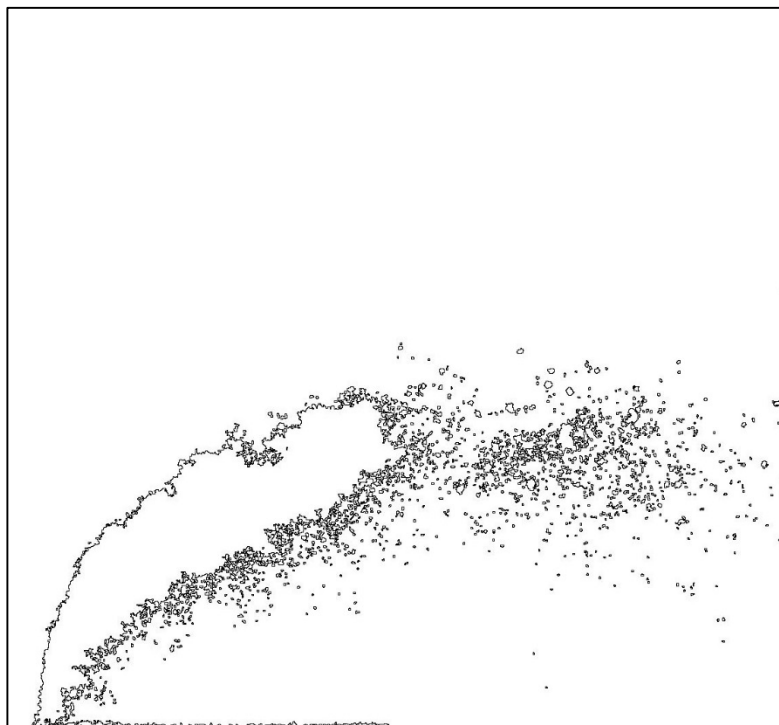


No.	Ref.	$V_{\text{Jet}}$ [m/s]	$V_{\text{Air}}$ [m/s]	q	$We_{\text{Air}}$	$We_{\text{Jet}}$	$Re_{\text{Air}}$	$Re_{\text{Jet}}$	$Oh_{\text{Air}}$ $\times 10^3$	$Oh_{\text{Jet}}$ $\times 10^3$	D10 [ $\mu\text{m}$ ]	D32 [ $\mu\text{m}$ ]
134	■	19	48	126	18	2330	925	9823	4.648	487.0	67.3	88.1

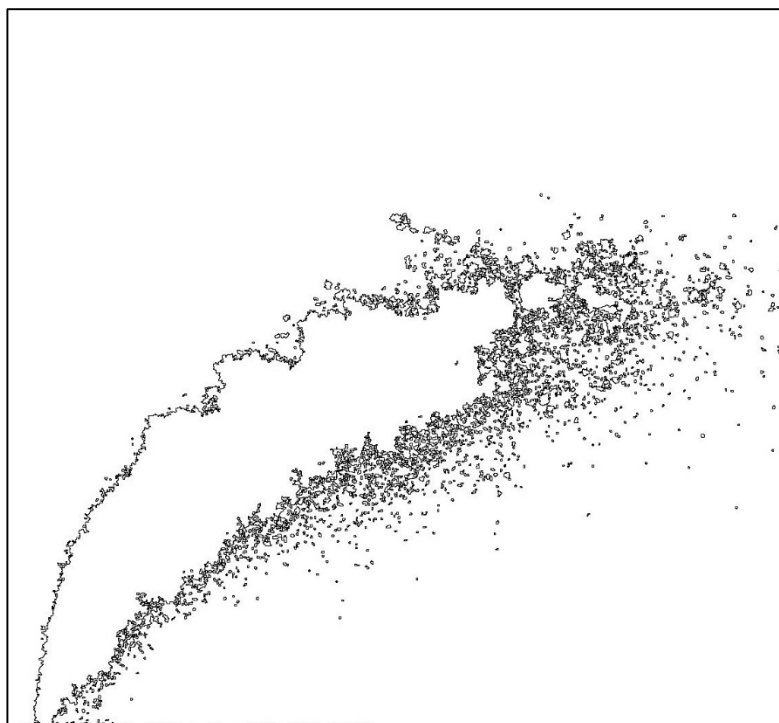




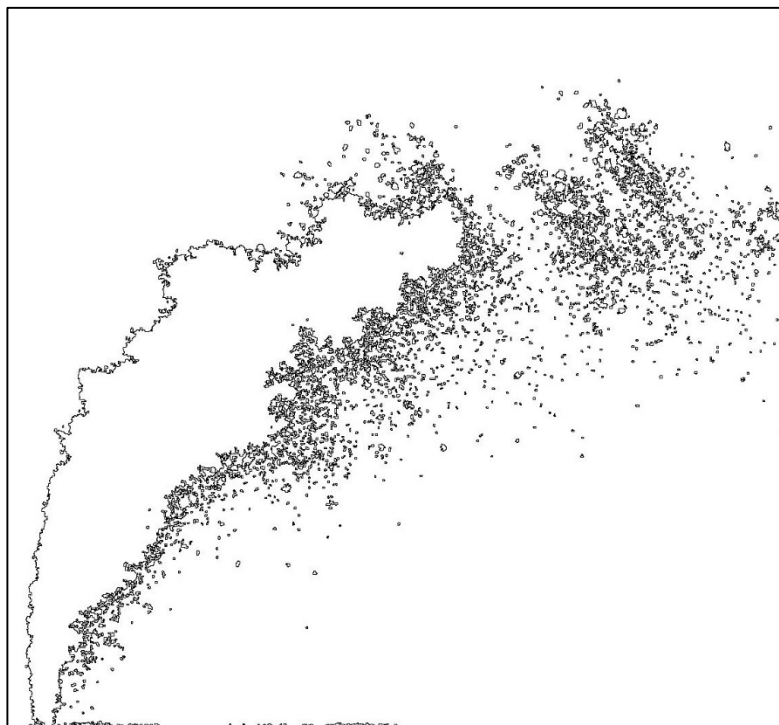
No.	Ref.	$V_{\text{Jet}}$ [m/s]	$V_{\text{Air}}$ [m/s]	q	$We_{\text{Air}}$	$We_{\text{Jet}}$	$Re_{\text{Air}}$	$Re_{\text{Jet}}$	$Oh_{\text{Air}}$ $\times 10^3$	$Oh_{\text{Jet}}$ $\times 10^3$	D10 [ $\mu\text{m}$ ]	D32 [ $\mu\text{m}$ ]
135	▲	18	88	10	217	2113	9632	9356	1.531	475.3	57.5	64.8



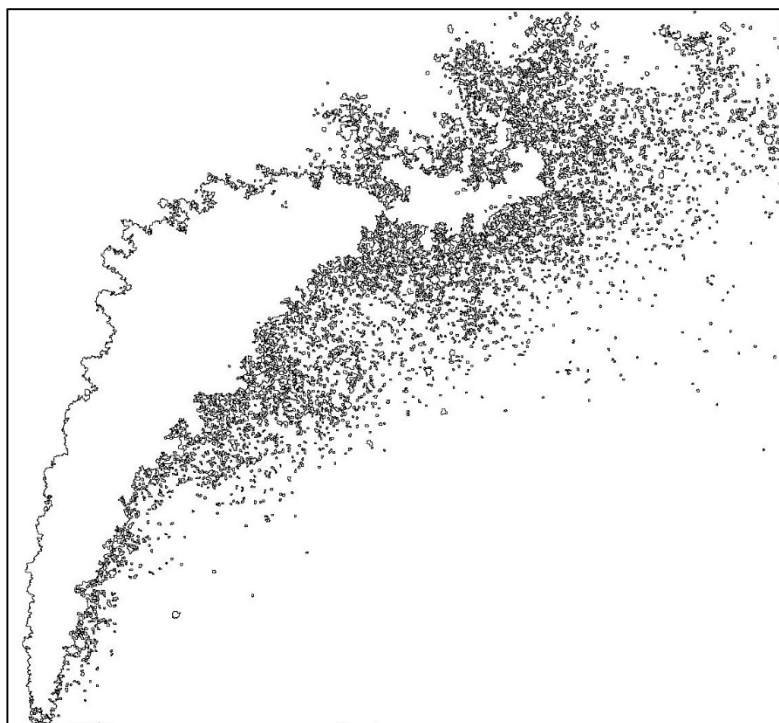
No.	Ref.	$V_{\text{Jet}}$ [m/s]	$V_{\text{Air}}$ [m/s]	q	$We_{\text{Air}}$	$We_{\text{Jet}}$	$Re_{\text{Air}}$	$Re_{\text{Jet}}$	$Oh_{\text{Air}}$ $\times 10^3$	$Oh_{\text{Jet}}$ $\times 10^3$	D10 [ $\mu\text{m}$ ]	D32 [ $\mu\text{m}$ ]
136	▲	26	88	19	217	4227	9632	13232	1.531	565.2	57.4	64.5



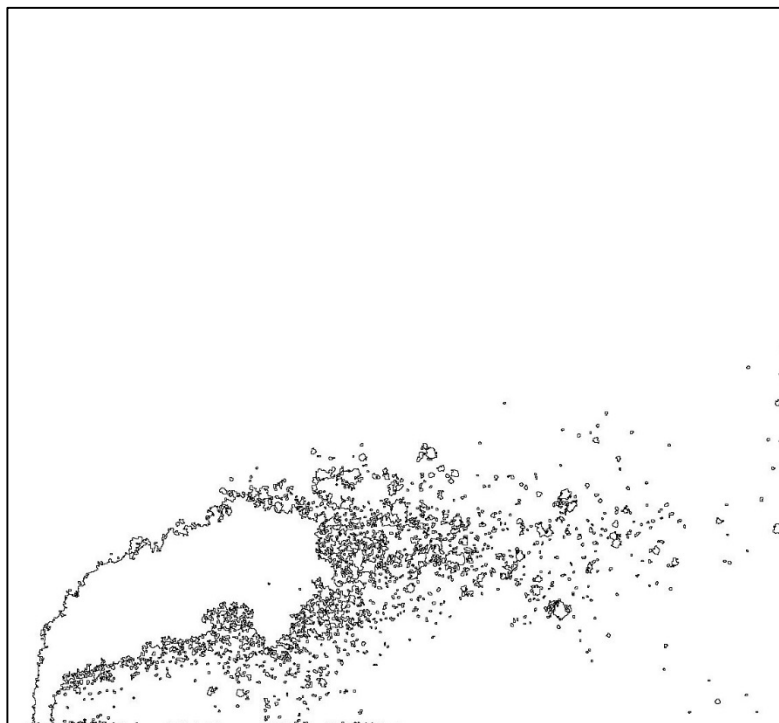
No.	Ref.	$V_{\text{Jet}}$ [m/s]	$V_{\text{Air}}$ [m/s]	q	$We_{\text{Air}}$	$We_{\text{Jet}}$	$Re_{\text{Air}}$	$Re_{\text{Jet}}$	$Oh_{\text{Air}}$ $\times 10^3$	$Oh_{\text{Jet}}$ $\times 10^3$	D10 [ $\mu\text{m}$ ]	D32 [ $\mu\text{m}$ ]
137	▲	41	88	49	217	10567	9632	20921	1.531	710.7	56.7	63.3



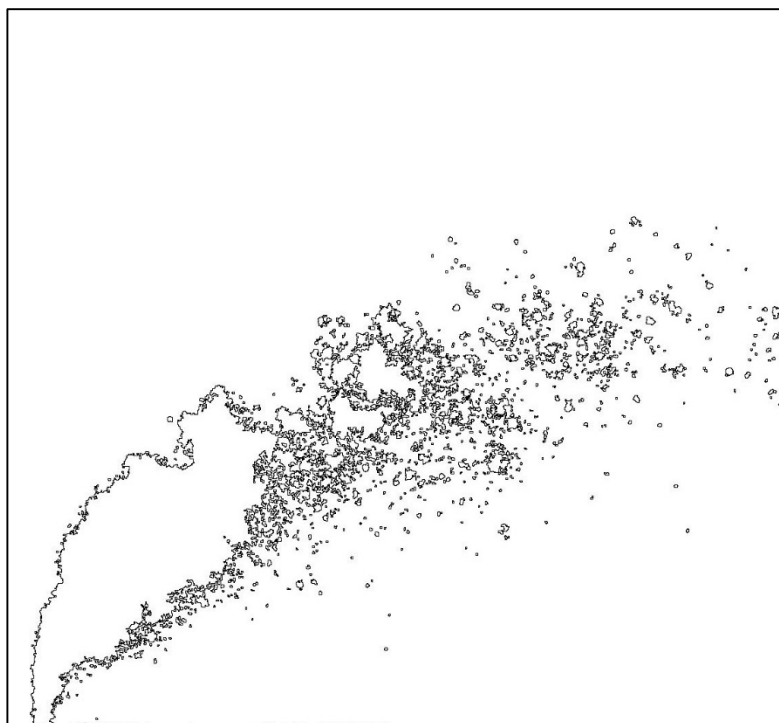
No.	Ref.	$V_{\text{Jet}}$ [m/s]	$V_{\text{Air}}$ [m/s]	q	$We_{\text{Air}}$	$We_{\text{Jet}}$	$Re_{\text{Air}}$	$Re_{\text{Jet}}$	$Oh_{\text{Air}}$ $\times 10^3$	$Oh_{\text{Jet}}$ $\times 10^3$	D10 [ $\mu\text{m}$ ]	D32 [ $\mu\text{m}$ ]
138	▲	52	88	78	217	16908	9632	26464	1.531	799.3	56.3	62.3



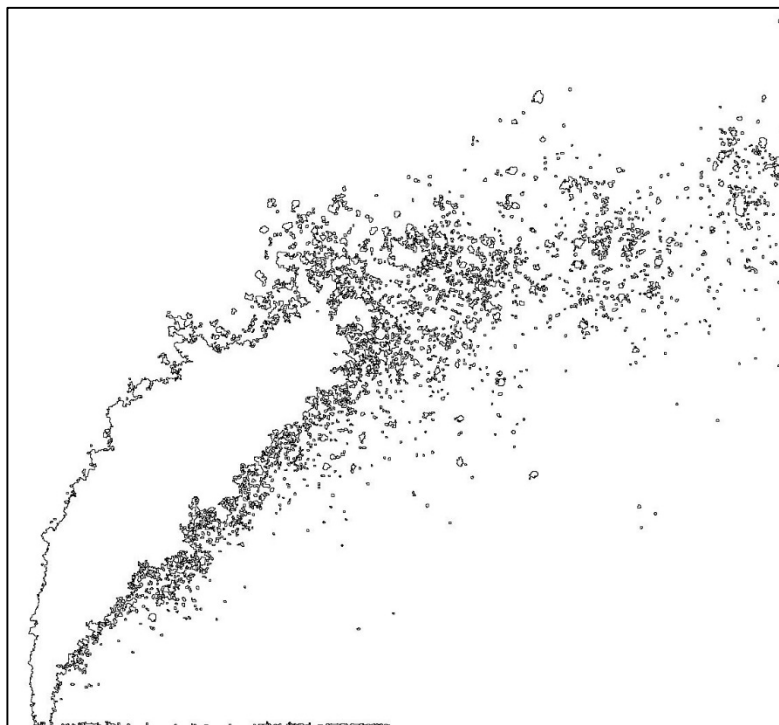
No.	Ref.	$V_{\text{Jet}}$ [m/s]	$V_{\text{Air}}$ [m/s]	q	$We_{\text{Air}}$	$We_{\text{Jet}}$	$Re_{\text{Air}}$	$Re_{\text{Jet}}$	$Oh_{\text{Air}}$ $\times 10^3$	$Oh_{\text{Jet}}$ $\times 10^3$	D10 [ $\mu\text{m}$ ]	D32 [ $\mu\text{m}$ ]
139	▲	14	68	9	129	1165	7432	6947	1.531	409.5	60.2	71.9



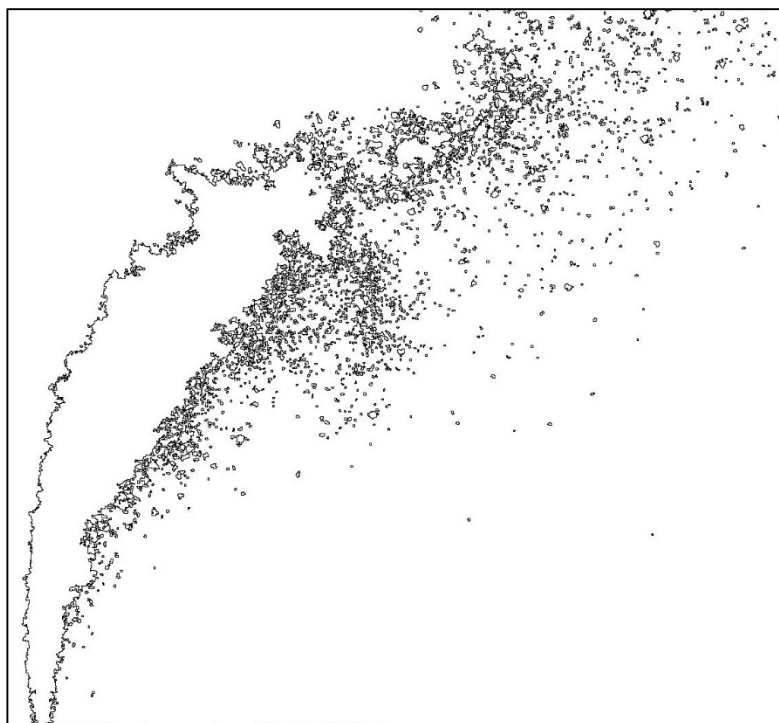
No.	Ref.	$V_{\text{Jet}}$ [m/s]	$V_{\text{Air}}$ [m/s]	q	$We_{\text{Air}}$	$We_{\text{Jet}}$	$Re_{\text{Air}}$	$Re_{\text{Jet}}$	$Oh_{\text{Air}}$ $\times 10^3$	$Oh_{\text{Jet}}$ $\times 10^3$	D10 [ $\mu\text{m}$ ]	D32 [ $\mu\text{m}$ ]
140	▲	19	68	18	129	2330	7432	9824	1.531	487.0	59.0	69.3



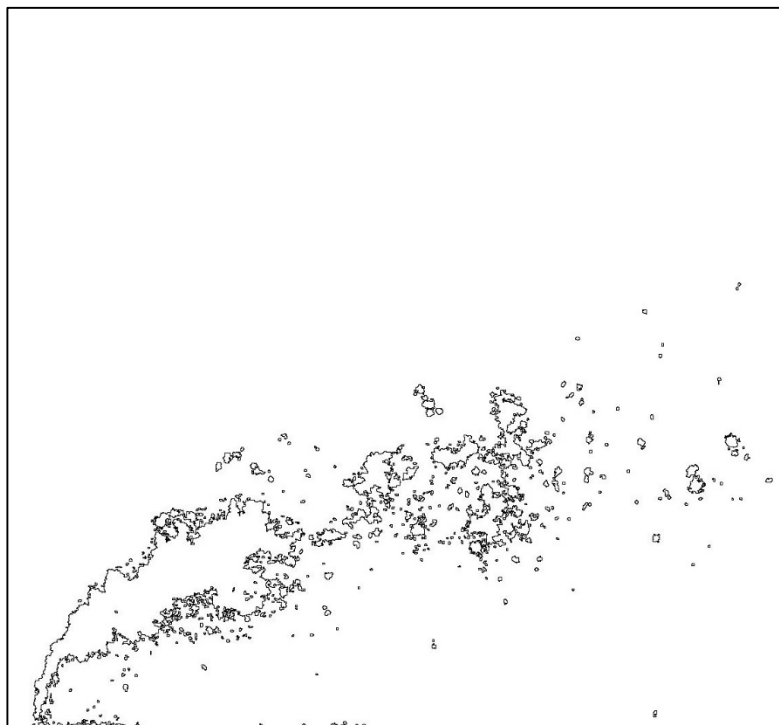
No.	Ref.	$V_{\text{Jet}}$ [m/s]	$V_{\text{Air}}$ [m/s]	q	$We_{\text{Air}}$	$We_{\text{Jet}}$	$Re_{\text{Air}}$	$Re_{\text{Jet}}$	$Oh_{\text{Air}}$ $\times 10^3$	$Oh_{\text{Jet}}$ $\times 10^3$	D10 [ $\mu\text{m}$ ]	D32 [ $\mu\text{m}$ ]
141	▲	30	68	45	129	5825	7432	15533	1.531	612.4	58.2	67.2



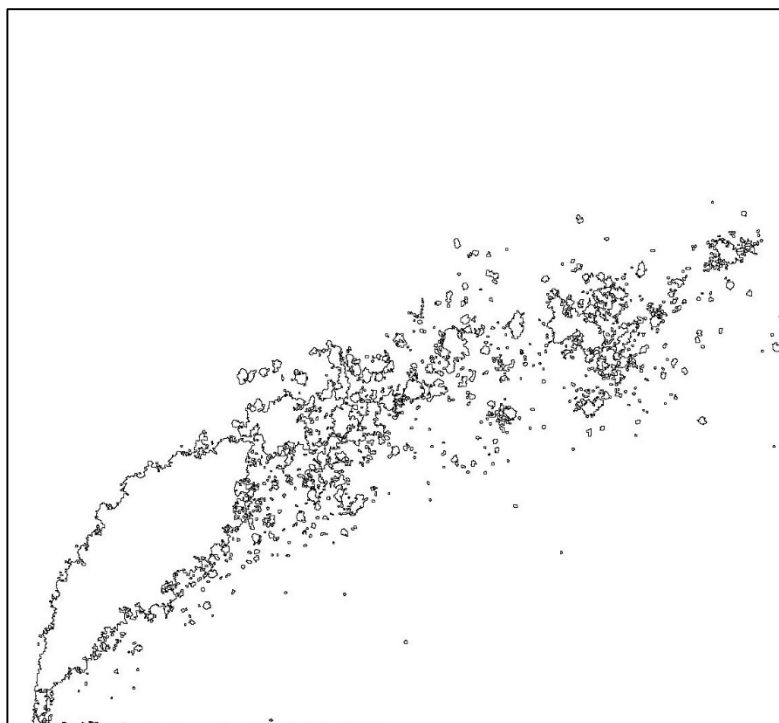
No.	Ref.	$V_{\text{Jet}}$ [m/s]	$V_{\text{Air}}$ [m/s]	q	$We_{\text{Air}}$	$We_{\text{Jet}}$	$Re_{\text{Air}}$	$Re_{\text{Jet}}$	$Oh_{\text{Air}}$ $\times 10^3$	$Oh_{\text{Jet}}$ $\times 10^3$	D10 [ $\mu\text{m}$ ]	D32 [ $\mu\text{m}$ ]
142	▲	38	68	72	129	9320	7432	19648	1.531	688.7	57.3	64.6



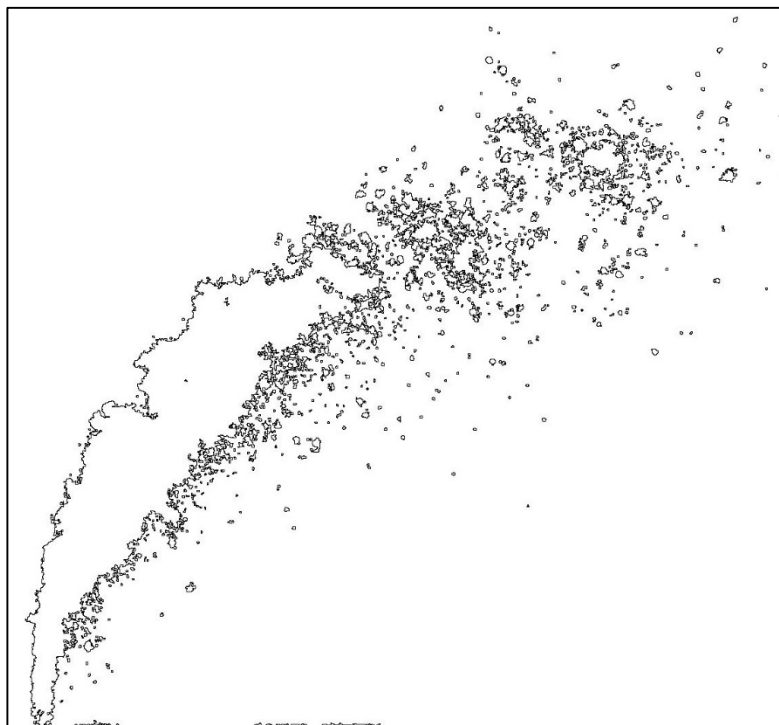
No.	Ref.	$V_{\text{Jet}}$ [m/s]	$V_{\text{Air}}$ [m/s]	q	$We_{\text{Air}}$	$We_{\text{Jet}}$	$Re_{\text{Air}}$	$Re_{\text{Jet}}$	$Oh_{\text{Air}}$ $\times 10^3$	$Oh_{\text{Jet}}$ $\times 10^3$	D10 [ $\mu\text{m}$ ]	D32 [ $\mu\text{m}$ ]
143	▲	9	44	9	55	466	4823	4394	1.531	325.7	61.6	76.3



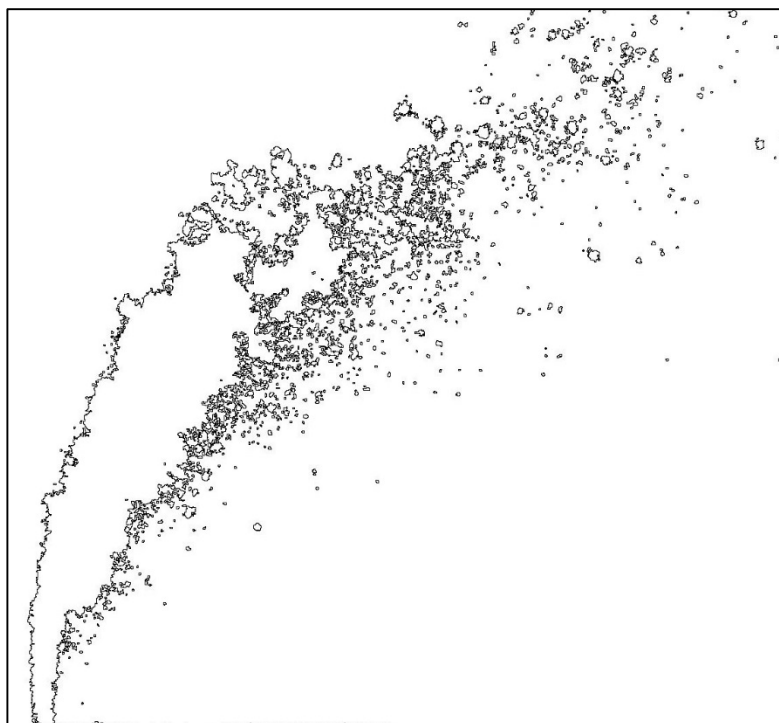
No.	Ref.	$V_{\text{Jet}}$ [m/s]	$V_{\text{Air}}$ [m/s]	q	$We_{\text{Air}}$	$We_{\text{Jet}}$	$Re_{\text{Air}}$	$Re_{\text{Jet}}$	$Oh_{\text{Air}}$ $\times 10^3$	$Oh_{\text{Jet}}$ $\times 10^3$	D10 [ $\mu\text{m}$ ]	D32 [ $\mu\text{m}$ ]
144	▲	12	44	17	55	932	4823	6213	1.531	387.3	61.5	75.3



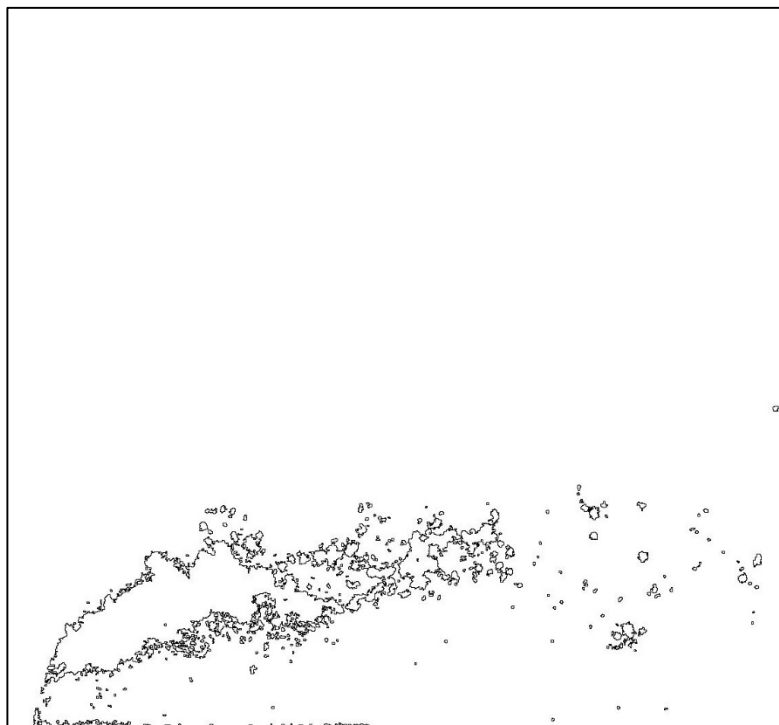
No.	Ref.	$V_{\text{Jet}}$ [m/s]	$V_{\text{Air}}$ [m/s]	q	$We_{\text{Air}}$	$We_{\text{Jet}}$	$Re_{\text{Air}}$	$Re_{\text{Jet}}$	$Oh_{\text{Air}}$ $\times 10^3$	$Oh_{\text{Jet}}$ $\times 10^3$	D10 [ $\mu\text{m}$ ]	D32 [ $\mu\text{m}$ ]
145	▲	19	44	43	55	2330	4823	9824	1.531	487.0	59.7	71.5



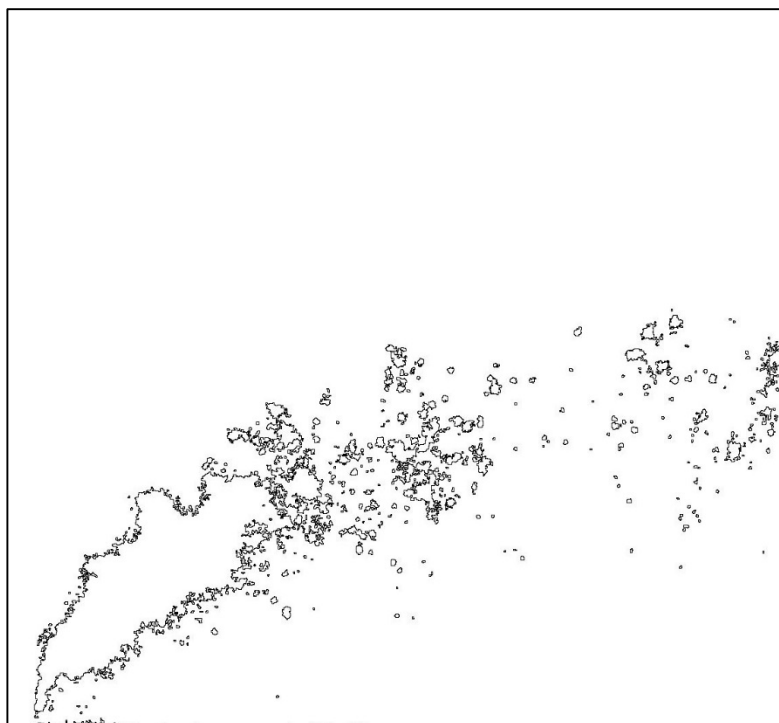
No.	Ref.	$V_{\text{Jet}}$ [m/s]	$V_{\text{Air}}$ [m/s]	q	$We_{\text{Air}}$	$We_{\text{Jet}}$	$Re_{\text{Air}}$	$Re_{\text{Jet}}$	$Oh_{\text{Air}}$ $\times 10^3$	$Oh_{\text{Jet}}$ $\times 10^3$	D10 [ $\mu\text{m}$ ]	D32 [ $\mu\text{m}$ ]
146	▲	24	44	68	55	3728	4823	12427	1.531	547.7	59.2	69.5



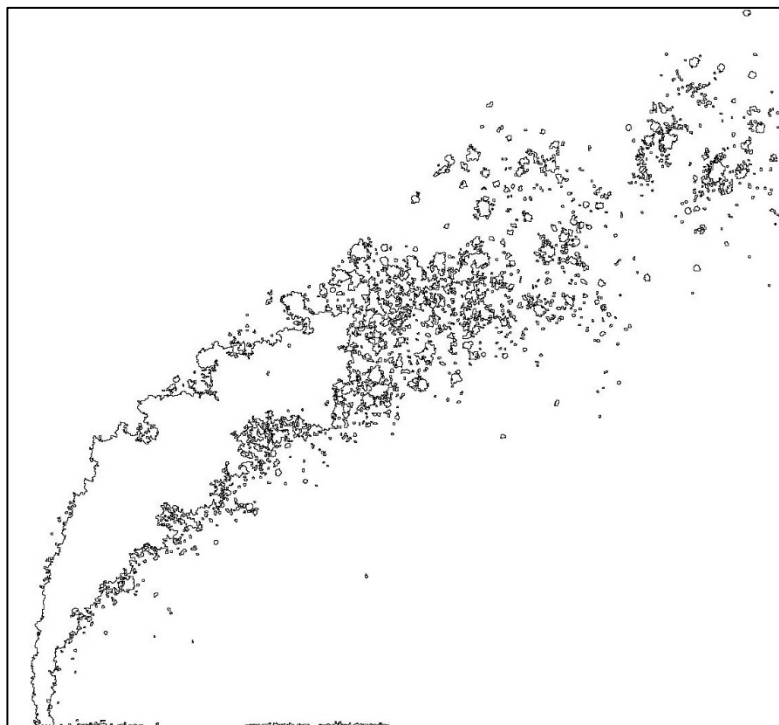
No.	Ref.	$V_{\text{Jet}}$ [m/s]	$V_{\text{Air}}$ [m/s]	q	$We_{\text{Air}}$	$We_{\text{Jet}}$	$Re_{\text{Air}}$	$Re_{\text{Jet}}$	$Oh_{\text{Air}}$ $\times 10^3$	$Oh_{\text{Jet}}$ $\times 10^3$	D10 [ $\mu\text{m}$ ]	D32 [ $\mu\text{m}$ ]
147	▲	7	35	9	34	291	3813	3473	1.531	289.6	60.9	74.1



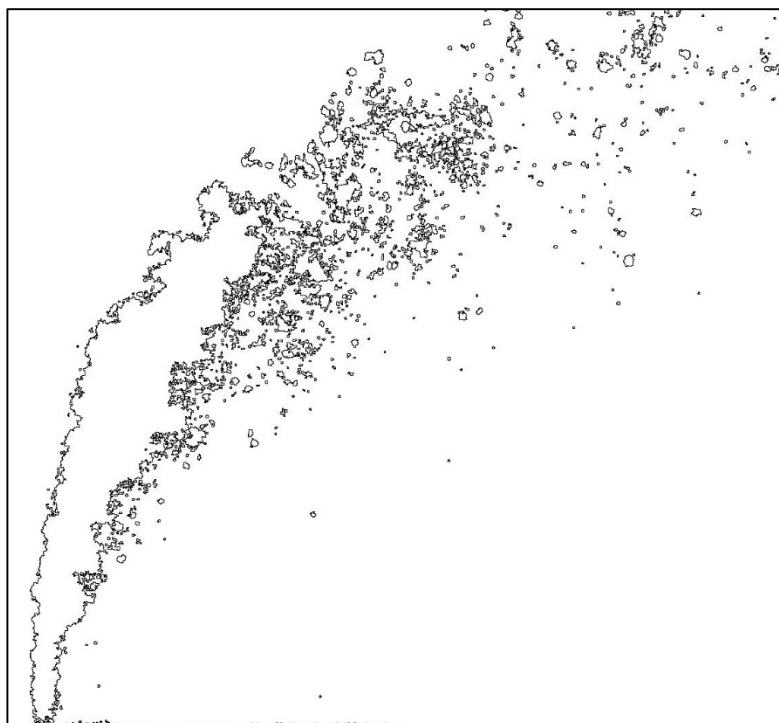
No.	Ref.	$V_{\text{Jet}}$ [m/s]	$V_{\text{Air}}$ [m/s]	q	$We_{\text{Air}}$	$We_{\text{Jet}}$	$Re_{\text{Air}}$	$Re_{\text{Jet}}$	$Oh_{\text{Air}}$ $\times 10^3$	$Oh_{\text{Jet}}$ $\times 10^3$	D10 [ $\mu\text{m}$ ]	D32 [ $\mu\text{m}$ ]
148	▲	10	35	17	34	583	3813	4912	1.531	344.4	61.9	76.5



No.	Ref.	$V_{\text{Jet}}$ [m/s]	$V_{\text{Air}}$ [m/s]	q	$We_{\text{Air}}$	$We_{\text{Jet}}$	$Re_{\text{Air}}$	$Re_{\text{Jet}}$	$Oh_{\text{Air}}$ $\times 10^3$	$Oh_{\text{Jet}}$ $\times 10^3$	D10 [ $\mu\text{m}$ ]	D32 [ $\mu\text{m}$ ]
149	▲	15	35	43	34	1456	3813	7767	1.531	433.0	60.2	73.0

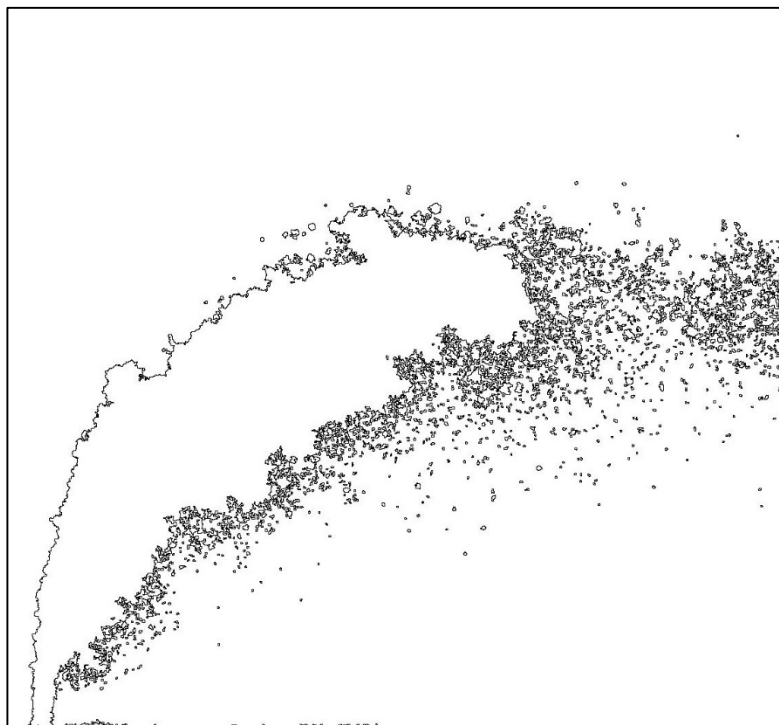


No.	Ref.	$V_{\text{Jet}}$ [m/s]	$V_{\text{Air}}$ [m/s]	q	$We_{\text{Air}}$	$We_{\text{Jet}}$	$Re_{\text{Air}}$	$Re_{\text{Jet}}$	$Oh_{\text{Air}}$ $\times 10^3$	$Oh_{\text{Jet}}$ $\times 10^3$	D10 [ $\mu\text{m}$ ]	D32 [ $\mu\text{m}$ ]
150	▲	19	35	68	34	2330	3813	9824	1.531	487.0	59.9	71.7

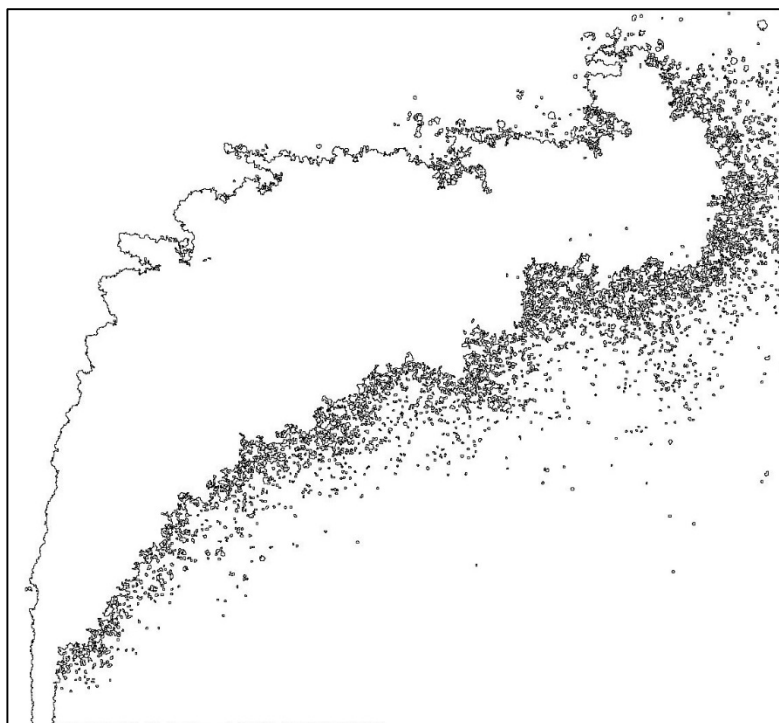




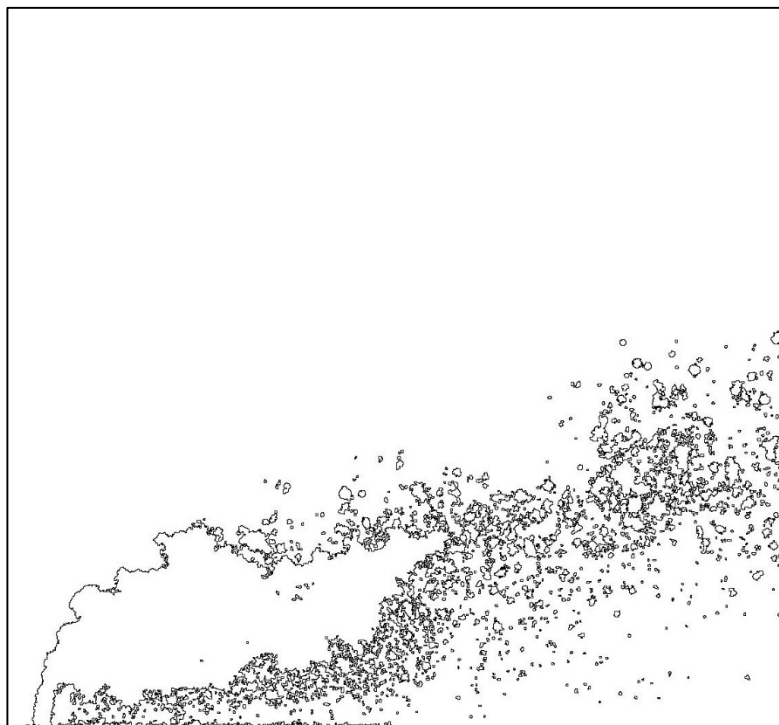
No.	Ref.	$V_{Jet}$ [m/s]	$V_{Air}$ [m/s]	q	$We_{Air}$	$We_{Jet}$	$Re_{Air}$	$Re_{Jet}$	$Oh_{Air}$ $\times 10^3$	$Oh_{Jet}$ $\times 10^3$	D10 [ $\mu m$ ]	D32 [ $\mu m$ ]
153	▲	43	93	77	152	11650	4520	21968	2.727	728.2	57.5	64.9



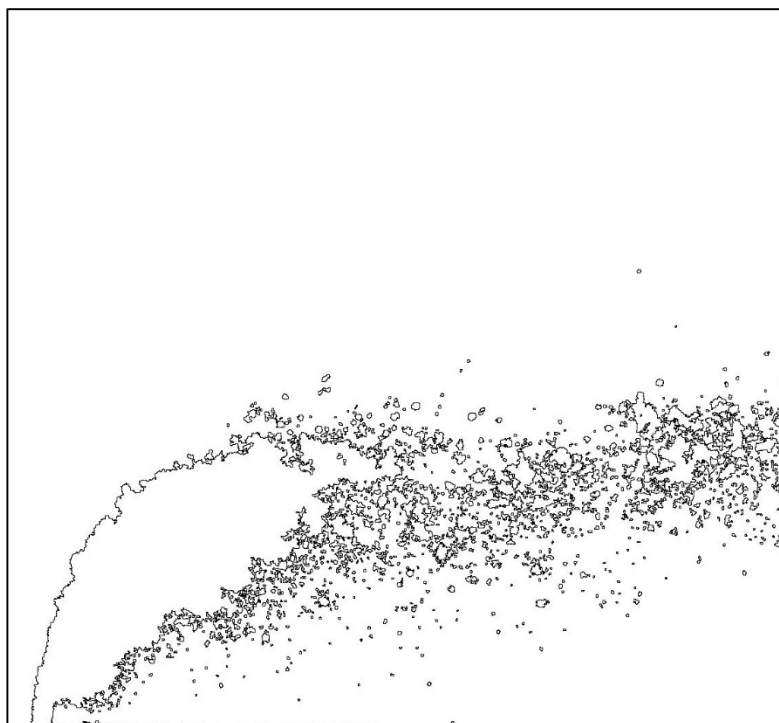
No.	Ref.	$V_{Jet}$ [m/s]	$V_{Air}$ [m/s]	q	$We_{Air}$	$We_{Jet}$	$Re_{Air}$	$Re_{Jet}$	$Oh_{Air}$ $\times 10^3$	$Oh_{Jet}$ $\times 10^3$	D10 [ $\mu m$ ]	D32 [ $\mu m$ ]
154	▲	54	93	123	152	18641	4520	27787	2.727	819.0	57.1	63.8



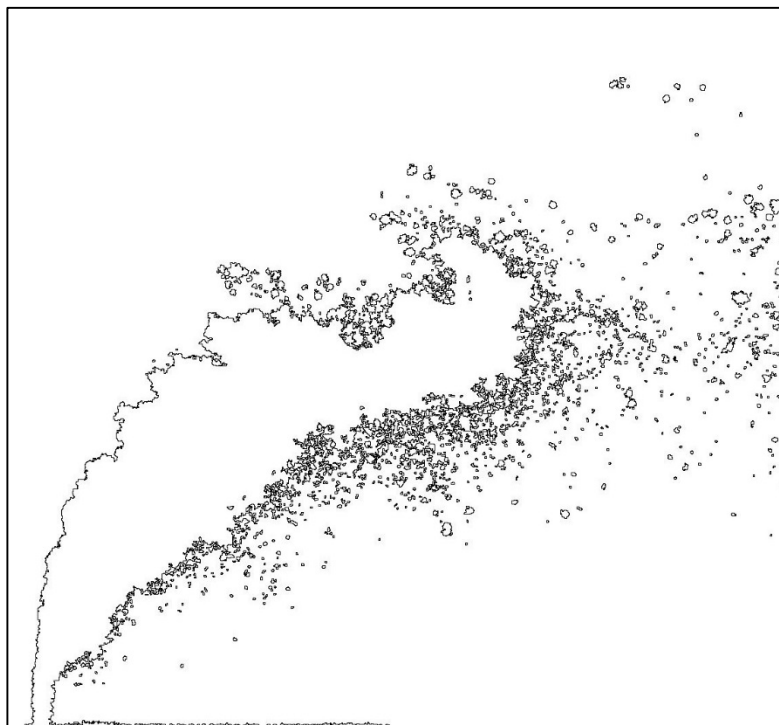
No.	Ref.	$V_{Jet}$ [m/s]	$V_{Air}$ [m/s]	q	$We_{Air}$	$We_{Jet}$	$Re_{Air}$	$Re_{Jet}$	$Oh_{Air}$ $\times 10^3$	$Oh_{Jet}$ $\times 10^3$	D10 [ $\mu m$ ]	D32 [ $\mu m$ ]
155	▲	14	68	14	82	1165	3327	6947	2.727	409.5	64.3	81.8



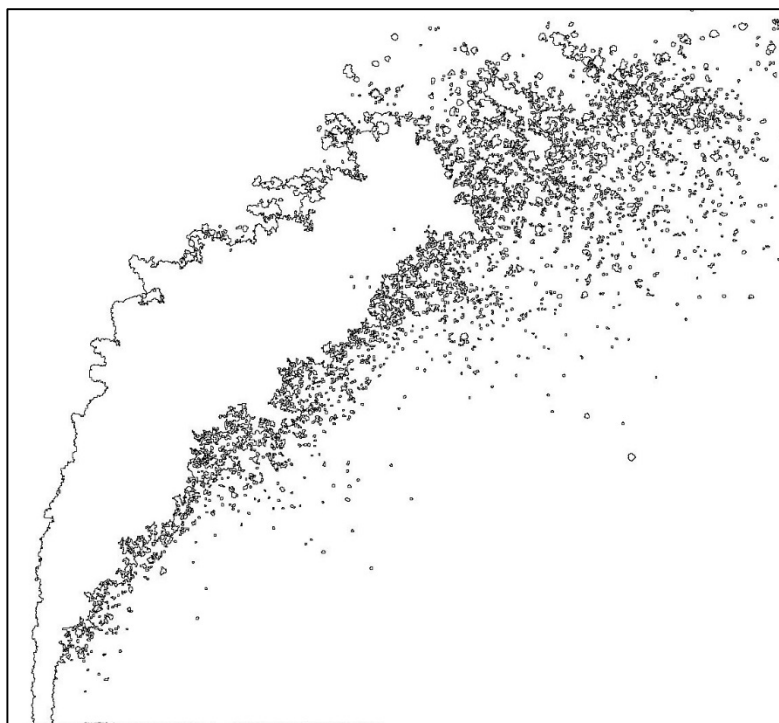
No.	Ref.	$V_{Jet}$ [m/s]	$V_{Air}$ [m/s]	q	$We_{Air}$	$We_{Jet}$	$Re_{Air}$	$Re_{Jet}$	$Oh_{Air}$ $\times 10^3$	$Oh_{Jet}$ $\times 10^3$	D10 [ $\mu m$ ]	D32 [ $\mu m$ ]
156	▲	19	68	28	82	2330	3327	9824	2.727	487.0	62.2	77.0



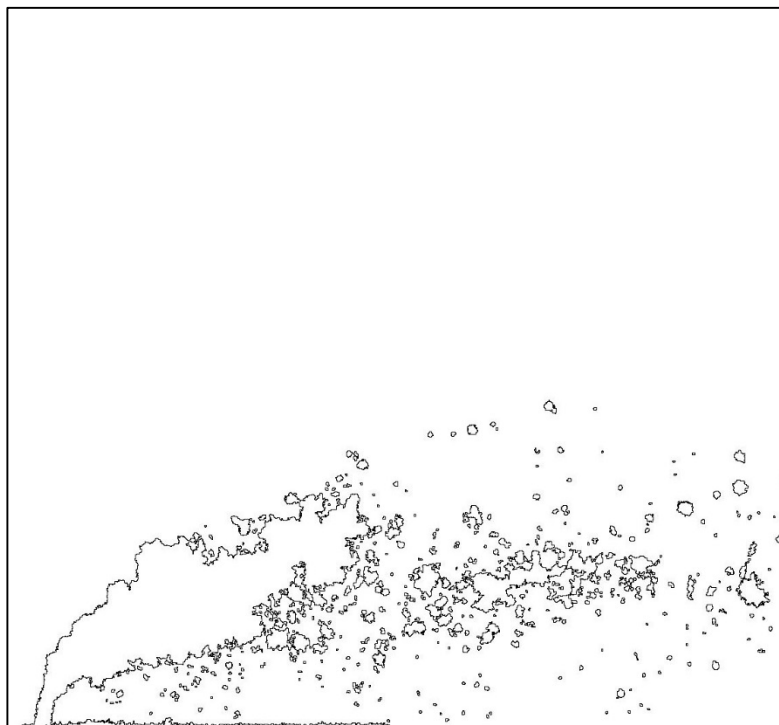
No.	Ref.	$V_{\text{Jet}}$ [m/s]	$V_{\text{Air}}$ [m/s]	q	$We_{\text{Air}}$	$We_{\text{Jet}}$	$Re_{\text{Air}}$	$Re_{\text{Jet}}$	$Oh_{\text{Air}}$ $\times 10^3$	$Oh_{\text{Jet}}$ $\times 10^3$	D10 [ $\mu\text{m}$ ]	D32 [ $\mu\text{m}$ ]
157	▲	30	68	71	82	5825	3327	15533	2.727	612.4	60.1	72.4



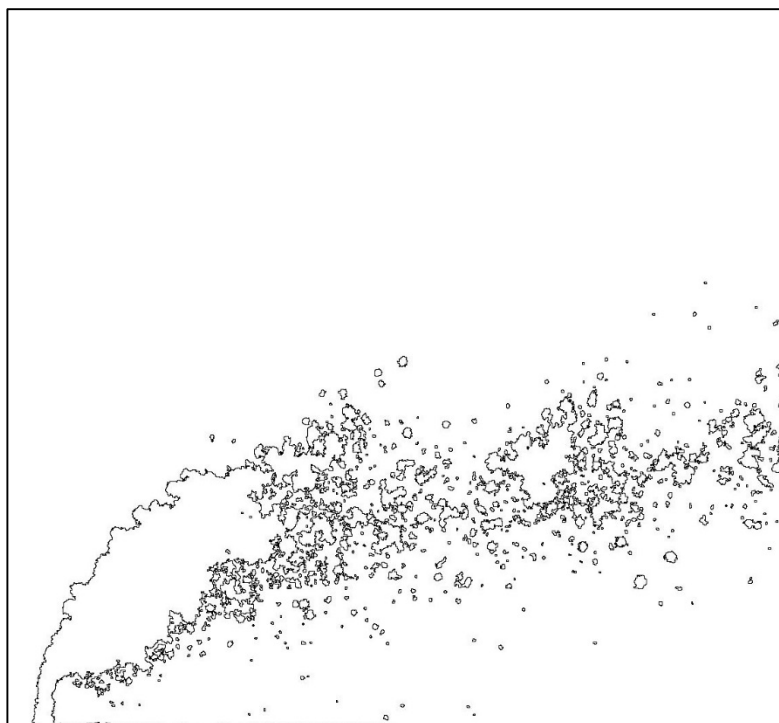
No.	Ref.	$V_{\text{Jet}}$ [m/s]	$V_{\text{Air}}$ [m/s]	q	$We_{\text{Air}}$	$We_{\text{Jet}}$	$Re_{\text{Air}}$	$Re_{\text{Jet}}$	$Oh_{\text{Air}}$ $\times 10^3$	$Oh_{\text{Jet}}$ $\times 10^3$	D10 [ $\mu\text{m}$ ]	D32 [ $\mu\text{m}$ ]
158	▲	38	68	113	82	9320	3327	19648	2.727	688.7	59.2	69.9



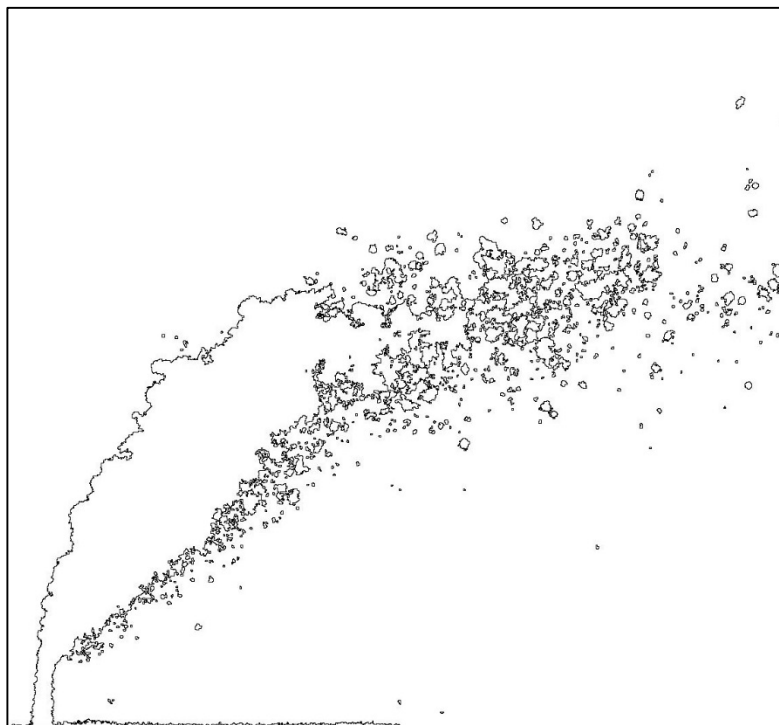
No.	Ref.	$V_{\text{Jet}}$ [m/s]	$V_{\text{Air}}$ [m/s]	q	$We_{\text{Air}}$	$We_{\text{Jet}}$	$Re_{\text{Air}}$	$Re_{\text{Jet}}$	$Oh_{\text{Air}}$ $\times 10^3$	$Oh_{\text{Jet}}$ $\times 10^3$	D10 [ $\mu\text{m}$ ]	D32 [ $\mu\text{m}$ ]
159	▲	9	44	14	33	466	2122	4394	2.727	325.7	70.7	92.8



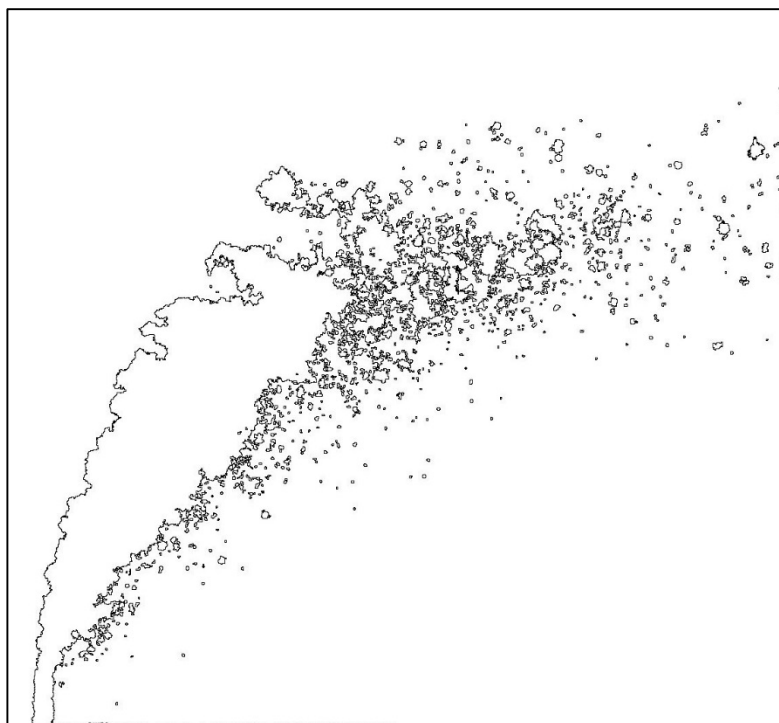
No.	Ref.	$V_{\text{Jet}}$ [m/s]	$V_{\text{Air}}$ [m/s]	q	$We_{\text{Air}}$	$We_{\text{Jet}}$	$Re_{\text{Air}}$	$Re_{\text{Jet}}$	$Oh_{\text{Air}}$ $\times 10^3$	$Oh_{\text{Jet}}$ $\times 10^3$	D10 [ $\mu\text{m}$ ]	D32 [ $\mu\text{m}$ ]
160	▲	12	44	28	33	932	2122	6213	2.727	387.3	68.2	89.5



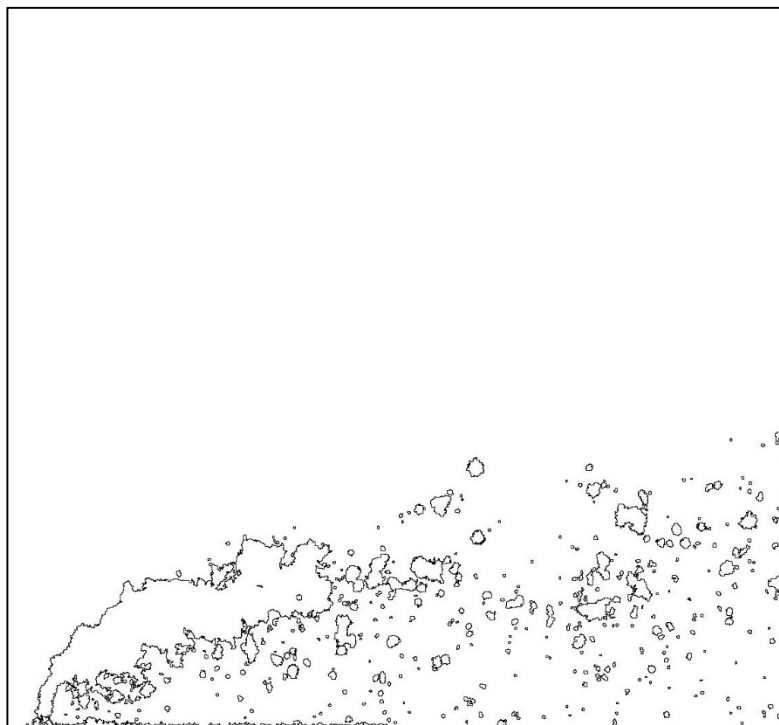
No.	Ref.	$V_{\text{Jet}}$ [m/s]	$V_{\text{Air}}$ [m/s]	q	$We_{\text{Air}}$	$We_{\text{Jet}}$	$Re_{\text{Air}}$	$Re_{\text{Jet}}$	$Oh_{\text{Air}}$ $\times 10^3$	$Oh_{\text{Jet}}$ $\times 10^3$	D10 [ $\mu\text{m}$ ]	D32 [ $\mu\text{m}$ ]
161	▲	19	44	70	33	2330	2122	9824	2.727	487.0	64.7	82.5



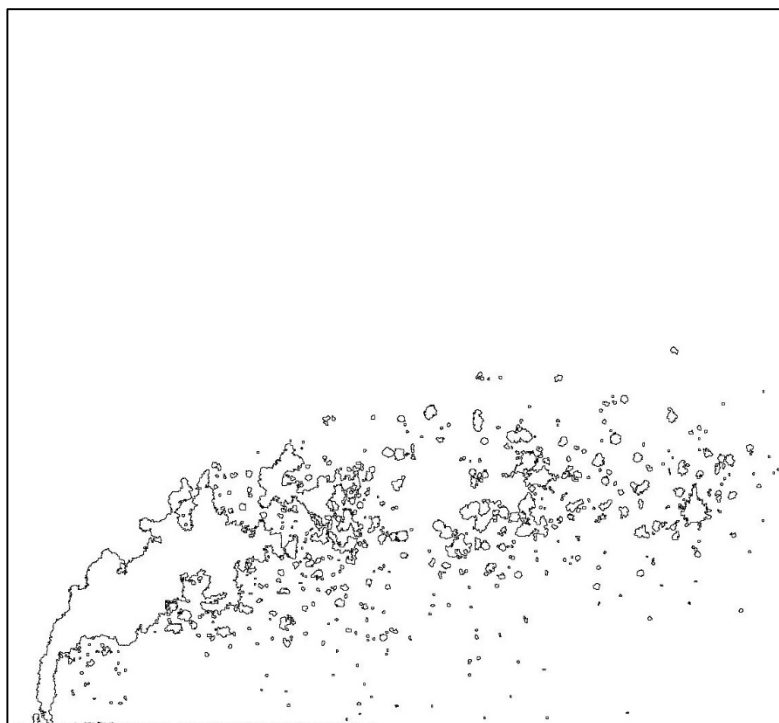
No.	Ref.	$V_{\text{Jet}}$ [m/s]	$V_{\text{Air}}$ [m/s]	q	$We_{\text{Air}}$	$We_{\text{Jet}}$	$Re_{\text{Air}}$	$Re_{\text{Jet}}$	$Oh_{\text{Air}}$ $\times 10^3$	$Oh_{\text{Jet}}$ $\times 10^3$	D10 [ $\mu\text{m}$ ]	D32 [ $\mu\text{m}$ ]
162	▲	24	44	111	33	3728	2122	12427	2.727	547.7	63.4	80.0



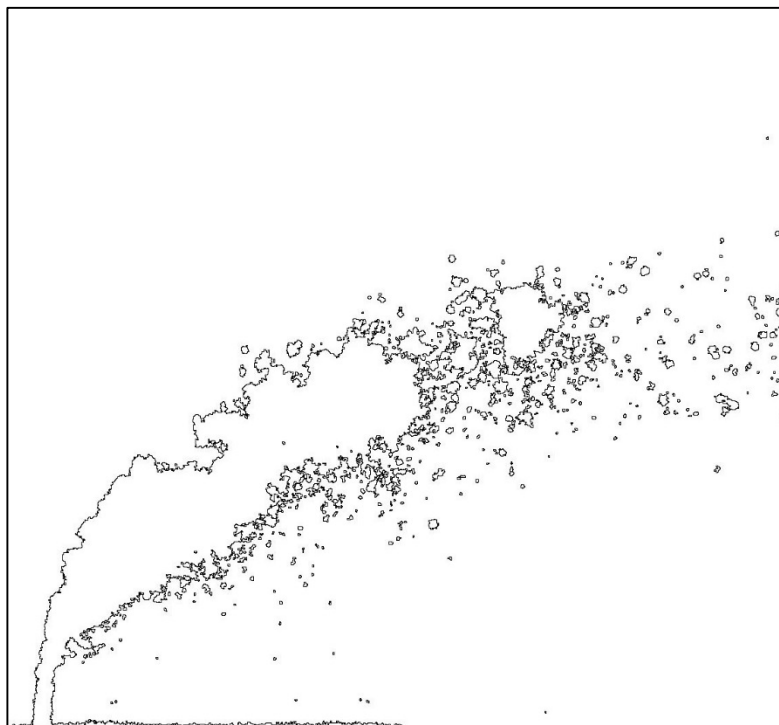
No.	Ref.	$V_{\text{Jet}}$ [m/s]	$V_{\text{Air}}$ [m/s]	q	$We_{\text{Air}}$	$We_{\text{Jet}}$	$Re_{\text{Air}}$	$Re_{\text{Jet}}$	$Oh_{\text{Air}}$ $\times 10^3$	$Oh_{\text{Jet}}$ $\times 10^3$	D10 [ $\mu\text{m}$ ]	D32 [ $\mu\text{m}$ ]
163	▲	7	34	14	21	291	1678	3473	2.727	289.6	72.1	94.8



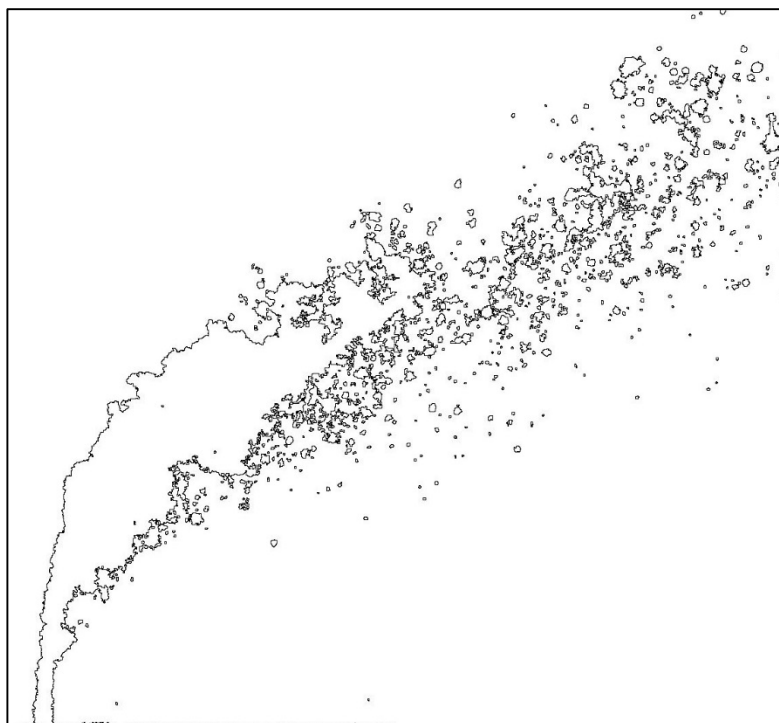
No.	Ref.	$V_{\text{Jet}}$ [m/s]	$V_{\text{Air}}$ [m/s]	q	$We_{\text{Air}}$	$We_{\text{Jet}}$	$Re_{\text{Air}}$	$Re_{\text{Jet}}$	$Oh_{\text{Air}}$ $\times 10^3$	$Oh_{\text{Jet}}$ $\times 10^3$	D10 [ $\mu\text{m}$ ]	D32 [ $\mu\text{m}$ ]
164	▲	10	34	28	21	583	1678	4912	2.727	344.4	70.1	92.8



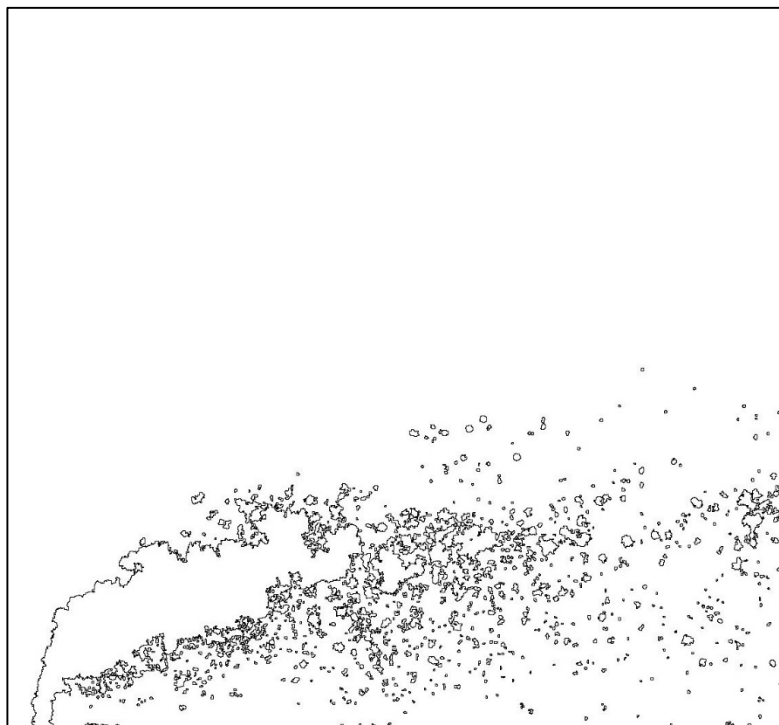
No.	Ref.	$V_{\text{Jet}}$ [m/s]	$V_{\text{Air}}$ [m/s]	q	$We_{\text{Air}}$	$We_{\text{Jet}}$	$Re_{\text{Air}}$	$Re_{\text{Jet}}$	$Oh_{\text{Air}}$ $\times 10^3$	$Oh_{\text{Jet}}$ $\times 10^3$	D10 [ $\mu\text{m}$ ]	D32 [ $\mu\text{m}$ ]
165	▲	15	34	70	21	1456	1678	7767	2.727	433.0	67.7	88.5



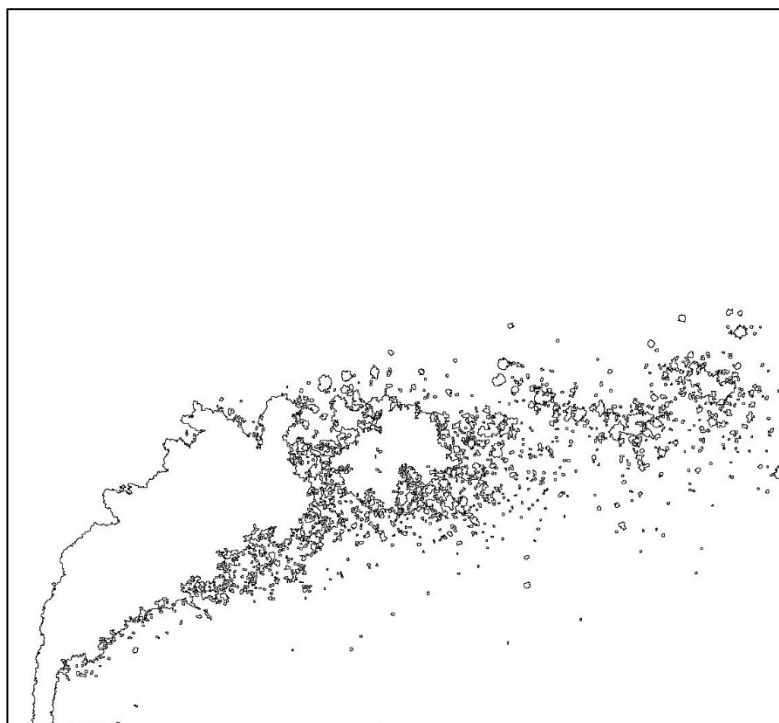
No.	Ref.	$V_{\text{Jet}}$ [m/s]	$V_{\text{Air}}$ [m/s]	q	$We_{\text{Air}}$	$We_{\text{Jet}}$	$Re_{\text{Air}}$	$Re_{\text{Jet}}$	$Oh_{\text{Air}}$ $\times 10^3$	$Oh_{\text{Jet}}$ $\times 10^3$	D10 [ $\mu\text{m}$ ]	D32 [ $\mu\text{m}$ ]
166	▲	19	34	111	21	2330	1678	9824	2.727	487.0	65.5	84.2



No.	Ref.	$V_{\text{Jet}}$ [m/s]	$V_{\text{Air}}$ [m/s]	q	$We_{\text{Air}}$	$We_{\text{Jet}}$	$Re_{\text{Air}}$	$Re_{\text{Jet}}$	$Oh_{\text{Air}}$ $\times 10^3$	$Oh_{\text{Jet}}$ $\times 10^3$	D10 [ $\mu\text{m}$ ]	D32 [ $\mu\text{m}$ ]
167	▲	14	68	17	67	1165	2384	6947	3.4342	409.5	64.8	83.1

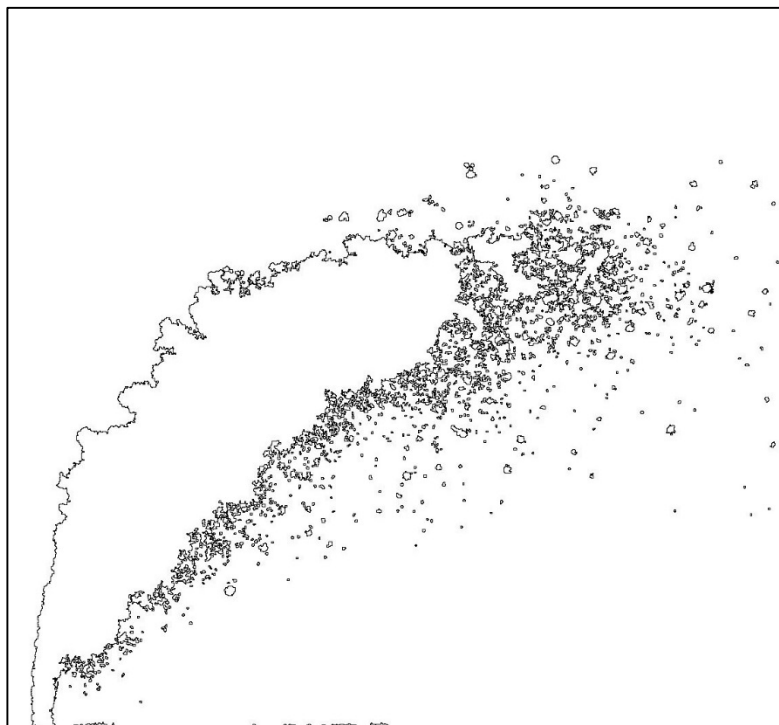


No.	Ref.	$V_{\text{Jet}}$ [m/s]	$V_{\text{Air}}$ [m/s]	q	$We_{\text{Air}}$	$We_{\text{Jet}}$	$Re_{\text{Air}}$	$Re_{\text{Jet}}$	$Oh_{\text{Air}}$ $\times 10^3$	$Oh_{\text{Jet}}$ $\times 10^3$	D10 [ $\mu\text{m}$ ]	D32 [ $\mu\text{m}$ ]
168	▲	19	68	35	67	2330	2384	9824	3.4342	487.0	62.4	78.0

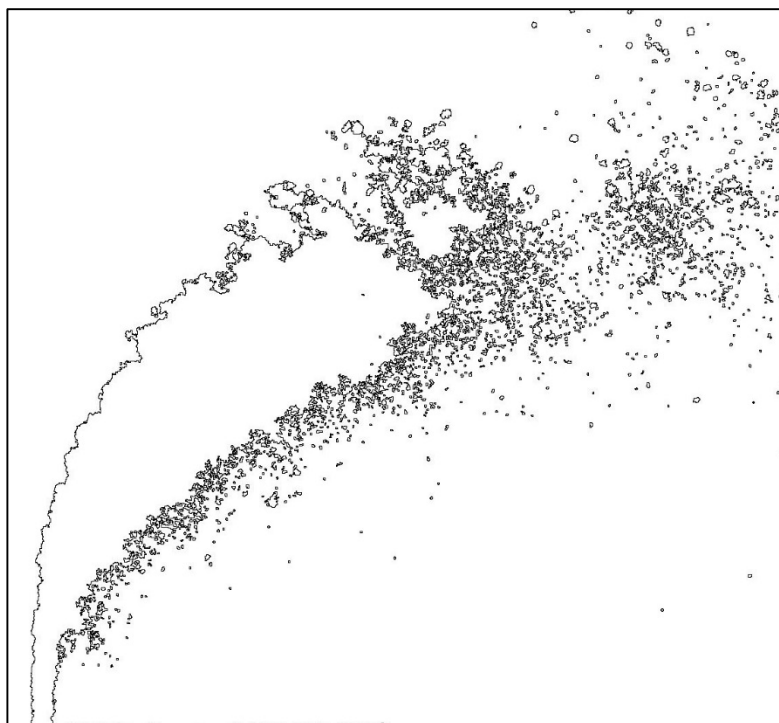




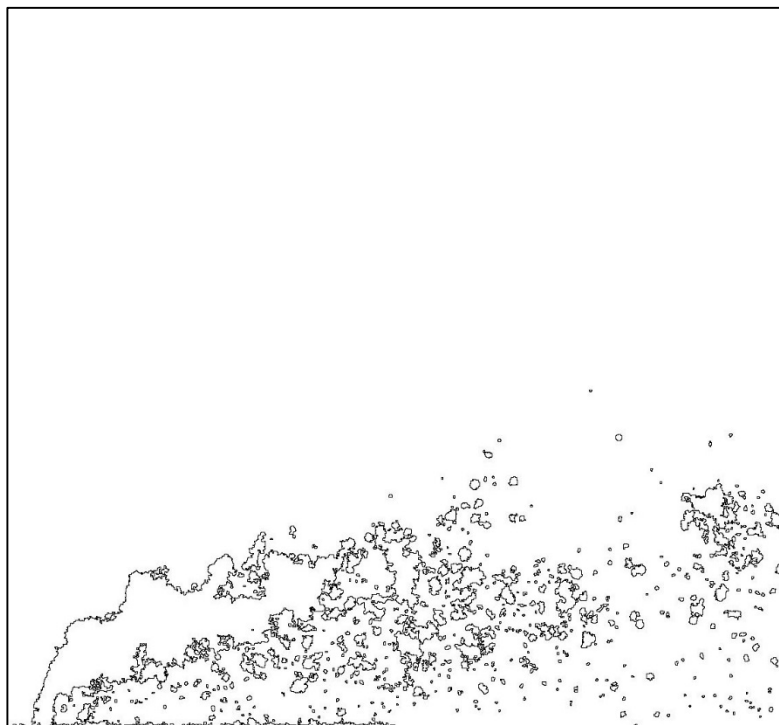
No.	Ref.	$V_{Jet}$ [m/s]	$V_{Air}$ [m/s]	q	$We_{Air}$	$We_{Jet}$	$Re_{Air}$	$Re_{Jet}$	$Oh_{Air}$ $\times 10^3$	$Oh_{Jet}$ $\times 10^3$	D10 [ $\mu m$ ]	D32 [ $\mu m$ ]
169	▲	30	68	87	67	5825	2384	15533	3.4342	612.4	60.4	72.8



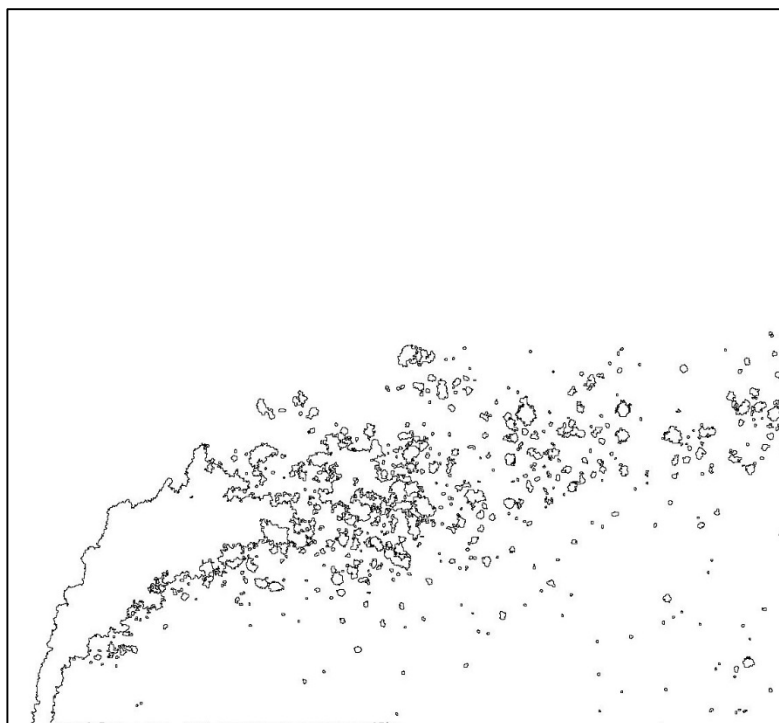
No.	Ref.	$V_{Jet}$ [m/s]	$V_{Air}$ [m/s]	q	$We_{Air}$	$We_{Jet}$	$Re_{Air}$	$Re_{Jet}$	$Oh_{Air}$ $\times 10^3$	$Oh_{Jet}$ $\times 10^3$	D10 [ $\mu m$ ]	D32 [ $\mu m$ ]
170	▲	38	68	139	67	9320	2384	19648	3.4342	688.7	59.3	70.3



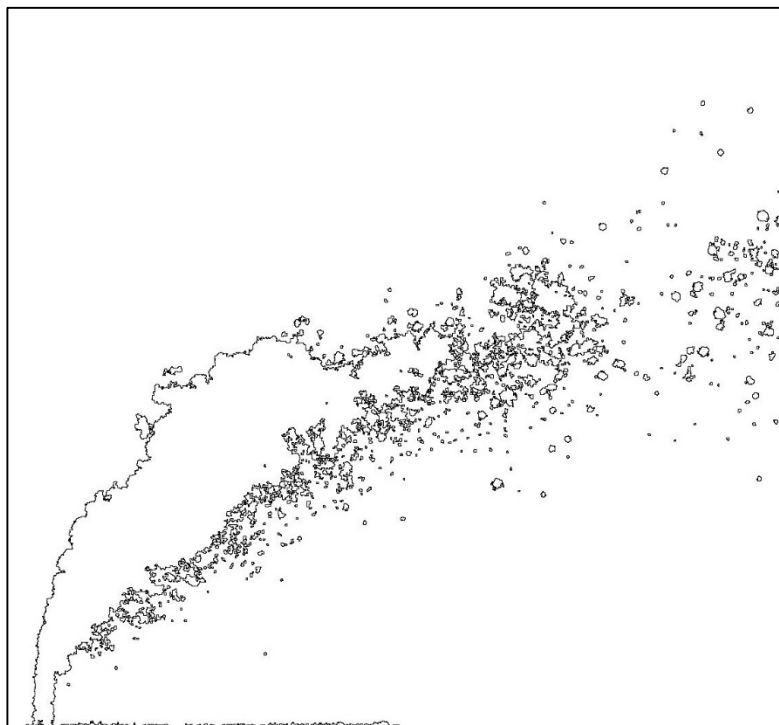
No.	Ref.	$V_{\text{Jet}}$ [m/s]	$V_{\text{Air}}$ [m/s]	q	$We_{\text{Air}}$	$We_{\text{Jet}}$	$Re_{\text{Air}}$	$Re_{\text{Jet}}$	$Oh_{\text{Air}}$ $\times 10^3$	$Oh_{\text{Jet}}$ $\times 10^3$	D10 [ $\mu\text{m}$ ]	D32 [ $\mu\text{m}$ ]
171	▲	9	44	17	28	466	1534	4394	3.4342	325.7	69.6	90.8



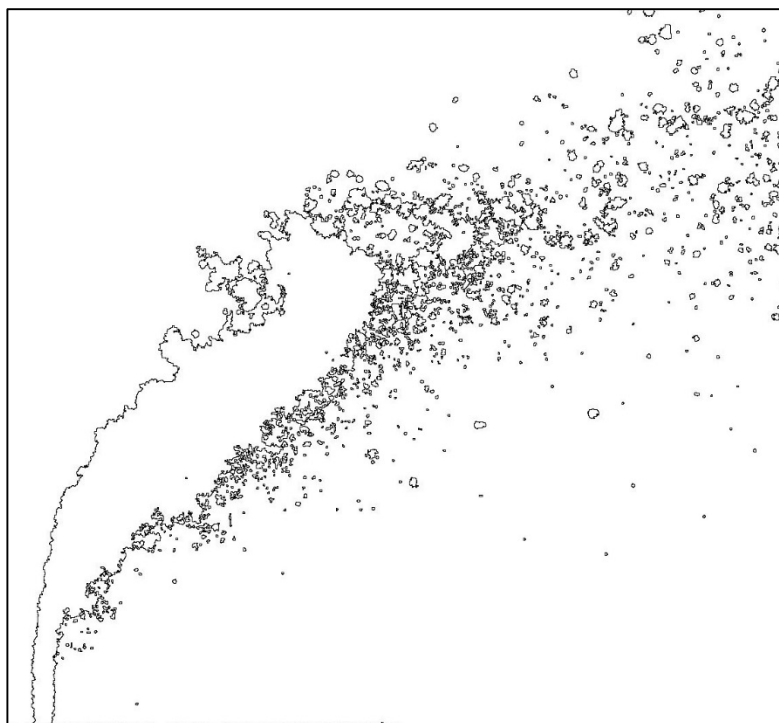
No.	Ref.	$V_{\text{Jet}}$ [m/s]	$V_{\text{Air}}$ [m/s]	q	$We_{\text{Air}}$	$We_{\text{Jet}}$	$Re_{\text{Air}}$	$Re_{\text{Jet}}$	$Oh_{\text{Air}}$ $\times 10^3$	$Oh_{\text{Jet}}$ $\times 10^3$	D10 [ $\mu\text{m}$ ]	D32 [ $\mu\text{m}$ ]
172	▲	12	44	34	28	932	1534	6213	3.4342	387.3	67.7	88.2



No.	Ref.	$V_{\text{Jet}}$ [m/s]	$V_{\text{Air}}$ [m/s]	q	$We_{\text{Air}}$	$We_{\text{Jet}}$	$Re_{\text{Air}}$	$Re_{\text{Jet}}$	$Oh_{\text{Air}}$ $\times 10^3$	$Oh_{\text{Jet}}$ $\times 10^3$	D10 [ $\mu\text{m}$ ]	D32 [ $\mu\text{m}$ ]
173	▲	19	44	84	28	2330	1534	9824	3.4342	487.0	65.1	83.5



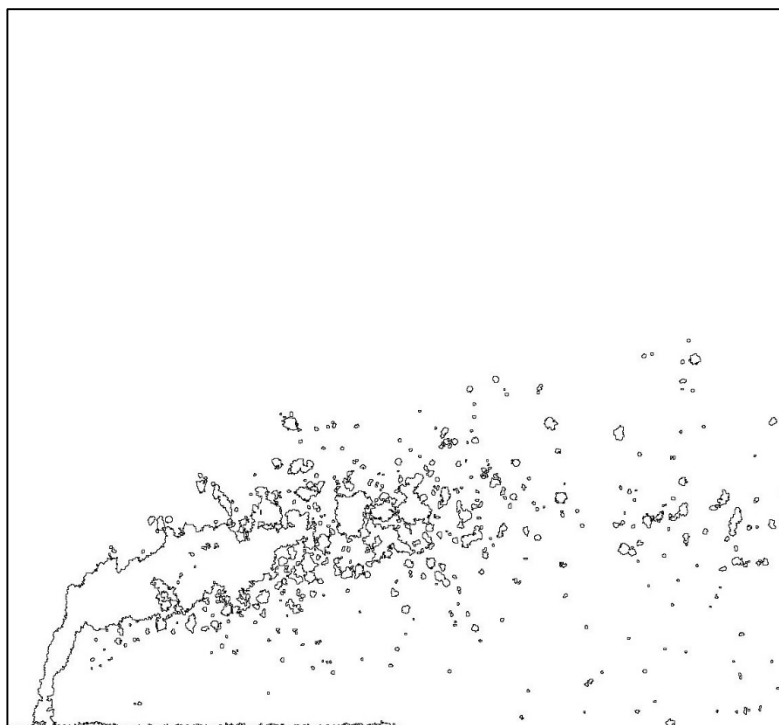
No.	Ref.	$V_{\text{Jet}}$ [m/s]	$V_{\text{Air}}$ [m/s]	q	$We_{\text{Air}}$	$We_{\text{Jet}}$	$Re_{\text{Air}}$	$Re_{\text{Jet}}$	$Oh_{\text{Air}}$ $\times 10^3$	$Oh_{\text{Jet}}$ $\times 10^3$	D10 [ $\mu\text{m}$ ]	D32 [ $\mu\text{m}$ ]
174	▲	24	44	134	28	3728	1534	12427	3.4342	547.7	64.3	81.5



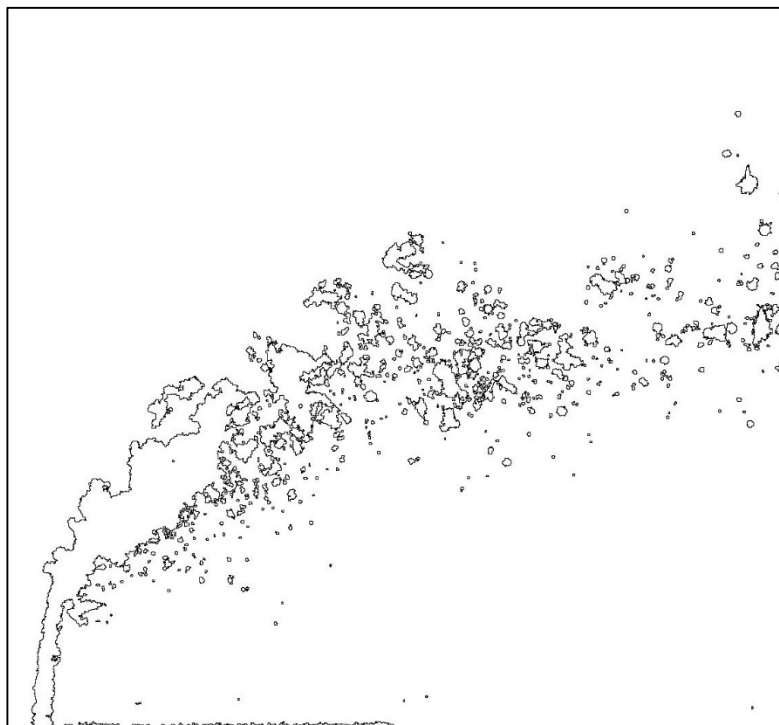
No.	Ref.	$V_{\text{Jet}}$ [m/s]	$V_{\text{Air}}$ [m/s]	q	$We_{\text{Air}}$	$We_{\text{Jet}}$	$Re_{\text{Air}}$	$Re_{\text{Jet}}$	$Oh_{\text{Air}}$ $\times 10^3$	$Oh_{\text{Jet}}$ $\times 10^3$	D10 [ $\mu\text{m}$ ]	D32 [ $\mu\text{m}$ ]
175	▲	7	35	17	18	291	1223	3473	3.4342	289.6	71.4	93.9



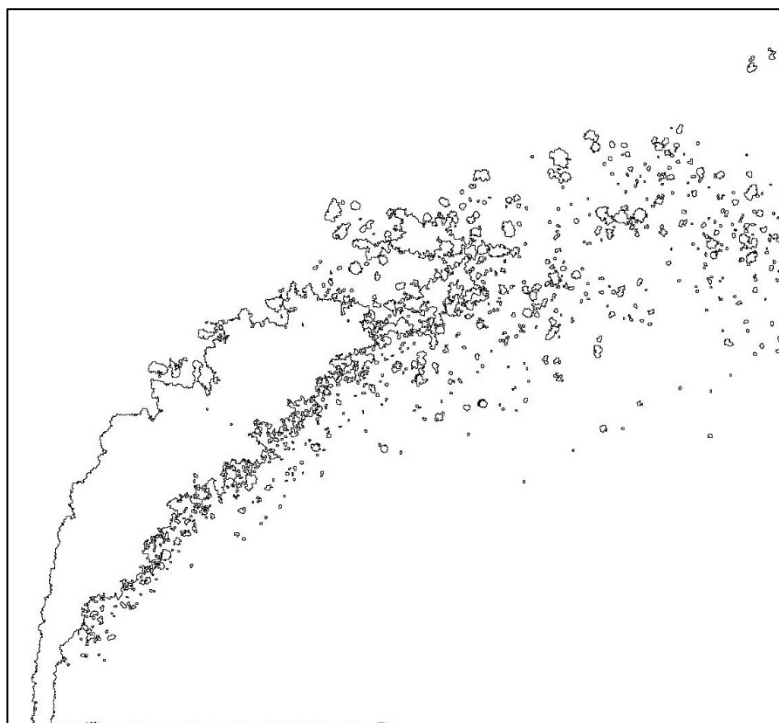
No.	Ref.	$V_{\text{Jet}}$ [m/s]	$V_{\text{Air}}$ [m/s]	q	$We_{\text{Air}}$	$We_{\text{Jet}}$	$Re_{\text{Air}}$	$Re_{\text{Jet}}$	$Oh_{\text{Air}}$ $\times 10^3$	$Oh_{\text{Jet}}$ $\times 10^3$	D10 [ $\mu\text{m}$ ]	D32 [ $\mu\text{m}$ ]
176	▲	10	35	33	18	583	1223	4912	3.4342	344.4	70.1	92.7



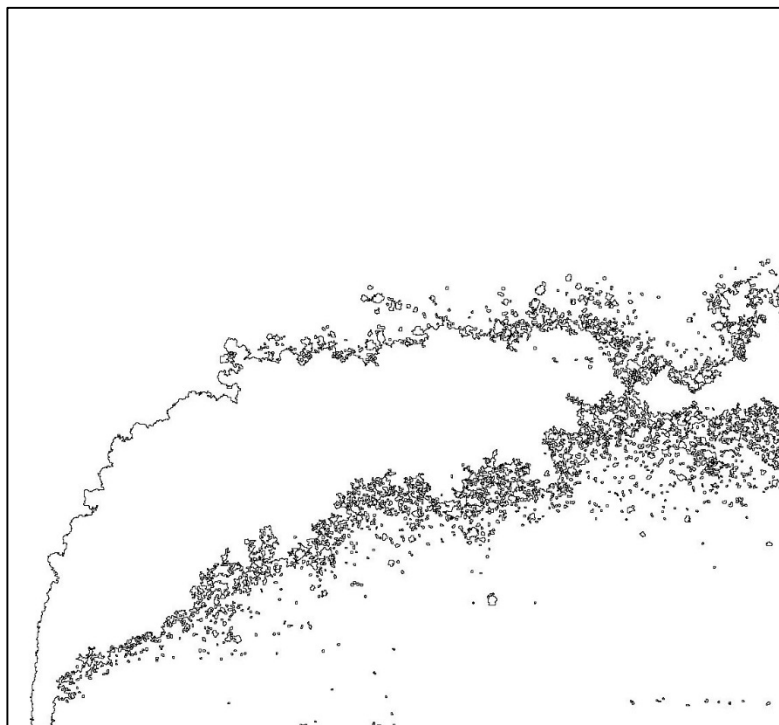
No.	Ref.	$V_{\text{Jet}}$ [m/s]	$V_{\text{Air}}$ [m/s]	q	$We_{\text{Air}}$	$We_{\text{Jet}}$	$Re_{\text{Air}}$	$Re_{\text{Jet}}$	$Oh_{\text{Air}}$ $\times 10^3$	$Oh_{\text{Jet}}$ $\times 10^3$	D10 [ $\mu\text{m}$ ]	D32 [ $\mu\text{m}$ ]
177	▲	15	35	83	18	1456	1223	7767	3.4342	433.0	68.5	90.5



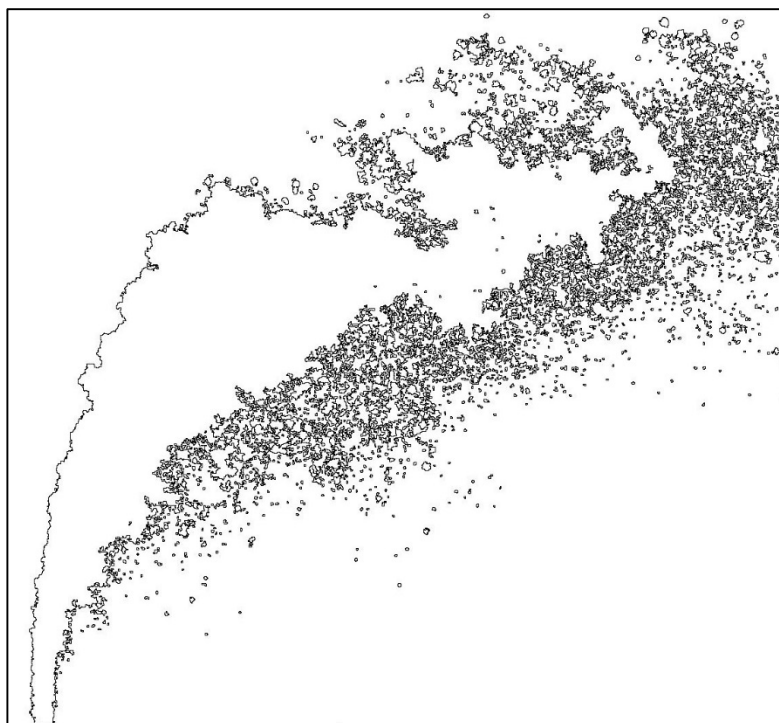
No.	Ref.	$V_{\text{Jet}}$ [m/s]	$V_{\text{Air}}$ [m/s]	q	$We_{\text{Air}}$	$We_{\text{Jet}}$	$Re_{\text{Air}}$	$Re_{\text{Jet}}$	$Oh_{\text{Air}}$ $\times 10^3$	$Oh_{\text{Jet}}$ $\times 10^3$	D10 [ $\mu\text{m}$ ]	D32 [ $\mu\text{m}$ ]
178	▲	19	35	132	18	2330	1223	9824	3.4342	487.0	67.2	87.5



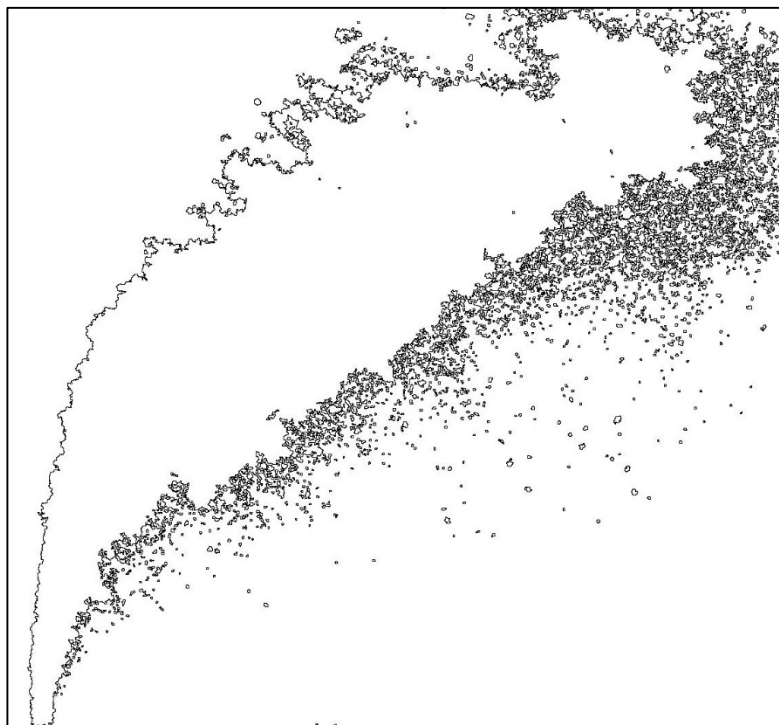
No.	Ref.	$V_{\text{Jet}}$ [m/s]	$V_{\text{Air}}$ [m/s]	q	$We_{\text{Air}}$	$We_{\text{Jet}}$	$Re_{\text{Air}}$	$Re_{\text{Jet}}$	$Oh_{\text{Air}}$ $\times 10^3$	$Oh_{\text{Jet}}$ $\times 10^3$	D10 [ $\mu\text{m}$ ]	D32 [ $\mu\text{m}$ ]
180	●	27	81	30	157	4660	5356	13895	2.3362	579.1	59.3	69.2



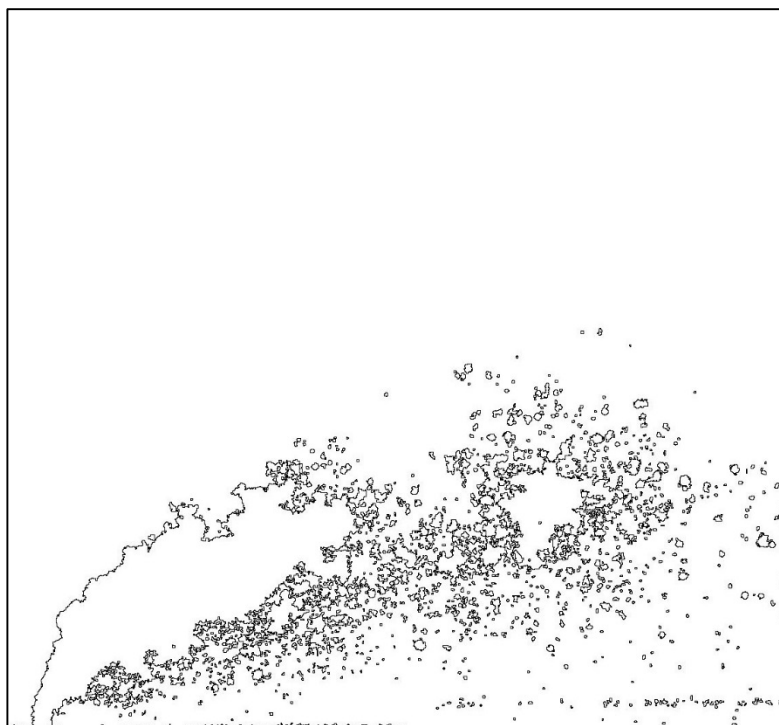
No.	Ref.	$V_{\text{Jet}}$ [m/s]	$V_{\text{Air}}$ [m/s]	q	$We_{\text{Air}}$	$We_{\text{Jet}}$	$Re_{\text{Air}}$	$Re_{\text{Jet}}$	$Oh_{\text{Air}}$ $\times 10^3$	$Oh_{\text{Jet}}$ $\times 10^3$	D10 [ $\mu\text{m}$ ]	D32 [ $\mu\text{m}$ ]
181	●	43	81	74	157	11651	5356	21970	2.3362	728.2	58.4	66.9



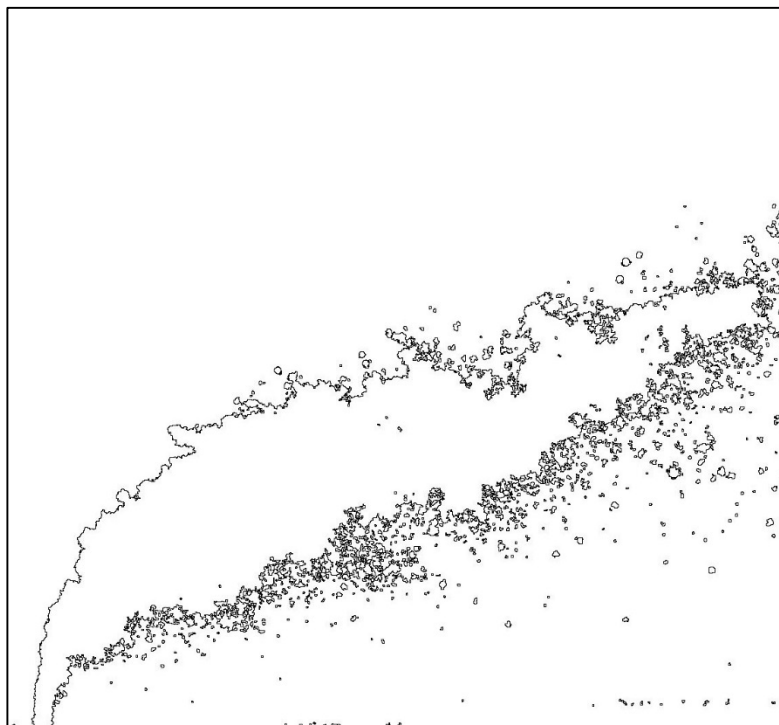
No.	Ref.	$V_{\text{Jet}}$ [m/s]	$V_{\text{Air}}$ [m/s]	q	$We_{\text{Air}}$	$We_{\text{Jet}}$	$Re_{\text{Air}}$	$Re_{\text{Jet}}$	$Oh_{\text{Air}}$ $\times 10^3$	$Oh_{\text{Jet}}$ $\times 10^3$	D10 [ $\mu\text{m}$ ]	D32 [ $\mu\text{m}$ ]
182	●	54	81	119	157	18642	5356	27790	2.3362	819.0	57.6	64.6



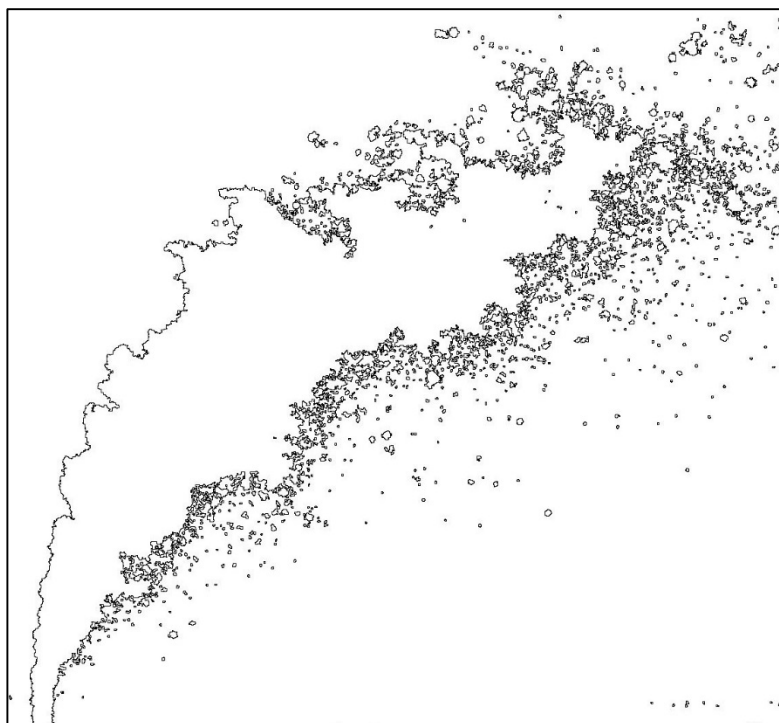
No.	Ref.	$V_{\text{Jet}}$ [m/s]	$V_{\text{Air}}$ [m/s]	q	$We_{\text{Air}}$	$We_{\text{Jet}}$	$Re_{\text{Air}}$	$Re_{\text{Jet}}$	$Oh_{\text{Air}}$ $\times 10^3$	$Oh_{\text{Jet}}$ $\times 10^3$	D10 [ $\mu\text{m}$ ]	D32 [ $\mu\text{m}$ ]
183	●	14	57	15	78	1165	3787	6947	2.3362	409.5	64.1	80.1



No.	Ref.	$V_{\text{Jet}}$ [m/s]	$V_{\text{Air}}$ [m/s]	q	$We_{\text{Air}}$	$We_{\text{Jet}}$	$Re_{\text{Air}}$	$Re_{\text{Jet}}$	$Oh_{\text{Air}}$ $\times 10^3$	$Oh_{\text{Jet}}$ $\times 10^3$	D10 [ $\mu\text{m}$ ]	D32 [ $\mu\text{m}$ ]
184	●	19	57	30	78	2330	3787	9825	2.3362	487.0	61.9	76.2

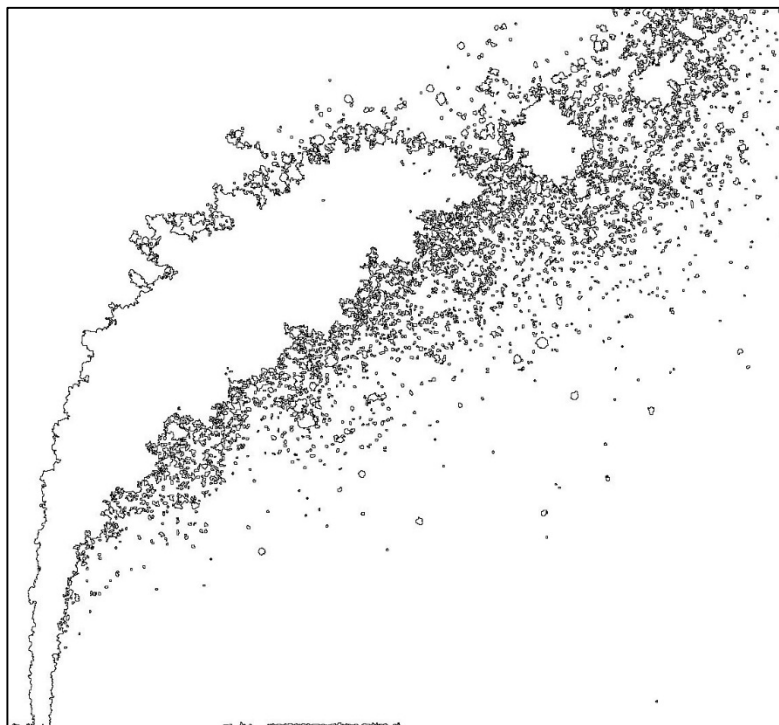


No.	Ref.	$V_{\text{Jet}}$ [m/s]	$V_{\text{Air}}$ [m/s]	q	$We_{\text{Air}}$	$We_{\text{Jet}}$	$Re_{\text{Air}}$	$Re_{\text{Jet}}$	$Oh_{\text{Air}}$ $\times 10^3$	$Oh_{\text{Jet}}$ $\times 10^3$	D10 [ $\mu\text{m}$ ]	D32 [ $\mu\text{m}$ ]
185	●	30	57	74	78	5826	3787	15535	2.3362	612.4	60.5	72.7

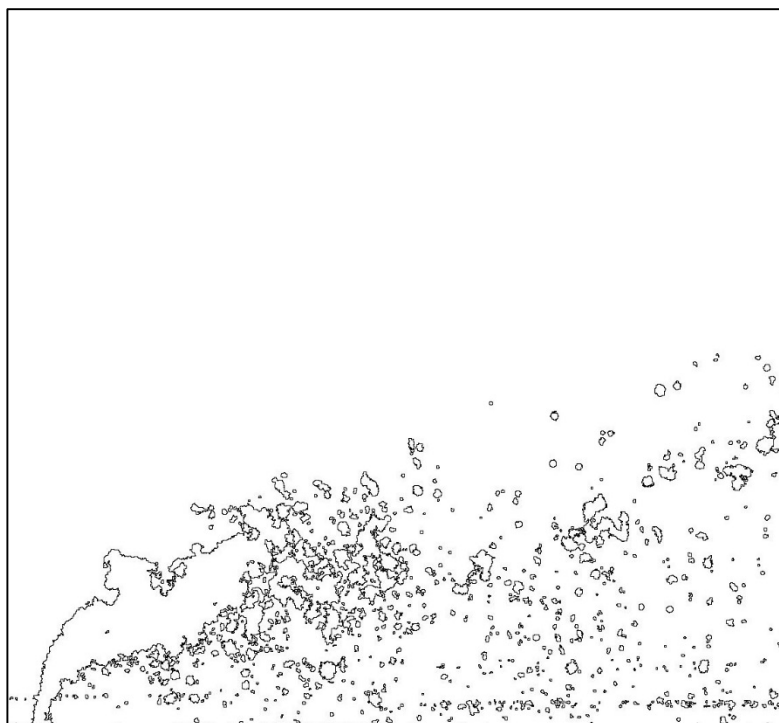




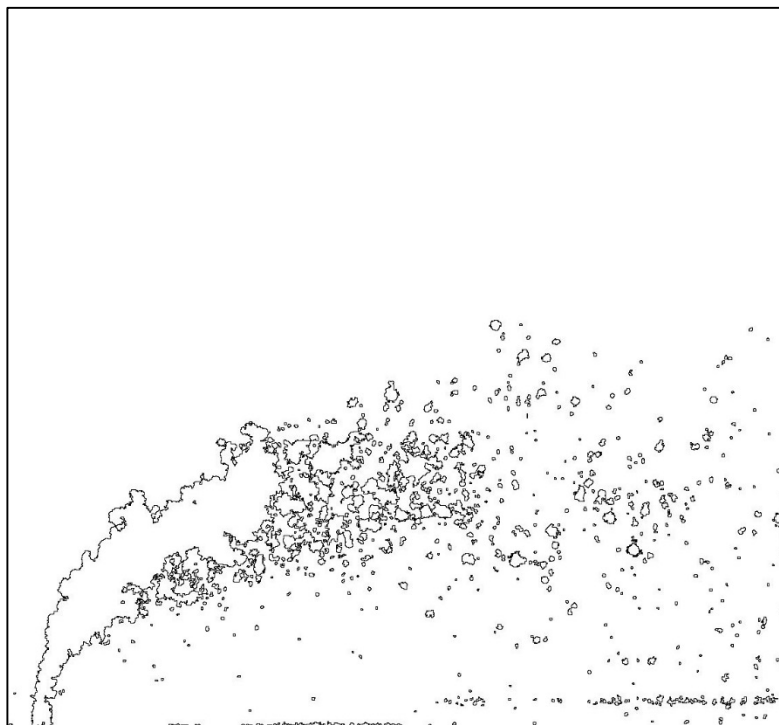
No.	Ref.	$V_{Jet}$ [m/s]	$V_{Air}$ [m/s]	q	$We_{Air}$	$We_{Jet}$	$Re_{Air}$	$Re_{Jet}$	$Oh_{Air}$ $\times 10^3$	$Oh_{Jet}$ $\times 10^3$	D10 [ $\mu m$ ]	D32 [ $\mu m$ ]
186	●	38	57	119	78	9321	3787	19650	2.3362	688.7	59.4	69.9



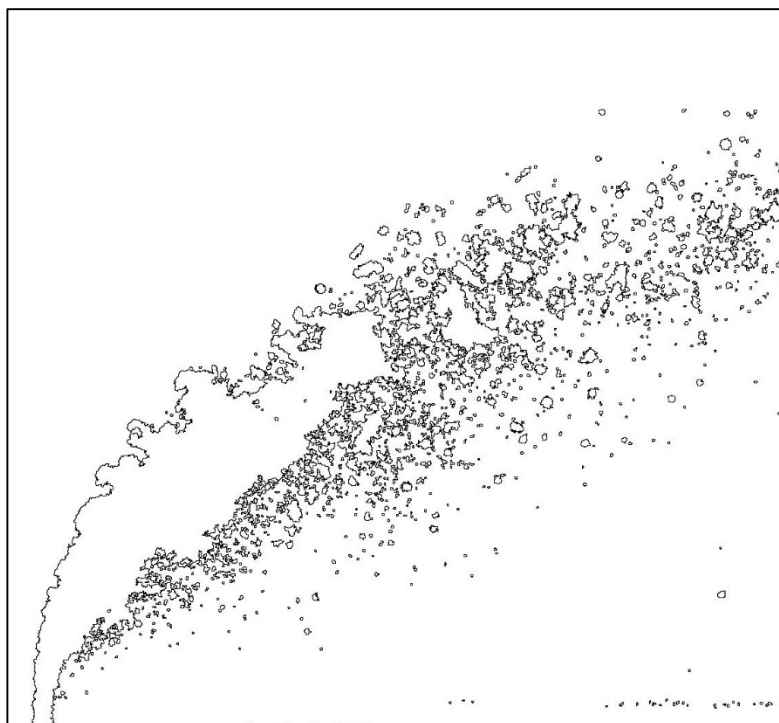
No.	Ref.	$V_{Jet}$ [m/s]	$V_{Air}$ [m/s]	q	$We_{Air}$	$We_{Jet}$	$Re_{Air}$	$Re_{Jet}$	$Oh_{Air}$ $\times 10^3$	$Oh_{Jet}$ $\times 10^3$	D10 [ $\mu m$ ]	D32 [ $\mu m$ ]
187	●	9	36	15	31	466	2395	4394	2.3362	325.7	68.9	88.8



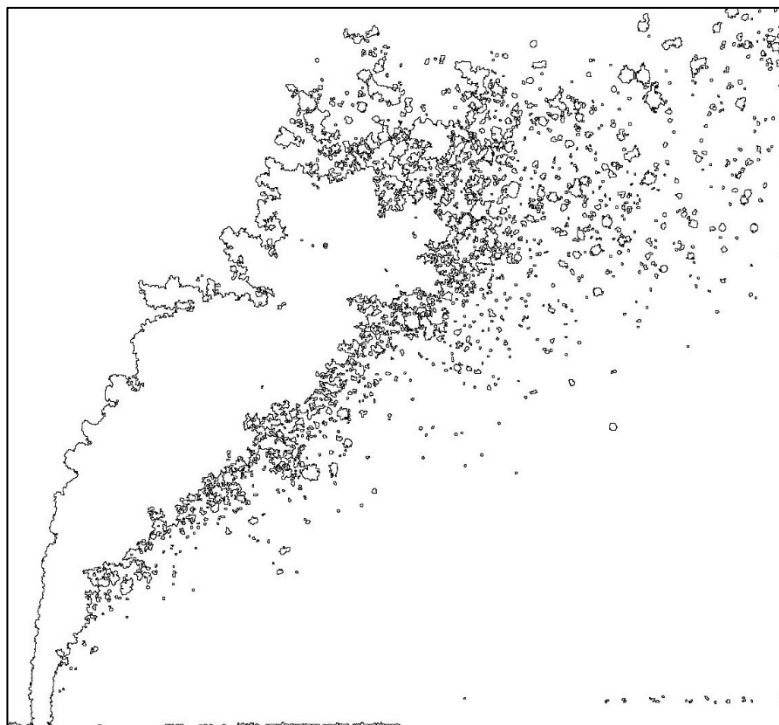
No.	Ref.	$V_{\text{Jet}}$ [m/s]	$V_{\text{Air}}$ [m/s]	q	$We_{\text{Air}}$	$We_{\text{Jet}}$	$Re_{\text{Air}}$	$Re_{\text{Jet}}$	$Oh_{\text{Air}}$ $\times 10^3$	$Oh_{\text{Jet}}$ $\times 10^3$	D10 [ $\mu\text{m}$ ]	D32 [ $\mu\text{m}$ ]
188	●	12	36	30	31	932	2395	6214	2.3362	387.3	68.1	87.2



No.	Ref.	$V_{\text{Jet}}$ [m/s]	$V_{\text{Air}}$ [m/s]	q	$We_{\text{Air}}$	$We_{\text{Jet}}$	$Re_{\text{Air}}$	$Re_{\text{Jet}}$	$Oh_{\text{Air}}$ $\times 10^3$	$Oh_{\text{Jet}}$ $\times 10^3$	D10 [ $\mu\text{m}$ ]	D32 [ $\mu\text{m}$ ]
189	●	19	36	74	31	2330	2395	9825	2.3362	487.0	65.0	82.0



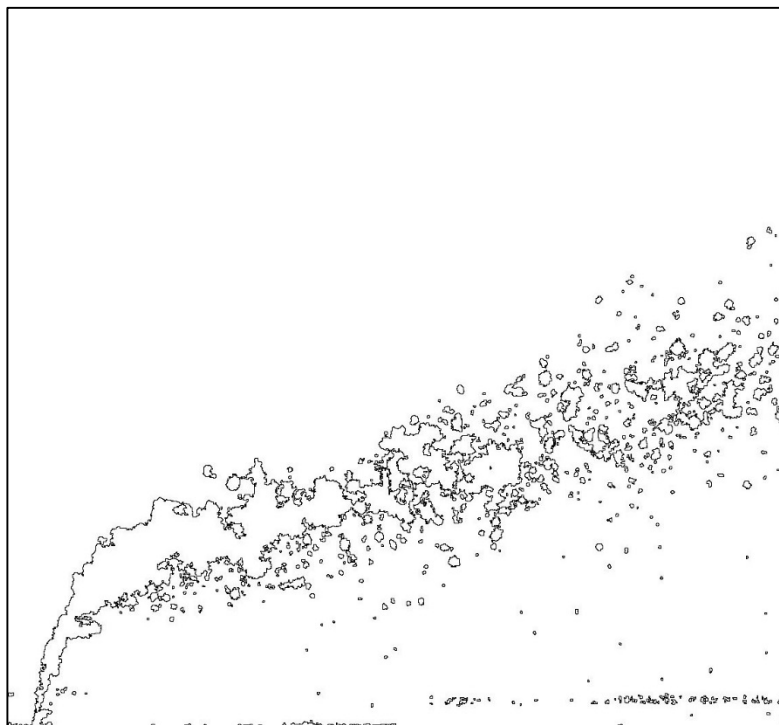
No.	Ref.	$V_{\text{Jet}}$ [m/s]	$V_{\text{Air}}$ [m/s]	q	$We_{\text{Air}}$	$We_{\text{Jet}}$	$Re_{\text{Air}}$	$Re_{\text{Jet}}$	$Oh_{\text{Air}}$ $\times 10^3$	$Oh_{\text{Jet}}$ $\times 10^3$	D10 [ $\mu\text{m}$ ]	D32 [ $\mu\text{m}$ ]
190	●	24	36	119	31	3728	2395	12428	2.3362	547.7	63.5	79.3



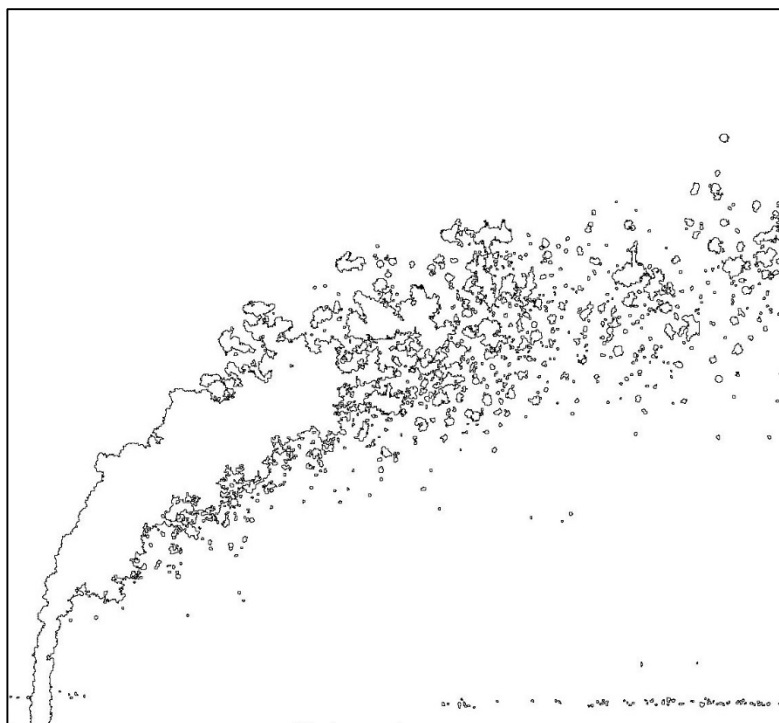
No.	Ref.	$V_{\text{Jet}}$ [m/s]	$V_{\text{Air}}$ [m/s]	q	$We_{\text{Air}}$	$We_{\text{Jet}}$	$Re_{\text{Air}}$	$Re_{\text{Jet}}$	$Oh_{\text{Air}}$ $\times 10^3$	$Oh_{\text{Jet}}$ $\times 10^3$	D10 [ $\mu\text{m}$ ]	D32 [ $\mu\text{m}$ ]
191	●	7	28	15	20	291	1894	3474	2.3362	289.6	70.3	91.8



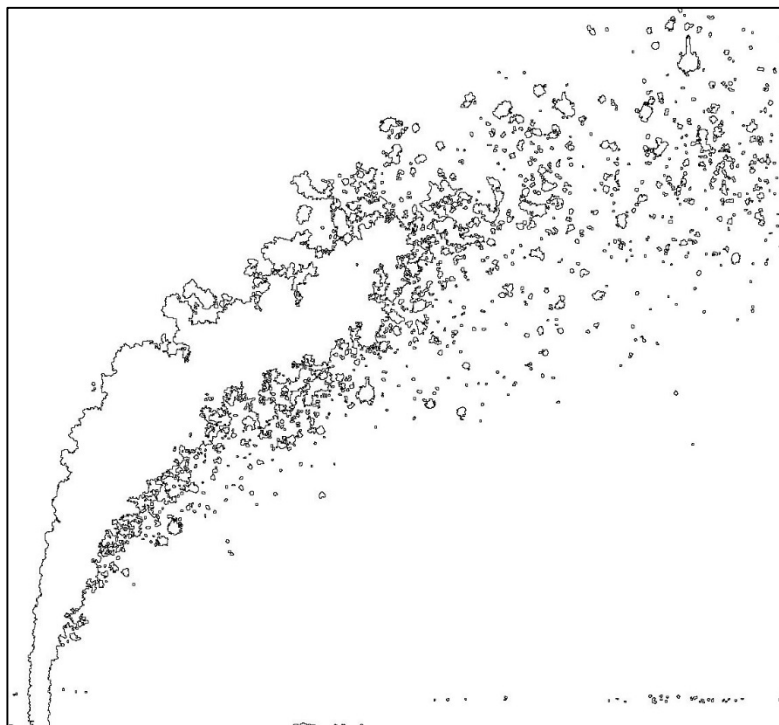
No.	Ref.	$V_{\text{Jet}}$ [m/s]	$V_{\text{Air}}$ [m/s]	q	$We_{\text{Air}}$	$We_{\text{Jet}}$	$Re_{\text{Air}}$	$Re_{\text{Jet}}$	$Oh_{\text{Air}}$ $\times 10^3$	$Oh_{\text{Jet}}$ $\times 10^3$	D10 [ $\mu\text{m}$ ]	D32 [ $\mu\text{m}$ ]
192	●	10	28	30	20	583	1894	4913	2.3362	344.4	70.2	91.4



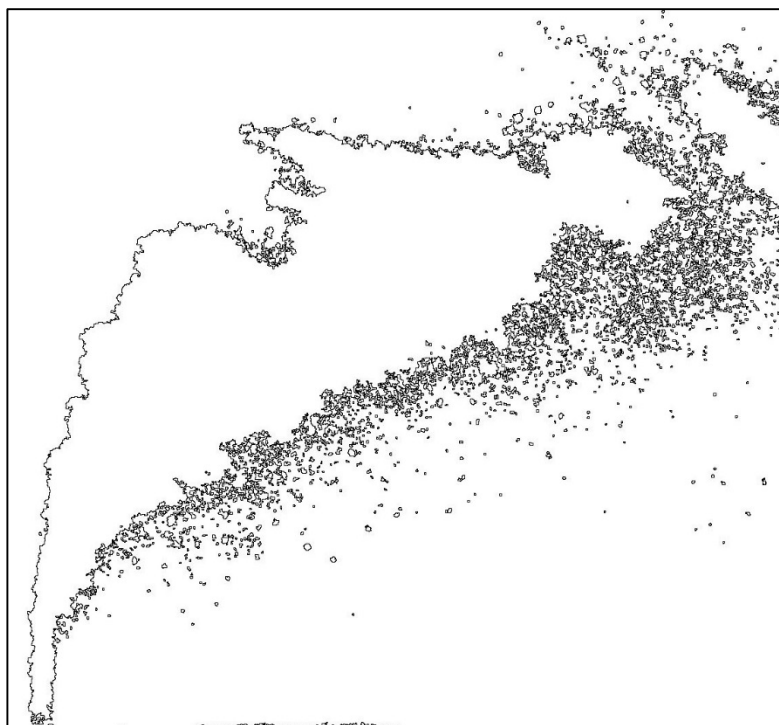
No.	Ref.	$V_{\text{Jet}}$ [m/s]	$V_{\text{Air}}$ [m/s]	q	$We_{\text{Air}}$	$We_{\text{Jet}}$	$Re_{\text{Air}}$	$Re_{\text{Jet}}$	$Oh_{\text{Air}}$ $\times 10^3$	$Oh_{\text{Jet}}$ $\times 10^3$	D10 [ $\mu\text{m}$ ]	D32 [ $\mu\text{m}$ ]
193	●	15	28	74	20	1456	1894	7767	2.3362	433.0	68.0	87.0



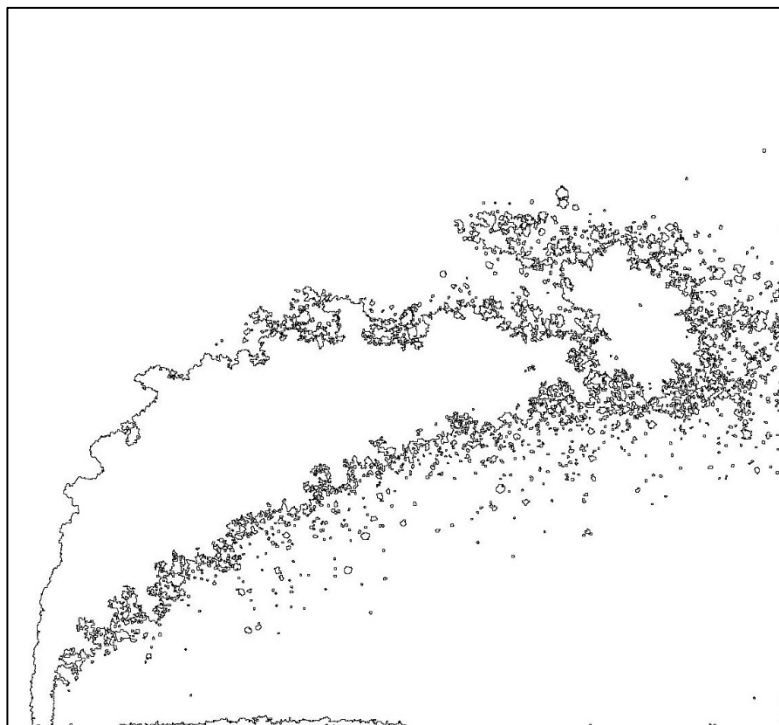
No.	Ref.	$V_{\text{Jet}}$ [m/s]	$V_{\text{Air}}$ [m/s]	q	$We_{\text{Air}}$	$We_{\text{Jet}}$	$Re_{\text{Air}}$	$Re_{\text{Jet}}$	$Oh_{\text{Air}}$ $\times 10^3$	$Oh_{\text{Jet}}$ $\times 10^3$	D10 [ $\mu\text{m}$ ]	D32 [ $\mu\text{m}$ ]
194	●	19	28	119	20	2330	1894	9825	2.3362	487.0	66.2	84.0



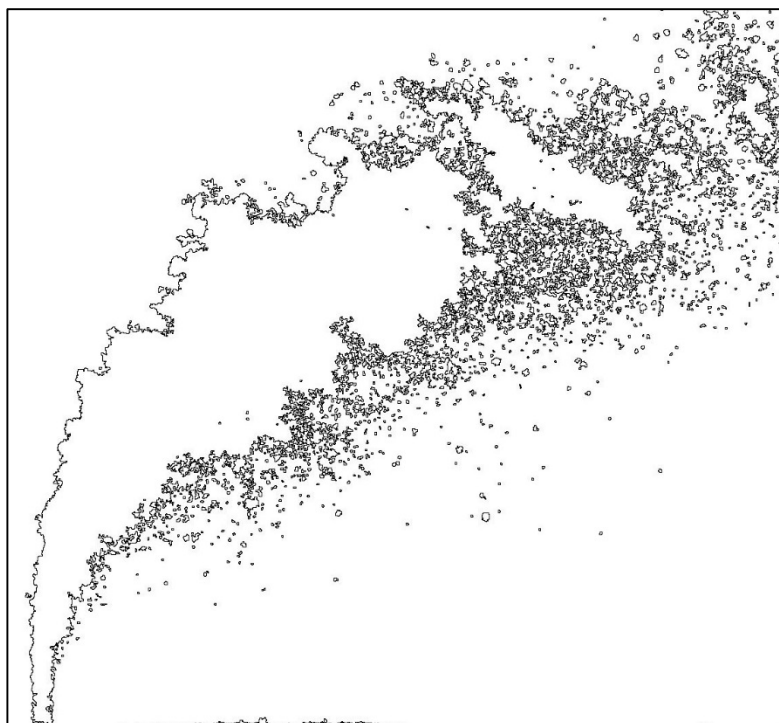
No.	Ref.	$V_{\text{Jet}}$ [m/s]	$V_{\text{Air}}$ [m/s]	q	$We_{\text{Air}}$	$We_{\text{Jet}}$	$Re_{\text{Air}}$	$Re_{\text{Jet}}$	$Oh_{\text{Air}}$ $\times 10^3$	$Oh_{\text{Jet}}$ $\times 10^3$	D10 [ $\mu\text{m}$ ]	D32 [ $\mu\text{m}$ ]
197	○	27	42	113	53	5973	3475	17599	2.0882	582.6	58.2	66.3



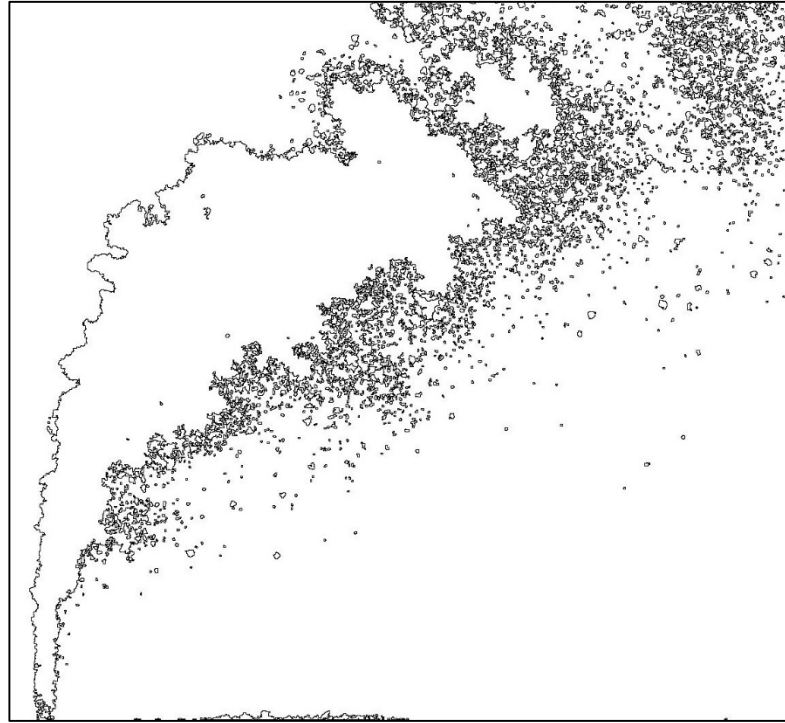
No.	Ref.	$V_{\text{Jet}}$ [m/s]	$V_{\text{Air}}$ [m/s]	q	$We_{\text{Air}}$	$We_{\text{Jet}}$	$Re_{\text{Air}}$	$Re_{\text{Jet}}$	$Oh_{\text{Air}}$ $\times 10^3$	$Oh_{\text{Jet}}$ $\times 10^3$	D10 [ $\mu\text{m}$ ]	D32 [ $\mu\text{m}$ ]
199	○	12	30	45	26	1195	2457	7870	2.0882	389.6	61.5	74.4



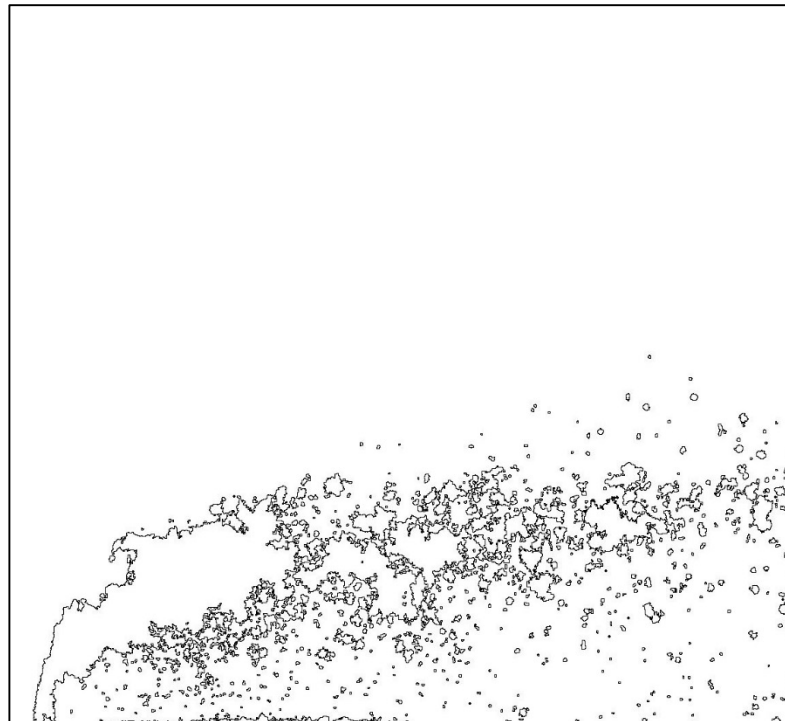
No.	Ref.	$V_{\text{Jet}}$ [m/s]	$V_{\text{Air}}$ [m/s]	q	$We_{\text{Air}}$	$We_{\text{Jet}}$	$Re_{\text{Air}}$	$Re_{\text{Jet}}$	$Oh_{\text{Air}}$ $\times 10^3$	$Oh_{\text{Jet}}$ $\times 10^3$	D10 [ $\mu\text{m}$ ]	D32 [ $\mu\text{m}$ ]
200	○	19	30	113	26	2987	2457	12444	2.0882	489.9	60.0	71.4



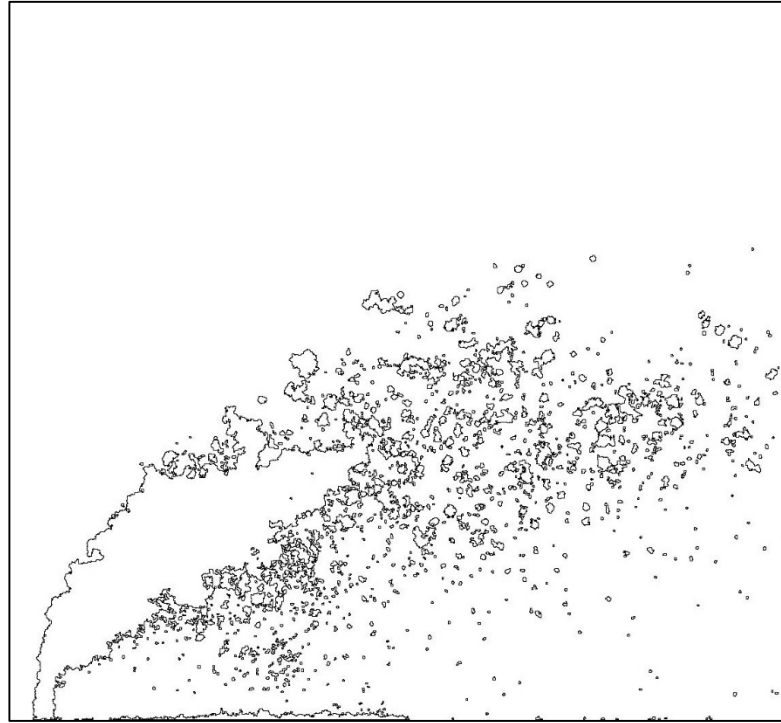
No.	Ref.	$V_{\text{Jet}}$ [m/s]	$V_{\text{Air}}$ [m/s]	q	$We_{\text{Air}}$	$We_{\text{Jet}}$	$Re_{\text{Air}}$	$Re_{\text{Jet}}$	$Oh_{\text{Air}}$ $\times 10^3$	$Oh_{\text{Jet}}$ $\times 10^3$	D10 [ $\mu\text{m}$ ]	D32 [ $\mu\text{m}$ ]
201	○	25	30	181	26	4779	2457	15741	2.0882	551.0	58.7	67.8



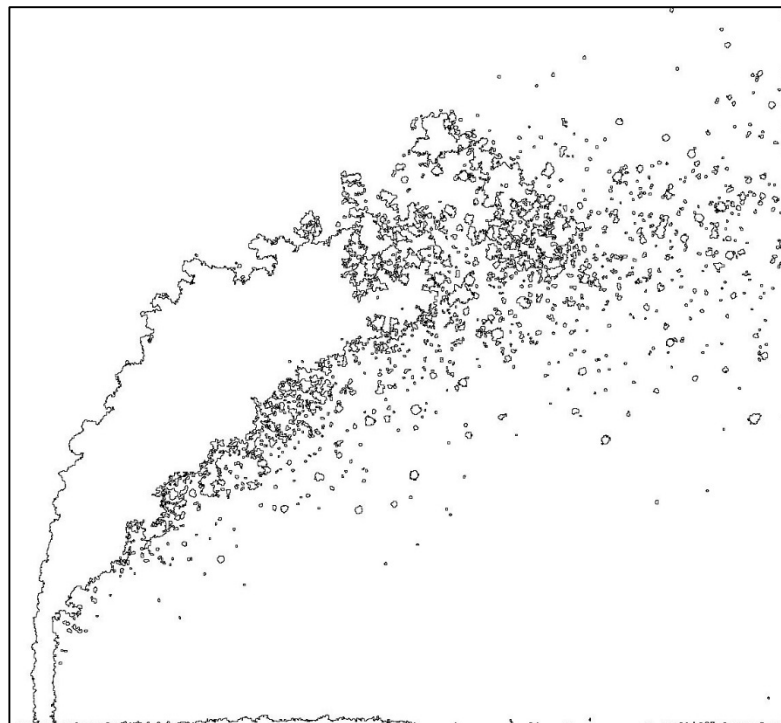
No.	Ref.	$V_{\text{Jet}}$ [m/s]	$V_{\text{Air}}$ [m/s]	q	$We_{\text{Air}}$	$We_{\text{Jet}}$	$Re_{\text{Air}}$	$Re_{\text{Jet}}$	$Oh_{\text{Air}}$ $\times 10^3$	$Oh_{\text{Jet}}$ $\times 10^3$	D10 [ $\mu\text{m}$ ]	D32 [ $\mu\text{m}$ ]
202	○	5	19	23	11	239	1554	3520	2.0882	260.5	67.1	85.0



No.	Ref.	$V_{\text{Jet}}$ [m/s]	$V_{\text{Air}}$ [m/s]	q	$We_{\text{Air}}$	$We_{\text{Jet}}$	$Re_{\text{Air}}$	$Re_{\text{Jet}}$	$Oh_{\text{Air}}$ $\times 10^3$	$Oh_{\text{Jet}}$ $\times 10^3$	D10 [ $\mu\text{m}$ ]	D32 [ $\mu\text{m}$ ]
203	○	8	19	45	11	478	1554	4978	2.0882	309.8	65.5	82.4

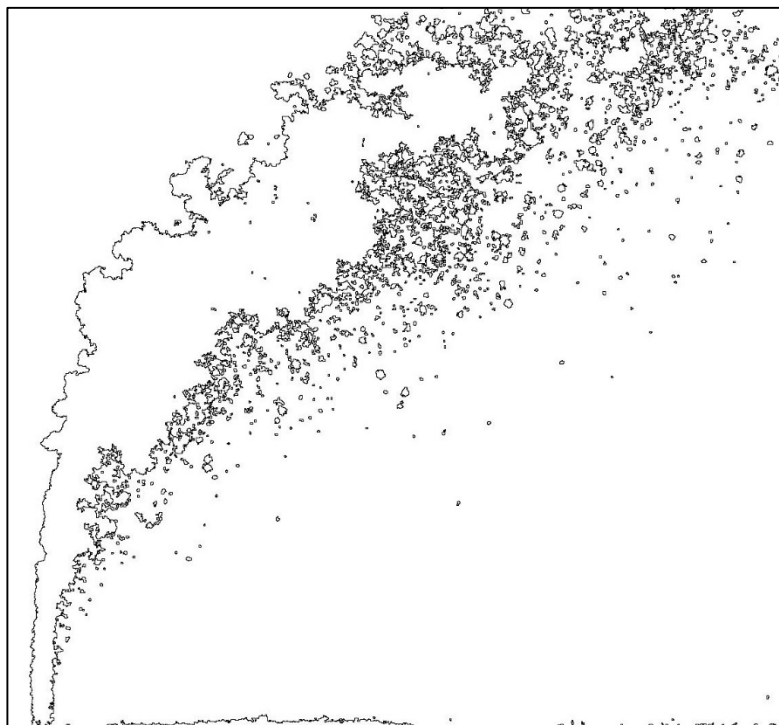


No.	Ref.	$V_{\text{Jet}}$ [m/s]	$V_{\text{Air}}$ [m/s]	q	$We_{\text{Air}}$	$We_{\text{Jet}}$	$Re_{\text{Air}}$	$Re_{\text{Jet}}$	$Oh_{\text{Air}}$ $\times 10^3$	$Oh_{\text{Jet}}$ $\times 10^3$	D10 [ $\mu\text{m}$ ]	D32 [ $\mu\text{m}$ ]
204	○	12	19	113	11	1195	1554	7870	2.0882	389.6	63.9	79.3





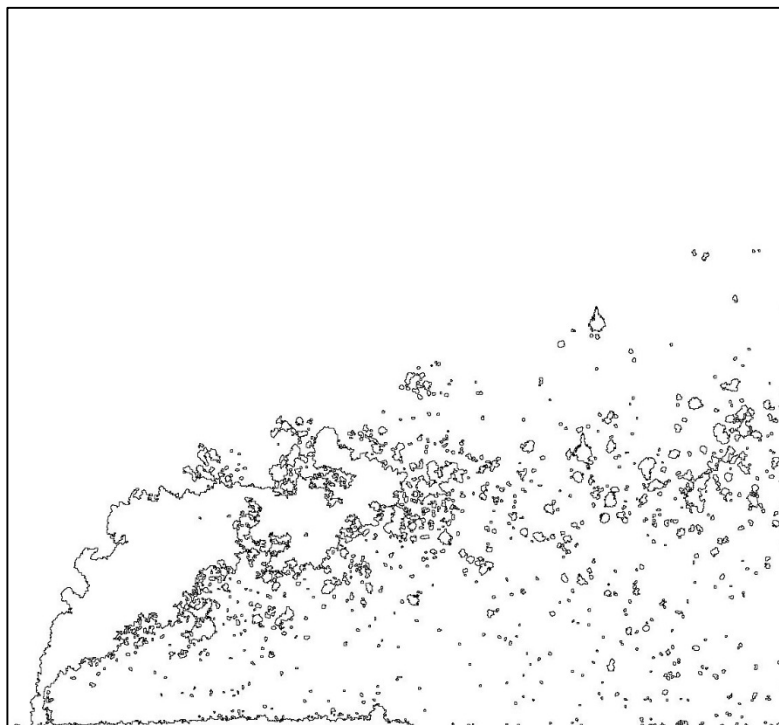
No.	Ref.	$V_{\text{Jet}}$ [m/s]	$V_{\text{Air}}$ [m/s]	q	$We_{\text{Air}}$	$We_{\text{Jet}}$	$Re_{\text{Air}}$	$Re_{\text{Jet}}$	$Oh_{\text{Air}}$ $\times 10^3$	$Oh_{\text{Jet}}$ $\times 10^3$	D10 [ $\mu\text{m}$ ]	D32 [ $\mu\text{m}$ ]
205	○	16	19	181	11	1911	1554	9955	2.0882	438.2	62.6	76.9



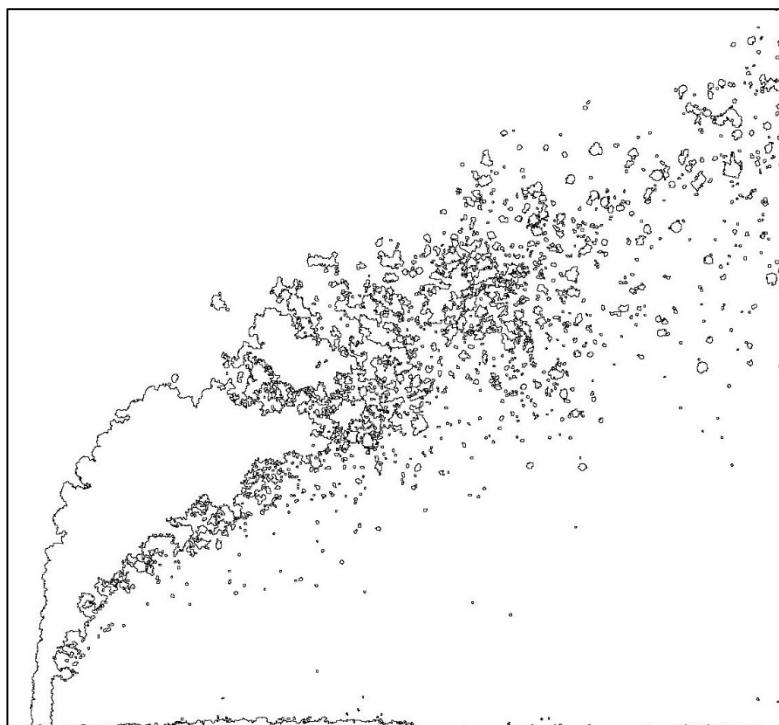
No.	Ref.	$V_{\text{Jet}}$ [m/s]	$V_{\text{Air}}$ [m/s]	q	$We_{\text{Air}}$	$We_{\text{Jet}}$	$Re_{\text{Air}}$	$Re_{\text{Jet}}$	$Oh_{\text{Air}}$ $\times 10^3$	$Oh_{\text{Jet}}$ $\times 10^3$	D10 [ $\mu\text{m}$ ]	D32 [ $\mu\text{m}$ ]
206	○	4	15	23	7	149	1229	2783	2.0882	231.7	68.8	88.3



No.	Ref.	$V_{\text{Jet}}$ [m/s]	$V_{\text{Air}}$ [m/s]	q	$We_{\text{Air}}$	$We_{\text{Jet}}$	$Re_{\text{Air}}$	$Re_{\text{Jet}}$	$Oh_{\text{Air}}$ $\times 10^3$	$Oh_{\text{Jet}}$ $\times 10^3$	D10 [ $\mu\text{m}$ ]	D32 [ $\mu\text{m}$ ]
207	○	6	15	45	7	299	1229	3935	2.0882	275.5	67.6	86.4



No.	Ref.	$V_{\text{Jet}}$ [m/s]	$V_{\text{Air}}$ [m/s]	q	$We_{\text{Air}}$	$We_{\text{Jet}}$	$Re_{\text{Air}}$	$Re_{\text{Jet}}$	$Oh_{\text{Air}}$ $\times 10^3$	$Oh_{\text{Jet}}$ $\times 10^3$	D10 [ $\mu\text{m}$ ]	D32 [ $\mu\text{m}$ ]
208	○	10	15	113	7	747	1229	6222	2.0882	346.4	66.2	83.6



No.	Ref.	$V_{\text{Jet}}$ [m/s]	$V_{\text{Air}}$ [m/s]	q	$We_{\text{Air}}$	$We_{\text{Jet}}$	$Re_{\text{Air}}$	$Re_{\text{Jet}}$	$Oh_{\text{Air}}$ $\times 10^3$	$Oh_{\text{Jet}}$ $\times 10^3$	D10 [ $\mu\text{m}$ ]	D32 [ $\mu\text{m}$ ]
209	○	12	15	181	7	1195	1229	7870	2.0882	389.6	64.8	80.6

